Report Title: Final Report for the ZERT II Project: Investigating the Fundamental Scientific Issues Affecting the Long-term Geologic Storage of Carbon Dioxide

Type of Report: Final Scientific/Technical Report

Reporting Period Start Date: August 4, 2010

Reporting Period End Date: September 30, 2014

Principal Authors:

Lee Spangler, Principal Investigator (MSU)
Alfred Cunningham (MSU)
Elliott Barnhart (MSU)
David Lageson (MSU)
Anita Moore-Nall (MSU)
Laura Dobeck (MSU)
Kevin Repasky (MSU)
Joseph A. Shaw (MSU)
Paul W. Nugent (MSU)
Jennifer Johnson (MSU)
Justin A. Hogan (MSU)
Sarah Codd (MSU)
Joshua Bray (MSU)
Cody Prather (MSU)
B. Peter McGrail (PNNL)
Curtis M. Oldenburg (LBNL)
Jeff Wagoner (LLNL)
Rajesh Pawar (LANL)

Date Report was Issued: December 19, 2014

DOE Award Number: DE-FE0000397

Name and Address of Submitting Organizations:

Montana State University (MSU)
Energy Research Institute
P.O. Box 172465
Bozeman, MT 59717-2465

Lawrence Livermore National Laboratory (LLNL)
P.O. Box 808
Livermore, CA 94551

Lawrence Berkeley National Laboratory (LBNL)
Earth Sciences Division 90-1116
1 Cyclotron Rd
Berkeley, CA 94720

Los Alamos National Laboratory (LANL)
Earth & Environmental Sciences Division (EES-16)
Los Alamos National Laboratory, MS T003
Los Alamos, NM 87545

Pacific Northwest National Laboratory (PNNL)
3110 Port of Benton Blvd
MS K6-81
Richland, WA 99352

DISCLAIMER

ABSTRACT

Overview

The Zero Emissions Research and Technology (ZERT) collaborative was formed to address basic science and engineering knowledge gaps relevant to geologic carbon sequestration. The original funding round of ZERT (ZERT I) identified and addressed many of these gaps. ZERT II has focused on specific science and technology areas identified in ZERT I that showed strong promise and needed greater effort to fully develop. Specific focal areas of ZERT II included:

- Continued use of the unique ZERT field site to test and prove detection technologies and methods developed by Montana State University, Stanford, University of Texas, several private sector companies, and others. Additionally, transport in the near surface was modelled.
- Further development of near-surface detection technologies that cover moderate area at relatively low cost (fiber sensors and compact infrared imagers).
- Investigation of analogs for escape mechanisms including characterization of impact of CO_2 and deeper brine on groundwater quality at a natural analog site in Chimayo, NM and characterization of fracture systems exposed in outcrops in the northern Rockies.
- Further investigation of biofilms and biomineralization for mitigation of small aperture leaks focusing on fundamental studies of rates that would allow engineered control of deposition in the subsurface.
- Development of magnetic resonance techniques to perform muti-phase fluid measurements in rock cores.
- Laboratory investigation of hysteretic relative permeability and its effect on residual gas trapping in large-scale reservoir simulations.
- Further development of computational tools including a new version (V2) of the LBNL reactive geochemical transport simulator, TOUGHREACT, extension of the coupled flow and stress simulation capabilities in LANL's FEHM simulator and an online gas-mixture-property estimation tool, WebGasEOS

Many of these efforts have resulted in technologies that are being utilized in other field tests or demonstration projects.

Biofilms and Biomineralization

The objective under this field of research was to perform a comprehensive evaluation of techniques for current and novel CO_2 sequestration concepts associated with microbial biofilms. Four distinct tasks were performed:

1. Determine the integrity of biomineralization deposits on flat coupons in response to brine and supercritical CO_2.
   Use of biomineralizing bacteria to plug preferential flow paths, such as cracks near well bores, is a novel strategy to mitigate escape of geologically sequestered carbon dioxide. Certain organisms *(i.e. Sporosarcina pasteurii*) have the capability to increase the pH of their

immediate environment by hydrolyzing urea which helps facilitate the precipitation of calcium carbonate ($CaCO_3$). These precipitated minerals will in turn plug the preferential escape pathways and may prevent gas escape. To ensure the $CaCO_3$ can indeed plug these pathways, it is important to examine the effect of brine and supercritical CO_2 ($scCO_2$) on the minerals under relevant subsurface conditions. After biomineral deposits were formed in batch systems on polycarbonate coupons, the coupons were challenged by (1) an atmospheric pressure, room temperature brine solution, (2) pure $scCO_2$, and (3) $scCO_2$ saturated brine at supercritical pressures and temperatures. The effects of the challenges were quantified by measuring the mass of minerals on the surface of the coupons and the mineralogy of the carbonates before and after the challenges. It was determined that brine at atmospheric conditions and pure $scCO_2$ at supercritical conditions had little to no effect on the biomineral deposits. Although significant mass loss was observed with exposure to $scCO_2$ and $scCO_2$ saturated brine, mechanical abrasion of $CaCO_3$, in addition to direct dissolution, may have contributed to the measured loss of minerals from these coupons.

2. Develop methods to understand and control the deposition rate of biomineralized calcium carbonate with distance in homogenous porous media.
   Under ZERT II, this task focused on two objectives: (1) developing methods to control the deposition of calcite along a porous media flow path, and (2) develop methods for quantifying the biomineralization process at the pore scale using mercury porosimetry. The research resulted in the following findings:

   - A standard, repeatable protocol, utilizing near injection-point calcium-medium displacement along with periods of bacterial resuscitation, was developed which resulted in a relatively uniform distribution of calcite along the flow path of packed sand columns. This operational protocol was validated both experimentally and computationally using a simulation model developed at the University of Stuttgart.

   - Balancing periods of biomineralization with periods of bacterial resuscitation during which additional growth nutrient was added counteracted (1) inactivation of bacterial cells (due to cell encapsulation), (2) reduced ureolysis, and (3) reduced calcium deposition efficiency. This balancing strategy contributed significantly to uniform calcite distribution.

   - Mercury porosimetry methods, which measure pore size distribution and porosity, have been developed for both sandstone and shale. These methods facilitate initial characterization of sandstone and shale samples along with providing valuable insight into how the biomineralization process changes rock properties at the pore scale.

3. Optimize biomineralization of isotopically labeled CO_2 carbon under variable head space pressure.
   The potential of microorganisms for enhancing Carbon Capture and Storage (CCS) via mineral-trapping and solubility-trapping was investigated where dissolved CO_2 is precipitated in carbonate minerals or held as dissolved carbonate species in solution. The bacterial hydrolysis of urea (ureolysis) was investigated in microcosms including synthetic

brine (SB) mimicking a prospective deep subsurface CCS site, with variable headspace pressures [p(CO_2)] of ^{13}C-CO_2. Dissolved Ca^{2+} in the SB was completely precipitated as calcite during microbially induced hydrolysis of 5 to 20 g L^{-1} urea. The incorporation of carbonate ions from ^{13}C-CO_2 (^{13}C-CO_3^{2-}) into calcite increased with increasing p($^{13}CO_2$) and increasing urea concentrations from 8.3% of total carbon in $CaCO_3$ at 1g L^{-1} to 31 % at 5g L^{-1}, and 37 % at 20g L^{-1}, demonstrated that ureolysis was effective at precipitating initially gaseous [CO_2(g)] originating from the headspace over the brine. Modeling the change in brine chemistry and carbonate precipitation after equilibration with the initial p(CO_2) demonstrated that no net precipitation of CO_2(g) via mineral-trapping occurred, since urea hydrolysis results in the production of dissolved inorganic carbon. However, the pH increase induced by bacterial ureolysis generated a net flux of CO_2(g) into the brine. This reduced the headspace concentration of CO_2 by up to 32 mM per 100 mM urea hydrolyzed because the capacity of the brine for carbonate ions was increased, thus enhancing the solubility-trapping capacity of the brine. Together with the previously demonstrated permeability reduction of rock cores at high pressure by microbial biofilms and resilience of biofilms to supercritical CO_2, this suggests that biomineralizing biofilms may enhance CCS via solubility-trapping, mineral formation, and CO_2(g) leakage reduction.

4. Evaluate the potential for coal-bed mediated CO_2 sequestration and enhanced methane production.
   The observation that methane production from coal can be stimulated by the presence of algae has been demonstrated. This finding has significant implications for improvement of current practices in coal bed methane (CBM) production in the Powder River basin and elsewhere, while simultaneously realizing increased CO_2 uptake from algae growth. This research provides a basis for future research into coupled biological systems (photosynthesis and methane production) that could sustainably enhance CBM production and generate algal biofuels while also sequestering carbon dioxide. CO_2 uptake as high as 187 kg CO_2/day could be achieved based on the assumption that 10 grams algae/m^2/day can be produced in production water facilities.

MR Studies of the Residual Trapping of Gases in Rock Cores

Effective exploitation of depleted hydrocarbon reservoirs for CO_2 storage or enhanced oil recovery (EOR) will require an understanding of complex multi-phase flow of native brine, residual hydrocarbons and injected CO_2. We performed NMR laboratory studies that will eventually complement the development of in-situ geophysical monitoring techniques by providing pore-scale to pore-network-scale observations of brine-hydrocarbon-scCO_2 (supercritical CO_2) flow and coupling of geochemical and geomechanical processes. Our experimental approach measured 1D profiles in rock cores during flow-through experiments in real-time. Results were obtained for the consecutive saturation, drainage and imbibition of water and CO_2, brine and scCO_2, and water and air. Preliminary data indicates that the fluids behave differently. Different behavior is anticipated for flow through rocks with distributed intergranular porosity and rocks with fracture-based flow paths.

Natural Analogs of Escape Mechanisms

Understanding the nature of rock formations that could potentially serve as carbon dioxide (CO_2) reservoirs is critical prior to subsurface CO_2 injection. The detailed mechanisms of fluid migration and trapping at multiple scales of observation are important for evaluating structural traps as sites for subsurface CO_2 sequestration. Faulting and tectonic fracturing can create fluid migration pathways, and often enhance the quality and potential for storage capacity of reservoir rocks within structural traps. Study of natural analogues includes systems currently storing CO_2 successfully, ancient systems that have stored CO_2 in the past, and modern "leaky" CO_2 systems to assess avenues for CO_2 escape. By studying natural analogs and potential storage structures, it is possible to learn more about the specific physical, chemical, lithologic and hydrologic conditions under which natural CO_2 is being trapped, as well as how porosity, permeability, fracture networks, temperature and pressure gradients and structural features control CO_2. The four study areas in this portion of the project each contributed aspects of exposed hydrothermally altered rock units which might be analogous of natural CO_2 escape mechanisms. The areas allowed for outcrop-scale investigation of the elements that comprise complex structural settings and an analysis of the relative timing of faulting, fracturing, fluid migration and structurally controlled diagenesis as well as detailed microscopic and geochemical studies. Analysis of the diagenetic history of the formations within the study areas indicate that they have all experienced significant fracturing and geochemical alteration that has influenced the porosity and permeability of the reservoir rocks. Fractures served as conduits for multiple episodes of fluid flow including hydrothermal brines, hydrocarbons, and CO_2. Additionally, textural evidence within these formations suggests that isothermal boiling of CO_2 caused forceful hydro-fracturing of the reservoir rocks creating vertical to sub-vertical breccia "pipes" that likely served as major fluid conduits. Field and petrographic evidence indicate that CO_2 - charged hydrothermal brines migrating along fractures and faults may have enhanced the secondary porosity and permeability of reservoir rocks, thus increasing their capacity for storage.

Underground Fiber Optic Sensors

An inline fiber sensor geometry was developed and demonstrated based on photonic bandgap (PBG) fibers for sub-surface detection of carbon dioxide. The inline fiber sensor utilizes a single mode optical fiber to deliver light to the PBG fiber where the laser light interacts with the carbon dioxide (CO_2). A small gap between the PBG fiber and a second single mode fiber allows a small portion of the light to be reflected back to a photodetector while the remainder of the light is coupled into the second single mode fiber that delivers light to the second inline fiber segment. Spectroscopic measurements were demonstrated in two consecutive fiber segments demonstrating the potential for this inline fiber geometry.

Work on a distributed fiber pressure sensor for seismic sensing was initiated. The fiber pressure sensor is based on a chirped laser source. The detected beat signal resulting from mixing a small portion of the outgoing laser beam with the light reflected from the fiber allows distance to be monitored based on the beat frequency. Simultaneously, amplitude of the beat signal provides information regarding the pressure.

Ultra-compact Infrared Imagers

Imaging of vegetation reflectance in the visible and near-infrared spectral bands and imaging of vegetation thermal emission in the long-wave infrared band have been shown to be capable of detecting CO_2 gas leaking from underground. The basic mechanism of both imaging modalities is that the vegetation is stressed by exposure to sustained high levels of soil gas. Both modalities were independently capable of detecting the leaking gas, but stronger correlations were found for the VIS-NIR imaging, using the Normalized Difference Vegetation Index (NDVI) as an indicator of vegetation health, computed from red and near-infrared reflectance values. An ultra-low-cost version of the VIS-NIR imager mounted on a tethered balloon was also shown to yield similar NDVI measurements as the more sophisticated imaging system, but it suffered from internal nonlinearities that made maintaining a consistent calibration impossible (but a newer version of the ultra-low-cost camera shows promise of negating this problem). Overall, the LWIR thermal images were found to be the most convenient imaging method for detecting leaking gas because no calibration target was required in the field, greatly simplifying the deployment. This advantage would be even greater in airborne measurements.

Validation of Near-surface CO_2 Detection Techniques and Transport Models

The ZERT controlled release field site completed its eighth successful season of CO_2 injection in 2014. Continued interest in the site has generated continued participation. Many groups maintained their involvement from ZERT I into ZERT II. The visibility of the facility led to interest of external groups and the addition of entirely new projects as well in ZERT II. The field site continues to produce advancements in the understanding of basic science as well as development of near surface CO_2 detection technologies for geological carbon sequestration.

TABLE OF CONTENTS

EXECUTIVE SUMMARY

Biofilms and Biomineralization

The objective under this field of research was to perform a comprehensive evaluation of techniques for current and novel CO_2 sequestration concepts associated with microbial biofilms. Four distinct tasks were performed:

1. Determine the integrity of biomineralization deposits on flat coupons in response to brine and supercritical CO_2.
   Research on this task was directed at understanding the effects of synthetic brine, supercritical CO_2 ($scCO_2$), and $scCO_2$-saturated brine on calcium carbonate ($CaCO_3$) precipitants on flat polycarbonate coupons. Biomineral deposits were formed on 1.2 cm (0.47 inch) diameter polycarbonate coupons by first growing a *Sporosarcina pasteurii* biofilm which is capable of hydrolyzing urea. Urea hydrolysis resulted in a pH increase which ultimately caused calcium carbonate to precipitate on the coupon surface. These biomineral-laden coupons were challenged by (1) an atmospheric pressure, room temperature brine solution, (2) pure $scCO_2$, and (3) $scCO_2$ saturated brine at supercritical pressures and temperatures. The effects of the challenges were quantified by measuring the mass of minerals on the surface of the coupons and the mineralogy of the carbonates before and after the challenges. It was determined that brine at atmospheric conditions and pure $scCO_2$ at supercritical conditions had little to no effect on the biomineral deposits. However the deposits did appear to be significantly affected by dissolution from exposure to $scCO_2$ and $scCO_2$ saturated brine. These observations were complicated by the fact that mechanical abrasion of $CaCO_3$, in addition to direct dissolution, may have contributed to the measured loss of minerals from the coupons. Overall, these data suggest that engineered biomineralization, with the purpose of reducing permeability in preferential leakage pathways during the operation of carbon capture and storage systems, are applicable in the $scCO_2$ region, the brine region, and the saturated $scCO_2$ region when subsurface fluid conditions are quasi-static.

2. Develop methods to understand and control the deposition rate of biomineralized calcium carbonate with distance in homogenous porous media.
   Under ZERT II this task is aimed at developing methods to understand and control the deposition rate of biomineralized calcium carbonate with distance in homogenous porous media. This research contributes to the overall investigation of ureolytic biomineralization as a possible technology for CO_2 leakage mitigation. The concept is based on the use of microbial biofilms which enzymatically hydrolyze urea, resulting in the precipitation of crystalline calcium carbonate (calcite), a process referred to as microbially induced calcite precipitation (MICP). Use of ureolytic, biofilm-forming bacteria (i.e. *Sporosarcina Pasteurii*) allows control over the distribution of the catalyst that induces calcite formation. This method has the potential to reduce near-well bore permeability, coat cement to reduce CO_2–related corrosion, and lower the risk of unwanted migration of CO_2 and other gasses. Laboratory research was conducted to develop a strategy for controlling the spatial distribution of calcium carbonate along a porous media flow path. The experimental system

involved the use of four vertically positioned columns 61 cm (2-feet) in length and 2.54 cm (1-inch) in diameter packed with 40 mesh (0.5 mm average diameter) quartz sand. The operational strategy for column operation was developed, which was based in part on simulation modeling conducted at the University of Stuttgart, resulted in uniform distributions of $CaCO_3$ (calcite) along the 61 cm (2-feet) column for the final three column experiments. Mercury porosimetry methods were developed to characterize pore size distribution and porosity in sandstone and shale. These methods were also developed to quantify effects of biomineralization at the pore scale. These ZERT II findings contribute to advancing MICP technology for subsurface applications.

3. Optimize biomineralization of isotopically labeled CO_2 carbon under variable head space pressure.
   The potential of microorganisms for enhancing CCS via mineral- and solubility-trapping where dissolved CO_2 is precipitated in carbonate minerals or held as dissolved carbonate species in solution was investigated. The bacterial hydrolysis of urea (ureolysis) was investigated in microcosms including synthetic brine (SB) mimicking a prospective deep subsurface CCS site, with variable headspace pressures [$p(CO_2)$] of ^{13}C-CO_2. Dissolved Ca^{2+} in the SB was completely precipitated as calcite during microbially induced hydrolysis of 5 to 20 g L^{-1} urea. The incorporation of carbonate ions from ^{13}C-CO_2 (^{13}C-CO_3^{2-}) into calcite increased with increasing $p(CO_2)$ and increasing urea concentrations from 8.3 % of total carbon in $CaCO_3$ at 1g L^{-1} to 31 % at 5g L^{-1}, and 37 % at 20g L^{-1}, demonstrating that ureolysis was effective at precipitating initially gaseous [$CO_2(g)$] originating from the headspace over the brine. Modeling the change in brine chemistry and carbonate precipitation after equilibration with the initial $p(CO_2)$ demonstrated that no net precipitation of $CO_2(g)$ via mineral-trapping occurred, since urea hydrolysis results in the production of CO_2. However, the pH increase induced by bacterial ureolysis generated a net flux of $CO_2(g)$ into the brine. This reduced the headspace concentration of CO_2 by up to 32 mM per 100 mM urea hydrolyzed because the capacity of the brine for carbonate ions was increased, thus enhancing the solubility-trapping capacity of the brine. Together with the previously demonstrated permeability reduction of rock cores at high pressure by microbial biofilms and resilience of biofilms to supercritical CO_2, this suggests that biomineralizing biofilms may enhance CCS via solubility-trapping, mineral-trapping, and $CO_2(g)$ leakage reduction (i.e. formation-trapping).

4. Evaluate the potential for coal-bed mediated CO_2 sequestration and enhanced methane production.
   According to the DOE Energy Information Administration, CBM currently makes up about 10% of U.S. natural gas production. CBM is produced by pumping water from coal beds, lowering the pressure in the coal beds to allow release and recovery of natural gas (methane) from the beds. The gas is then separated and recovered above ground from the produced water. CBM is naturally present in the coal bed, due primarily to the activity of microbial communities capable of degrading coal and producing methane (biogenic methane production). Research under ZERT II has been directed toward evaluating the ability of algae to enhance coal-to-methane production in laboratory reactor systems containing produced water, coal, and microbial inoculum recovered from groundwater wells in coal formations in

the Powder River Basin in eastern Montana. These experiments indicate that by applying a carefully designed nutrient recipe which includes algae extract, coal-to-methane conversion can be stimulated resulting in a more diverse and active methanogenic biofilm community and enhanced methane production. These results point to the possibility of growing large quantities of algae in coal bed methane produced water stored in surface impoundments and processing the algae for multiple benefits. Large-scale algae production in CBM impoundments will offer the benefit of sequestering atmospheric CO_2 thereby reducing the carbon footprint of traditional CBM production. Algae growth will also sequester metals and consume organics thereby enhancing the overall quality of produced water. The algae can then be harvested and lipids extracted to produce a variety of products including biofuels. The residual algal extract after lipid production can conceivably be re-injected into the original CBM formation thus serving as stimulant for further methane production. Enhancing production of domestic natural gas and phototrophic biofuel while at the same time recycling wastewater, nutrients, and sequestering CO_2 will substantially reduce impacts to the atmosphere, surface waters, and subsurface environments associated with CBM production for the Powder River Basin in eastern Montana and Wyoming as well as other similar locations.

MR Studies of the Residual Trapping of Gases in Rock Cores

Effective exploitation of depleted hydrocarbon reservoirs for CO_2 storage or enhanced oil recovery will require an understanding of complex multi-phase flow of native brine, residual hydrocarbons and injected CO_2. We performed NMR laboratory studies that will eventually complement the development of in-situ geophysical monitoring techniques by providing pore-scale to pore-network-scale observations of brine-hydrocarbon-$scCO_2$ (supercritical CO_2) flow and coupling of geochemical and geomechanical processes. Our experimental approach measured 1D profiles in rock cores during flow-through experiments in real-time. Results were obtained for a cycle that involved consecutive: saturation with water; then drainage with a gas of either air, CO_2, or $scCO_2$; and finally imbibition of water. Preliminary data indicates that the fluids behave differently. Different behavior is anticipated for flow through rocks with distributed intergranular porosity and rocks with fracture-based flow paths. MRI 1D images were used to monitor the wetting phase at each stage in the saturation. Drainage, imbibition cycle. Most significantly the residual trapping of the gas was less for the $scCO_2$ than for the CO_2 or air.

Natural Analogs of Escape Mechanisms

The four study areas include the Stewart Peak culmination study area (SPC), Thermopolis Anticline study area (TSA), Pryor Mountain study area (PMSA) and Big Snowy Mountains study area (BSMSA). SPC is a surface analogue for fractured reservoirs located in compressive thrust belts. The TSA, PMSA and BSMSA are Laramide style uplifts that have been breached by erosion. The TSA and PMSA also both have naturally occurring active geothermal features within the areas. The BSMSA is an area influenced by widespread Eocene igneous activity, which introduced a heating mechanism for hydrothermal fluid flow. Many of the breccias, recognized in each of the study areas are hydrothermal in origin based on their morphology, distribution, and geochemical signature. Hydrothermal activity is related to crustal shortening

during the Sevier and Laramide orogenies in the study areas. Taking into account the regional tectonic features that influenced and may possibly influence potential subsurface sites for CO_2 sequestration is also important. Brecciation is accompanied by dolomitization, dedolomitization, late-stage calcite precipitation, and porosity occlusion, especially in outcrop reservoir rocks observed in the study areas. Multiple episodes of fluid flow are evident in each study area with chemical zoning recognized in fracture fill and cross-cutting relationships. Tectonic-hydrothermal late-stage calcite may reduce permeability in outcrops and, potentially, high-quality subsurface reservoir rocks.

Underground Fiber Optic Sensors

The ability to monitor carbon sequestration sites will require detectors capable of monitoring large areas. Fiber optic sensor arrays offer the ability to utilize a scalable array of point sensors for monitoring the large areas associated with sequestration sites. The inline fiber sensor work developed and demonstrated provides a method of increasing the number of point sensors available for a fiber sensor array. The inline fiber sensor utilizes a series of fiber segments that consist of a single mode optical fiber and a photonic bandgap (PBG) fiber. The single mode optical fiber delivers light to the PBG fiber where the light interacts with the carbon dioxide. A small portion of the light is reflected by the single mode fiber making up the second segment of the inline fiber sensor. Carbon dioxide (CO_2) concentrations in the PBG fiber are measured using an integrated path differential absorption measurement where the distributed feedback diode laser operating nominally at 2.004 □m is tuned across a CO_2 absorption feature. Two segments of the inline fiber sensor were demonstrated in a laboratory experiment.

The ability to monitor the injected CO_2 plume is a second important monitoring need. One plume monitoring technique involves using seismic waves to map out the sub-surface CO_2 plume. Initial work on a fiber pressure sensor was begun. The fiber pressure sensor utilizes a chirped laser source. A small portion of this chirped source is picked off and is beat against the light scattered from the fiber optical cable place down-well. The frequency of the beat signal can be used to determine the location in the fiber where the scattering occurred while the amplitude of the beat signal is related to the fiber strain. Initial laboratory experiments and modeling were conducted to study the feasibility of the chirped fiber pressure sensor.

Ultra-compact Infrared Imagers

The purpose of this project was to determine if CO_2 gas leaking from underground could be detected with passive imaging of overlying vegetation in visible (VIS), near-infrared (NIR), and long-wave infrared (LWIR) spectral bands. The basic concept driving the use of vegetation imaging to locate leaking CO_2 is that higher soil gas concentrations of CO_2 will stress the vegetation, leading to measurable changes in VIS and NIR reflectance and LWIR emission. Higher soil gas concentrations of CO_2 could result in less oxygen and water being drawn from the soil into the plants, resulting in a leaf stomata response and changing the reflectance and radiative properties of the vegetation. The increased plant stress results in increased red reflectance and decreased NIR reflectance. A side-by-side deployment of reflective and emissive imagers enabled direct comparisons of VIS and NIR imaging with LWIR imaging for CO_2 gas

leak detection. Our analysis showed that data from the two types of imagers are statistically significant alone, and either wavelength band can be used effectively. There was no evidence that using the two methods together yielded a significant advantage, and the VIS-NIR imaging alone yielded the highest statistical correlations. However, the practical advantage of not requiring an in-field calibration source made LWIR imaging more convenient, especially for aerial monitoring of large areas.

A final component of the project was to explore the feasibility of using an even lower-cost imaging system deployed on a tethered balloon. An imaging system originally developed for outreach use (Shaw et al. 2012) was deployed periodically during the 2012 ZERT field experiment on a tethered balloon. This vantage point enabled imaging of a larger area without the higher cost of airplane deployment, but the ultra-low-cost imaging system data required extra effort before a reliable calibration was achieved. However, the final calibrated data did yield favorable agreement with the surface-mounted imager, and was able to measure the vegetation response to the leaking CO_2 gas.

Validation of Near-surface CO_2 Detection Techniques and Transport Models

The ZERT field site has provided a much needed controlled release facility for use by the carbon sequestration community. Study of transport through and the influence of CO_2 on soil, water, plants, and the atmosphere continued. Several projects initiated in ZERT I carried on into ZERT II as many groups used information learned in previous years to optimize instrumentation and define new experimental goals. Three entirely new projects were added in ZERT II. As hosts of the site, MSU helped design, install, maintain, and operate the infrastructure to release CO_2 into the shallow subsurface. Operation of the site included obtaining and complying with an Environmental Protection Agency (EPA) Underground Injection Control (UIC) injection permit as well as supplying supporting data to participants. MSU also contributed to the scientific goals of the ZERT project. Kevin Repasky and Joseph Shaw of the MSU Electrical and Computer Engineering Department both developed optically based instrumentation to study CO_2 in the gas phase and the effect of CO_2 on plant health, respectively.

Experimental Methods, Results and Discussion, and Conclusions are given by task.

EXPERIMENTAL METHODS: BIOFILMS AND BIOMINERALIZATION

Ureolytic biomineralization is being investigated as a possible technology for CO_2 leakage mitigation (Phillips, et al. 2013, Mitchell et al., 2013), Mitchell, et al. 2010). The concept is based on the use of microbial biofilms which enzymatically hydrolyze urea, resulting in the precipitation of crystalline calcium carbonate ($CaCO_3$ or calcite), a process referred to as microbially induced calcite precipitation (MICP) (Cunningham et al., 2013). Use of ureolytic, biofilm-forming bacteria (i.e. *Sporosarcina Pasteurii*) allows control over the distribution of the catalyst that induces calcite formation. This method has the potential to reduce near-well bore permeability, coat cement to reduce CO_2–related corrosion, and lower the risk of unwanted migration of CO_2 and other gasses.

Under ZERT II this task has been focused on two objectives: (1) developing methods to control the deposition of calcite along a porous media flow path, and (2) develop methods for quantifying the biomineralization process at the pore scale using mercury porosimetry. The reporting format for Subtask 2.2 has been organized to address both of these objectives.

Subtask 2.1: Determine the integrity of biomineralization deposits on flat coupons in response to brine and supercritical CO_2.

$CaCO_3$ Coated Coupon Preparation

Sporosarcina pasteurii was used for this study based on relevance to previous work (5, 8). Liquid culture growth (BHI+Urea; CMM-) and calcium-rich (CMM+) growth media were produced by adding the constituents in Table 1 to one liter of distilled water and stirring continuously (3). As necessary, the pH of the media was adjusted to between 6.0 and 6.3 with concentrated hydrochloric acid. Complete medium was filter sterilized using a SteriTop (Fisher, Fair Lawn, NJ) 0.22 μm vacuum filter.

Table 1. Growth and Calcium-Rich Growth Media Constituents (all mass in grams)

BHI + Urea		***CMM-***		***CMM+***	
Brain Heart Infusion Broth (BD, Sparks, MD)	37	Difco Nutrient Broth (BD, Sparks, MD)	3	Difco Nutrient Broth (BD, Sparks, MD)	3
Urea (Fisher, Fair Lawn, NJ)	20	Urea (Fisher, Fair Lawn, NJ)	20	Urea (Fisher, Fair Lawn, NJ)	20
		Ammonium chloride (Fisher, Fair Lawn, NJ)	10	Ammonium chloride (Fisher, Fair Lawn, NJ)	10
		Sodium Bicarbonate (Fisher, Fair Lawn, NJ)	1.05	Sodium Bicarbonate (Fisher, Fair Lawn, NJ)	1.05

			Calcium Chloride Dihydrate (Acros, NJ)	4.62

For all experiments, *S. pasteurii* (ATCC 11859) cultures were obtained after culturing from frozen stocks using aseptic techniques (two times 1% inoculum transfers to fresh BHI+Urea or CMM- media). The cultures were grown on an incubated shaker at 30°C at 150 rpm. After the final transfer and 13-15 hours of growth, 1 ml of the cultures were used to inoculate CMM+ filter sterilized media in sterile Pyrex bottles loaded with 4 pre-weighed polycarbonate coupons each.

Inoculated calcium-rich media in 250 ml Pyrex bottles were placed into a 30°C incubator. Two coupons were also incubated in sterile, un-inoculated media to confirm abiotic precipitation was not occurring. After 24-48 hours of incubation and precipitation all coupons were removed with sterilized tweezers. The coupons were dried for greater than 24 hours at 65°C until constant weight was achieved. Excess mineral not firmly attached to the coupon was blown off the coupon using compressed air (Falcon Dust Off, Branchburg, NJ). The coupons were weighed and also imaged on a stereoscope.

Exposure to Room Temperature, Atmospheric Pressure Brine

Coupons were randomly selected from the precipitated, dried, weighed and imaged coupons and two coupons each were placed into four 250 mL Pyrex bottles containing 200 mL of brine (Table 2)(4). Brine constituents were dissolved by stirring continuously in distilled water and then filter sterilized. The pH of brine (7.61) was assessed with a Fisher Scientific pH meter (model AR-25) equipped with a Corning glass electrode, which was calibrated with pH 7 and 10 buffers.

Table 2. Growth and Calcium-Rich Growth Media Constituents (all mass in grams)

Ingredient	**Amount (mM)**
NaCl	683.7
$MgSO_4 \cdot 7H_2O$	16.4
$CaCl_2 \cdot 2H_2O$	5.5
$MgCl_2 \cdot 6H_2O$	480.4
KCl	264.4
KBr	1.79

Coupons were challenged with the brine for 4 hours, 24 hours, and one week of exposure. Additionally, two coupons without precipitated mineral were placed in brine for 24 hours as sterile controls. After removal from the brine, coupons were rinsed in deionized water to remove residual brine and then dried, weighed, and imaged. Finally, the coupons and attached minerals from each exposure set were dissolved in acid for calcium analysis via ICP-MS.

Exposure to supercritical CO_2

Five coupons were randomly selected from the precipitated, dried, weighed and imaged coupons and loaded into the view-ported high pressure vessel (HPV) system (Figure 1). The system was pressurized and $scCO_2$ was pumped under constant flow via a Teledyne Isco high pressure pump to the HPV until pressure stabilized at 1300 psi. The high pressure system is maintained inside of

an incubator so temperature can be controlled and maintained above the critical point (Mitchell et al., 2009). During the two hour exposure to $scCO_2$ at 1300 psi the temperature was maintained at 33°C. One precipitated coupon was left outside the reactor as a control. Immediately after the exposure the coupons were removed from the reactor and imaged with the stereoscope as previously described. The coupons were then dried for 24 hours and weighed periodically until constant weight was achieved. Finally, coupons and attached minerals from the exposure and controls were dissolved in acid for calcium analysis via ICP-MS.

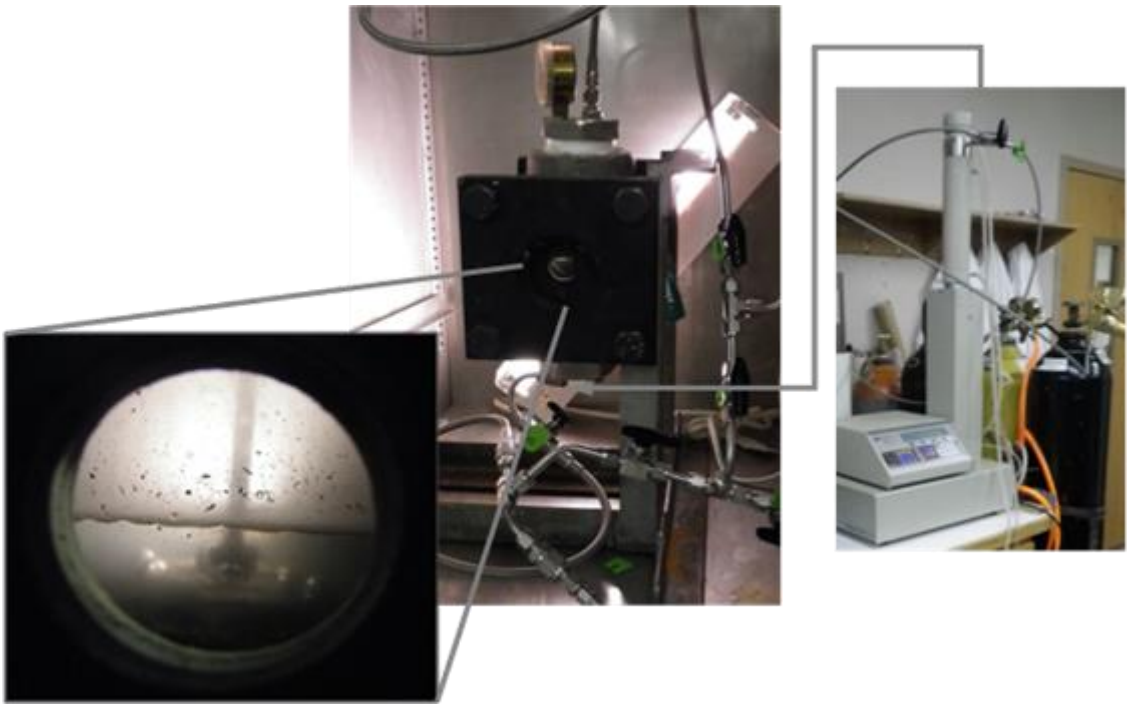

Figure 1. Supercritical CO_2 is pumped by a Teledyne Isco (Lincoln, Nebraska) pump into the view-ported (HPV)

(From right to left) Supercritical CO_2 is pumped by a Teledyne Isco (Lincoln, Nebraska) pump into the view-ported (HPV). The view port image of the HPV shows $scCO_2$ in the headspace and $scCO_2$ saturated brine in the bottom of the HPV during an exposure.

Exposure to supercritical CO_2 and supercritical CO_2 saturated brine

As described above, 350 ml of brine was added under ambient pressure conditions into the high pressure vessel. Coupons were randomly selected from the precipitated, dried, weighed and imaged coupons and were loaded into the reactor so three coupons were wetted in the brine (bottom portion of reactor) and three were in the headspace of the reactor. Two coupons were left outside of the reactor as controls. The system was pressurized and $scCO_2$ was pumped into the HPV through the brine until pressure in the reactor stabilized at 1250 psi. The coupons in the HPV were exposed to $scCO_2$ (in the headspace portion) and supercritical CO_2 saturated brine (bottom portion of the reactor) at 1250 psi and 37°C as a batch system for two hours and also 48 hours. Throughout the exposures, CO_2 was added periodically to maintain 1250 psi in the HPV. Immediately after each (2 hour and 48 hour) exposure the coupons were removed from the HPV

rinsed in DI water to remove any residual brine and imaged, dried for 24 hours, and weighed until constant weight was achieved. Additionally, pH of the brine was measured as described previously. After weighing, the minerals from each set ($scCO_2$, $scCO_2$ saturated brine, and controls) were examined with XRD to determine state of mineral formation. Finally, the coupons and minerals from each set were dissolved in acid for calcium analysis via ICP-MS.

A summary of the brine, $scCO_2$, and $scCO_2$ saturated brine exposure conditions is presented in Table 3.

Table 3. Summary of Exposure Scenarios

Exposure	Pressure	Temperature	Description
1	Ambient	Room	Expose coupons to brine for 4 hours
2	Ambient	Room	Expose coupons to brine for 24 hours
3	Ambient	Room	Expose coupons to brine for 1 week
4	1300	33°C	Expose coupons to $scCO_2$ in HPV for 2 hours
5	1250	37°C	Expose coupons to $scCO_2$ (headspace) in ½ brine-filled HPV for 2 hours
6	1250	37°C	Expose coupons to $scCO_2$ (headspace) in ½ brine-filled HPV for 48 hours
7	1250	37°C	Expose coupons to $scCO_2$ saturate brine in HPV for 2 hours
8	1250	37°C	Expose coupons to $scCO_2$ saturate brine in HPV for 48 hours
9	Ambient	Room	Sterile control

Subtask 2.2: Develop methods to understand and control the deposition rate of biomineralized calcium carbonate with distance in homogenous porous media.

Controlled deposition of biomineralization in sand columns

Materials and Methods. The strategy for controlling the spatial distribution of calcium carbonate resulting from biomineralization was developed using saturated packed sand columns. Four vertically positioned columns (61 cm (2-feet) in length, 2.54 cm (1-inch) in diameter) were packed with 40 mesh (0.5 mm effective filtration size) quartz sand (Unimin Corporation, Emmet, ID) under water to minimize air inclusions. Columns were disinfected and rinsed by injecting two pore volumes followed by 30 minute stagnation periods of each of the four following solutions:

- 1% bleach (Clorox, Oakland, Calif.) v/v and 3.5% Tween 80 (Acros, N. J.) w/v solution ;
- 10% w/v NaCl (Fisher, Fair Lawn, N. J.) solution ;
- 1.26% w/v sodium thiosulfate (Fisher, Fair Lawn, N. J.) solution ; and
- 10% w/v ammonium chloride (Fisher, Fair Lawn, N. J.) solution.

Cultures of *Sporosarcina pasteurii* were grown overnight from a frozen stock culture and washed via centrifugation and resuspened in fresh sterile medium prior to injection into the

column in up-flow configuration. A cell attachment period (no flow) of ~6 h was followed by 18 h of pumping growth medium to develop biofilm. After biofilm establishment and an overnight delay, two pore volumes of calcium-rich (1.25 M calcium) growth medium were injected to initiate biomineralization. The columns were then allowed to remain static for 24 h (biomineralization stage). For columns 2–4, calcium-rich medium from the first 7.6 cm of the columns was displaced immediately after injection with calcium-free medium to minimize injectivity reduction near the injection point. Between biomineralizing stages, the columns were flushed with two pore volumes of calcium and urea-free medium to restore a low saturation state. Periodically, throughout the experiments, the biofilm was resuscitated by injecting at least two pore volumes of fresh growth medium without calcium. Flow rates were controlled by a Masterflex (model 755370) pump and controller (Cole Parmer, Vernon Hills, Ill.).

Column Injection. The filling and flushing strategy for all four columns is described in Table 4. The experiments were terminated when the systems' pressure limits were reached. However, column 4 was terminated when as much calcium had been injected as for columns 2 and 3.

Table 4. Column injection summary

Column	Biomass concentration of Inoculum (cfu/ml)	Ca^{2+} Rich Medium Pulses	Mass of Total Ca^{2+} Injected (g)	Resuscitation Events	Avg. Flow Rate ($mL\ s^{-1}$)	Rinse Influent Region
1	$4.0x10^9$	35	303.4	15	10.7	No
2	$1.1x10^8$	20	130.3	10	8.0	Yes
3	$6.2x10^9$	11	83.3	4	8.9	Yes
4	$1.3x10^7$	22	135.2	9	9.1	Yes

Growth medium was prepared by mixing 3 g of Difco Nutrient Broth (BD, Sparks, Md.), 20 g of urea (Fisher, Fair Lawn, N. J.), 10 g of ammonium chloride (Fisher, Fair Lawn, N. J.), and 185 g of calcium chloride dihydrate (not included in calcium-free growth medium) (Acros, N. J.) and stirring continuously until dissolved in 1 L of nanopure water. As necessary, the pH of the medium was adjusted to between 6.0 and 6.3 (the final pH of calcium-rich medium was 5.4–5.6).

Monitoring and Sampling Methods. Column effluent was collected and monitored for ammonium and residual calcium concentration after each biomineralization stage. A portion of the effluent sample was filtered using a 0.2 μm SFCA Corning syringe filter (Corning Incorporated, N. Y.) and analyzed with a modified Nessler assay for ammonium production. The unfiltered remainder of the effluent sample was used to monitor pH. During the experiments, the activity in the column was monitored as follows:

- Ammonium concentration was determined with a modified Nessler assay; effluent samples were diluted in deionized water and compared to standards made from $(NH_4)_2SO_4$. Each sample and standard (250mL) was added in triplicate to a 96-well microplate (Fisher, Fair Lawn N. J.) to which 3 mL of mineral stabilizer and polyvinyl alcohol, and 10 mL of Nessler reagent (potassium tetraiodomercurate(II)) (Hach,

Loveland, Colo.) were added. Ammonium concentration was quantified in the resulting solution after 13 min reaction time via spectrophotometry at 425 nm (Bio-Tek, Synergy HT).

- The pH of effluent samples was assessed with a Fisher Scientific pH meter (model 50) equipped with a Corning glass electrode, which was calibrated daily with pH 7 and 10 buffers.

- At the termination of the experiment, each column was destructively sampled by cutting it into eight 7.6 cm sections and digesting triplicate portions of each section's sand contents with 10% trace-metal grade nitric acid (Fisher, Fair Lawn, N. J.). Calcium analysis was performed on an Agilent 7500 ICPMS after a 1:5000 or 1:10,000 dilution in 5% trace-metal grade nitric acid (Fisher, Fair Lawn, N. J.) and compared with certified standards (Agilent Technologies, Environmental Calibration Standard 5183–4688) to estimate the total $CaCO_3$ mineral per mass of sand.

Mercury Porosimetry for porosity and pore size distribution

As part of ZERT II methods to measure pore size distribution and porosity in sandstone were developed using mercury porosity. This activity was motivated by the need to compare changes in pore size distribution and porosity in response to biomineralization of sand stone cores. Subsequently mercury porosity methods were used to analyze shale samples from a parallel project funded by The CO_2 Capture Project (CCP). CCP is a partnership of several major energy companies working together to advance the technologies that will underpin the deployment of industrial-scale CO_2 capture and storage (CCS).

Figure 2. Micromeritics Porosimeter

Collaboration between ZERT II and CCP. Resources from ZERT II were used to augment the scope of work funded by CCP. Overall the total effort funded by ZERT was approximately 25%

of the total CCP effort—which was aimed at testing the biomineralization concept in shale cores obtained from the Mont Terri test site in Switzerland. The mercury porosimetry work, together with some additional ZERT-funded laboratory technetium effort, contributed significantly to the overall CCP shale testing project. A copy of the final project report submitted to CCP in November 2013 is attached in an Appendix. This report has been submitted as a potential chapter in Carbon Dioxide Capture for Storage in Deep Geological Formations, Vol. 4, 2014 CPL Press and BP, and is currently under review. ZERT II is credited in the Acknowledgements.

Mercury Porosimetry methods. Mercury porosimetry or mercury intrusion is based on the principle that the amount of pressure required for a non-wetting fluid, such as mercury, to intrude into a porous substance is inversely proportional to the size of the pores. Material properties that can be determined from this porosimetry test include pore size distribution, total pore volume, median pore diameter, bulk density, and material density. A Micromeritics Autopore IV Model 9500 Mercury Porosimeter (Figure 2) was used. This porosimeter has a 33,000 psi pressure capability which allows it to accurately measure pore sizes over a wide range, from 900 µm to 0.005 µm.

Porous media chips (sandstone and shale were examined under ZERT II) with an area roughly 1 cm^2 and a few mm in thickness were placed in a bulb penetrometer and evacuated to remove air and volatile substances. The bulb was then filled with mercury and pressurized in discrete steps. The incremental volume of mercury that intruded into the sample was recorded for each pressure point up to 33,000 psi. The analysis results in graphs show in how much mercury is intruded (mL/g) in relation to pore size (µm), as shown below in the Results and Discussion section.

Subtask 2.3: Optimize biomineralization of isotopically labeled CO_2 carbon under variable head space pressure.

Experimental setup

Batch CO_2 precipitation microcosms were prepared in sterile 35 ml serum bottles in a laminar flow hood. Each microcosm included 20 ml of a synthetic brine (SB) with approximately 5 g L^{-1} Total Dissolved Solids (TDS), mimicking the ionic ratios present in the proposed Powder River Basin CO_2 injection site (Busby et al. 1995). Three SBs were produced with different urea [$(NH_2)_2CO$] concentrations of 1, 5, or 20 g L^{-1}, to simulate the addition of varying concentrations of urea to the aquifer. Test and control SB microcosms were prepared. Test SB microcosms included the ureolytic organism *Sporosarcina pasteurii* (ATCC 11859, gram-positive, spore-forming, urease positive), known to induce $CaCO_3$ precipitation. Biotic control experiments included the non-ureolytic gram-positive bacterium *Bacillus subtilis* strain 186 (ATCC 23857). Abiotic control experiments included just the SB with no bacterial amendment. The headspace (15 cm^3) of each vial was then purged with 0.2µm filter sterilized 99% $\delta^{13}C$-CO_2 (Cambridge Isotope Laboratories, MA) for 1 minute, and final headspace p(CO_2) of 1, 1.35 and 1.7 atm were attained by measurement with a headspace pressure gauge. A set of microcosms was also retained with an atmospheric pressure air headspace [390 ppm CO_2 at 1 atm = 0.00039 atm p(CO_2)]. The microcosms were incubated at 22ºC on a shaker at 100 rpm for 8 days. While headspace pressures are far lower than expected during deep subsurface SC-CO_2 injection (up to 73 atm, these microcosms allow investigation of the general relationship of p(CO_2) and ureolysis on carbonate speciation. Additionally, even in deep subsurface brines the p(CO_2) will likely vary

significantly due to the advective and diffusive transport of CO_2 from the injection point over time. The SB was characterized for pH, dissolved Ca, and NH_4^+ immediately after inoculation and headspace adjustment [time (t) = 0, t_0], and again after 8 days (t_8). At the termination of the experiments any $CaCO_3$ precipitates formed in the microcosms were characterized by X-ray Diffraction System (XRD) and analyzed for $\delta^{13}C$.

Speciation and saturation modeling

PHREEQC (Parkhurst and Appelo, 1999) was used to model inorganic carbon speciation and carbonate mineral saturation in microcosm experiments simulating CO_2 injection into the Powder River Basin brine with $p(CO_2)$ of 0.00039, 1 and 1.7 atm. All calculations were carried out at 25°C and used the MINTEQ database (Allison et al., 1990).

Subtask 2.4: Evaluate the potential for coal-bed mediated CO_2 sequestration and enhanced methane production.

Sampling microbial inoculum from coal beds

The data and process described reported here are the result of collaboration with the U.S. Geological Survey in Reston VA, and the Montana Bureau of Mines and Geology. This study team has developed a novel microbial sampler, referred to as the diffusive microbial sampler (DSM), which can be placed down-well in coal bed methane formations and colonized with native coal-degrading methanogenic cultures as shown in Figure 3.

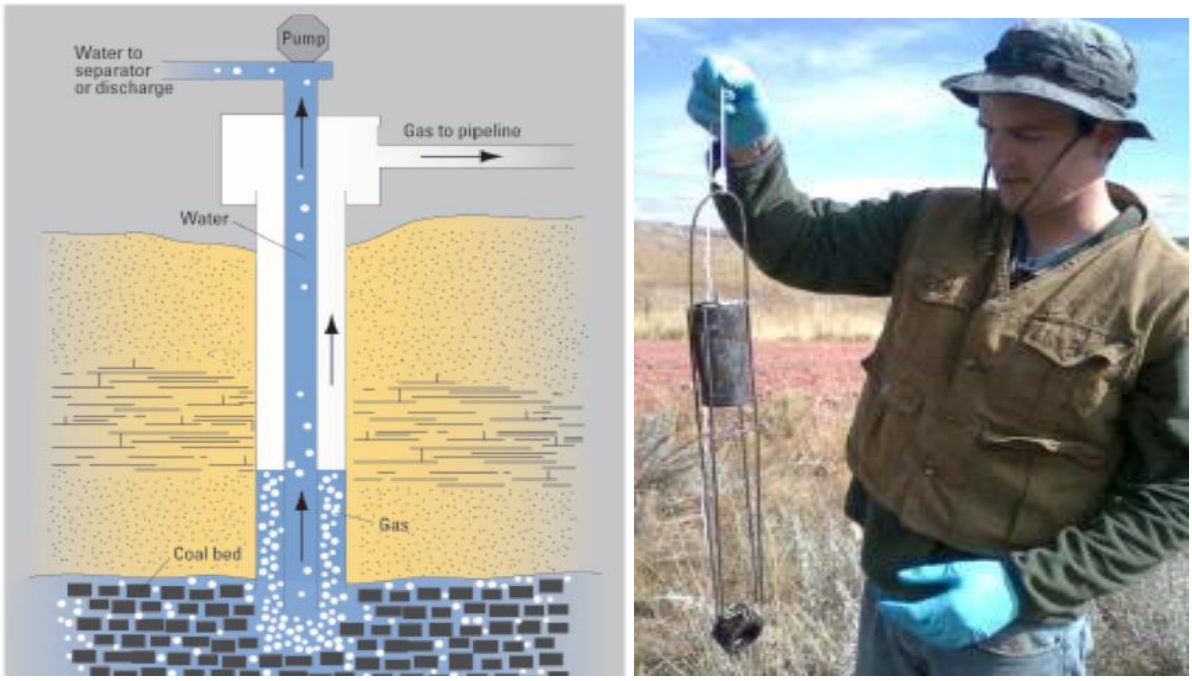

Figure 3. Diffusive Microbial Sampler

The DSM is lowered down-well into the coal bed methane-producing formation. The sampler contains approximately 200 grams of sub-bituminous coal particles from the Powder River

Basin, wrapped inside a porous mesh. The construction of the sampler insures that the sediment (coal) inside the sampler is only exposed to water inside the coal seam where methanogenisis takes place. Over time a microbial population indicative of that in the actual coal seam develops on the coal inside the sampler.

The DMS consists of a cylinder 6.35 cm (2.5 inches) in diameter and 12.7 cm (5 inches) long with 2 rods extending from the top of the cylinder to a weight 30.4 cm (12 inches) below the cylinder (Barnhart et al., 2013). The weight seals the DMS, due to gravity, until contacting the bottom of the well where the rods extending from the weight lift the coal out of the sealed cylinder allowing colonization by indigenous microorganisms. Coal within the sampler is composed of approximately 200 g of sub-bituminous coal particles (>2 mm but <4 mm diameter) from the Decker Coal Mine in the Powder River Basin (PRB. The coal particles are encased with #8 stainless steel mesh. The DMS is autoclaved prior to being placed in the well allowing autoclaved coal to act as the negative control in our DNA analysis.

The DSM was placed down an existing coal bed methane observation well (HWC-01) operated by the Montana Bureau of Mines and Geology and located in the Powder River basin in Montana. The DMS was retrieved from well HWC-01 after three months (Summer 2010) using aseptic techniques and samples of the recovered microbial population extracted and stabilized.

Batch enrichment experiments to measure methane production

The native microbial cultures recovered from well HWC-01 were subsequently used to inoculate batch microcosms (shown in Figure 4). The microcosms contained 50 mg of coal and 50 ml of simulated coal bed media (minimal salts media) which contained concentrations of ions that reflected the chemistry of the sampled well: (per liter) 3.86 mg $MgCl_2 \cdot 6H_2O$, 5.21 mg $CaCl_2 \cdot 2H_2O$, 0.5 g NH_4Cl, and 5.0 mg KCl. The medium was buffered using 1.1 mM K_2HPO_4 and 12.37 mM $NaHCO_3$ with 1 ml of 1000X per liter nonchelated trace elements and 1 ml of 1000X per liter vitamin solution amended with 2.0 g/liter choline chlorideadded as growth supplements. L-Cysteine • HCl (1 mM) and sulfide (1 mM as $Na_2S \cdot 9H_2O$) were added as reducing agents. Resazurin (1 mg/liter) was added as a redox indicator.

Figure 4. Batch flasks (50 ml serum bottles) containing Powder River coal, simulated coal bed media, and field inoculum.

Methane stimulation nutrients, including yeast extract and algae/algae extract were also added. All samples were run in triplicate as shown. Methane production was monitored in the head space.

The enrichments (batch flasks) were incubated in the dark at 25°C and microbially produced methane was monitored in the head space by a direct injection SRI 8610C gas chromatograph (GC) with a thermal conductivity detector (TCD) and a S.S. Molecular Sieve 13X Packed Column. This system allowed the investigation of various nutrient stimulants (i.e. algae extract and yeast extract) on the rate and extent of methane production.

Three sets of enrichment experiments were set up and are continuing at present. These microcosm experiments all involve the addition of algae extract as a stimulant to methane production form coal, compared to methane production from the same coal without algae addition. Yeast extract was also added in the first experiment. The description of each experiment is as follows.

Experiment #1. Coal from a surface mine in Decker, MT, inoculum from a USGS well HWC-01 in the Powder River Basin, media consisting of synthetic CBM produced water (described above). Experiment 1 included addition of yeast extract (1 ml) and algae extract (1 ml) to stimulate methane (started 9/10/2010).

Experiment #2. Decker coal, Inoculum from well HWC-01 well, media consisting of synthetic CBM water plus sulfate. Methane production stimulated by adding 1ml algae extract (started 5/4/2011).

*Experiment #3***.** Decker coal, filtered CBM produced water, inoculum from well HWC-01. Methane production was stimulated by adding 1 ml algae extract (started 4/5/2012).

RESULTS AND DISCUSSION: BIOFILMS AND BIOMINERALIZATION

Subtask 2.1: Determine the integrity of biomineralization deposits on flat coupons in response to brine and supercritical CO_2.

Mass Differences

Figure 5 shows the relative difference between the coupon mass before exposure and after exposure. Exposure to brine (Exposure 1, 2, 3) caused minor changes to mineral mass on the coupons after exposure, however there is no clear trend from the data to indicate whether minerals were dissolving. Exposure to brine after 4 hours caused a 7% reduction in mass, where exposure to 24 hours revealed a 32% increase in mass and finally one week of exposure showed a 22% decrease in mineral mass after exposure. Exposure to $scCO_2$ without brine for 2 hours (Exposure 4) did not significantly change the mineral mass on the coupons, whereas, coupons exposed to $scCO_2$ for 2 and 48 hours (Exposure 5 and 6) did show 37% and 17%, respectively, reductions in mass post exposure. A significant reduction of mineral mass was observed (83% and 92%) on coupons exposed to $scCO_2$ saturated brine for 2 and 48 hours (Exposure 7 and 8). Exposure 9 indicates a 10% mass difference was observed on sterile control coupons exposed to brine for 24 hours.

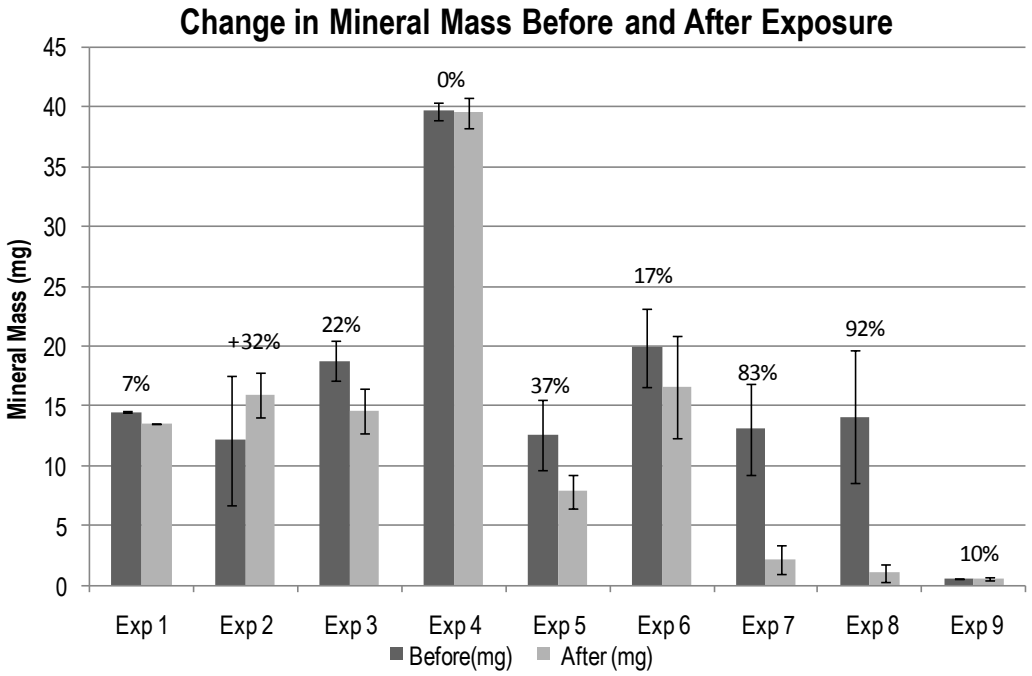

Figure 5. Change in mass of the minerals on coupons before and after exposure with percentage change of mass listed above each bar.

Dissolved Calcium Analysis

ICP-MS results (Table 5) indicate little calcium is lost from the coupons during the exposure to brine (Exposure 1, 2, 3). Brine exposure causes from 4-20% loss of calcium from coupons versus

the measured mass of minerals deposited on coupons before exposure. It is presumed the mineral mass measured is all in the form of calcium carbonate in order to be able to make these comparisons. Measured calcium from ICP_MS results is adjusted to calcium carbonate by multiplying mass measured by 100/40.

Table 5. Comparison of mass of $CaCO_3$ as determined by ICP-MS to the measured weight of minerals deposited on coupons before brine and $scCO_2$ challenges.

	Exp 1	Exp 2	Exp 3	Exp 4	Exp 5	Exp 6	Exp 7	Exp 8	Exp 9
Percent Reduction	20%	6%	4%	-10%	62%	33%	92%	91%	0%

Exposure to $scCO_2$ alone (Exposure 4) did not cause a reduction in the mass of calcium measured before and after exposure. However, exposure to $scCO_2$ in the headspace of the brine-filled HPV did effect a reduction in the measured mass of calcium before and after exposure. Some of the presumed mineral loss, however, might be attributed to the XRD analysis sample prep and recovery. Although efforts were made to recover the minerals from the XRD prep mount, it is likely some of the mineral mass was compromised and thus not digested prior to ICP-MS analysis. It is unclear from these results whether exposure to $scCO_2$ alone causes loss of calcium from the coupons.

Minerals attached to coupons exposed to $scCO_2$ saturated brine show a significant (92 and 91%) calcium loss vs. the measured weight of minerals before the exposure. These observations were complicated by the fact that mechanical abrasion of $CaCO_3$, in addition to direct dissolution, may have contributed to the measured loss of minerals from the coupons. Mechanical abrasion was the result of $scCO_2$ intensely bubbling through the brine phase, causing mechanical shear stress on the biomineral deposits on the coupons. These samples also were processed for XRD analysis so these results might also reflect loss during sample prep. Not all of the reduction may be attributable to actual exposure.

Stereoscope Analysis

The coupons used in the brine exposures (Exposure 1, 2, and 3) were not properly colored to provide contrast needed in the Metavue software to perform threshold analysis. As such, threshold analysis was not able to be performed on images of coupons from before and after exposure to brine. However, a qualitative analysis of the photos shows that there is no visual difference in mineral coverage after exposure to brine (Figure 6). This problem was remedied prior to the $scCO_2$ exposure by coloring the coupons black so as to provide contrast from the whitish minerals for threshold image analysis.

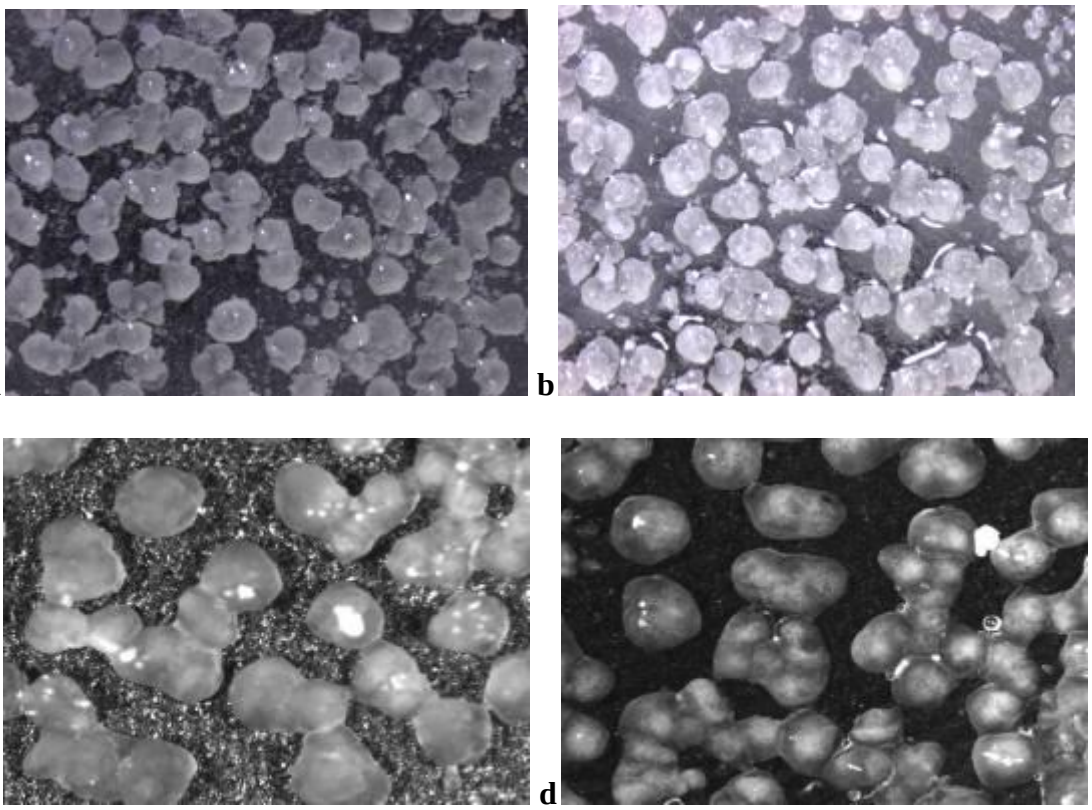

Figure 6. Stereoscope images of coupons exposed brine and $scCO_2$ before (a and c) and after (b and d) challenge. Images are at 40x magnification

Table 6 lists the averages and difference of percent area covered by minerals before and after $scCO_2$ exposure.

Table 6. Coupon surface area covered by solids on coupons before and after $scCO_2$ and $scCO_2$ saturated brine challenges. Data shown is the average of images for each coupon taken at 40x and 80x magnification.

Exposure	% Covered Before Exposure	% Covered After Exposure	Difference
4	79.08	75.60	3.48 ± 5.62
5	69.66	32.47	37.18 ± 17.78
6	82.45	34.38	48.06 ± 35.59
7	63.12	22.71	40.41 ± 9.4
8	76.21	9.83	66.38 ± 29.16
9	49.76	50.61	(0.85) ± 6.77

As indicated by Table 6, $scCO_2$ exposure (Exposure 4) did not significantly impact the percentage of coupon area covered by mineral. However, exposure to $scCO_2$ in the headspace of the brine-filled HPV and the coupons exposed to $scCO_2$ saturated brine all show reduced area

covered by mineral after exposure (37-66% reduction in coverage area). Control coupons do not show statistically significant changes in coverage after soaking in brine for 24 hours.

XRD Analysis

Minerals from coupons were analyzed to determine the form of calcium carbonate after exposure to $scCO_2$ and $scCO_2$ saturated brine compared with minerals not subjected to any exposure. Sample mineral spectra were compared to reference spectra to determine crystal formation by DMSNT analysis software. It was observed that mineralogy did not change after exposure to $scCO_2$ and $scCO_2$ saturated brine. Calcite was detected as the predominant form of calcium carbonate in both the controls and exposed samples. No vaterite or aragonite minerals were detected.

Subtask 2.2: Develop methods to understand and control the deposition rate of biomineralized calcium carbonate with distance in homogenous porous media.

Controlled deposition of biomineralization in sand columns.

Biomineralization Injection strategy. The goal for the sand packed column experiments was to develop a repeatable strategy for achieving a uniform distribution of calcite deposition along the 61 cm flow path, thereby avoiding excessive calcite buildup near the entrance (Whiffin et al., 2007; Fujita et al., 2008; Cunningham et al., 2009). After inoculation and significant biofilm growth has occurred, subsequent $CaCO_3$ precipitation may inactivate microorganisms or create nutrient diffusion limitation (De Muynck et al.,2010; Whiffin et al., 2007; Parks, 2009; Dupraz et al., 2009), leading to reduced ureolysis and subsequently less biomineralization. To counteract these phenomena, the biofilm in the column was periodically resuscitated by injecting at least two pore volumes of fresh growth medium without calcium to stimulate the recovery of bacterial populations after precipitation events. As a result both pH and NH_4^+ concentrations (an indication of ureolysis) were greater directly after the biofilm resuscitation events, while these parameters were observed to decrease during active biomineralization periods (Figure 7). As Figure 5 shows, directly after resuscitation events, effluent pH was restored to above 9 and the NH_4^+ concentrations rose to above 12 g L^{-1}, while during active biomineralizing periods, the pH averaged 6.9 and NH_4^+ concentrations dropped as low as 5.1 g L^{-1}.

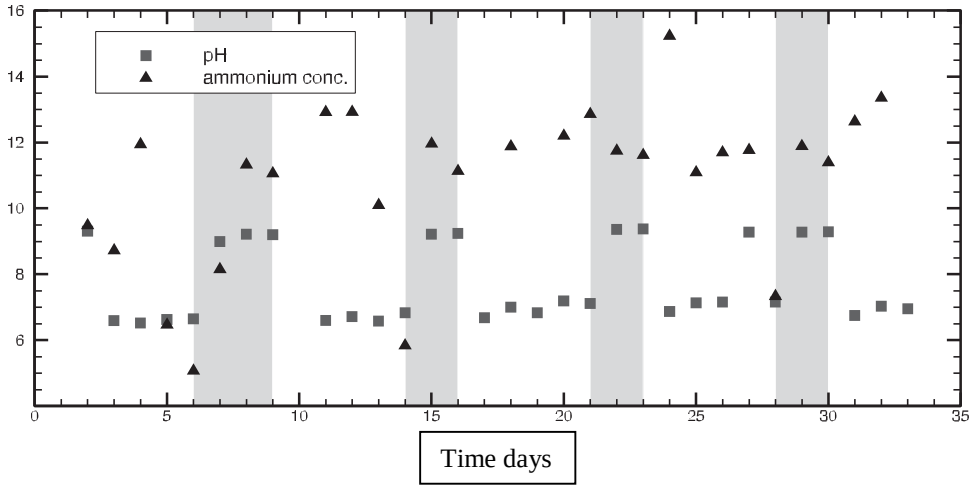

Figure 7. Effluent NH_4^+ concentration and pH data from column 4.

In Figure 7, the gray areas indicate resuscitation periods. Directly after resuscitation events, effluent pH was restored to above 9 and the NH4+ concentrations rose to above 12 g L-1, while during active biomineralizing periods, the pH averaged 6.9 and NH4+ concentrations dropped as low as 5.1 g L-1. Similar results were observed for the other columns. Note that the injected medium contained 3.4 g L^{-1} of NH_4^+.

Distribution of $CaCO_3$ Deposition. The average $CaCO_3$ contents from each column study are summarized in Table 7, while plots of $CaCO_3$ deposition along the column flow path appear in Figure 6. Calcium carbonate distribution results for columns 2-4 clearly indicate that the injection strategy developed results in a very uniform mineral distribution along the 61 cm (2-foot) column flow path. Unlike columns 2–4, column 1 did not employ a calcium-medium displacement strategy for the injection region and, as a result, higher $CaCO_3$ concentrations per mass of sand were observed in column 1 in the first section near the injection point. Concerns regarding locally reduced injectivity near the injection point of the column led to a modified injection strategy (used for columns 2–4) which involved rinsing Ca^{2+} rich medium from the influent area before significant ureolysis, and thus $CaCO_3$ precipitation could occur.

Table 7. Average calcite concentration per column section (§) per experiment (mg $CaCO_3$/per gram of sand)

Exp #	§1	§2	§3	§4	§5	§6	§7	§8
1	479 ± 29	256 ± 61	274 ± 30	227± 29	250 ± 74	254 ± 71	211 ± 22	202 ± 73
2	222 ± 30	193 ± 13	196 ± 10	188 ± 8	174 ± 6	178 ± 10	169 ± 15	173 ± 24
3	150 ± 10	136 ± 6	130 ± 4	154 ± 29	132 ± 12	133 ± 11	134 ± 6	201 ± 34
4	112 ± 18	165 ± 40	141 ± 40	118 ± 21	117 ± 24	121 ± 12	117 ± 8	109 ± 8

Simulation modeling. In parallel with ZERT II, the University of Stuttgart funded a simulation modeling project aimed at modeling the biomineralization process along a porous media flow path. This collaboration made possible the analysis of the calcite distribution data in Figure 8

using the Stuttgart biomineralization model. The solid lines in Figure 8 show these modeling results which were obtained by using the actual experimental protocol described above as model input. It is important to point out that these simulation modeling predictions were made prior to running the corresponding column experiment—thereby increasing the confidence in the use of this simulation model for predictive purposes in the lab as well in the field. The description of the Stuttgart biomineralization model as well as the analysis of the ZERT II data in Figure 8, are presented in Ebigbo, et al. 2012.

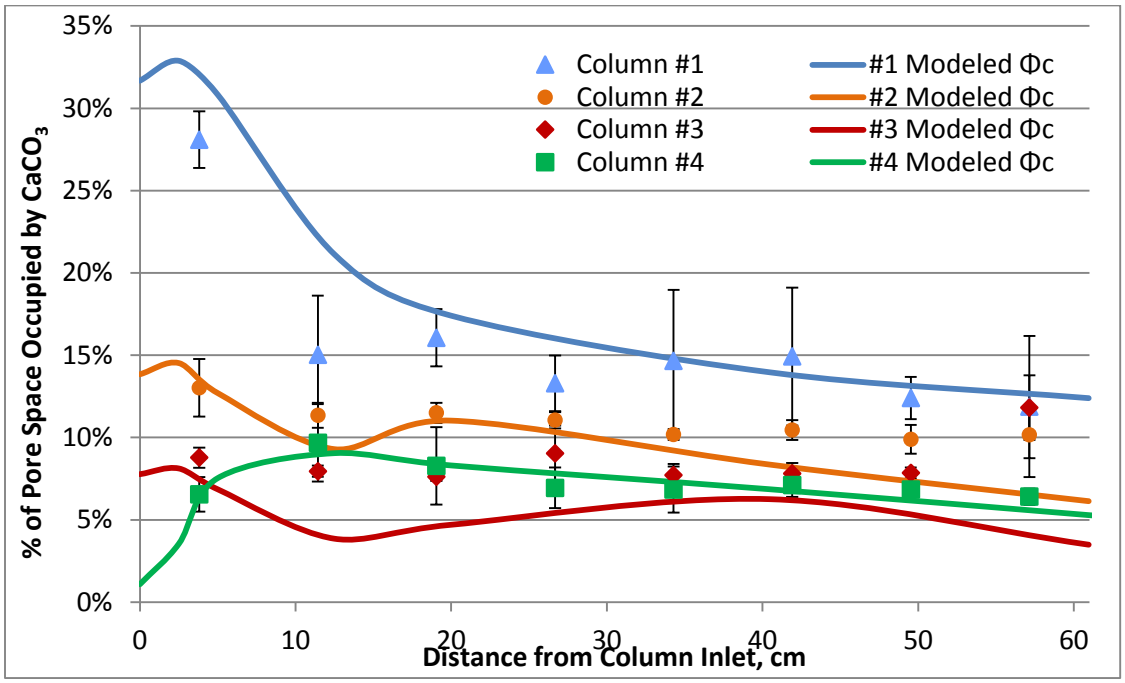

Figure 8. Summary of biomineralization distribution along the axes of 2.54 cm diameter, 61 cm long sand-packed columns.

In Figure 8, biomineralization is measured as the per cent of pore space occupied by precipitated $CaCO_3$. The lines shown through the experimental data points represent simulation modeling results as describe in Ebigbo, et al. 2012.

Mercury Porosimetry for porosity and pore size distribution

Berea sandstone. Mercury porosimetry was used to estimate pore size distribution and porosity changes resulting from biomineralization in Berea sandstone cores with initial porosity of 18 - 20%. Two 2.54 cm (one inch) diameter core plugs were drilled from the same block of Berea sandstone. Both cores were 5.08 cm (2 inches) in length. One core was subjected to biomineralization using the standard protocol described in the previous section. The other core was used as a control. After biomineralization was completed subsamples were broken off the influent and effluent ends of both cores and analyzed using mercury porosimetry. Resulting pore size distributions are shown in Figure 9 and Table 8 below. Figure 9 shows the incremental intrusion of mercury in relation to mean pore diameter for both the control and biomineralized cores. Here it is seen that the intrusion curves are similar for the control and biomineralized cores with the exception of the range between roughly 6 and 20 µm. In this range the amount of

mercury intrusion is significantly higher for the control core. This is interpreted to mean that biomineralization significantly reduced the overall pore space in this range.

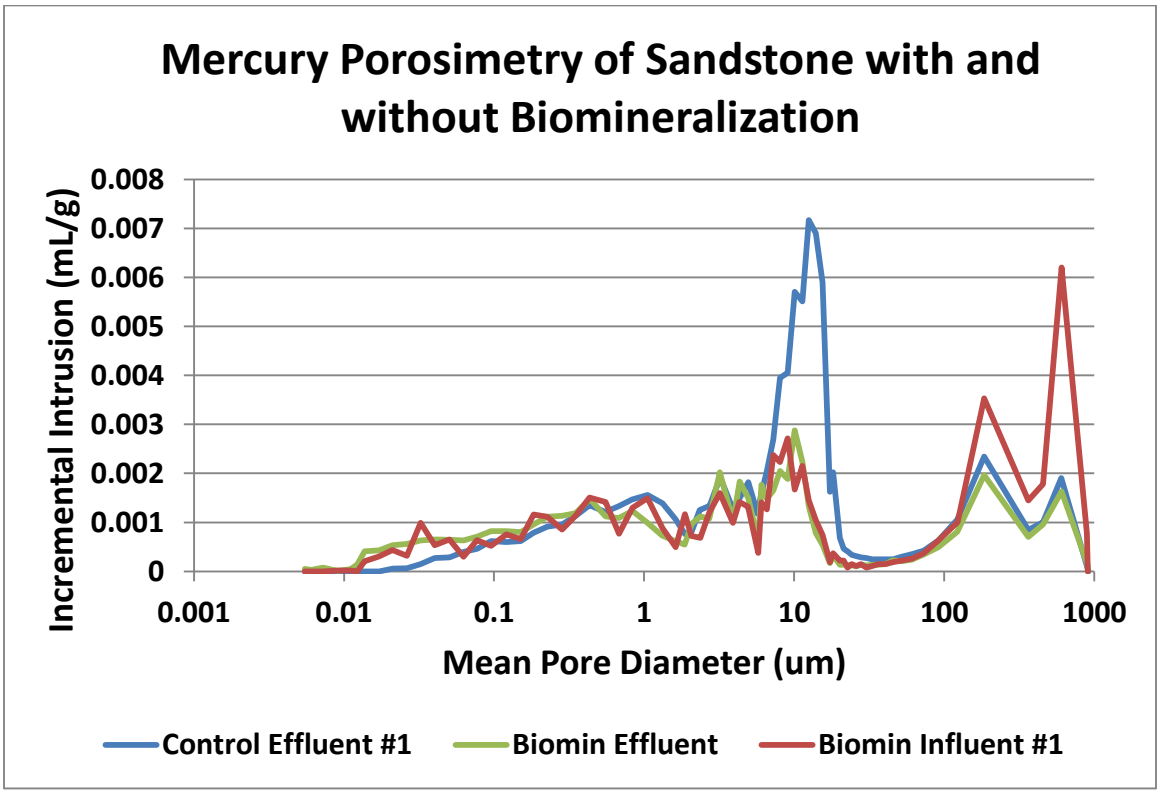

Figure 9. Mercury intrusion vs mean pore diameter for biomineralized Berea sandstone and non-biomineralized control.

Table 8. Comparison of pore size distributions between biomineralized Berea sandstone core (influent and effluent ends) and the non-mineralized control core.

Pore volume diameter	Control average	Biomin Influent Average	Biomin Effluent Average
less than 1 µm	15%	22%	28%
1-10 µm	33%	26%	38%
10-100 µm	42%	29%	22%
100-1000 µm	10%	23%	13%
6-16 µm	51%	33%	31%

This result is further documented in Table 3. Here the row highlighted in green shows that biomineralization substantially reduces the number of pores between 6 – 16 µm. In addition it was observed that the porosity was reduced from 18-20.4% down to 10.4-15% due to biomineralization. The results provided by mercury porosimetry provide valuable insight regarding how the biomineralization process behaves at the pore scale.

Mont Terri shale. The mercury porosimetry methods developed under ZERT II for Berea sandstone were subsequently used to support the work plan for a parallel project which involved laboratory bench-scale tests to evaluate the potential for biomineralization sealing in fractured shale. The tests were conducted using samples of Opalinus shale obtained from the Mont Terri underground testing facility in Switzerland and was funded by CCP. Mercury porosimetry methods were used to analyze two samples of the Opalinas shale (labeled OP1 and OP2), along with shales from the Bakken formation (North Dakota) and Green River formation (Utah).

As shown in Figure 10 all shales contained very little porosity between 0.1 and 10 µm. However, since the Bakken Shale had almost no porosity less than about 50 µm, both OP1 and OP2 were more similar to the Green River shale.

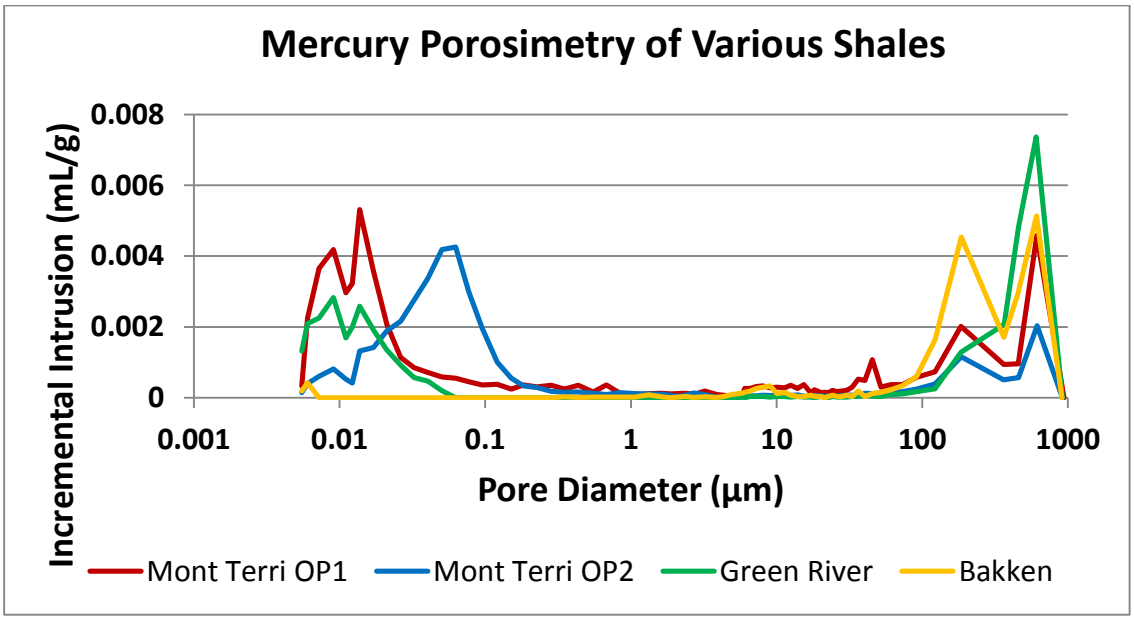

Figure 10. Comparison of Mont Terri shale pore sizes with other shales.

Table 9 shows the porosity for each shale sample along with the summary pore size categories. The average porosity for the two Mont Terri shales was 11.0 %

Table 9. Shale pore size summary.

Core	Porosity		
	Total	Less than 10 µm	Between 1-10 µm

Mont Terri #OP1	12.31%	8.59%	0.65%
Mont Terri #OP2	9.71%	8.13%	0.27%
Green River	8.25%	4.53%	0.03%
Bakken	4.50%	0.51%	0.39%

In summary the majority of the porosity for all shale types tested is contained in pores less than 0.1 µm and those greater than 10 µm. The overall pore size distributions for both OP1 and OP2 were very similar. All four shale samples contained very little porosity between 0.1 and 10 µm. The average porosity for the two Mont Terri shale blocks tested was 11.0%.

These results demonstrate the value of mercury porosimetry as a tool for characterizing shale as well as sandstone rock samples.

Subtask 2.3: Optimize biomineralization of isotopically labeled CO_2 carbon under variable head space pressure.

The capacity of the brine for carbonate ions and the precipitation of $CaCO_3$ is controlled by the complex interplay of carbonate equilibrium and pH [7]. We therefore evaluated the detailed evolution of the brine chemistry and carbonate precipitation using PHREEQC in order to elucidate the detailed changes in carbonate speciation and fluxes between the gas, solid, and solution phases. PHREEQC modeling results for synthetic brine ammonium (NH4+) concentration, pH, and Ca2+ concentration in CO_2 biomineralization experiments for four different head space conditions are shown in Figure 11.

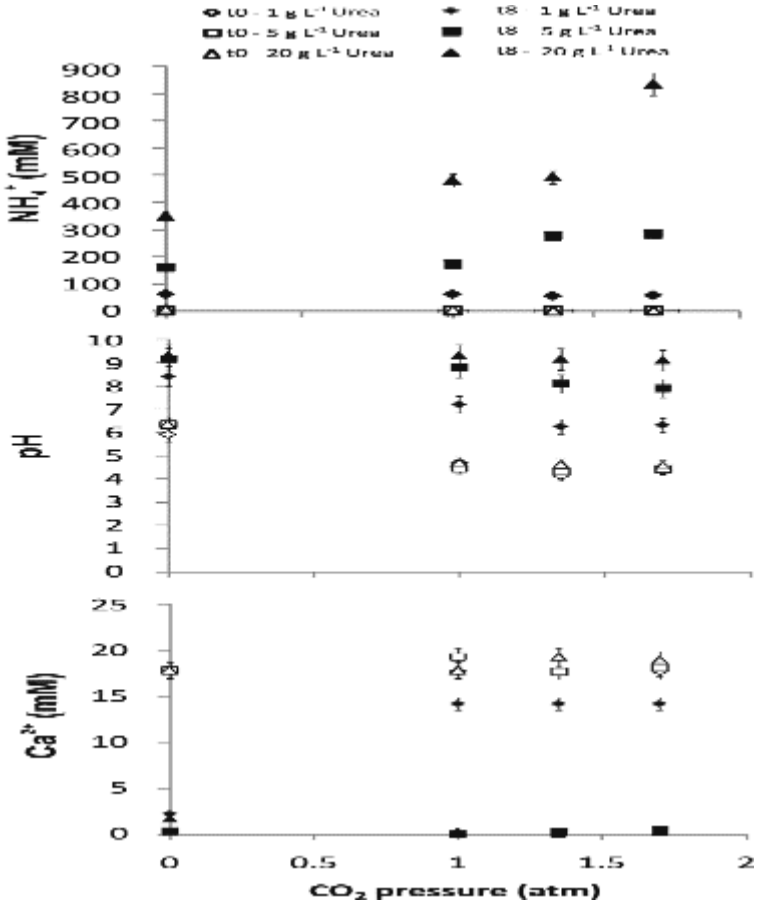

Figure 11. Synthetic brine ammonium (NH4+) concentration, pH, and Ca2+ concentration in CO_2 biomineralization experiments inoculated with Sporosarcina pasteurii, at varying CO_2(g) headspace pressures and urea concentrations at time t0 (0 days) and t8 (8 days).

The modeling demonstrates that after equilibration of the aqueous solutions with the headspace CO_2(g), for p(CO_2) above atmospheric pressure, (i) *ureolysis increases pH, via the net production of hydroxide ions and consumption of protons. (ii) Once supersaturated, $CaCO_3$ precipitates*, the degree of ureolysis required for the induction of precipitation is greater at higher initial p(CO_2), because it takes longer for the pH to increase to the point where the solution is saturated with respect to calcite. In addition, at higher initial p(CO_2), the proportion of carbonate ions precipitated in $CaCO_3$ decreases at a given degree of ureolysis, with a greater proportion remaining as aqueous carbonate ions [CO_3(aq)]. (iii) *Headspace p(CO_2) decreases, as long as ureolysis continues and pH is increasing, as the carbonate ion capacity and aqueous carbonate ion concentration increases in response to the increasing pH*. Here, at higher initial p(CO_2), the mass of CO_2 gassing into the groundwater solutions, and thus the concentration of CO_3(aq), increases, at a given degree of ureolysis. This reduced the headspace concentration of CO_2 by up to 32 mM per 100 mM urea hydrolyzed. Modeling results for calcium concentrations of 2mM and 125 mM demonstrate the same general trends. However, increased calcium concentrations lower the pH attained at a given degree of ureolysis due to the precipitation of $CaCO_3$, which results in the liberation of protons during the conversion of HCO_3^- to CO_3^{2-}.

The modeled C isotope compositions are shown in Figure 12 where they are compared with experimental values. The modeled C isotope compositions are more positive than those determined experimentally, especially for the experiments with 1 g L^{-1} urea.

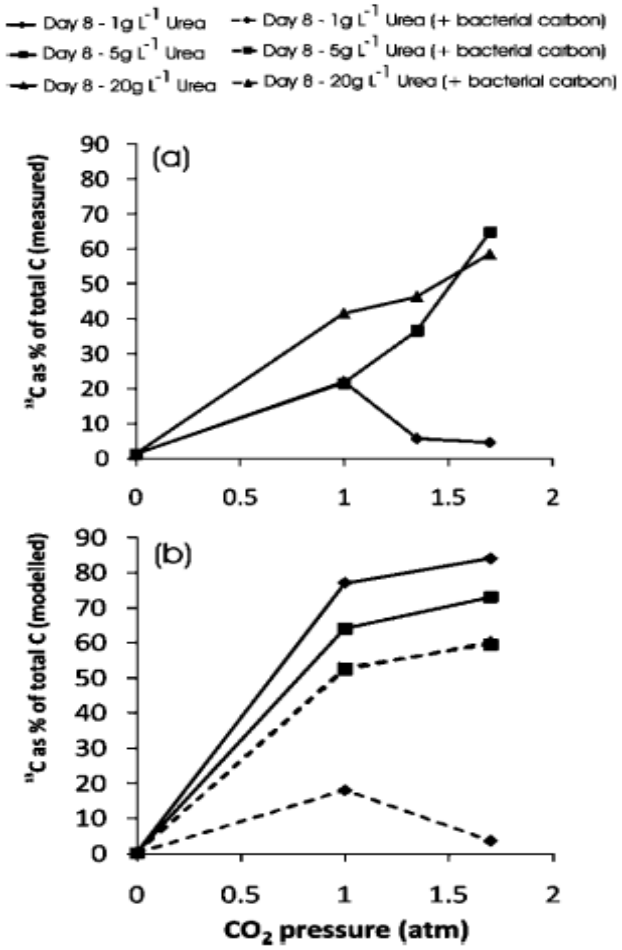

Figure 12. Measured and modeled ^{13}C as a percentage of total C in precipitated $CaCO_3$ in CO_2 biomineralization experiments inoculated with Sporosarcina pasteurii by t8 (8 days).

These data in Figure 12 demonstrate that the ^{13}C as a % of total C in $CaCO_3$ increased with increasing $p(CO_2)$ for each urea concentration.

The potential of microbially enhanced CCS

These data reveal that microbial ureolysis can enhance the mineral-trapping and solubility-trapping capacity of brine and other groundwater. This occurs primarily via the pH increase induced by urea hydrolysis which increases the carbonate capacity of the SB, according to carbonate equilibration and speciation in a CO_2-H_2O system as a function of pH. This increases the net flux of CO_2 (g) from the headspace into solution thereby enhancing the resulting solubility trapping and mineral trapping of CO_2 (g). A journal article summarizing these findings has been recently published in 2010 in *Environmental Science and Technology* (Mitchell, et al., 2010).

Subtask 2.4: Evaluate the potential for coal-bed mediated CO_2 sequestration and enhanced methane production.

Results from the three long-term batch flask experiments form the basis for evaluating microbial coal-to-methane conversion. The primary focus under the ZERT II project is the study of the rate and extent of biogenic methane production in response to the addition of algae extract as a stimulant. These results are summarized below.

Algae Enhanced CBM Production

Short term experiments. The CBM enhancement potential of algae extract was investigated by adding algal biomass with lipids removed to the batch experiments shown in Figure 4. Figure 13 below shows head space methane production for the first 125 days of Experiment #1. Comparison of the production curves reveals that the presence of either yeast or algae significantly enhances methane production compared to the curve for media + coal. Similar observations from other investigators studying CBM enhancement using yeast extract are summarized in Barnhart (2014).

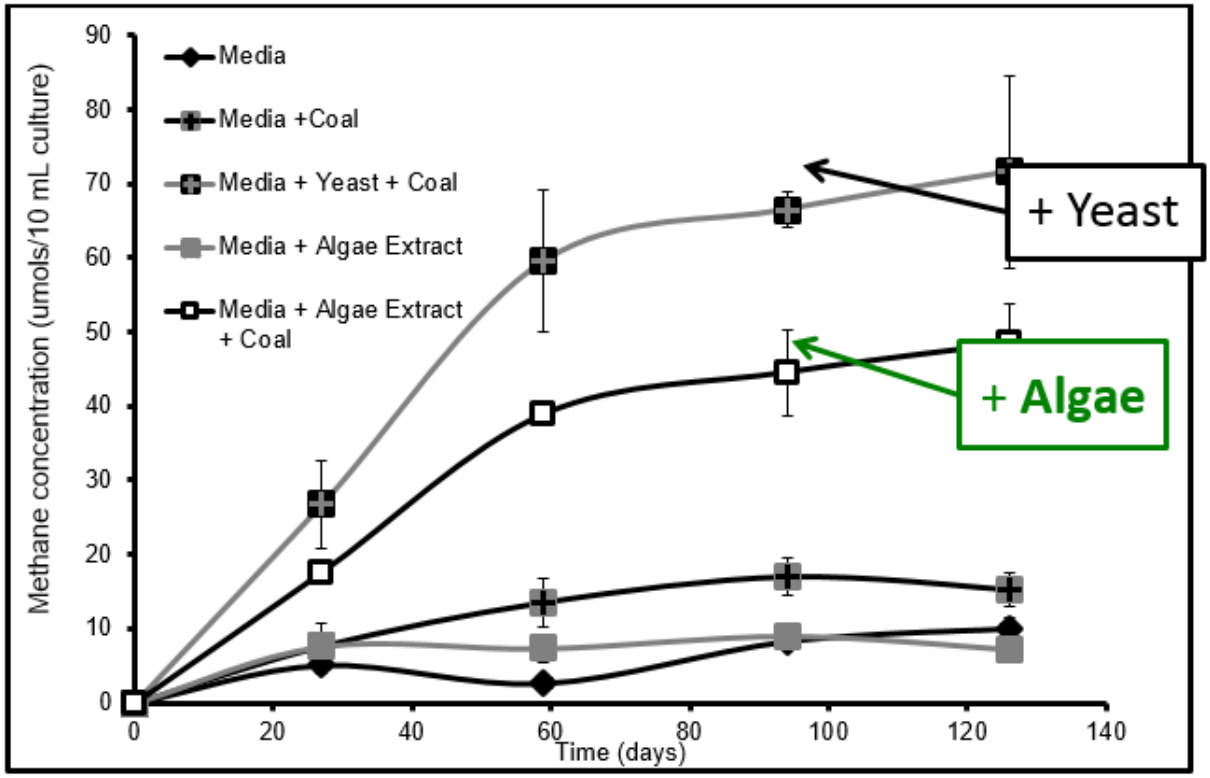

Figure 13. Methane production for first 125 days of batch microcosms for Experiment #1.

Experiment #1 utilized coal from a surface mine in Decker, MT, inoculum from a USGS well HWC-01 in the Powder River Basin, media consisting of synthetic CBM produced water (described above). Experiment #1 included addition of yeast extract (1 ml) and algae extract (1 ml) to stimulate methane (main ingredients mg, k, ca ammonium chloride, sodium bicarbonate,

K2Hpo4). All data points represent the average of triplicate experiments. Experiment #1 was started 9/10/2010.

Long term Experiments. Batch serm bottles for Experiment #1 were sampled after 165 days and then again in July 2014, 1406 days (3yrs and 10 months) after the experiment began. As shown in Figure 14, methane has continued to be produced in all three systems over the 1406 day period. These methane production curves reveal relatively rapid methane production for the first 165 days then a substantially reduced rate thereafter. This reductionin methane production rate this is very likely the caused by nutrient depletion with time inside the serum bottle. However it is important to note that methane production has continued after the initial 165 days--albiet at a significantly reduced rate. Because regular sampling was suspended until the final (1406 day) data point it is not possible to know if the methane rate has remained constant or is behaving in an asymtotic fashion. The most significant observation that can be made from the long term data in Experiment #1 is that the algae-amended methane production (green line) ultimately approached the yeast-amended line. Clearly both algae and yeast amendents significantly enhanced methane production relative to the Media+coal system.

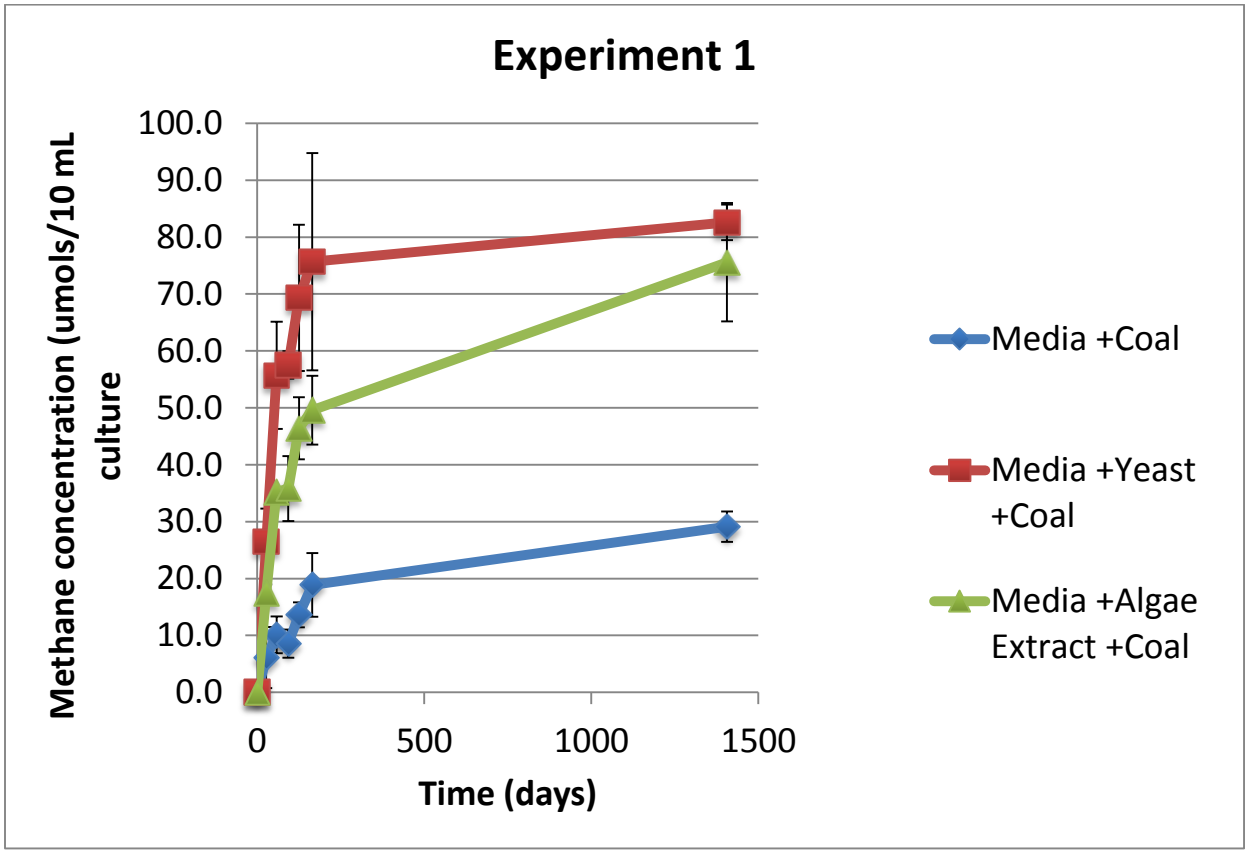

Figure 14. Long term (1406 day) methane production for Experiment #1.

Algal-enhanced methane production was also observed for Experiments #2 and #3. Figure 15 shows the total methane accumulation for Experiment #2 after 261 and 1169 days of operation. This experiment compared Media+coal with Media+coal+algae extract. Figure 16 makes the

same comparison for Experiment #3. As is the case with Experiment #1 both sets of results for Experiments #2 and #3 demonstrate significant enhancement of methane accumulation in the algae-amended systems.

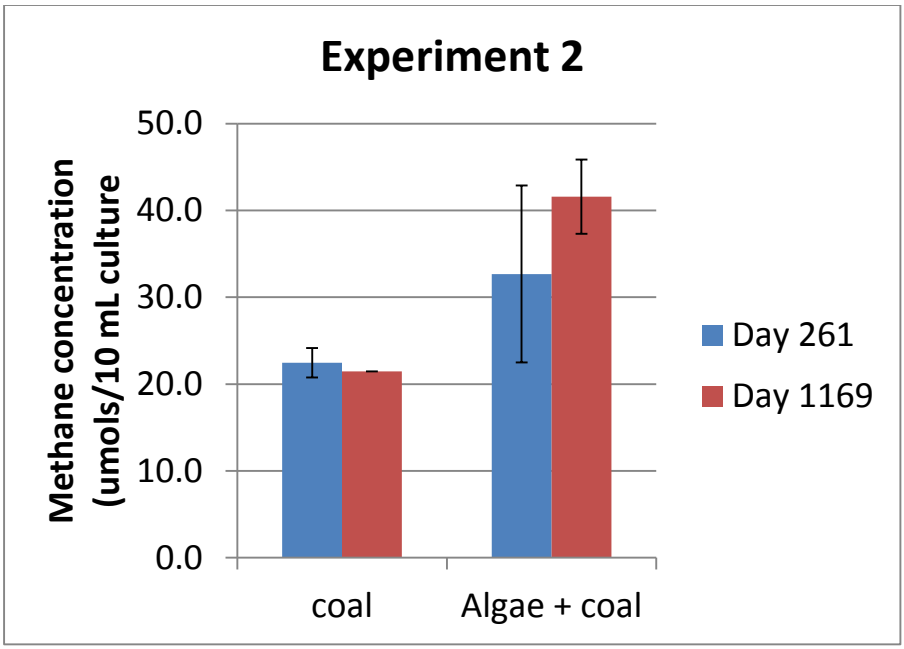

Figure 15. Methane production for Experiment #2 which contained Decker coal, Inoculum from well HWC-01 well, media consisting of synthetic CBM water plus sulfate. Methane production stimulated by adding 1ml algae extract (started 5/4/201)

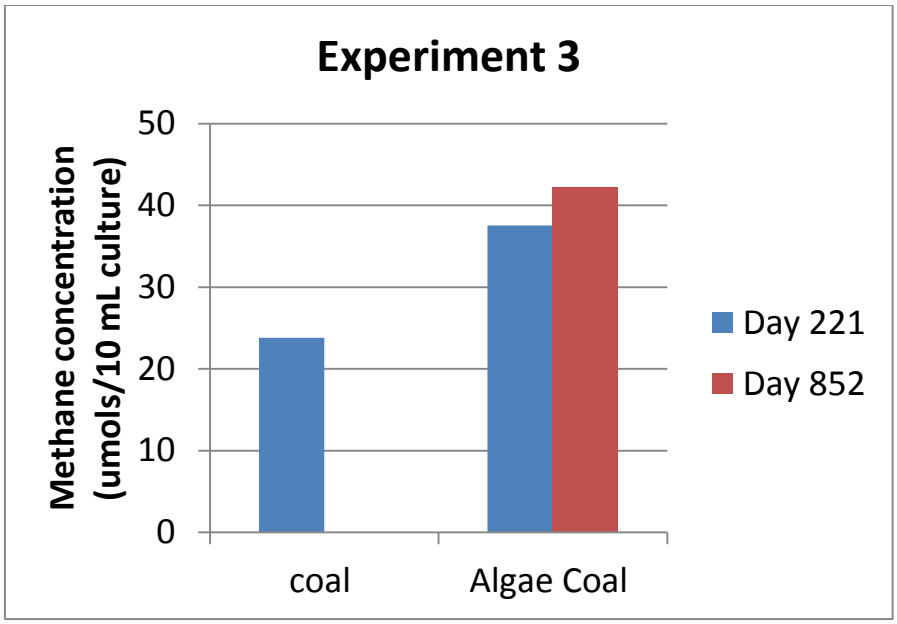

Figure 16. Methane production from Experiment #3 which contained Decker coal, filtered CBM produced water, and inoculum from well HWC-01. Methane production was stimulated by adding 1 ml algae extract (started 4/5/2012).

Energy-water quality synergies

Results from these three long-term batch experiments clearly demonstrate that biogenic methane production of methane from coal can be enhanced when algae extract is added as a stimulant. These observations point to the possibility of realizing some very important synergies at the field scale. Figure 17 illustrates the overall concept for field scale application of algal/nutrient technology for the enhancement of CBM production. After a well field's gas production has dropped off such that it is not economically viable, the stimulation cycle can begin. Produced water, stored in existing ponds, could be used for growth of algae. Algae that have the ability to produce lipids (*i.e.*, bio-oil) will be used, and the lipids can be extracted for production of biodiesel and other algae-derived products. After lipid extraction, the remaining algal biomass will be returned to the coal bearing formation as a nutrient source for stimulating subsurface coal-bed microbial communities.

The CBM production water is considered a waste stream often with high concentrations of metals and organics present. The growth of algae in produced water will increase algal uptake of metals and organics—thus improving overall water quality. Also the re-injection of algae/nutrient-amended water back down-hole to the coal-beds will reduce the amount of produced which must be otherwise treated and discharged to other receptors. The recycled water will flow through the coal seam delivering nutrients to indigenous microorganisms to facilitate additional methane production via methanogenisis. This cycle, as shown in Figure 17, will facilitate sustainable CBM production.

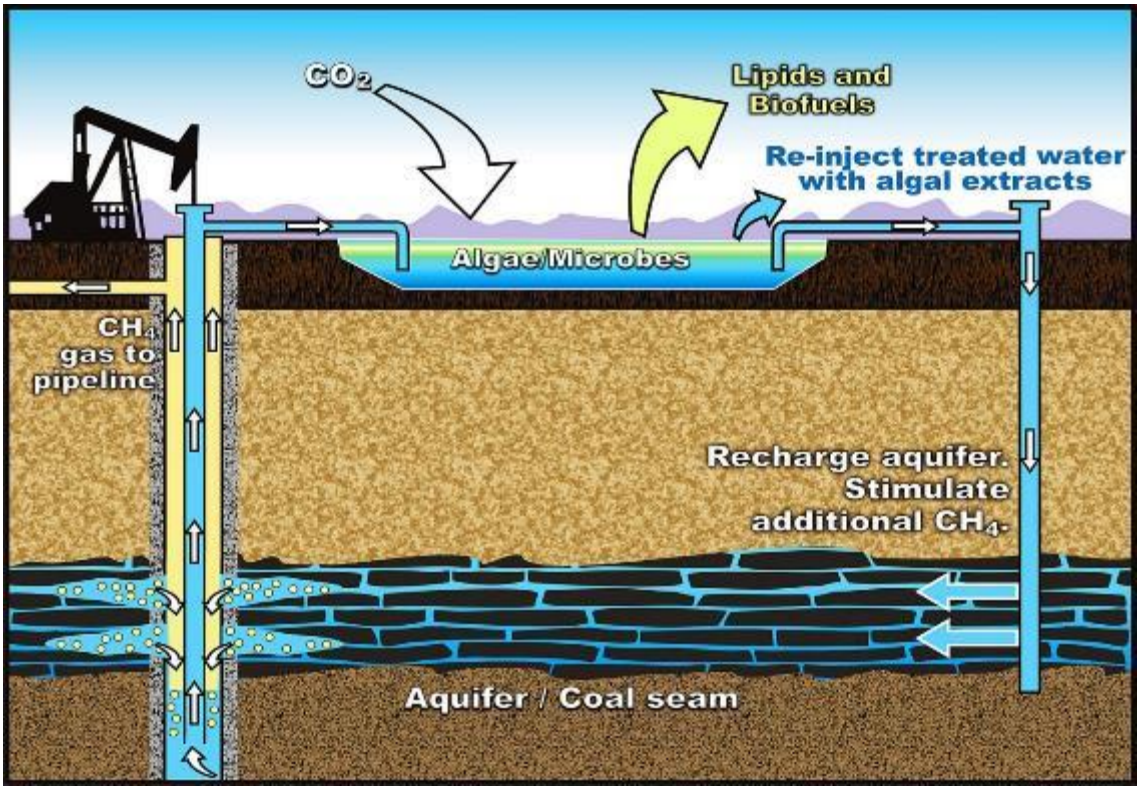

Figure 17. Conceptual scheme for stimulating CBM production by injecting CBM production water amended with algae extract and other nutrients. Enhanced CO_2 Uptake and CBM produced water recycle are added benefits resulting from this approach to CBM production stimulation.

Large-scale algal production in CBM ponds will also substantially increase CO_2 uptake from the atmosphere there by decreasing the carbon footprint of conventional CBM operations. In a parallel DOE-funded algal-biofuel research program at MSU (*Integration of Nutrient and Water Recycling for Sustainable Algal Biorefineries*, DOE-EERE (DE-EE0005993), R. Gerlach PI) It was observed that maximum algae biomass production in field-scale raceway systems could be as high as 10 grams algae/m^2/day. Assuming that algae biomass is 50% carbon (which comes from CO_2), corresponding estimate for CO_2 uptake from the atmosphere for a field system like that shown in Figure 2 would be 5 g C/m^2/day. Converting carbon to CO_2 gives a value of 18.75 g CO_2/m^2/day from the surface of a field-scale algal production system. For a one-hectare surface area 187,500 g or 187 kg CO_2/day could be taken up.

CONCLUSIONS: BIOFILMS AND BIOMINERALIZATION

Subtask 2.1: Determine the integrity of biomineralization deposits on flat coupons in response to brine and supercritical CO_2.

For subtask 2.1 we conclude that brine at atmospheric conditions and pure $scCO_2$ at supercritical conditions has little to no effect on biomineral deposits formed by S. pasteurii. Biominerals do appear affected by dissolution from exposure to $scCO_2$ in the headspace of a brine-filled HPV

and $scCO_2$ saturated brine, however, several experimental conditions may have contributed to the measured loss of minerals from the coupons. First, during the depressurization of the reactor, the brine was vigorously bubbling as CO_2 left the brine solution. This agitation may have contributed to knocking minerals off of the coupons. Second pH of the final brine solution after the HPV was depressurized was measured at 4.85 and 5.91 (Exposure 7 and 8 respectively). Calcium carbonate mineral dissolution is possible at these pHs. These data suggest that microbially-induced mineralization with the purpose of reducing the permeability of preferential leakage pathways during the operation of CCS may be most applicable in the pure $scCO_2$ region and the $scCO_2$ saturated brine region of the subsurface storage site where subsurface fluids are quasi static.

Subtask 2.2 Develop methods to understand and control the deposition rate of biomineralized calcium carbonate with distance in homogenous porous media.

Under ZERT II Subtask 2.2 has been focused on two objectives: (1) developing methods to control the deposition of calcite along a porous media flow path, and (2) develop methods for quantifying the biomineralization process at the pore scale using mercury porosimetry.

The following conclusions were reached:

- A standard, repeatable protocol, utilizing near-injection-point calcium-medium displacement along with periods of bacterial resuscitation, was developed which resulted in a relatively uniform distribution of calcite along the flow path of packed sand columns. This operational protocol was validated both experimentally and computationally using a simulation model developed at the University of Stuttgart.
- Balancing periods of biomineralization with periods of bacterial resuscitation which additional growth nutrient was added counteracted inactivation of bacterial cells (due to cell encapsulation), reduced ureolysis, and, ultimately, reduced calcium deposition efficiency.
- Mercury porosimetry methods, which measure pore size distribution and porosity, have been developed for both sandstone and shale. These methods facilitate initial characterization of sandstone and shale samples along with providing valuable insight into how the biomineralization process changes rock properties at the pore scale.

These ZERT II findings contribute to advancing MICP technology for subsurface applications. Primarily ZERT II research has advanced understanding of how to manipulate ureolytic, biofilm-forming bacteria (i.e. *Sporosarcina Pasteurii*) to control the distribution of $CaCO_3$ along the axis of flow through porous media. The MICP technology has the potential to reduce near-well bore permeability, coat cement to reduce CO_2–related corrosion, and lower the risk of unwanted migration of CO_2 and other gasses.

Subtask 2.3. Optimize biomineralization of isotopically labeled CO_2 carbon under variable head space pressure.

By controlling the supply of Ca^{2+} and HCO_3^- in the subsurface water, injecting microbial inocula, growth nutrients and urea, calcium carbonate precipitation in the subsurface can be engineered by bacterial hydrolysis of urea (aka ureolysis). Ureolysis results in the production of ammonium (NH_4^+) and an increase in pH via a net production of OH^- ions. This increase in pH and alkalinity favors $CaCO_3$ precipitation. As reported previously, our research team has determined that the ureolytic biomineralization process, when properly engineered, can precipitate copious quantities of calcium carbonate into aquifer pores and fractures, thus providing a potential technology for plugging leakage pathways available to injected CO_2 (i.e. enhanced formation trapping).

Under subtask 2.3 we present results from the bacterial hydrolysis of urea (ureolysis) in microcosms containing synthetic brine with variable headspace pressures [p(CO_2)] of $^{13}CO_2$. These experiments demonstrate a net flux of head space $^{13}CO_2$ into the brine and precipitated mineral phases. These results suggest that ureolytic biomineralization is capable of sequestering anthropogenic CO_2 from the gas phase into the mineral phase as $CaCO_3$--thereby facilitating enhanced mineral-trapping of injected CO_2 in the subsurface as well as from waste streams above ground. Of equal importance we have found that ureolytic biomineralization enhances the capacity of the brine for CO_2 (g) and dissolved carbonate ions, thus increasing the potential for solubility-trapping of injected CO_2.

Subtask 2.4 Evaluate the potential for coal-bed mediated CO_2 sequestration and enhanced methane production.

The observation that methane production from coal can be stimulated by the presence of algae has been demonstrated. This finding has significant implications for improvement of current practices in CBM production in the Powder River basin and elsewhere, while simultaneously realizing increased CO_2 uptake from algae growth. This research provides a basis for future research into coupled biological systems (photosynthesis and methane production) that could sustainably enhance CBM production and generate algal biofuels while also sequestering carbon dioxide (CO_2). CO_2 uptake as high as 187 kg CO_2/day could be taken up based on the assumption that10 grams algae/m^2/day can be produced in production water facilities.

EXPERIMENTAL METHODS: MR STUDIES OF THE RESIDUAL TRAPPING OF GASES IN ROCK CORES

A custom Temco FCH core holder was used to maintain rock cores under scCO$_2$ temperatures and pressures, see Figure 18.

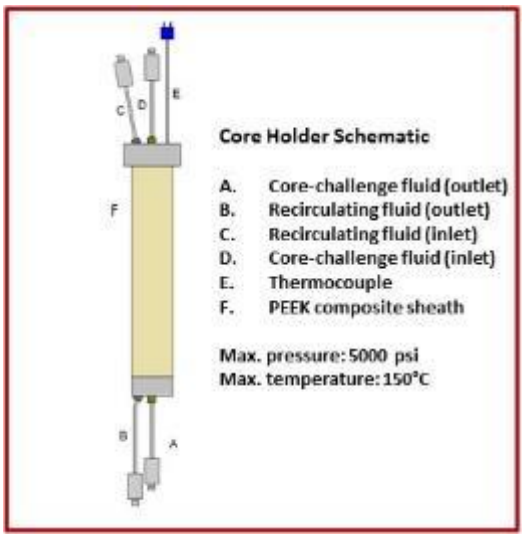

Figure 18: Core Holder Schematic

The Temco core holder was attached to two ISCO 500D syringe pumps. One pump provided the overburden pressure using Fluorinert, which is not visible to the NMR system. The other pump was used to flow either the CO_2 or the water through the rock core. A back pressure regulator kept the entire system at high pressure, see Figure 19 and Figure 20.

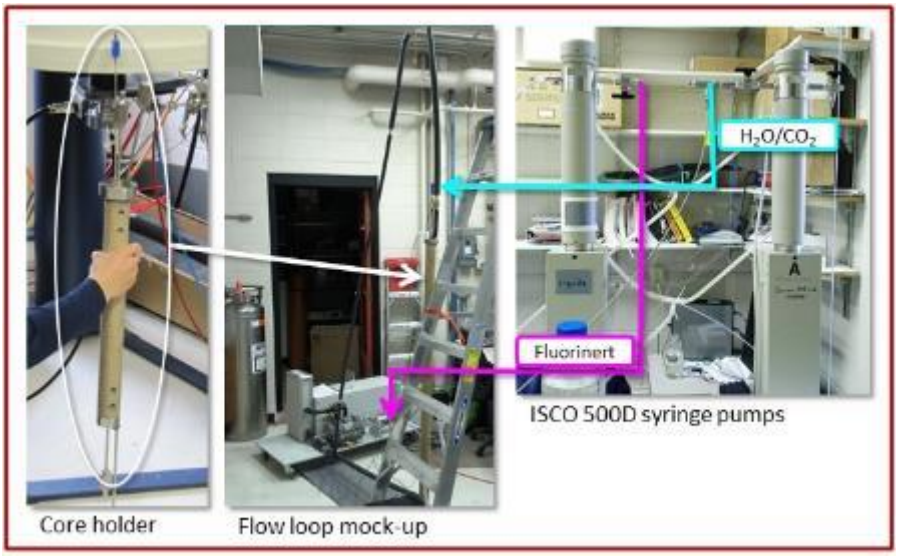

Figure 19: Flow Loop Equipment Components

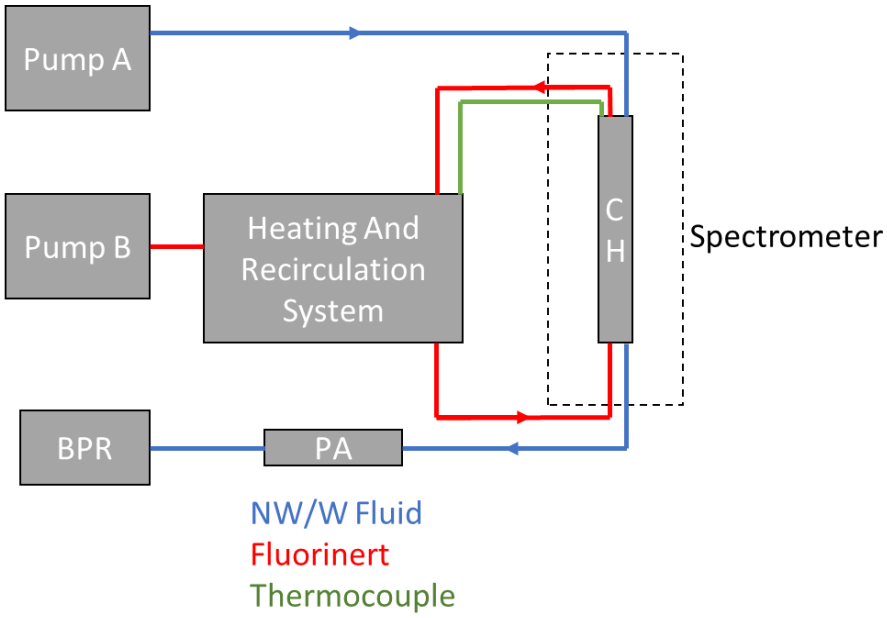

Figure 20: Flow Loop Schematic

One dimensional profiles of the water were obtained using the Zero Echo Time Imaging sequence (ZTE). This sequence allowed 1D profiles to be obtained in less than a minute. See Figure 21.

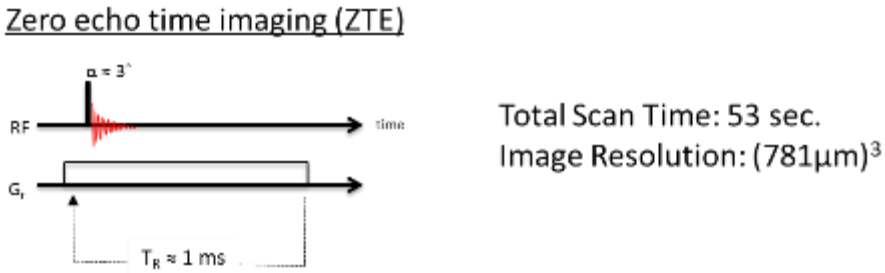

Figure 21: Zero Time Imaging ZTE 1D MRI Sequence

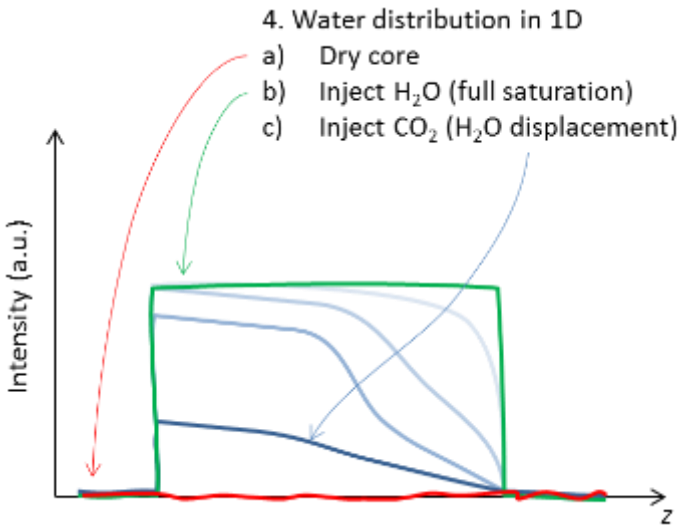

Figure 22: Expected 1D Profile Results

The experimental protocol involved initially fully saturating several rock cores with water at 1100 PSI. The water was then allowed to drain at 0.5 ml/min with a gas at 1100 PSI being used for the drainage. Following the drainage, water at 1100 was imbibed at the same rate or 0.5 ml/min. The fluids used for the drainage were either: air (1100 PSI, 293 K), CO_2 (1100 PSI, 293 K) or $scCO_2$ (1100 PSI, 308 K). Figure 22 is a schematic of the expected 1D magnetic resonance imaging MRI images obtained with the ZTE sequence.

RESULTS AND DISCUSSION: MR STUDIES OF THE RESIDUAL TRAPPING OF GASES IN ROCK CORES

A typical set of 1D MRI images is shown in Figure 23. The initial 1D profile after full saturation is shown in red. The profiles obtained each minute during the drainage are shown in green. The profile after imbibition of the water again is shown in blue.

Preliminary data calculated from these profiles is shown in Table 10. The air drains about 40 % of the water whereas the CO_2 and $scCO_2$ drains 50% of the water, see $S_{initial}$. The final saturation levels vary for the two samples and the three gases, see $S_{residual}$. However, interestingly, the percentage of gas trapped ($S_{initial}$ /$S_{residual}$) is less for the $scCO_2$ than for the air or CO_2, 60-65% compared to 70-75%.

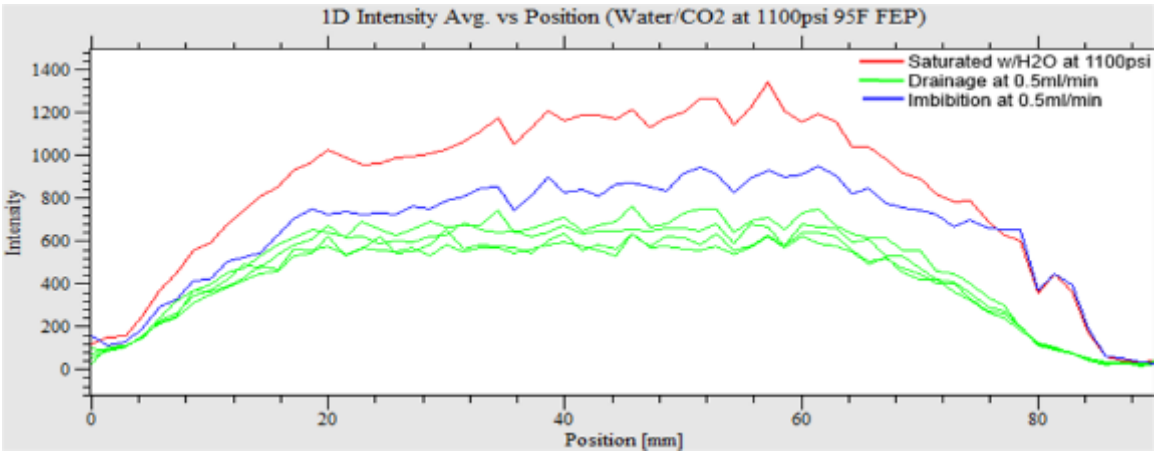

Figure 23. Representative 1D profile results - $scCO_2$ and Water

Table 10. Non-Wetting NW Phase Fractions at Different Stages of the drainage and imbibition cycle

Scan (Non-Wetting Phase)	Normalized 1D Avg. Intensity from 28-54mm for Core #2					
Run	Air (AFLAS)	Air (FEP)	CO2 (FEP)	CO2 (FEP)	scCO2 (FEP)	scCO2 (FEP)
Fully Saturated	0	0	0	0	0	0
Drainage Final ($S_{Initial}$)	0.408	0.418	0.509	0.511	0.507	0.466
Imbibition Final ($S_{Residual}$)	0.277	0.320	0.359	0.366	0.267	0.302
$S_{Residual}/S_{Initial}$	0.679	0.766	0.705	0.716	0.527	0.648

Max NW phase after drainage

Residual NW phase after imbibition

Trapping efficiency (Residual/Max)

Scan (Non-Wetting Phase)	Normalized 1D Avg. Intensity from 28-54mm for Core #3					
Run	Air (FEP)	Air (FEP)	CO2 (FEP)	CO2 (FEP)	scCO2 (FEP)	scCO2 (FEP)
Fully Saturated	0	0	0	0	0	0
Drainage Final ($S_{Initial}$)	0.402	0.439	0.467	0.481	0.491	0.478
Imbibition Final ($S_{Residual}$)	0.299	0.316	0.328	0.354	0.294	0.290
$S_{Residual}/S_{Initial}$	0.744	0.712	0.702	0.736	0.599	0.607

Max NW phase after drainage

Residual NW phase after imbibition

Trapping efficiency (Residual/Max)

NMR relaxation T_2 measurements are shown here for interest. No conclusions are clear yet, but to the extent that T_2 can be correlated to pores size in the rock (Callaghan and Washburn, 2006)) the gas seems to be preferentially trapped in the larger pores. It is important to note that due to the large sample size, and necessary long RF pulses in the NMR CPMG measurement, the only signal detected in these T_2 measurements is longer than a millisecond and hence much of the water signal in the smallest pores is undetectable.

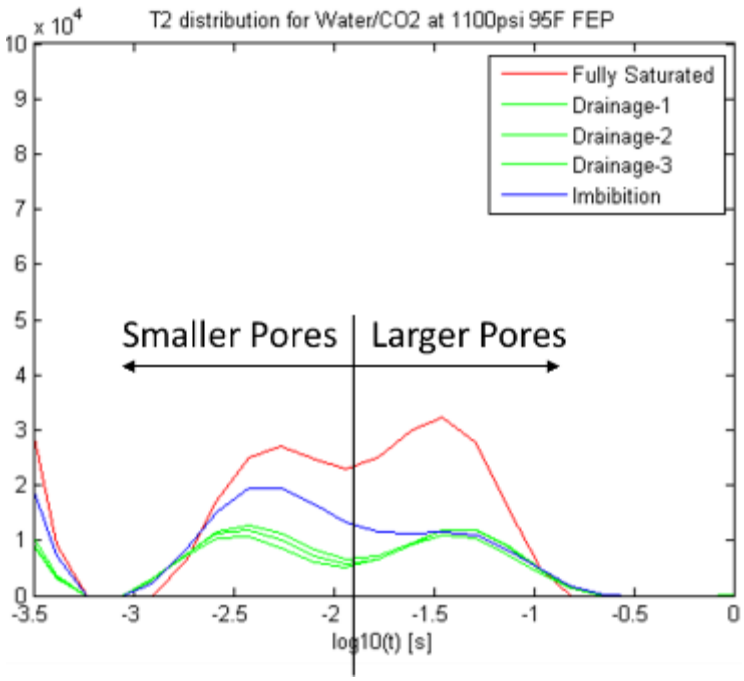

Figure 24. T2 Distribution and Pore Size Correlation for the residual water following a drainage cycle with CO_2

CONCLUSIONS: MR STUDIES OF THE RESIDUAL TRAPPING OF GASES IN ROCK CORES

The most significant conclusion is that even with this initial preliminary data, it is clear that NMR can non-invasively monitor drainage and imbibition and determine the percentage of trapping. This could be critical in understanding how supercritical CO_2 can be trapped in different porous subsurface materials. Rock cores have high magnetic susceptibility and future plans hope to use a low field Rock Core Analyser to study these processes and obtain more detailed information.

EXPERIMENTAL METHODS: NATURAL ANALOGS OF ESCAPE MECHANISMS

During the course of the project rock samples from each study area were collected and prepared for analysis. These rock samples were chosen to provide data on geologic processes caused by subsurface migration of natural CO_2 across faults and fracture networks (Figure 20). Breccia clasts and matrix samples were collected as well both altered and unaltered host rock, and generations of cements from veins from each study area. The work performed to complete analyses in the study areas included standard petrography, cathodoluminescence (CL), scanning electron microscopy (SEM) with energy-dispersive x-ray spectrometry (EDS), field emission scanning electron microscopy (FE SEM), powder x-ray diffraction (XRD) spectroscopy, x-ray fluorescence (XRF), stable isotope analysis (carbon and oxygen), radiogenic isotope analysis

(strontium), carbonate staining of hand samples and petrographic thin sections, fluid inclusion work and field examinations. Computer aided fracture analysis was also used to see trends in the areas and then field checked. Most of the analytical work was performed using instrumentation in the Imaging and Chemical Analysis Laboratory (ICAL) facility at Montana State University (MSU) in Bozeman, Montana.

Figure 25. Location Map for study areas in the Natural Analogs of CO_2 Escape Mechanisms portion of the project.

Figure 25 shows South to North: Stewart Peak Culmination study area, Thermopolis study area, Pryor Mountain study area and Big Snowy Mountain Study area. The Kevin Dome area is located in north western Montana near the Canadian border.

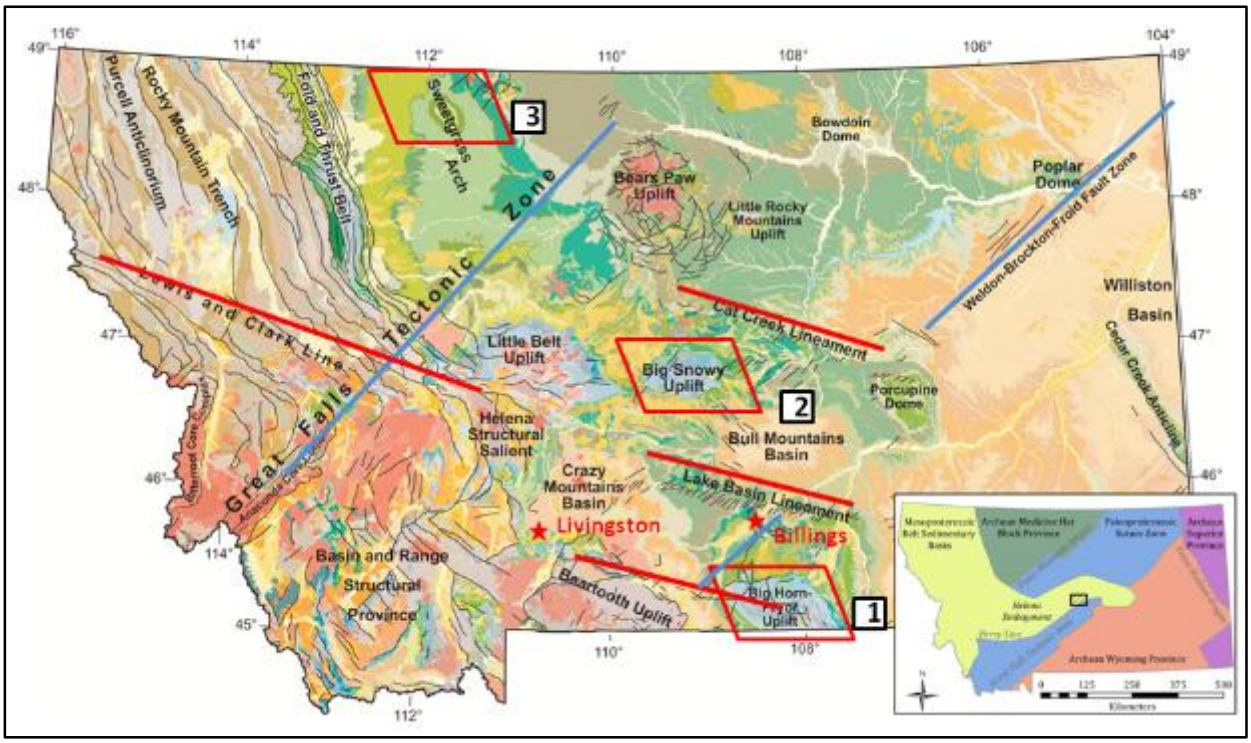

Figure 26. Major tectonic features base map and faults of Montana

Figure 26 is modified from the Geology of Montana Map Montana Bureau of Mines and Geology map and shows PMSA (1) and BSMSA (2) study areas in Montana and the location of the Big Sky Carbon Sequestration Partnership Kevin Dome Carbon Storage Project (3). The blue and red lines show NW-SE and NE-SW trending lineaments. Lower right inset shows Archean provinces of Montana. The location of the Big Snowy Mountains (outlined in the hachured box) is superimposed on top of Archean-Proterozoic orogenic and tectonic features (modified from Sims et al., 2004; Jeffrey, 2014).

Field work:

Field work was conducted in all of the study areas. Samples were selected which could be examined and chemically characterized (Figure 28) in the laboratory to gain a sense of the relative timing of faulting, fracturing, fluid migration and structurally controlled diagenesis of each area. Fracture analyses (Figure 29) were done across faults and fracture networks associated with subsurface migration of natural CO_2 bearing fluids around mineralized areas to access the geologic processes associated in these study areas. A portable XRF was utilized in the field in the PMSA and also in the structure lab at MSU. The instrument was recently acquired and initial analyses were performed for quick mineral identification such as dolomite vs. calcite. When fully calibrated to perform quantitative analyses this instrument may yield a good first

approximation of chemical composition of many geologic materials and be a useful exploration tool for use both in the field and in the lab.

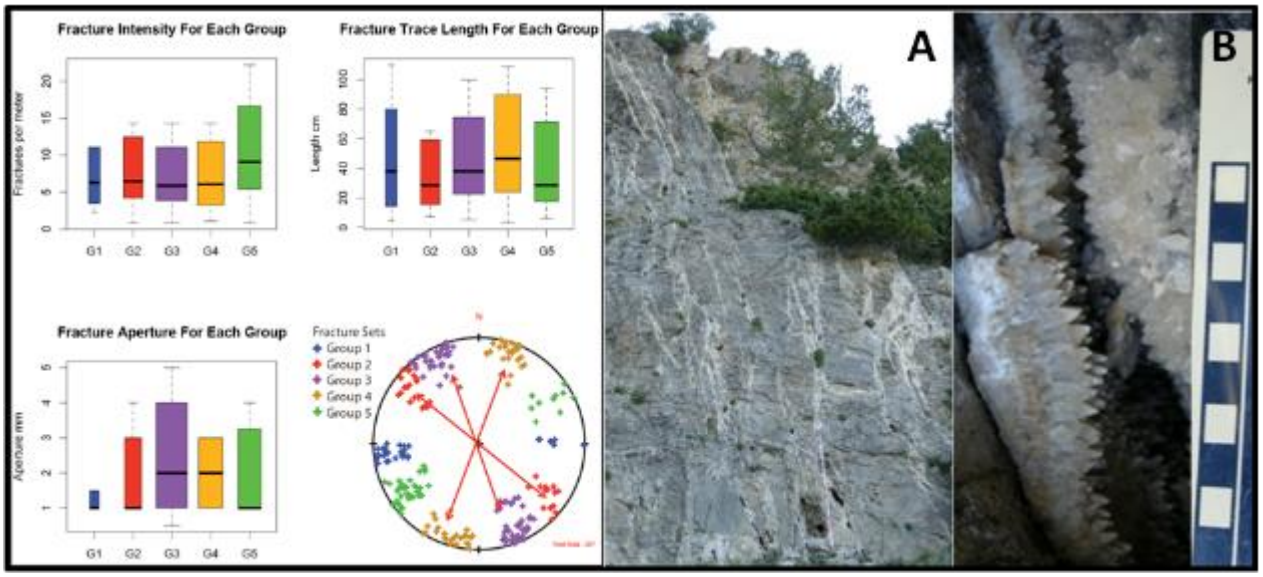

Figure 27. (A) Large anastomosing group 4 fractures SPC area with vein fill material (B) demonstrating multiple episodes of fluid flow.

Figure 27 shows the left figure boxplots showing the values of fracture attributes as well as a stereonet plot showing poles to planes of fractures belonging to the 5 designated groups of the SPC.

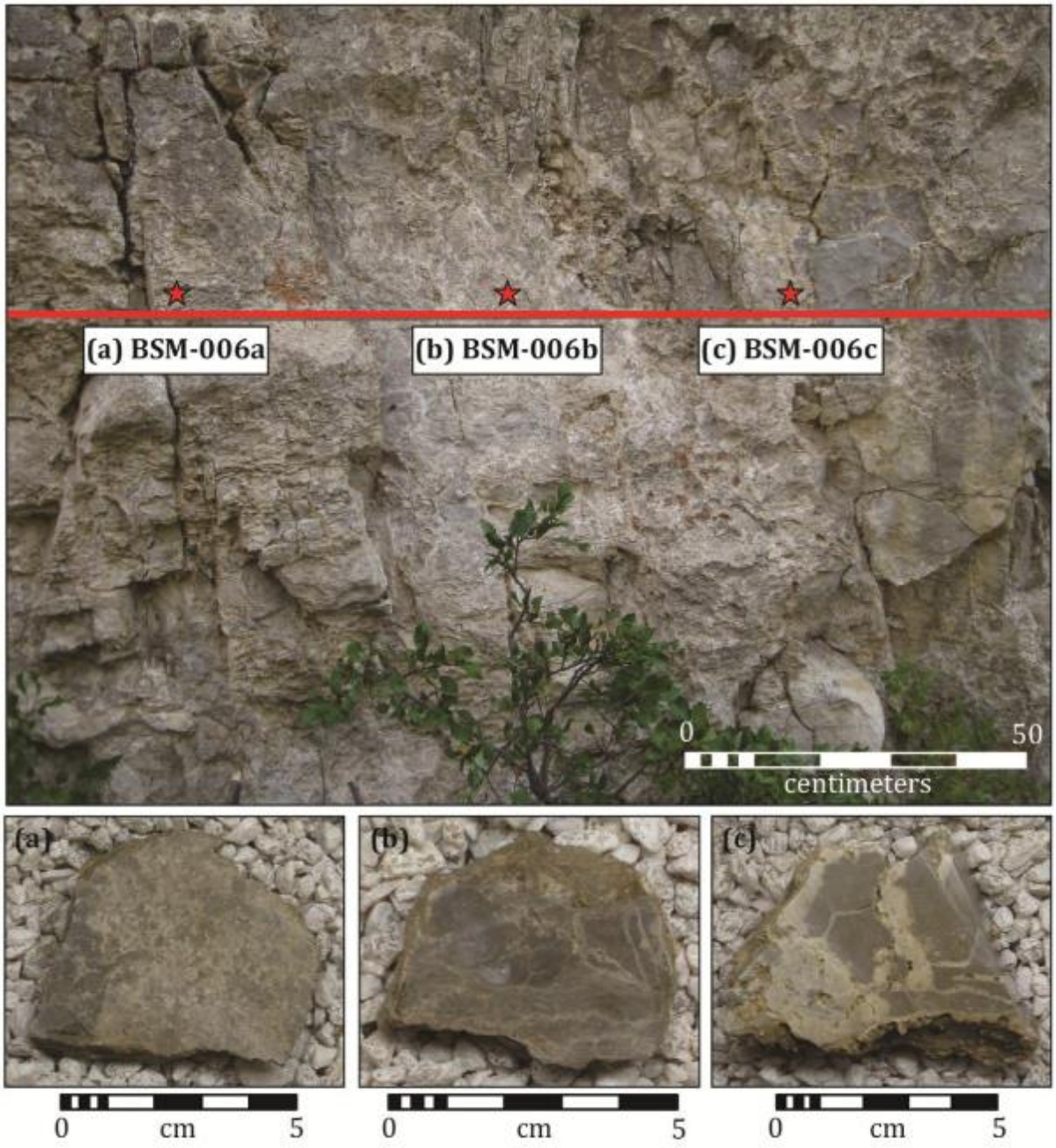

Figure 28. Brecciated samples from the BSMSA display the internal zonation of a breccia pipe.

Breccia pipe BSM-006 (top) shows the progression from outer (left) to inner (right) regions of the pipe. Sample BSM-006a (a) was taken from a matrix-poor, clastsupported crackle breccia near the contact with the undeformed wall rock. Sample BSM-006b (b) was taken in a patch of more deformed material, resulting in a more fractured mosaic breccia exhibiting a slight rotation of clasts and a higher matrix content. Sample BSM-006c (c) was taken from the internal conduit of the breccia pipe, where the matrix concentration was highest and there was a maximum

separation of clasts, resulting in a chaotic breccia. All three samples were taken within one meter of each other, exemplifying their extremely heterogeneous nature.

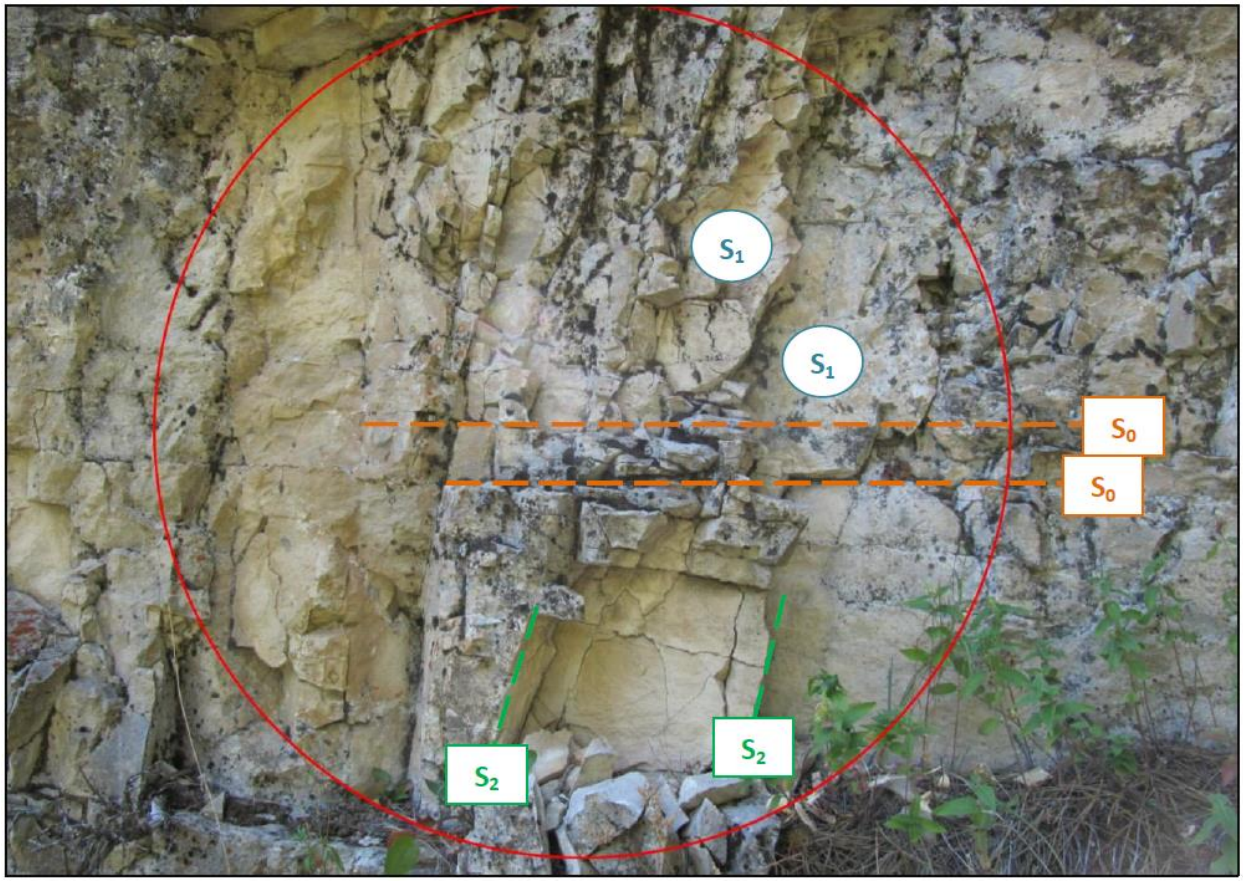

Figure 29. Fracture station along the BSFS.

Station BSM-020 E (the wall rock on the east side of breccia pipe BSM-020) exhibits two dominant systematic fracture sets in the Mission Canyon Limestone. The red circle is approximately one meter in diameter. Within this circle, dip, average dip direction, and fracture length for each of the sets was measured. "S0" (orange) is the bedding plane; "S1" (blue) is the primary shear fracture face; and "S2" (green) is the secondary shear fracture plane (figure from Jeffrey, 2014).

Laboratory work:

During this fourth fiscal quarter July 1- September 30, 2014 laboratory work including XRD, SEM, XRF and standard petrography was performed to aid in the interpretation of fluid migration associated with the tectonic hydrothermal breccias in the PMSA. Powdered samples were prepared for radiogenic Sr isotope analysis. Samples of late stage calcites, matrix material from breccia samples, and fluorite were prepared for isotope analysis using a battery powered hand held drill equipped with a Dremel™ tool rounded bit with a diameter of 1/8 inch and/or a diamond alloy steel mortar and pestle. These were analyzed in the ICAL facility at MSU using XRD, SEM, with EDS to determine mineralogy type. Sr isotope work was done at the University

of Wyoming High Precision Isotope Laboratory in Laramie, Wyoming. Analyses were done on the NEPTUNE Plus, a next-generation Multicollector-Inductively Coupled Plasma Mass Spectrometer (MC-ICPMS). The following descriptions of methods and procedures are typical for each field study area in the project.

Powder X-Ray Diffraction Spectrometry

XRD spectrometry is a useful technique that aids in identifying bulk mineral phase compositions from a well-mixed, homogenized rock sample approximately 5-10 micrometers (μm) in size (Jeffrey, 2014). XRD spectrometry was performed on samples from the SPC to aid in carbonate identification for Carbon and Oxygen stable isotope analysis. Samples were drilled out and analyzed at the ICAL facility at MSU and then sent to Michigan for isotope analysis. Samples from BSFS along the western flank of the Big Snowy Mountains and samples from Swimming Woman Canyon (SWC) along the southern edge of the range were also analyzed for XRD prior to stable isotope analysis. Samples from the PMSA were drilled out to select specific regions of the sample that would be hard to obtain by other methods. Samples were sometimes stained for carbonate identification (Figure 30) using a mixture of alizarin red and potassium cyanide solution. Staining can aid in identifying variations in iron content which might be hard to do without more extensive testing.

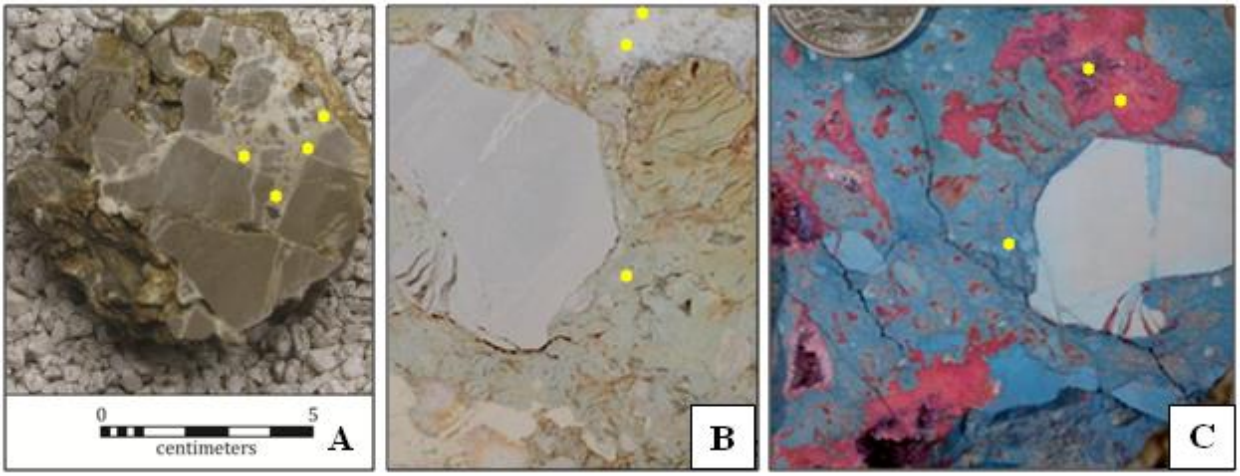

Figure 30. Samples which were selected for isotope analysis were drilled out to get only the desired portion of each sample, yellow dots depict areas which were drilled.

In (A) of Figure 30 the sample was drilled in the vein cement portion of the rock. Sample is from a well cemented breccia in the BSMSA. Images B and C are the same sample. C has been stained for carbonate identification using alizarin red and potassium cyanide solution. The turquoise color is ferroan dolomite, the red is calcite (late-stage) and the violet is ferroan calcite, the last stage fluid. The samples were drilled for XRD and then those samples were used for isotope analysis.

Two loading techniques were used for each of the powdered samples. For samples with ample (greater than one teaspoon) powder, metal cup mounts were used. Each mount was affixed with a glass plate and filled using a metal scoop. Care was taken not to tap or knock the mount to ensure

random orientations of grains within the sample holder before removing the glass plate. For samples with very small amounts of powder, the sample was sprinkled carefully and evenly on a petrographic slide lightly coated in petroleum jelly. Using either method the mount or slide could then be centered onto the XRD sample holder so that the maximum width of the powdered sample would be hit by the X-rays. To ensure that all directions of the randomly-oriented crystals are sampled by X-rays, the machine's goniometer rotates the arm of the machine containing the cathode tube at an angle of 2Θ, thus producing numerous peak diffraction patterns (Bish et al., 1989).

The ICAL facility at MSU possesses a SCINTAG X1 Diffraction Spectrometer and computer-aided mineral identification system. This model of diffractometer operates by heating a filament within the cathode tube to produce electrons, which are then accelerated toward the sample holder by applying a voltage of 1.00 kilovolts (kV) at a sample distance of 250 millimeters (mm). Once the emitted electrons dislodge the inner shell electrons of the powdered sample, an X-ray spectrum (CuKα1) is produced with a wavelength of 1.540562 angstroms (Å). The intensity of the reflected X-ray is then recorded, and a relative peak height in intensity occurs, which is recorded in counts. The detector setup is a liquid nitrogen cooled solid state detector with a Bragg-Brentano theta: theta configuration and the diffractometer is accurate to within 0.2 degrees.

At the beginning of each XRD session at ICAL, the goniometer was initialized using SCINTAG Diffraction Management System for NT (DMSNT) software and automatically aligned using a brass plate using both a coarse (0.3 second preset time, 0.05 degree step size, 1 degree start/stop offset) and fine (0.3 second preset time, 0.01 degree step size, 0.2 degree start/stop offset) alignments. The purpose of these alignments is to maximize the peak intensity and minimize the offsets added to the experimental diffraction pattern. Peak intensities were generally between ~10,000-12,000 and offsets <0.05, so as not to be too high to compare to standards in the computer database. Each of the 43 samples was then run using the same parameters. The slit sizes were kept fixed for each run, with the tube having 2 mm (divergence) and 4 mm (scatter) slit widths, and the detector having 0.5 mm (scatter) and 0.2 mm (receiving) slid widths. The scan event operated with a 0.02° step size with a start angle of 20° and a stop angle of 80°. Each scan ran continuously at 0.6 seconds per step at a rate of 2.00 degrees per minute.

Once each scan was complete, a raw curve was saved to the computer. Using DMSNT software, the background was subtracted and peaks found by converting peaks to lines, with a more in-depth visual confirmation that all peaks were identified by the computer software. The International Centre for Diffraction Data (ICDD) was used in conjunction with LookPDF software using search match techniques to match diffraction patterns from each scan with standard patterns in the diffraction database. Each card was then superimposed on the experimental pattern to identify the individual crystal structures within the sample. Once X-ray diffraction was performed on the samples from the BSFS and SWC, the relative compositions of minerals within the sample could be quantified. Chave (1952) was the first to determine a partial solid-state solution between calcite ($CaCO_3$) and dolomite ($CaMg(CO_3)_2$) using XRD.

This method is particularly useful because it relates the differences in ionic sizes between substituting and host cations, which are expressed by the interplanar d-spacing for the major cleavage (104) of calcite. This experiment, chemically determined, resulted in an empirical curve relating calcite and dolomite, it has been utilized and refined in later experiments by Goldsmith et al. (1955, 1961), Goldsmith and Graf (1958), Milliman et al. (1971), Bischoff et al. (1983), and most recently, Zhang et al. (2010). The results from this project's X-ray diffraction analyses were compared with the experimental curve from the Zhang et al. (2010) paper, which characterized the ordered and disordered magnesium content of samples based on numerous researchers' findings (Figure 31).

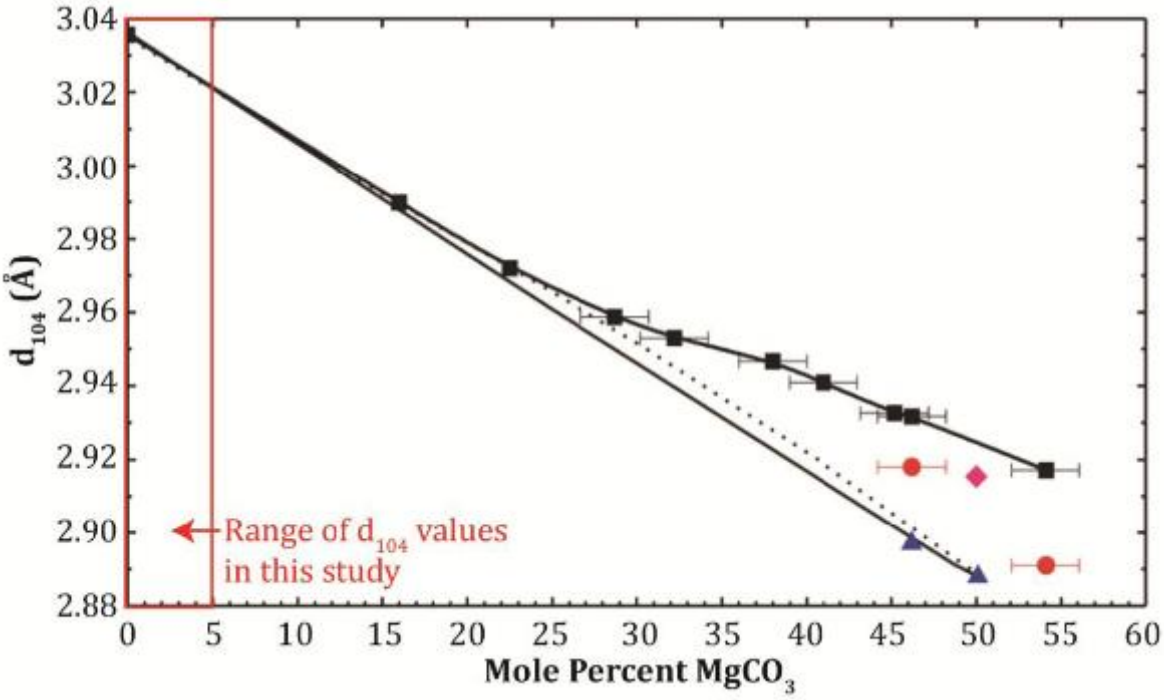

Figure 31. Empirical curve between d_{104} values and mole percent dolomite.

In Figure 31, black squares are disordered dolomite data points from the Zhang et al. (2010) study; purple triangles are from ordered dolomite samples; the pink diamond is from an almost-ordered dolomite sample; and red circles are from weakly ordered dolomite. The straight solid and dashed black lines are the idealized curves from Goldsmith and Graf (1958) and Goldsmith et al. (1961) (modified from Zhang et al., 2010; figure from Jeffrey, 2014).

Stable C and O isotope analyses

Stable isotope analysis is a useful tool for studying the influences of meteoric and/or marine waters on a carbonate system, and aims to identify the different sources of dissolved carbonate as well as the rock-water interactions that commonly drive carbonate diagenesis (Arthur et al., 1983). In each study area stable carbon and oxygen isotope values were measured at the University of Michigan Stable Isotope Laboratory to determine the source of the water as given by the isotopic signature within matrix material of the brecciated samples, vein fill material and

host rocks (Figure 32). The same powdered samples were used as in the XRD analysis; therefore, no additional preparations were necessary if enough sample was prepared.

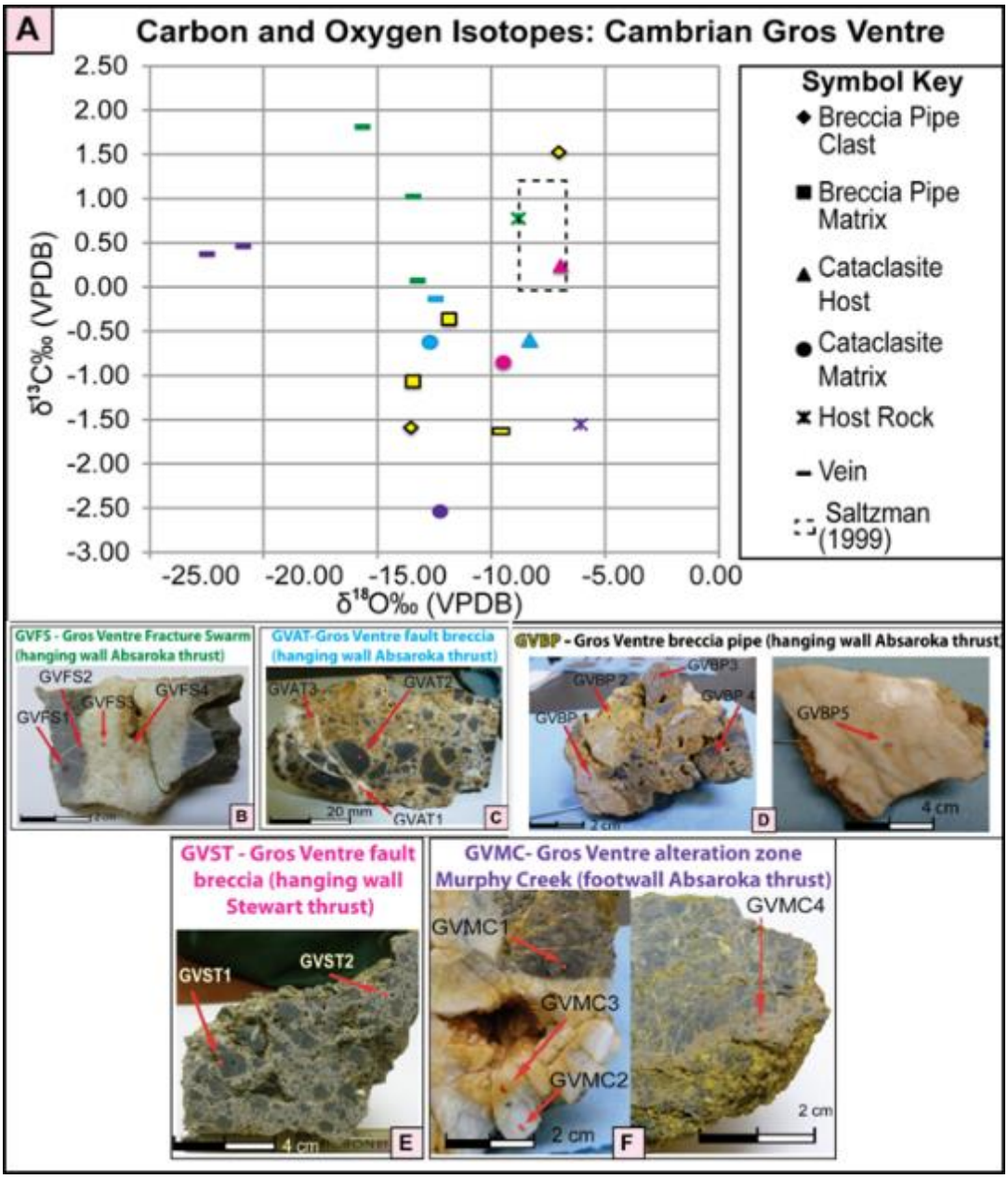

Figure 32. Stable carbon and oxygen isotope values were measured

Figure 32.A) Carbon and oxygen stable isotopic compositions of Cambrian samples from the SPC. Stable isotopic compositions of Late Cambrian rocks sampled across Montana and Wyoming by Saltzman (1999) are shown in the dotted box for comparison. These isotopic data were used to correlate regional chemostratigraphic boundaries. These carbon and oxygen isotopic values from Saltzman (1999) are within the range of expected values for marine carbonates (Hoefs, 2009). B) Samples analyzed from the Gros Ventre Fracture Swarm. C)

Samples analyzed from the hanging wall fault core of the Absaroka thrust. D) Samples analyzed from the Gros Ventre Breccia pipe in the hanging wall of the Absaroka thrust –GVBP 5 not shown. E) Samples analyzed from the hanging wall fault core of the Stewart thrust. F) Samples analyzed from the Murphy Creek alteration zone (figure adapted from Lynn, 2012).

An isotopic analysis was performed by reacting a minimum of ten micrograms of the powdered sample in stainless steel boats with four drops of anhydrous phosphoric acid for eight minutes (twelve for predominately dolomitic samples) in a borosilicate reaction vessel at 77 ± 1°C. These reaction vessels were then placed in a Finnigan MAT Kiel IV preparation device coupled with a Finnigan MAT 253 triple collector isotope mass spectrometer. O^{17} data was corrected for acid fractionation by correcting to a best-fit regression line determined by the standard NBS 19. This method is accurate within 0.1‰ (Wingate, 2013). Results were categorized in a spreadsheet based on breccia pipe location and sample material, and then graphed as a scatter plot with laboratory standards.

Stable isotope results are given in comparison to the standard VPDB, which is calibrated through the analysis of an international reference laboratory standard from the U.S. Natural Bureau of Standards (NBS) (Arthur et al., 1983). The δ (delta) values for oxygen and carbon stable isotopic ratios discussed in this report are referenced to the following standard materials: Vienna Pee Dee Belemnite (VPDB) and Pee Dee Belemnite (PDB) based on Veizer et al., (1999). Most Current literature report values based on VPDB because its use implies that the measurements have been calibrated according to IAEA (International Atomic Energy Agency) guidelines for expression of delta (δ)values relative to available reference materials on normalized per mil scales (Coplen, 1994). Older literature may refer to PDB which is the original standard from which the equivalent VPDB has been derived since there is no longer a supply of PDB material. NBS-19 is a standard derived from a homogenized white marble of unknown origin. The Standard Mean Ocean Water (SMOW) is a hypothetical standard in which oxygen and hydrogen ratios are similar to that of the average ocean water, which can be compared to VPDB values by the equation

$$(1) \quad \delta^{18}O_{SMOW} = 1.03086\ \delta^{18}O_{VPBD} + 30.86$$

Results are reported in delta (δ) notation, which is a ratio of stable isotopes given by the equation

$$(2)\ \delta = \frac{R_{sample} - R_{standard}}{R_{standard}} \text{ x } 1000$$

where "R" is the ratio between either $^{13}C/^{12}C$ or $^{18}O/^{16}O$, the standard is either VPDB or SMOW, and units are per mil (‰) (Faure, 1998).

Radiogenic Strontium Isotope analysis

The isotopic composition of strontium (Sr) in rocks, minerals, and fluids carries geochronologic stratigraphic and provenance information due to ß$^-$ decay of ^{87}Rb to ^{87}Sr. Resulting variations in the radiogenic $^{87}Sr/^{86}Sr$ ratio generally vary with age and Rb/Sr ratios making the $^{87}Sr/^{86}Sr$ ratio

an excellent tracer for the source(s) of Sr (Scher, et al., 2013). Strontium isotopes can be used to trace fluid interactions with different rock types.

Sr isotope methodology
Powdered samples were prepared as described for XRD portion above at MSU. Work to separate Sr from the powdered rock samples was performed in a clean lab in Laramie, Wyoming. Approximately 100 mg of each of the powdered samples was weighed on a Metler Toledo model AX204 scale and put into 60 ml Teflon beakers. Working under a hood calcite, limestone and dolomite were each dissolved with 3 ml 1N hydrochloric acid (HCl) and let sit for 48 hours to dissolve. Fluorite was dissolved with 1ml concentrated nitric acid (HNO_3) then 3 ml perchloric acid ($HClO_4$) was added; the samples were placed in an Analab Eurotherm 2132 model gas collector under a hood to dissolve. Breccia samples were dissolved with 3 ml concentrated HNO3 + 1ml $HClO_4$ + 2ml concentrated hydrofluoric acid (HF) and placed on a hot plate set at 130°C to dissolve for 48 hours.

After calcite, limestone and dolomite samples had sat in 3N HCL for at least 24 hours each sample was poured into 5 ml centrifuge tubes, rinsing down beaker with 1N HCL to remove all detritus to centrifuge tube. If some detritus remained in the beaker it was rinsed with H_2O and discarded. The samples in tubes were centrifuged for 2 minutes at 3000 rpm on an Eppendorf centrifuge model 5702 (with caps wrapped in parafilm). For each sample, supernatant was pipetted back into the Teflon beaker that was rinsed out prior to centrifuging. The precipitate (or detritus) was left stored and labeled in the 5 ml centrifuge tubes with a small amount of HCL for possible further study. The Teflon beakers of calcite, limestone and dolomite samples were placed open containered, on a hot plate set at 130°C overnight to dry down.

In the morning the dried down calcite, limestone and dolomite samples were described prior to adding 8-10 ml 7N HNO_3 to each sample. The samples were capped and placed on a hot plate set at 130°C for approximately 8 hours. Removed caps and returned samples to hot plate to dry down overnight.

Sr Resin microcolumns – snipped-off HDPE transfer pipettes fitted with train-ticket punched out polyethylene frit at bottom

- Column ~ 500 µl Sr resin
- reservoir capacity is approximately 4 ml
- Drip rate: ca. 20 min/ml or 1h20 min./reservoir

Resin prep: Make slurry of resin with H_2O* (*if sample in chloride form, convert to nitrate prior to loading step), shake, let settle several hours or best overnight, pipette off floating surface material with transfer pipette.

Day 1 Sr Resin microcolumns (cleaning step) - cleaned out resin pipettes which were fitted with polyethylene frit at bottom with 50% HCL, then with nano purified water. Set up batch (8-12 microcolumns) of pipettes on a stand with waste beakers below each microcolumn. Loaded resin

into columns with 1 reservoir of H_2O. Then added 1 reservoir of 6N HCL; cleaned with 1 reservoir of H_2O. *each loading step takes about 1h20 min from last column added.

Day 2 Strontium columns – (Condition columns) conditioned Sr columns with 1 reservoir (pipetted) 3N HNO_3 . Rinsed Sr columns with 1 ml 3N HNO_3 Elute matrix with 4 ml 3N HNO_3

Next 6 ml 3N HNO_3 was added to samples that had been dried down to a salt sized grain; put on hot plate for 30 minutes. Removed and let cool then loaded samples into 5 ml centrifuge tubes; spun these down. If no precipitate was present loaded samples.

Collect Sr – add 3 ml H_2O to each column with collection beakers below columns to collect Sr in solution. Removed collection beakers from below Sr columns and placed on hotplate set at 90°C to dry overnight. The next day added 3 drops from syringe concentrated HNO_3 and 1 drop hydrogen peroxide H_2O_2 and let these dry down.

In the mass spectrometer room added 1 ml 1N HNO_3 to each sample and let these dissolve. Sample ready to run on NEPTUNE Plus MC-ICPMS. Sample was diluted and tested for Sr strength before being analyzed by the instrument. Isotopic analysis was performed on the NEPTUNE Plus, a next-generation Multicollector-Inductively Coupled Plasma Mass Spectrometer (MC-ICPMS). $^{87}Sr/^{86}Sr$ reported relative to NBS987 = 0.710240 and two other standards were used during the analyses including BCR (Columbia River basalt) and SRM915 a $CaCO_3$ standard.

This procedure was repeated for each batch. The fluorites and breccias took longer to dry down and had to be on the analab to dry down. The extra time needed to dry down may have been due to organics in the solution once the elements were disassociated in the acids.

Scanning Electron Microscopy

SEM was used at ICAL at Montana State University to take high resolution images of samples from each of the study areas. It is a JEOL JSM-6100. A SEM uses a highly-focused beam of electrons from a LaB6 source to scan a sample. It operates off of the principle that kinetic energies which are much lower than primary incident electrons (containing lower energies and lower penetration depths) can detect secondary electrons as a consequence of the position of the beam. This results in magnifications up to 100,000 times and resolutions up to 40 amperes (A) in some samples (Montana State University Department of Physics, 2011). The SEM at ICAL has EDS capabilities and this part of the SEM was used to determine the composition of some samples from the different study areas. Energy-Dispersive x-ray spectrometry works by the interaction of an electron beam with a sample target. This produces a variety of emissions, including x-rays. An energy-dispersive (EDS) detector is used to separate the characteristic x-rays of different elements into an energy spectrum, and EDS system software is used to analyze the energy spectrum in order to determine the abundance of specific elements. EDS can be used to find the chemical composition of materials down to a spot size of a few microns, and to create element composition maps over a much broader raster area. Together, these capabilities provide fundamental compositional information for a wide variety of materials

Secondary Electron Imaging and ImageJ Statistical Calculations

The SEM at ICAL was used to take topographical images of ten samples from the BSFS and six samples from SWC. Rock samples were whole chips approximately 3-5 mm in length. Samples were mounted on a coater tray and secured using carbon tape, then sputter coated with iridium at 20 milli-amperes (mA) for 20 seconds. Digital images were taken using MImage version 1.0. Greyscale SEM images were then imported into BoneJ, a plug-in of the freeware ImageJ version 1.47 in order to determine the two-dimensional cross-sectional porosity present within the brecciated samples. This was accomplished by correcting each photo with a color threshold, which then aided in calculating percent area porosity (Figure 33).

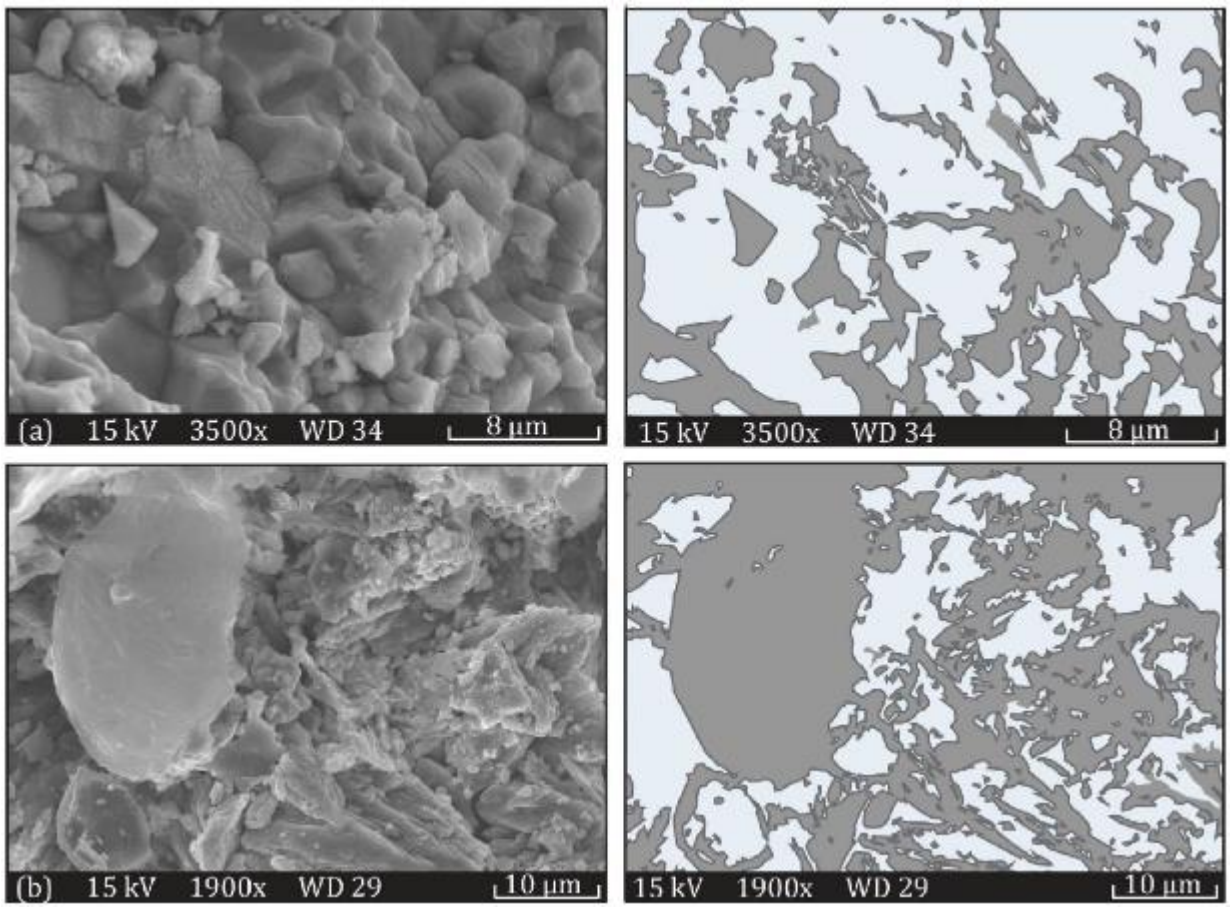

Figure 33. SEM and BoneJ analyses of matrix material from breccias highlighting the amount of porosity present.

Figure 33 shows SEM (left) and the BoneJ plug-in of ImageJ (right) analyses were of matrix material from breccias BSM-007a (a) and BSM-013a (b). Color thresholds (dark grey enhancement in the images on the right) were applied, which emphasize the increase in two-dimensional area porosity. Calculations revealed a 5 to 25% increase in area porosity.

Cathodoluminescence

CL Optical cathodoluminescence (optical-CL) permits optical examination or imaging of a sample through the attachment of an evacuated CL-stage to an optical microscope. The CL-stage attachment uses a cathode gun to bombard a sample with a beam of high-energy electrons. The resulting luminescence in minerals allows textures and compositional variations to be viewed that are not otherwise evident using light microscopy. The stage allows X-Y movement of the sample to examine much of the surface area in the sample (serc.carleton.edu website). The Earth Science Department at MSU has a RELIOTRON CL instrument which is attached to a Nikon Microscope. Thin sections were polished and left uncovered to perform CL analysis on. The CL was used to look at vein fill material as well as matrix material in several of the study areas. The CL shows multiple episodes of vein fill in Figure 34.

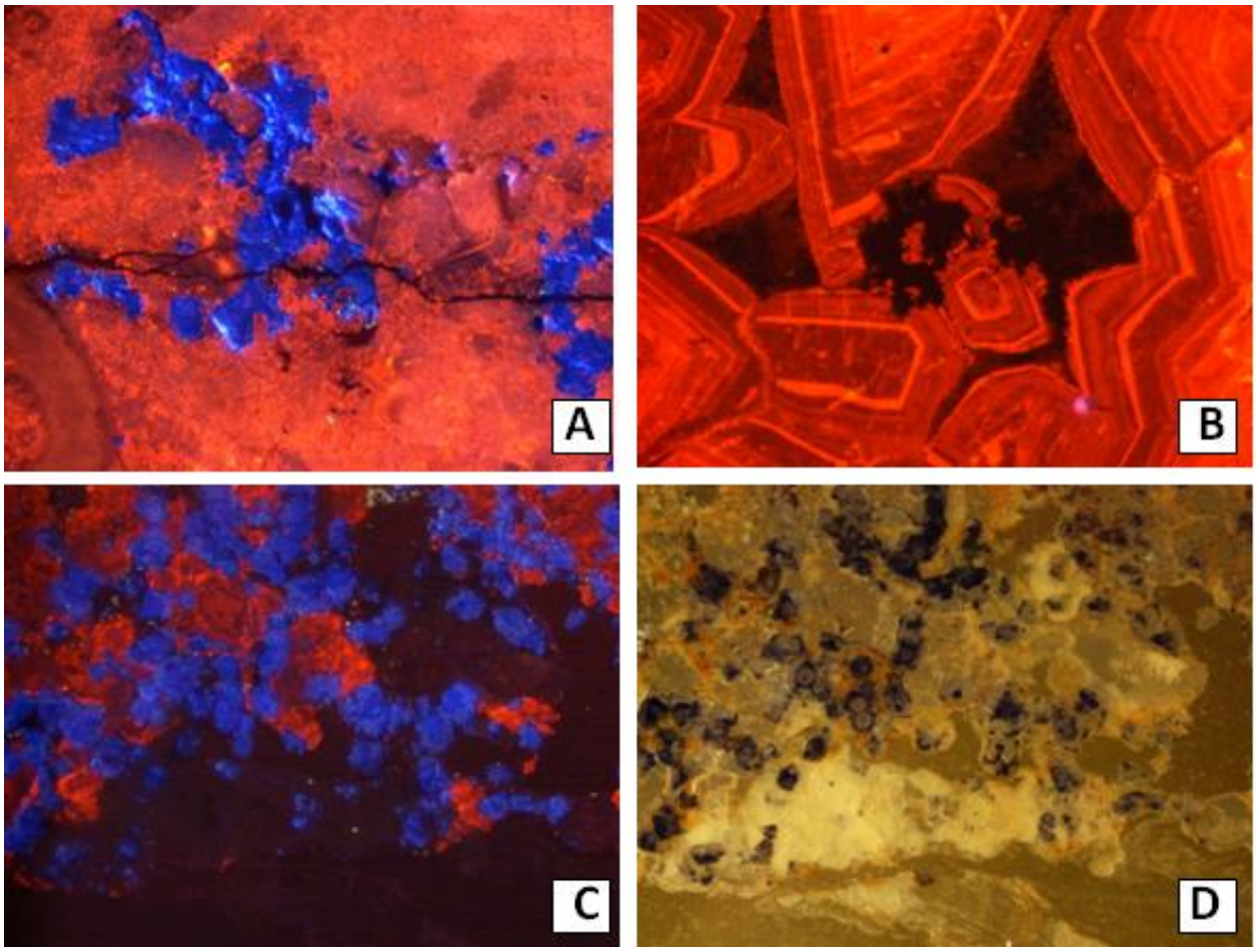

Figure 34. CL shows multiple episodes of vein fill

In Figure 34, CL images A, B. and C. D is the same view as C viewed without the CL under plane polarized light, magnification is 4X. With CL the fluorite shows up bright blue in A and C. It is replacing oolites visible in D. The red color is calcite and the darker part of C & D is mostly dolomite. Image B (10 X magnification) shows zoning of iron rich calcite and also sulfides and bitumen filling in the void spaces and replacing some of the calcite. The samples are from the PMSA.

Standard Petrography
All of the study areas in the project utilized standard petrography techniques to examine samples which were collected in the field. Samples were brought back to MSU and billets were cut from selected areas of each sample. Many thin sections were made without cover slips so that CL and SEM techniques might also be applied. Some thin sections were prepared as double polished slides for fluid inclusion work. Some thin sections were stained for carbonate (Figure 35, Figure 36, and Figure 37).

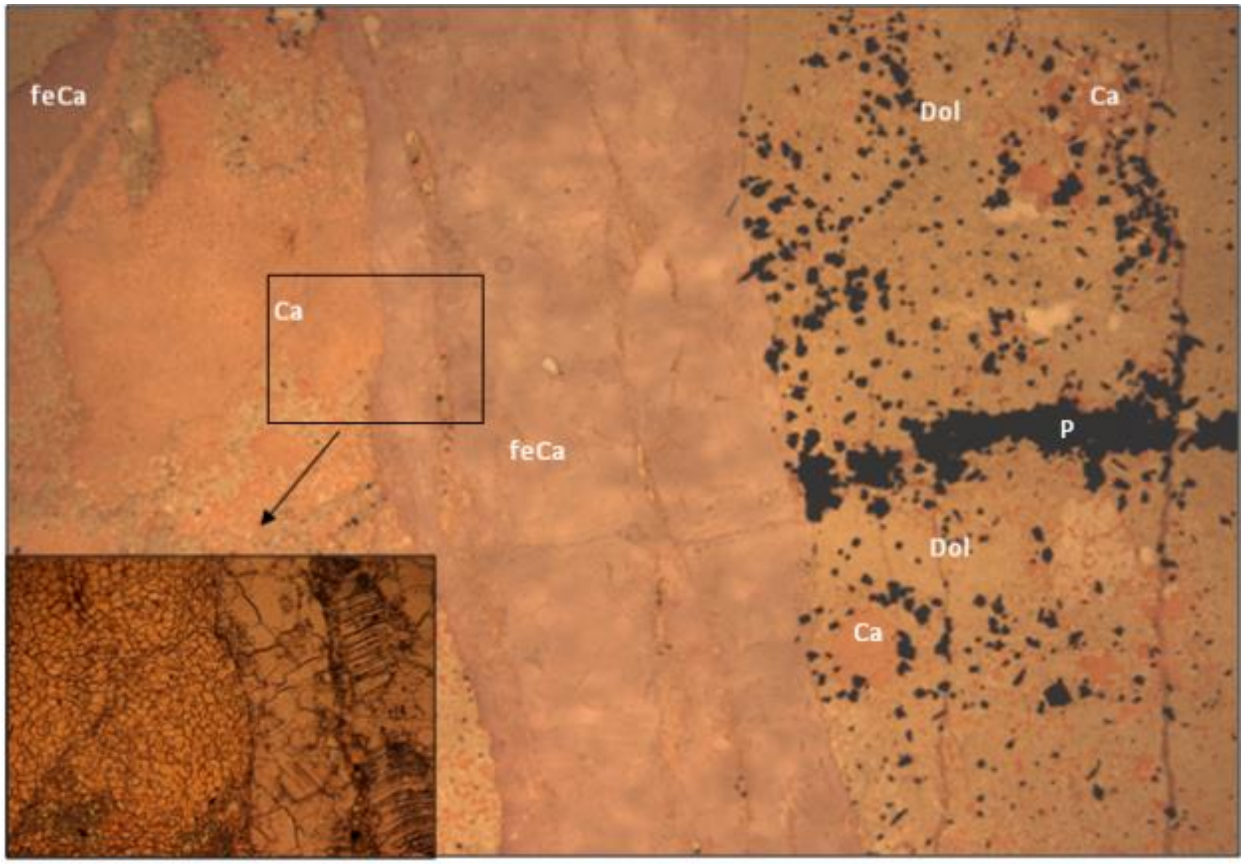

Figure 35. Thin sections stained for carbonate.

Figure 35 is a photomicrograph of thin section using the white card method to see textures easily in the stained thin section from PMSA, 2X magnification and plain polarized light. Section was stained with alizarin red and potassium ferricyanide. The red portions of the stained sample are mainly microspar calcite filling in voids in the dolomite host rock; the central light violet vein is coarse sparry late-stage ferroan calcite, and no color change is dolomite. The dark areas are sulfides, mainly pyrite. Area in black rectangle bottom left detail of section with arrow is ppl and 10X magnification. Dol, Ca, feCa and P are labels for dolomite, calcite, ferroan calcite and pyrite.

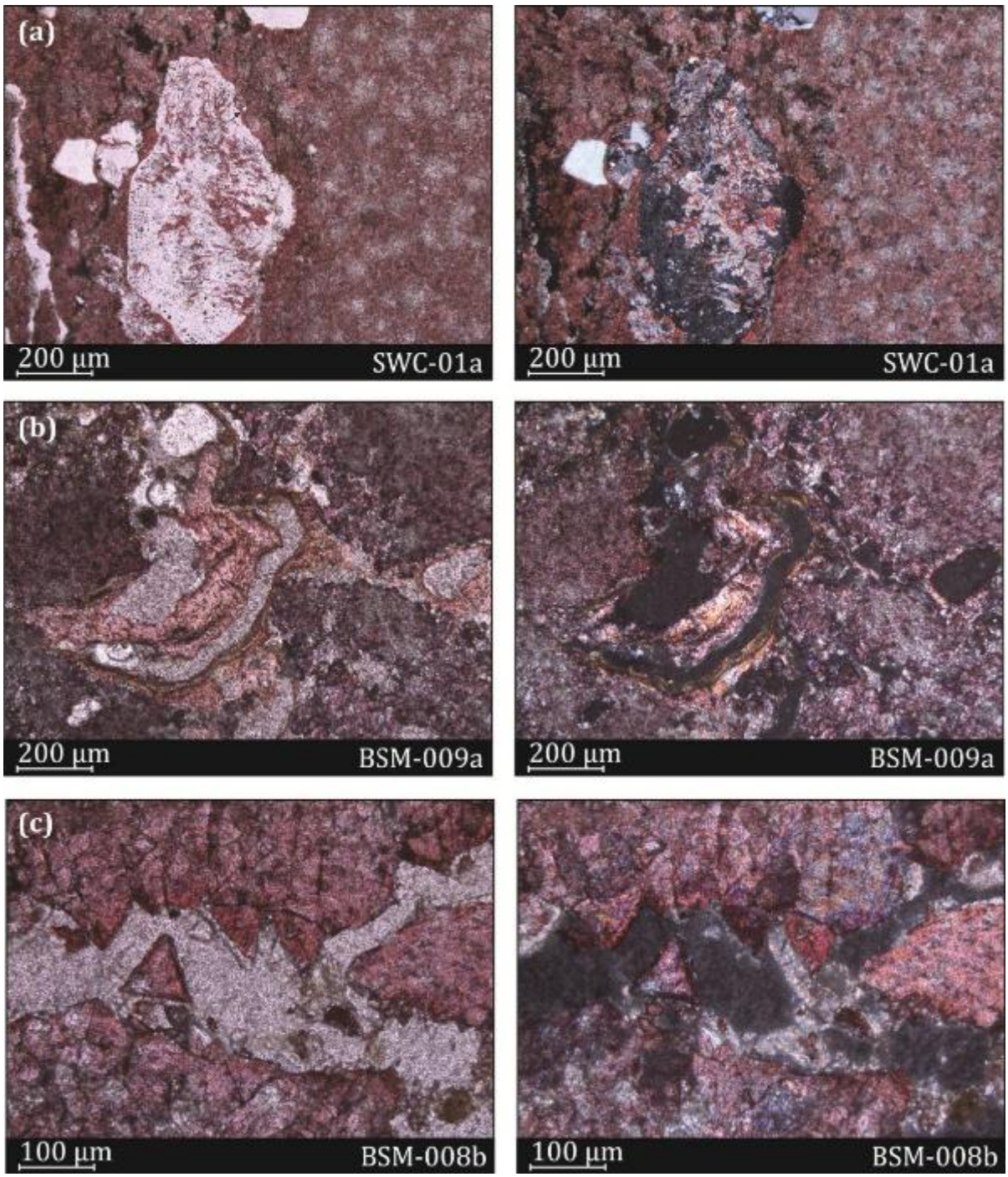

Figure 36. Petrographic images of hydrothermal breccias from BSMSA exhibiting the variations in secondary mineral precipitation and porosity development.

In Figure 36, the left column displays samples in plane-polarized light; the right in cross-polarized light. SWC- 01a (a) shows a highly replaced Herkimer quartz crystal surrounded by calcite rhombs and matrix dolomitization. BSM-009a (b) displays a vug lined with early calcite and dolomite cements and late-stage iron. BSM-008b (c) is of a void that had been created by

fracturing, and is lined by coarse calcitic cements. This void has been bridged by a late-stage dolomite cement event, which is interpreted to reduce the permeability that had been created by tectonic events. *These thin sections were stained for carbonates.

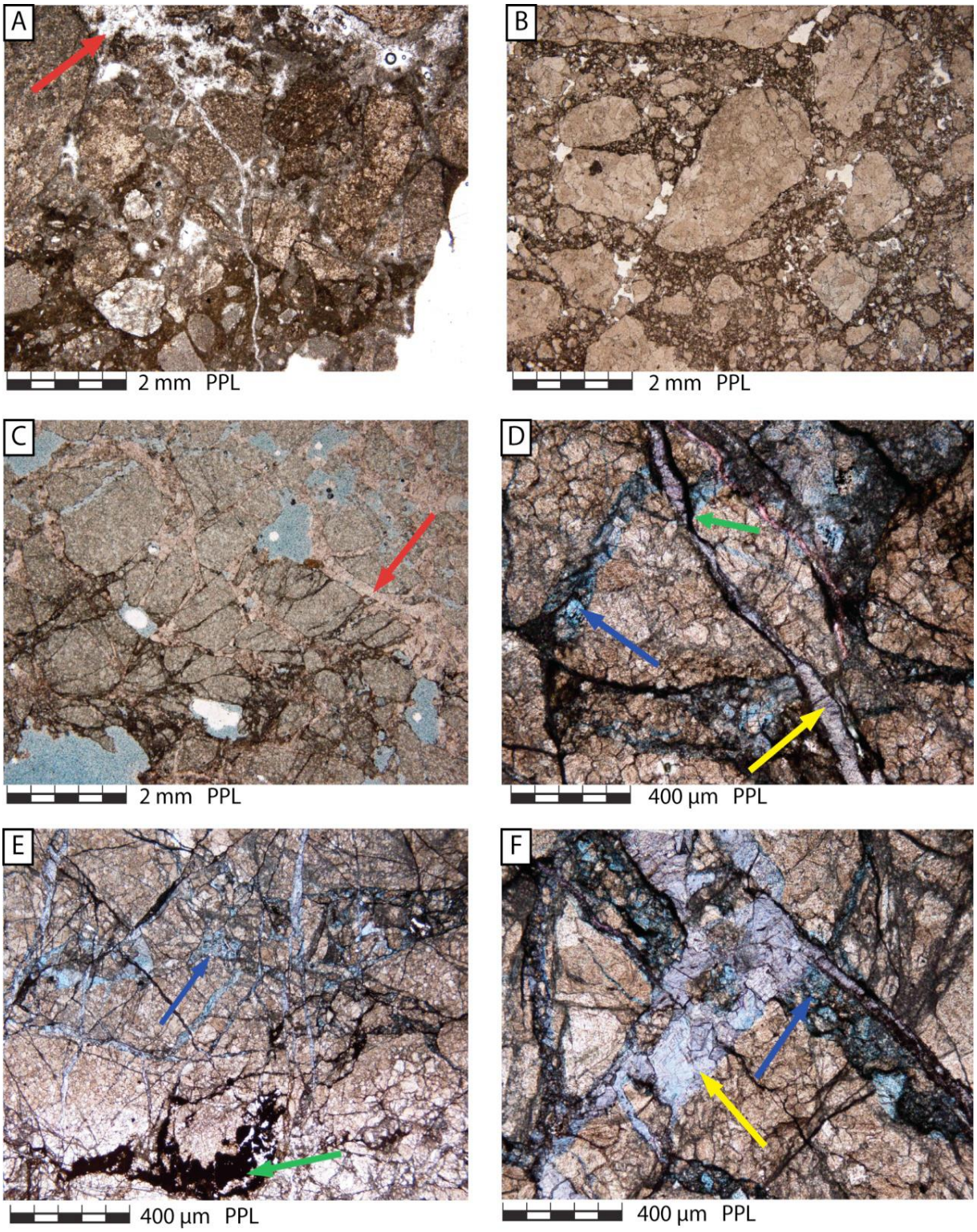

Figure 37. Thin section photomicrographs showing fault breccias in the Cambrian Gros Ventre Formation (photos C-F are of stained thin sections).

Figure 37 A) is fault breccia from the hanging wall of the Absaroka thrust showing recrystallization of the matrix (arrow) and a late stage calcite vein. B) Fault breccia from the hanging wall of the Stewart thrust. Note the general matrix porosity. C-F) Brecciated Gros Ventre samples collected near a small-scale fault in the Murphy Creek area C) Late-stage calcite (stained pink) has recrystallized much of the cataclastic matrix (red arrow). The teal areas are stained epoxy, not ferroan dolomite. D-F) Ferroan dolomite (stained turquoise – blue arrows) and ferroan calcite (stained purple – yellow arrows) veins precipitated along fractures and in intercrystalline porosity. Early ferroan dolomite (Blue arrows) was offset, by later ferroan calcite-filled fractures. The dark material lining fracture walls is bitumen (hydrocarbon residue – green arrows). The matrix is a coarse sparry dolomite, which was likely an early diagenetic product postdated by fracturing and cementation.

RESULTS AND DISCUSSION: NATURAL ANALOGS OF ESCAPE MECHANISMS

Two theses were completed and published based on this work and one is in review. These areas have been referenced during the duration of this project, following are the abstracts and location maps and a few figures from the areas.

Stewart Peak Culmination Study Area – SPC
Helen Lynn's abstract from her master's thesis
The Stewart Peak culmination is a duplex fault zone of the Absaroka thrust sheet, which is part of the Sevier fold-and-thrust belt in western Wyoming. Duplex structures can serve as subsurface oil, gas and carbon dioxide (CO_2) traps. The culmination lies east and up-dip from naturally occurring CO_2 traps in Idaho and west of the Moxa arch in Wyoming, another naturally occurring CO_2 trap and potential target for CO_2 sequestration. The culmination has been uplifted and breached by erosion, exposing traps and reservoir rocks analogous to proximal subsurface structures, thus allowing for outcrop-scale investigation of the elements that comprise a complex trap and an analysis of the relative timing of faulting, fracturing, fluid migration and structurally-controlled diagenesis.

The purpose of this study was to characterize structural elements of the Stewart Peak culmination that controlled fluid flow. Field-based analyses of fractures, fault damage zones and breccia pipes were conducted in order to assess how these structures affected fluid flow. Rocks were sampled in order to elucidate the diagenetic characteristics of alteration associated with episodes of fluid migration and document the qualities of reservoir rocks.
Faulting has led to extensive fracturing and brecciation of rocks in the culmination. The geometry of faults and fracture sets initially controlled fluid migration pathways. Brecciated fault zones of large-displacement thrusts served as focused fluid conduits. Fracturing also facilitated fluid flow, locally enhancing porosity and permeability. The protracted history of deformation in the culmination helped maintain fluid flow pathways through fractures zones. Fault zones and fractures display complex diagenetic alteration as a result of multiple episodes of deformation and fluid migration. Sub-vertical fracture swarms and breccia bodies dissect some fault zones and represent discrete vertical fluid pathways through which CO_2-charged hydrothermal fluids

were focused. Hydrothermal brines may have enhanced structurally controlled fluid migration pathways through interrelated processes of effervescence-induced brecciation and dolomitization.

Faulting, fracturing, brecciation and diagenetic alteration generally enhanced the quality of reservoir rocks and increased the hydraulic connectivity within the culmination. The enhanced porosity and permeability of the Madison Limestone and Bighorn Dolomite indicate that these reservoirs have good potential for CO_2 sequestration.

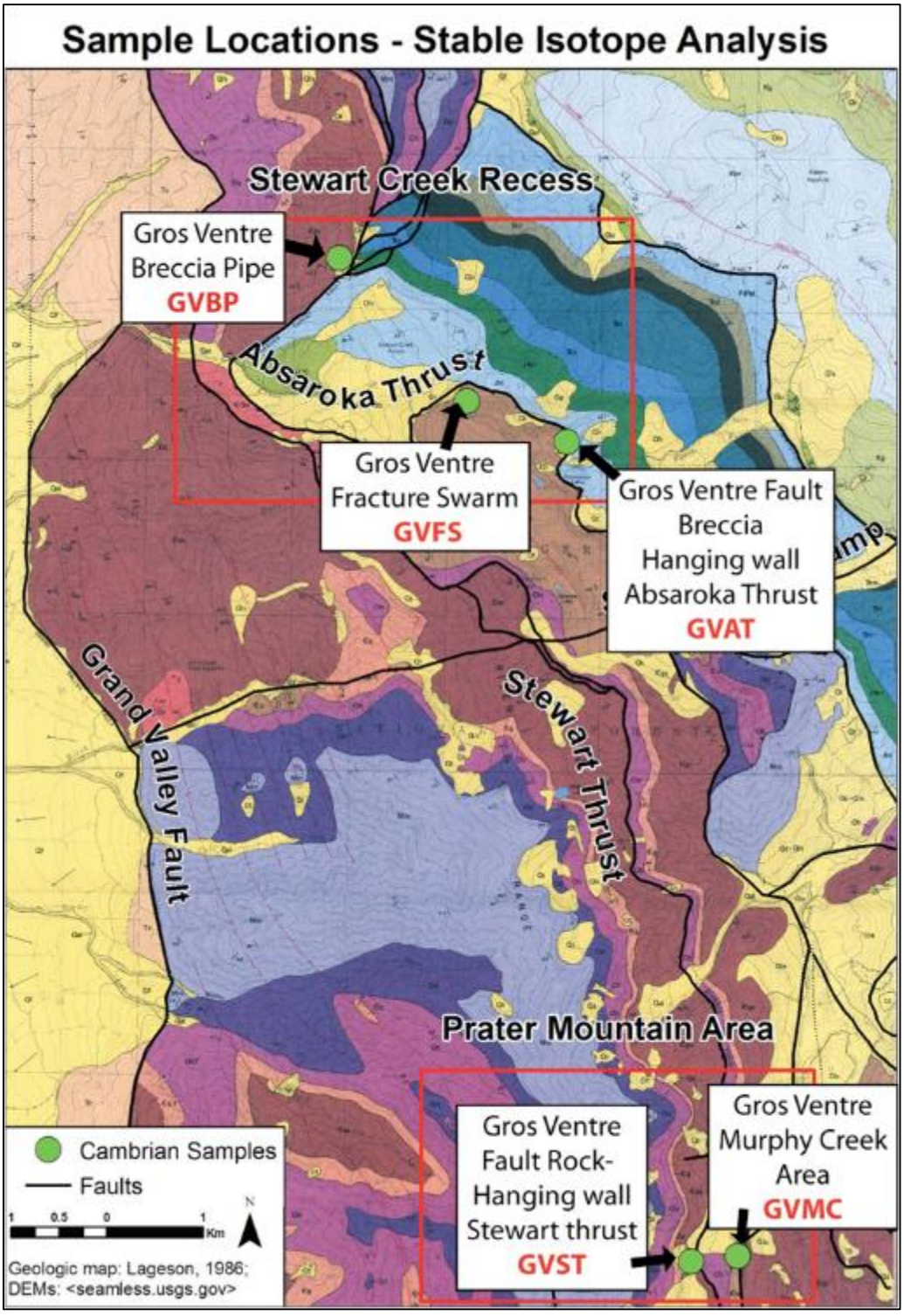

Figure 38. Locations of Cambrian samples collected for stable isotope analysis in the SPC. Several of the samples from these locations are shown in **Figure** 32.

The samples were chosen for both stable C and O stable isotope work and referenced to the fracture stations which spanned the hydrothermally altered field site. Having multiple geological analyses in an area such as thin sections, fracture stations, and chemical analyses including isotope work supports the characterization of the unit being studied.

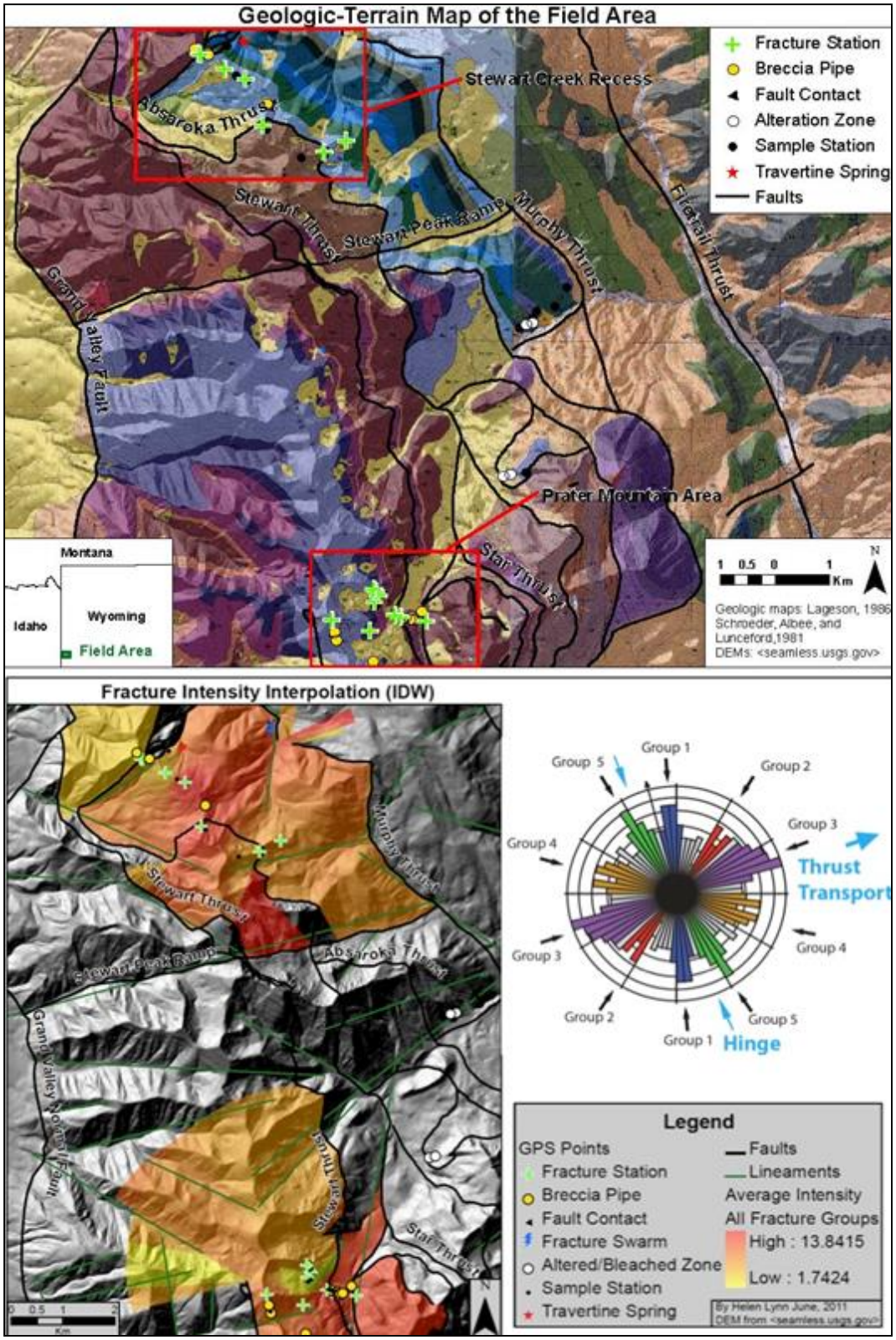

Figure 39. Top figure shows locations of study areas in the SPC. Bottom shows fracture intensity in the areas. The rose diagram shows the orientations of fractures measured in the field.

Thermopolis Anticline Study Area – TSA

Whitney Treadway's abstract from her master's thesis (thesis is under review):

As global greenhouse gas emissions increase, it is necessary to find ways to mitigate these gases in order to decrease the effects of anthropogenic climate change. One mitigation strategy is to capture and store CO_2 in viable geologic structures. This project focused on a geologic structure similar to those being used as CO_2 storage sites and potential leakage. This study was intended to gain insight on fracture patterns at a leaky CO_2 system. The geologic structure studied in this project is a Laramide-style, fault-propagation fold in the southern Bighorn Basin in Wyoming. During the course of this project, measurements on fractures were collected and analyzed in order to gain understanding of potential leakage in other similar structures. Measurements were taken on fractures throughout the anticline, including orientation, length, vein fill, and fracture aperture. Fracture orientations were grouped into hinge-parallel, hinge-perpendicular, and conjugate fractures. Hinge-parallel fractures are dominant throughout the field area because these fractures developed early on in folding and continued throughout folding. Other fracture orientations develop at variations in curvature and along basement weaknesses. Fracture intensity was greatest in the steep, southern limb and along the crest of the anticline, as well as in the more resistant, thinner formations. Vein fill is also greatest in the southern limb and crest of the anticline near the Bighorn River. Less vein fill occurs further from the river and hot springs. Multiple generations of vein material was found, resulting from multiple fracture opening events and/or recrystallization of previous vein material. Vein fill material and hot springs water migrate through the same pathways along the fractured south limb and crest, and at the strike-slip fault along the Bighorn River. While vein fill material and travertine deposits vary in age, both were formed from meteoric water percolating into the system; vein material formation water interacts more with host rock and other vein material, while travertine formation water has less interaction with adjacent rock. Implications for CO_2 storage are as follows; storage sites must have thick, less resistant caprock overlying entire structure, and structure must not be cut by sub-vertical faults that reach the surface.

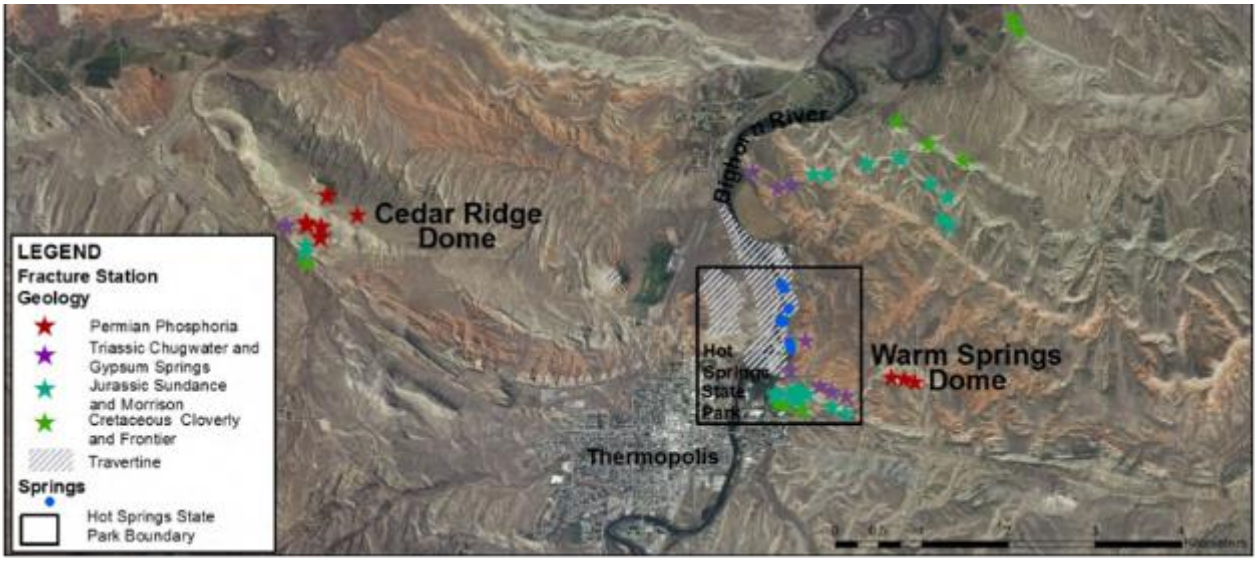

Figure 40. Fracture stations in the TSA study areas, Cedar Ridge Dome and Warm Springs Dome.

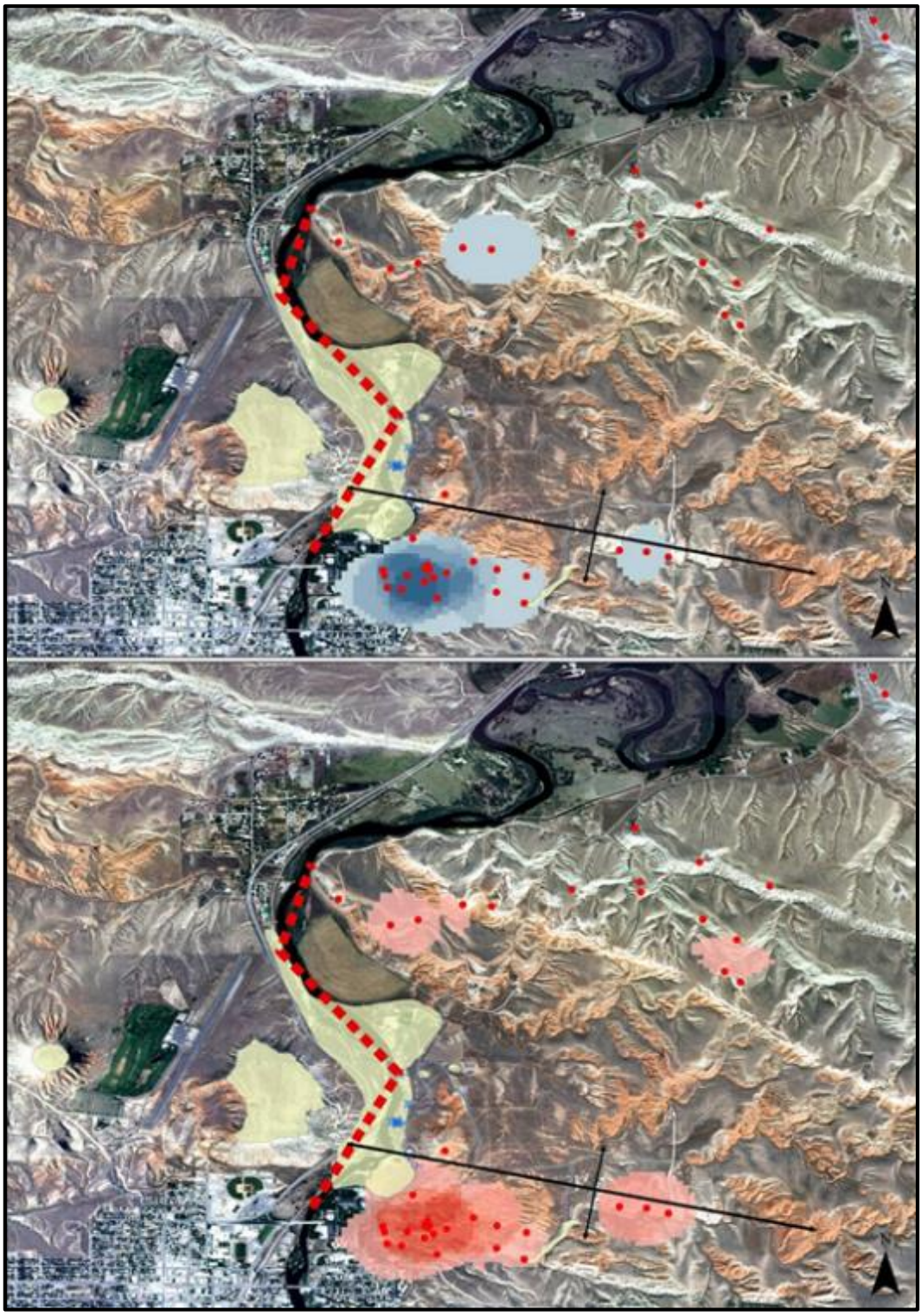

Figure 41. Top map showing vein fill in blue; darker blue shows higher vein fill values and travertine deposits are shown in yellow. Bottom map shows fracture intensity in red, with darker red indicating denser fracture intensity. Fracture stations in the TSA study areas are in red in this figure.

Big Snowy Mountain Study Area – BSMA

Sarah Jeffrey's abstract from her master's thesis:

The subsurface characterization of three-dimensional structural traps is becoming increasingly important with the advent of new technologies for the sequestration of anthropogenic carbon dioxide, which often takes place within pre-existing, sealed reservoirs to permanently store greenhouse gasses that are detrimental to the global climate. Within the Big Snowy Arch, central Montana, reservoir units that are targets for carbon sequestration have experienced Laramide and younger deformation and widespread Eocene igneous activity, which introduced a heating mechanism for hydrothermal fluid flow and created anisotropy in Mississippian strata. One particular region of interest is the western flank of the Big Snowy Mountains, which contains a northeast-southwest striking, high-angle fault zone which has acted as a conduit for hydrothermal brine solutions into the overlying Phanerozoic rocks. Such fault zones often branch and bifurcate as they propagate up-section through the overburden, until a loss of thermally-driven hydrodynamic pressure terminates the upward movement of carbon dioxide-rich brines, leaving a distinct assemblage of collapse breccia rich in hydrothermal minerals, such as saddle dolomite and sulfide precipitates. To determine the degree of structurally-induced anisotropy within the reservoir units, field techniques (detailed structural measurements and lithologic descriptions) coupled with analytical methods (X-ray diffraction spectrometry, stable carbon and oxygen isotope analyses, secondary electron imagery, and petrography) were utilized. These techniques presented concrete evidence of hydrothermal mineralization and episodic fluid flow within the brecciated region of the fault zone. These areas are major avenues of enhanced porosity and permeability in the subsurface, which has important applications at some sites in Montana where carbon sequestration is under consideration (e.g., Kevin Dome).

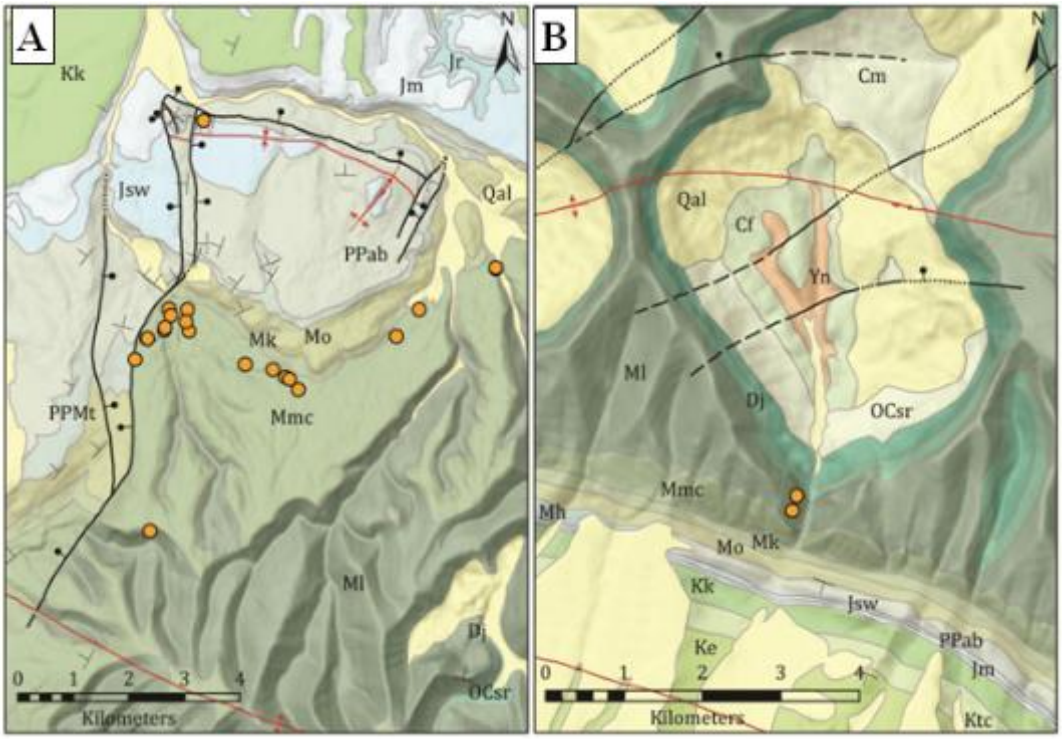

Figure 42. The BSFS field area (A) displays the location of 22 breccia pipes along the trace of the fault under study; the SWC field area (B) displays the location of two breccia pipes at the canyon entrance. These areas are shown in the following Figure 44.

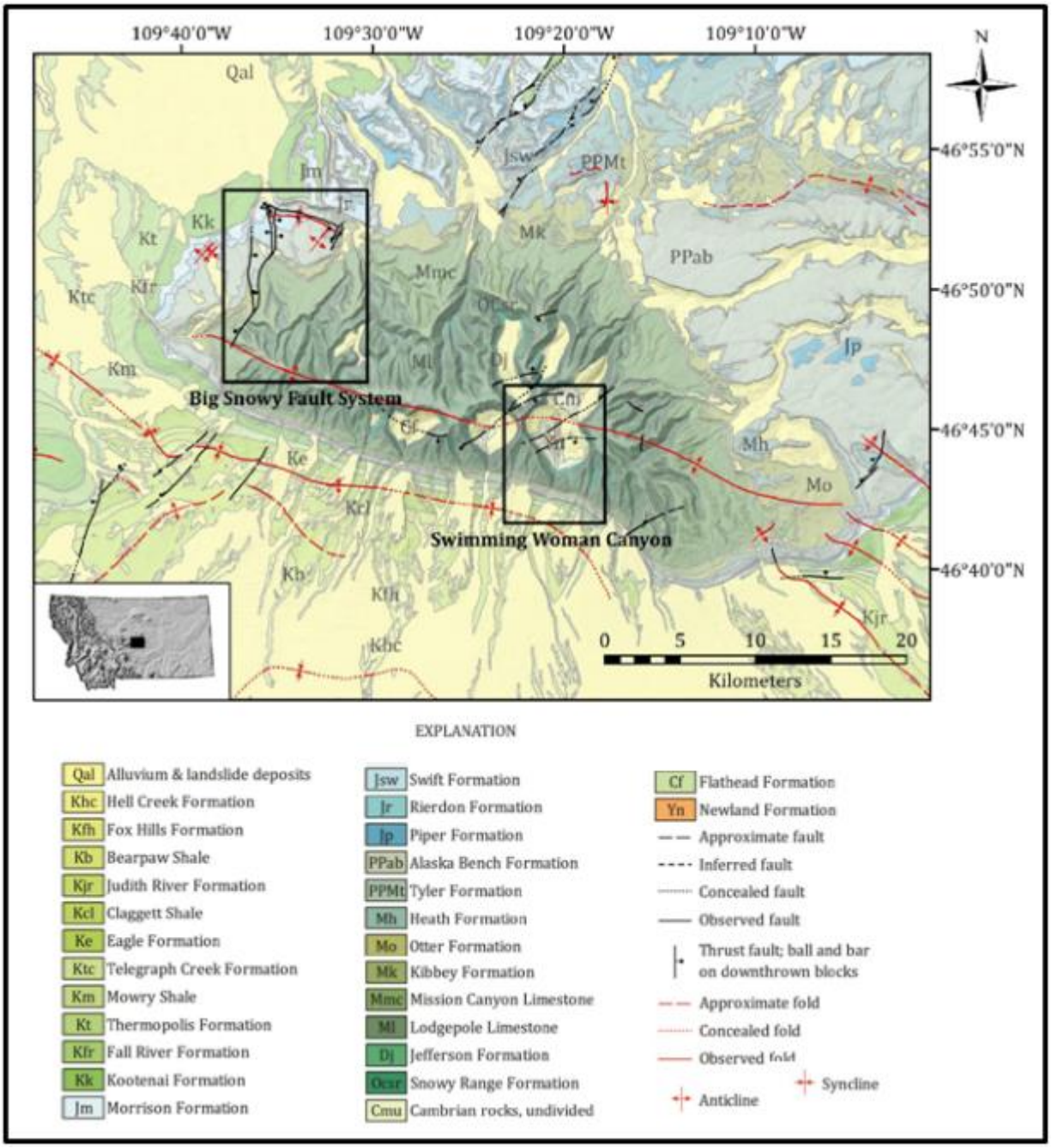

Figure 43. Field area map of the BSMSA. The Big Snowy fault system (BSF) and Swimming Woman Canyon (SWC) field areas are outlined and displayed over the geologic map for central Montana. Inset shows location within Montana.

The Big Snowy Mountain Study Area located at the western end of the Big Snowy Arch, is focused on a northeast-southwest-striking high-angle fault zone that transects the entire range and is rooted in the Precambrian basement (Figure 45) (Jeffrey, 2014). Basement-rooted faults are well known for their conductivity of warm, hydrothermal brine solutions into the overlying Phanerozoic rocks (Davies and Smith, 2006).

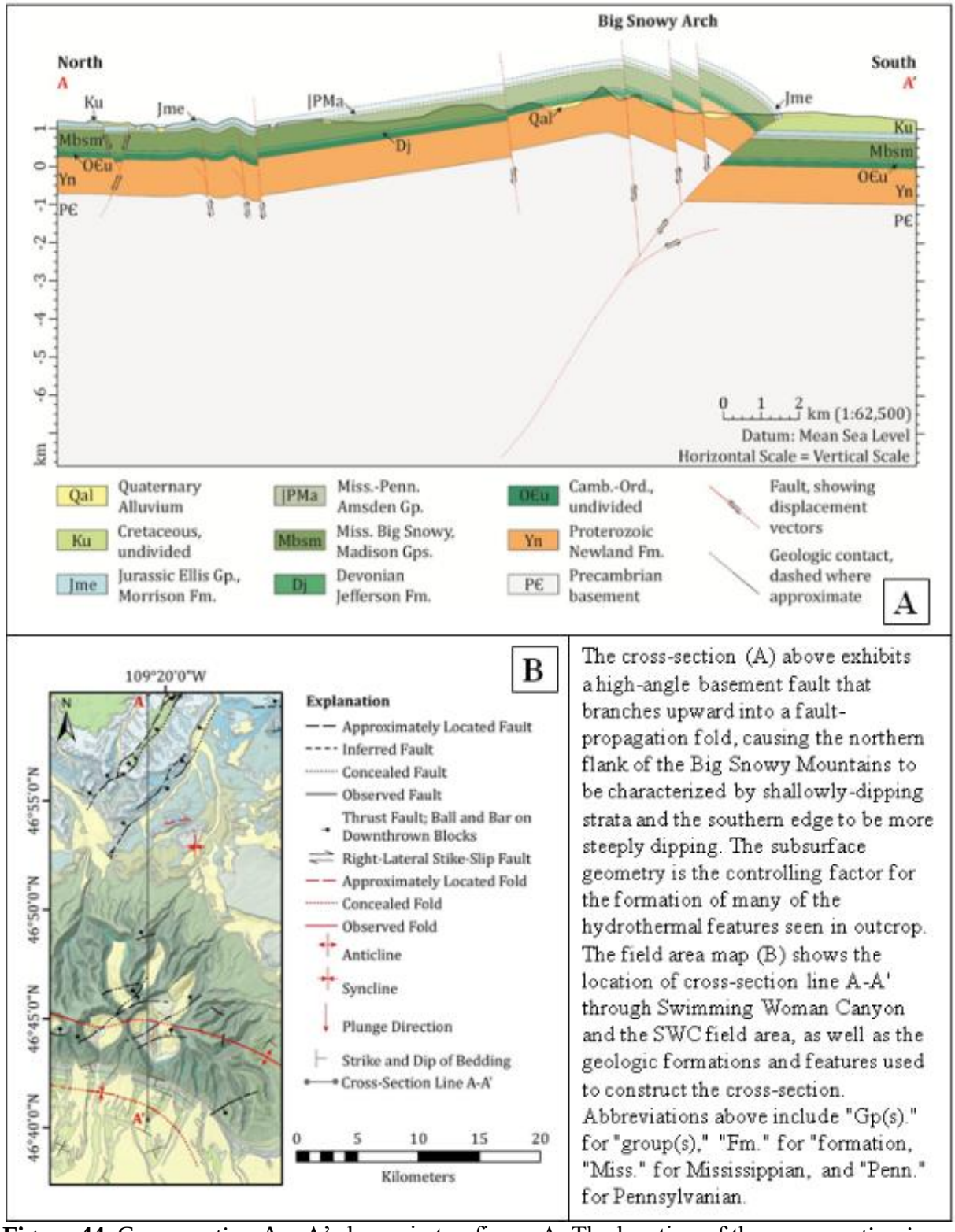

Figure 44. Cross-section A – A' shown in top figure A. The location of the cross-section is shown in map of the figure B.

Table 11. Stable C and O Isotope Results. Colors correspond to Figure 45.

Breccia Pipe ID	$\delta^{13}C$ (‰ VPDB)	$\delta^{18}O$ (‰ VPDB)
BSM-001c	1.06	-15.72
BSM-002b	1.54	-15.35
BSM-003a	-0.47	-17.05
BSM-004d	1.57	-11.56
BSM-005b	1.43	-12.71
BSM-006c	0.32	-16.47
BSM-007b	0.65	-17.99
BSM-007b clast	2.73	-8.98
BSM-007c	1.26	-14.98
BSM-008b	-0.10	-16.79
BSM-009e	0.73	-16.34
BSM-010c	2.14	-10.91
BSM-011a vein	3.27	-12.25
BSM-012a	-2.63	-18.70
BSM-013a	0.91	-14.10
BSM-014a	-0.64	-15.45
BSM-015b	1.53	-12.21
BSM-016a	0.70	-12.60
BSM-017c	0.08	-15.81
BSM-018b	1.14	-16.29
BSM-019a whole	0.82	-19.62
BSM-019b vugs	0.58	-17.85
BSM-019c whole	0.59	-19.15
BSM-020a	1.52	-14.06
BSM-020c clast	2.97	-5.56
BSM-021b	0.92	-15.16
BSM-022a	1.60	-10.91
BSM-F2c	-6.38	-7.09
BSM-F3b	-4.23	-16.59
SWC-01a whole	0.58	-14.12
SWC-01b	0.61	-9.97
SWC-01c	0.60	-11.59
SWC-01d	0.25	-12.31
SWC-01e	0.84	-11.18
SWC-01f	0.50	-11.79
SWC-02a whole	4.01	-3.28
SWC-03a replacement	-2.04	-12.13
SWC-03b whole	0.74	-12.20
SWC-03c	0.96	-12.37
SWC-03c rind	0.97	-11.40
SWC-03d	0.34	-13.05
SWC-03e	1.72	-9.02
SWC-03f whole	1.60	-9.60
Standard	1.94	-2.20
Standard	1.90	-2.22

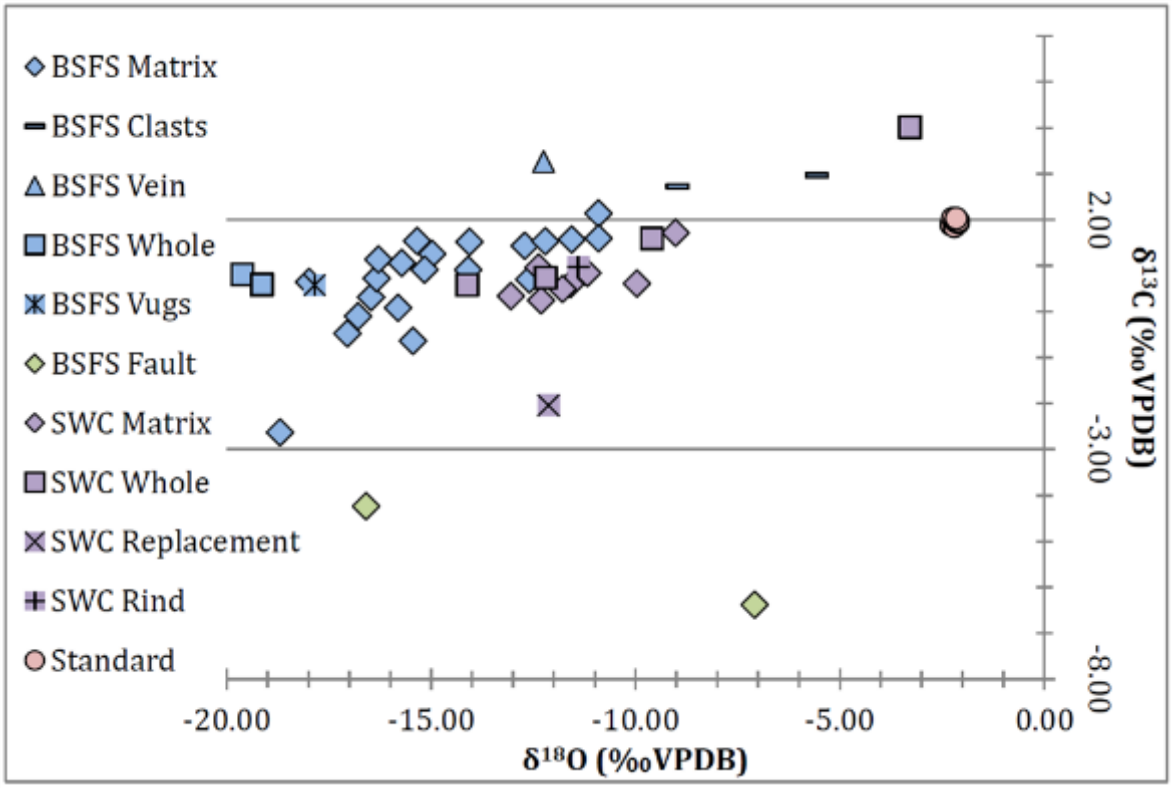

Figure 45. Stable C and O isotope results. Stable isotope analysis contrasts samples from various parts of a breccia pipe in comparison to standard laboratory samples (pink circles).

Figure 45 shows there is a slight downward linear trend (down to the left on the graph) indicating mixing between marine and meteoric waters. Marine waters, which may originally be trapped within the pore spaces or layers of a sedimentary rock, are often isotopically altered by isotope exchange reactions with the host rocks and downward-percolating meteoric fluids (Faure, 1998). This results in connate waters whose isotopic signature is a mixture of formational and meteoric fluids.

Pryor Mountain Study Area – PMSA

Small uranium vanadium deposits are present in the PMSA. The deposits are hosted in mineralized collapse breccia features within a paleokarst horizon of the Madison Limestone. Some of these features show multiple episodes of brecciation including hydrothermal breccias along the same fractures. Faults and fractures are critical factors in enhancing the porosity and permeability of otherwise tight carbonate reservoirs and have important implications for fluid migration. Both districts are located in Laramide structures. A similar structure located at the near Lovell, Wyoming, the Little Sheep Mountain anticline, hosts the active Lower Kane Cave bearing hydrothermal fluids with radioactive mud and water. The cave is still forming through sulfuric acid speleogenesis, a mechanism in which limestone dissolves due to sulfuric acid instead of carbonic acid, aided by microbial processes. This structure may provide a modern day analogue to the depositional mode of mineralization for these districts and provide a natural analog to CO_2 escape mechanisms. Rock samples were chosen to provide data on geologic processes caused by subsurface migration of natural CO_2 across faults and fracture networks ie.

along the crest of the anticlines. Breccia clasts and matrix samples were collected as well as both altered and unaltered host rock, and generations of cements from veins from each study area.

Figure 46. Index map of the Pryor Mountain study area includes Big Pryor Mountain, East Pryor Mountain, Red Pryor Mountain, Montana and the Little Mountain area, Lower Kane Cave and

Little Sheep Mountain anticline, Wyoming. Fracture studies were conducted on Red Pryor Mountain and Little Sheep Mountain anticline and these areas are denoted with red stars.

Stable C and O and radiogenic Sr isotopes

The PMSA was the only study area which had Sr isotope analyses done over the course of this project. All of the study areas had stable C and O isotope analyses done on breccia, host rock, and vein fill cement with very similar results. The late stage calcites and breccias generally have have the most depleted $\delta^{18}O$ values. The more negative $\delta^{18}O$ values of carbonate cements may reflect high temperatures during vein filling, precipitation from isotopically depleted fluids, or some combination of both factors (Budai and Wiltschko, 1987; Katz et al., 2006). At elevated temperatures the oxygen fractionation between water and calcite is decreased, resulting in calcite precipitates with more negative oxygen isotopic compositions. In all four study areas the more depleted $\delta^{18}O$ values have been from areas that show physical signs of hydrothermal alteration. The values are also similar to nearby study areas when comparing literature.

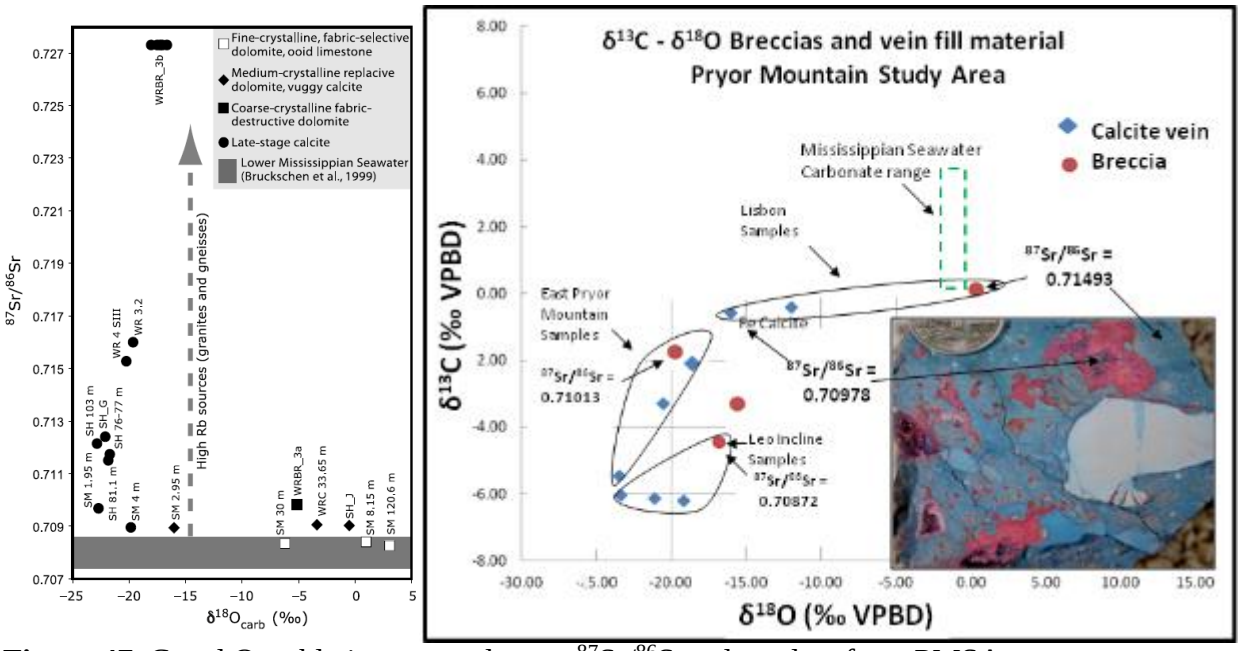

Figure 47. C and O stable isotope and some $^{87}Sr/^{86}Sr$ values data from PMSA.

In Figure 47, the turquoise stained portion of the rock is the dolomite host rock (LISBON001A), the red vug filling is the calcite and the last episode of vein fill is the purple ferroan calcite (LISBON001C). Green dashed box represents Mississippian carbonate range based on Cooley et al., 2011. Sample groups are circled. for the two ferroan carbonates are shown. Figure to left (from Katz et al, 2006) shows Sr and O isotope crossplot of Madison Formation rocks in the Owl Creek thrust sheet. The dark grey line represents the Mississippian seawater Sr value as defined by Bruckschen, et al., 1999. $\delta^{18}O$ values are the most depleted in both figures in the late –stage calcites. The breccias in the PMSA have more radiogenic values than the late-stage calcites.

When deciding which samples to have analyzed for Sr isotopes, values of stable C and O isotope data was reviewed from the PMSA. The same powdered samples that were used for XRD and

stable C and O isotope analyses were analyzed. Samples were chosen to get a wide representation of the sample set based on the previous isotope data. Four Madison Limestone host rock samples which seemed the closest to Madison sea water values were chosen, 8 breccia samples with 2 being silicified and not having any stable C and O isotope data, 3 fluorite and 2 barite samples also not having stable C and O isotope data, 12 calcite vein and cement samples with some of the more depleted $\delta^{18}O$ values, and several limestone and dolomite samples.

In the PMSA the host rock for the hydrothermal breccias is the Mississippian age Madison Limestone. The Sr isotope analysis was used to determine if the fluids responsible for late-stage calcite precipitation and breccia matrix interacted with high Rb source rocks such as granites and gneisses. All $^{87}Sr/^{86}Sr$ isotope results are presented in Table 13 along with $\delta^{18}O$ and $\delta^{13}C$ values from the carbonates tested. Barite and fluorite are present in most of the silicified hydrothermal breccias in the PMSA so these samples were also analyzed for Sr isotopes. The barite Sr isotopes were analyzed at the Institute of Marine Sciences, University of California, Santa Cruz, California, using the methods described by Scher et al., 2013. The barites, fluorites and a few carbonates did not have stable C and O isotope work done on them. The $\delta^{18}O$ carbonate values versus $^{87}Sr/^{86}Sr$ ratios are shown in Figure 48. Table 12 shows $^{87}Sr/^{86}Sr$ ratio for some geologic materials. It shows Phanerozic seawater with the same range of values as the Madison Limestone host in the PMSA. The results in Table 13 and Figure 48, show that the Madison Limestone host rocks $^{87}Sr/^{86}Sr$ values (0.707913-0.708914) fall within and slightly above to the Upper Carboniferous seawater range as based on Burke et al., 1982 (~0.70804−0.70828; Burke et al., 1982). One limestone PSE002A is host to a mineralized calcite vein and has a much more radiogenic value of 0.710047 suggesting the fluids that produced the mineralization were not in equilibrium with the host rock. Two breccia samples and one calcite sample have values less than 0.709 while all the other samples have 0.709 or greater excluding the Madison Limestone host rock samples. The 3 fluorite and 2 barite samples have a similar radiogenic signal to each other suggesting they were derived from the same migrating fluid source, more radiogenic than the Madison Limestone host. All the other samples have a more radiogenic or continental signature in terms of $^{87}Sr/^{86}Sr$ than the host limestone formation. The most radiogenic sample is a ferroan dolomite pictured in Figure 47 which came from a large floating clast breccia on the Red Pryor portion of the PMSA. The sample had the least depleted stable C and O values of all the samples with $\delta^{13}C$ value of 0.20 and a $\delta^{18}O$ value of 0.15. Figure 47 shows C and O stable isotope data from PMSA and several Sr results. The turquoise stained portion of the rock is the dolomite host rock (LISBON001A), the red stained vug filling is the calcite (LISBON001B) and the last episode of vein fill is the purple stained ferroan calcite (LISBON001C). $^{87}Sr/^{86}Sr$ values for the two ferroan carbonates are shown. $^{87}Sr/^{86}Sr$ analysis was not done on LISBON001B, the red vug calcite. The wide range of values for $^{87}Sr/^{86}Sr$ seems to suggest that most of the hydrothermally altered materials have been in contact with fluids that migrated from the burial environment while dissolving and incorporating radiogenic Sr from the dissolution of the surrounding carbonates and the felsic basement, respectively. The strontium isotope values of the breccias are between 0.7087 and 0.7149 and document the incorporation of strontium from basement rocks like the pink granites (0.726) of the Beartooth Mountains, Montana (Lafrenz et al., 1986), the continental crust (0.7155–0.7165; Burke et al., 1982), feldspathic basement (0.7195; Tucker and Wright, 1990), and/or Precambrian gneisses (0.712–0.726; Faure et al.,1963).

Table 12. Ranges and average $^{87}Sr/^{86}Sr$ ratios of some geologic materials

Ranges and average $^{87}Sr/^{86}Sr$ ratios of some geologic materials

	$^{87}Sr/^{86}Sr$		$\delta^{87}Sr$		Reference [a]
	average	range	average	range	
Continental crust	0.716		9.7		1
Continental volcanics		0.702–0.714		−10.1 to +6.8	2
Oceanic island basalts	0.704	0.702–0.707	−7.3	−10.1 to −3.1	2
River water	0.712	0.704–0.922	4.0	−7.3 to 300	3–8
Modern seawater	0.7092		0		9–10
Phanerozoic seawater		0.707–0.709		−3.1 to +0.2	9, 11–13
Proterozoic seawater		0.702–0.709		−10.1 to +0.2	14, 15

[a] 1 = Goldstein and Jacobsen (1988); 2 = Faure (1986); 3 = Brass (1976); 4 = Wadleigh et al. (1985); 5 = Goldstein and Jacobsen (1987); 6 = Palmer and Edmond (1989); 7 = Palmer and Edmond (1992); 8 = Krishnaswami et al. (1992); 9 = Burke et al. (1982); 10 = Capo and DePaolo (1992); 11 = Hess et al. (1986); 12 = DePaolo (1986); 13 = Elderfield (1986); 14 = Veizer et al. (1983); 15 = Derry et al. (1992).

Table 13. δ13C, δ18O, & 87Sr/86Sr values of some samples from the PMSA

Lab No.	Sample ID Number	Composition of sample	$\delta^{13}C$	$\delta^{18}O$	$^{87}Sr/^{86}Sr$	2σ
AM44	OGMF	Fluorite	none	none	0.709974	0.000009
AM45	MBEPryor02	Fluorite	none	none	0.709458	0.000011
AM46	DandyF	Fluorite	none	none	0.709933	0.000009
*UCSC lab	OGM B	Barite	0.00	none	0.709509	0.000003
*UCSC lab	SWMP B	Barite	0.00	none	0.709907	0.000024
AM2	DH22; dremel tool	Madison LS	-1.02	-6.74	0.708232	0.000009
AM3	DH22;M/pestle	Madison LS	-1.02	-6.74	0.708340	0.000012
AM11	DH22 chips	Madison LS	-1.02	-6.74	0.708336	0.000007
AM4	Mm1021A; dremel tool	Madison LS	2.04	-2.87	0.708625	0.000009
AM5	Mm1021A;M/pestle	Madison LS	2.04	-2.87	0.708116	0.000015
AM12	MM1021A chips	Madison LS	2.04	-2.87	0.708167	0.000010
AM6	PSE003; dremel tool	Madison LS	1.14	-3.75	0.708914	0.000007
AM7	PSE003; M/pestle	Madison LS	1.14	-3.75	0.708754	0.000010
AM13	PSE003 chips	Madison LS	1.14	-3.75	0.708764	0.000010
AM8	Salamander;dremel tool	Madison LS	1.30	-6.93	0.707968	0.000010
AM9	Salamander; M/pestle	Madison LS	1.30	-6.93	0.707913	0.000008
AM14	Salamander Chips	Madison LS	1.30	-6.93	0.708004	0.000009
AM43	PSE002A	Limestone	-1.76	-18.33	0.710048	0.000010
AM27	LEOINCLINE_A	Calcite	-6.20	-19.18	0.708316	0.000009
AM28	DANDY_SPMV	Calcite	-2.33	-24.80	0.709220	0.000007
AM29	D2001C	Calcite	-4.55	-23.60	0.709090	0.000006
AM29(2) dup.	D2001C	Calcite	-4.55	-23.60	0.709087	0.000008
AM30	FS139	Calcite	-1.86	-17.36	0.709342	0.000007
AM31	OGM-715GC	Calcite	-5.60	-19.49	0.708718	0.000008
AM32	LSM-RRC005	Calcite	-2.26	-23.72	0.709473	0.000007
AM33	LSM-RRC007C	Calcite	-1.92	-19.82	0.709433	0.000010
AM34	SBRX	Calcite	-2.07	-21.87	0.709591	0.000007
AM36	LM_LISBON	Calcite	none	none	0.708845	0.000010
AM37	2PSE001GC	Calcite	-4.35	-19.57	0.709294	0.000007
AM38	PSE002	Calcite	-3.28	-19.01	0.709375	0.000013
AM39	UKC004	Calcite	none	none	0.709363	0.000006
AM40	1028_LSH	Dolomite	2.61	-1.00	0.709207	0.000009
AM41	SWMP_0IV	Dolomite	-0.79	-15.28	0.709676	0.000008
AM42	UMB018	Dolomite	-1.59	-19.06	0.709855	0.000008
AM26	LISBON001C	Ferroan Calcite	-0.59	-15.99	0.709781	0.000009
AM47	LISBON001A	Ferroan Dolomite Breccia	0.20	0.15	0.714931	0.000008
AM48	LM_LEOINCLINE	Limestone Breccia	-4.43	-16.79	0.708726	0.000009
AM49	EPOO2_DB	Limestone Breccia	-1.94	-19.22	0.710132	0.000009
AM50	EPOO2_B	Limestone Breccia	-0.81	-16.47	0.709589	0.000010
AM51	MB15_UV	Silicified LS Breccia	none	none	0.709874	0.000007
AM52	OGM04	Silicified LS Breccia	none	none	0.709544	0.000009
AM53	UKC002	Limestone Breccia	none	none	0.709333	0.000006
AM54	LSM-RRC004	Limestone Breccia	0.03	-12.80	0.709431	0.000008
NBS987 (mean n = 21)	(mean n= 21)	Reference Standard			0.710265	0.000003

* Barite samples were analyzed on a Neptune MC-ICPMS in the lab of Dr. Adina Paytan at the Institute of Marine Sciences, University of California Santa Cruz, California; 87Sr/86Sr reported relative to NBS987 = 0.710240

*All other 87Sr/86Sr work was done on a Neptune MC-ICPMS Plus in the High Precision Isotope Laboratory of Dr. Kenneth Sims at the University of Wyoming; 87Sr/86Sr reported relative to NBS987 = 0.710240

*C and O stable isotopes were analyzed by Lora Wingate at the University of Michigan. C and O values reported relative to VPBD using the calcite standard NBS 19 = 1.95 per mil

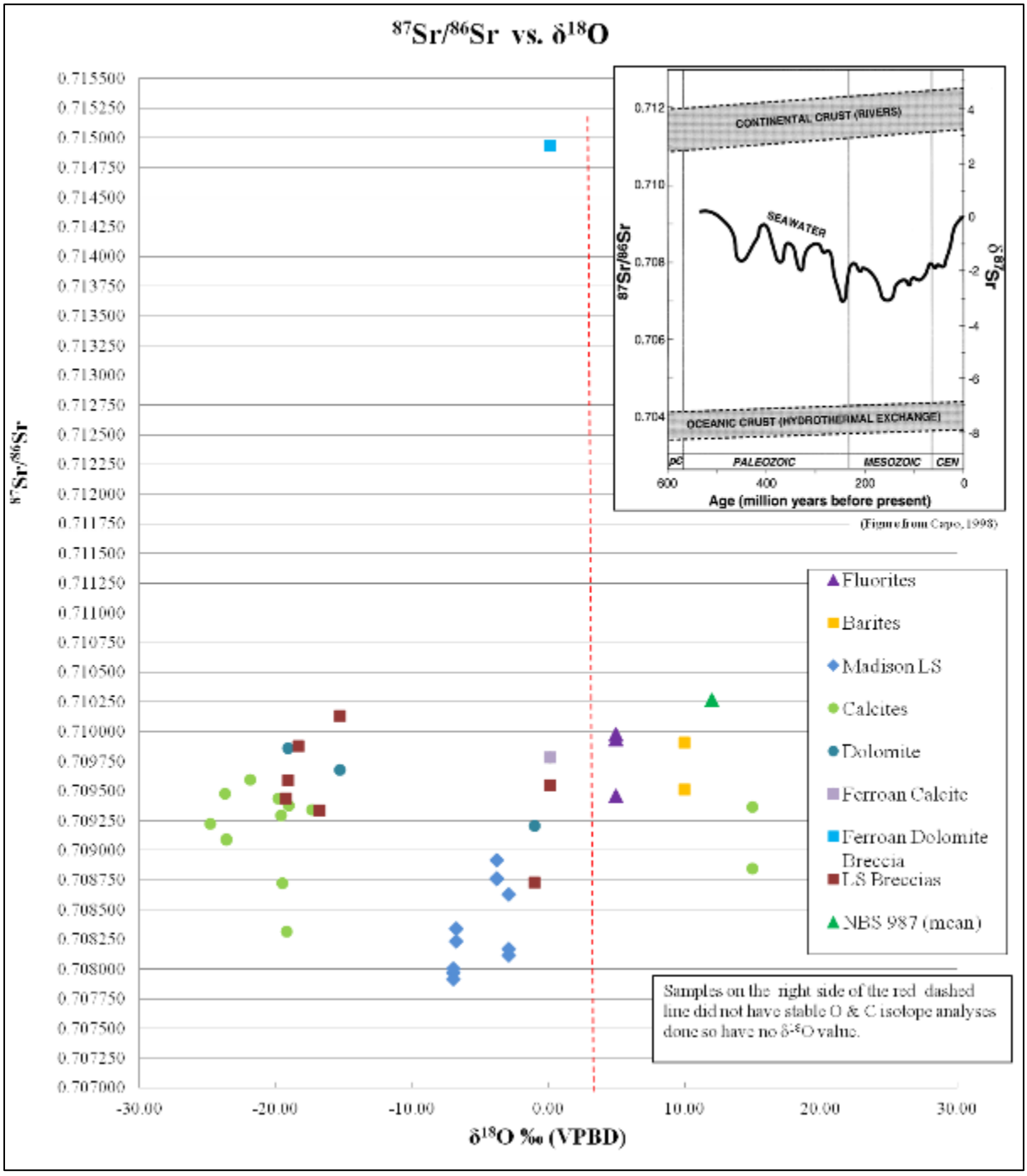

Figure 48. The $\delta^{18}O$ carbonate values versus $^{87}Sr/^{86}Sr$ ratios from some samples from the PMSA. Inset figure showing variation of the strontium isotopic composition of Phanerozoic oceans.

In Figure 48, the $^{87}Sr/^{86}Sr$ of seawater has fluctuated between the average values of terrestrial weathering and hydrothermal exchange with mid-ocean ridge basalts. The isotopic composition at any time in the past reflects that of unaltered marine carbonate of that age (Capo et al., 1998).

Summary of Petrographic and Fieldwork Findings

Petrographic analyses of formations sampled in the study areas demonstrate that fractures have served as fluid conduits at all scales of observation (outcrop, hand sample and microscopic scales). Veins with sharp host rock contacts and a crystal size increasing towards the interior of the mineralized fractures (drusy fabric) indicate that precipitation occurred in fluid-filled spaces generated by tensile fracturing (Roberts, 1990). Separate generations of vein fill cements, replacement textures, dissolution and hydrothermal mineralization are localized along fractures, small-scale faults, and pressure solution seams, which indicates that tectonic fabrics have controlled the location and extent of diagenetic alteration for multiple episodes of fluid migration. Additionally, dead oil or bitumen is localized along fracture walls, along bedding planes, within dissolution vugs, and in the intercrystalline porosity of the more extensively dolomitized limestones, indicating that fractures influenced the migration and accumulation of hydrocarbons in the study areas.Generally highly fractured and dolomitized facies display the largest concentrations of bitumen and minor sulfides namely pyrite. Although the diagenetic history of each formation examined varies widely, the late-stage diagenesis affecting those units have some consistent similarities. Fracturing provides migration pathways for many episodes of fluid migration, with some still active at the TSA, within the SPC and Little Sheep Mountain areas. The late diagenetic products of those fluid migration episodes vary between the different formations examined within each field area, but they consistently display a general sequence of fluid migration, mineralization and alteration that includes the following:

1. Precipitation of dolomite cements and and/or replacement of early formed carbonates with dolomites that often have ferroan composition and sometimes have a saddle shaped morphology. These late-stage dolomites differ from early diagenetic dolomites in their shape (euhedral to subhedral), size (coarsely crystalline) and location (proximal to fractures, faults and stylolites).
2. Hydrocarbon migration and accumulation along fractures and within porous and permeable facies. This episode of fluid migration may be coeval with, or slightly postdate migration of the dolomitizing fluids.
3. Dolomite dissolution and the development of moldic porosity in some of the dolomitic and biomicritic units.
4. Sulfide mineralization (largely pyrite) localized along fractures, faults, stylolites, dissolution vugs and within porous facies.
5. Coarse, blocky ferroan calcite precipitation that may be genetically associated with sulfide mineralization.
6. Precipitation of coarse, non-ferroan blocky calcite cement often occludes porosity, fills fractures, molds and dissolution vugs, and replaces earlier generations of carbonates- late stage calcite.
7. Oxidation and weathering of sulfides into limonite and hematite.
8. Vadose calcite cementation and precipitation of pendant cements and speleothems.

This generalized history of fluid migration is an oversimplified description of the paragenetic sequence of late diagenesis affecting reservoir rocks of the four study areas. The late-diagenetic

history of the rocks examined is more intricate than the sequence discussed above. There are numerous fine-scale overprinting deformation and brecciation textures and complex recrystallization, dissolution, and cementation textures. The TSA and PMSA also have a component of active geothermal fluids migrating through parts of the areas that are likely more enriched in H_2S. Volatilization and oxidation of H_2S to sulfuric acid on cave-wall surfaces causes aggressive carbonate rock dissolution and replacement by gypsum during sulfuric acid speleogenesis (Engle et. al, 2003). This is the process that is forming the Lower Kane Cave, Wyoming and is now recognized worldwide as a prominent cave forming process. Hydrogen sulfide bearing fluids migrate upward along fractures, bedding planes and joints in structures in this process and may be particularly relevant in sites being considered for storage of CO_2 which are proximal to producing or past productive hydrocarbon reservoirs.

The similarities of structurally controlled, late-stage diagenesis between each formation suggest that the pervasive deformation in the culmination allowed for similar fluids to migrate through the entire stratigraphic package studied. Fractures and small-scale faults appear to be critical in facilitating fluid flow, and maintaining structural permeability in the SPC. Most outcrop-scale fractures are open, and many fractures in thin section remain open, or are only partially bridged by cements. This may be a result of recent meteoric dissolution. The presence of multiple generations of cements and multiple diagenetic alteration products that are localized along fractures indicates that they remained open to fluid migration for an extended period of time. The history of fluid migration is more complex than the simple summary presented here. Petrographic examination indicates that there were many pulses of fluid migration associated with episodic deformation and tectonic pumping in the study areas.

Hydrothermal fluid systems are characterized by dynamic processes controlled by the interplay of deformation and fluid migration; fluid flow is episodic in nature with abrupt changes in pore fluid pressures and applied stress in response to preseismic processes, coseismic fault rupture, and post seismic aftershock processes that can control fault zone permeability (Davies and Smith, 2006). The presence of saddle dolomite and sulfide minerals suggests that the sources of mineralizing fluids were hydrothermal in nature. The suite of minerals that developed as a result of late-diagenetic alteration in the SPC and the PMSA are often associated with Mississippi-Valley-type hydrothermal ore deposits (Davies and Smith, 2006). Coarse, blocky, anhedral to subhedral calcite cements are typically the latest diagenetic product in the samples examined. These cements are often associated with mosaic breccias, floating clast breccias and/or multiple overprinting breccia textures. The coarse nature of these cements and the floating breccia textures suggest that the calcite was precipitated rapidly, and that it was associated with a late episode of deformation. The development of floating clast breccias and mosaic breccias are sometimes attributed to hydro-fracturing of a host rock as a result of isothermal CO_2 effervescence; effervescence and hydro-fracturing occur due to rapid changes in fluid pressures following rupture along a fault (Sibson, 1986; Davies and Smith, 2006; Katz et al., 2006). Effervescence causes an increase in the fluid pressure within a vein, and a decrease in the effective confining pressure of the surrounding host rock, which allows for fracture propagation (Jébrak, 1997).

CONCLUSIONS: NATURAL ANALOGS OF ESCAPE MECHANISMS

Extensional fracturing and brecciation are two important deformation mechanisms which increase porosity and permeability in reservoir rocks. In all four areas fractures play a large role in the transport of fluids through the structures. These areas have been influenced by several tectonic events with the Laramide orogeny imparting many tectonic breccias along existing and new fracture systems. The quality of these reservoirs and their capacity for CO_2 storage, are dependent upon reservoir porosity and permeability, the architecture of sub-surface traps and fracture-controlled permeability networks that affect fluid dynamics in a system. Faults and fractures may serve as conduits or barriers to fluid flow in structural traps. These structures could be potential leakage avenues if they breach seal rocks and/or direct fluid flow towards the surface; conversely faults and fractures can also compartmentalize reservoirs and create anisotropy in fluid flow systems if they are sealed with impermeable cements. Carefully examining paleo fluid flow systems at outcrops found in breached exhumed structures like the Little Sheep Mountain anticline, Thermopolis anticline, and Gypsum creek anticline can lend insight into the fluid dynamics of similar subsurface structures being considered for storage of CO_2. Different chemical and isotopic compositions within vein fill material indicate that fluid flow has occurred in more than one episode. Some of the possible sources of fluids related to veining include Cretaceous marine or meteoric water, connate fluids, and basinal brines (Budai and Wiltchko, 1987; Katz et al, 2006).

The following conclusions can be made about potential CO_2 reservoir rocks:

1) Early dolomitization of carbonates (the Madison and Bighorn Formations) enhanced host rock porosity, thus increasing reservoir quality (Budai, 1987) in the four study areas.

2) Fracturing associated with Sevier tectonic deformation and development of the Stewart Peak Culmination created pathways for migrating fluids and enhanced the secondary porosity and permeability of reservoir rocks. Later Laramide tectonic deformation enhanced fluid pathways within reservoir rocks in the PMSA, BSMSA and TSA; fractures and paleokarst features served as conduits for the migrating fluids from the Bighorn Basin area. At Thermopolis and Little Sheep Mountain anticlines, fractures and Laramide faults continue to serve as the main fluid conduits controlling the locations of active hot spring deposits and the development of hydrogen sulfide speleogenesis.

3) Tectonic deformation associated with the development of the culmination in the SPC, and later Laramide tectonic deformation of TSA, PMSA, and BSMSA, led to the formation of fault-fracture permeability networks that enhanced reservoir quality and storage capacity in host reservoir rocks.

4) Hydrocarbons migrated into the Stewart Peak culmination and the basement cored Laramide structures via faults and fractures and were stored within the pore-space created by deformation and related structural/diagenetic alteration.

5) Hydrothermal fluids migrating along permeability networks caused dissolution of early carbonate cements and host rocks and fabric-selective dolomitization, which increased porosity and permeability of reservoirs in the four study areas.

6) CO_2 migration likely formed vertical fracture swarms and breccia pipes associated with hydrothermal fluids and boiling of CO_2 due to a loss of pressure in the four study areas.

In the SPC fault damage zones allowed fluids to migrate parallel to the strike of faults. Fractures geometrically "fit" with Sevier tectonic deformation and are consistent with the regional tectonic fabric. Fluid flow was facilitated by the linking and intersection of systematic fracture sets, which increased the hydraulic connectivity of the duplex, and allowed fluids to migrate and pool under well-sealed structural highs. Travertine springs and zones of extensive alteration are products of fluid migration along some of these major fluid conduits, which appear to be long-lived, fault-controlled permeability networks. Permeability networks in structurally complex areas such as displacement transfer zones should be assessed as potential leakage points for possible CO_2 storage sites.

There is a clear tectonic control over the late-stage diagenesis that has affected the rocks examined in all four study areas. The similarity of the late diagenetic episodes between examined formations suggests that fractures and faults transmitted fluids through the structures, allowing fluids to infiltrate and alter the entire package of examined strata. Hydrothermal fluids likely enhanced structurally controlled conduits via the processes of dolomitization, dissolution, fracturing, and brecciation. The presence of saddle dolomite, Herkimer style quartz, barite, fluorite and disseminated sulfides suggest multiple episodes of low temperature hydrothermal fluid migration. Petrographic analysis and geochemical isotope analyses demonstrate that fractures have served as fluid conduits at all scales of observation (outcrop, hand sample and microscopic scales).

EXPERIMENTAL METHODS: UNDERGROUND FIBER OPTIC SENSORS

The work on the inline fiber sensor, described in detail in the results and discussion section, was completed in the Applied Optics Research Laboratory. The inline fiber sensor work utilized a distributed feedback (DFB) diode laser with a nominal operating wavelength of 2.004 μm with tuning achieved by varying the operating temperature via a thermoelectric cooler. All optic splicing was completed using a commercial fusion splicer. The silicon V-grooves were developed and processed in the Montana Micro-Fabrication Facility located on the Montana State University campus. All optical components used in the development of the fiber sensor are available commercially and described in the Results and Discussion section of this report.

The work on the seismic sensor, described in detail in the results and discussion section, was also completed in the Applied Optics Research Laboratory. The components used for the developing a laboratory based fiber seismic sensor are all commercially available and described in detail in the Results and Discussion section of this report.

RESULTS AND DISCUSSION: UNDERGROUND FIBER OPTIC SENSORS

The major goal for the ZERT phase II is to develop an in-line fiber sensor based on photonic bandgap (PBG) fibers for underground monitoring of carbon dioxide (CO_2). A schematic of the proposed is shown in Figure 49. Light from a fiber coupled tunable distributed feedback laser is split using a 50/50 beam splitter with half of the light going to a transmission detector while the remainder of the light travels through a segment of single mode optical fiber (SMF). The SMF fiber is fusion spliced to a PBG fiber with a hollow core and the end of the PBG fiber, a small gap allows the CO_2 to diffuse into the hollow core of the PBG fiber. A reflection at this gap sends light back towards the inline fiber splitter where the light is monitored using a transmission detector. Several segments of the SMF fiber, PBG fiber, and gap can be used to create an inline fiber sensor. The Phase II ZERT effort is aimed at demonstrating one segment of this fiber sensor.

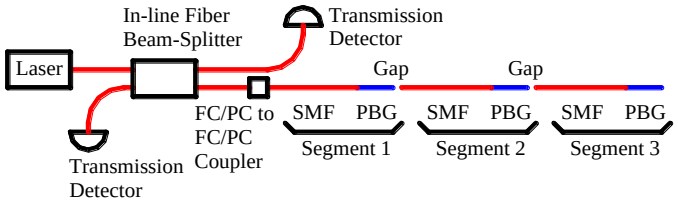

Figure 49. Schematic of the in-line fiber sensor.

The implementation of the inline fiber sensor is dependent on the quality of the fusion splice between the SMF and PBG fibers and the reflection of the light from the gap and amount of light coupled into the next segment of the optical fiber. The optical power of the return signal can be estimated using

$$P_T = \frac{1}{4} P_0 T_S^{2N} R_S (1 - R_S)^{N-1} F_C^{2N-1}$$

where P_T is the optical power seen be the transmission detector, P_0 is the output optical power from the DFB laser, T_S is the transmission for the SMF/PBG fiber splice, R_S is the reflection from the SMF fiber after the gap, F_C is the fraction of light coupled into the fiber through each gap, and N is the segment number.

Initial efforts in fusion splicing SMF and PBG fibers produce highly variable transmission through the splices and highly variable splice strengths. Initial investigation into the variability of the splice transmission and splice strength indicate the cleave of both the SMF and PBG fibers is critical. A cleave of the PBG fiber using the York cleaver, which is an automated cleaver that uses a diamond tip to score the fiber and a settable tension to produce the cleaved end is shown in Figure 50 for a tension of 205 gf. Several issues are apparent from this figure including the collapsed core structure used to guide the light down the hollow core and the damaged outer core. Furthermore, using an interferometric setup, the splice shown in Figure 50 showed a large angular variation across the surface. The damage of the hollow core structure and the large

angular variability across the surface of the fiber are the most likely causes of the variable transmission through the splice and splice strength.

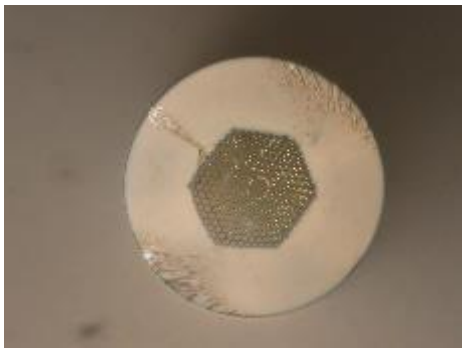

Figure 50. Cleave using a tension of 205 gf.

The ability to produce repeatable cleaves between the SMF and PBG fibers requires the inspection of each cleaved surface. A setup for inspection of the cleaved ends of fibers has been assembled and set up in the optics laboratory. The inspection microscope, shown in Figure 51 was identified and purchased. Using this microscope, it was confirmed that a tension on the fiber cleaver of 165 gf produces a clean (undamaged fiber core) cleave.

Figure 51. Inspection microscope for the cleaved fiber ends.

The splicing of a single mode fiber (SMF) to a PBG fiber was study as a function of the optical alignment of the two fibers in the fusion splicer. A table of the starting parameters for the fusion splicing of a SMF to PBG fiber are given in Table 14. The PBG fiber under investigation has a 12 μm core diameter so the parameters for the HC-1550-02 were used as the starting point. The fiber transmission for the splice was check after each splice by measuring the fiber couple light in the SMF fiber after the SMF fiber was cleaved. A table of the fiber splicing results is provided in Table 15.

Table 14. Fusion splicing parameters for the SMF to PBG splice.

Fiber Type	HC-1550-02 (10.9 μm core)	HC19-1550-01 (20 μm core)
Prefuse Time	.2 s	.2 s
Prefuse Current	10 mA	10 mA
Gap	10 μm	10 μm
Overlap	10 μm	15 μm
Fusion Time 1	.2 s	.2 s
Fusion Current 1	10 mA	10 mA
Fusion Time 2	12 s	12 s
Fusion Current 2	7 mA	7 mA
Fusion Time 3	3 s	3 s
Fusion Curent 3	6.5 mA	6.5 mA
Offset	260	260

Table 15. Summary of the parametric study of the fusion splice parameters on the properties of the fusion splice between the PBG and single mode optical fiber.

Parameters on Splicer	Gap	30 µm	50 µm	50 µm	50 µm	50 µm	50 µm	50 µm	50 µm	50 µm	50 µm	50 µm
	Overlap	20 µm	25 µm	25 µm	25 µm	25 µm	25 µm	25 µm	25 µm	25 µm	25 µm	20 µm
	Fusion Time 1	0.4 s	0.4 s	0.4 s	0.4 s	0.4 s	0.4 s	0.4 s	0.4 s	0.4 s	0.5 s	0.5 s
	Fusion Current 1	11.0 mA	11.5 mA	11.5 mA	11.0 mA	11.5 mA	11.5 mA	11.5 mA	11.5 mA	12.0 mA	11.5 mA	11.5 mA
	Fusion Time 2	1.0 s	6.0 s	6.0 s	6.0 s	6.0 s	6.0 s	2.0 s	3.0 s	3.0 s	3.0 s	6.0 s
	Fusion Current 2	11.5 mA	12.5 mA	12.0 mA	12.0 mA	12.0 mA	11.5 mA	12.0 mA	12.0 mA	12.0 mA	12.0 mA	12.0 mA
	Fusion Time 3	15.0 s	3.0 s	3.0 s	3.0 s	3.0 s	3.0 s	6.0 s	6.0 s	6.0 s	6.0 s	3.0 s
	Fusion Current 3	8.0 mA	6.5 mA	6.5 mA	6.5 mA	6.5 mA	6.5 mA	6.5 mA	6.5 mA	6.5 mA	6.5 mA	6.5 mA
	Set Center	265	270	270	270	270	270	270	270	270	270	270
	Alignment	Peak Trans.	Peak Trans.	Peak Trans.	Peak Trans.	Peak Trans.	Peak Trans.	Peak Trans.	Peak Trans.	Peak Trans.	Peak Trans.	Peak Trans.
	Cleave	Ok	Good	Good	Good	Good	Good	Bad	Good	Good	Good	Good
Results	Bowing	Yes	Slight&back	Slight&back	Yes	Yes&back	Yes	Yes	Yes&back	Yes	Yes	Slight&back
	Deformed	No	Yes	Yes	No	Slight	No	No	No	No	No	Yes
	Strength	1	5	6	1	5	1	1	****	1	1	2
	Voltage Before (mV)	225	240	235	220	225	260	200	245	240	255	245
	Voltage After (mV)	185	15	0	150	60	185	175	135	205	110	12
	Voltage out SMF (mV)	495	495	495	495	495	495	495	495	495	495	495
	Transmission Before (%)	45.4545	48.4848	47.4747	44.4444	45.4545	52.5253	40.4040	49.4949	48.4848	51.5152	49.4949
	Transmission After (%)	37.3737	3.0303	0.0000	30.3030	12.1212	37.3737	35.3535	27.2727	41.4141	22.2222	2.4242

Continued on next page

Parameters on Splicer	Gap	50 µm	50 µm	50 µm	50 µm	50 µm	**50 µm**	45 µm	50 µm
	Overlap	20 µm	20 µm	20 µm	20 µm	20 µm	**20 µm**	20 µm	20 µm
	Fusion Time 1	0.5 s	0.5 s	0.5 s	0.5 s	0.5 s	**0.5 s**	0.5 s	0.5 s
	Fusion Current 1	11.5 mA	11.5 mA	11.5 mA	11.5 mA	11.5 mA	**11.5 mA**	11.5 mA	11.5 mA
	Fusion Time 2	2.0 s	1.0 s	1.0 s	1.0 s	1.0 s	**0.6 s**	1.0 s	1.0 s
	Fusion Current 2	12.0 mA	12.0 mA	12.0 mA	12.0 mA	11.5 mA	**12.0 mA**	11.5 mA	11.5 mA
	Fusion Time 3	8.0 s	8.0 s	8.0 s	8.0 s	8.0 s	**8.0 s**	8.0 s	8.0 s
	Fusion Current 3	6.5 mA	6.5 mA	6.5 mA	6.5 mA	6.5 mA	**6.5 mA**	6.5 mA	6.5 mA
	Set Center	270	270	270	270	270	**270**	270	270
	Alignment	Peak Trans.	Peak Trans.	Peak Trans.	Peak Trans.	Peak Trans.	**Peak Trans.**	Peak Trans.	Peak Trans.
	Cleave	Good	Good	Bad	Good	Good	**Good**	Good	Good
Results	Bowing	Slight&back	Slight	Slight&back	Slight&back	Slight&back	**Yes**	Yes	Slight&back
	Deformed	No	No	No	No	No	**No**	No	No
	Strength	4	2	3	3	3	**3**	1	3
	Voltage Before (mV)	240	210	245	245	220	**240**	260	260
	Voltage After (mV)	130	170	115	150	170	**170**	195	125
	Voltage out SMF (mV)	495	495	495	495	495	**495**	495	495
	Transmission Before (%)	48.4848	42.4242	49.4949	49.4949	44.4444	**48.4848**	52.5253	52.5253
	Transmission After (%)	26.2626	34.3434	23.2323	30.3030	34.3434	**34.3434**	39.3939	25.2525

An initial experiment was set up to measure the fiber coupling from a first fiber into a second fiber as a function of gap distance. This measurement provides an important result that will be used for the micro-machined fiber couplers. A plot of the transmission as a function of the gap spacing is shown in Figure 52 indicating that greater than 80% transmission can be achieved for gaps of less than 40 μm, a distance that can be achieved using mechanical positioners. Furthermore, this type of measurement allows us to set the gap spacing between the fibers by monitoring the transmission. These measurements were made using FC/PC fiber connectors on the end of a fiber pigtail. Fiber optic ports with x-y-z and θ–ϕ control was used to obtain the results shown in Figure 52.

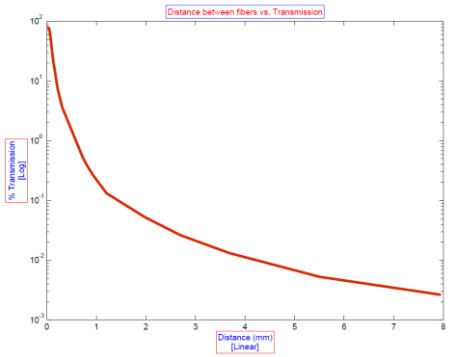

Figure 52. Plot of the transmission as a function of the fiber gap distance.

To achieve these results with the bare fiber envisioned for the multi-segment in-line fiber sensor, fiber couplers need to be designed. Because of the mechanical tolerances, we have decided, after a thorough literature search, to utilized silicon based micro-machining techniques to develop these fiber couplers. The initial design utilizes two pieces of silicon to create three points of contact which is described as the best method for fiber coupling in the literature. The bottom fiber will contain a V-groove. Because of the etching process in silicon the angles of the V-groove are set providing an angle of 109.4° at the base of the V-groove. The width of the V-groove is chosen, based on this angle to provide an appropriate depth so that the fiber sits in the V-groove making two points of contact with the top of the fiber 50 μm above the silicon substrate. The second piece of silicon will make contact at a third point with glue holding the fiber coupler together. This design provides the flexibility to add a waveguide between the two fibers to enhance the coupling efficiency.

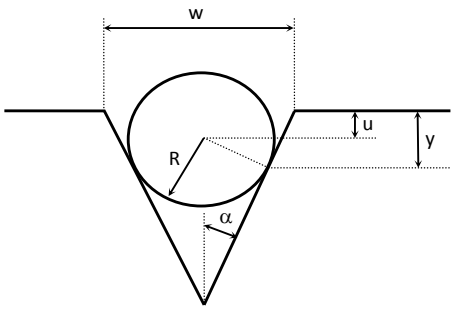

Figure 53. V-groove design parameters.

The initial photolithographic mask design was designed with several features. First, the cladding diameter of the single mode (SMF) optical fiber is 125 μm in diameter while the cladding of the photonic bandgap (PBG) fiber is 155 μm in diameter. To match the center of the optical cores of the two fiber, a relationship between the center of the optical fiber and the width of the v-groove was developed. The relevant v-groove parameters are shown in Figure 53. The dimension u is a design parameter which locates the center of the fiber with respect to the top of the silicon material. The parameter y located the contact point between the optical fiber and sidewall. The angle α=35.3° is a material parameter of the silicon and results from the unit cell structure. R is the cladding diameter and w is the v-groove width. From the geometry shown in Figure 53,

$$w = \frac{2(R + usin(\alpha))}{\cos(\alpha)}$$

Using this relationship a new mask with a variety of V-groove widths has been design to allow alignment of the core centers for SMF to SMF coupling and SMF to PBG coupling. Furthermore, because the etch process and mask transfer are process based and can vary depending on the etch time for example, several V-groove widths have been accommodated to provide a testing for the most efficient SMF to SMF and SMF-PBG coupling. Once the design of the V-groove structure was completed, L-Edit software, available at Montana State University, was use to design the photolithographic mask needed for processing of the fiber couplers. The photolithographic mask design produced using L-Edit is shown in Figure 54. Several variations on the initial design have been included on the photolithographic mask design allowing for variations in the design to be tested using a single processed silicon wafer. Jordan Creveling, the undergraduate student working on this project completed training in the Montana Micro-fabrication Facility (MMF) operated by the Electrical and Computer Engineering Department at Montana State University. This training was necessary so Jordan can process the silicon based on the photolithograph mask allowing for the continued development of the fiber sensors. The completed V-groove structure is shown in Figure 55.

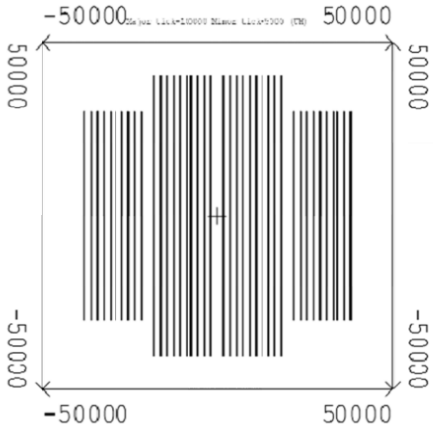

Figure 54. Final mask design fof photolithographic development of coupling microstructures for the in-line fiber sensor.

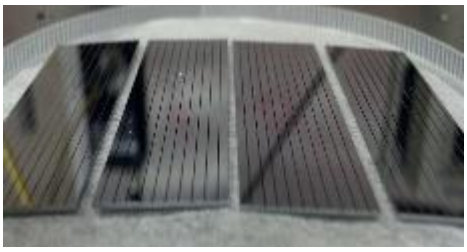

Figure 55. The completed V-groove structures. Being prepared for testing.

The mechanical V-Groove splice was tested using a 2µm laser that was controlled by an ILX laser diode Controller with the function input connected to a function generator that supplied a 50kHz 1V amplitude sine wave. The 2µm beam was launched into a 50/50 beam splitter. One end of the beam splitter was launched into a 2µm photo-detector for a reference. The other end was coupled to a strand of single mode fiber with one tip that was bare fiber. This Large Non-Uniform V-Groove chip was used to splice the bare single mode (SM) fiber to a bare photonic bandgap (PBG) fiber. The other end of the PBG fiber was launched into another photo-detector. The photo-detectors were connected to an oscilloscope where the transmission was monitored using a Fast Fourier Transform to find the AC and DC components of the signal in an attempt to gain resolution on the measurement. The V-Groove Chip was placed on a platform that was controlled by a differential micrometer. This allowed for a steady and constant way to control the fibers when they were placed in the Groove. It also allowed for a distance vs. transmission measurement to be taken. The micrometer stage setup can be seen in Figure 56.

As can be seen in Figure 56 the V-Groove Chip is placed on the platform with the two fibers held in the 6th Groove (from the top of the chip) by two pieces of extra silicon wafer and electrical tape. In the two adjacent grooves there are pieces of striped SM fiber and striped PBG fiber. These extra pieces sit next to the main fibers of the same type to space the extra silicon holding pieces. The spacing fibers help decrease friction on the main fibers so that they may be moved back and forth in the grooves while still sitting securely in the groove. The SM fiber in Figure 56 is held only by the groove so it moves with the Groove when the micrometer stage is

adjusted, the PBG fiber however is held in place by the bare fiber launch. When the micrometer was adjusted the PBG fiber did not move with the groove but instead moved back and forth in the groove. This allowed for some controlled movement of the fibers in the groove while still holding the fibers down in the grooves. In addition to the set up used in Figure 57 another set up was created to help in placing the fibers in the grooves. Figure 57 shows this set up were the SM fiber is also held by a bare fiber launch. However this extra launch is only meant to assist in laying the SM fiber in the desired groove which in this setup is the 2nd groove (from the top of the chip). The bare fiber launch holding the SM fiber was not clamped down on the fiber allowing it to move back and forth freely in the launch and keep the fiber in a constant position within the groove. This is compared to the PBG fiber launch that was clamped down on the fiber holding it in a fixed position, making the fiber slide in the groove when the micrometer stage was adjusted. Ultimately the functionality of the two setups was the same however the setup in Figure 57 was more convenient to work with because it held the SM fiber up to the groove allowing for easier application of the SM fiber in the groove.

Table 16. Repeatability of the transmission measurements

Attempt	SM Fiber Output	PBG Fiber Output	% Transmission
1	133.7 mV	63 mV	47%
2	133.7 mV	56.5 mV	42.2%
3	135 mV	67 mV	49.6%
Avg. % Transmission	X	X	46.2%

Finding peak transmission between the two fibers was a trial and error process. A method for placing the fibers in the grooves was created and can be seen below. Table 16 records the measured transmission attempts using this method. It should also be noted that when these measurements were taken the two fiber ends were touching as this is when maximum transmission was seen. The two fibers were known to be touching because when they were brought together and made contact the fixed PBG fiber pushed the SM fiber back, this was visually confirmed by seeing the junction between the two fibers move in the groove. The alignment procedure is discussed below.

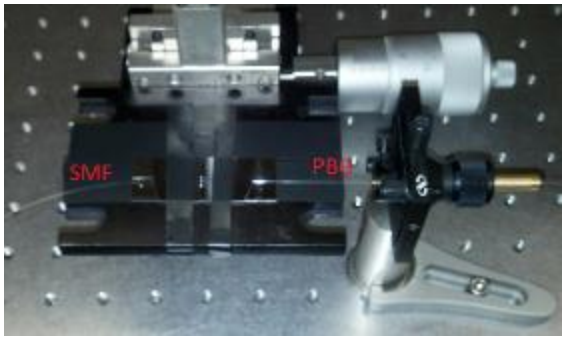

Figure 56. Single Fiber Launch

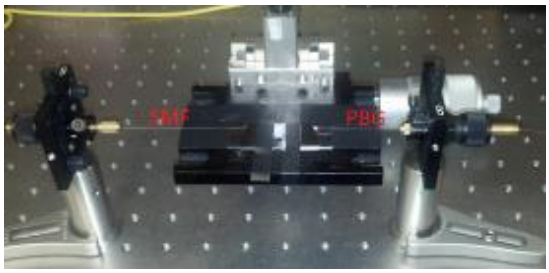

Figure 57. Double Fiber Launch Micrometer Stage Setup

Assembling V-Groove Fiber Splice

1.) Clean V-Groove With Isopropyl Alcohol (IPA) Solution and a Chem Wipe
- Drop some IPA on a Chem wipe
- Gently wipe down Large Non-Uniform V-Groove Chip from smaller groove to larger groove

2.) Cleave SM Fiber
- Strip protective coating with a fiber striping tool
- Run fiber between two Q-tips with IPA
- Place fiber in fiber cleaving tool
    - Just nicking the fiber with the cleaving blade, this creates a better cleave, a good cleave is crucial for good transmission between fibers
- Inspect cleaved fiber end piece under microscope, re-cleave if necessary

3.) Place SM Fiber in Desired Groove
- Place 2 bare SM fiber tips in the adjacent grooves of the desired splicing groove as spacers.
    - Cleaved fiber end pieces work well for this purpose
    - The desired grooves used for these measurements were the 6^{th} and 2^{nd} grooves from the top of the Large Non-Uniform V-Groove chip seen in Figure 53-Figure 54
- Place the main fiber in the groove so that it hangs over into the larger part of the groove that holds the PBG fiber
    - The fiber should hang over into the larger part of the groove by about 0.25mm as shown in Figure 58.

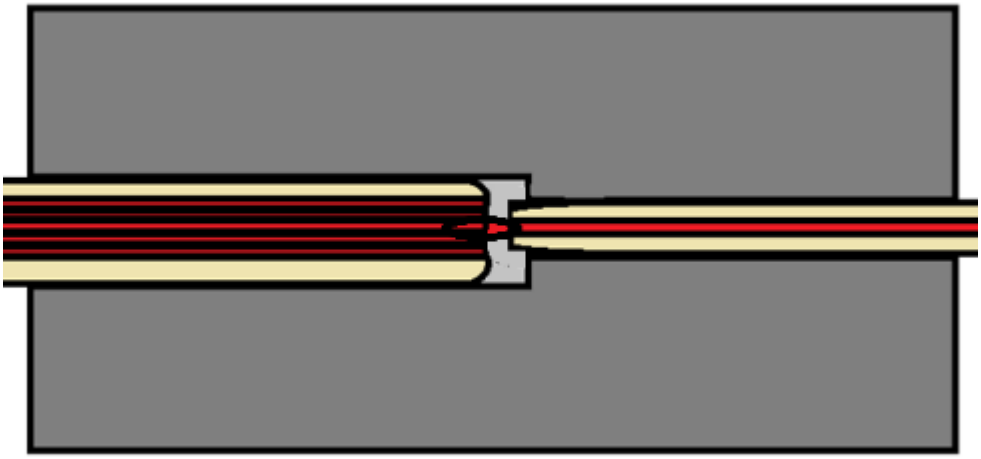

Figure 58. Alignment of the PBG fiber in the V-groove.

- When the non-uniform grooves were etching they did not etch in an ideal manner where the two different size grooves would meet and form right angles at the junction. Instead they gradually slope down forming imperfections in the grooves that can be seen in Figure 49 and Figure 50. This is why it is necessary to hang the SM fiber about 0.25mm over the edge, so that it may bypass the imperfections made by the junction of the two different sized grooves.

4.) Secure the extra silicon piece over the fiber to hold it down into the groove.

- This was done with electrical tape in this set up.
  - To permanently hold the fiber in the groove optical glue could be used to glue the extra silicon piece in place with the fiber. However this was not tested in the lab.

5.) Cleave PBG Fiber

- Strip protective coating from fiber by applying epoxy remover with a Q-tip.
  - Let Sit 12-15 min
  - When done run two dry Q-tips along fiber to pull covered region of jacket off.
- Run fiber between two Q-tips with IPA
- Place fiber in fiber cleaving tool
  - Just nicking the fiber with the cleaving blade, this creates a better cleave, a good cleave is crucial for good transmission between fibers
- Inspect cleaved fiber end piece under microscope, re-cleave if necessary

6.) Place PBG Fiber in Desired Groove

- Place 2 bare PBG fiber tips in the adjacent grooves of the desired splicing groove as spacers.
  - Cleaved fiber end pieces work well for this purpose

- The desired grooves used for these measurements were the 6th and 2nd grooves from the top of the Large Non-Uniform V-Groove chip seen in Figure 53-Figure 54

- Place the PBG fiber in the groove so that its end is almost touching the end of the SM fiber
  - The distance between the SM and PBG fiber can be adjusted using the micrometer stage.

7.) Secure the extra silicon piece over the fiber to hold it down into the groove.

- This was done with electrical tape in this set up.
  - To permanently hold the fiber in the groove optical glue could be used to glue the extra silicon piece in place with the fiber. However this was not tested in the lab.

A distance vs. transmission measurement was taken by using the 3rd attempt of gaining maximum transmission seen in Table 16 as the first measurement at µm spacing. When the 3rd attempt was done the two fibers were pushed together with the micrometer until it was seen that the SM fiber moved back in the groove. The maximum measurement of 49.6% transmission was seen here when the fibers were touching. Using the micrometer the PBG fiber was backed away from SM fibers by 2µm intervals for 100µm. Figure 59 is a plot of the DC transmission value as a function of distance. In Figure 59 it can be seen that the transmission decreases as expected until around 62 µm when the transmission flattens out around 35.5% transmission where it stays for the remainder of the measurement. This seemed odd because one would expect the transmission to continue to decrease, a reason it plateaued may be because the silicon holding pieces holding the fibers to the grooves became lose and allowed the fibers to move in the groove and keep their relative distance constant regardless of the micrometer stage movement. Regardless the data up until 62µm seams consistent to what would be expected from a distance vs. transmission relationship.

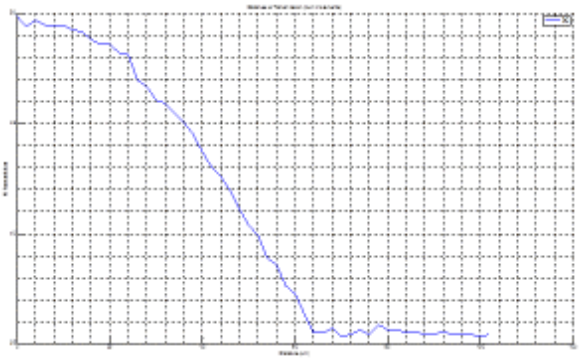

Figure 59. Transmission as a function of distance

The first experimental setups used to demonstrate a single segment of the in-line fiber sensor is shown in Figure 60. Light from the tunable 2 µm DFB laser is launched into single mode optical fiber with FC/APC connectors at both ends. Using a fiber coupled detector, the amount of light coupled into the first fiber can accurately be measured. A second single mode fiber with an

FC/APC connector was then connected to the first single mode optical fiber. At the other end of the single mode optical fiber, a section of PBG fiber has been spliced. This first experiment was set up to monitor the transmission of the PBG fiber using an optical detector. The PBG fiber and optical detector were placed in a container with dry ice to elevate the CO_2 concentration to levels that would be expected for sub-surface measurements. Tuning the laser is achieved by adjusting the operating temperature and monitoring the temperature set point is achieved using a temperature dependent resistor (thermistor). A plot of the transmission through the PBG fiber as a function of the operating temperature of the the DFB laser is shown in Figure 61 as the DFB laser is tuned across a single CO_2 absorption feature.

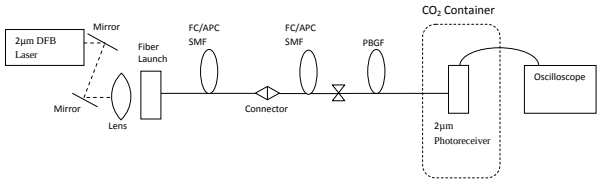

Figure 60. Experimental setup for measuring the transmission through the PBG fiber.

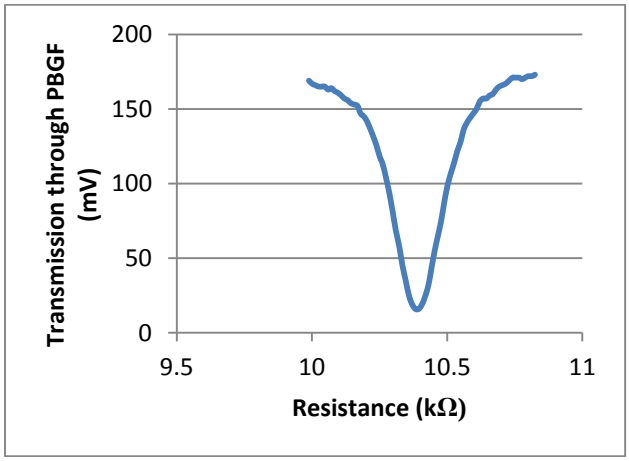

Figure 61. A CO_2 absorption feature as a function of the DFB operating temperature measured using a thermistor.

The second experimental setup used to further explore the in-line fiber sensor is shown in Figure 62. Light from the 2 μm DFB laser is launched into a port of a 2 x 2 optical fiber splitter. The input light is split with half of the light directed to a first transmission detector while the remaining light is coupled to a second single mode optical fiber that is spliced to a PBG fiber. Light exiting the PBG fiber is reflected back into the PBG fiber using a mirror. The PBG fiber and mirror are housed in a container and dry ice is used to elevate the CO_2 concentration within the container to mimic underground CO_2 concentrations. The light then propagates back to the 2 x 2 fiber splitter where half of the reflected light is directed to a second transmission detector. A function generator is connected to the current controller of the DFB laser to allow modulation of the operating wavelength through changes in the drive current. In this way the DFB laser is scanned over an absorption feature of CO_2.

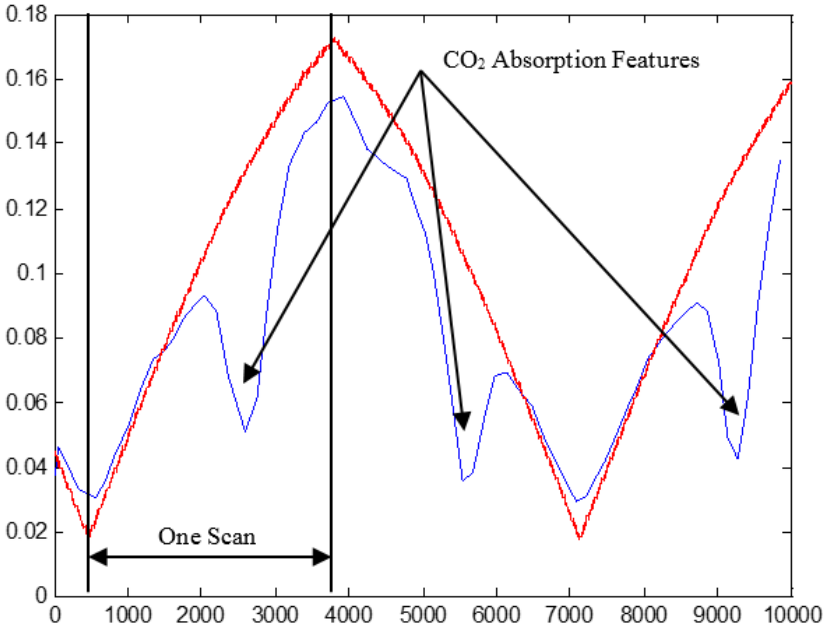

Figure 62. The reference power signal seen be the first transmission detector (Red Line) and the transmission signal (Blue Line) seen by the second transmission detector as a function of time. One CO_2 absorption feature was scanned over.

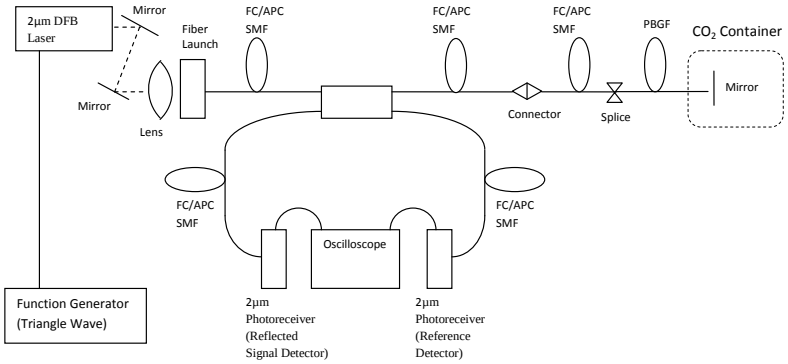

Figure 63. Experimental setup for measuring the transmission through the PBG fiber using a double pass geometry.

A plot of the voltage seen by the first and second transmission detectors as a function of time is shown in Figure 63. The red line indicates the optical power seen be the first transmission detector, which is proportional to the output power of the DFB laser and can be used to normalize the transmissions through the PBG fiber. The blue line indicates the power seen by the second transmission detector. This signal is a measure of the optical power after the light has passed through the PBG fiber, been reflected from the mirror, and passes through the PBG fiber a second time. The DFB laser scans over one absorption feature which is indicated in Figure 63. Figure indicates that the double pass geometry through the PBG fiber can and the 2 x 2 fiber splitter can be used to successful measure CO_2.

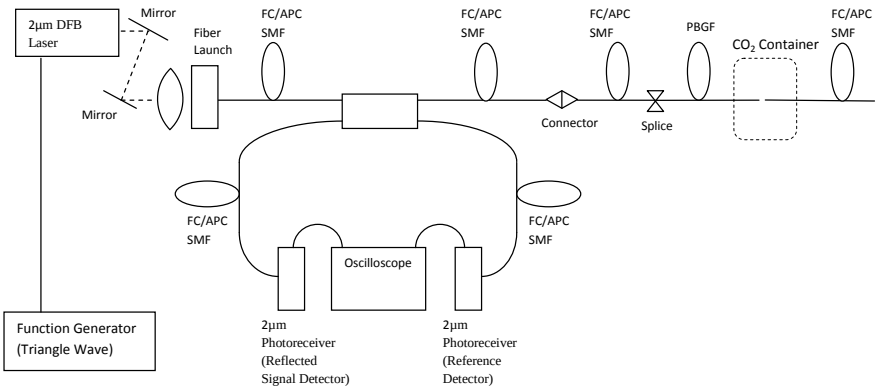

Figure 64. Experimental setup used to study a single segment of the in-line optical fiber sensor.

The third experimental setup used to demonstrate a single segment of the in-line fiber sensor is shown in Figure 64. The experimental setup is similar to that described in Figure 52 with the main difference being that the mirror used to reflect the light back through the PBG fiber has been replaced with a single mode optical fiber. Thus the experimental setup shown in Figure 64 represents a single segment of the in-line fiber sensor shown in Figure 49. The first measurement made with the experimental setup shown in Figure 54 was the amount of light coupled into the second single mode optical fiber that would be available for the second segment of the in-line fiber sensor. This amount of light coupled into the second single mode optical fiber was measured at 40.5%. A plot of the optical power at the two transmission detectors is using the experimental setup shown in Figure 64 is presented in Figure 65a when no CO_2 is present in the container surrounding the air gap between the PBG fiber and second single mode optical fiber. The red line indicates the optical power measured by the first transmission detector, which is proportional to the output power of the DFB laser. The blue line represents the optical power that passes through the PBG, is reflected from the second single mode optical fiber, is coupled back into the PBG, passes through the PBG a second time and is the incident on the second transmission detector after the 2 x 2 fiber coupler. Carbon dioxide was then added to the container via dry ice and spectroscopic measurements of CO_2 where made using the two transmission detectors. A plot of the optical power for the two transmission detectors is shown in Figure 66 with the CO_2 absorption feature indicated in the figure. This result indicates that a single segment of the in-line fiber sensor can be used to monitor sub-surface CO_2

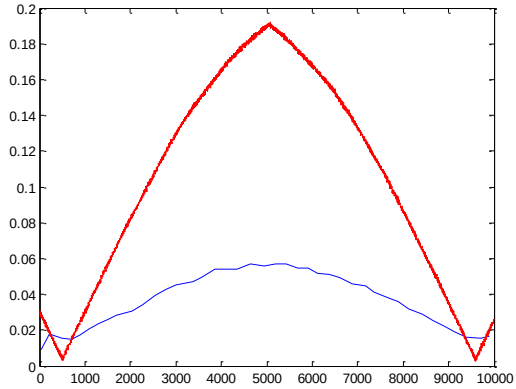

Figure 65. The reference power signal seen be the first transmission detector (Red Line) and the transmission signal (Blue Line) seen by the second transmission detector as a function of time. No CO_2 was placed in the container so no absorption features are seen in this figure.

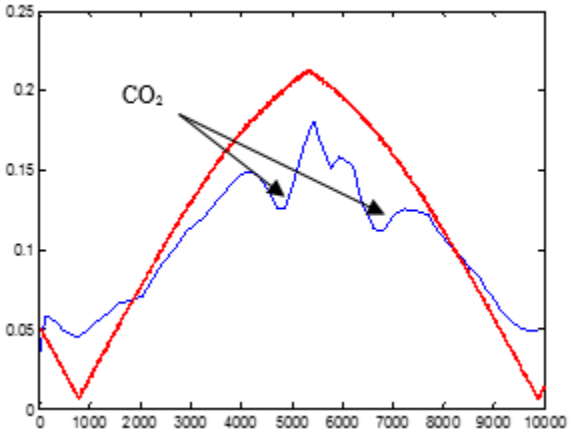

Figure 66. The reference power signal seen be the first transmission detector (Red Line) and the transmission signal (Blue Line) seen by the second transmission detector as a function of time. The CO_2 absortion features are indicated in this figure.

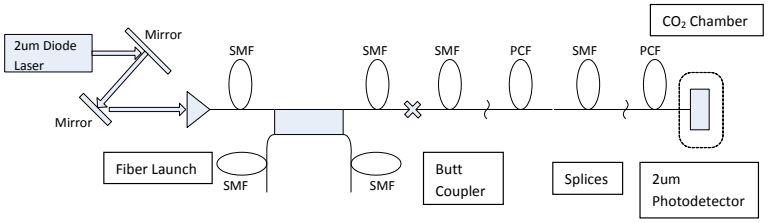

Figure 67. Two segment setup of the in-line fiber sensor using the PCF.

The two segment in-line fiber sensor was reconstructed as shown in Figure 67. Light from the 2 μm is coupled in to a single mode optical fiber. This single mode optical fiber is then but coupled into the first in-line segment of the in-line fiber sensor that utilizes a single mode optical fiber fusion spliced to the PCF. A small gap after this first segment allows carbon dioxide (CO_2) to

diffusion into the core of the PCF allowing for the spectroscopic absorption measurements to be made. A second segment of the inline fiber sensor is then aligned using the fiber couplers shown in Figure 51.

Laboratory based CO_2 spectra were measured using dry-ice to mimic the elevated CO_2 levels expected underground. A plot of the transmission as a function of time is shown in Figure 68 with no dry ice allowing for a background measurement to be made. The DFB laser is tuned using a sawtooth waveform so the time axis is proportional to the operating wavelength of the laser. A plot of the transmission as a function of time is shown in Figure 69 with dry ice present for the second in-line fiber segment. The CO_2 absorption features are visible in this figure indicating that that CO_2 absorption measurements can be made from this second segment.

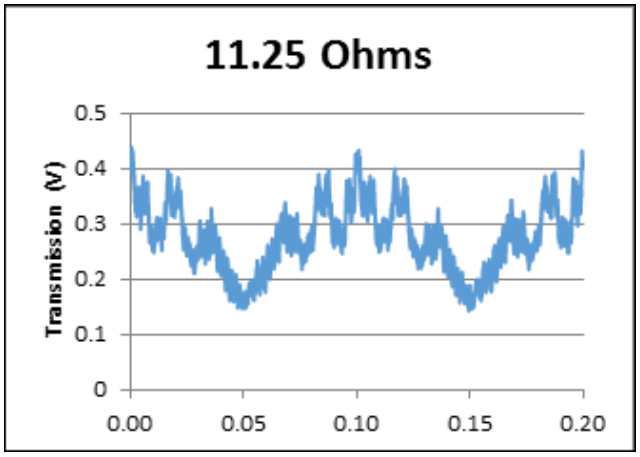

Figure 68. Transmission as a function of time (proportional to wavelength) with no dry ice

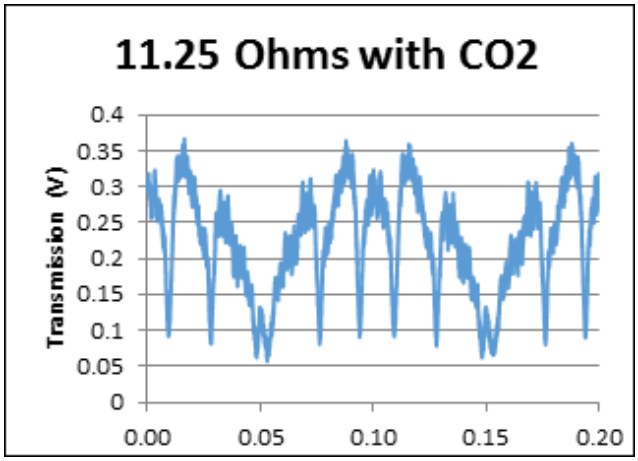

Figure 69. Transmission as a function of time (proportional to wavelength) with dry ice. The CO_2 absorption lines can be seen in this plot.

The fiber optic sensor will be assembled as shown in Figure 70. The cw intensity from a PM fiber-coupled, single frequency laser at 1550 nm is injected into a PM fiber coupled, electro-optic modulator that will form 400 nanosecond pulses at a pulse rate of 10 kHz. Each pulse will then be injected into a PM fiber-coupled phase shifter that will put a linear phase shift on the

pulse. The pulse is then injected into port 1 of a PM fiber-coupled circulator. The output of port 2 of the circulator is injected into a fiber Bragg grating (FBG#1). After a length of PM single mode fiber, the pulse will see a second fiber Bragg grating. The reflections from the two FBG's will return to port 2 of the circulator and exit from port 3 into a detector. The length of the fiber between the two FBG's will initially be set to 20 m so that the two reflected pulses will overlap over a 200 ns window and hence the interference of the two returning pulses can be studied. The linear phase shift put on the pulse is intended to increase the sensitivity of the interference signal.

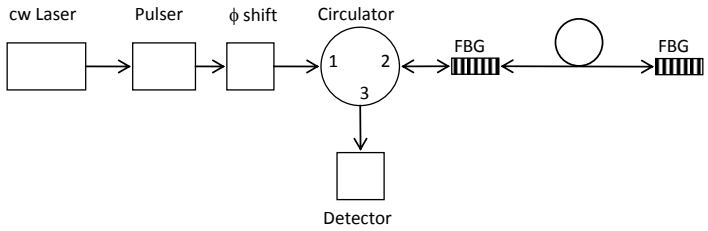

Figure 70. Schematic used for modeling and initial laboratory demonstration.

To understand the beat signal, the linear frequency chirp applied to the laser beam is $\omega(t) = \omega_o + \frac{\beta t}{2}$ where ω_o is the laser operating frequency and β is the chirp rate. The electric fields that combine at the detector can be written as

$$E_1(\omega, t) = E_0 \exp\left(j\left(\omega_o t + \frac{\beta t^2}{2}\right)\right) rect\left(\frac{t}{\tau}\right)$$

and

$$E_2(\omega, t) = \alpha S E_0 \exp\left(j\left(\omega_o + \frac{\beta t}{2}\right)(t + T_d)\right) rect\left(\frac{t}{\tau}\right)$$

where rect(t/τ) is the rectangle function and τ is the pulse width. Calculating the intensity seen be the detector as a function of frequency and position yields

$$I(x, \omega) = |E_o|^2 \frac{\tau}{\sqrt{2\pi}}\left[sinc\left(\frac{\omega\tau}{2\pi}\right) + \alpha S sinc\left(\frac{\omega\tau - \frac{\beta x \tau}{v}}{2\pi}\right)\right]$$

where sinc(x) is the sinc function x is the position in the fiber at which the scattering occurred and v is the velocity of light in the fiber. The first term in the square bracket is a function center at ω = 0 while the second term in the square bracket is a function centered at frequency $\omega = \frac{x\tau}{v}$ and its amplitude depends on the scattering strength which changes as the pressure changes. Using a spectrum analyzer to monitor the detector, the amplitude at each frequency will be proportional to the pressure while the frequency is directly related to the where in the fiber the scattering occurred. Thus, the potential exists using a pulsed chirped laser source to monitor in real time the distributed pressure along an optical fiber.

The modeling of the scattered signal in an optical fiber was also worked on this past quarter and is summarized here. The amount of light that is scattered and collected by the optical fiber can be calculated from

$$s = \left(\frac{NA}{n_o}\right)^2 \frac{1}{4.55}$$

Where NA is the numerical aperture of the fiber and n_o is the index of refraction for the fiber core. To calculate the fraction of light lost due to scattering, we can calculate the scattering coefficient, α, in dB/km where

$$\alpha = \frac{0.76 + 0.51(n_{core} - n_{cladding})}{\lambda^4}$$

where n_{core} and $n_{cladding}$ are the core and cladding index of refraction and λ is the wavelength in μm. Modeling of the fiber optic Rayleigh scattering indicates that the amount of scattered light will be $\alpha S = 1.2 * 10^{-4}\ km^{-1}$.Using this loss term due to scattering, the optical power after the light travels a distance z through the fiber is

$$P(z) = P_0 10^{\frac{-\alpha}{10}z}$$

The amount of light that is scatter from the fiber between a position L and L+ΔL can be calculated from

$$I(t) = I_0 \alpha S \Delta L 10^{\frac{-\alpha}{5}L}$$

where $\Delta L = \frac{c\tau}{2n}$ is the spatial resolution of the detection system where c is the speed of light, □ is the pulse duration, n is the index of refraction, and t is the time of flight for the light pulse and is $t = 2nL/c$.

With this general model for the light seen at a detector resulting from Rayleigh scattering, the perturbation of the detected signal can be estimated by looking at how the scattered signal is affected by pressure, strain, and temperature. The attenuation for the optical fiber resulting from strain (due to pressure) can be calculated by looking at how strain affects the optical fiber. The index of refraction for the optical fiber can be written $n = n' - in''$ where n' is the real part of the index of refraction and n'' is the imaginary part of the index of refraction. Taking the partial derivative of the optical path length yields

$$\frac{\partial(n''L)}{\partial\sigma} = n''\frac{\partial L}{\partial\sigma} + L\frac{\partial n''}{\partial\sigma}$$

The first term on the right side of the equation relates to the added absorption due to the changing length of the fiber resulting from the strain and is negligible. The second term relates the variations in the attenuation coefficicent due to strain and plays a role in determining how the

strain will affect he light collected by the receiver. This value is discussed in the literature and is approximately 5% per micron of displacement. Using the bulk modulus of the optical fiber, the strain and stress can be related resulting in a connection between the applied pressure and the change in the attenuation for the fiber.

The fiber optic sensor shown schematyically in Figure 49 was constructed using commercially available components. The benchtop assembly is shown in Figure 71 with the major components listed in Table 17.

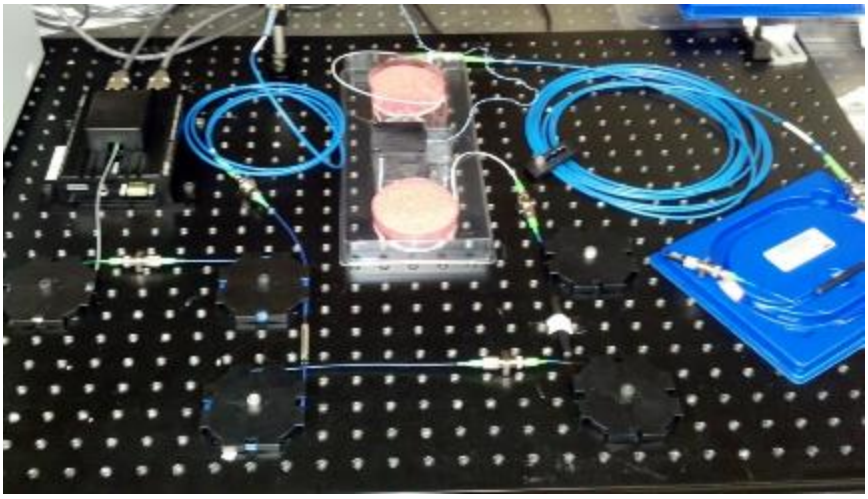

Figure 71. Fiber Optic Bragg Grating Seismic Wave Sensing system

Table 17. Major components used in the benchtop fiber seismic sensor

Component	**Description**
Laser	Thorlabs SFL 1550P Diode Laser
Detector	New Focus 2011
FBG	MPB Comm. Inc Athermal 1550nm R = 10% PM
Fiber Stretcher	Optiphase PZ1-PM4
Circulator	Thorlabs CIR1550PM

The sensor is meant to measure only the change in path length due to strain effects. However, the fiber itself is also sensitive to small changes in temperature. These temperature changes cause a random drift in the detected signal shown in Figure 72. The fiber Bragg grating (FBG) frequency response is highly dependent on the periodic structure inside its fiber and any expansion or contraction of the structure would cause signal degradation. However, thermal expansion was assumed not to be a significant factor for the FBGs since the packaging should be athermal. Thus these drifts are attributed mainly due to changes in the effective cavity length from room temperature variations. Literature on compensating for these thermal drifts reported using active feedback with another PZT cylinder to null the effects of these unwanted oscillations. Some sort of system could be implemented in the future if deemed necessary for

signal fidelity. Figure 72a also shows that the output seems to have some saturation at a maximum value. Investigations into this were inconclusive, but it does not seem to be due to sensor saturation. When the drive current was increased the output level scaled with it exhibiting the exact behavior seen in Figure 72a. When the fiber stretcher is driven with a sinusoidal input, the detected output shows a superposition of the random environmental effects with the driving signal. Figure 73 shows a typical output.

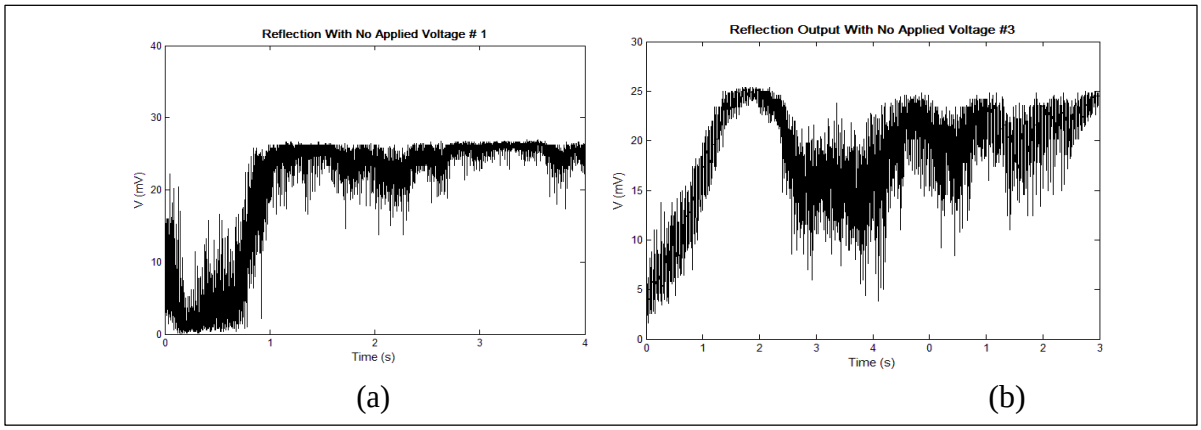

Figure 72. Thermal Effects on Detected Signal

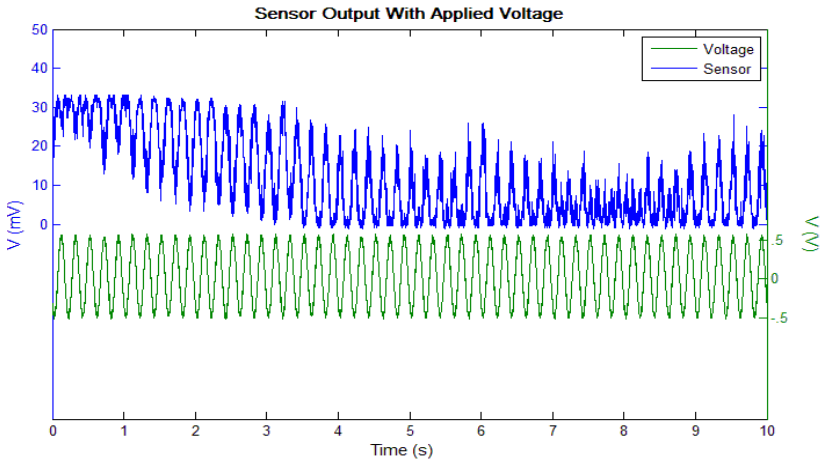

Figure 73. The sensor Output is shown in blue for the corresponding fiber stretcher signal shown in green.

It is clear from Figure 73 that the strain resulting from the fiber being stressed due to the fiber stretcher, however the signal has other frequency content that is not necessary for seismic applications. The frequency range of seismic type events ranges from the mHz up to several kHz. Therefore, any frequencies above that can be filtered out without loss of information. To that end, a 4th order active low pass filter was inserted to help remove the unwanted signals. It was made adjustable by implementing a DIP switch that selects one of three resistor settings. A schematic of the filter is shown in Figure 74. The circuit is implemented using two 2nd order

Butterworth Sallen-Key topographies. The last stage is a simple buffer.

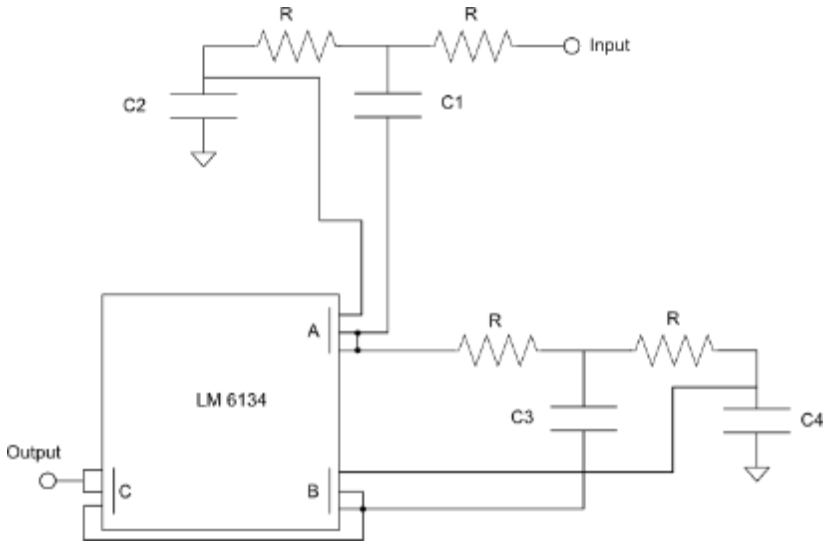

Figure 74. Filter Schematic

The different resistor settings correspond to different cutoff frequencies. Originally implemented with 1 kHz, 10kHz and 30kHz settings, the 30kHz cutoff frequency was replaced with 7 kHz. The Network Analyzer HP 3589A was used to look at the frequency response with the results for the 7 kHz filter shown in Figure 75.

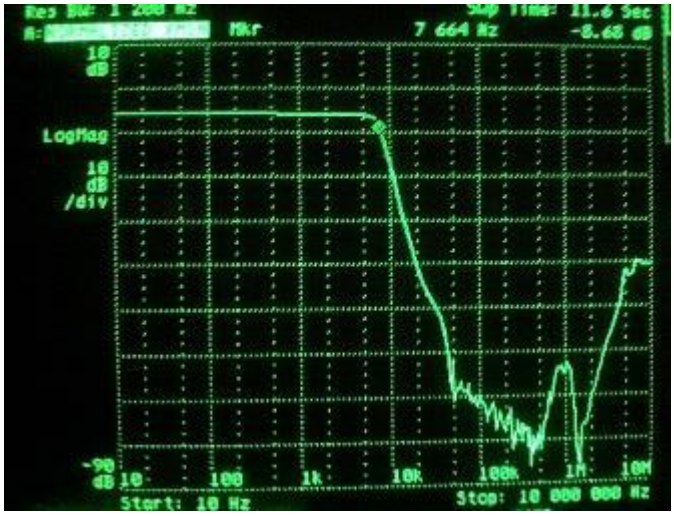

Figure 75. Frequency Response of Filter

The filter shows a very flat response typical of the Butterworth filter and from the corner frequency upwards to ~30 kHz exhibits a rough attenuation greater than 70 dB. Beyond that the frequency characteristics of the operational amp start to affect the filters performance. The trade off for the great flat passband performance is that the filter design does alter the phase

information. Figure 76 shows the output from the system with decreasing cutoff frequency. A definite improvement can be seen between the unfiltered and filtered signals.

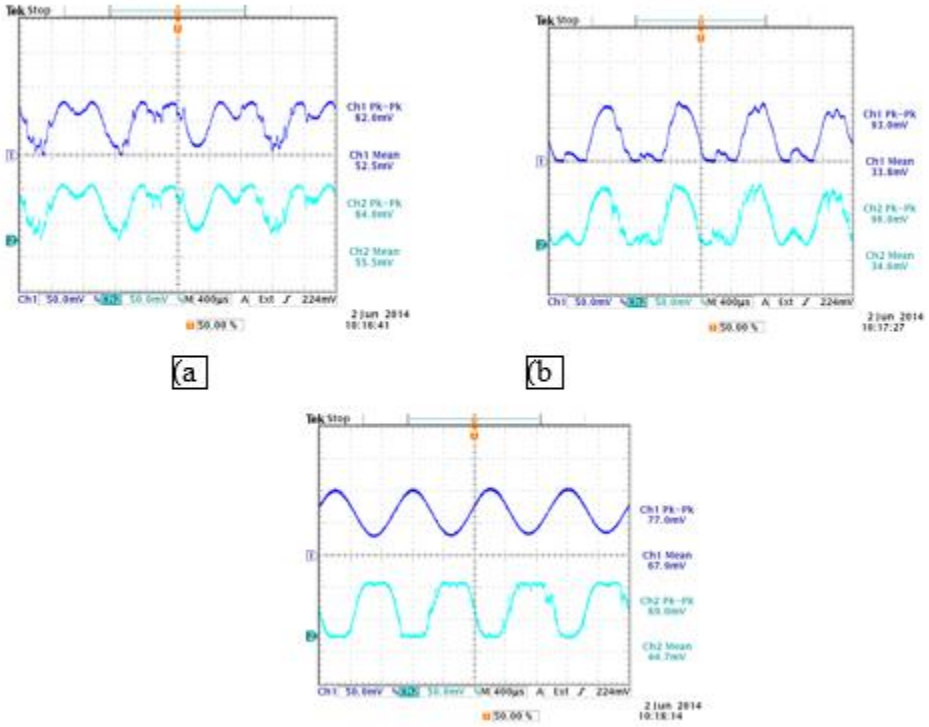

Figure 76. Output with Filter Implemented. For all three cases the driving signal was 1 kHz. In (a) fc was 30 kHz, (b) was at 10 kHz and (c) was at 1 kHz. The blue (top) signal is the filtered output while the teal (bottom) signal is not filtered.

Another approach to cleaning up the signal could be simply averaging. Some sample data was taken from the oscilloscope and a running average algorithm was applied to both the filtered and unfiltered output data. The results show that for higher frequency signals using both the filter and averaging produce a nice clean signal to work with. For slower frequency signals, using both is not as useful. In Figure 77, the blue represents the unfiltered and the red, the filtered signal.

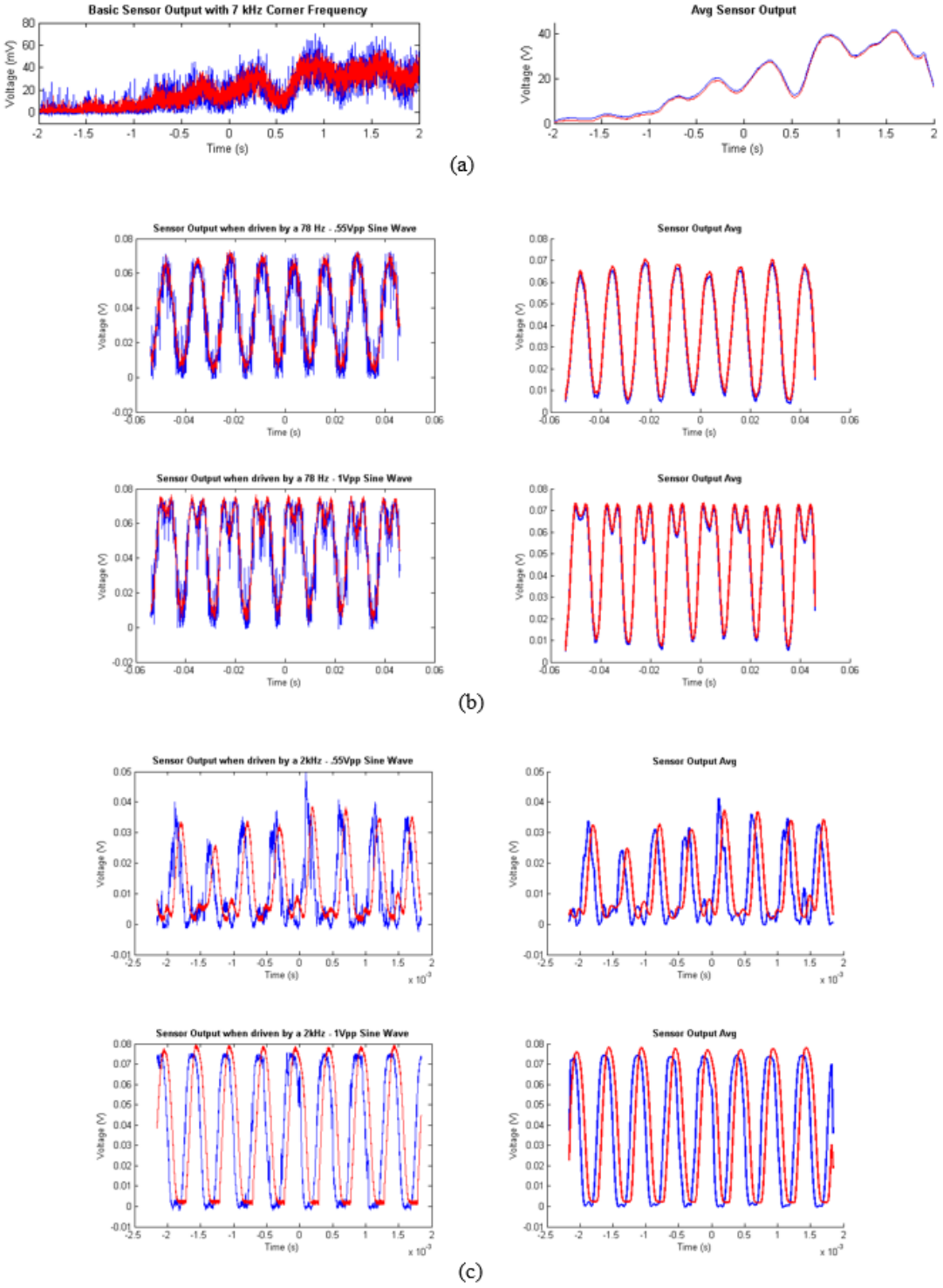

Figure 77. Comparisons between filtering and averaging.

In Figure 77, the plots on the left are the raw data from the scope while the right plots are after averaging. Blue represents unfiltered and red represents the filtered signal. The fc for all three

parts is set at 7 kHz. The output without any driving signal is shown in (a). Plots (b) and (c) are for driving frequencies in the fiber stretcher of 78 Hz and 2 kHz, respectively.

As expected, the averaging is helpful when the signal noise is larger and the phase does shift as the frequency of the signal approaches the filter's cutoff frequency.

Currently, the sensor is using an Optiphase fiber stretcher to simulate a signal to be detected. The fiber stretcher is essentially a large cylinder wrap with fiber. The cylinder can expand or contract and this creates stresses in the fiber wrapped along it. The specifications sheet for the device states that fiber stretches .14 μm per volt. After some investigation, it was determined that in order to be measurable, a minimum input of 40mV was necessary. This was based on looking at the noise of the sensor without any driving signal and then slowly increasing the drive signal from 0mV to 100mV. The signal emerged from the noise at around 40mV. With 40mV as the minimum detectable signal, a basic estimation for the sensitivity of the current sensor can be obtained. Assuming that roughly 10m of the 12.3m of fiber attached to the stretcher is actually wrapped around the cylinder, this gives a rough strain resolution of .56 nano-strain. This strain level indicates that this fiber sensor has the needed sensitivity to measure the seismic events.

CONCLUSIONS: UNDERGROUND FIBER OPTIC SENSORS

The inline fiber sensor can allow several point measurements to be made along a single segment of the optical fiber. For this work, two segments of the inline fiber sensor were demonstrated. Combining this result with other fiber sensor work ("Field demonstration of a 1 x 4 Fiber Sensor Array for Sub-Surface Carbon Dioxide Monitoring for Carbon Sequestration", Benjamin Soukup, Kevin S. Repasky, John L. Carlsten, and Geoff Wicks, Journal of Applied Remote Sensing, Vol. 8, 083699-1, 083699-13, 2014.) has the potential of allowing up to two hundred point measurements to be made using a single laser source and inexpensive fiber optic components. This fiber sensor array has the potential to cover large areas and is easily configurable allowing flexible deployment at carbon sequestration sites.

The chirped laser fiber pressure sensor has the potential to allow for distributed strain measurements along an optical fiber. The beat signal frequency and amplitude allow location and strain amplitude respectively to be determined along a fiber deployed along a well.

EXPERIMENTAL METHODS: ULTRA-COMPACT INFRARED IMAGERS

The methods used in this study all relied on compact, field-deployable imaging systems custom designed for long-term outdoor deployment. The basic concept driving the use of vegetation imaging to locate leaking CO_2 is that higher soil gas concentrations of CO_2 will stress the vegetation, leading to measurable changes in VIS and NIR reflectance and LWIR emission. Similar methods have been used with airborne and satellite-based sensors to identify regions of natural CO_2 seepage from VIS/NIR and infrared images of vegetation and soil (Bateson et al.

2008, Govindan et al. 2010, Govindan et al. 2011). Some studies have suggested that leaks can be identified through CO_2-induced changes in plant species (Krüger et al. 2009, Noble et al. 2012), although most have been based on measuring changes in plant stress. The earlier study by Bateson et al. (2008) showed that CO_2 gas vents appeared as warm regions in thermal infrared images, and hypothesized that this might be a result of the leaking gas or the soil at the gas vent being warmer than the surrounding vegetation. Our study added the more complete interpretation of the LWIR image response in terms of plant stress leading to impaired thermo-regulation by vegetation, which leads to increased vegetation temperature during day and increased variation of vegetation temperature during day and night (Johnson et al. 2012).

Our VIS and NIR reflectance imaging experiments were conducted initially with a commercial multispectral imager (Rouse et al. 2010), and later with a custom wide-angle imager that used red and NIR reflective bands (Hogan et al. 2012a,b,). In comparing measured reflectance values of healthy vegetation to those of vegetation exposed to the leaking CO_2, there were statistically significant temporal and spatial variations of VIS and NIR reflectance and vegetation indices derived from the reflectance. The CO_2 leak location was identified by a more rapid rate of plant stress relative to the usual seasonal decay in the control regions.

During the summer 2011, 2012, and 2013 controlled release experiments, we also deployed a LWIR imager to measure vegetation stress and thereby indirectly identify the gas leak location from thermal emission (Johnson et al. 2012). The mechanism was expected to be essentially the same, but in this case the stress caused by high soil gas concentrations of CO_2 at the plant roots was hypothesized to result in an impairment of the vegetation's temperature regulation. A consequence of this was that over time the vegetation nearest the leak exhibited larger diurnal temperature variations and, most significantly, higher maximum daytime brightness temperatures (temperature of an ideal blackbody emitting the same amount of radiation).

The vegetation imagers were mounted on a 3-m scaffold, looking down at approximately 45° onto a vegetation test area (Figure 78). The horizontal well, buried at a nominal depth of 2 m, ran just in front of the scaffold, across the bottom of the images. The released CO_2 exited the ground in a highly nonuniform pattern (Oldenburg 2010, Lewicki 2008, 2009), creating localized regions of elevated CO_2 concentrations that we refer to as "hot spots." The 2011 release ran from July 18 to August 15, 2011, with a flow rate of 0.15 tons/day. Images were acquired once per minute throughout daylight hours for the reflective imager and throughout both day and night for the emissive imager. Images were analyzed in a hotspot region known to have high CO_2 flux and two control regions with near background-level CO_2 flux (Figure 79). The use of two control regions allowed us to find that there was no substantial view-angle dependence in the results (Johnson et al. 2012).

Figure 78. Side-by-side vis/NIR imager and LWIR imager mounted on a scaffold

Figure 78 shows side-by-side vis/NIR imager and LWIR imager mounted on a scaffold to measure vegetation reflectance and emission, respectively, at the ZERT field in Bozeman, Montana. The tripod in front of the scaffold is a mount that holds a Spectralon reflectance panel to calibrate the vis/NIR images.

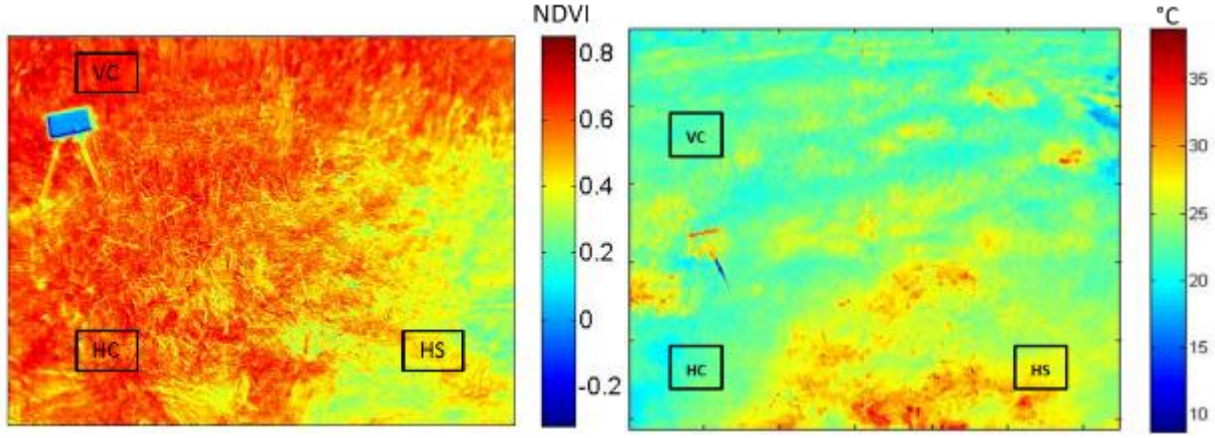

Figure 79. Approximate locations of the hotspot (HS), horizontal control (HC), and vertical control (VC) regions shown on images of the vegetation test area from 14 Aug 2011: (left) NDVI, and (right) LWIR brightness temperature in degrees C.

The reflective imager had 1280×1024 pixels and custom front-end optics that provide wide-angle imaging through interference filters mounted in a rotating filter wheel. The filters had 40-nm half-power bandwidths, centered at 800 nm for the NIR channel and 630 nm for the red channel (Hogan 2012a). The reflective imager had an embedded computer running custom software to control the instrument. During this deployment, red and NIR image pairs were acquired once each minute. A Spectralon 99%-reflectance panel was deployed on a tripod mount in the midst of the vegetation test area so that it was included in a portion of each image. A laboratory calibration was used to relate the pixels in that particular portion of each image to all of the

pixels throughout the image, resulting in a calibration that converted digital numbers to reflectance. From these reflectance data, Normalized Difference Vegetation Index (NDVI) values were calculated from equation (1), and then the 1-minute reflectance and NDVI data in the hotspot and two control regions were averaged from 10 AM to 2 PM (when the Sun is sufficiently high to reduce shadows in the vegetation) to create a single value of red reflectance, NIR reflectance, and NDVI for each region on each day.

$$NDVI = \frac{\text{NIR-Red}}{\text{NIR + Red}}. \quad (1)$$

Note that the NDVI is a non-independent interaction term for red and NIR reflectance (Lawrence & Ripple 1998) that has been shown in previous studies to have substantial statistical explanatory effect (Rouse et al. 2010, Hogan et al. 2012a,b, Lawrence & Ripple 1998).

The LWIR imager was mounted on the same scaffold, immediately beside the reflective imager (Figure 78). The FLIR photon 320 LWIR camera with 320×240 pixel produced 14-bit digital images, whose digital numbers were calibrated using a method developed at Montana State University for maintaining radiometric calibration even with widely varying camera temperature and no calibration target in the field (Nugent et al. 2013, Nugent and Shaw 2014, Nugent et al. 2015). The resulting values of radiance [W/(m^2 sr)] at each pixel were converted to brightness temperature (T_b) in degrees C with a lookup table computed by integrating the product of the Planck blackbody function and the 8-14 μm spectral response function of the imager. The T_b values in all the thermal images were spatially averaged within the hotspot region and the two control regions to produce a time series of region-average T_b.

In the final component of this project, an ultra-low-cost VIS-NIR imaging system was deployed on a tethered balloon over the ZERT field to determine if this simple system would be capable of detecting leaking CO_2 and to demonstrate the advantage of a tethered balloon platform that enables viewing of a larger area than was possible with the scaffold-mounted imagers. This very simple imaging system, originally designed for outreach, used three very basic board-level cameras, each outfitted with low-cost optical filters to define blue, red, and NIR spectral images (Shaw et al. 2012). Figure 80 is a photograph of the system, with its three filter-covered cameras on the left side and the electronics boards on the right side of the transparent plastic enclosure. The "balloon camera" was deployed four times during the 2012 experiment on a balloon tethered above the ZERT field (limited by balloon availability) and was deployed on the scaffold alongside the "scaffold camera" during the 2013 field experiment.

Figure 80. Photograph of the ultra-low-cost spectral imager designed and built at Montana State University for deployment on a tethered balloon.

RESULTS AND DISCUSSION: ULTRA-COMPACT INFRARED IMAGERS

The high sensitivity and rapid response of vegetation reflectance imaging to changes in the CO_2 flow are demonstrated by Figure 81, which is a time-series plot of the NDVI calculated from red and NIR images recorded during the 2012 experiment with the scaffold-mounted spectral imager built at Montana State University (these data are from the "scaffold camera," not the ultra-low-cost "balloon camera"). The gas flow was started on 10 July and interrupted soon after by a lightning strike. The NDVI previously was on a downward trend because of naturally occurring senescence of the grass as summer progressed, but its rate of decline slowed and even tended to reverse. Causes of this change could include vegetation nourishment by rainfall or the initial burst of CO_2, or a combination of the two. The downward trend resumed again as soon as the gas flow was resumed on 16 July. A curious and significant pattern of NDVI fluctuations occurred in mid-July in the same time period that saw the gas flow twice interrupted briefly by power outages. We do not have the biological data necessary to completely interpret these fluctuations, but it is clear that the NDVI responds in a significant and rapid manner to changes in the flow of the leaking gas.

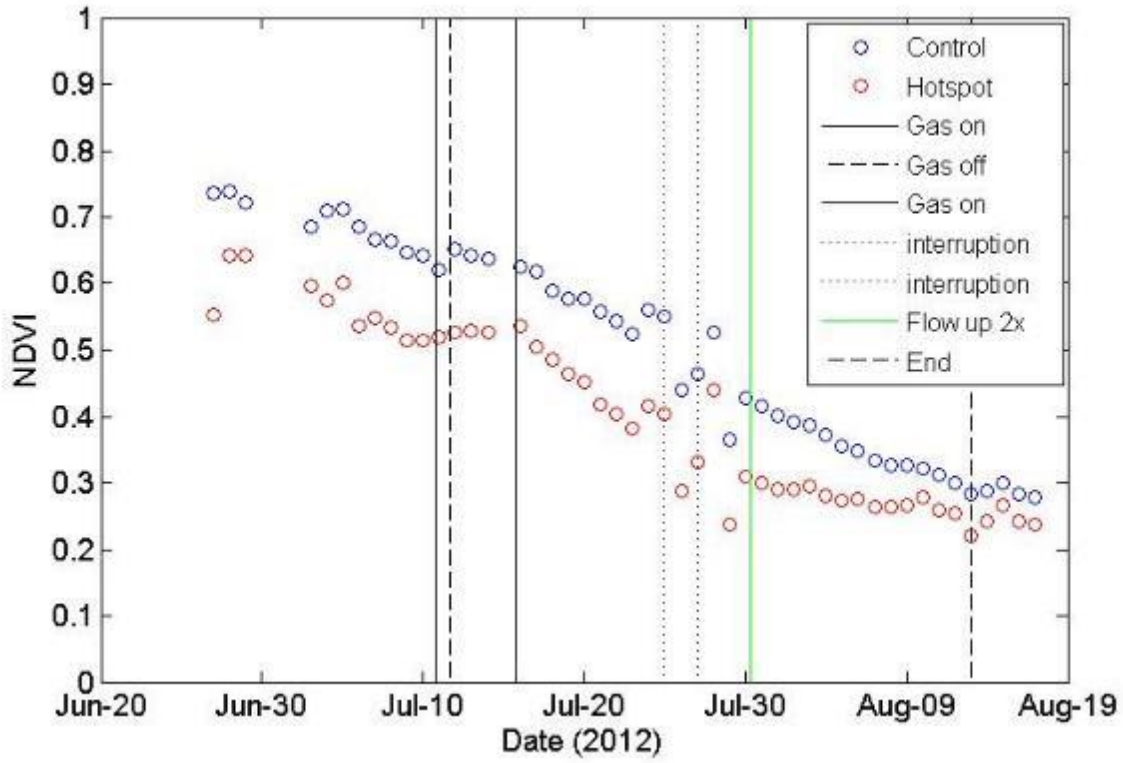

Figure 81. VIS & NIR imager data from the 2012 CO_2 release experiment, demonstrating that vegetation reflectance image data show high sensitivity to changes in CO_2 flow.

We entered the ZERT II program having already established that NDVI imaging was capable of detecting leaking CO_2 (Rouse et al. 2010) but the 2011 experiment demonstrated this with much greater statistical significance (Hogan et al. 2012b). Additionally, an LWIR camera was deployed for the entire 2011 and 2012 experiments to test the hypothesis that there would be a detectable thermal response of the vegetation to the leaking gas and to enable a quantitative comparison of the VIS-NIR imager and the LWIR thermal imager.

To facilitate a statistical comparison of the performance of the two types of imagers during the 2011 CO_2 release experiment, linear regressions were calculated using DAY (number of days since the start of operation with side-by-side imagers) as the response variable and reflectance, NDVI, and T_b as predictors. We used DAY as the response variable, because, although DAY does not respond to the spectral responses, it enables comparison of the correlations between DAY and spectral responses even when there are multiple spectral responses being tested in a single regression. Furthermore, DAY acts as a surrogate for exposure level to the constantly flowing CO_2 gas, which is the biophysical driver of the response we are measuring.

This procedure was similar to the analysis implemented in prior years for the reflective data alone [Rouse et al. 2010, Hogan et al. 2012a,b), but this iteration added thermal brightness temperature data and the second control region. Thermal images were acquired during day and night, starting in early June 2011, whereas reflective images were acquired only during day,

starting in early July 2011. Although there is some evidence that the extra images acquired prior to the start of the release and during hours other than at midday increased the amount of variance explained by the thermal data (Johnson et al. 2012), the comparison reported here uses images only from midday (10 AM – 2 PM) on the common days when both the reflective and emissive imagers were operating together (14 July – 23 August 2011, with gas flowing from 18 July to 15 August).

We began the analysis by performing separate linear regressions on NDVI data alone, red and NIR data alone, and thermal brightness temperature data alone to determine whether each of these data types by itself was able to produce statistically significant results that allowed us to distinguish between the hotspot and control regions (Johnson et al. 2012). The linear regression model for the NDVI was formulated as follows:

$$\mathrm{DAY} = \beta_0 + \beta_1 \mathrm{NDVI} + \beta_2 \mathrm{REGION} + (\beta_3 \mathrm{NDVI} \times \mathrm{REGION}) \quad (2)$$

In this equation, DAY is the response variable representing the number of days elapsed since the start of operation for both side-by-side imagers, REGION is a categorical variable that selects from the three regions of interest (hotspot, horizontal control, or vertical control), and the β terms are the regression coefficients. We created a reduced model by removing terms that were not found to be statistically significant, starting with the least significant term. Statistical significance was determined by a term having a *p*-value less than or equal to 0.05 (the *p*-value is the probability of observing a sample statistic that is as extreme as the test statistic). The reduced model for the NDVI regression (eq. 3) resulted in a residual standard error of 3.76 on 109 degrees of freedom, with an adjusted R^2 value of 0.90.

$$\mathrm{DAY} = 144.47 - 164.19\,\mathrm{NDVI} - 1.71\,\mathrm{VC} - 78.91\mathrm{HS} + (95.61\,\mathrm{NDVI} \times \mathrm{HS}), \quad (3)$$

In eq. (3), VC and HS are the values of the categorical variable REGION, representing the vertical control or hotspot regions, respectively. In this case, both regions were compared with the horizontal control region in the regression; i.e., for observations in VC, VC = 1 and HS = 0, for observations in HS, VC = 0 and HS = 1, and for observations in HC, VC = 0 and HS = 0. This enables three possible models, depending on the value of VC and HS. In fact, the three models are represented by the three regression lines shown in Figure 82, Figure 83, and Figure 84.

These results show that there was a statistically significant difference between the vertical control and hot spot regions. The coefficient estimated for the hot spot intercept was substantially larger than the coefficient for the vertical control intercept, meaning the hot spot had a much greater difference from the horizontal control than the vertical control, which was quite similar to the horizontal control.

Figure 82 is a time-series plot of daily average NDVI, plotted with time on the horizontal axis for convenience (although to interpret the regression values in the table, it is important to keep in mind that the regressions were actually performed with experiment day as the response variable).

The vertical lines indicate the start and end of the CO_2 release. This figure shows that the NDVI data from all three regions started out similar, but decayed with different rates for the control and hotspot regions after the onset of the CO_2 release. The similarity of the curves from the two control regions indicates that there is no substantial view-angle difference in the data. As expected, the NDVI data from the hotspot region decayed at a much higher rate than in either control region.

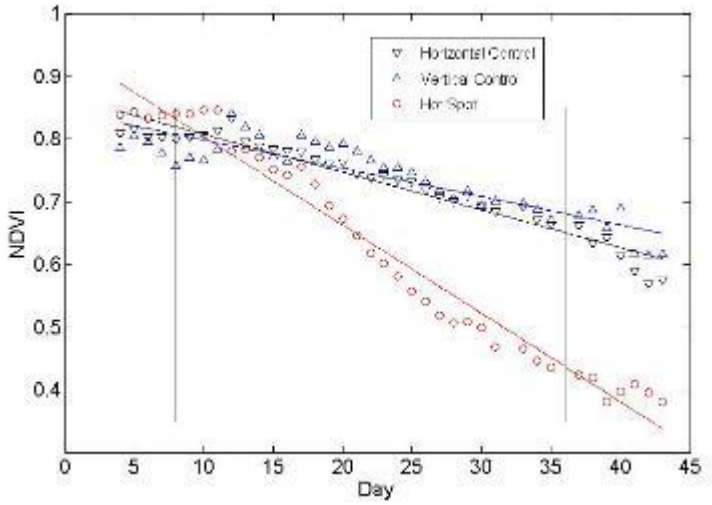

Figure 82. NDVI plotted vs. day of the 2011 experiment for three test regions. The vertical lines mark the start and end of the CO_2 gas release on 18 July 2011 and 15 August 2011, respectively.

A similar linear regression was calculated for the red and NIR reflectance data:
$\mathrm{DAY} = \beta_0 + \beta_1 \mathrm{NIR} + \beta_2 \mathrm{RED} + \beta_3 \mathrm{REGION} + (\beta_4 \mathrm{NIR} * \mathrm{REGION}) + (\beta_5 \mathrm{RED} \times \mathrm{REGION})$. (4)

Again, a reduced model was obtained by eliminating terms that were found to not have statistical significance according to the requirement that p-value ≤ 0.05. This regression gave a residual standard error of 2.39 on 106 degrees of freedom with an adjusted R^2 value of 0.96. The reduced reflectance regression model is shown in equation (5), and the reflectance is plotted vs. experiment day in Figure 83. The temporal trends were as expected, with the red reflectance rising and the NIR reflectance falling as the vegetation dried out through the summer, but with the highest rate of change in the hotspot region because of the additional stress caused by the high soil gas concentration. It is interesting to note the similarity in the slope of the Hotspot and Vertical Control lines for the NIR reflectance in Figure 83. The NIR reflectance is primarily responsive to leaf structure, but the lack of biophysical measurements prevents us from interpreting this with confidence.

$$\mathrm{DAY} = 75.66 - 126.65\,\mathrm{NIR} + 323.92\,\mathrm{RED} - 30.94\,\mathrm{VC} - 42.05\,\mathrm{HS} + 37.64\,(\mathrm{NIR} \times \mathrm{VC}) + 71.34\,(\mathrm{NIR} \times \mathrm{HS}) - 172.57\,(\mathrm{RED} \times \mathrm{HS}) \quad (5)$$

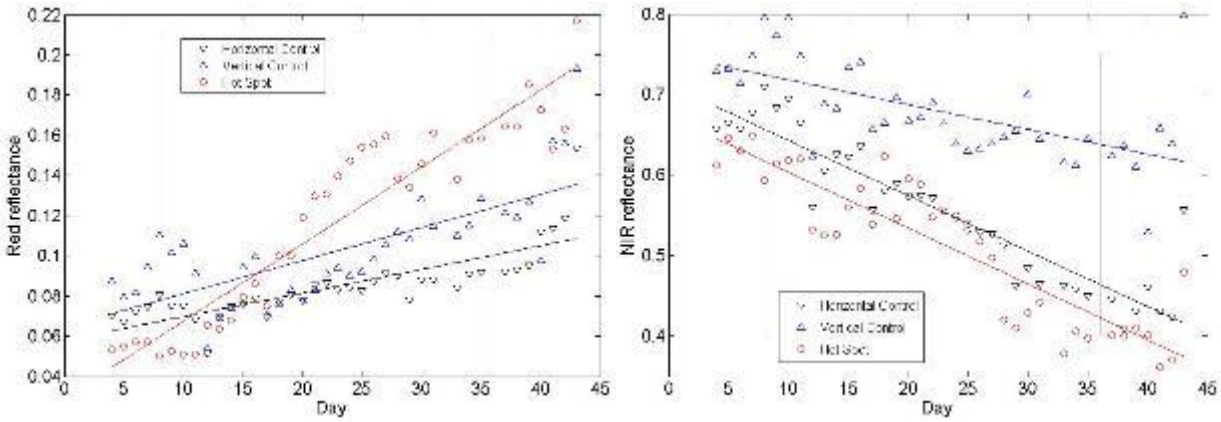

Figure 83. Reflectance plotted vs. day of the 2011 experiment for all three test regions: (left) red and (right) NIR.

The same type of analysis was performed on the infrared brightness temperatures for the days when both imagers were operating together. To isolate the plant-health-related thermal signature from the meteorological variations, the ambient air temperature was subtracted from the infrared brightness temperature for all readings. The full linear regression model for the emissive data used the same REGION categorical variable as the previous models, along with a ΔT term representing the difference of IR brightness temperature and air temperature ($\Delta T = T_b - T_a$), as follows:

$$DAY = \beta_0 + \beta_1\, REGION + \beta_2\, \Delta T + \beta_3(\Delta T \times REGION) \qquad (6)$$

The reduced ΔT regression model in equation (7) resulted in a residual standard error of 8.71 on 110 degrees of freedom with an adjusted R^2 value of 0.44. Again, the temporal trend shown in Figure 84 was as expected, with ΔT increasing as the vegetation became stressed while summer progressed, but with the highest rate of increase in the hotspot region. This trend was expected because ΔT increased as the stressed vegetation lost its ability to regulate its own temperature, resulting in an IR T_b that was much higher than the ambient air temperature because of solar heating during the day. The vegetation nearest to the hot spot region showed markedly higher ΔT values than the unexposed vegetation. In this case, the difference between the slopes of the regression lines for the two control regions was slightly significant, indicating that there is no substantial concern with view angle.

$$\mathrm{DAY} = 6.03 - 6.95\,\mathrm{HS} + 9.18\,\mathrm{VC} + 2.81\Delta T \qquad (7)$$

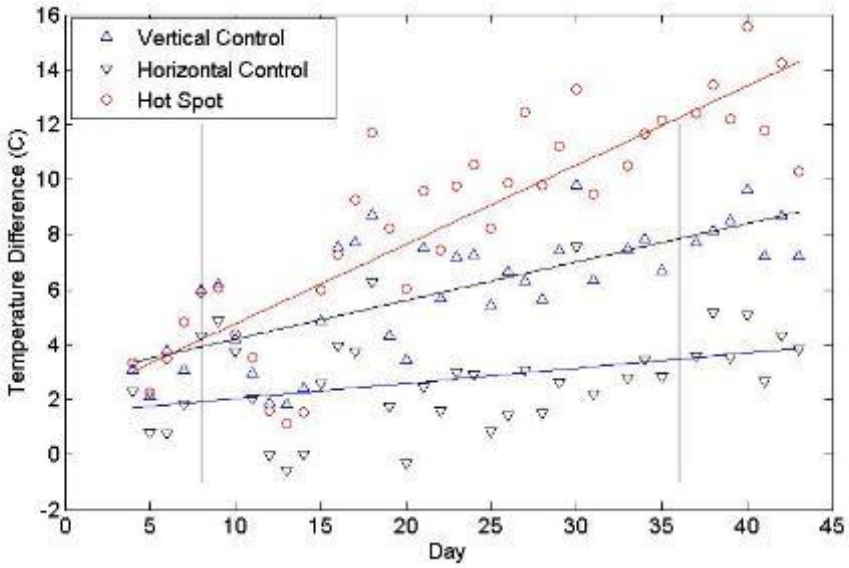

Figure 84. Difference of LWIR brightness temperature and air temperature, plotted vs. day of the 2011 experiment for the three test regions.

Having shown that both the vis/NIR imager data and the LWIR imager data independently yielded statistically significant results, we next combined the NDVI, reflectance, and brightness temperature data into the following single regression model.

$$\mathrm{DAY} = \beta_0 + \beta_1\mathrm{NDVI} + \beta_2\mathrm{NIR} + \beta_3\mathrm{RED} + \beta_4\Delta T + \beta_5\mathrm{REGION} + \beta_6(\mathrm{NDVI} * \mathrm{REGION}) + \beta_7(\mathrm{NIR} * \mathrm{REGION}) + \beta_8(\mathrm{RED} * \mathrm{REGION}) + \beta_9(\Delta T \times \mathrm{REGION}) \quad (8)$$

The full-model reduced regression in equation (9) resulted in a residual standard error of 2.24 on 103 degrees of freedom with an adjusted R^2 value of 0.96.

$$\mathrm{DAY} = 1.02 + 66.73\mathrm{NDVI} - 120.75\mathrm{NIR} + 469.2\,\mathrm{RED} + 0.13\Delta T + 66.34\mathrm{HS} + 26.15\mathrm{VC} - 129.81(\mathrm{NDVI} \times \mathrm{HS}) + 109.90(\mathrm{NIR} \times \mathrm{HS}) - 30.20(\mathrm{NIR} \times \mathrm{VC}) - 475.03(\mathrm{RED} \times \mathrm{HS}) \quad (9)$$

This full regression model using combined reflective and emissive data shows that the reflectance, NDVI, and thermal infrared measurements are all significant for identifying CO_2-affected regions from unaffected regions of vegetation. The individual regressions (equations 3, 5 and 7) also are each strong by themselves, indicating that a CO_2-affected region can be identified by one method alone (reflectance, NDVI, or LWIR emission). The highest R^2 value (0.96) occurred for both the reflectance regression and the combined reflective-and-emissive regression. This suggests that the most effective single type of measurement would be visible and near-infrared vegetation reflectance, although there is statistically significant value in measuring both reflectance and emission.

In the 2012 experiment, we added to the study the ultra-low-cost VIS-NIR imager deployed on a balloon tethered above the ZERT field. Figure 85 is an NDVI image derived from the red and

NIR channels of this balloon-mounted camera on 5 July 2012. The image shows the entire ZERT vegetation test area as the dark rectangular area near the center of the image, and also shows a good amount of the surrounding field. Recent haying had left piles of freshly cut grass, which produce easily discernible rows of higher NDVI, separated by rows of lower NDVI where the underlying soil is visible through the remaining vegetation stalks. The locations of the camera scaffold, the Spectralon reflectance calibration target, and the CO_2 "hot spot" are marked on the image. A path also can be discerned, where people had been walking between the scaffold and the Spectralon mount.

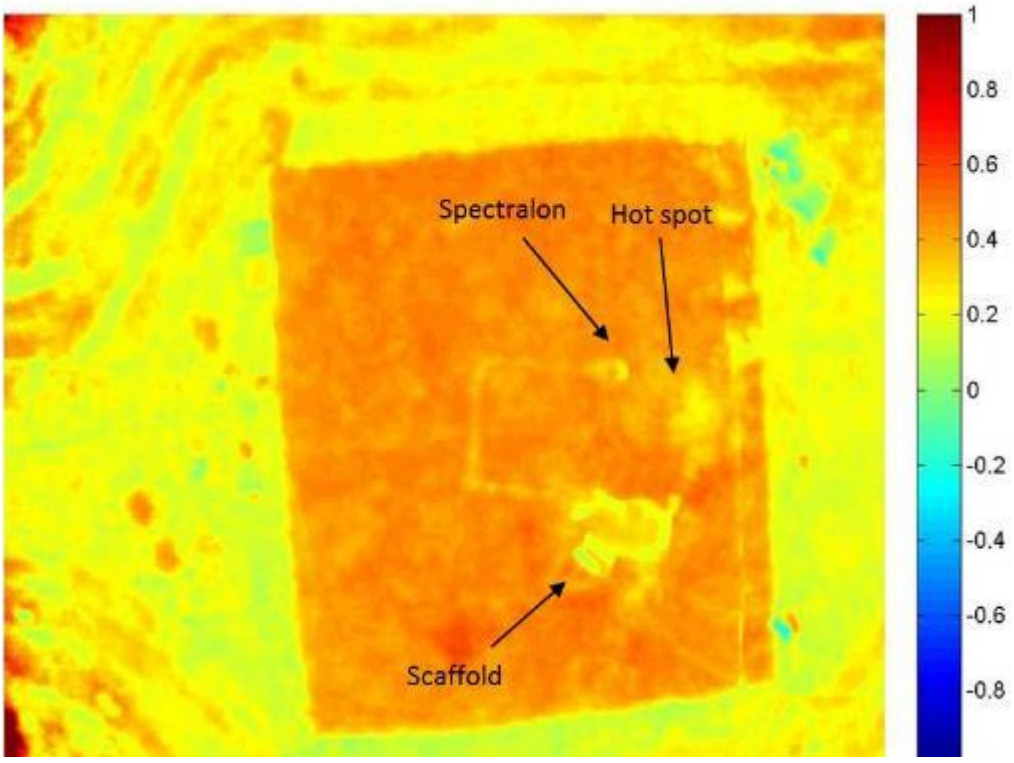

Figure 85. NDVI image of the ZERT vegetation test area and surroundings, obtained on July 5, 2012 with ultra-low-cost imager mounted on a balloon tethered above the ground.

A time-series plot of NDVI measured by the balloon camera and the scaffold camera is shown in Figure 86. This plot includes the same vertical lines that were shown on Figure 81 to mark the onset, interruptions, and end of CO_2 gas flow. Error bars have been added to the NDVI data from both cameras, based on a standard error-propagation method (Bevington and Roberts 2002) using experimentally determined uncertainties of the calibration for each camera. The figure shows that a similar trend was evident in both cameras, but the larger uncertainties of the balloon camera data raise a question of whether there was statistically significant separation of the NDVI data in the control and hot spot regions of the field. This larger uncertainty arose because the calibration of the ultra-low-cost balloon camera was found to be not stable, owing to apparent nonlinearities within the camera electronics. However, post processing based on a side-by-side deployment of the balloon camera and scaffold camera during the 2013 field experiment allowed us to recover a reasonable estimate of the NDVI from the balloon camera images. We note that

since then, a newer, even lower-cost camera has been identified that seems to eliminate the problems experienced with the original ultra-low-cost cameras. Experiments with this newer system are continuing beyond the end of the ZERT II project for other remote sensing purposes.

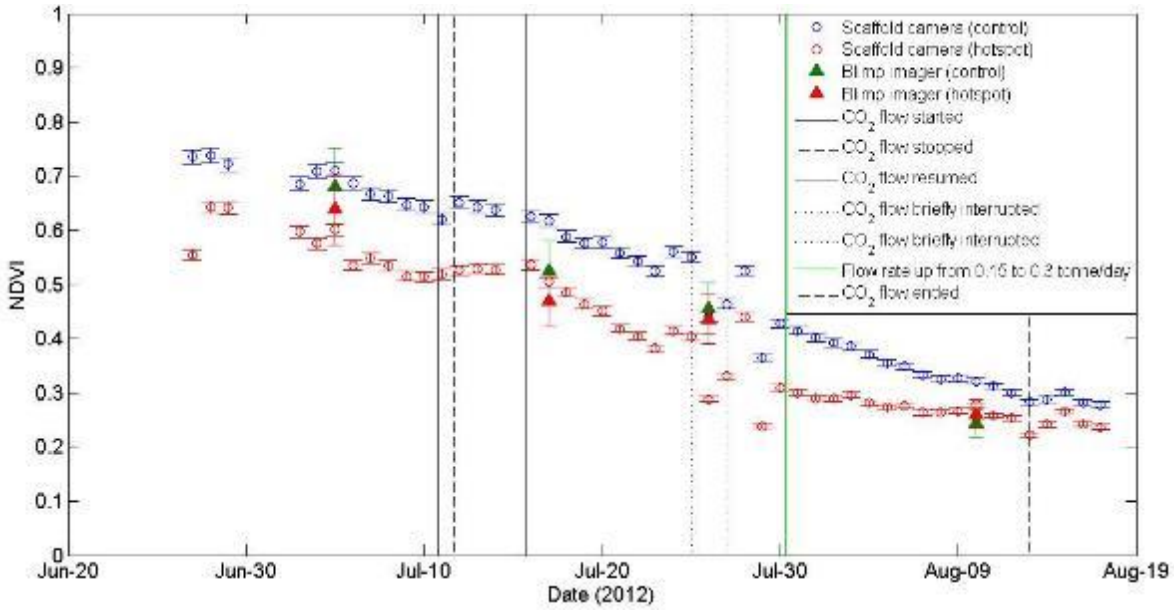

Figure 86. Time-series plot of NDVI data from scaffold and balloon cameras during the 2012 ZERT field experiment.

CONCLUSIONS: ULTRA-COMPACT INFRARED IMAGERS

This study showed that leaking CO_2 was readily detectable using VIS-NIR imaging of vegetation reflectance or LWIR imaging of vegetation thermal emission. The comparison of these two imaging modalities showed that the emissive data combine in a statistically significant manner with the reflectance-band data. However, either reflective or emissive imaging alone can distinguish between regions with and without a CO_2 leak. An ultra-low-cost version of the VIS-NIR camera was deployed on a tethered balloon and obtained consistent NDVI measurements, but was hampered by internal electronic nonlinearities that made calibration difficult. Newer versions of this camera without the nonlinearity are showing promise, but are not completely characterized as of this writing. Overall, in our study, the LWIR imaging method was simplest because it did not require a reflectance calibration panel in the field, only air temperature data, which are generally readily available. If this method were used for airborne monitoring, thermal imaging would therefore require deployment of air temperature sensors in the area being monitored, while visible/NIR imaging would require either field deployment of a sufficiently large reflectance calibration panel, deployment of downwelling solar irradiance sensors in the field, or use of other calibration methods that allow the images to be processed for reflectance.

EXPERIMENTAL METHODS: VALIDATION OF NEAR-

SURFACE CO_2 DETECTION TECHNIQUES AND TRANSPORT MODELS

The field site and infrastructure required to release CO_2 has been described in detail previously (Spangler, Dobeck et al. 2010). In order to perform the CO_2 releases Montana State University (MSU) every year procures a source of CO_2 with a large negative $\delta^{13}C$, installs, maintains, operates, and disassembles the injection infrastructure, samples the injected CO_2 for $\delta^{13}C$, and performs the necessary water collection and reporting to comply with the requirements of the EPA UIC permit issued in 2012. MSU also continues to collect and provide supporting data to participants such as CO_2 injection flow logs, meteorological variables, vertical wind profile, and soil flux measurements.

During the releases conducted in the summers of 2011-2014 six national labs, six universities, two companies, and the United States Geological Survey (USGS) conducted experiments at the site. Fourteen activities begun in ZERT I continued into ZERT II. Transport of CO_2 through soil was studied by several groups. Pacific Northwest National Laboratory (PNNL), Lawrence Berkeley National Laboratory (LBNL) and MSU investigated soil CO_2 flux from the ground surface with accumulation chambers. The PNNL steady state system is described in (Amonette, Barr et al. 2010). LBNL and MSU used commercial systems (WEST Systems, Pisa, Italy) based on the accumulation chamber method (Chiodini 1998). Refinements of the MSU underground fiber sensor system (Barr, Humphries et al. 2011) measuring CO_2 soil gas concentration at approximately 1 m depth continued through the 2012 season. Brookhaven National Laboratory (BNL) finished up their inelastic neutron scattering (INS) measurements of total carbon in soil in 2011. (The technique is described in (Wielopolski and Mitra 2010)). Montana Tech continued to investigate the influence of CO_2 on the physical properties of soil. The types of techniques used are described in (Zhou, Lakkaraju et al. 2012; Zhou, Apple et al. 2013). In 2011, the University of Montana completed sampling for the soil microbial studies they began in ZERT I.

Changes in water chemistry as a result of CO_2 injection into the shallow groundwater was a continued area of experimental activity by USGS in ZERT II. Studies of the reflectance spectra as indicators of plant health advanced by multispectral (Hogan 2012) based methods, as well as by measuring other leaf physiological responses to upwelling soil CO_2 (Sharma 2014).

National Energy Technology Laboratory (NETL) and Apogee again co-injected perfluorocarbon tracers (PFTs) with CO_2 in one well zone to investigate atmospheric transport of CO_2. MSU purchased two eddy covariance towers to continue net CO_2 flux measurements after Lewicki finished her involvement in ZERT. Several types of laser based systems measured various quantities of interest in the air. Los Alamos National Laboratory (LANL) made measurements in the 2011 season of the ratio of O_2 and CO_2 with a system described in (Fessenden, Clegg et al. 2010). Measurements exploiting the large negative $\delta^{13}C$ of the injected CO_2 relative to the isotopic signature of background CO_2 at the site were made with a frequency modulated spectroscopy (FMS) laser system from LANL (Fessenden, Clegg et al. 2010). A mobile sensing platform (Krevor, Perrin et al. 2010) based on a commercial (Picarro) cavity ringdown (CRD) laser was developed further to make real time measurements of ^{13}C and ^{12}C in 2013 and 2014.

In addition to work advancing on from ZERT I, there were three new projects introduced during ZERT II. Kevin Respasky (MSU) field tested a scanning differential absorption lidar (DIAL) system with the goal of developing a CO_2 detection based method capable of scanning wide areas. The technique is described in (Johnson 2013). Kathryn Romanak from Bureau of Economic Geology (BEG) at University of Texas-Austin used the head space in the water monitoring wells in 2012 to test her process-based soil gas technique (Romanak 2012) at a controlled release site. In 2014 a private company, Exelis, used the ZERT field site to test a laser imaging tomography system that is in the development phase.

RESULTS AND DISCUSSION: VALIDATION OF NEAR-SURFACE CO_2 DETECTION TECHNIQUES AND TRANSPORT MODELS

Carbon dioxide flow rates and duration of release varied from year to year. The minimum rate of CO_2 flow was 0.1 tonne/day. The maximum was 0.3 tonne/day. All releases took place within the months of July and September of a given year. A continuous record of meteorological values at the site including atmospheric pressure, temperature, wind direction and speed, precipitation, relative humidity, and dew point was provided by Joe Shaw. The data is archived and accessible on an MSU website. MSU also collected and recorded flow logs of all the CO_2 injections.

In 2011, PNNL modified and continued to optimize the multi-channel, steady-state flow-through soil CO_2 flux monitoring system they designed and originally deployed during ZERT I. The correlation of the spatial distribution of CO_2 flux with soil moisture content and wind velocity was studied. Results of a comparison with a commercial (non-steady state) system owned and operated by MSU are given in (Amonette, Barr et al. 2013).

Jennifer Lewicki of LBNL made portable accumulation chamber measurements of soil CO_2 flux along the pipeline. This data is very useful to other experimenter since it maps the surface expression of the injected CO_2 as well as the relative magnitude of the hotspots. Lewicki concluded her participation in ZERT after the 2011 season. These flux maps were important enough to the project that MSU purchased a portable accumulation chamber and made these flux measurements in subsequent years. There has been little variation in location and relative intensity of the hot spots over the 8 years the field site has been in operation.

Soil Gas (fiber sensor)

Beginning in ZERT I changes in the geophysical properties of the soil in response to introduced CO_2 were investigated by Montana Tech. (Zhou, Lakkaraju et al. 2012) details the results of collecting data on soil moisture, soil temperature, rainfall rate, and soil CO_2 concentration to help determine what influences bulk soil electrical conductivity. Variation of O_2 gas in the soil with changing CO_2 concentrations was also investigated (Zhou, Apple et al. 2013). This work continued into the 2013 field season.

University of Montana collected soil samples at the ZERT field site to determine how elevated levels of CO_2 influence microbial communities. (Morales 2013; Morales 2014) discuss the response and shifts seen in the soil microbial communities.

Water sampling of the shallow aquifer underlying the site continued to yield information about the potential groundwater quality impacts of CO_2 leakage. The USGS supplemented their previous work (Kharaka, Thordsen et al. 2010; Zheng, Apps et al. 2012) on water chemistry with measurements made in the 2011 season.

Refinement of the multispectral detection of plant health degradation continued through 2013.

Multispectral

Montana Tech also measured plant health before and after exposure to injected CO_2 by measuring the physiological properties of stomatal conductance, chlorophyll content, and specific leaf area in dandelion and orchard grass. The work is detailed in (Sharma 2014).

NETL expanded on previous work (Strazisar, Wells et al. 2009; Wells, Strazisar et al. 2010; Pekney, Wells et al. 2012) to refine technologies capable of monitoring larger areas at reduced cost. Experiments in 2011 again used PFT's co-injected with CO_2 and detection on three 10 m high towers was automated to sample only during optimal atmospheric conditions.

Stanford re-initiated work on a mobile real-time CO_2 detection platform that they began in ZERT I. In 2013 and 2014 they tested improvements made to a portable system based on a Picarro CRD laser measuring $^{13}CO_2$ and $^{12}CO_2$ in the air. Advances were described in (Moriarty 2013) and (Moriarty 2014).

CO_2 DIAL

In 2012 Katherine Romanak of the University of Texas-Austin chose the ZERT site to test her process-based soil gas method. The technique relies on measuring various ratios of four gases (N_2, O_2, CO_2, and CH_4) to determine the origin of the CO_2 present. She had previously applied this method at a natural CO_2 site, a CO_2 EOR site, and a farm whose landowners claimed CO_2 was leaking from the Weyburn CO_2 sequestration site in Saskatchewan, Canada. ZERT provided a controlled release site where the source and quantity of the CO_2 is known, and no hydrocarbons are present to complicate the chemistry. Measurements of both soil gas and dissolved gases in groundwater were consistent with predictions of the process-based method (Romanak, Dobeck et al. 2013). Comparison of the ZERT results with the other settings mentioned above are given in (Romanak 2014).

Exelis, a private company and new participant in ZERT, took part in the 2014 release. They are developing a laser imaging tomography system ("Green LITE") and wanted to verify whether the system could detect anomalous CO_2 levels at a controlled release. ZERT aided in their development process by providing them with a realistic field setting and helped reveal what is needed to take the instrument from the lab to a field deployable system.

CONCLUSIONS: VALIDATION OF NEAR-SURFACE CO_2 DETECTION TECHNIQUES AND TRANSPORT MODELS

The ZERT site has successfully released CO_2 into the shallow subsurface every summer from 2007 through 2014. It has provided a valuable test bed with a robust baseline established over 8 years of data for daily, seasonal, and interannual variability. Over the duration of the ZERT experiment we have had participation in the field from seven universities, six national laboratories, six private companies, and the USGS. This work has generated over 40 publications. The site has gained world-wide recognition that has consistently generated interest of groups wanting to bring new detection techniques to test at ZERT. The visibility of work at the site has led to substantial international collaborations. The project director and site manager have been asked to provide technical advice on design and operation to other controlled release facilities. The ZERT field site was relevant enough to development of monitoring technologies to attract the International Energy Agency Greenhouse Gas (IEAGHG) Environmental Impact of CO_2 Storage Workshop July 17-19, 2012 conference. MSU hosted the conference and the ZERT site was a featured field trip of the conference.

GRAPHICAL MATERIALS LIST

Figures

Tables

REFERENCES

http://www.mmf.montana.edu/

Allison, J. D.; Brown, D. S.; Novo-Gradac, K. J. (1990), MINTEQA2/PRODEFA2—A Geochemical Assessment Model for Environmental Systems: Version 3.0 User's Manual. *U.S. Environmental Protection Agency.*

Amonette, J. E., J. L. Barr, et al. (2010). "Spatiotemporal changes in CO2 emissions during the second ZERT injection, August-September 2008." Environmental Earth Sciences 60(2): 263-272.

Amonette, J. E., J. L. Barr, et al. (2013). "Measurement of advective soil gas flux: results of field and laboratory experiments with CO2." Environmental Earth Sciences 70(4): 1717-1726.

Anderson, T.F., and Aruthur, M.A., 1983, Stable isotopes of oxygen and carbon and their application to sedimentologic and paleoenvironmental problems, *in* Stable Isotopes in Sedimentary Geology: SEPM Shourt Course no. 10, p. 1.1-1.151.

Arthur, M.A., Anderson, T.F., Kaplan, I.R., Veizer, J., and Land, L.S., 1983, Stable isotopes in sedimentary geology: SEPM Short Course, no. 10, p. 5–54.

Barnaby, R., Oetting, G.C. and Gao, G., 2004, Strontium isotopic signatures of oil-field waters: applications for reservoir characterization, AAPG Bulletin, vol. 88, no. 12, p. 1677–1704.

Barnhart, E.P. In Situ and Enhanced Coal-Bed Methane Production from the Powder River Basin. PhD Dissertation, Microbiology, Montana State University, June 2014.

Barnhart, E.P., De Le´on, K.B., Ramsay, B.D., Cunningham, A.B., and Fields, M.W., 2013, Investigation of Coal-Associated Bacterial and Archaeal Populations from a Diffusive Microbial Sampler (DMS): International Journal of Coal Geology, no. doi: 10.1016/j.coal.2013.03.006.

Barr, J. L., S. D. Humphries, et al. (2011). "Laser-based carbon dioxide monitoring instrument testing during a 30-day controlled underground carbon release field experiment." International Journal of Greenhouse Gas Control 5(1): 138-145.

Bateson, L., M. Vellico, S. E. Beaubien, J. M. Pearce, A. Annunziatellis, G. Ciotoli, F. Coren, S. Lombardi, and S. Marsh, "The application of remote-sensing techniques to monitor CO2-storage sites for surface leakage: Method development and testing at Latera (Italy) where naturally produced CO2 is leaking to the atmosphere," Int. J. Greenhouse Gas Control, v. 2, pp. 388-400 (2008).

Berthold, John E., "Historical Review of Microbend Fiber-Optic Sensors", Journal of Lightwave Technology, 13, 1193-1199, 1995.

Bevington, P. and D. K. Robinson, Data reduction and error analysis in the physical sciences, 3rd ed., McGraw-Hill (2002).

Bischoff, W.D., Bishop, F.C., and Mackenzie, F.T., 1983, Biogenically produced magnesian calcite inhomogeneities in chemical and physical-properties comparison with synthetic phases: American Mineralogist, v. 68, p. 1183–1188.

Bish, D.L., and Reynolds, R.C., Jr, 1989, Sample preparation for X-ray diffraction *in* Bish, D.L., and Post, J.E., eds., Reviews in Mineralogy, v. 20, p. 73–99.

Brown, W. G., 1993, Structural style of Laramide basement-cored uplifts and associated folds, *in* Snoke, A. W., Steidtmann, J. R., and Roberts, S. M., eds., Geology of Wyoming: Geological Survey of Wyoming Memoir, no. 5, p. 312-371.

Bruckschen, P., Bruhn, F., Veizer, J. and Buhl, D., 1995, 87Sr/86Sr isotopic evolution of Lower Carboniferous seawater: Dinatian of Western Europe, Sedimentary Geology, vol. 100, p. 63–81.

Bruckschen, P., S. Oesmann, and J. Veizer, 1999, Isotope stratigraphy of the European Carboniferous: Proxy signals for ocean chemistry, climate and tectonics: Chemical Geology, v. 161, p. 127– 163.

Burke, W. H., Denison, R. E., Hetherington, E. A., Koepnick, R. B., Nelson, H. F., and Otto, J. B., 1982, Variation of seawater 87Sr/86Sr throughout Phanerozoic time: Geology, v. 10, p. 516–519.

Burke, W.H., Denison, R.E., Hetherington, E.A., Koepnick, R.B., Nelson, H.F. and Otto, J.B., 1982, Variation of seawater 87Sr/86Sr through Phanerozoic time, Geology, vol.16, p. 516–519.

Busby, J. F.; Kimball, B. A.; Downey, J. S.; Peter, K. D. (1995), Geochemistry of water in aquifers and confining units of the Northern Great Plains in parts of Montana, North Dakota, South Dakota, and Wyoming, . *U.S.G.S. Professional Paper 1402-F* **1995**, 146 pp.

Butler, A.W., III, 1982, Case history of the north Caribou prospect, Bonneville County, Idaho, *in* Powers, R.B., ed., Geologic Studies of the Cordilleran Thrust Belt, Volume II: Denver, Colorado, USA, Rocky Mountain Association of Geologists, p. 649-655.

Capo, R.C., Stewart, B.W., and Chadwick, O.A., 1998, Strontium isotopes as tracers of ecosystem processes: theory and methods, Geoderma, vol. 82, p. 197-225.

Chaudhuri, S. and Clauer, N., 1993, Strontium isotopic compositions and potassium and rubidium contents of formation waters in sedimentary basins: clues to the origin of the solutes, Geochimica et Cosmochimica Acta, vol. 57, p. 429–437.

Chave, K.E., 1952, A solid solution between calcite and dolomite: The Journal of Geology, v. 60, p. 190–192.

Chiodini, G. C., G. R.; Guidi, M.; Raco, B.; Marini, L. (1998). "Soil CO2 flux measurements in volcanic and geothermal areas." Appl. Geochem. 13: 543-552.

Connolly, C.A., Walter, L.M., Baadsgard, H. and Longstaffe, F.J., 1990, Origin and evolution of formation waters, Alberta Basin, Western Canada sedimentary basin: II, Isotopic systematics and water mixing, Applied Geochemistry, vol. 5, p. 397– 413.

Cooley, M. A., Price, R. A., Kyser, T. K., and Dixon, J. M., 2011, Stable-isotope geochemistry of syntectonic veins in Paleozoic carbonate rocks in the Livingstone Range anticlinorium and their significance to the thermal and fluid evolution of the southern Canadian foreland thrust and fold belt: AAPG Bulletin, v. 95, no. 11, p. 1851–1882.

Cunningham A.B., Lauchnor E., Eldring J., Esposito R., Mitchell A.C., Gerlach R., Phillips A.J., Ebigbo A., Spangler L.(2013) Abandoned Well CO_2 Leakage Mitigation Using Biologically Induced Mineralization: Current Progress and Future Directions. Greenhouse *Gas Sci Technol.* **3**:40–49. DOI: 10.1002/ghg.1331.

Cunningham, A. B., R. Gerlach, L. Spangler, and A. C. Mitchell (2009), Microbially enhanced geologic containment of sequestered supercritical CO_2, Energy Procedia, 1(1), 3245–3252.

Davies, G.R., and Smith, L.B., 2006, Structurally controlled hydrothermal dolomite reservoir facies: An overview: AAPG Bulletin, v. 90, p. 1641–1690.

De Muynck, W., K. Verbeken, N. De Belie, and W. Verstraete (2010b), Influence of urea and calcium dosage on the effectiveness of bacterially induced carbonate precipitation on limestone, Ecol. Eng., 36(2), 99–111.

Derickson, Dennis, Fiber Optic Test and Measurement, (Prentice Hall, Upper Saddle River, New Jersey, 1998, ISBN 0-13-534330-5).

Dupraz, S., B. Menez, P. Gouze, R. Leprovost, P. Benezeth, O. S. Pokrovsky, and F. Guyot (2009a), Experimental approach of CO_2 biomineralization in deep saline aquifers, Chem. Geol., 265(1–2), 54–62.

Ebigbo, A., A. Phillips, R. Gerlach, R. Helmig, A. Cunningham, H. Class, and L. Spangler (2012), Darcy-scale modeling of microbially induced carbonate mineral precipitation in sand columns, *Water Resources Research* 2012; 48(7):1–17. doi:10.1029/2011WR011714.

Faure, G., 1998, Principles and Applications of Geochemistry: Prentice Hall, ed. 2, 544 p.

Faure, G., Hurley, P. M., and Fairbairn, H. W., 1963, An estimate of the isotopic composition of strontium in rocks of the Precambrian shield of North America: Journal of Geophysical Research, v. 68, p. 2323– 2329.

Fessenden, J. E., S. M. Clegg, et al. (2010). "Novel MVA tools to track CO2 seepage, tested at the ZERT controlled release site in Bozeman, MT." Environmental Earth Sciences 60(2): 325-334.

Fujita, Y., J. L. Taylor, T. L. T. Gresham, M. E. Delwiche, F. S. Colwell, T. L. McLing, L. M. Petzke, and R. W. Smith (2008), Stimulation of microbial urea hydrolysis in groundwater to enhance calcite precipitation, Environ. Sci. Technol., 42(8), 3025–3032.

Goldsmith, J.R. and Graf, D.l., 1958, Relation between lattice constants and composition of the Ca-Mg carbonate: American Mineralogist, v. 43, p. 84–101.

Goldsmith, J.R., Graf, D.l., and Heard, H.C., 1961, Lattice constants of the calcium-magnesium carbonates: American Mineralogist, v. 46, p. 453–459.

Goldsmith, J.R., Graf, D.l., and Joensuu, O., 1955, The occurrence of magnesian calcite in nature: Geochimica et Cosmochimica Acta, v. 7, p. 212–230.

Govindan, R., A. Korre, S. Durucan, C. E. Imrie, "A geostatistical and probabilistic spectral image processing methodology for monitoring potential CO2 leakages on the surface," Int. J. Greenhouse Gas Control, doi:10.1016/j.ijggc.2010.04.014 (2010).

Govindan, R., A. Korre, S. Durucan, C. E. Imrie, "Comparative assessment of the performance of airborne and spaceborne spectral data for monitoring surface CO2 leakages," Energy Procedia, vol. 4, pp. 3421-3427 (2011).

Hoefs, J., 2009, Stable Isotope Geochemistry: Springer, ed. 6, 285p.

Hogan, J. A. S., J.A., Lawrence, R.L., Larimer, R.M. (2012). "Low-cost multispectral vegetation imaging system for detecting leaking CO2 gas." Applied Optics 51(4): A59-A66.

Hogan, J. A., J. A. Shaw, R. L. Lawrence, J. L. Lewicki, L. M. Dobeck and L. H. Spangler, "Detection of leaking CO2 gas with vegetation reflectances measured by a low-cost multispectral imager," IEEE J. Selected Topics Appl. Earth Obs. Remote Sensing, vol. 5, no. 3, pp. 699-706 (2012).

Hogan, J. A., J. A. Shaw, R. L. Lawrence, R. L. and R. M. Larimer, "Low-cost multispectral vegetation imaging system for detecting leaking CO2 gas," Appl. Opt., vol. 51, no. 4, pp. 59-66 (2012).

Huntoon, P.W., 1993, The influence of Laramide foreland structures on modern ground-water circulation in Wyoming artesian basins, *in* Snoke, A.W., Steidtmann, J.R., and Roberts, S.M., editors, Geology of Wyoming: Geological Survey of Wyoming Memoir No. 5, p. 756-789.

Jébrak, M., 1997, Hydrothermal breccias in vein-type ore deposits: A review of mechanisms, morphology and size distribution: Ore Geology Reviews, v. 12, p. 111-134.

Jeffrey, Sarah Rae, 2014, Structurally-controlled hydrothermal diagenesis of Mississippian reservoir rocks exposed in the Big Snowy Arch, central Montana [master's thesis] Montana State University, 208 p. URI: http://scholarworks.montana.edu/xmlui/handle/1/3352

Johnson, J. E., J. A. Shaw, R. L. Lawrence, P. W. Nugent, L. M. Dobeck, and L. H. Spangler, "Long-wave infrared imaging of vegetation for detecting leaking CO2 gas," J. Appl. Rem. Sens., vol. 6, 063612-1, doi:10.1117/1.JRS.6.063612 (2012).

Johnson, W. R., K. S.; Carlsten, J. L. (2013). "Micropulse differential absorption lidar for identification of carbon sequestration site leakage." Applied Optics 52(13): 2994-3003.

Keating, E.H., Fessenden, J., Kanjorski, N., Koning, D.J., and Pawar, R., 2010, The impact of CO_2 on shallow groundwater chemistry: Observations at a natural analog site and implications for carbon sequestration: Environmental Earth Sciences, v. 60, p. 521–536.

Kersey, A.D., T.A. Berkoff, and W.W. Morey, "Fiber-optic Bragg grating strain sensor with drift compensated high-resolution interferometric wavelength shift detection", Optics Letters, 18, 72-74, 1993.

Kharaka, Y. K., J. J. Thordsen, et al. (2010). "Changes in the chemistry of shallow groundwater related to the 2008 injection of CO2 at the ZERT field site, Bozeman, Montana." Environmental Earth Sciences 60(2): 273-284.

Kislak, J., L. Smith, D. Peacock, G. Eberli, and P. Swart, 2001, Classification, distribution, and origin of hydrothermal breccias, Madison Formation, Wyoming (abs.): AAPG Annual Meeting Program, v. 10, p. A105.

Krevor, S., J. C. Perrin, et al. (2010). "Rapid detection and characterization of surface CO2 leakage through the real-time measurement of delta(13) C signatures in CO2 flux from the ground." International Journal of Greenhouse Gas Control 4(5): 811-815.

Krüger, M., J. West, J. Frerichs, B. Oppermann, M. C. Dictor, C. Joulian, D. Jones, P. Coombs, K. Green, J. Pearce, F. May, I. Moller, "Ecosystem effects of elevated CO2 concentrations on microbial populations at a terrestrial CO2 vent at Laacher See, Germany," Energy Procedia, vol. 1, pp. 1933-1939 (2009).

Lageson, D.R., 2008, Interim assessment of naturally occurring CO_2 traps in SE Idaho (Bonneville County) and up-dip CO_2 pathways in the northern Salt River Range, Lincoln County, Wyoming: Unpublished Research, 33 p.

Lawrence, R. L., and W. J. Ripple, "Comparisons among vegetation indices and bandwise regression in a highly disturbed, heterogeneous landscape: Mount St. Helens, Washington," Remote Sens. Environ 64:1453–1463 (1998).

Lewicki, J. L., C. M. Oldenburg, L. Dobeck, and L. H. Spangler, "Surface CO2 leakage during the first shallow subsurface CO2 release experiment," Lawrence Berkeley National Laboratory report, http://escholarship.org/uc/item/44g635nc (2008).

Lewicki, J. L., G. E. Hilley, M. L. Fischer, L. Pan, C. M. Oldenburg, L. Dobeck, L. Spangler, "Detection of CO2 leakage by eddy covariance during the ZERT project's CO2 release experiments," Energy Procedia, vol. 1, pp. 2301-2306 (2009).

Luo, Fei, Jingyuan Liu, Naibing Ma, and T.F. Morse, "A fiber optic microbend sensor for distributed sensing application in the structural strain monitoring", Sensors and Actuators, 77, 41-44, 1999.

Lynn, Helen Beatrice, 2012, Structural controls on subsurface fluid migration through thrust sheets of the Stewart Peak culmination, northern Salt River Range, Wyoming [master's thesis] Montana State University, 306 p. URI:http://scholarworks.montana.edu/xmlui/handle/1/1768

Machel, H.G., and Lonnee, J., 2002, Hydrothermal dolomite – A product of poor definition and imagination: Sedimentary Geology, v. 152, p. 163–171.

Marshak, S., and Mitra, G., 1988, Basic Methods of Structural Geology: Prentice Hall, 446 p.

Marshall, D. J., 1988, Cathodoluminescence of Geological Materials. Boston, Unwin Hyman, 146 p.

Maughan, E.K., 1989, Geology and petroleum potential, Central Montana Province: Open-File Report – U.S. Geological Survey, p. 41–41. 121

Maughan, E.K., 1993, Stratigraphic and structural summary for central Montana *in* Hunter, L.D.V., ed., 1993 Montana Geological Society field conference: Montana Geological Society, p. 3–20.

McNutt, R.H., Frape S.K., Fritz, P., Jones, M.G. and McDonald, I.M., 1990, The 87Sr/86Sr values of Canadian shield brines and fracture minerals with applications to groundwater mixing, fracture history and geochronology, Geochimica et Cosmochimica Acta, vol. 54, p. 205–215.

Milliman, J.D., Gastner, M., and Muller, J., 1971, Utilization of magnesium in coralline algae: Geological Society of America Bulletin, v. 82, p. 573–580.

Mitchell A.C., K. Dideriksen, L.H. Spangler, A. B. Cunningham, R. Gerlach **(2010).** Microbially enhanced carbon capture and storage by mineral-trapping and solubility-trapping. *Environ. Sci. Technol.*, 44(13):5270-5276. doi: 10.1021/es903270w

Mitchell, A. C.; Phillips, A. J.; Schultz, L.; Parks, S.; Spangler, L.; Cunningham, A. B.; Gerlach, R.(2013) Microbial CaCO3 mineral formation and stability in a simulated high pressure saline aquifer with supercritical CO_2. *International Journal of Greenhouse Gas Control, Volume 15, July 2013, Pages 86-96*. DOI: 10.1016/j.ijggc.2013.02.001

Mitchell, A., A. Phillips, R. Hiebert, R. Gerlach, L. Spangler, and A. Cunningham. 2009. Biofilm enhanced geologic sequestration of supercritical CO_2. International Journal of Greenhouse Gas Control:90-99.

Montana State University Department of Physics, 2011, Scanning Electron Microscope JEOL JSM-6100: ICAL, Web.

Morales, S. E. H., W.E. (2013). "Functional Response of a Near-Surface Soil Microbial Community to a Simulated Underground CO2 Storage Leak." PLOS ONE 8(11): e81742.

Morales, S. E. H., W.E. (2014). "Simulated geologic carbon storage leak reduces baterial richness and alters bacterial community composition in surface soil." Soil Biology & Biochemistry 76: 286-296.

Moriarty, D. D., L.; Benson, S. (2014). "Rapid surface detection of CO2 leaks from geological sequestration sites." GHGT-12 Energy Procedia.

Moriarty, D. D., L.; Spangler, L.; Krevor, S.; Benson, S. (2013). Rapid Detection of CO2 Leaks from Carbon Sequestration Sites. AGU. San Francisco, CA.

Noble, R. R. P., L. Stalker, S. A. Wakelin. B. Pejcic, M. I Leybourne, A. L. Hortle, and K. Michael, "Biological monitoring for carbon capture and storage – a review and potential future developments," Int. J. Greenhouse Gas Control, vol. 10, pp. 520-535 (2012).

Nugent, P. W., and J. A. Shaw, "Calibration of uncooled LWIR microbolometer imagers to enable long-term field deployment," Proc. SPIE 9071 (Infrared Imaging Systems: Design, Analysis, Modeling, and Testing XXV, G. C. Holst, K. A. Krapels, G. H. Ballard, J. A. Buford, and R. L. Murrer, eds.), 90710V, doi:10.1117/12.2053082 (2014).

Nugent, P. W., J. A. Shaw, and N. J. Pust, “Correcting for focal plane array temperature dependence in microbolometer infrared cameras lacking thermal stabilization,” Opt. Eng. 52(6), 061304, doi:10.1117/1.OE.52.6.061304 (2013).

Nugent, P. W., J. A. Shaw, and N. J. Pust, “Radiometric calibration of infrared imagers using an internal shutter as an equivalent external blackbody,” Opt. Eng. 53(11), pages TBD (2015).

Oldenburg, C. M., J. L. Lewicki, L. Pan, L. M. Dobeck, and L. H. Spangler, “Origin of the patchy emission pattern at the ZERT CO2 release site,” Env. Earth Sci., vol. 60, no. 2, pp. 241-250 (2010).

Parkhust, D.; Appelo, C. (1999), USER’S GUIDE TO PHREEQC (VERSION 2)— A COMPUTER PROGRAM FOR SPECIATION, BATCH-REACTION, ONE-DIMENSIONAL TRANSPORT, AND INVERSE GEOCHEMICAL CALCULATIONS. *U.S. Geological Survey, Water-Resources Investigations Report 99-4259* **1999**, 312 pp.

Parks, S. L. (2009), Kinetics of calcite precipitation by ureolytic bacteria under aerobic and anaerobic conditions, Master’s thesis, Montana State University, Bozeman.

Pekney, N., A. Wells, et al. (2012). "Atmospheric monitoring of a perfluorocarbon tracer at the 2009 ZERT Center experiment." Atmospheric Environment 47: 124-132.

Phillips, A.J., R. Gerlach, R., Lauchnor, E., Mitchell, A.C, Cunningham, A.B. Spangler L. Engineered applications of ureolytic biomineralization: a review (2013). *Biofouling*, Vol. 29, No. 6, 715–733, http://dx.doi.org/10.1080/08927014.2013.796550.

Phillips, W.J., 1972, Hydraulic fracturing and mineralization: Journal of the Geological Society, v. 128, p. 337–359.

Quattrocchi, F., Barbieri, M., Bencini, R., Cinti, D., Durocher, K., Galli, G., Pizzino, L., Shevalier, M., and Voltattorni, N., 2006, Strontium isotope ($^{87}Sr/^{86}Sr$) chemistry in produced oil field waters: the IEA CO_2 monitoring and storage project, Advances in the Geological Storage of Carbon Dioxide Nato Science Series: IV: Earth and Environmental Sciences, Volume 65, p. 243-259.

Roberts, G., 1990, Structural controls on fluid migration in foreland thrust belts, *in* Letouzey, J., ed., Petroleum and tectonics in mobile belts: Paris, FR, Editions Technip, p. 193-210.

Rogers, A.J., “Distributed optical-fiber sensors for measurement of pressure, strain and temperature”, Physics reports, 169, 99-143, 1988.

Romanak, K. B., P. C.; Yang, C.; Hovorka, S. D. (2012). "Process-based approach to CO2 leakage detection by vadose zone gas monitoring at geological CO2 storage sites." Geophysical Research Letters 39: L15405.

Romanak, K. W., B., Yang, C., Sherk, G.W., Dale, J., Dobeck, L.M., Spangler, L.H. (2014). "Process-based soil gas leakage assessment at the Kerr Farm: Comparison of results to leakage proxies at ZERT and Mt. Etna." International Journal of Greenhouse Gas Control 30: 42-57.

Romanak, K., L. Dobeck, et al. (2013). "Potential for a process-based monitoring method above geologic carbon storage sites using dissolved gases in freshwater aquifers." Proceedings of the Fourteenth International Symposium on Water-Rock Interaction, Wri 14 7: 746-749.

Rouse, J. H., J. A. Shaw, R. L. Lawrence, J. L. Lewicki, L. M. Dobeck, K. S. Repasky, and L. H. Spangler, "Multi-spectral imaging of vegetation for detecting CO2 leaking from underground." Env. Earth Sci., vol. 60, no. 2, 313-323 (2010).

Scher, H. D., Griffith, E. M. and Buckley, W. P., 2014, Accuracy and precision of $^{88}Sr/^{86}Sr$ and $^{87}Sr/^{86}Sr$ measurements by MC-ICPMS compromised by high barium concentrations, Geochemistry, Geophysics, Geosystems, vol.15, p. 499–508.

Serc.carleton website http://serc.carleton.edu/research_education/geochemsheets/index.html accessed: October 29, 2014.

Sharma, B. A., M.E., Zhou, X., Olson, J.M., Dorshorst, C., Dobeck, L.M., Cunningham, A.B., Spangler, L.H. (2014). "Physiological responses of dandelion and orchard grass leaves to experimentally released upwelling soil CO2." International Journal of Greenhouse Gas Control 24: 139-148.

Shaw, J. A., P. W. Nugent, N. Kaufman, N. J. Pust, D. Mikes, C. Knierim, N. Faulconer, R. Larimer, A. DesJardins, B. Knighton, "Multispectral imaging system on tethered balloons for optical remote sensing education and research," J. Appl. Rem. Sens. 6(1), 063613, doi:10.1117/1.JRS.6.063613 (2012).

Sibson, R.H., 1986, Brecciation processes in fault zones: Inferences from earthquake rupturing: Pure and Applied Geophysics, v. 124, p. 159-175.

Sibson, R.H., 1990, Faulting and fluid flow, in B.E. Nesbitt, ed., Fluids in tectonically active regimes of the continental crust: Mineralogical Association of Canada Short Coarse Handbook, v. 18, ch. 4, p. 93-132.

Smith, L.B., and Davies, G.R., 2006, Structurally controlled hydrothermal alteration of carbonate reservoirs: Introduction: AAPG Bulletin, v. 90, p. 1635–1640.

Soukup, Benjamin, Kevin S. Repasky, John L. Carlsten, and Geoff Wicks, "Field demonstration of a 1 x 4 Fiber Sensor Array for Sub-Surface Carbon Dioxide Monitoring for Carbon Sequestration", Journal of Applied Remote Sensing, Vol. 8, 083699-1, 083699-13, 2014.

Spangler, L. H., L. M. Dobeck, et al. (2010). "A shallow subsurface controlled release facility in Bozeman, Montana, USA, for testing near surface CO2 detection techniques and transport models." Environmental Earth Sciences 60(2): 227-239.

Strazisar, B. R., A. W. Wells, et al. (2009). "Near-surface monitoring for the ZERT shallow CO2 injection project." International Journal of Greenhouse Gas Control 3(6): 736-744.

Thyne, G.D., Tomasso, M., Bywater-Reyes, S.V., Budd, D.A., and Reyes, B.M., 2010, Characterization of porosity and permeability for CO_2 sequestration models in the Mississippian Madison Group, Moxa Arch-LaBarge Platform, southwestern Wyoming: Rocky Mountain Geology, v. 45, no. 2, p. 133–150.

Tucker, M. E., and Wright, V. P., 1990, Radiogenic isotopes, *in* Tucker, M. E., Wright, P. V., and Dickson, J. A. D., eds., Carbonate sedimentology: Oxford, United Kingdom, Blackwell Science Publishing (GBR), p. 312.

Veizer, J. and Compston, W., 2004, 87Sr/86Sr composition of seawater during the Phanerozoic, Geochimica et Cosmochimica Acta, vol. 38, p. 1461–1484.

Washburn K.E., Callaghan P.T. (2006). "Tracking pore to pore exchange using relaxation exchange spectroscopy" Phys. Rev. Lett. 97(17):175502.

Wells, A., B. Strazisar, et al. (2010). "Atmospheric tracer monitoring and surface plume development at the ZERT pilot test in Bozeman, Montana, USA." Environmental Earth Sciences 60(2): 299-305.

Whiffin, V. S., L. A. van Paassen, and M. P. Harkes (2007), Microbial carbonate precipitation as a soil improvement technique, Geomicrobiol. J., 24(5), 417–423.

Wielopolski, L. and S. Mitra (2010). "Near-surface soil carbon detection for monitoring CO2 seepage from a geological reservoir." Environmental Earth Sciences 60(2): 307-312.

Wingate, L., 2013, C and O isotope protocol, personal communication

Zhang, F., Xu, H., Konishi, H., and Roden, E.E., 2010, A relationship between d104 value and composition in the calcite-disordered dolomite solid-solution series: American Mineralogist, v. 95, p. 1650–1656.

Zheng, L. G., J. A. Apps, et al. (2012). "Geochemical modeling of changes in shallow groundwater chemistry observed during the MSU-ZERT CO2 injection experiment." International Journal of Greenhouse Gas Control 7: 202-217.

Zhou, X. B., M. E. Apple, et al. (2013). "Observed response of soil O-2 concentration to leaked CO2 from an engineered CO2 leakage experiment." International Journal of Greenhouse Gas Control 16: 116-128.

Zhou, X. B., V. R. Lakkaraju, et al. (2012). "Experimental observation of signature changes in bulk soil electrical conductivity in response to engineered surface CO2 leakage." International Journal of Greenhouse Gas Control 7: 20-29.

BIBLIOGRAPHY

Anderson, T.F., and Aruthur, M.A., 1983, Stable isotopes of oxygen and carbon and their application to sedimentologic and paleoenvironmental problems, *in* Stable Isotopes in Sedimentary Geology: SEPM Shourt Course no. 10, p. 1.1-1.151.

Barr, J. L., S. D. Humphries, A. R. Nehrir, K. S. Repasky, L. M. Dobeck, J. L. Carlsten, and L. H. Spangler, “Laser-based carbon dioxide monitoring instrument testing during a 30-day controlled underground carbon release field experiment,” Int. J. Greenhouse Gas Control, vol. 5, no. 1, pp. 138-145, 2011.

Bateson, L., M. Vellico, S. E. Beaubien, J. M. Pearce, A. Annunziatellis, G. Ciotoli, F. Coren, S. Lombardi, and S. Marsh, “The application of remote-sensing techniques to monitor CO2-storage sites for surface leakage: Method development and testing at Latera (Italy) where naturally produced CO2 is leaking to the atmosphere,” Int. J. Greenhouse Gas Control, v. 2, pp. 388-400 (2008).

Bellante, G. J., S. L. Powell, R. L. Lawrence, K. S. Repasky, T. A. O. Dougher, “Aerial detection of a simulated CO2 leak from a geologic sequestration site using hyperspectral imagery,” Int. J. Greenhouse Gas Control, vol. 13, pp. 124–137, 2013.

Benson, S., and Cook, P., 2005, Underground geological storage, *in* Metz, B., Davidson, O., Coninck, H.d., Loos, M., and Meyer, L. eds.: IPCC Special Report on Carbon Dioxide Capture and Storage, p. 195–276.

Bevington, P., and D. K. Robinson, Data reduction and error analysis in the physical sciences, 3rd ed., McGraw-Hill (2002).

Blackstone, D. L., Jr., 1940, Structure of the Pryor Mountains, Montana: Journal Geology, v, 48, no. 6, p. 590-618.

Blackstone, D.L., Jr., 1973, Analysis of linear photo elements, Big Horn-Pryor Mountains, Montana-Wyoming: Special Report for Goddard Space Flight Center, 14 p.

Blackstone, D.L., Jr., and Huntoon, P.W., 1984, Tectonic structures responsible for anisotropic transmissivities in the Paleozoic aquifers of the southern Bighorn Basin: Wyoming: U.S. Geological Survey Research Project Technical Completion Report G-879, no. 2, p. 1-74.

Bottrell, S.H., Crowley, S., Self, C., 2001, Invasion of a karst aquifer by hydrothermal fluids: evidence from stable isotopic compositions of cave mineralization, Geofluids, v. 1 p. 1103–1121.

Davies, G.R., and Smith, L.B., 2006, Structurally controlled hydrothermal dolomite reservoir facies: An overview: AAPG Bulletin, v. 90, p. 1641–1690.

Dicken, A.P., 2005, Radiogenic Isotope Geology, Second Edition, Cambridge University Press, New York, 492 p.

Egemeier, S. J., 1981, Cave development by thermal waters, National Speleological Society Bulletin, v. 43, no. 2, p. 31–51.

Fessenden, J. E., S. M. Clegg, T. A. Rahn, S. D. Humphries, and W. S. Baldridge, "Novel MVA tools to track CO2 seepage, tested at the ZERT controlled release site in Bozeman, MT," Env. Earth Sci., vol. 60, no. 2, pp. 325-334, 2010.

Fetter, C.W., Applied Hydrogeology, Prentice Hall, Third edition, 1994.

Figueroa, J. D., T. Fout, S. Plasynski, H. McIlvried, R. D. Srivastava, "Advances in CO2 capture technology – The U.S. Department of Energy's carbon sequestration program," Int. J. Greenhouse Gas Control, vol. 2, no. 1, pp. 9-20, 2008.

Friedmann, S. J., "Geological Carbon Dioxide Sequestration," Elements, vol. 3, no. 3, pp. 179-184, 2007.

Govindan, R., A. Korre, S. Durucan, C. E. Imrie, "A geostatistical and probabilistic spectral image processing methodology for monitoring potential CO2 leakages on the surface," Int. J. Greenhouse Gas Control, doi:10.1016/j.ijggc.2010.04.014 (2010).

Govindan, R., A. Korre, S. Durucan, C. E. Imrie, "Comparative assessment of the performance of airborne and spaceborne spectral data for monitoring surface CO2 leakages," Energy Procedia, vol. 4, pp. 3421-3427 (2011).

Herring, A. L., E. J. Harper, et al. (2013). "Effect of fluid topology on residual nonwetting phase trapping: Implications for geologic CO2 sequestration." Advances in Water Resources 62: 47-58.

Hogan, J. A., J. A. Shaw, R. L. Lawrence, J. L. Lewicki, L. M. Dobeck and L. H. Spangler, "Detection of leaking CO2 gas with vegetation reflectances measured by a low-cost multispectral imager," IEEE J. Selected Topics Appl. Earth Obs. Remote Sensing, vol. 5, no. 3, pp. 699-706 (2012).

Hogan, J. A., J. A. Shaw, R. L. Lawrence, R. L. and R. M. Larimer, "Low-cost multispectral vegetation imaging system for detecting leaking CO2 gas," Appl. Opt., vol. 51, no. 4, pp. 59-66 (2012).

Humphries, S. D., A. R. Nehrir, C. J. Keith, K. S. Repasky, L. M. Dobeck, J. L. Carlsten, and L. H. Spangler, "Testing carbon sequestration site monitor instruments using a controlled carbon dioxide release facility," Appl. Opt., vol. 47, no. 4, pp. 548-555, 2008.

Huntoon, P.W., 1983. Fault Severing of Aquifers and Other Geologically Controlled Permeability Contrasts in the Basin-Mountain Interface, and the Implications for Ground Water Recharge to and Development from the Major Artesian Basins of Wyoming. Technical Completion Report to the U.S. Department of the Interior (Agreement No. 14-34-0001-2154, Project A-034-WYO), 64 p.

Huntoon, P.W., 2000, Variability of karstic permeability between unconfined and confined aquifers, Grand Canyon region, Arizona, Environmental and Engineering Geoscience, vol. 6, no. 2, p. 155-170.

Johnson, J. E., J. A. Shaw, R. L. Lawrence, P. W. Nugent, L. M. Dobeck, and L. H. Spangler, "Long-wave infrared imaging of vegetation for detecting leaking CO2 gas," J. Appl. Rem. Sens., vol. 6, 063612-1, doi:10.1117/1.JRS.6.063612 (2012).

Johnson, W., K. S. Repasky, and J. L. Carlsten, "Micropulse differential absorption lidar for identification of carbon sequestration site leakage," Appl. Opt., vol. 52, no. 13, pp. 2994-3003, 2013.

Keith, C. J., K. S. Repasky, R. L. Lawrence, S. C. Jay, J. L. Carlsten, "Monitoring effects of a controlled subsurface carbon dioxide release on vegetation using a hyperspectral imager," Int. J. Greenhouse Gas Control, vol. 3, no. 5, pp. 626-632, 2009.

Krüger, M., J. West, J. Frerichs, B. Oppermann, M. C. Dictor, C. Joulian, D. Jones, P. Coombs, K. Green, J. Pearce, F. May, I. Moller, "Ecosystem effects of elevated CO2 concentrations on microbial populations at a terrestrial CO2 vent at Laacher See, Germany," Energy Procedia, vol. 1, pp. 1933-1939 (2009).

Kyser, K., 2000, Fluids and Basin Evolution, Mineralogical Association of Canada, Short course Series vol. 28, 262 p.

Lafrenz,W. B., Shuster, R. D., Mueller, P. A., and Bowes, D. R., 1986, Archean and Proterozoic granitoids of the Hawley Mountain area, Beartooth Mountains, Montana: Montana Geological Society, Yellowstone-Bighorn Research Association (YBRA) Field Conference, p. 79– 89.

Lawrence, R. L., and W. J. Ripple, "Comparisons among vegetation indices and bandwise regression in a highly disturbed, heterogeneous landscape: Mount St. Helens, Washington," Remote Sens. Environ 64:1453–1463 (1998).

Lewicki, J. L., and G. E. Hilley, "Eddy covariance network design for mapping and quantification of surface CO2 leakage fluxes," Int. J. Greenhouse Gas Control, vol. 7, pp. 137-144, 2012.

Lewicki, J. L., C. M. Oldenburg, L. Dobeck, and L. H. Spangler, "Surface CO2 leakage during the first shallow subsurface CO2 release experiment," Lawrence Berkeley National Laboratory report, http://escholarship.org/uc/item/44g635nc (2008).

Lewicki, J. L., G. E. Hilley, M. L. Fischer, L. Pan, C. M. Oldenburg, L. Dobeck, L. Spangler, "Detection of CO2 leakage by eddy covariance during the ZERT project's CO2 release experiments," Energy Procedia, vol. 1, pp. 2301-2306 (2009).

Lewicki, J. L., G. E. Hilley, M. L. Fischer, L. Pana, C. M. Oldenburg, L. M. Dobeck, and L. H. Spangler, "Detection of CO2 leakage by eddy covariance during the ZERT project's CO2 release experiments," Energy Procedia, vol. 1, no. 1, pp. 2301-2306, 2009.

Lonnee, J., and Machel, H.G., 2006, Pervasive dolomitization with subsequent hydrothermal alteration in the Clarke Lake gas field, Middle Devonian Slave Point Formation, BritishColumbia, Canada, The American Association of Petroleum Geologists, AAPG Bulletin, v. 90, no. 11, p. 1739–1761.

Male, E. J., W. L. Pickles, E. A. Silver, G. D. Hoffmann, J. L. Lewicki, M. Apple, K. S. Repasky, and E. A. Burton, "Using hyperspectral plant signatures for CO2 leak detection during the 2008 ZERT CO2 sequestration field experiment in Bozeman, Montana," Env. Earth Sciences, vol. 60, no. 2, pp. 251-261, 2010.

Marshak, S., and Mitra, G., 1988, Basic methods of structural geology: Englewood Cliffs, New Jersey, Prentice Hall Publishing, 446 p.

McAlexander, I., G. H. Rau, J. Liem, T. Owano, R. Fellers, D. Baer, and M. Gupta, "Deployment of a carbon isotope ratiometer for the monitoring of CO2 sequestration leakage," Analytical Chemistry, vol. 83, pp. 6223-6229, 2011.

McCaleb, J.A., 1988, Significance of Paleokarst on Petroleum Recovery, Elk Basin Field, Big Horn Basin, *in* Goolsby S.M., and Longman, M.W., eds., Occurrence and Petrophysical Properties of Carbonate Reservoirs in the Rocky Mountain Region, Rocky Mountain Association of Geologists Carbonate Symposium, p. 139-147.

Noble, R. R. P., L. Stalker, S. A. Wakelin. B. Pejcic, M. I Leybourne, A. L. Hortle, and K. Michael, "Biological monitoring for carbon capture and storage – a review and potential future developments," Int. J. Greenhouse Gas Control, vol. 10, pp. 520-535 (2012).

Nugent, P. W., and J. A. Shaw, "Calibration of uncooled LWIR microbolometer imagers to enable long-term field deployment," Proc. SPIE 9071 (Infrared Imaging Systems: Design, Analysis, Modeling, and Testing XXV, G. C. Holst, K. A. Krapels, G. H. Ballard, J. A. Buford, and R. L. Murrer, eds.), 90710V, doi:10.1117/12.2053082 (2014).

Nugent, P. W., J. A. Shaw, and N. J. Pust, "Correcting for focal plane array temperature dependence in microbolometer infrared cameras lacking thermal stabilization," Opt. Eng. 52(6), 061304, doi:10.1117/1.OE.52.6.061304 (2013).

Nugent, P. W., J. A. Shaw, and N. J. Pust, "Radiometric calibration of infrared imagers using an internal shutter as an equivalent external blackbody," Opt. Eng. 53(11), pages TBD (2015).

Oldenburg, C. M., and A. J. A. Unger, "On leakage and seepage from geologic carbon sequestration sites: Unsaturated zone attenuation," Vadose Zone J., vol. 2, no. 3, pp. 287-296 2003.

Oldenburg, C. M., J. L. Lewicki, and R. P. Hepple, "Near-surface monitoring strategies for geologic carbon dioxide storage verification," Lawrence Berkeley National Lab Report, http://escholarship.org/uc/item/1cg241jb, 2003.

Oldenburg, C. M., J. L. Lewicki, L. Pan, L. M. Dobeck, and L. H. Spangler, "Origin of the patchy emission pattern at the ZERT CO2 release site," Env. Earth Sci., vol. 60, no. 2, pp. 241-250 (2010).

Palmer, A.N., Palmer, M.V., and DuChene, H., 2011, Karst and Carbonate Geochemistry of the Bighorn Basin, Wyoming, and Surrounding Regions, *in* Carbonate Geochemistry: Reactions and Processes in Aquifers and Reservoirs, Field Trip Guide book, Karst Waters Institute, Cody, Wyoming, 9 p.

Ramsay, J.G., and Huber, M.I., 1987, The techniques of modern structural geology,volume 2: folds and fractures: London, Academic Press, 700 p.

Rouse, J. H., J. A. Shaw, R. L. Lawrence, J. L. Lewicki, L. M. Dobeck, K. S. Repasky, and L. H. Spangler, "Multi-spectral imaging of vegetation for detecting CO2 leaking from underground." Env. Earth Sci., vol. 60, no. 2, 313-323 (2010).

Sando, W. J., 1988, Madison Limestone (Mississippian) paleokarst: a geologic synthesis, *in* James, N. P., and Choquette, P.W., eds., Paleokarst: Springer-Verlag, New York, p. 256-277.

Sando, W. J., and B. L. Mamet, 1974, New evidence on the age of the top of the Madison Limestone (Mississippian), Big Horn Mountains, Wyoming and Montana: Journal of Research, U.S. Geological Survey, v. 2, no. 5, p. 619-624.

Sando, W.J.., 1974, Ancient solution phenomena in the Madison Limestone (Mississippian) of north-central Wyoming: Journal of Research, U.S. Geological Survey, v. 2, no. 2, p. 133-141.

Shaw, J. A., P. W. Nugent, N. Kaufman, N. J. Pust, D. Mikes, C. Knierim, N. Faulconer, R. Larimer, A. DesJardins, B. Knighton, "Multispectral imaging system on tethered balloons for optical remote sensing education and research," J. Appl. Rem. Sens. 6(1), 063613, doi:10.1117/1.JRS.6.063613 (2012).

Shukla, V., and Baker, P.A., 1988, Sedimentology and geochemistry of dolostones : based on a symposium sponsored by the Society of Economic Paleontologists and Mineralogists, Society of Economic Paleontologists and Mineralogists, Special Publication No. 43, 266 p.

Smith, L.B., and Davis, G.R., 2006, Structurally controlled hydrothermal alteration of carbonate reservoirs: Introduction, AAPG Bulletin, v. 90, p. 1635-1640.

Spangler, L. H., L. M. Dobeck, K. S. Repasky, A. R. Nehrir, S. D. Humphries, J. L. Barr, C. J. Keith, J. A. Shaw, J. H. Rouse, A. B. Cunningham, S. M. Benson, C. M. Oldenburg, J. L. Lewicki, A. W. Wells, J. R. Diehl, B. R. Strazisar, J. E. Fessenden, T. A. Rahn, J. E. Amonette, J. L. Barr, W. L. Pickles, J. D. Jacobson, E. A. Silver, E. J. Male, H. W. Rauch, K. S. Gullickson, R. Trautz, Y. Kharaka, J. Birkholzer, L. Wielopolski, "A shallow subsurface controlled release facility in Bozeman, Montana, USA, for testing near surface CO2 detection techniques," Env. Earth Sci. vol. 60, no. 2, pp. 227-239, 2010.

Surdam, R.C., 2013, Geological CO_2 Storage Characterization: The Key to Deploying Clean Fossil Energy Technology, *in*: Springer Environmental Science and Engineering, Springer Science & Business Media, 316 p.

Wells, A., B. Strazisar, J. R. Diehl, and G. Veloski, "Atmospheric tracer monitoring and surface plume development at the ZERT pilot test in Bozeman, Montana, USA, Env. Earth Sci., vol. 60, no. 2, pp. 299-305, 2010.

Wielopolski, L., and S. Mitra, “Near-surface soil carbon detection for monitoring CO2 seepage from a geological reservoir,” Env. Earth Sci. vol. 60, no. 2, pp. 307-312, 2010.

Yang, H., Z. Xu, M. Fan, R. Gupta, R. B. Slimane, A. E. Bland, I. Wright, “Progress in carbon dioxide capture and separation: A review,” J. Env. Sci., vol. 20, no. 1, pp. 14-27, 2008.

Zhou, X., V. R. Lakkaraju, M. Apple, L. M. Dobeck, K. Gullickson, J. A. Shaw, A. B. Cunningham, L. Wielopolski, and L. H. Spangler, “Experimental observation of signature changes in bulk soil electrical conductivity in response to engineered surface CO2 leakage,” Int. J. Greenhouse Gas Control, vol. 7, pp. 20-29, 2012.

LIST OF ACRONYMS AND ABBREVIATIONS

‰	per mil notation is used to describe a unit expressing the ratio of stable-isotopic abundances of an element in a sample to those of a standard material.
δ	delta Delta is the notation used when describing isotope species fractionation
AC	Alternating Current
BEG	Bureau of Economic Geology
BNL	Brookhaven National Laboratory
BSFS	Big Snowy fault system one of the field areas for the BSMSA; a northeast-southwest-striking high-angle fault zone
BSMSA	Big Snowy Mountains Study Area located at the western end of the Big Snowy Arch The study focused on a northeast-southwest-striking high-angle fault zone that transects the entire range and is rooted in the Precambrian basement. Field work in the BSMSA was concentrated along outcrops exposed in canyons following the traces of the Big Snowy Fault system and Swimming Woman Canyon.
C	Carbon
CBM	Coal bed methane
CCP	Carbon Capture Project (CCP is a partnership of several major energy companies working together to advance the technologies that will underpin the deployment of industrial-scale CO_2 capture and storage (CCS).
CCS	Carbon Capture and Storage.
CL	Cathodoluminescence Optical cathodoluminescence (optical-CL) permits optical examination or imaging of a sample through the attachment of an evacuated CL-stage to an optical microscope. The CL-stage attachment uses a cathode gun to bombard a sample with a beam of high-energy electrons. The resulting luminescence in minerals allows textures and compositional variations to be viewed that are not otherwise evident using light microscopy. The stage allows X-Y movement of the sample to examine much of the surface area in the sample (serc.carleton.edu website).
CO_2	Carbon dioxide
CRD	Cavity ring down

DC	Direct Current
DFB	Distributed Feedback
DIAL	differential absorption lidar
EDS	Energy-Dispersive x-ray spectrometry - Interaction of an electron beam with a sample target produces a variety of emissions, including x-rays. An energy-dispersive (EDS) detector is used to separate the characteristic x-rays of different elements into an energy spectrum, and EDS system software is used to analyze the energy spectrum in order to determine the abundance of specific elements. EDS can be used to find the chemical composition of materials down to a spot size of a few microns, and to create element composition maps over a much broader raster area. Together, these capabilities provide fundamental compositional information for a wide variety of materials (serc.carleton.edu website).
EOR	Enhanced oil recovery
EPA	Environmental Protection Agency
FBG	Fiber Bragg Grating
FC/APC	Fiber Coupler/Angled Physical Contact
FC/PC	Fiber Coupler/Physical Contact
FE SEM	Field emission scanning electron microscopy – FE SEM provides topographical and elemental information at magnifications of 10x to over 100,000x, with virtually unlimited depth of field. Compared with convention scanning electron microscopy (SEM), field emission SEM (FESEM) produces clearer, less electrostatically distorted images with spatial resolution down to 1 1/2 nanometers – three to six times better. The ICAL facility at MSU has a Zeiss SUPRA 55VP model FE SEM. http://www.physics.montana.edu/ical/instrumentation/fesem.asp
FMS	frequency modulation spectroscopy
HTD	hydrothermal dolomite
ICAL	Imaging and Chemical Analysis Laboratory at Montana State University
IEAGHG	International Energy Agency Greenhouse Gas
INS	inelastic neutron scattering
IPA	Isopropyl Alcohol
LANL	Los Alamos National Laboratory
LBNL	Lawrence Berkeley National Laboratory
LWIR	Long-wave Infrared (wavelengths of approximately 8 – 14 μm)
MC-ICPMS	Multicollector-Inductively Coupled Plasma Mass Spectrometer - is an instrument that measures isotopic ratios. It is a hybrid mass spectrometer that combines the advantages of superior ionization of an inductively coupled plasma source and the precise measurements of a magnetic sector multicollector mass spectrometer. As a hybrid mass spectrometer, MC-ICPMS combines an inductively coupled plasma (ICP) plasma source, an energy filter, a magnetic

	sector analyzer, and multiple collectors for the measurement of ions. The ions are produced by introducing the sample into an inductively coupled plasma which strips off electrons thereby creating positively charged ions. These ions are accelerated across an electrical potential gradient (up to 10 KV) and focused into a beam via a series of slits and electrostatically charged plates. This ion beam then passes through an energy filter, which results in a consistent energy spectrum in the ion beam and then through a magnetic field where the ions are separated on the basis of their mass to charge ratio. These mass-resolved beams are then directed into collectors where the ions reaching the collectors are converted into voltage. Isotope ratios are calculated by comparing voltages from the different collectors. (serc.carleton.edu website) http://serc.carleton.edu/research_education/geochemsheets/techniques/MCICPMS.html
MICP	Microbially Induced Calcite Precipitation.
MMF	Montana Micro-fabrication Facility
MRI	Magnetic Resonance Imaging
MSU	Montana State University
NA	Numerical Aperture
NDVI	Normalized Difference Vegetation Index
NETL	National Energy Technology Laboratory
NIR	Near Infrared (wavelengths of approximately 700–1000 nm)
NMR	Nuclear Magnetic Resonance
$p(CO_2)$	Head space pressure of CO_2 in microcosms
PBG	Photonic Bandgap
PDB	Pee Dee Belemnite
PFT	perfluorocarbon tracer
PM	Polarization Maintaining
PMSA	Pryor Mountain Study Area - The PMSA includes the Big Pryor, Red Pryor and East Pryor Mountain areas of the Pryor Mountains, Montana and the Little Mountain and Little Sheep Mountain Anticlines in Wyoming. These are Laramide structures that expose the Mississippian age Madison Formation, allowing for outcrop and petrographic examination of this reservoir rock.
PNNL	Pacific Northwest National Laboratory
$scCO_2$	Supercritical CO_2
SEM	Scanning electron microscopy - SEM uses a focused beam of high-energy electrons to generate a variety of signals at the surface of solid specimens. The signals that derive from electron-sample interactions reveal information about the sample including external morphology (texture), chemical composition, and crystalline structure and orientation of materials making up the sample (serc.carleton.edu website).
SM	Single Mode

SMF	Single Mode Fiber
SMOW	Standard Mean Ocean Water
SPC	Stewart Peak Culmination Study Area - The SPC is located in the Salt River Range in western Wyoming along the Absaroka thrust sheet.
Sr	strontium
SWC	Swimming Woman Canyon – one of the field areas in the BSMSA
TSA	Thermopolis Anticline Study Area - The TSA is located in the southern Bighorn Basin just north of the Owl Creek Mountains. TSA is a Laramide-style basement-involved uplift, i.e. a trishear anticline with a subtending thrust fault. Investigation of the Thermopolis anticline included seal and caprock formations such as the Triassic Chugwater Formation. There is a large mineral hot spring located on the anticline at the Bighorn River, providing a suitable field site to study causes of leakage to the surface.
UIC	Underground Injection Control
USGS	United States Geological Survey
VIS	Visible (wavelengths of approximately 400-700 nm)
VPDB	Vienna Pee Dee Belemnite
XRD	X-ray powder diffraction spectroscopy - XRD is a rapid analytical technique primarily used for phase identification of a crystalline material and can provide information on unit cell dimensions. The analyzed material is finely ground, homogenized, and average bulk composition is determined (serc.carleton.edu website).
XRF	X-ray fluorescence An XRF spectrometer is an x-ray instrument used for routine, relatively non-destructive chemical analyses of rocks, minerals, sediments and fluids. It works on wavelength-dispersive spectroscopic principles that are similar to an electron microprobe (EPMA). However, an XRF cannot generally make analyses at the small spot sizes typical of EPMA work (2-5 microns), so it is typically used for bulk analyses of larger fractions of geological materials. The relative ease and low cost of sample preparation, and the stability and ease of use of x-ray spectrometers make this one of the most widely used methods for analysis of major and trace elements in rocks, minerals, and sediment (serc.carleton.edu website).
ZERT	Zero Emissions Research Technology
ZTE	Zero Echo Time Imaging sequence

PUBLICATIONS

Amonette, J.E., Barr, J.L., Erikson, R.L., Dobeck, L. and Shaw, J.A., Measurement of Advective Soil Gas Flux: Results of Field and Laboratory Experiments with CO2. Environmental Earth Sciences, 2012. Published online(February 17, 2013) DOI: 10.1007/s12665-013-2259-5. (ZERT I)

Amonette, J.E., Barr, J.L., Dobeck, L.M., Gullickson, K. and Walsh, S.J., Spatiotemporal changes in CO2 emissions during the second ZERT injection, August-September 2008. Environmental Earth Sciences, 2010. 60(2): p. 263-272 DOI: 10.1007/s12665-009-0402-0.

Amonette, J.E., Barr, J.L., Dobeck, L.M., Gullickson, K. and Walsh, S.J., Spatiotemporal changes in CO2 emissions during the second ZERT injection, August-September 2008. Environmental Earth Sciences, 2010. 60(2): p. 263-272 DOI: 10.1007/s12665-009-0402-0.

Amonette, J.E., Barr, J.L., Erikson, R.L., Dobeck, L.M. and Shaw, J.A., Measurement of advective soil gas flux: results of field and laboratory experiments with CO2. Environmental Earth Sciences, 2013. 70(4): p. 1717-1726 DOI: 10.1007/s12665-013-2259-5.

Amonette, J.E., Barr, J.L., Erikson, R.L., Dobeck, L.M. and Shaw, J.A., Measurement of advective soil gas flux: results of field and laboratory experiments with CO2. Environmental Earth Sciences, 2013. 70(4): p. 1717-1726 DOI: 10.1007/s12665-013-2259-5.

Amonette, J.E., Barr, J.L., Erikson, R.L., Dobeck, L.M. and Shaw, J.A., Measurement of advective soil gas flux: results of field and laboratory experiments with CO2. Environmental Earth Sciences, 2013. 70(4): p. 1717-1726 DOI: 10.1007/s12665-013-2259-5.

Barr, J.L., Humphries, S.D., Nehrir, A.R., Repasky, K.S., Dobeck, L.M., Carlsten, J.L. and Spangler, L.H., Laser-based carbon dioxide monitoring instrument testing during a 30-day controlled underground carbon release field experiment. International Journal of Greenhouse Gas Control, 2011. 5(1): p. 138-145 DOI: 10.1016/j.ijggc.2010.03.002.

Barr, J.L., Humphries, S.D., Nehrir, A.R., Repasky, K.S., Dobeck, L.M., Carlsten, J.L. and Spangler, L.H., Laser-based carbon dioxide monitoring instrument testing during a 30-day controlled underground carbon release field experiment. International Journal of Greenhouse Gas Control, 2011. 5(1): p. 138-145 DOI: 10.1016/j.ijggc.2010.03.002.

Barnhart, E., Bowen, D., Ramsay, B., Cunningham, A.B. and Fields, M., Coal-Associated Bacterial and Archaeal Populations: Coal-Dependant Increased Bacterial Diversity. International Journal of Coal Geology, 2012. 115(2013): p. 64-70 DOI: 10.1016/j.coal.2013.03.006.

Barnhart, E., De Le'on, K.B., Ramsay, B., Cunningham, A. and Fields, M., Investigation of coal-associated bacterial and archaeal populations from a diffusive microbial sampler (DMS). International Journal of Coal Geology, 2013. 115(August 2013): p. 64-70 DOI: 10.1016/j.coal.2013.03.006.

Bellante, G.J., Powell, S.L., Lawrence, R.L., Repasky, K.S. and Dougher, T.A.O., Aerial detection of a simulated CO2 leak from a geologic sequestration site using hyperspectral imagery. International Journal of Greenhouse Gas Control, 2013. 13: p. 124-137 (ZERT I)

Chiodini, G.C., G. R.; Guidi, M.; Raco, B.; Marini, L., Soil CO2 flux measurements in volcanic and geothermal areas. Appl. Geochem., 1998. 13: p. 543-552

Chiodini, G.C., G. R.; Guidi, M.; Raco, B.; Marini, L., Soil CO2 flux measurements in volcanic and geothermal areas. Appl. Geochem., 1998. 13: p. 543-552

Bonneville, A., Dermond, J., Strickland, M., Sweeney, M., Sullivan, E.C., Heggy, E. and Normand, J., Monitoring Surface Deformation Associated with an Aquifer Storage and

Recovery (ASR) Site In Pendleton, OR, as an Analog for Subsurface CO2 Sequestration. Water Resources Research, 2012. Submitted

Cunningham, A.B., Gerlach, R., Spangler, L., Mitchell, A., Parks, S. and Phillips, A., Reducing the risk of well bore leakage of CO2 using engineered biomineralization barriers. Energy Procedia, 2011. 4: p. 5178-5185 DOI: 10.1016/j.egypro.2011.02.495.

Cunningham, A.B., Lauchnor, E., Eldring, J., Esposito, R., Mitchell, A., Gerlach, R., Phillips, Ebigbo, A. and Spangler, L., Abandoned Well CO2 Leakage Mitigation Using Biologically Induced Mineralization: Current Progress and Future Directions. Greenhouse Gases: Science and Technology, 2013. 3(1): p. 40-49 DOI: 10.1002/ghg.1331.

Ebigbo, A., Phillips, Gerlach, R., Helmig, R., Cunningham, A.B., Class, H. and Spangler, L., Darcy-Scale modeling of Microbially Induced Carbonate Material Precipitation In Sand Columns Water Resources Research, 2013. 48(W07519) DOI: 10.1029/2011WR011714.

Fang, Y., Nguyen, K., Carroll, M., Xu, Y., Yabusaki, T., Scheibe, A. and Bonneville, A., Development of a coupled thermo-hydro-mechanical model in discontinuous media for carbon sequestration. Int. J. Rock Mech. Min. Sci., 2013. 62(September 2013): p. 138–147 DOI: 10.1016/j.ijrmms.2013.05.002.

Fessenden, J.E., Clegg, S.M., Rahn, T.A., Humphries, S.D. and Baldridge, W.S., Novel MVA tools to track CO2 seepage, tested at the ZERT controlled release site in Bozeman, MT. Environmental Earth Sciences, 2010. 60(2): p. 325-334 DOI: 10.1007/s12665-010-0489-3.

Fessenden, J.E., Clegg, S.M., Rahn, T.A., Humphries, S.D. and Baldridge, W.S., Novel MVA tools to track CO2 seepage, tested at the ZERT controlled release site in Bozeman, MT. Environmental Earth Sciences, 2010. 60(2): p. 325-334 DOI: 10.1007/s12665-010-0489-3.

Hogan, J.A., Shaw, J.A., Lawrence, R.L. and Larimer, R.L., A low-cost multi-spectral imager for detecting gas leaks indirectly from changes in vegetation reflectance. Appl. Opt., 2012. 51(4): p. A59-A66 DOI: 10.1364/AO.51.000A59.

Hogan, J.A., Shaw, J.A., Lawrence, R.L., Lewicki, J.L., Dobeck, L. and Spangler, L., Detection of leaking CO2 gas with vegetation reflectances measured by a low-cost multispectral imager. IEEE J. Selected Topics Appl. Earth Obs. And Rem. Sens, 2012. 5(3): p. 699-706 DOI: 10.1109/JSTARS.2012.2202880. (ZERT I)

Hogan, J.A., Shaw, J.A., Lawrence, R.L., Lewicki, J.L., Dobeck, L.M. and Spangler, L.H., Detection of Leaking CO2 Gas With Vegetation Reflectances Measured By a Low-Cost Multispectral Imager. Ieee Journal of Selected Topics in Applied Earth Observations and Remote Sensing, 2012. 5(3): p. 699-706 DOI: 10.1109/jstars.2012.2202880.

Hogan, J.A.S., J.A., Lawrence, R.L., Larimer, R.M., Low-cost multispectral vegetation imaging system for detecting leaking CO2 gas. Applied Optics, 2012. 51(4): p. A59-A66 (ZERT I)

Jeffrey, Sarah Rae, 2014, “Structurally-controlled hydrothermal diagenesis of Mississippian reservoir rocks exposed in the Big Snowy Arch, central Montana,” master’s thesis Montana State University URI: http://scholarworks.montana.edu/xmlui/handle/1/3352

Johnson, J., Shaw, J.A., Lawrence, R.L., Nugent, P., Dobeck, L. and Spangler, L., Long-wave Infrared Imaging of Vegetation For Detecting Leaking CO2 Gas. Journal of Applied Remote Sensing 2012. 6(063612) DOI: 10.1117/1.JRS.6.063612.

Johnson, J., Shaw, J.A., Lawrence, R.L., Nugent, P., Hogan, J.A., Dobeck, L. and Spangler, L., Comparison of long-wave infrared and visible/near-infrared imaging of vegetation for detecting leaking CO2 gas. IEEE Journal Selected Topics in Applied Earth Observation & Remote Sensing, 2014. 7(5): p. 1651-1657 DOI: 10.1109/JSTARS.2013.2295760

Johnson, J. E., Remote sensing applications of uncooled long-wave infrared thermal imagers," M.S. Thesis, Department of Electrical and Computer Engineering, Montana State University, Bozeman, Montana, http://scholarworks.montana.edu/xmlui/handle/1/1573 (2012).

Johnson, W.R., K. S.; Carlsten, J. L., Micropulse differential absorption lidar for identification of carbon sequestration site leakage. Applied Optics, 2013. 52(13): p. 2994-3003

Keating, E., Hakala, J.A., Viswanathan, H.S., Capo, R., Stewart, B., Gardiner, J., Guthrie, G.D., Casey, J.W. and Fessenden, J., The challenge of predicting groundwater quality impacts in a CO2 leakage scenario: Results from field, laboratory, and modeling studies at a natural analog site in New Mexico, U.S.A. Energy Procedia, 2010. 4: p. 3239-3245 DOI: 10.1016/j.egypro.2011.02.242.

Keating, E., Hakala, Viswanathan, H.S., Carey, R., Pawar, R.J., Guthrie, G.D. and Fessenden, J., CO2 leakage impacts on shallow groundwater: field-scale reactive-transport simulations informed by Observations at a natural analog site. Applied Geochemistry, 2013. 30: p. 136-147 DOI: 10.1016/j.apgeochem.2012.08.007.

Kharaka, Y.K., Thordsen, J.J., Kakouros, E., Ambats, G., Herkelrath, W.N., Beers, S.R., Birkholzer, J.T., Apps, J.A., Spycher, N.F., Zheng, L.E., Trautz, R.C., Rauch, H.W. and Gullickson, K.S., Changes in the chemistry of shallow groundwater related to the 2008 injection of CO2 at the ZERT field site, Bozeman, Montana. Environmental Earth Sciences, 2010. 60(2): p. 273-284 DOI: 10.1007/s12665-009-0401-1.

Kihm, J., Kim, J.M., Wang, C. and Xu, T., Hydrogeochemical numerical simulation of impacts of mineralogical compositions and convective fluid flow on trapping mechanisms and efficiency of carbon dioxide injected into deep saline sandstone aquifers. Journal of Geophysical Research, 2012. 117(B06204) DOI: 10.1029/2011JB008906.

Kneafsey, T., Silin, D. and Ajo-Franklin, J., Supercritical CO2 flow through a layered silica sand/calcite sand system: Experiment and modified Maximal Inscribed Spheres analysis,. International Journal of Greenhouse Gas Control, 2013. 14: p. 141-150 DOI: 10.1016/j.ijggc.2012.12.031

Krevor, S., Perrin, J.C., Esposito, A., Rella, C. and Benson, S., Rapid detection and characterization of surface CO2 leakage through the real-time measurement of delta(13) C signatures in CO2 flux from the ground. International Journal of Greenhouse Gas Control, 2010. 4(5): p. 811-815 DOI: 10.1016/j.ijggc.2010.05.002.

Krupa, K.M., Cantrell, K.J. and McGrail, B.P., Thermodynamic Data for Geochemical Modeling of Carbonate Reactions Associated with CO2 Sequestration –Literature Review. PNNL-19766, 2010

Lageson, D.R., Larsen, M.C., Lynn, H.B. and Treadway, W.A., Applications Of Google Earth Pro to Fracture and Fault Studies of Laramide Anticlines in the Rocky Mountain Foreland Whitmeyer, S.J., Bailey, J.E., De Paor, D.G., and Ornduff, T., eds., Google Earth and Virtual Visualizations in Geoscience Education and Research, 2012. 492: p. 209-220 DOI: 10.1130/2012.2492(15).

Lauchnor, E., Schultz, L., Bugni, S., Mitchell, A., Cunningham, A. and Gerlach, R., Bacterially induced calcium carbonate precipitation and strontium co-precipitation in a porous media flow system. Environmental Science & Technology Journal, 2013. 47(3): p. 1557-1564 DOI: 10.1021/es304240y.

Lewicki, J.L. and Hilley, G.E., Eddy covariance network design for mapping and quantification of surface CO2 leakage fluxes. International Journal of Greenhouse Gas Control, 2012. 7: p. 137-144 DOI:10.1016/j.ijggc.2012.01.010. (ZERT I)

Lynn, Helen Beatrice, 2012, "Structural controls on subsurface fluid migration through thrust sheets of the Stewart Peak culmination, northern Salt River Range, Wyoming" master's thesis Montana State University URI: http://scholarworks.montana.edu/xmlui/handle/1/1768

McAlexander, I., Rau, G.H., Liem, J., Owano, T., Fellers, R., Baer, D. and Gupta, M., Deployment of a Carbon Isotope Ratiometer for the Monitoring of CO2 Sequestration Leakage. Analytical Chemistry, 2011. 83(16): p. 6223-6229 DOI: 10.1021/ac2007834. (ZERT I)

Mitchell, A., Phillips, A., Schultz, L., Parks, S., Spangler, L., Cunningham, A. and Gerlach, R., Microbial CaCO3 mineral formation and stability in a simulated high pressure saline aquifer with supercritical CO2. International Journal of Greenhouse Gas Control, 2013. 15: p. 86-96 DOI: 10.1016/j.ijggc.2013.02.001.

Morales, S.E.H., W.E., Functional Response of a Near-Surface Soil Microbial Community to a Simulated Underground CO2 Storage Leak. PLOS ONE, 2013. 8(11): p. e81742 (ZERT I)

Morales, S.E.H., W.E., Simulated geologic carbon storage leak reduces baterial richness and alters bacterial community composition in surface soil. Soil Biology & Biochemistry, 2014. 76: p. 286-296 (ZERT I)

Pekney, N., Wells, A., Diehl, J.R., McNeil, M., Lesko, N., Armstrong, J. and Ference, R., Atmospheric monitoring of a perfluorocarbon tracer at the 2009 ZERT Center experiment. Atmospheric Environment, 2012. 47: p. 124-132 DOI: 10.1016/j.atmosenv.2011.11.024. (ZERT I)

Phillips, A., Gerlach, R., Lauchnor, E., Cunningham, A. and Spangler, L., Engineered applications of ureolytic biomineralization: a review Biofouling, 2013. 29(6): p. 715-733 DOI: http://dx.doi.org/10.1080/08927014.2013.796550.

Phillips, A., Lauchnor, E., Eldring, J., Esposito, R., Mitchell, A., Gerlach, R., Cunningham, A.B. and Spangler, L., Potential CO2 Leakage Reduction through Biofilm-Induced Calcium Carbonate Precipitation Environmental Science & Technology Journal, 2013. 47(1): p. 142-149 DOI: http://dx.doi.org/10.1021/es301294q.

Pruess, K., Integrated Modeling of CO2 Storage and Leakage Scenarios Including Transitions between Super- and Sub-Critical Conditions, and Phase Change between Liquid and Gaseous CO2. Greenhouse Gases: Science and Technology, 2011. 1(3): p. 237-247 DOI: 10.1002/ghg.024.

Romanak, K., Dobeck, L., Dixon, T. and Spangler, L., Potential for a process-based monitoring method above geologic carbon storage sites using dissolved gases in freshwater aquifers. Proceedings of the Fourteenth International Symposium on Water-Rock Interaction, Wri 14, 2013. 7: p. 746-749 DOI: 10.1016/j.proeps.2013.03.122.

Romanak, K.B., P. C.; Yang, C.; Hovorka, S. D., Process-based approach to CO2 leakage detection by vadose zone gas monitoring at geological CO2 storage sites. Geophysical Research Letters, 2012. 39: p. L15405

Romanak, K.W., B.; Yang, C.; Sherk, G.W.; Dale, J.; Dobeck, L.M., Spangler, L.H., Process-based soil gas leakage assessment at the Kerr Farm: Comparison of results to leadage proxies at ZERT and Mt. Etna. International Journal of Greenhouse Gas Control, 2014. 30: p. 42-57

Rouse, J. H., J. A. Shaw, R. L. Lawrence, J. L. Lewicki, L. Dobeck, K. S. Repasky, and L. H. Spangler, "Multispectral imaging of vegetation for detecting CO2 leaking from underground," J. Env. Earth Sci. 60(2), 313-323, doi:10.1007/s12665-010-0483-9 (2010).

Silin, D., Tomutsa, L., Benson, S.M. and Patzek, T., Microtomography and Pore Scale Modeling of Two-Phase Fluid Distribution. Transport in Porous Media, 2010: p. 1-21 DOI: 10.1007/s11242-010-9636-2.

Sharma, B.A., M.E.; Zhou, X., Olson, J.M.; Dorshorst, C.; Dobeck, L.M.; Cunningham, A.B.; Spangler, L.H., Physiological responses of dandelion and orchard grass leaves to experimentally released upwelling soil CO2. International Journal of Greenhouse Gas Control, 2014. 24: p. 139-148

Shaw, J. A., P. W. Nugent, N. Kaufman, N. J. Pust, D. Mikes, C. Knierim, N. Faulconer, R. Larimer, A. DesJardins, B. Knighton, "Multispectral imaging system on tethered balloons for optical remote sensing education and research," J. Appl. Rem. Sens. 6(1), 063613, DOI:10.1117/1.JRS.6.063613 (2012).

Spangler, L.H., Dobeck, L.M., Repasky, K.S., Nehrir, A.R., Humphries, S.D., Barr, J.L., Keith, C.J., Shaw, J.A., Rouse, J.H., Cunningham, A.B., Benson, S.M., Oldenburg, C.M., Lewicki, J.L., Wells, A.W., Diehl, J.R., Strazisar, B.R., Fessenden, J.E., Rahn, T.A., Amonette, J.E., Pickles, W.L., Jacobson, J.D., Silver, E.A., Male, E.J., Rauch, H.W., Gullickson, K.S., Trautz, R., Kharaka, Y., Birkholzer, J. and Wielopolski, L., A shallow subsurface controlled release facility in Bozeman, Montana, USA, for testing near surface CO2 detection techniques and transport models. Environmental Earth Sciences, 2010. 60(2): p. 227-239 DOI: 10.1007/s12665-009-0400-2.

Strazisar, B.R., Wells, A.W., Diehl, J.R., Hammack, R.W. and Veloski, G.A., Near-surface monitoring for the ZERT shallow CO2 injection project. International Journal of Greenhouse Gas Control, 2009. 3(6): p. 736-744 DOI: 10.1016/j.ijggc.2009.07.005.

Viswanathan, H.S., Z., D., C., L., Keating, E., Hakala, K., S., Zheng, L. and Pawar, R.J., Developing a robust geochemical and reactive transport model to evaluate possible sources of arsenic at the CO2 sequestration natural analog site in Chimayo, New Mexico. International Journal of Greenhouse Gas Control, 2012. 10: p. 199-214 DOI: 10.1016/j.ijggc.2012.06.007.

Vogt, S.J., Shaw, C.A., Maneval, J.E., Brox, T., Skidmore, M., Codd, S.L. and Seymour, J.D., Magnetic resonance measurements of flow-path enhancement during supercritical CO2 injection in sandstone and carbonate rock cores. Journal of Petroleum Science and Engineering, 2014. In Press

Wells, A., Strazisar, B., Diehl, J.R. and Veloski, G., Atmospheric tracer monitoring and surface plume development at the ZERT pilot test in Bozeman, Montana, USA. Environmental Earth Sciences, 2010. 60(2): p. 299-305 DOI: 10.1007/s12665-009-0371-3.

Wielopolski, L. and Mitra, S., Near-surface soil carbon detection for monitoring CO2 seepage from a geological reservoir. Environmental Earth Sciences, 2010. 60(2): p. 307-312 DOI: 10.1007/s12665-009-0397-6.

White, M.D., Bacon, D.H., McGrail, B.P., Watson, T.L., White, S.K. and Zhang, G., STOMP: Subsurface Transport Over Multiple Phases: STOMP-CO2 and -CO2e Guide. PNNL-21268, 2012

Windisch, C.F., Maupin, J.G.D. and McGrail, B.P., Soret Effect Study on High- Pressure CO2-Water Solutions Using UV-Raman Spectroscopy and a Concentric-Tube Optical Cell. Technical Report PNNL-21156, 2012

Windisch, C.F., Maupin, J.G.D. and McGrail, B.P., Ultraviolet (UV) Raman Spectroscopy Study of the Soret Effect in High-Pressure CO2-Water Solutions. Applied Spectroscopy, 2012. 66(7): p. 731-739 DOI: 10.1366/12-06591.

Xu, T., Spycher, N., Sonnenthal, N., Zhang, G., Zheng, L. and Pruess, K., TOUGHREACT Version 2.0: A Simulator for Subsurface Reactive Transport under Non-isothermal Multiphase Flow Conditions, Computers & Geosciences, 2011. 37(6): p. 763-774 DOI: 10.1016/j.cageo.2010.10.007.

Xu, T., Zheng, L. and Tian, H., Reactive Transport Modeling for CO2 Geological Sequestration. Petroleum and Science and Engineering, 2011. 78(3-4): p. 765-777 DOI: 10.1016/j.petrol.2011.09.005.

Yang, Y.M., Small, M.J., Ogretim, E.O., Gray, D.D., Wells, A.W., Bromhal, G.S. and Strazisar, B.R., A Bayesian belief network (BBN) for combining evidence from multiple CO2 leak detection technologies. Greenhouse Gases-Science and Technology, 2012. 2(3): p. 185-199 DOI: 10.1002/ghg.1284. (ZERT I)

Zhang, W., Xu, T. and Li, Y., Modeling of fate and transport of coinjection of H2S with CO2 in deep saline formations. Journal of Geophysical Research-Solid Earth, 2011. 116(B02202): p. 13 DOI: 10.1029/2010JB007652.

Zheng, L.G., Apps, J.A., Spycher, N., Birkholzer, J.T., Kharaka, Y.K., Thordsen, J., Beers, S.R., Herkelrath, W.N., Kakouros, E. and Trautz, R.C., Geochemical modeling of changes in

shallow groundwater chemistry observed during the MSU-ZERT CO2 injection experiment. International Journal of Greenhouse Gas Control, 2012. 7: p. 202-217 DOI: 10.1016/j.ijggc.2011.10.003. (ZERT I)

Zhou, X.B., Lakkaraju, V.R., Apple, M., Dobeck, L., Gullickson, K.S., Shaw, J.A., Cunningham, A.B., Wielopolski, L. and Spangler, L., Experimental observation of signature changes in bulk soil electrical conductivity in response to engineered surface CO2 leakage. International Journal of Greenhouse Gas Control, 2012. 7: p. 20-29 DOI: 10.1016/j.ijggc.2011.12.006. (ZERT I)

Zhou, X.B., Apple, M.E., Dobeck, L.M., Cunningham, A.B. and Spangler, L.H., Observed response of soil O-2 concentration to leaked CO2 from an engineered CO2 leakage experiment. International Journal of Greenhouse Gas Control, 2013. 16: p. 116-128 DOI: 10.1016/j.ijggc.2013.03.005. (ZERT I)

PRESENTATIONS

Apple, M. E., B. Sharma, X. Zhou, J. A. Shaw, L. M. Dobeck, A. Cunningham. L. H. Spangler, "Plants as indicators of past and present zones of upwelling soil CO2 at the ZERT facility," American Geophysical Union (AGU) Fall meeting, San Francisco, CA (5-9 Dec. 2011).

Barnhart, E., McIntosh, M., Clark, A., Orem, W., Cunningham, A.B. and Fields, M., In-Situ and Enriched Microbial Community Compostion and Function Associated With Coal-bed Mathane From Powder River Basin Coals, in 14th International Society of Microbial Ecology (ISME). 2012: Copenhagen, Denmark

Barnhart, E., Mclure, M., Hunt, K. and Fields, M., Genomic Insight into the Evolution of Acetoclastic Methanogenesis, in 14th International Society of Microbial Ecology (ISME) 2012: Copenhagen, Denmark

Bonneville, A., Sullivan, E.C., Heggy, E., Dermond, J. and Sweeney, M., Using large Aquifer Storage and Recovery (ASR) Sites as Analogs to Study the Mechanical Behavior of Large CO2 Storage, in Fall Meeting American Geophysical Union. 2010: San Francisco, CA

Bowen, D., Lageson, D.R. and Spangler, L., Hydrothermal Systems as Analogs for Breached Traps and Subsurface Healing: Outcrop and Subsurface Examples and Escape Mechanisms, in IEAGHG workshop: Overview of Monitoring Controlled Releases: IEAGHG workshop on Natural Releases of CO2: Building Knowledge for CO2 Storage Environmental Impact Assessments. 2010: Maria Laach, Germany

Chen, H., Buscheck, T., Wagoner, J., Sun, Y., White, J. and Chiaramonte, L., A three-dimensional gas migration model for the Leroy underground natural gas storage facility, in International Conference on Water Resources CMWR. 2012

Connolly, J., Jackson, B., Klapper, I., Cunningham, A.B. and Gerlach, R., The Potential of Microbial Activity to Increase the Efficacy of Geologic Carbon Capture and Storage, in 4th International Conference on Porous Media and its Applications in Science, Engineering and Industry. 2012: Potsdam, Germany

Connolly, J., Pitts, B., Cunningham, A.B. and Gerlach, R., Imaging and Analysis of Microbially Induced Calcium Carbonate Precipitates and Biofilm at the Center for Biofilm Engineering, in Microscopy of America, Microscopy and Microanalysis Meeting. 2012: Phoenix, AZ

Connolly, J., Rothman, A., Jackson, B., Klapper, I., Cunningham, A.B. and Gerlach, R., Pore Scale Processes in Microbially Induced CaCO3 Precipitation in Montana Biofilm Meeting 2012: Bozeman, MT

Cunningham, A.B., Energy Related Biofilms, in Biofilm Science and Technology Meeting. 2011: Center for Biofilm Engineering, Bozeman, Montana

Cunningham, A.B., Gerlach, R., Phillips, Eldring, J., Lauchnor, E., Klapper, I., Ebigbo, A., Mitchell, A. and Spangler, L., The Potential of Microbial Activity To Increase The Efficacy Of Geologic Carbon Capture and Storage, in American Geophysical Union Fall Meeting. 2012: San Francisco, CA

Cunningham, A.B., Phillips, Spangler, L., Mitchell, A. and Gerlach, R., Controlling well bore leakage of CO2 using engineered biomineralization barriers, in Proceedings of the 10th annual Carbon Capture and Sequestration. 2011: Pittsburg, PA

Cunningham, A.B., Spangler, L., Mitchell, A., Phillips and Gerlach, R., Controlling wellbore leakage of CO2 using engineered biomineralization barriers, in Montana Biofilm Meeting. 2011: Montana State University-Bozeman

Ebigbo, A., Helmig, R., Gerlach, R., Cunningham, A.B. and Phillips, Modeling Microbially Induced Carbonate Precipitation And Its Influence On CO2 And Water Flow In The Subsurface, in Fall Meeting American Geophysical Union. 2011: San Francisco, CA

Gerlach, R., Chromium (VI) reduction by environmental microbes – Influence of common soil constituents and carbon sources on chromium (VI) reduction and toxicity, in Montana Biofilm Meeting. 2011: Montana State University-Bozeman

Gerlach, R., Connolly, J., Ebigbo, A., Klapper, I., Lauchnor, E., Mitchell, A., Phillips, Schultz, L., Spangler, L., Zhang, T. and Cunningham, A.B., The Potential of Microbial Activity to Increase the Efficacy of Geologic Carbon Capture and Storage, in 4th International Conference on Porous Media and its Applications in Science, Engineering and Industry. 2012: Potsdam, Germany

Gerlach, R., Connolly, J., Ebigbo, A., Klapper, T., Lauchnor, E., Mitchell, A., Phillips, Schultz, L., Spangler, L., Zhang, T. and Cunningham, A.B., The Potential of Microbial Activity to Increase the Efficacy of Geologic Carbon Capture and Storage, in 4th International Conference on Porous Media and its Applications in Science, Engineering and Industry. 2012: Potsdam, Germany

Gerlach, R., Microbe and Mineral Mediated Transformation of Heavy Metals, Radionuclides, and Organic Contaminants, in Fall Meeting American Geophysical Union. 2011: San Francisco, CA

Gerlach, R., Mitchell, A., Cunningham, A.B., Spangler, L., Zhang, G., Klapper, T. and Ebigbo, A., Microbially Enhanced Carbon Capture and Storage: Pore and Core Scale Experiments and Modeling, in 242nd ACS National Meeting & Exposition. 2011: Denver, CO

Gerlach, R., Mitchell, A., Ebigbo, A., Phillips and Cunningham, A.B., Potential of Microbes to Increase Geologic CO2 Storage Security, in Fall Meeting American Geophysical Union. 2011: San Francisco, CA

Gerlach, R., Mitchell, A., Spangler, L. and Cunningham, A.B., Utility of Biofilms and Biologically-Induced Mineralization in Geologic Carbon Sequestration, in Fall Meeting American Geophysical Union. 2010: San Francisco, CA

Gerlach, R., Phillips, Lauchnor, E., Ebigbo, A., Connolly, J., Mitchell, A., Helmig, R., Cunningham, A.B. and Spangler, L., Improving Control of Microbially-Induced Mineral Precipitation In Flow Systems- Experiments and Modeling, in American Geophysical Union Fall Meeting 2012: San Francisco, CA

Gerlach, R., Phillips, Lauchnor, E., Ebigbo, A., Connolly, J., Zhang, T., Mitchell, A., Klapper, I., Helmig, R., Cunningham, A.B. and Spangler, L., Improving Control of Microbial Activity and Microbially-Induced Mineral Precipitation in Flow Systems - Experiments and Modeling, in 4th International Conference on Porous Media. 2012: Purdue University, West Lafayette, Indiana

Gerlach, R., Schultz, L., Mitchell, A. and Cunningham, A.B., Bacterially Induced Calcite Precipitation and Strontium Co-Precipitation under Flow Conditions in a Porous Media System, in 242nd ACS National Meeting & Exposition. 2011: Denver, CO

Gerlach, R., Spangler, L., Mitchell, A. and Cunningham, A.B., Utility of Biofilms and biologically induced mineralization in geologic carbon sequestration, in Biofilm Science and Technology Meeting. 2011: Center for Biofilm Engineering, Montana State University, Bozeman, Montana

Gerlach, R., Utility of Biofilms and Biologically-Induced Mineralization in Biotechnology and Geologic Carbon Sequestration, in 8th European Congress of Chemical Engineering/1st European Congress of Applied Biotechnology. 2011: Berlin, Germany

Hogan, J. A., and J. A. Shaw, "A field-deployable multi-spectral imaging system for indirect CO2 leak detection through vegetation imaging," Proc. Optical Instrumentation for Applications in Energy and the Environment (OSA), Austin, TX (2-3 Nov. 2011). http://www.opticsinfobase.org/abstract.cfm?URI=E2-2011-EThB6

Hogan, J.A., Shaw, J.A., Lawrence, R.L., Dobeck, L. and Spangler, L., Multispectral imaging of vegetation for CO2 leak detection, in Fall Meeting American Geophysical Union. 2010: San Francisco, CA

Hommel, J., Cunningham, A., Helmig, R., Ebigbo, A. and Class, H., Numerical investigation of microbially induced calcite precipitation as leakage mitigation, in European Geosciences Union. 2013: Vienna, Austria

Hommel, J., Cunningham, A., Helmig, R., Ebigbo, A. and Class, H., Numerical investigation of microbially induced calcite precipitation as leakage mitigation, in The International Research Training Group NUPUS Conference. 2013: Bergen, Norway

Jeffrey, S.R., 2013, Hydrothermal Characteristics of a Fault/Fracture System in the Western Big Snowy Arch, Montana, MSU Earth Sciences Colloquium, April 12-13, 2013 (poster).

Jeffrey, S.R., 2013, Structurally-controlled hydrothermal diagenesis of Paleozoic reservoir rocks exposed in the western Big Snowy Arch, central Montana, Geological Society of America Annual Meeting, Denver, CO, October 27-30, 2013 (poster).

Jeffrey, S.R., and Lageson, D.R., 2014, Structurally-controlled hydrothermal diagenesis of Mississippian reservoir rocks exposed in the Big Snowy Arch, central Montana, Geological Society of America Rocky Mountain (66th Annual) and Cordilleran (110th Annual) Joint Meeting (19–21 May 2014), abstract (oral presentation).

Jeffrey, S.R., Structurally-controlled hydrothermal diagenesis of Paleozoic reservoir rocks exposed in the western Big Snowy Arch, central Montana, in Geological Society of America Annual Meeting. 2013: Denver, CO

Johnson, J., Shaw, J.A., Lawrence, R.L., Nugent, P., Dobeck, L. and Spangler, L., Long-wave Infrared Imaging of Vegetation for Detecting Leaking CO2 Gas, in Remote Sensing and Modeling of Ecosystems for Sustainability IX (SPIE) 2012: San Diego, CA

Johnson, J., J. A. Shaw, P. W. Nugent, J. A. Hogan, "Thermal imaging of vegetation to detect CO2 leaks," Optical Technology Center (OpTeC) Annual Meeting, Montana State University, Bozeman, Montana (18 Aug. 2011).

Johnson, J., J. A. Shaw, P. W. Nugent, R. L. Lawrence, L. M. Dobeck, L. H. Spangler, "Long-wave infrared imaging of vegetation for detecting leaking CO2 gas," Optical Technology Center (OpTeC) annual meeting, Montana State University, Bozeman, MT (17 Aug. 2012).

Kaufman, N., B. Staal, J. A. Shaw, P. W. Nugent, N. J. Pust, D. Mikes, C. Knierim, R. Torgerson, R. Larimer, "Optical sensors for education and outreach," Optical Technology Center (OpTeC) annual meeting, Montana State University, Bozeman, MT (26 Aug. 2010).

Keating, E. and al, e., The challenge of predicting groundwater quality impacts in CO2 leakage scenarios: Results from field, laboratory and modeling studies at a natural analog site in New Mexico, U.S.A., in Geological Society of America Annual Meeting. 2010: Denver, CO

Keating, E. and al, e., The challenge of predicting groundwater quality impacts in CO2 leakage scenarios: Results from field, laboratory and modeling studies at a natural analog site in New Mexico, U.S.A., in IEAGHG Workshop: Natural release of CO2: Building knowledge for CO2 storage environmental impacts assessments. 2010: Maria Leach, Germany

Keating, E., Assessing risk to shallow groundwater from CO2 leaks: Synthesis of two field studies with contrasting results, in 10th Annual conference on Carbon Capture & Sequestration. 2011: Pittsburg, PA

Keating, E., Assessing the impact of CO2 and brine leakage on shallow groundwater quality: Results from a natural analog study in New Mexico, USA, in American Geophysical Union 2011 Fall Meeting. 2011: San Francisco, CA

Kelkar, S. and al, e. Coupled plastic failure and permeability in rocks: a modeling approach. in 46th US Rock Mechanics/Geomechanics Symposium of the American Rock Mechanics Association. 2012. Chicago, IL.

Lageson, D.R. and Lynn, H.B., Characterization of CO2 reservoirs in the Absaroka thrust sheet, Idaho-Wyoming fold-and-thrust belt, in National Meeting of the Geological Society of America. 2010: Denver, CO

Lageson, D.R. and Lynn, H.B., Fault rock and hydrothermal "pipes" associated with the Absaroka thrust system, western Wyoming, in Geological Society of America Annual Meeting. 2011: Minneapolis, Minnesota

Lageson, D.R., Larsen, M.C., Lynn, H.B. and Treadway, W.A., Applications of Google earth pro© to fault and fracture studies of Laramide anticlines in the Rocky mountain foreland, in Geological Society of America Annual Meeting, Virtual Reality in Geoscience Education I. 2011: Minneapolis, Minnesota

Lageson, D.R., Structural controls on naturally occurring CO2 reservoir systems, in Department of Geology and Geophysics Distinguished Lecturer Series. 2010: University of Wyoming, Laramie, WY

Lauchnor, E., Phillips, Cunningham, A.B. and Gerlach, R., Laboratory-scale Column Studies To Evaluate Ureolytically Drive CaCO3 Mineralization in American Geophysical Union Fall Meeting 2012: San Francisco, CA

Lauchnor, E., Schultz, L., Mitchell, A. and Gerlach, R., Microbially induced CaCO3 mineralization and strontium co-precipitation in porous media reactors, in 4th International Conference on Porous Media and its Applications in Science, Engineering and Industry. 2012: Potsdam, Germany

Lewicki, J.L., What can we learn from natural releases of CO2?, in IEAGHG Workshop: Natural releases of CO2: building knowledge for CO2 storage environmental impact assessments. 2010: Maria Laach, Germany

Lynn, H.B. and Lageson, D.R., Structural Controls on Fluid Migration Through the Stewart Peak Culmination, Rocky Mountain Section, in American Association of Petroleum Geologists annual meeting. 2011

Lynn, H.B., Lageson, D.R. and Treadway, W.A., Structural controls on subsurface fluid migration through thrust sheets of the Stewart Peak culmination, Northern Salt River Range, Wyoming, in National Meeting of the Geological Society of America. 2010: Denver, CO

Lynn, H.B., Structural controls on fluid migration (brine + hydrocarbons + CO2) through thrust sheets of the Stewart Peak duplex culmination, western Wyoming, in MSU Earth Sciences Colloquium 2011. 2011: Bozeman, Montana

Maneval, J.E, J., Shaw, J.A., W, N.P. and Hogan, J.A., Thermal imaging of vegetation to detect CO2 leaks, in Optical Technology Center annual meeting. 2011: Montana State University, Bozeman, MT

Mitchell, A., Phillips, Lauchnor, E., Connolly, J., Schultz, L., Gerlach, R. and Cunningham, A.B., Potential of Microbiologically Induced Mineralization to Increase Geologic CO2 Storage Security. Platform Presentation, in Goldschmidt Conference - Earth in Evolution. 2012: Montreal, Canada

Mitchell, A., Phillips, Schultz, L., Lauchnor, E., Gerlach, R. and Cunningham, A.B., Engineered Biofilm and Bio-mineral Plugging of Leakage Pathways., in 17th Reservoir Microbiology Forum 2011. 2011: Energy Institute, London. UK

Mitchell, A., Spangler, L., Cunningham, A.B. and Gerlach, R., Microbially enhanced carbon capture and storage – from pores to cores, in Fall Meeting American Geophysical Union. 2010: San Francisco, CA

Moore-Nall, A. and Lageson, D.R., Elevated Lead in the Bighorn River may be linked to groundwater distribution through reactivated Precambrian fault systems, in Montana Section of American Water Resources Association annual meeting. 2011: Great Falls, Montana

Moore-Nall, A. and Lageson, D.R., Elevated lead in the Bighorn River may be naturally distributed through reactivated Precambrian fault systems, in Geological Society of America Annual Meeting, Potentially Toxic Elements in the Environment: A Session for Students. 2011: Minneapolis, Minnesota

Moore-Nall, A. and Lageson, D.R., Elevated lead in water shows a direct relationship to the Lake Basin fault system of south central Montana, in Montana Section of American Water Resources Association annual meeting. 2011: Great Falls, Montana

Moore-Nall, A. and Lageson, D.R., Francevillite [(Ba,Pb)(UO2)2(V2O8)•5H2O] identified in the Uranium Vanadium deposits in the Pryor Mountain Mining District, Montana and the Little Mountain Mining District, Wyoming may provide a link to the elevated lead in the Bighorn River and be related to fluid migration of the Lower Kane Cave, Wyoming, in 9th Annual Earth Science Colloquium, Earth Sciences. 2014: Bozeman, MT Montana State University

Moore-Nall, A. and Lageson, D.R., Francevillite [(Ba,Pb)(UO2)2(V2O8)•5H2O] identified in the Uranium Vanadium deposits in the Pryor Mountain Mining District, Montana and the Little Mountain Mining District, Wyoming may provide a link to the elevated lead in the Bighorn River and be related to fluid migration of the Lower Kane Cave, Wyoming, in Geological Society of America Annual Meeting. 2014: Denver, CO

Moore-Nall, A. and Lageson, D.R., Francevillite [(Ba,Pb)(UO2)2(V2O8)•5H2O] identified in the Uranium Vanadium deposits in the Pryor Mountain Mining District, Montana and the Little Mountain Mining District, Wyoming may provide a link to the elevated lead in the Bighorn River, in SACNAS (Society for the Advancement of Chicano and Native American Scientists) 40th Anniversary Annual Conference 2013: San Antonio, Texas

Moore-Nall, A. and Lageson, D.R., Herkimer Diamonds in the Pennsylvanian Tensleep Formation may indicate hydrothermal influences for mineralization of the Red Pryor Mountain Uranium/Vanadium deposits, in MSU Earth Sciences Colloquium. 2012: Montana State University, Bozeman, MT

Moore-Nall, A. and Lageson, D.R., Herkimer diamonds in the Pennsylvanian Tensleep Formation may indicate hydrothermal influences for mineralization of the Red Pryor Mountain uranium/vanadium deposits, in Geological Society of America Annual Meeting, Mineralogy/Crystallography. 2011: Minneapolis, Minnesota

Moore-Nall, A. and Lageson, D.R., Hydrothermal influences for U-V mineralization in the Madison Limestone and adjacent units, Pryor Mountains, Montana-Wyoming and a possible link to elevated Pb and Hg in the Big Horn River in Montana, in National Meeting of the Geological Society of America. 2010: Denver, CO

Moore-Nall, A. and Lageson, D.R., Isotopic Evidence from Late-stage Calcite and Brecciated Host Rocks from Abandoned Uranium Vanadium Deposits in Montana and Wyoming Suggests a Possible Hydrothermal Source, in SACNAS National Conference. 2012: Seattle, WA

Moore-Nall, A. and Lageson, D.R., Isotopic Evidence of Late-stage Calcite in Brecciated Host Rocks from Abandoned Uranium Vanadium Deposits in Montana and Wyoming Suggests a Possible Hydrothermal Source, in Geological Society of America Annual Meeting 2012: Charlotte, NC

Moore-Nall, A.L., and Lageson, D.R., 2013, Isotopic Evidence from Late-Stage Calcite and Brecciated Host Rocks from Abandoned Uranium Vanadium Deposits in Montana and Wyoming Suggests a Possible Hydrothermal Source, MSU Earth Sciences Colloquium, April 12-13, 2013 (poster).

Moore-Nall, A. and Lageson, D.R., The Pryor Mountains, a pop-up structure, in the scheme of things, in MSU Earth Sciences Colloquium. 2012: Montana State University, Bozeman

Moore-Nall, A.L., Fault-related hydrothermal dolomitization as a model for U-V mineralization in the Madison Limestone and adjacent units, Pryor Mountains, Montana, in MSU Earth Sciences Colloquium 2011. 2011: Bozeman, Montana

Moriarty, D.D., L.; Benson, S., Rapid surface detection of CO2 leaks from geological sequestration sites. GHGT-12 Energy Procedia, 2014

Moriarty, D.D., L.; Spangler, L.; Krevor, S.; Benson, S., Rapid Detection of CO2 Leaks from Carbon Sequestration Sites, in AGU. 2013: San Francisco, CA

Nicolaysen, S., J. A. Shaw, P. W. Nugent, "A multispectral approach to the detection of leaking CO2," Optical Technology Center (OpTeC) annual meeting, Montana State University, Bozeman, MT (17 Aug. 2012).

Phillips, Eldring, J., Lauchnor, E., Hiebert, R., Gerlach, R., Mitchell, A., Esposito, R., Cunningham, A.B. and Spangler, L., Biofilm-induced Calcium Carbonate Precipitation: Application In The Subsurface, in American Geophysical Union Fall Meeting 2012: San Francisco, CA

Rapaka, S. and al, e., Modeling permeability enhancement due to coupled Thermal-Hydrological-Mechanical processes in geothermal reservoirs, in Fall Meeting American Geophysical Union. 2010: San Francisco, CA

Rapaka, S. and Pawar, R.J., Application of Satellite-based Surface Deformation Monitoring for Leakage Detection, in 10th Annual conference on Carbon Capture & Sequestration. 2011: Pittsburg, PA

Rapaka, S., Kelkar, S., Zyvoloski, G.A. and Pawar, R.J., Non-linear geomechanical modeling with the Finite Element Heat and Mass transfer (FEHM) code, in 9th Annual CO2 Sequestration Conference. 2010: Pittsburgh, PA.

Repasky, K.S., Large area detection for carbon sequestration site monitoring, in International Energy Agency Greenhouse Gas Research and Development Workshop. 2012: Bozeman, MT

Shaw, J. A., "Optical remote sensing of the environment: a tutorial," invited presentation, Optical instrumentation for applications in energy and the environment (OSA), Austin, TX (2-3 Nov. 2011).

Shaw, J. A., "Optical remote sensing systems for environmental studies," seminar at Land Resources and Environmental Sciences Department, Montana State University, Bozeman, Montana, 25 Feb. 2013.

Shaw, J. A., J. Johnson, R. L. Lawrence, and P. W. Nugent, "Thermal imaging of vegetation to detect CO2 gas leaking from underground," invited paper, Optical Instrumentation for Energy and Environmental Applications (E2), Optical Society of America, Tucson, AZ (3-6 Nov. 2013).

Shaw, J. A., P. W. Nugent, J. Johnson, "Radiometric infrared imaging with compact microbolometer cameras: from clouds to beehives," invited talk at Infrared: science, technology, and applications, 506th Wilhelm and Else Heraeus-Seminar, Bad Honnef, Germany (21-23 May 2012).

Shaw, J. A., P. W. Nugent, N. Kaufman, N. J. Pust, D. Mikes, C. Knierim, N. Faulconer, R. L. Larimer, A. DesJardins, "Multispectral imaging system on tethered balloons for optical remote sensing education and outreach," Proc. SPIE 8481 (Optics education and outreach II), 84810T-1-9, San Diego, CA (2012).

Spangler, L., Gerlach, R. and Cunningham, A.B., MSU Energy Research, in Biofilm Science and Technology Meeting. 2011: Center for Biofilm Engineering, Montana State University, Bozeman, Montana

Spangler, L., Overview of Monitoring Controlled Releases, in IEAGHG workshop on Natural Releases of CO2: Building Knowledge for CO2 Storage Environmental Impact Assessments. 2010: Maria Laach, Germany

Treadway, W.A., Fracture analysis and risk assessment of a "leaky" CO2 system in the Rocky Mountain foreland, Thermopolis anticline, Wyoming, in MSU Earth Sciences Colloquium 2011. 2011: Bozeman, Montana

Treadway, W.A., Lageson, D.R. and Lynn, H.B., Fracture Analysis and Geological Characterization of a "Leaky" CO2 System in the Rocky Mountain Foreland, Rocky Mountain Section, in American Association of Petroleum Geologists annual meeting. 2011

Treadway, W.A., Lageson, D.R. and Lynn, H.B., Fracture analysis and risk assessment for a "leaky" CO2 system in the Rocky Mountain foreland, in National Meeting of the Geological Society of America. 2010: Denver, CO

Viswanathan, H.S., Mechanisms for Arsenic Release at the CO2 Sequestration Natural Analog Site in Chimayo, New Mexico, in American Geophysical Union 2011 Fall Meeting. 2011: San Francisco, CA

Viswanathan, H.S., Mechanisms Of Arsenic And Uranium Release At The CO2 Sequestration Natural analog Site, Chimayo, New Mexico, in 10th Annual conference on Carbon Capture & Sequestration. 2011: Pittsburg, PA

Zyvoloski, G.A. and al, e., Thermal-Hydrologic-Mechanical behavior of single fracture in EGS reservoirs, in Fall Meeting American Geophysical Union. 2010: San Francisco, CA

Appendix A

Biofilms and Biomineralization

Assessing Potential for Biomineralization Sealing in Fractured Shale at the Mont Terri Underground Research Facility, Switzerland

APPENDIX A. Project report submitted to CCP. This report has been submitted for consideration as a chapter in Carbon Dioxide Capture for Storage in Deep Geological Formations, Vol. 4, 2014 CPL Press and BP. It is currently under review.

ASSESSING POTENTIAL FOR BIOMINERALIZATION SEALING IN FRACTURED SHALE AT THE MONT TERRI UNDERGROUND RESEARCH FACILITY, SWITZERLAND

Cunningham A.B.[1*], R. Gerlach[1,2], A. Phillips[1], E. Lauchnor[1], A. Rothman[1], R. Hiebert[1], A. Busch[4], B.P. Lomans[4] and L. Spangler[1,3]

[1]Center for Biofilm Engineering, Montana State University, Bozeman, Montana, USA 59717
[2]Chemical and Biological Engineering, Montana State University, Bozeman, Montana, USA 59717
[3]Energy Research Institute, Montana State University, Bozeman, Montana, USA 59717
[4] Shell Global Solutions, Rijswijk, The Netherlands
[*]Corresponding author

ABSTRACT: This report summarizes the methods and results of laboratory testing to evaluate the potential for biomineralization sealing in fractured shale. The tests were conducted using samples of Opalinus shale obtained from the Mont Terri underground testing facility in Switzerland [1]. These results will provide the basis for development of a work plan to test biomineralization sealing in a planned future Mont Terri field demonstration, if appropriate.

Important findings include:

- Porosity and pore size distribution were measured for two blocks of Mont Terri shale (OP1 and OP2) using mercury porosimetry. Mont Terri porosimetry measurements were compared with shale samples from other formations (i.e. Green River (Utah) and Bakken (North Dakota)). The majority of the porosity for all shale types tested is contained in pores less than 0.1 µm and those greater than 10 µm. All four shale samples contained very little porosity between 0.1 and 10 µm. The average porosity for the Mont Terri samples was 11.0%.
- Two cores designated as OP2-3 and OP2-4 were used to conduct biomineralization sealing tests under ambient pressure. Both cores had a single fully-penetrating fracture along the axis of flow. Sand proppant was added to the fracture in core OP2-4, resulting in an initial permeability of 2420 millidarcies. Core OP2-3 had an initial permeability of 249 millidarcies with no sand added. Both were biomineralized to approximately the same final permeability (approximately 0.2 millidarcies) after 4 days, corresponding to a four and three order of magnitude reduction in permeability, respectively.
- Another fractured shale core (OP1-4) was loaded into the high pressure testing system and permeability was measured in response to a range of overburden pressures. Applying overburden pressures in the range of 13.6 to 61.2 bar (200 - 900 psi) resulted in fractured core permeabilities ranging from 14.2µd down to 1.6µd. The highest overburden pressure (61.2 bar or 6.12 MPa) corresponds to the estimated overburden pressure at the Mont Terri site of between 6 -7 MPa.
- Following the overburden permeability tests the OP1-4 shale core was biomineralized in the high pressure system with an overburden pressure of 61.2 bar (900 psi, 6.12 MPa) to mimic Mont Terri pressure conditions. The initial permeability of 2.9 µd was reduced to approximately 0.1 µd due to biomineralization sealing (an order of magnitude reduction). This test indicates that the biomineralization process was successful in the pressures range tested. X-Ray CT scans showed very little evidence of fractures remaining in core OP1-4 after biomineralization sealing.
- In this testing, pre-biomineralization fracture aperture widths ranged from a high of 84.3 µm (OP2-4) down to 0.72 µm (OP1-4). The intermediate values of 39.6 µm (OP2.3) and 43.4 µm (OP1-2) are close to the reported hydraulic aperture range of 20-30 µm estimated for the Mont Terri shale after hydraulic fracturing—indicating that tests reported here have bracketed the range of fracture apertures expected at the Mont Terri site. Biomineralization sealing was successful for all initial fractures tested.

KEYWORDS: Fracture sealant, biomineralization, Opalinus Shale, Mont Terri Underground Research Laboratory, CCS leakage mitigation

INTRODUCTION & BACKGROUND

DOE is currently funding the Center for Biofilm Engineering (CBE) at Montana State University (MSU) on two CO_2 sequestration-related projects (DE-FE0004478 and DE-FE0009599) aimed at developing technology for sealing unwanted CO_2 leakage pathways. This technology is based on bacterial ureolysis-induced biomineralization, a process that promotes the deposition of carbonate minerals in porous media or fractures to seal preferential leakage pathways. Specific leakage pathways of interest include fractures, cracks and delaminations between well casing, well cement, and surrounding aquifer or caprock, and potentially the pore space of the rock. The on-going DOE projects focus entirely on proving the concept of biomineralization sealing in sandstone rock environments. This research and testing methodology has been previously published by the CBE study team [2-11, 13, 15-16].

The work for phase three of the CO_2 Capture Project (CCP3) described here was focused on extending the sandstone-based biomineralization research to evaluate the potential for biomineralization sealing using 2.54 cm (one-inch) diameter cores of fractured Opalinus shale from the Mont Terri test site.

SCOPE OF WORK

This research has demonstrated the feasibility of biomineralization technology to seal fractured shale in laboratory scale tests. This was accomplished by establishing biomineralized seals in cores at both ambient and field relevant pressure and temperature conditions. Seals were evaluated by measuring the reduction in permeability of the fractured core as biomineralization seal development progressed. X-ray computed tomography (X-ray CT) measurements before and after the tests were done to compare the original pore and fracture structure to the structure after biomineralization.

Pore size distribution and porosity were also measured on shale samples using mercury porosimetry. Porosimetry results for Opalinus shale were compared with results for shale samples from other geologic formations.

The principal tasks for this work plan were:

- Task 1. Prepare shale core samples.
- Task 2. Characterize shale porosity and pore size distribution.
- Task 3. Perform core sealing tests at ambient pressure and temperature.
- Task 4. Perform core sealing tests at field relevant pressure and temperature.
- Task 5. Relate findings to field conditions at Mont Terri field site

TASK 1. PREPARE SHALE CORE SAMPLES

Two blocks of Opalinus shale from the Mont Terri test site were used for this study. From these shale blocks multiple 2.54 cm (one-inch) diameter core samples were drilled which were subsequently used in biomineralization sealing tests. Six cores were drilled from the first shale block as shown in Figure 1 (note that the "OP1" designation refers to the cores from the first shale block while "OP2" refers to cores drilled from the second shale block). All cores were drilled parallel to the bedding planes. The attempt at wet drilling (core OP1-6) did not yield satisfactory results. All other OP1 cores were drilled dry, yielding cores which were largely intact but with a few well developed fractures. Cores OP1-1 and OP1-2 were sacrificed to develop the apparatus and experimental protocol for performing biomineralization of shale cores and simultaneous measurement of core permeability. No data from cores OP-1 and OP-2 are reported herein with the exception of the 330 md permeability for OP-2 as reported in Table 5. Biomineralization sealing test results for OP1-4 are reported under Task 4 below. The description of the OP2 shale cores is provided below under Task 3.

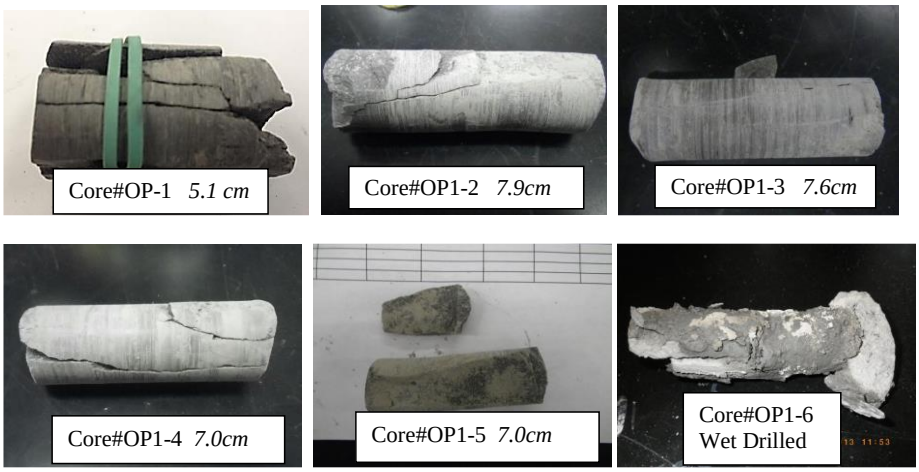

Figure 1. Cores drilled from the OP1 shale block.

TASK 2. CHARACTERIZE SHALE POROSITY AND PORE SIZE DISTRIBUTION

Characterization of Opalinus shale samples consisted primarily of using mercury porosimetry to measure porosity and pore size distribution. X-Ray CT was also used to visually characterize core fractures before and after biomineralization. CT results are reported under Task 4.

Pore Size Distribution and porosity using mercury porosimetry.

Mercury porosimetry was carried out in the laboratories of Montana Emergent Technologies (MET) on the campus of Montana Tech of the University of Montana, located in Butte MT. To evaluate the pore characteristics of the Mont Terri shale, a Micromeritics Autopore IV Model 9500 Mercury Porosimeter (Figure 2) was used. This porosimeter has a 33,000 psi pressure capability which allows it to accurately measure pore sizes over a wide range, from approximately 900 µm to approximately 0.005 µm.

Figure 2. Micromeritics Mercury Porosimeter

Mercury porosimetry or mercury intrusion is based on the principle that the amount of pressure required for a non-wetting fluid, such as mercury, to intrude into a porous substance is inversely proportional to the size of the pores. Material properties that can be determined from this porosimetry test include pore size distribution, total pore volume, median pore diameter, bulk density, and material density.

Samples of both OP1 and OP2 shales were tested. Shale chips with an area roughly 1 cm^2 and a few mm in thickness were placed in a bulb penetrometer which was evacuated to remove air and volatile substances. The bulb was then filled with mercury and pressurized in discrete steps. The incremental volume of mercury that intruded into the sample was recorded for each pressure point up to 33,000 psi.

The majority of the porosity for all shale types tested was contained either in pores less than 0.1 µm or those greater than 10 µm. The portion of porosity greater than 100 µm typically consists of surface roughness and indentations, rather than easily accessible pores. Cracks in the shale would fall in this category.

As shown in Figure 3, the pore size distributions for both OP1 and OP2 were very similar. However, OP2 had significant porosity around the 0.1 µm range while OP1 had pores that were an order of magnitude smaller (around 0.01 µm).

In Figure 4, the pore size distribution for both samples of Mont Terri shale were compared with shale from the Bakken formation (North Dakota) and the Green River formation (Utah). All shales contained very little porosity between 0.1 and 10 µm. However, since the Bakken Shale had almost no porosity less than about 50 µm, both OP1 and OP2 were more similar to the Green River shale.

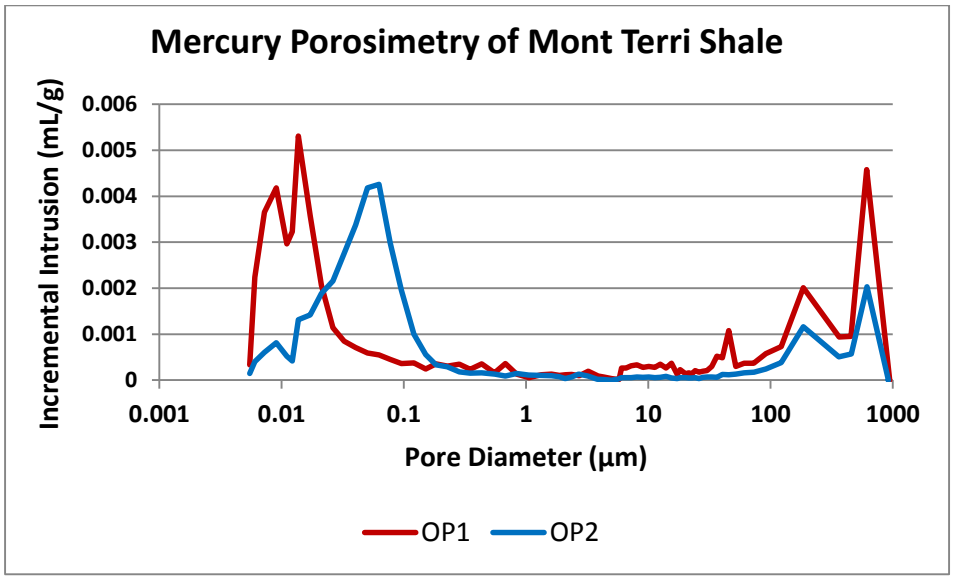

Figure 3. Pore size distribution for OP1 and OP2 shales.

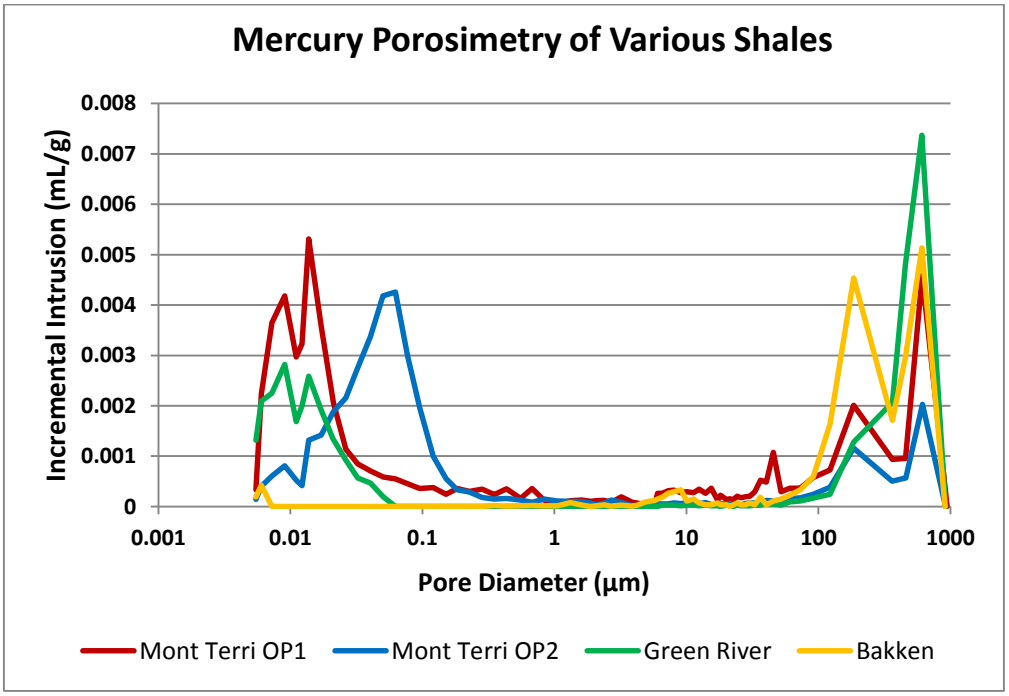

Figure 4. Comparison of Mont Terri shale pore sizes with other shales.

Table 1 shows the porosity for each shale sample along with the summary pore size categories. The average porosity for the two Mont Terri shales was 11.0 %.

Table 1. Mont Terri shale pore size summary.

Core	Porosity		
	Total	Less than 10 µm	Between 1-10 µm
Mont Terri #OP1	12.31%	8.59%	0.65%
Mont Terri #OP2	9.71%	8.13%	0.27%
Green River	8.25%	4.53%	0.03%
Bakken	4.50%	0.51%	0.39%

TASK 3. PERFORM CORE SEALING TESTS AT AMBIENT PRESSURE

Core Preparation.

Four 2.54 cm (one inch) diameter cores were drilled from the second Opalinus shale block (designated OP2). Two of these cores (OP2-3 and OP2-4) were used to conduct biomineralization sealing tests under ambient pressure.

Using a hammer and a sharp object, both cores were split longitudinally. Core OP2-3 fractured into three pieces as shown in Figure 5. Core OP2-4 split cleanly into two pieces (Figure 6). Both cores were soaked in Mont Terri Brine overnight (about 16 hours). The liquid caused OP2-3 to separate into many additional pieces as shown in Figure 5. These pieces were pieced together as well as possible and wrapped in several layers of Polytetrafluoroethylene (PTFE) tape. The wrapped core was then inserted into a reinforced PVC tube for permeability testing.

The overnight soak in Mont Terri Brine caused less damage to OP2-4; the two pieces stayed intact. As shown in Figure 7, approximately one layer of 30/50 proppant sand was placed on one piece and the core was reassembled and wrapped in PTFE tape. The wrapped core was then inserted into a reinforced PVC tube for permeability testing.

Figure 5. Split OP2-3 core and core wrapped in PTFE tape. Core length was 5.77 cm (2.27 inches).

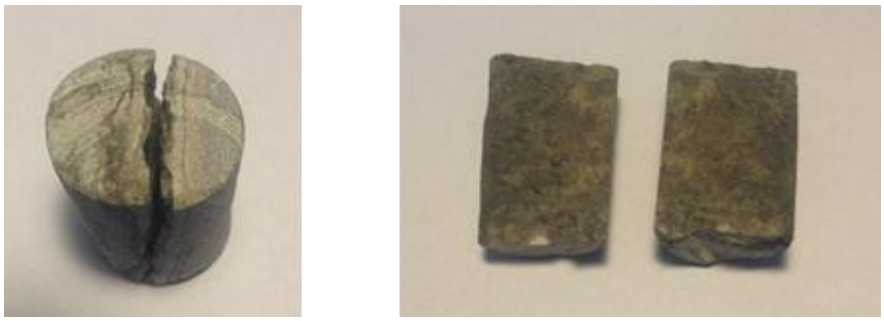

Figure 6. Split OP2-4 Core. Core length was 4.01 cm (1.58 inches).

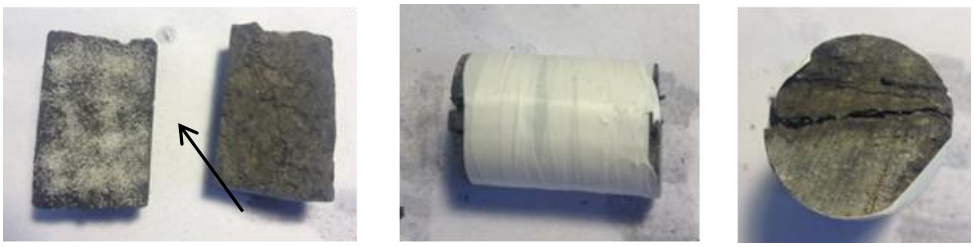

Figure 7. OP2-4 Core showing proppant placement (arrow) and wrapping pieces with PTFE tape.

System for developing biomineralization seal and measuring permeability.

The flow-through system used to develop the biomineralization seal while simultaneously measuring permeability through 2.54 cm (one-inch) diameter shale cores is shown in Figures 8 and 9. This system consisted of a pump for fluid injection, a pressure transducer (Omega) for determination of differential pressure across the core, and a holder around the core with sufficient overburden pressure to prevent bypass of flow around the core. A Cole Palmer peristaltic pump was used to inject fluid for initial permeability measurements. A KD Scientific syringe pump was used for injection of biomineralization fluids. Pump flow rate and influent pressure were recorded periodically and logged. The core holder consisted of PVC reinforced tubing with an inner diameter of one inch and the overburden pressure was provided by a heavy duty hose clamp placed around the core, which was tightened with a torque wrench to 20-40 in-lbs. The core holder was connected to the system via ¼-inch plastic tubing and oriented vertically with upward fluid flow. The effluent fluid that collected at the top of the core overflowed to a waste vessel.

The establishment of the biomineralization seal was monitored using standard pH measurements as well as flow rate and pressure differential monitoring [6,8,13].

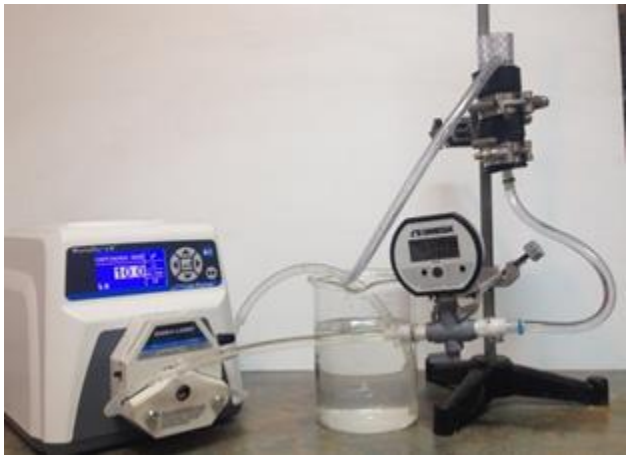

Figure 8. Apparatus for performing biomineralization sealing of shale cores and simultaneously measuring core permeability.

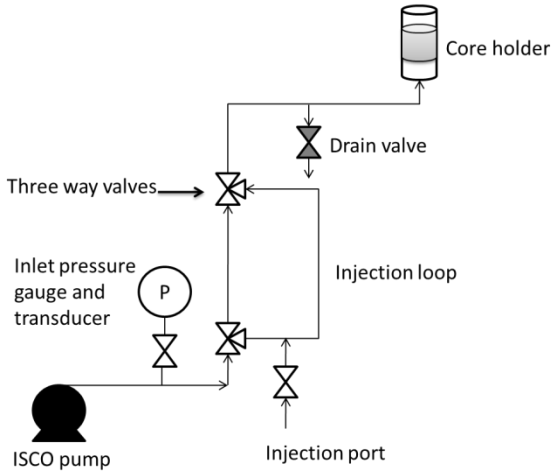

Figure 9. Process flow diagram (schematic) of apparatus for performing biomineralization sealing of shale cores and simultaneously measuring core permeability.

Initial permeability measurements.

A solution of 10 g/L ammonium chloride was used to measure the initial permeability of the cores. This solution corresponds to the ammonium chloride content of the media used for biomineralization, without urea and nutrient broth added. The measured permeability was based on the cross sectional area of the core face perpendicular to flow and the average of the shortest and longest measured core length. Fluid was recirculated with a peristaltic pump at a rate sufficient to measure a reasonable pressure drop across the core. The permeability was calculated using Darcy's Law and results for both OP2 cores are shown in Table 2. The permeability OP2-4 was an order of magnitude greater (249 millidarcies vs 2420 millidarcies) than that of OP2-3, presumably due to the presence of proppant in the fracture. This is as expected since proppant is used to for instance enhance the permeability of fractured shale for oil recovery.

Table 2. Initial Permeability values prior to biomineralization

Core	Area (cm^2)	Average Length (cm)	Flow Rate (ml/min)	Pressure drop (meters H_2O)	Calculated Permeability (md)
OP2-3	5.43	5.77	10.0	7.3	249
OP2-4	5.43	4.01	40.0	2.2	2,420

Biomineralization sealing procedure.

The two OP2 cores (OP2-3 and OP2-4) cores were biomineralized using procedures developed by Montana State University. The biomineralization procedure consisted of first inoculating the core with the ureolytic organism *Sporosarcina pasteurii*, then pumping a nutrient solution containing microbial growth medium and urea without calcium (designated CMM-) into the core, followed by the same growth medium with calcium (CMM+). Alternating pulses of CMM- and CMM+ were applied to build up the calcium carbonate sealing deposits. As the mineralization deposits built up, the flow rate was periodically reduced to keep the pressure drop at or below 25 psig as higher pressures might have caused leaks in the system.

Biomineralized core permeability measurements.

Core permeabilities following biomineralization are shown in Table 3. Although OP2-4 had an initial permeability 10 times greater than OP2-3, both were biomineralized to approximately the same final permeability (approximately 0.2 millidarcies) after 4 days. A plot of permeability vs time is shown in Figure 10. Significant calcium carbonate precipitate was observed in the fractures and on the outside of the biomineralized cores, OP2-3 and OP2-4 (Figure 11). The mineralization process effectively blocked the flow of fluid through the cracks in the shale.

Table 3. Permeability values following biomineralization

Core	Flow Rate (ml/min)	Pressure drop (meters H_2O)	Final Permeability (md)	Permeability Reduction
OP2-3	0.015	15.6	0.18	99.93%
OP2-4	0.03	19.5	0.20	99.99%

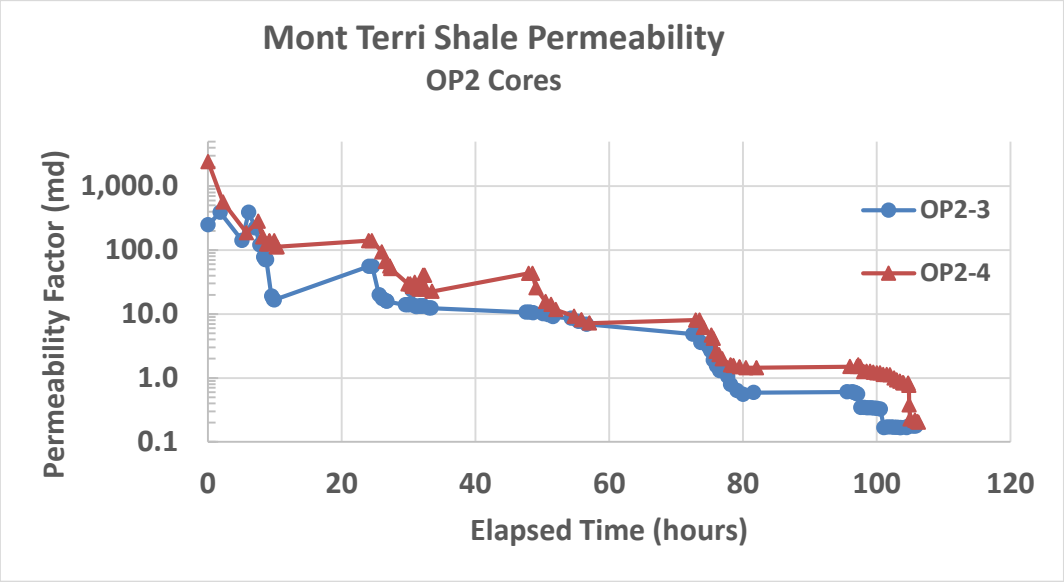

Figure 10. Permeability reduction with time during biomineralization of cores OP2-3 (blue dots) and OP2-4 (red triangles).

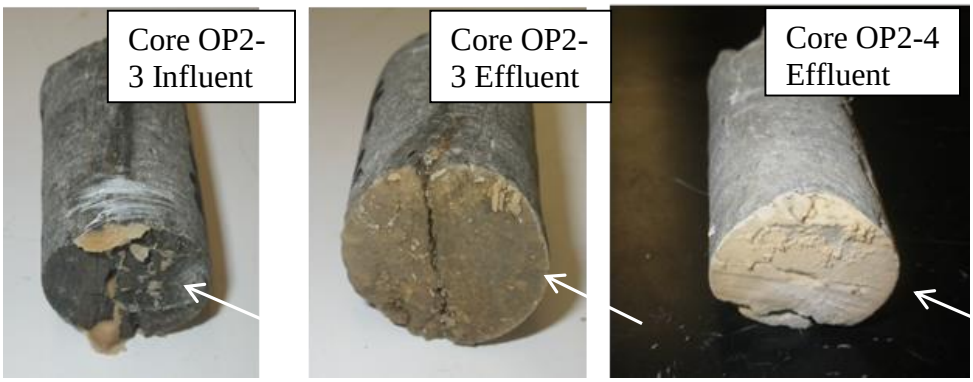

Figure 11. Significant calcium carbonate (arrows) was observed in the fractures and on the outside of cores OP2-3 and OP2-4 following biomineralization. All OP2 cores were drilled wet.

TASK 4 - PERFORM CORE SEALING TESTS AT FIELD-RELEVANT PRESSURE

High pressure core test system.

MSU/CBE has developed a high pressure, elevated temperature rock core testing system [2,3,4,17]. A Hassler-type core holder housed in an incubator to control temperature (Figure 12) has been utilized to test biofilm- and biomineral-based sealing of 2.54 cm (1 inch) diameter Berea sandstone cores. Both biofilm-only and biofilm-induced biomineralization sealing has been shown to reduce the permeability approximately 3 to 5 orders of magnitude in Berea sandstone cores under high and low pressure

[9,10,13,17]. In addition, it was demonstrated that the biofilms and the deposited minerals were resistant to supercritical CO_2 exposure [9,10,12].

Permeability vs. overburden pressure.

A fractured shale core (OP1-4) was loaded into the high pressure testing system and permeability was measured in response to a range of overburden pressures (a picture of core OP1-4 is shown in Figure 1 and below in Figure 15).

The core was wrapped in PTFE tape to ensure a tight seal against the Viton sleeve inside the core holder. The core was loaded into the core holder and the overburden reservoir was filled. Synthetic Mont Terri brine was pumped through the core over a 5 day period. After this time the core was assumed to be saturated and permeability testing was performed. Each permeability test had a constant differential pressure across the core and a constant overburden pressure. The inlet pressure and overburden pressure were controlled by high pressure syringe pumps (Teledyne Isco 500D). The outlet of the core was open to atmospheric pressure. Both the inlet and overburden pressures were raised slowly in 50-100 psi intervals, while keeping the overburden pressure above the inlet pressure to prevent bypass of the brine solution. Once the desired inlet pressure was reached data logging for both pumps was started. Volume dispensed from the pump was monitored over time to determine an average flow rate. Permeability was calculated using Darcy's law when the flow rate through the core was stable for approximately 2 hours. The experiments were carried out in sequence from low pressures to higher pressure.

Figure 12. The high pressure core test system. The Hassler type core holder is in the center of the picture. Flow was from left to right. Overburden pressure was controlled via a high pressure flexible stainless steel hose connected to an Isco pump operated in constant pressure mode which was connected to the core holder (bottom of the picture).

Table 4 and Figure 13 show that applying overburden pressures ranging from 13.6 to 61.2 bar (200 to 900 psi) substantially reduces the permeability of the (saturated) fractured shale core into the microdarcy range. The upper range of overburden pressure (61.2 bar), which corresponds to the estimated overburden pressure at the Mont Terri site, results in a permeability of about 1.6 microdarcies. The variability in permeability values observed for 20.4 and 61.2 bar overburden pressures indicates the possibility that the effective fracture aperture is exhibiting a dynamic response to changes in overburden pressure and flow rate. This response may be the result of random opening and closing of micro flow channels along the original fracture.

Table 4. Permeability of the fractured OP1-4 shale core in response to increasing overburden pressure

Flow Rate (mL/hr)	Differential Pressure (bar)	Overburden Pressure (bar)	Permeability (μd)	Standard deviation (μd)
0.347	10.2	13.6	14.2	0.810
0.176	17.0	20.4	4.34	0.239
0.104	10.2	20.4	4.22	0.526
0.125	54.4	61.2	0.99	0.053
0.144	57.8	61.2	1.05	0.078

0.210	54.4	61.2	1.63	0.056

Biomineralization sealing.

Following the overburden permeability tests the OP1-4 shale core was biomineralized. For this test the overburden pressure was set at 61.2 bar (900 psi) and the injection pressure was set to 54.4 bar (800 psi). Biomineralization sealing was promoted using the same methods and protocols as described in Task 3. Results shown in Figure 14 indicate that the initial permeability of 2.9 microdarcies was reduced to approximately 0.1 microdarcies during the first 50 hours. This permeability reduction was entirely due to bacterial plugging. After 50 hours calcium was added and biomineralization began, however no further permeability reduction was observed. This result is not surprising since the estimated original aperture width of approximately 0.74 µm (shown in Table 5 below) is substantially smaller than the size of the *S. pasteurii* cells (2-4 microns). This test does however indicate that the biomineralization process was not affected by pressures in the range tested as significant calcium carbonate deposits were observed in the system.

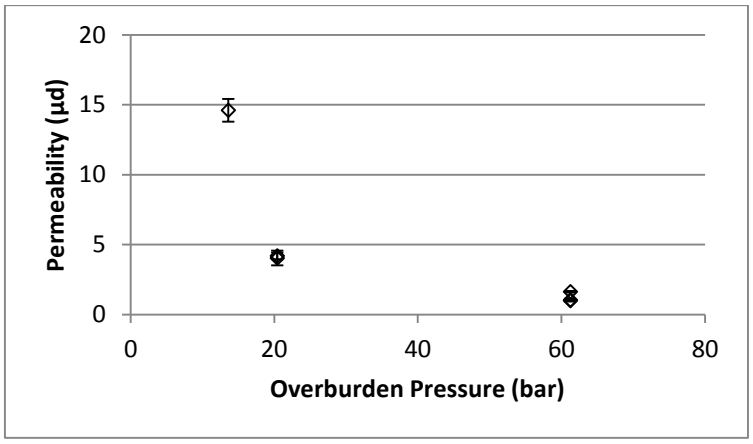

Figure 13. Observed permeability vs. overburden pressure, error bars represent the standard deviations of five measurements.

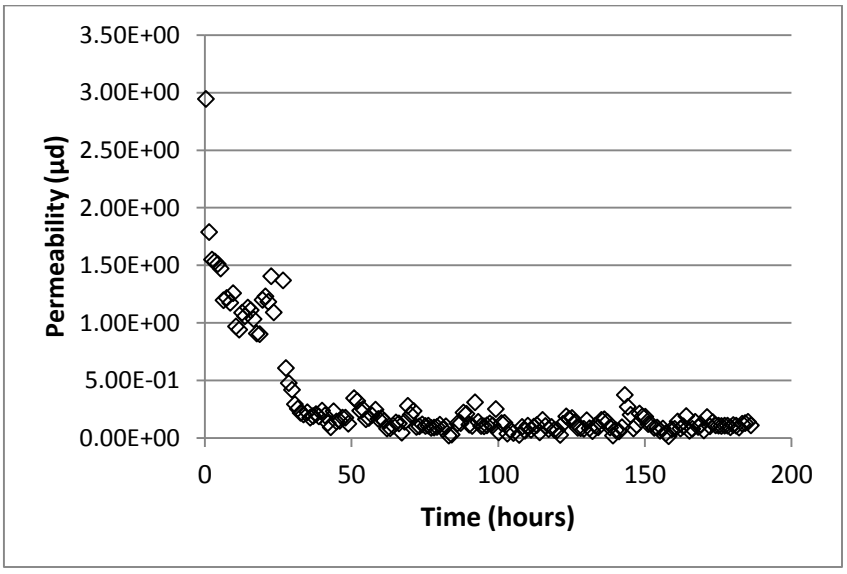

Figure 14. Permeability of core OP1-4 over time. At 24 hours the system was depressurized and switched from injecting the organisms to the growth medium. At 50 hours the system was switched from the growth medium to the calcium-containing medium. Permeability calculations accounted for the differences in fluid viscosity, since the calcium-free medium has a viscosity of 1.006 10^{-3} kg m^{-1} s^{-1} and the calcium-containing medium has a viscosity of 1.051 10^{-3} kg m^{-1} s^{-1}.

Following biomineralization sealing, core OP1-4 was scanned using X-Ray CT. Figure 15 shows the OP1-4 core before and after high pressure biomineralization along with the locations where the CT scans were performed.

Figure 16 shows the results of the X-Ray CT scans for two locations along the axis of core OP1-4 before and after biomineralization. It should be noted that the "before biomineralization" scans were taken while the core was wrapped in PTFE tape. This condition corresponds to a very small, but unknown overburden condition. As a result it is not possible to directly compare the size of the fractures before and after biomineralization as the biomineralization sealing was performed at very high (61.2 bar) overburden pressure. However the X-Ray CT scans do show very little evidence of fractures remaining after biomineralization sealing was completed.

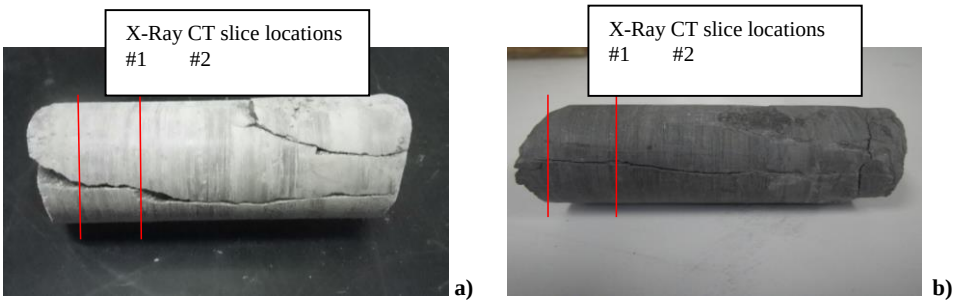

a) **b)**

Figure 15. Core OP1-4 **a)** before biomineralization and **b)** after biomineralization.

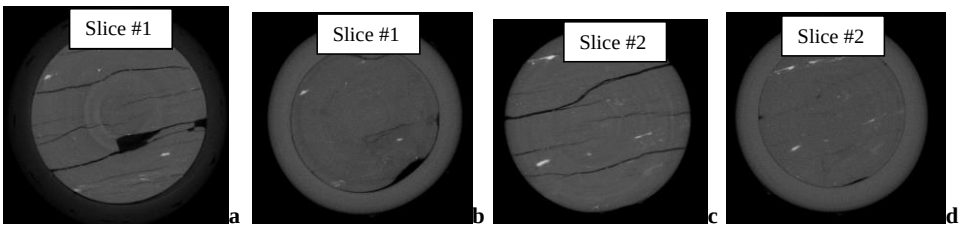

a **b** **c** **d**

Figure 16. X-Ray CT scans of core OP1-4 before (16a & 16c,) and after (16b & 16d,) biomineralization sealing. After applying overburden pressure of 61.2 bar and completing biomineralization sealing figures 16b and 16d reveal very little evidence of residual fracturing in the shale.

TASK 5 RELATE FINDINGS TO FIELD CONDITIONS AT MONT TERRI FIELD SITE

The confining stresses at the Mont Terri site are in the range of 6-7 MPa and fracture apertures can be expected in the range of 20 to 30 μm when fractures are kept open by an overpressure (above reopening pressure). These data are reported in "Hydro-fracturing Design Studies for Sealing Experiment at Mont Terri" by Rutqvist *et al* at LBNL. Ambient temperature at the site is assumed to be 20 degrees C.

The high pressure permeability and biomineralization experiment described was carried out with an overburden pressure of 61.2 bar (900 psi or 6.12 MPa). This 6.12 MPa pressure is therefore in the rage of possible confining stresses assumed for Mont Terri.

Core fracture aperture width calculation

Published equations were used to relate average permeability fractured cores (as measured for Task 3 & 4) to the corresponding (calculated) fracture aperture widths. The following derivation shows the mathematical development of the equation used to calculate fracture width from measured average fractured core permeabilities.

Derivation

The analytical solution to the Navier Stokes equation for incompressible flow through two equally spaced plates was combined with Darcy's law to yield an expression for effective fracture hydraulic conductivity, $K_{fracture}$ [=] $^{m}/_{s}$.

$$K_{fracture} = \frac{w^2}{12} \cdot \frac{\rho g}{\mu}$$

Where: w = the aperture of the fracture in meters

ρ is the density of the fluid in $\frac{kg}{m^3}$,

g is the gravitational acceleration constant in $\frac{m}{s^2}$

and μ is the viscosity of the fluid in $\frac{kg}{m\,s}$.

A second relation, from [14], was used to relate matrix, average and fracture hydraulic conductivities:

$$K_{fracture} = \frac{K_{average}A - K_{matrix}(A - wl)}{wl} \qquad \text{Equ. 1}$$

Where: $K_{average}$ = hydraulic conductivity of the rock and core system (m/s). This was measured experimentally at different overburden and differential pressures.

A = cross sectional area of the core (m^2)

K_{matrix} = hydraulic conductivity of unfractured shale, $1.0 * 10^{-14}\frac{m}{s}$ was used. This was the observed hydraulic conductivity at the end of the first high pressure experiment.

l =width of the fracture (m)

Combining these equations leads to: $\frac{w^3 l}{12}\frac{\rho g}{\mu} - k_{av}A + k_m(A - wl) = 0$ Equ. 2

Which was solved for w, the aperture of the fracture.

Calculated aperture values

Calculated fracture apertures for all (pre-biomineralization) tests are shown below in Table 5.

Results shown in Table 5 indicate that the biomineralized cores exhibit pre-biomineralization fracture widths ranging from 84.3 µm (OP2-4) down to 0.74 µm (OP1-4). The intermediate values of 39.6 µm (OP2-3) and 43.4 µm (OP1-2) are close to the range of 20-30 µm estimated above for the Mont Terri shale after hydraulic fracturing. These findings indicate that the biomineralization tests described here have bracketed the range of fracture apertures expected at the Mont Terri site. Biomineralization sealing was successful for all initial fractures apertures tested.

Table 5. Results from varying overburden pressure and differential pressure in the high pressure system. Overburden pressure tests were run on core OP1-4. The permeability and fracture aperture for cores OP1-2, OP2-3, and OP2-4 measured under ambient pressure are also included in this Table.

Differential Pressure (psi)	Overburden Pressure (psi)	Permeability (µd)	Fracture Aperture (µm)
150	200	14.2	1.5
250	300	4.34	1.0
150	300	4.22	1.0
850	900	1.05	0.64
800	900	1.63	0.74

Ambient experiments	Permeability (md)	Fracture Aperture (µm)
Proppant Core (OP2-4)	2420	84.3
No Proppant (OP2-3)	250	39.6
No Proppant (OP1-2)	330	43.4

SUMMARY

Porosity and pore size distribution were measured for two blocks of Mont Terri shale (OP1 and OP2) using mercury porosimetry. Mont Terri porosimetry measurements were also compared with shale samples from other formations (i.e. Green River (Utah) and Bakken (North Dakota)). The majority of the porosity for all shale types tested is contained in pores less than 0.1 μm and those greater than 10 μm. The overall pore size distributions for both OP1 and OP2 were very similar. All four shale samples contained very little porosity between 0.1 and 10 μm. The average porosity for the two Mont Terri shale blocks tested was 11.0%

Cores OP2-3 and OP2-4 were used to conduct biomineralization sealing tests under ambient pressure. Both cores had a single fully-penetrating fracture along the axis of flow. Sand proppant was added to the fracture in core OP2-4 resulting in an initial permeability of 2490 millidarcies. Core OP2-3 had an initial permeability of 249 millidarcies. Both were biomineralized to approximately the same final permeability (approximately 0.2 millidarcies) after 4 days. This corresponds to a four and three order of magnitude reduction in permeability, respectively.

Fractured shale core (OP1-4) was inserted into the high pressure testing system and permeability was measured in response to a range of overburden pressures. Applying overburden pressures in the range of 13.6 to 61.2 bar (200 - 900 psi) resulted in fractured core permeabilities ranging from 14.2μd down to 1.6μd. The highest overburden pressure (61.2 bar or 6.12 MPa) corresponds to the estimated overburden pressure at the Mont Terri site of between 6 -7 MPa.

Following the overburden-permeability tests the OP1-4 shale core was biomineralized at an overburden pressure of 61.2 bar (900 psi). The initial permeability of 2.9 microdarcies was reduced to approximately 0.1 microdarcies due to biomineralization sealing (two order of magnitude reduction). This test indicates that the biomineralization process was not affected by pressures in the range tested. X-Ray CT scans showed very little evidence of fractures remaining in core OP1-4 after biomineralization sealing was completed.

In Phase I testing pre-biomineralization fracture widths ranged from a high of 84.3 μm (OP2-4) down to 0.74 μm (OP1-4). The intermediate values of 39.6 μm (OP2.3) and 43.4 μm (OP1-2) are close to the range of 20-30 μm estimated above for the Mont Terri shale after hydraulic fracturing—indicating that Phase I tests have bracketed the range of fracture apertures expected at the Mont Terri site. Biomineralization sealing was successful for all initial fracture apertures tested.

CONCLUSIONS

1) The two blocks of Opalinus shale tests were found to have similar pore size distributions (<0.1 μm and > 10 μm) and porosities (11% average porosity).

2) Applying overburden pressures in the range of 13.6 to 61.2 bar (200 - 900 psi) reduced the saturated, fractured shale core permeability into the microdarcy range (14.2μd to 1.6μd).

3) All shale samples tested were successfully biomineralized. Initial average fractured core permeabilities were reduced by up to four orders of magnitude. Shale fracture apertures tested bracketed the aperture range (20-30 microns) predicted at Mont Terri.

4) Results from this testing indicate that the biomineralization sealing alternative has a high probability of success in the planned Mont Terri field test.

ACKNOWLEDGEMENTS

This research was sponsored by CCP3 with supplemental funding from DOE Project #DE-FE0000397. Additional Technical review was provided by Joseph J.T. Westrich of Shell Global Solutions.

REFERENCES

Thury, M.; The characteristics of the Opalinus Clay investigated in the Mont Terri underground rock laboratory in Switzerland. Comptes Rendus Physique, Volume 3, Issue 7, Pages 923-933, 2002.

Cunningham, A.B.; Gerlach, R.; Spangler, L.; Mitchell, A.C. (2009): Microbially enhanced geologic containment of sequestered supercritical CO_2. *Energy Procedia*. 1(1):3245-3252. doi: 10.1016/j.egypro.2009.02.109

Cunningham, A.B., Gerlach, R.; Spangler, L.; Mitchell, A.C.; Parks, S.; Phillips, A. (2011): Reducing the risk of well bore leakage using engineered biomineralization barriers. *Energy Procedia*. 4:5178-5185. doi:10.1016/j.egypro.2011.02.49.

Cunningham, A.B.; Lauchnor, E.; Eldring, J. Esposito, R.; Mitchell, A.C.; Gerlach, R.; Connolly, J.; Phillips, A.J.; Ebigbo, A.; Spangler, L.H. (2013): Abandoned Well CO2 Leakage Mitigation Using Biologically Induced Mineralization: Current Progress and Future Directions. *Greenhouse Gases: Science and Technology*.

Ebigbo A.; Helmig, R.; Cunningham, A.B.; Class, H.; Gerlach, R. (2010): Modelling biofilm growth in the presence of carbon dioxide and water flow in the subsurface. *Advances in Water Resources*. 33:762–781. doi: 10.1016/j.advwatres.2010.04.004

Ebigbo A.; Phillips, A; Gerlach, R.; Helmig, R.; Cunningham, A.B.; Class, H.; Spangler, L. (2012): Darcy-scale modeling of microbially induced carbonate mineral precipitation in sand columns. *Water Resources Research*. 48, W07519, doi:10.1029/2011WR011714.

Fridjonsson, E.O.; Seymour, J.D.; Schultz, L.N.; Gerlach, R; Cunningham, A.B.; Codd, S.L. (2011): NMR Measurement of Hydrodynamic Dispersion in Porous Media Subject to Biofilm Mediated Precipitation Reactions. *Journal of Contaminant Hydrology*. 120-121:79-88. doi:10.1016/j.jconhyd.2010.07.009

Lauchnor, E.G.; Schultz, L.; Mitchell, A.C.; Cunningham, A.B.; Gerlach, R. Bacterially Induced Calcium Carbonate Precipitation and Strontium Co-Precipitation under Flow Conditions in a Porous Media System. *Environmental Science and Technology*. es-2010-02968v. Accepted. Jan 02, 2013. http://dx.doi.org/10.1021/es304240y,

Mitchell, A.C.; Phillips, A.J.; Hamilton, M.A.; Gerlach, R.; Hollis, K.; Kaszuba, J.P.; Cunningham, A.B. (2008): Resilience of planktonic and biofilm cultures to supercritical CO_2. *The Journal of Supercritical Fluids*. 47(2):318-325. doi:10.1016/j.supflu.2008.07.005

Mitchell, A.C.; Phillips, A.J.; Hiebert, R.; Gerlach, R.; Spangler, L.; Cunningham, A.B. (2009): Biofilm enhanced geologic sequestration of supercritical CO2. *The International Journal on Greenhouse Gas Control*. 3:90-99. doi:10.1016/j.ijggc.2008.05.002

Mitchell, A.C.; Dideriksen, K.; Spangler, L.H.; Cunningham, A.B.; Gerlach, R. (2010): Microbially enhanced carbon capture and storage by mineral-trapping and solubility-trapping. *Environmental Science and Technology*. 44(13):5270-5276. doi: 10.1021/es903270w

Mitchell, A.C.; Phillips, A.J.; Schultz, L.N.; Parks, S.L.; Spangler, L.H.; Cunningham, A.B.; Gerlach, R. Microbial $CaCO_3$ mineral formation and stability in an experimentally simulated high pressure saline aquifer with supercritical CO_2. *International Journal of Greenhouse Gas Control*. Accepted February 03, 2013.

Phillips, A.J., R. Gerlach, R., Lauchnor, E., Mitchell, A.C, Cunningham, A.B. Spangler L. Engineered applications of ureolytic biomineralization: a review (2013). *Biofouling*, Vol. 29, No. 6, 715–733, http://dx.doi.org/10.1080/08927014.2013.796550.

Putra, E., V. Muralidharan, and D. S. Schechter. "Overburden pressure affects fracture aperture and fracture permeability in a fracture reservoir." *Saudi Aramco Journal of Technology* (2003): 57-63.

Schultz, L.; Pitts, B.; Mitchell, A.C.; Cunningham, A.B.; Gerlach, R. (2011): Imaging Biologically-Induced Mineralization in Fully Hydrated Flow Systems. *Microscopy Today*. September 2011:10-13. doi:10.1017/S1551929511000848 (with cover image feature).

Phillips, AJ; Lauchnor, E; Eldring, J; Esposito R; Mitchell, A.C.; Gerlach, R; Cunningham, A; and Spangler, L. (2013): Potential CO_2 Leakage Reduction through Biofilm-Induced Calcium Carbonate Precipitation. *Environmental Science & Technology*. 47 (1):142-149

Phillips, AJ. (2013): Biofilm-Induced Calcium Carbonate Precipitation: Application in the Subsurface, Montana State University, PhD Thesis. 223 pp.

Appendix B

Lawrence Berkeley National Laboratory Final Report

ZERT II Final Scientific Report

DE-FE0000397

Lawrence Berkeley National Laboratory

AUTHORS/CONTRIBUTORS:

Curt Oldenburg (PI)
Paul Cook
Andrea Cortis[1]
Christine Doughty
Timothy Kneafsey
Jennifer L. Lewicki[2]
Alex Morales
Karsten Pruess[3]
Matthew Reagan
Dmitriy Silin[4]
Nic Spycher
Tetsu Tokunaga
Jiamin Wan
Jong-Won Jung[5]
Tianfu Xu[6]

[1]Now at Ayasdi, Palo Alto, CA
[2]Now at USGS, Menlo Park, CA
[3]Retired
[4]Now at Shell, Houston, TX
[5]Now at Louisiana State University, Baton Rouge, LA
[6]Now at Jilin University, China

October 29, 2014

ABSTRACT

Work at LBNL under ZERT II consisted of three technical tasks focused on numerical simulation applications and development, field monitoring, and laboratory studies of two-phase CO_2-water flow and trapping. In this report, simulation results and programming effort are described for long-term CO_2 migration and leakage up a fault, hysteretic relative permeability, reactive geochemical transport, shallow CO_2 flow and transport, and web-based gas-mixture property estimation. Field-based research on monitoring CO_2 surface flux using eddy-covariance and accumulation chamber methods, and related field and modeling support are presented next. Finally, we present laboratory studies of fluid and gas flow and retention in porous media focused on surface-tension-related phenomena. This is complemented by presentation of an example of a computational approach to modeling pore occupancy and its verification using high-resolution imaging.

EXECUTIVE SUMMARY

Simulation studies suggest that complex phase-change and related phase-interference phenomena are predicted to occur during CO_2 leakage up a fault resulting in oscillatory leakage fluxes of CO_2 and water. We finalized and released a new version (V2) of the reactive geochemical transport simulator, TOUGHREACT. Hysteresis in relative permeability is an important property of porous media systems undergoing drainage (CO_2 injection) and imbibition (water migrating into pore space vacated by CO_2. Upscaling of laboratory-measured hysteretic relative permeability is feasible and can provide input parameters for residual gas trapping in large-scale reservoir simulations of geologic carbon sequestration. A relevant test problem and user guide for the shallow CO_2-air transport model EOS7CA was developed for expanding the user base of the code. The LBNL online gas-mixture-property estimation tool, WebGasEOS, was ported to an LBNL-wide server and is receiving considerable use from around the nation and the world. Eddy covariance and accumulation chamber approaches to monitoring and detection of CO_2 leakage were demonstrated at the ZERT shallow release test site along with related modeling approaches to analyze and interpret the data. LBNL provided critical technical assistance in the field in support of the experiments. In the laboratory, LBNL research demonstrated the importance of mixed wettability in the flow of CO_2 and brine through grains of calcite and silica sand, details of CO_2 capillary pressure relative to air as an analog, and a useful computational approach to modeling pore occupancy by a non-wetting fluid such as $scCO_2$.

EXPERIMENTAL METHODS

The ZERT II project at LBNL comprised three technical tasks aimed at improving performance prediction of geologic carbon sequestration, developing approaches to monitor and verify storage, and improving understanding of trapping processes. The methods used included computer modeling, field investigations at the ZERT shallow-release facility in Montana, and laboratory work. The computer modeling work included programming new capabilities into the TOUGH codes, testing, and applications of these new capabilities. In the field, we used accumulation chamber and eddy covariance approaches to monitor CO_2 emissions from the ground surface at the Montana State University ZERT release facility. LBNL also installed the packer and CO_2 delivery and flow controller system (that LBNL previously designed and built) used inside the shallow horizontal well previously drilled by Montana State University. In the laboratory, a variety of experimental methods was used including high-pressure core-flow analysis, imaging using X-ray CT and other methods, and a high-pressure cell for visual interfacial tension measurements.

RESULTS AND DISCUSSION

The project was organized into a management task (Task 1) and three technical tasks (Tasks 2-4) with a single task lead assigned to each task. There was close integration between Tasks 2 and 3 as the computer models of Task 2 are useful in Task 3 for predicting CO_2 leakage fluxes. Here we present a summary of results of the project organized by Task and Subtask.

Task 2: Performance Prediction for Long-Term Underground Fate of CO_2

Goal: To develop reliable techniques to predict and model CO_2 migration and trapping mechanisms.

Subtask 2.1. Long-term CO_2 migration and leakage

In order to analyze long-term CO_2 migration and leakage, we performed numerical simulations using the fluid property module ECO2M (Pruess, 2011a), which can represent all possible phase combinations in the CO_2-brine system, including transitions between super- and sub-critical conditions, and phase change between liquid and gaseous CO_2. This allows a seamless modeling of CO_2 storage and leakage, all the way from a deep storage reservoir to the land surface. An example of our ZERT II research test problem is shown in Figure 1 by the sketch of a plume migration scenario consisting of a sloping reservoir and overlying cap rock with a vertical fault zone extending all the way to the land surface. The model domain as shown in Figure 1 dips at an angle $\alpha = 1.5^o$.

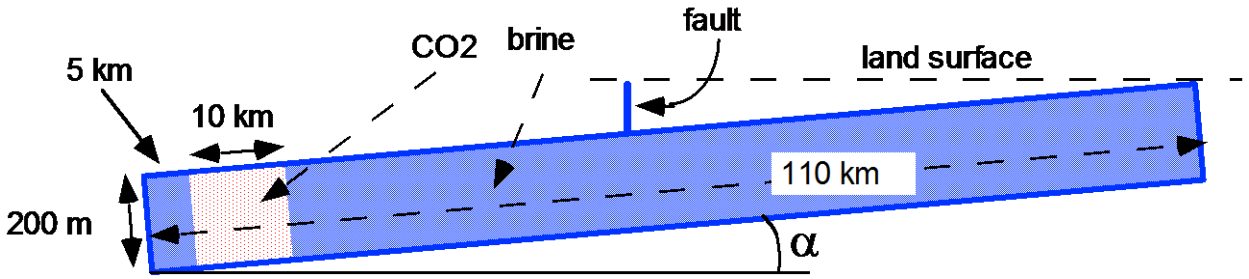

Figure 1. *Geometric dimensions of the flow system modeled. The initial CO_2 plume is shown by light shading. The fault intersects the aquifer at a distance of 50 km (32 mi) from the left boundary.*

Results are illustrated in Figures 2-4. As shown in Figure 2, the CO_2 plume reaches the fault zone after about 185 years (5.8×10^9 s), at which time CO_2 begins to flow up the fault while water flow in the fault changes from small up flow to down flow (Figure 3). Subsequently, both CO_2 and water fluxes show cyclic variations (Figures 2, 3) which arise from an interplay of the following three processes with different time constants: (1) multiphase flow of CO_2 and water in the fault zone accompanied by strong cooling effects from liquid CO_2 boiling into gas, and gaseous CO_2 expanding on approach to the land surface (Joule-Thomson effect); (2) heat exchange between fluids in the fault zone and the surrounding wall rocks; and (3) multiphase flow in the storage aquifer. Figure 4 shows that the advancement of the CO_2 plume stalls when the fault zone is reached, but after a period of about 50 years, plume advancement continues with the same speed as for the case without a leaky fault. This behavior can be understood by noting that the leading edge of the plume is rather thin, so that fault-zone leakage initially amounts to a large fraction of total up-dip CO_2 flow. Over time the CO_2 plume at the bottom of the fault thickens, so that leakage up the fault becomes a small fraction of total CO_2 flow, and consequently the effect of fault leakage on the speed of plume advancement becomes small. Complete descriptions and further analysis of this problem are published in Pruess (2011b) and Pruess and Nordbotten, 2011).

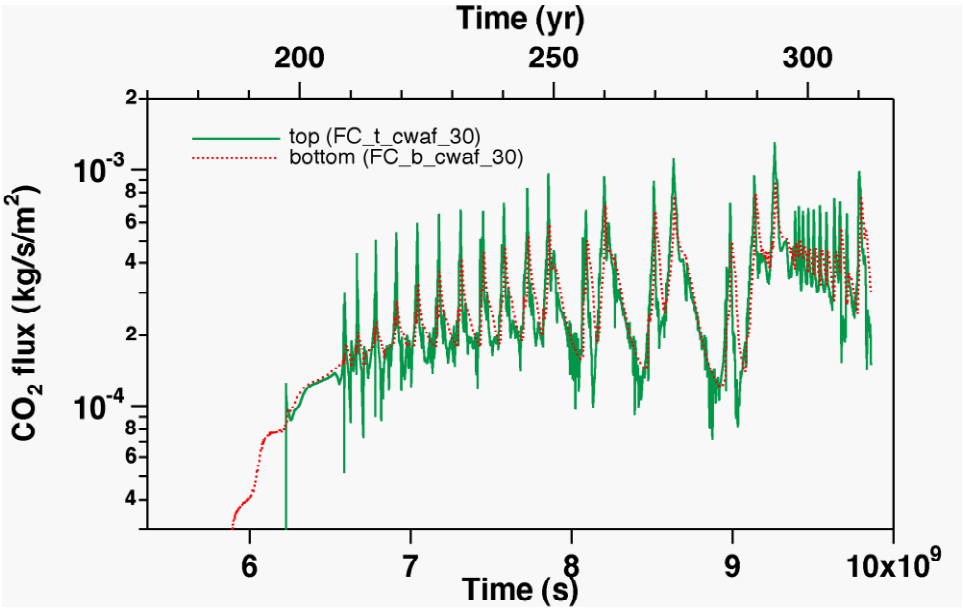

Figure 2. *CO_2 fluxes at the bottom and the top of the fault.*

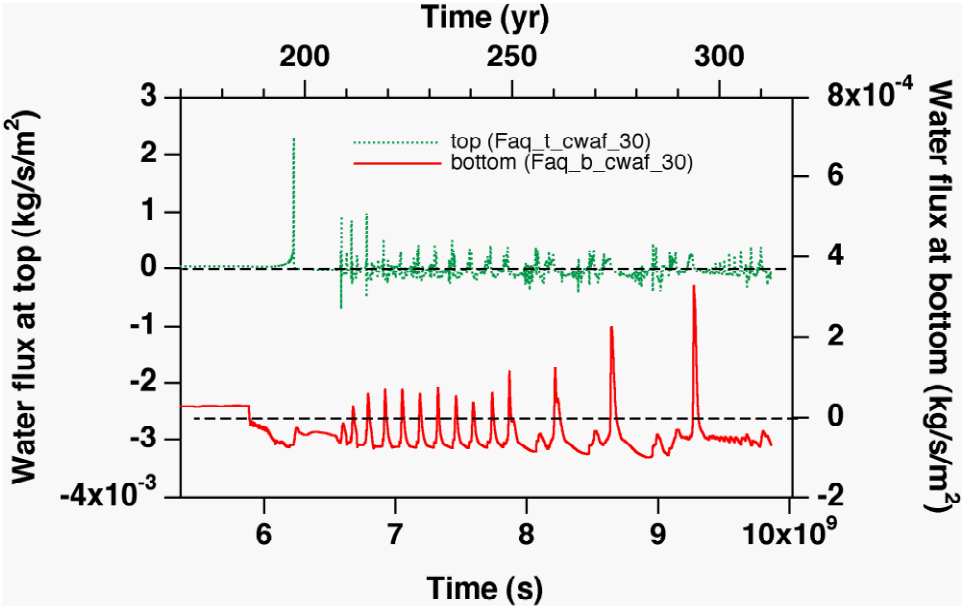

Figure 3. *Water fluxes at the top and bottom of the fault.*

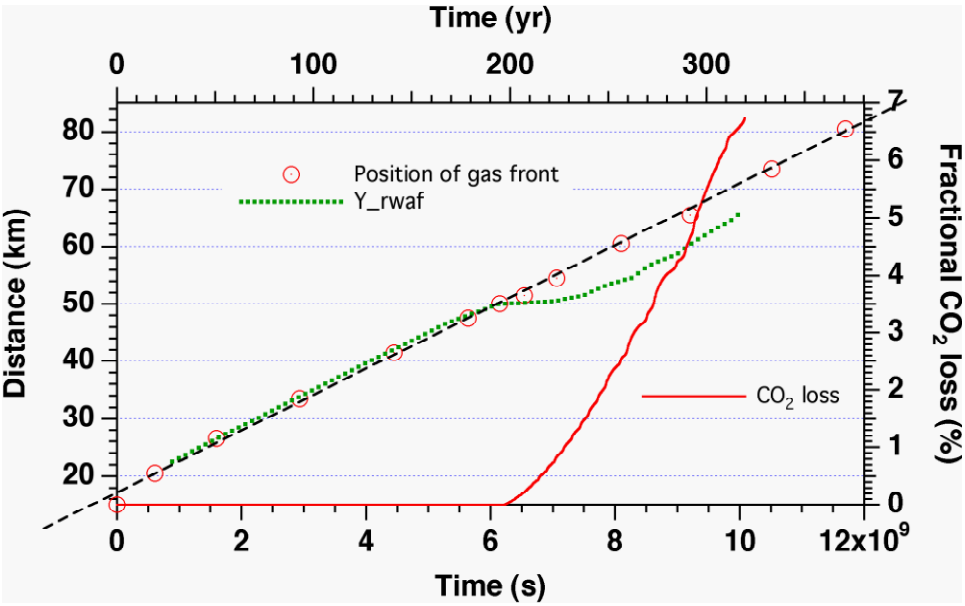

Figure 4. *Up-dip advancement of the CO_2 plume. Open circles are for the case without a fault, while the dotted line is with a fault zone present. CO_2 loss from the fault zone is also shown.*

Subtask 2.2. TOUGHREACT V2 Development

TOUGHREACT is a reactive geochemical modeling flow and transport code in wide use in the geologic carbon sequestration research community. Over the years since about 2004, there have been numerous additions in capabilities to the TOUGHREACT code that motivated development of a second version (i.e., V2, Xu et al., 2011). Work in the ZERT II project was carried out to finish up testing and release of TOUGHREACT V2. The result of this effort was the release to the public for licensing of TOUGHREACT V2:
(http://esd.lbl.gov/research/projects/tough/licensing/toughreact.html)

Subtask 2.3. Hysteresis and Heterogeneity

Hysteresis in the geologic carbon sequestration context is the term given to the differences in relative permeability of CO_2 and water (gas and aqueous phases, respectively) arising from differences in how water (the wetting phase) enters (wets, or imbibes) or exits (drains) from a porous medium. This difference is responsible for a fundamental CO_2 trapping mechanism called residual gas trapping. The inclusion of accurate hysteretic relative permeability functions is critical for reliable CO_2 trapping simulations. In ZERT II, we continued our study of hysteresis upscaling and its coding into TOUGH2.

A literature review of laboratory experiments on relative permeability was conducted to provide baseline information at the core scale for upscaling studies. Key features of the relative permeability curves that were examined include residual liquid saturation, S_{lr}, maximum gas

relative permeability, $K_{rg}(S_{lr})$, and concavity of relative permeability curves (amount of phase interference). The characteristics of the two fluids control relative permeability primarily through the interfacial tension and viscosity ratio, which makes relative permeability curves not merely a function of the reservoir rock, but also of the in situ pressure, temperature, and salinity conditions and the composition of the fluids themselves. When these fluid effects are significant, results of experiments done using analog fluids or lower temperature, pressure conditions must be viewed with caution.

A procedure for using numerical simulation to upscale relative permeability from the core scale (~10 cm (3.94 in)) to the scale required for models of pilot-scale field experiments (~10-m (32.8-ft) gridblocks for a few 100-m (328.08-ft) simulation domain) was devised and applied to two example relative permeability curves. The first example has strongly interfering gas and liquid relative permeability (strongly concave curves) and the second example has much weaker interference (closer to linear curves). The reason for scaling up to the pilot scale is that there may be opportunities to compare to field data at that scale, to validate the method. For commercial-scale operations another factor of 10 - 50 upscaling will probably be required (100-m - 500-m (328.08-ft to 1,640.42-ft) gridblocks for a many-kilometer (many-mile) simulation domain). The numerical-simulation upscaling technique appears valid for that upscaling also.

Upscaling studies from 10 cm - 10 m (3.94 in - 32.81 ft) with a slightly heterogeneous formation (Figure 5) show no scale dependence for the strongly interfering relative permeability curves and a slight increase in interference for the weakly interfering curves (Figure 6). These findings support the use of laboratory-derived relative permeability curves for pilot-scale models in which discretization is adequate so that each grid block represents a single facies, and intra-facies variability is small (Doughty, 2013).

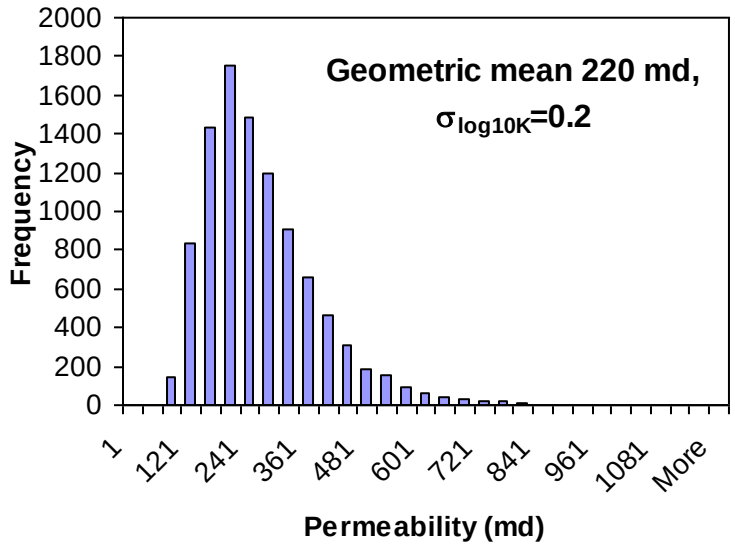

Figure 5. *Permeability distribution with small heterogeneity, applicable to heterogeneity within a single sand facies.*

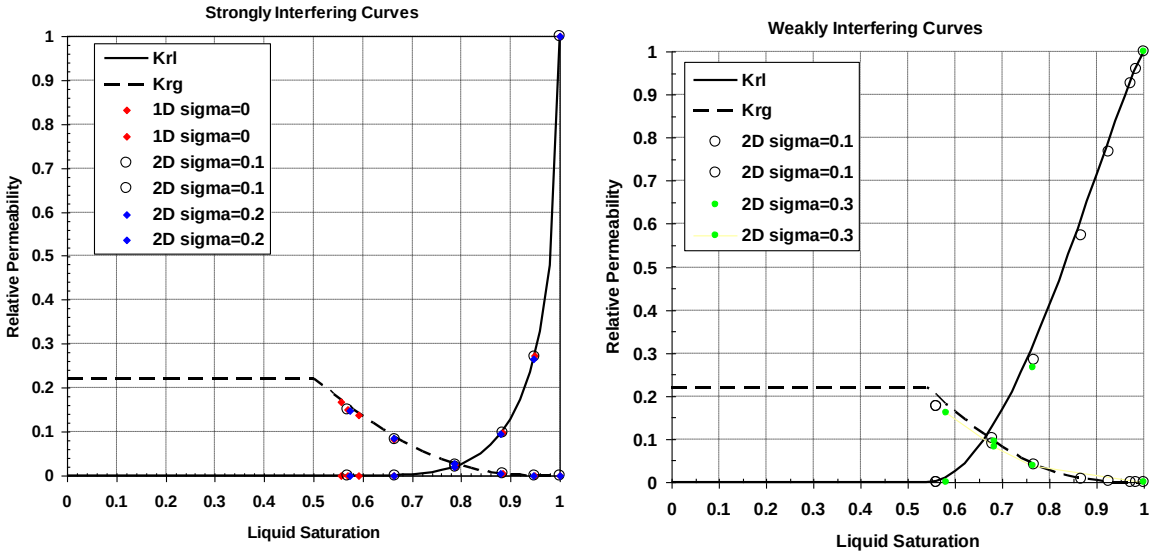

Figure 6. *Results of upscaling from 10 cm (3.94 in, lab scale) to 10 m (32.81 ft, pilot-scale grid block). Lines show the relative permeability curves specified for the model (based on laboratory experiments). Symbols show the effective relative permeability obtained for a 10-m (32.81-ft) model, with sigma indicating the standard deviation of log_{10}-permeability.*

Next, we extended the 10 cm - 10 m (3.94 in - 32.81 ft) upscaling with slight heterogeneity in the formation presented above to include cases with greater heterogeneity. As shown in Figure 7, for strongly interfering curves, the gas relative permeability decreases a modest amount for the most heterogeneous case ($\sigma_{log10k} = 1$) while the liquid relative permeability remains unchanged. For the weakly interfering curves, the previously seen trend of modest increase in interference as heterogeneity increases is extended. These findings support the use of laboratory-derived relative permeability curves for pilot-scale models in which discretization is adequate so that each grid block represents a single facies, and intra-facies variability is small.

To provide an idea of the character of the heterogeneous permeability distribution and the resulting saturation distribution, Figure 8 illustrates the permeability field and steady-state saturation distribution for $\sigma l_{og10k} = 0.3$ and an inlet boundary condition with $S_l = 0.6$, slightly greater than the residual liquid saturation of $S_{lr} = 0.5$. This simulation produces the purple points with $S_{lr} = 0.67$ in the left-hand frame of Figure 7. As heterogeneity increases, the numerical simulations become much more time-consuming, and $\sigma l_{og10k} = 0.3$ provides a good compromise between the desire to model heterogeneous formations and the need for numerical efficiency.

The results presented here apply to drainage conditions, in which non-wetting-phase CO_2 replaces brine in the pore space. Analogous simulations have been done for imbibition, in which brine replaces CO_2 in the pore space, and we found that the upscaled imbibition response is comparable to the upscaled drainage response.

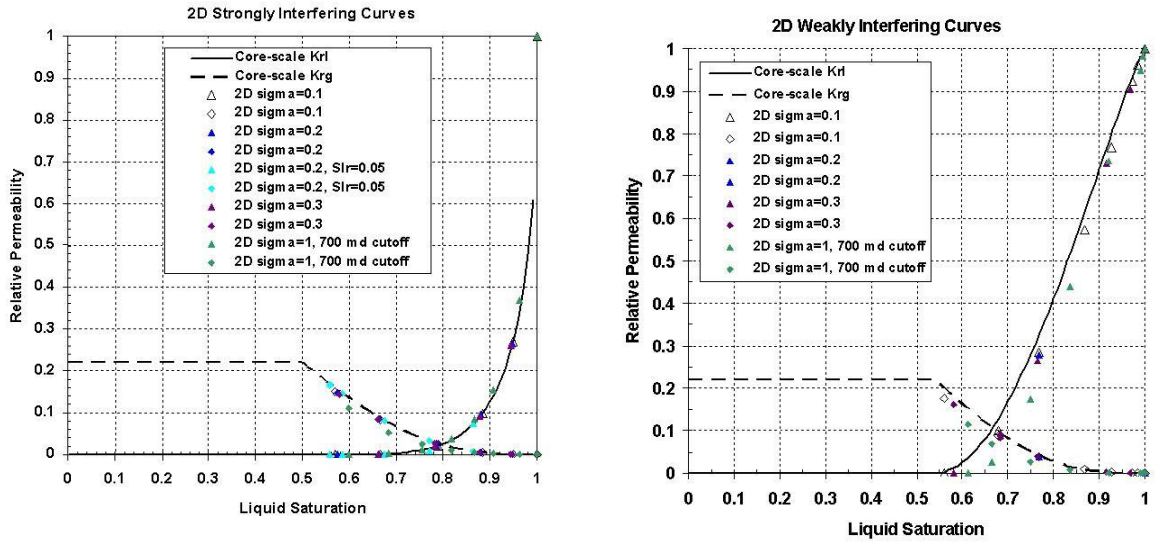

Figure 7. *Upscaled relative permeability (symbols) compared to core-scale relative permeability (lines) for two classes of relative permeability curves, those that are strongly interfering (strongly concave) on the left, and those that are weakly interfering (more linear) on the right. These two cases provide an envelope for a wide range of laboratory experiment results.*

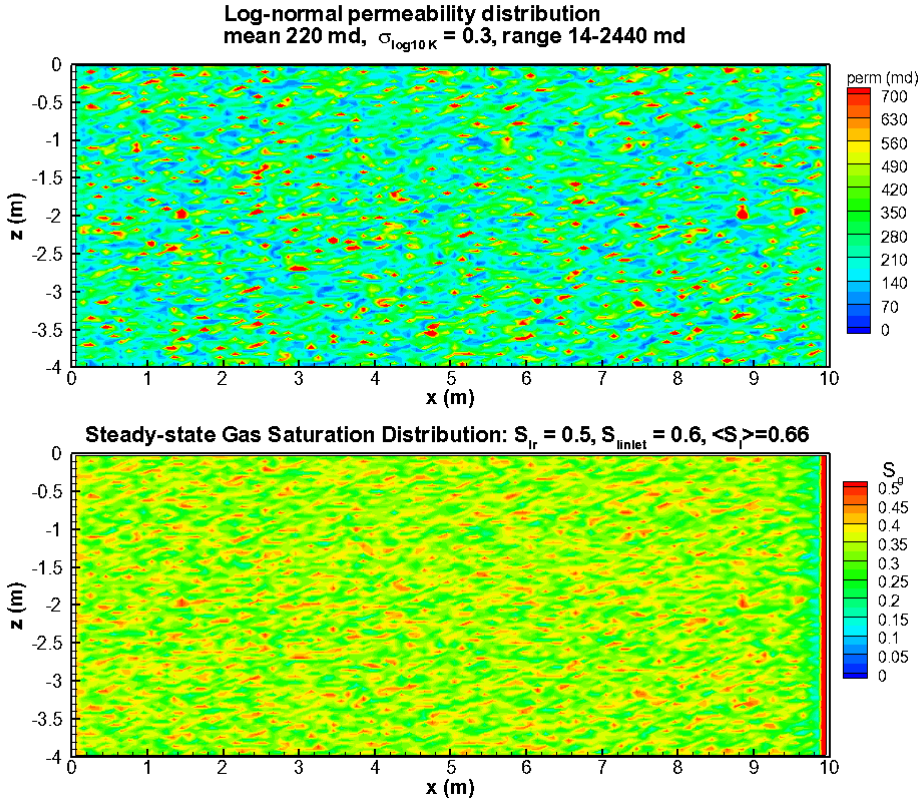

Figure 8. *Example permeability distribution (top) and steady-state gas saturation distribution (bottom) for the strongly interfering relative permeability curves.*

Subtask 2.4. Near-surface modeling

Under Subtask 2.4, we tested and wrote a user guide for EOS7CA, a TOUGH2 module for near-surface CO_2 flow and transport modeling. EOS7CA models mixtures of water (aqueous and/or vapor phase), a non-condensible gas (NCG) and air with or without a gas tracer. The user can select the NCG as being CO_2, N_2, or CH_4. EOS7CA uses a cubic equation of state with a multiphase version of Darcy's Law to model flow and transport of gas and aqueous phase mixtures over a range of pressures and temperatures appropriate to shallow subsurface porous media systems. The limitation to shallow systems arises from the use of Henry's Law for gas solubility which is accurate for low pressures but over-predicts solubility at pressures greater than approximately 1 MPa (10 bar). The components modeled in EOS7CA are water, brine, NCG, gas tracer, air, and optional heat. The real gas properties module (ZEVCA) has options for Peng-Robinson, Redlich-Kwong, or Soave-Redlich-Kwong equations of state to calculate gas mixture density, enthalpy departure, and viscosity. Transport of the gaseous and dissolved components is by advection and Fickian molecular diffusion. The user guide provides instructions for use and two sample problems as verification and demonstration of EOS7CA.

The second sample problem is prototypical of the kinds of injection and migration problems that EOS7CA was designed to handle. The problem consists of a shallow vadose zone with a water table at a depth of approximately 3 m (9.8 ft). We assume there is a horizontal injection well at a depth of approximately 2.4 m (7.9 ft), and that the well is long enough that the flow domain can be approximated as a two-dimensional (2D) Cartesian slice transverse (perpendicular) to the well. This test problem is designed to model field experiments aimed at studying how CO_2 will flow and migrate within the shallow subsurface following its arrival from a deep leaking geologic carbon sequestration site through a leakage pathway such as an abandoned well, fault, or fracture zone (e.g., Oldenburg et al., 2010). Table 1 provides properties of the system.

***Table 1**. Properties of the homogeneous vadose zone.*

	Soil
Temperature (T)	15 °C (59 °F)
Porosity (ϕ)	0.30
Permeability (k)	1 x 10^{-12} m^2 (1 Darcy)
Capillary Pressure (P_c)	van Genuchten λ = 0.2, S_{lr} = 0.11, α = 8.5 x 10^{-4} Pa^{-1}, P_{max} = 1 x 10^{10} Pa, S_{ls} = 1.
Relative permeability (k_r)	van Genuchten S_{lr} = 0.10, S_{gr} = 0.01
Molec. diffusivity coefficients (d_β^κ)	Liquid: 10^{-10} m^2 s^{-1} Gas: 10^{-5} m^2 s^{-1} θ = 1.0, P_0 = 10^5 Pa (1 bar)
Tortuosity (τ_0)	1.0
Saturation-dependent tortuosity (τ_β)	Equal to relative permeability

Figure 9a shows the Cartesian 2D transverse model system discretization and water table location. The top boundary is held at a constant pressure of 1 bar (10^5 Pa), zero CO_2 concentration, and 15 °C (59 °F) temperature. The right-hand side boundary is held at constant conditions corresponding to the initial condition which has a gravity-capillary equilibrium above the water table and liquid saturation equal to 0.5 at the top of the domain. The bottom boundary of the system is held at constant (aqueous-phase) fully saturated conditions and P = 1.194 bar (i.e., hydrostatic below the initial water table). The left-hand side boundary is closed to flow representing a mirror symmetry plane.

Figure 9b-d shows model results for three times during simulation of CO_2 injection from the horizontal well with an injection rate of 2.43 kg d^{-1} (5.35 lb d^{-1}) As shown in Figure 9, the CO_2 exits the well directly into the unsaturated zone and creates a CO_2-rich zone around the well. The CO_2 spreads in all directions by pressure-gradient driving forces. Note the CO_2 gas pushes the water table down as shown by the deflection of the light-blue contour lines, and by the high CO_2 concentration in the gas where formerly saturated aqueous phase conditions prevailed. The CO_2 exits out the ground surface (top of model domain) at some time between 0.5 and 1 day. By 5 days, the region of CO_2 flux out the ground surface extends to more than 3 m (9.84 ft) from the trace of the well. Note the high mass fractions of CO_2 in the gas phase (nearly pure CO_2) and high soil-gas concentration gradient near the ground surface.

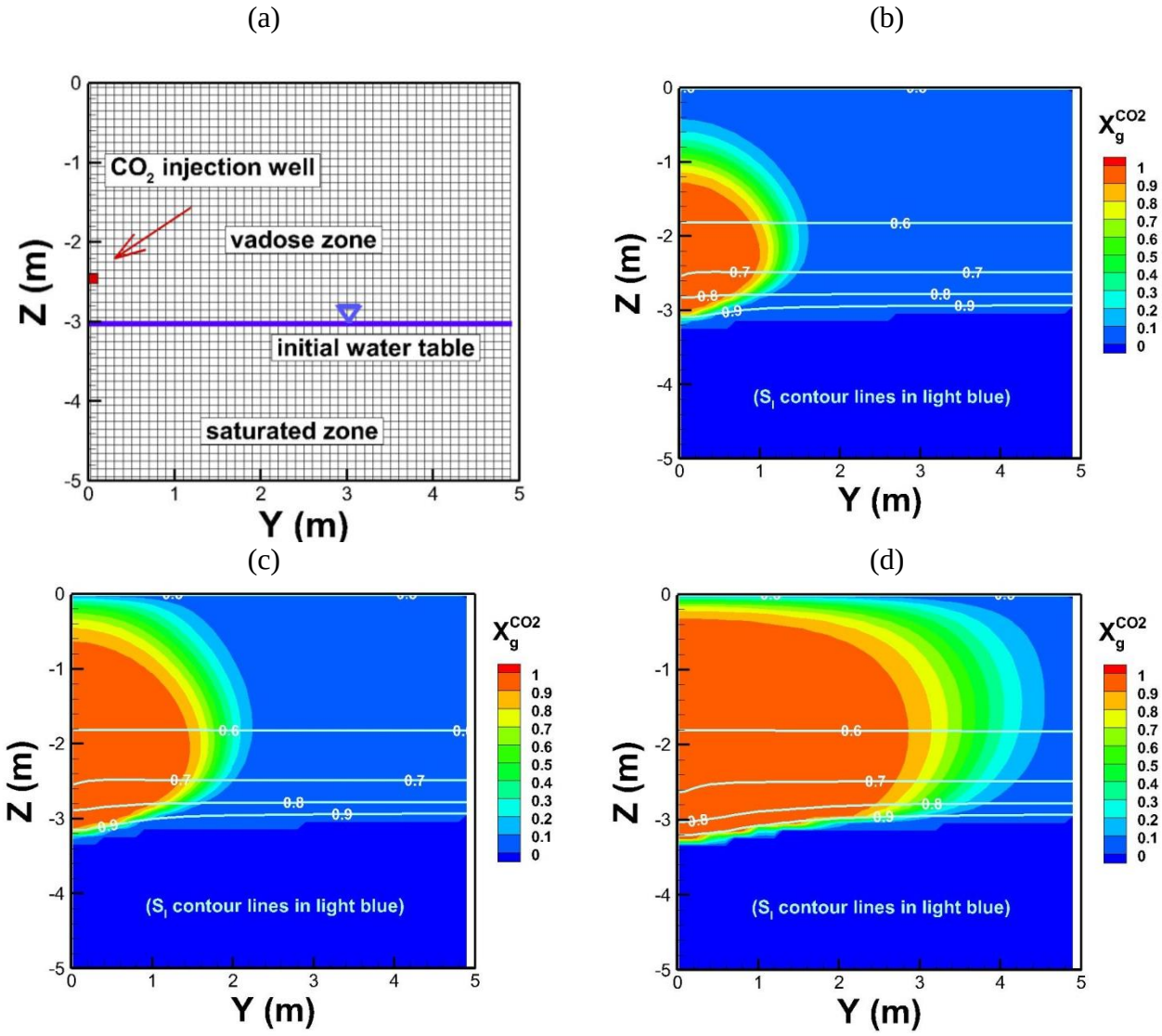

Figure 9. *EOS7CA simulation results for the SAM7CA2 vadose zone problem showing discretization and locations of injection well and water table (a), and color contours of CO_2 mass fraction in the gas phase and light blue lines of aqueous phase saturation at (b) 0.5 days, (c) 1 day, and (d) 5 days.*

Task 2 (supplemental). WebGasEOS Usage Report

We developed WebGasEOS as an off-shoot of prior development of EOS7C, the TOUGH2 module for CO_2 and CH_4. WebGasEOS is a publicly available web-based tool for calculating the properties of gas mixtures. WebGasEOS complements other available online tools such as those provided by the National Institute of Science and Technology (NIST) because WebGasEOS allows gas mixtures whereas the NIST Chemistry Webbook only provides properties of pure gases. Under ZERT II, we worked with a contract programmer to update WebGasEOS for access from an LBNL-wide server rather than Earth Sciences Division-wide (ESD-wide) web-hosting

system. This was necessary because the ESD hosting system became out of date, difficult to maintain, and experienced frequent hardware outages, leading to decreased usage. With this change to an LBNL-wide system, we were able to provide a robust and up-to-date web server for our WebGasEOS users. In addition, modernization of the WebGasEOS code continued, with legacy programming removed to ensure future robustness.

For the six-year period from January 28, 2008 (when analytics were installed) through January 13, 2014, the WebGasEOS site was visited 10,275 times by 4,550 unique visitors from 84 countries, for a total of 39,240 pageviews. The time line of site visits is shown in Figure 10. Visitors from the US composed 44.3% of all visits, with the remainder spread across the globe, with heaviest international use in Western Europe, Canada, Japan, Brazil, and China (Figure 11). LBNL provided 15% of the visitors, with other top users (University of Texas, BRGM (France), and Texas A&M University) generating an additional 18.3% of traffic.

WebGasEOS can be accessed at http://esdtools.lbl.gov/gaseos/gaseos.html

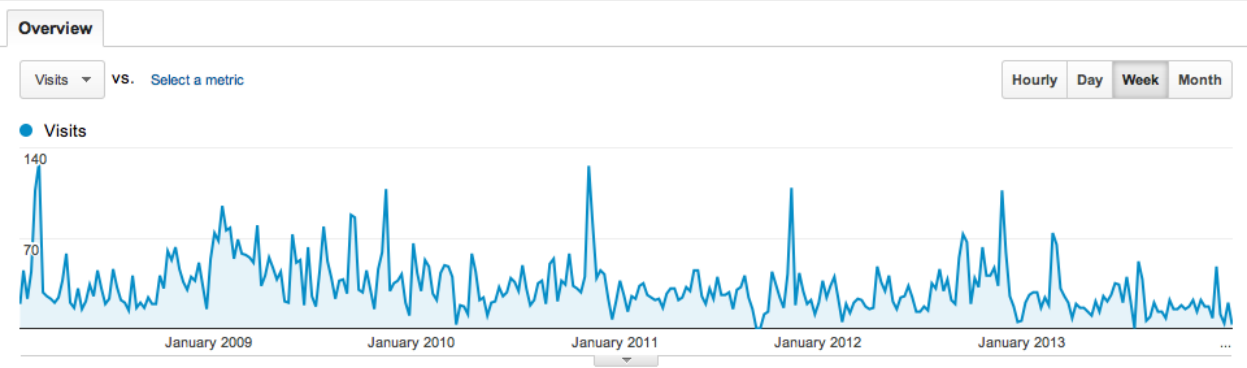

Figure 10. *WebGasEOS weekly usage, 2008-2014.*

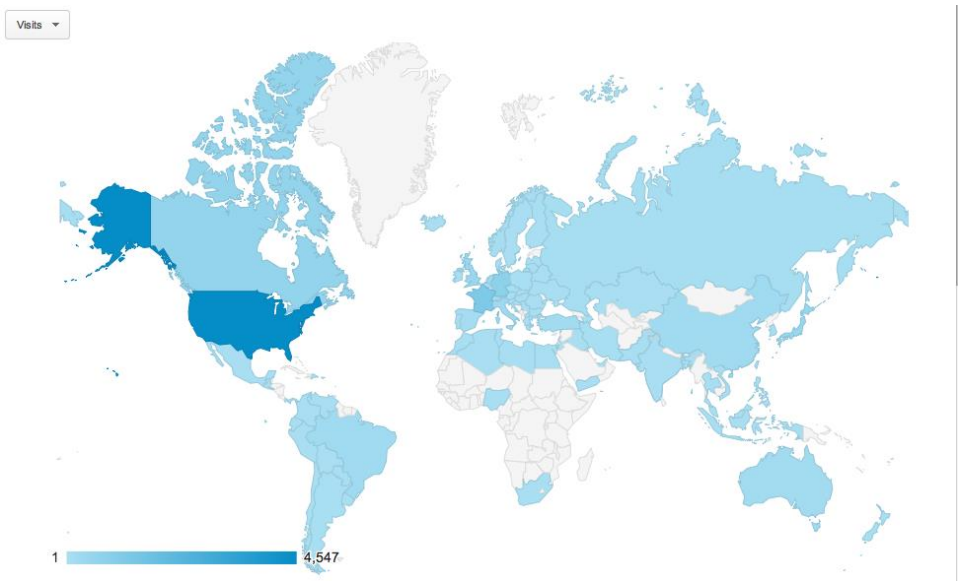

Figure 11. *WebGasEOS usage by geographic location, 2008-2014.*

3. Task 3: Measurement and Monitoring to Verify Storage and Track Migration of CO_2

Goal: To develop reliable techniques to demonstrate storage effectiveness and quantify migration out of the storage formation and release rates at the surface.

Subtask 3.1. Assess detection limits and optimal deployment strategies for monitoring

We carried out field monitoring of CO_2 release from the horizontal well at the ZERT shallow-release field site. We made measurements of soil CO_2 fluxes using the accumulation chamber method to characterize the spatial distribution of surface CO_2 leakage fluxes during the release. An example of measurements made during the first week of the release in summer 2011 is shown in Figure 12. As shown, measurements were made at 1-m spacing along the surface trace of the horizontal well on 21 July (Figure 12) and on a grid surrounding the release well on 20 and 22 July (Figure 13). The spatial distribution of surface CO_2 leakage fluxes was similar to that observed throughout the ZERT shallow release experiments, characterized by five to six focused zones of elevated CO_2 emissions ("hot spots") aligned along the surface trace of the well (Figures 12 and 13). These CO_2 leakage maps provided project investigators with a reference flux map to which they could compare their own measurements made using different CO_2 leakage detection techniques. LBNL work under ZERT II is reported in Lewicki et al. (2010) and Lewicki and Hilley (2012).

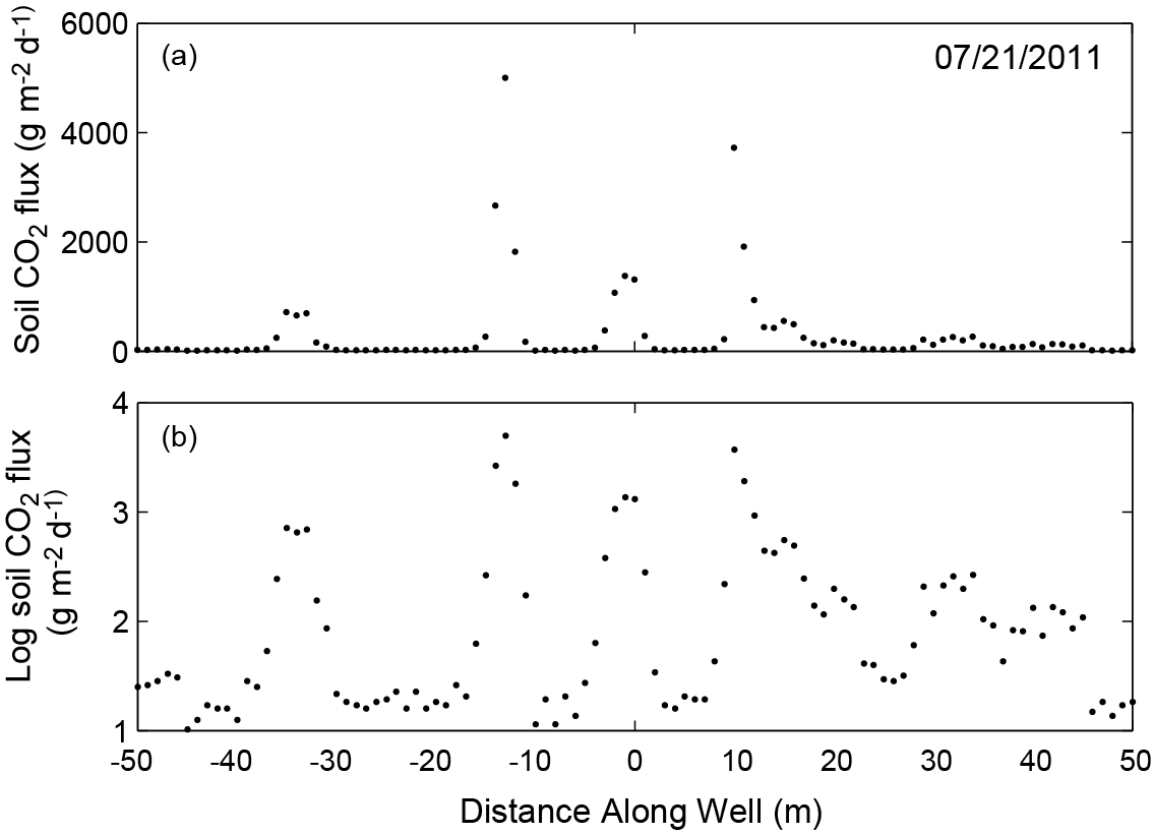

Figure 12. *Plots of (a) soil CO_2 flux and (b) log soil CO_2 flux measured using the accumulation chamber technique along the surface trace of the release well on 21 July 2011.*

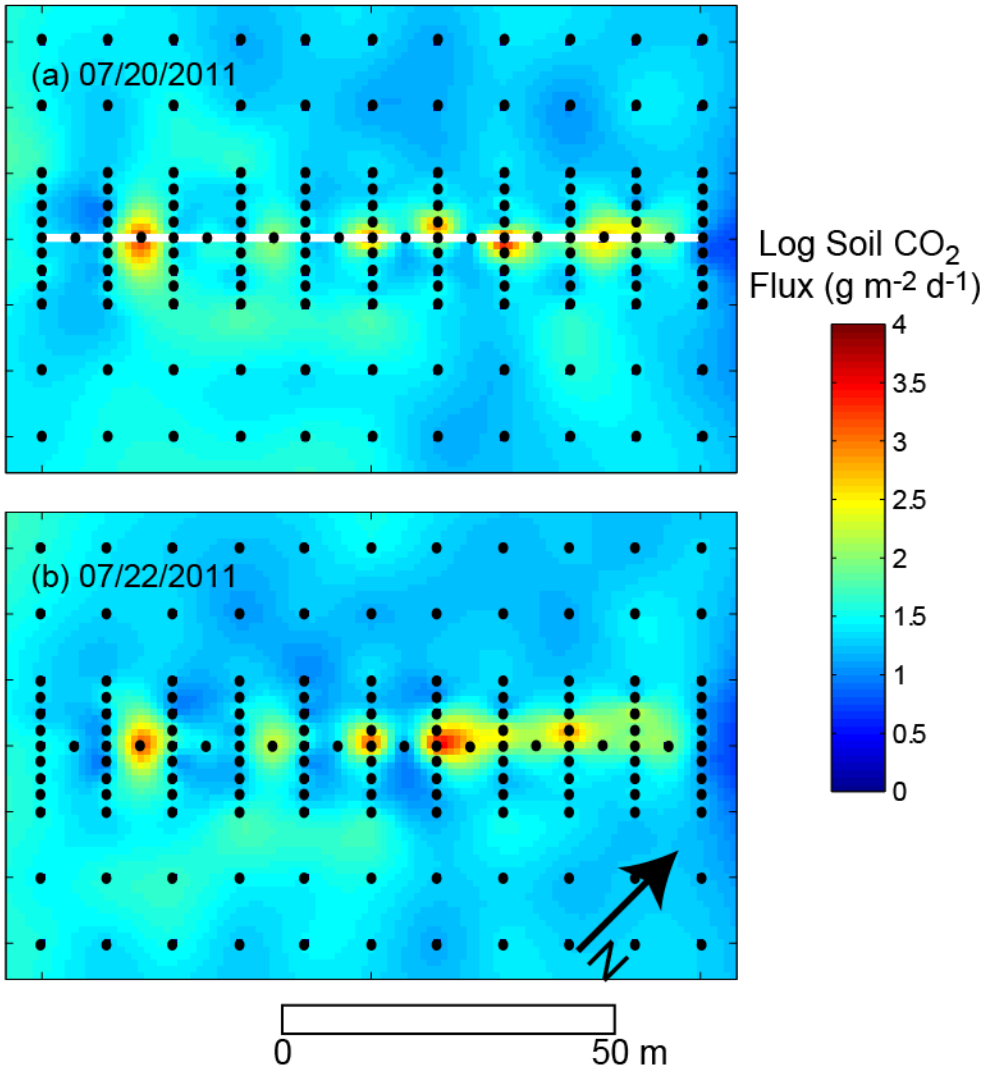

Figure 13. *Maps of log soil CO_2 flux, interpolated based on accumulation chamber measurements made at the black dots on (a) 20 July 2010 and (b) 22 July 2010. White line on (a) shows surface trace of release well.*

Subtask 3.2. Perform simulations for the ZERT shallow-release experiment.

The TOUGH2/EOS7CA code and user guide were developed for application to the ZERT shallow-release experiment. Under ZERT II, the test problem based on the ZERT release experiment was developed as described under Subtask 2.4.

Subtask 3.3. Support field activities at the MSU shallow-release facility.

The CO_2 shallow-subsurface release system was pulled out of the shallow horizontal pipe in winter and redeployed for the summer test season(s). During the ZERT II project, LBNL staff (Cook and Morales) traveled to Bozeman multiple times to deploy and disassemble the underground CO_2 release system.

Upon re-deployment, LBNL staff installed and tested the CO_2 release control system hardware and software. In August, LBNL met the 8/3/14 milestone to support the ZERT II field experiment through assistance with packers and CO_2 release system.

Subtask 3.4. Conduct field experiments to verify surface monitoring techniques.

LBNL staff (Lewicki) traveled to Bozeman multiple times to participate in the shallow CO_2 release experiments and collect data on CO_2 flux, concentration, and meteorological parameters. An example of this work is summarized under Subtask 3.1.

4. Task 4: Fundamental Geochemical and Hydrological Investigations of CO_2 Storage

Goal: To develop understanding and confidence in solubility trapping, residual gas trapping and mineral trapping, and to identify new trapping mechanisms that can contribute to even greater storage security.

Subtask 4.1. Core flow-through and scanning

Under ZERT II, we investigated the effects of mixed wettability during CO_2 migration in the subsurface. The sequence of laboratory tests included a series of core floods through a sample with regions that have different water and CO_2 wettabilities (i.e., the sample contains different kinds of solid materials). In this test, the brine flood provides the system permeability, while the nitrogen flood reveals the behavior of a fluid that is nonwetting to both regions, and the $scCO_2$ flood shows the influence of wettability on CO_2 migration. Subsamples of the material used in the core floods were investigated using X-ray microtomography. The various approaches are sketched in Figure 14. The data from microtomography were used to extend the Maximal Inscribed Spheres technique to account for fluid wettability.

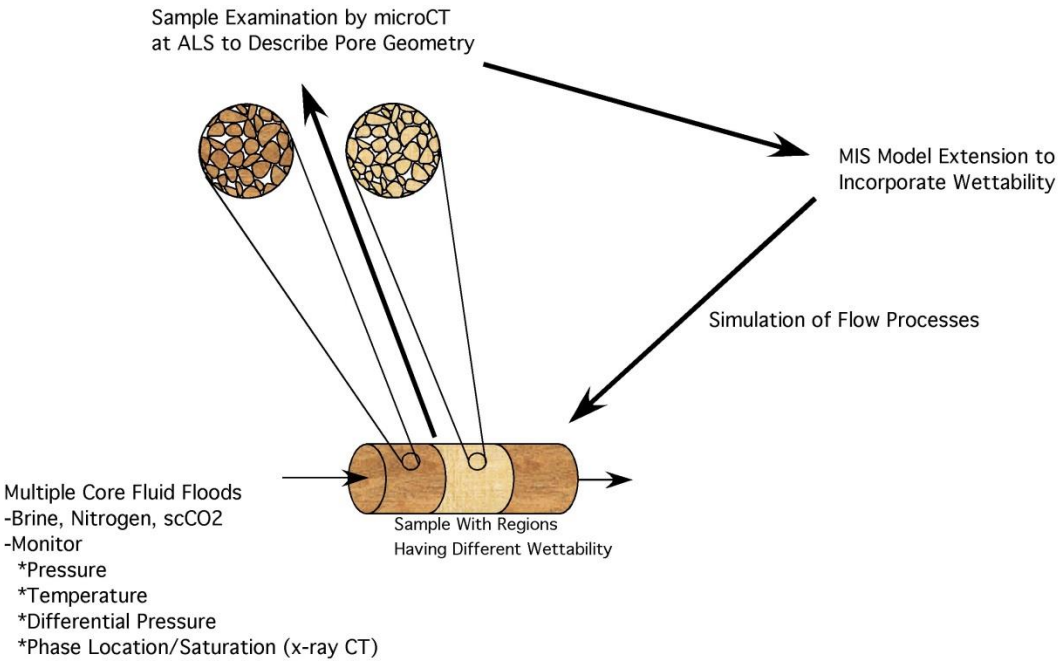

Figure 14. *Schematic of approaches to investigate effects of mixed wettability.*

To examine characteristics when CO_2 flows through a medium with varying surface chemistry, an experiment was performed in which invading fluids (1. nitrogen and 2. CO_2) were flowed through a brine-saturated layered silica sand – calcite sand – silica sand sample. Following the nitrogen and CO_2 floods, brine was flowed through the system to examine residual saturation and dissolution. The center of the sample was calcite sand with grain sizes passing the 150 micron (5.9×10^{-3} in) sieve and retained on the 75 micron (2.95×10^{-3} in) sieve, while the sand layers on the two ends were composed of silica passing the 177 micron (6.97×10^{-3} in) sieve and retained on the 125 micron (4.92×10^{-3} in) sieve (Figure 15). The size difference was intended to provide a capillary barrier at the first silica sand/calcite sand boundary for nonwetting fluids to allow the invading fluids to build up there before penetrating into the calcite. The sand was contained in an elastomer sleeve between two endcaps and placed in an X-ray transparent pressure vessel contained within a temperature-controlled jacket (Figure 16). The space between the elastomer sleeve surrounding the sample and the pressure vessel was filled with a mixture of propylene glycol and water, and the pressure of this fluid was controlled with a high-pressure syringe pump. The effective stress on the sand (confining pressure – pore pressure) was maintained at 1.38 MPa (200 psi), but variations in the effective stress of 0.34 MPa (50 psi) were allowed when increasing or decreasing system pressure.

The sample was CT scanned while dry to provide a baseline density distribution. The sand sample was saturated with 5 M NaCl brine, and the pore pressure was increased to 1.38 MPa (200 psi) and flowed overnight using high-pressure syringe pumps on the inlet and outlet. The sample was CT scanned while saturated to provide a density distribution at the highest density.

The nitrogen flood was performed at 46.7±0.5 °C (116 °F) and a pore pressure of 1.38 MPa (200 psi). Nitrogen was flowed at 1 ml/min into the sample, controlled by extracting 1 ml/min of brine

at the effluent end. The flood was stopped intermittently to CT scan to allow observation of the gas location in the sample. Following breakthrough, the gas flow was stopped, and two pore volumes of brine were flowed through the sample before the sample was CT scanned again. The sample was then re-saturated with brine by pulling a vacuum on the sample followed by brine injection to 8.27 MPa (1,200 psi). The CO_2 flood was performed in the same manner at 8.27 MPa (1,200 psi) and 46.7±0.5 °C (116 °F) with a confining pressure of 9.65 MPa (1,400 psi).

a. 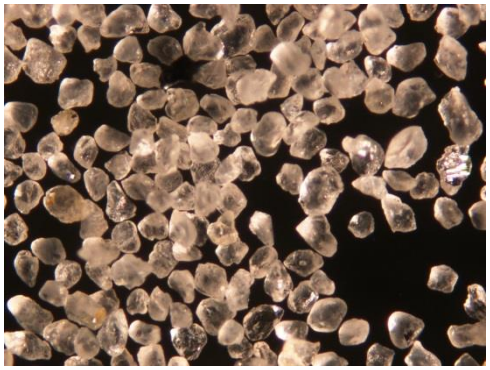 b. 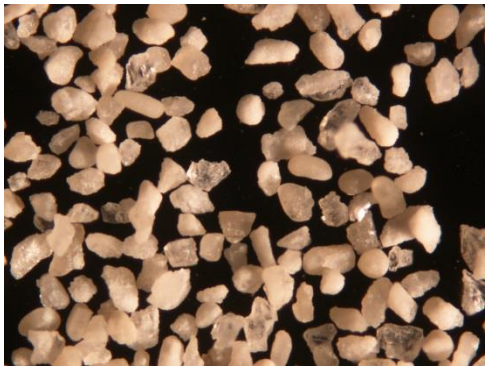

Figure 15. *Silica (a) and calcite (b) sand.*

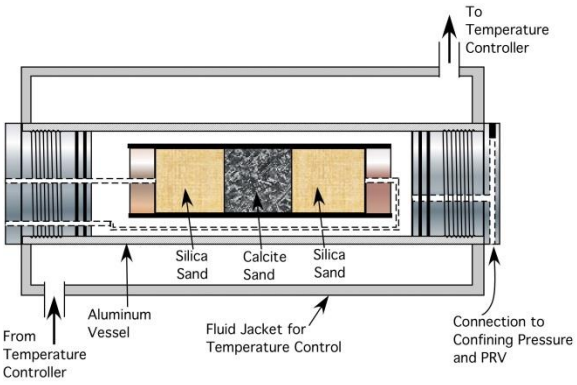

Figure 16. *Experiment setup.*

Samples of the two sands were micro-CT scanned at the Advanced Light Source at LBNL (Figure 17), and results from the CT scanning were analyzed using LBNL's modified Maximal Inscribed Spheres technique (Silin and Patzek, 2006, Tomutsa et al., 2007, Silin et al., 2010), with the modification allowing the technique to incorporate contact angle. The analysis was used to provide capillary pressure curves for a set of contact angles (Figure 18).

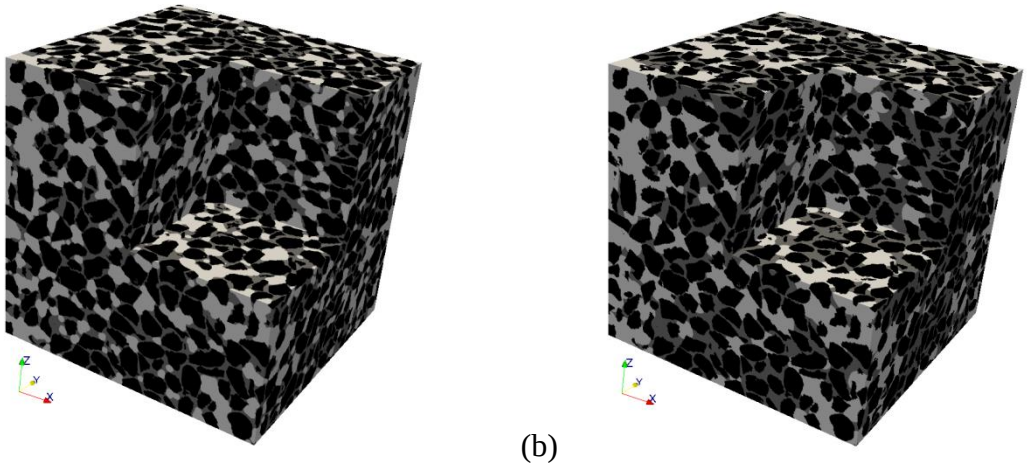

(a) (b)

Figure 17. *Results of micro CT imaging with computed gas and brine capillary equilibrium for contact angles of (a) 0° and (b) 60°. Black color – mineral grains, dark gray – wetting fluid, light gray – nonwetting fluid. Brine saturation in both cases is near 48%.*

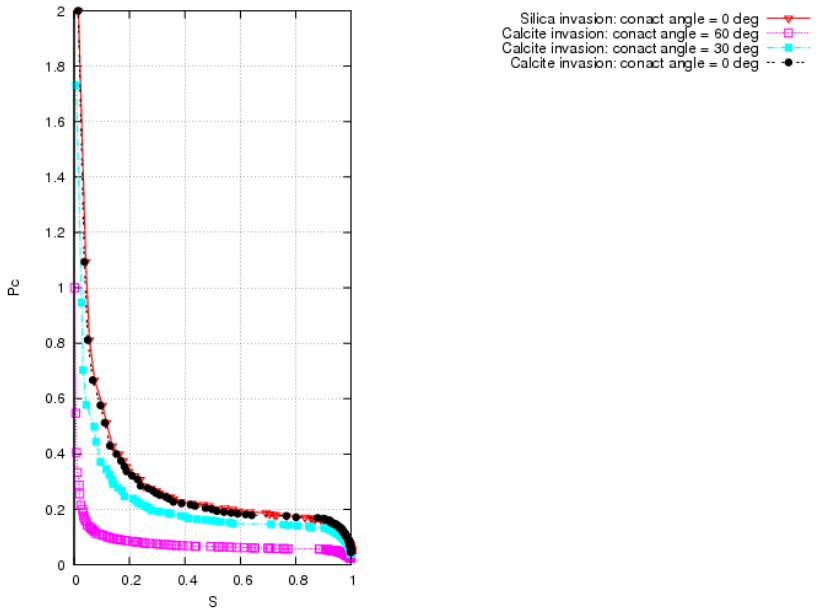

Figure 18. *MIS-evaluated dimensionless invasion capillary pressure curves for silica sand and calcite sand packs with various assumed contact angles.*

Nitrogen and CO_2 saturations throughout the sample at breakthrough are shown in Figure 19. It is clear that there is significant gravity override as the lighter phases invade over the brine phase. The densities of the nitrogen, CO_2, and brine at the experiment conditions are estimated to be 15.55 and 258.39 kg/m^3 (0.97 lb/ft^3 and 16.1 lb/ft^3) and 1,181 kg/m^3 (73.7 lb/ft^3) and interfacial

tensions between the brine and nitrogen, and the brine and CO_2 are estimated to be 75 mN/m (5.14×10^{-3} lb-force/ft) and 47.11 mN/m (3.23×10^{-3} lb-force/ft), respectively.

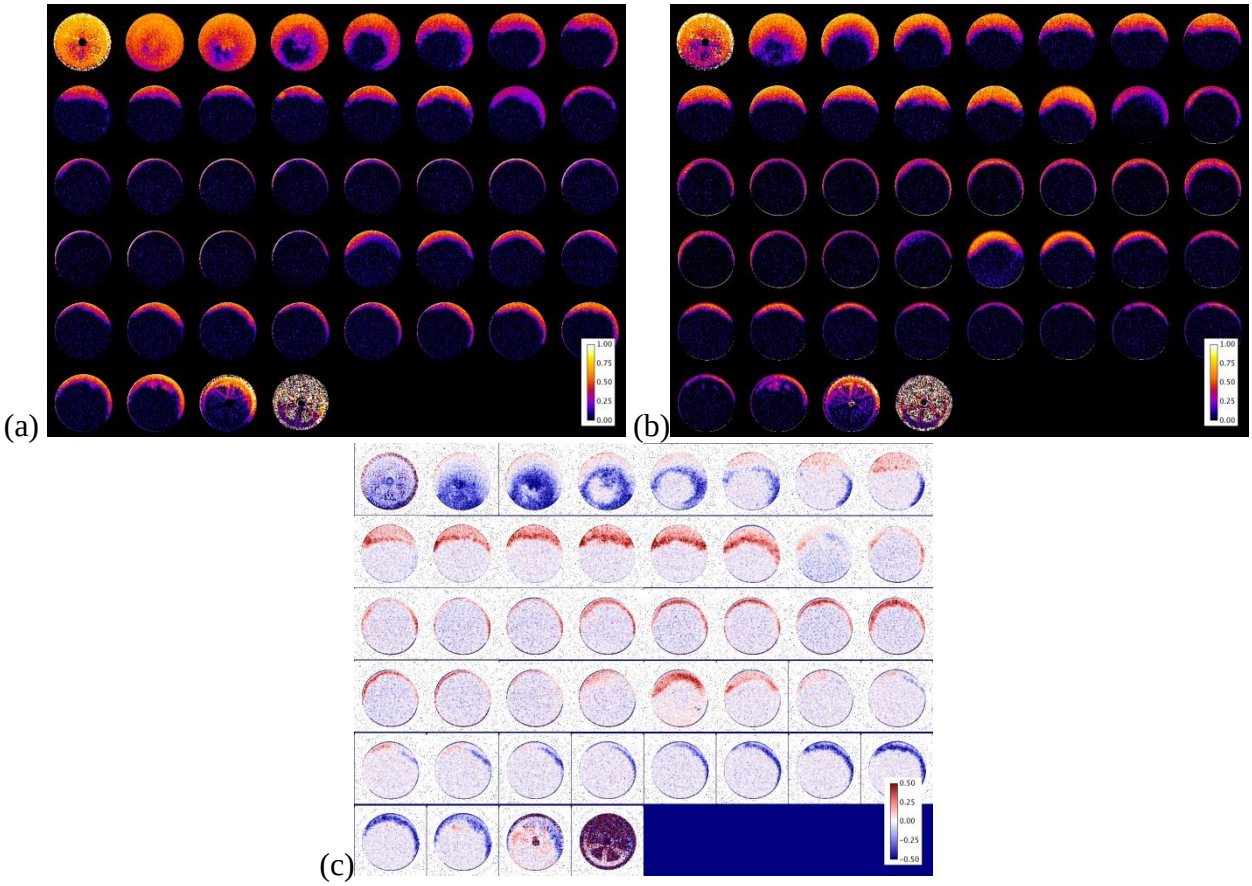

Figure 19. *Nitrogen (a) and CO_2 (b) saturations at breakthrough. Each circle shows the saturation in a 3 mm slice of the 50 mm diameter cylindrical sample. The inlet is at the top left, and sequential slices proceed left to right, top to bottom. Brighter colors indicate higher saturations. The first 14 slices contain the inlet silica sand, the center 14 slices contain the calcite sand, and the final 14 slices contain the outlet silica sand. Differences (c) between the CO_2 and nitrogen saturations with CO_2 > nitrogen in red and nitrogen > CO_2 in blue.*

Average saturations over 2.7 - 3.6 cm (1.06 – 1.42 in) thicknesses for each layer along a vertical profile are shown in Figure 20. As can be seen in Figures 20b and 20c, both invading fluids (nitrogen and CO_2) exhibited higher saturations at the inlet and along the top of the sample. This would be expected because the invading fluid pressure would be higher at the inlet, and gravity override causes the less dense phase to flow at the top. The invading fluids penetrated farther (from the sample top) into both silica sand layers than into the calcite sand layer. Figure 20c shows regions where the CO_2 saturation at breakthrough exceeded the breakthrough nitrogen saturation (red) or vice-versa (blue). Both fluids flowed in crescent-shaped regions at the outer radii of the sample. This is indicative of a higher porosity layer there. This porosity difference was not observed in the CT data.

The CO_2 penetrated more deeply into the upstream silica sand and calcite sand than the nitrogen (Figure 20b). This would be expected because the interfacial tension of the CO_2-brine system is approximately 63% of the nitrogen-brine system. A higher capillary pressure would be needed to cause the nitrogen to penetrate deeper. In the downstream silica sand, the nitrogen penetrated farther than the CO_2.

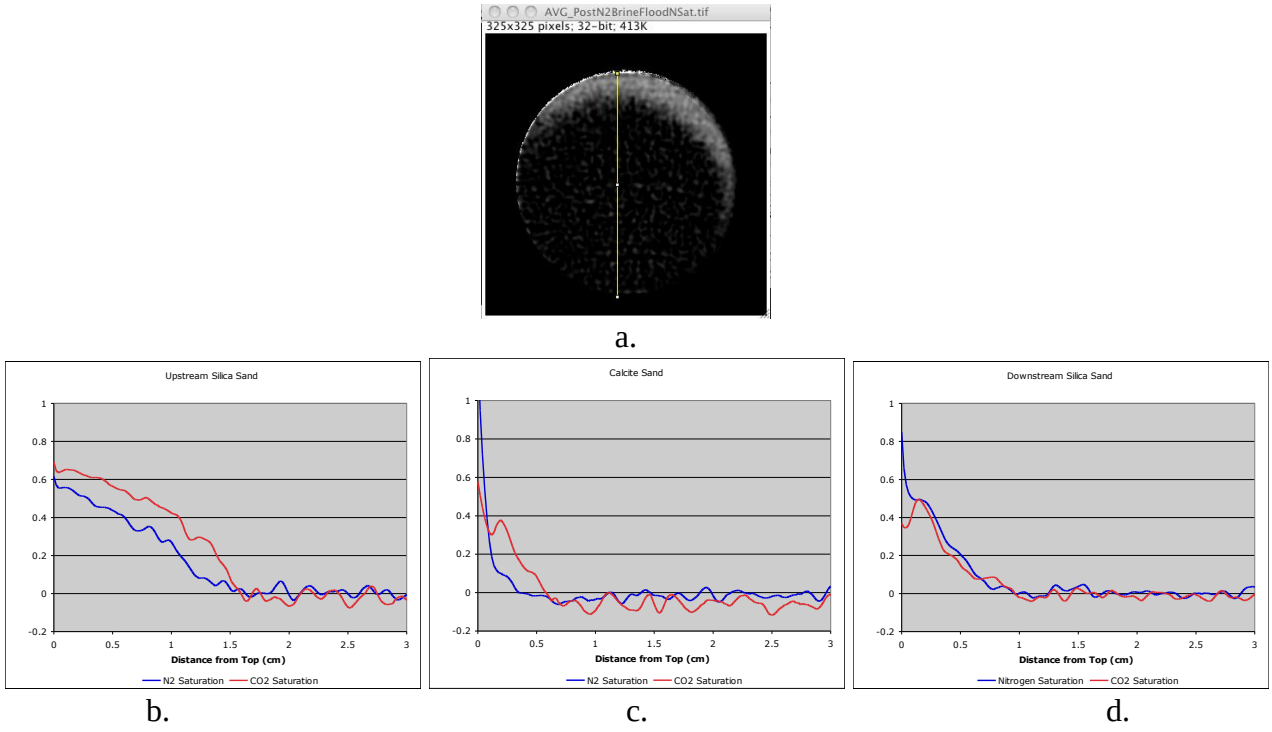

Figure 20. *Average saturations along the vertical profile (a) for the upstream silica sand (b), calcite sand (c) and downstream silica sand (d).*

Following breakthrough of the invading fluids, two pore volumes of nitrogen and CO_2-free brine were flowed through the sample to displace and dissolve the invading fluids. Figure 21 shows the residual saturations following the brine floods. For the nitrogen, the saturations were reduced from around 50 - 70% before the brine flood to around 20%. For the CO_2, however, saturations were lowered from around 50 - 70% before the brine flood to nearly zero in the upstream silica sand and calcite sand, and around 10 - 20% in the downstream silica sand. The primary difference for this behavior is the much higher solubility of CO_2 than nitrogen in the brine. Further details and analysis can be found in Kneafsey et al. (2013).

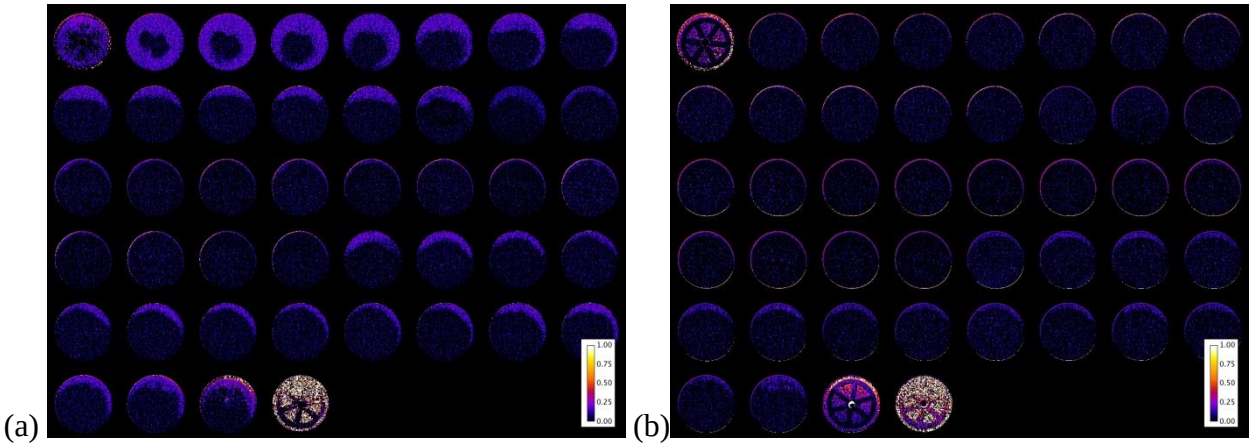

Figure 21. *Nitrogen (a) and CO_2 (b) saturation following two pore volumes of brine.*

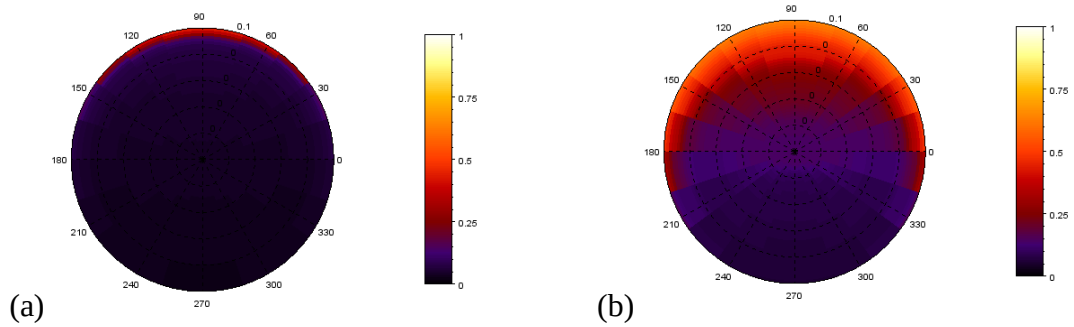

Figure 22. *Computed saturation distribution in the core for contact angles of (a) 0° and (b) 20°.*

Subtask 4.2. Interfacial tension studies

The goals of this effort were to measure the relation between capillary pressure (P_c) and brine saturation (S) in a sand pack with $scCO_2$ as the nonwetting fluid, in order to (i) make this basic information available, and (ii) to test the commonly invoked assumption that such $S(P_c)$ relations can be predicted through capillary scaling. Given the common use of capillary scaling and the importance of correctly representing $S(P_c)$ relations in geologic CO_2 sequestration, the extent of validity of capillary scaling needs to be determined. For this purpose, $scCO_2$ and air are being compared as the nonwetting phases in $S(P_c)$ relations for brine (the wetting fluid) in homogeneous (300-350 μm (1.18×10^{-2}-1.38×10^{-2} in)) quartz sand packs. For $scCO_2$ and brine, $S(P_c)$ relations were measured at 8.5 MPa (85 bar) total pressure, and 45 °C (113 °F) (representative of a reservoir depth of about 0.8 km (0.5 mi)). The air-brine $S(P_c)$ relations were measured at atmospheric pressure and room temperature (ca. 22 °C) (71.6 °F). All measurements were obtained on the same sand pack, contained in a high-pressure reaction vessel, modified with a hydrophilic stainless steel bottom filter plate (1 μm pore size), and a Hastelloy upper filter plate (60 μm (2.4×10^{-3} in)). Equilibrium brine (1 M NaCl) drainage and imbibition curves were

obtained in duplicate runs for both $scCO_2$ and air as the nonwetting phase. In addition, we measured the $S(P_c)$ relation for deionized water and air at atmosphere in the sand-pack to serve as a reference for deionized water-$scCO_2$ experiments. Properties of the fluids are shown in Table 2.

Table 2. *Properties of fluids used in experiments.*

Temperature	˚C (˚F)	21 (69.8)	45 (113)	45 (113)
Pressure	MPa	0.102	8.5	120
1.00 M NaCl density, ρ_w	kg m^{-3}	1,036	1,032	1,034
Nonaqueous phase		air	$scCO_2$	$scCO_2$
Nonaqueous phase density, ρ_n	kg m^{-3}	1.2	281.8	657.7
$\rho_w - \rho_n$	kg m^{-3}	1,035	750	376
$(\rho_w - \rho_n)g$	kg m^{-2} s^{-2}	10,151	7,358	3,689
Fluid-fluid interfacial tension	mN m^{-1}	74.4	34	31

Drainage $S(P_c)$ curves for brine-air and brine-$scCO_2$ showed fairly good reproducibility, with drainage of brine by $scCO_2$ occurring at lower magnitude P_c because of lower interfacial tension and lower fluid-fluid density differences (Figure 23a). Similar offsets and good reproducibility in imbibition measurements were obtained for bine-air and brine-$scCO_2$ (Figure 23b). Scaled capillary potentials are obtained by multiplying P_c values by the characteristic grain size (325 µm (1.28×10^{-3} in)), and dividing by interfacial tension (74 mN m^{-1} for brine-air (5.07×10^{-3} lb-force/ft, and 31 mN m^{-1} (2.12×10^{-3} lb-force/ft) for brine-$scCO_2$). Applying this transformation to the drainage and wetting curves shows convergence toward unique scaled drainage (Figure 23c) and scaled wetting (Figure 23d) curves. However, important differences in capillary behavior become evident in these scaled plots. Brine drainage through displacement with $scCO_2$ occurs at slightly lower scaled Pc, indicative of decreased wettability. Decreased wettability of the brine-$scCO_2$ system is further reflected in lower "residual" saturations, and greater trapping of the nonwetting phase ($scCO_2$) at the end of the imbibition cycle ($P_c = 0$). Larger changes in wettability are anticipated with longer mineral-brine-$scCO_2$ reaction times, and under higher total pressure. Further details of this work can be found in Tokunaga et al. (2013).

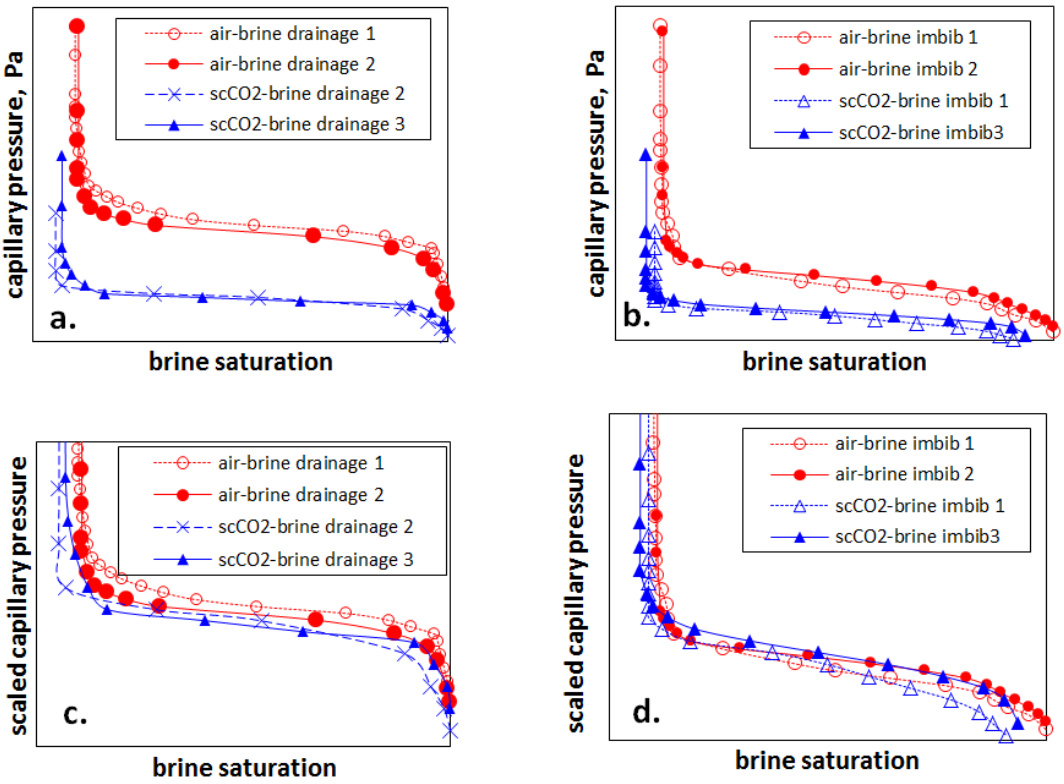

Figure 23. *Capillary pressure-saturation relations for 300-350 µm sand, obtained with 1 M NaCl "brine" and air at atmospheric pressure and room temperature, and brine-scCO$_2$ at 8.5 MPa (85 bar) and 45˚C (113 ˚F); (a) drainage and (b) imbibition S(Pc) curves, (c) capillary-scaled drainage and (d) capillary-scaled imbibition results, with the scaling involving normalization with respect to fluid density differences, interfacial tension, and grain size.*

Subtask 4.3. Evolution of rock flow properties by mineral trapping

In this subtask, we examined the effects on rock properties of the changes in porosity and pore geometry that accompany mineral trapping. To address this problem, we used an updated version of the Maximal Inscribed Spheres (MIS) algorithm to evaluate capillary-equilibrium two-phase fluid distributions assuming various wettability properties of the rock as controlled by mineral formation in the pore space. A colleague (Jonathan Ajo-Franklin, LBNL) obtained 3D high-resolution images of supercritcal CO_2-flooding experiment in a core plug. Customized ImageJ scripts were developed for evaluation of the experiments and preparation of input data for the MIS algorithm. Figure 24 displays a gray-scale micro-CT image obtained at the ALS compared to a 3D fluid distribution evaluated with MIS calculations. As shown, the agreement between simulation and experiment is very good. We note that the best-matching experimental data fluid configuration was found by simulating directed drainage assuming a contact angle of 30° with direction of invasion the same in the simulations and in the experiment. The good match with non-zero contact angle may mean that the grains are not completely water-wet, or that the fluid displacement is affected by the roughness of the pore walls.

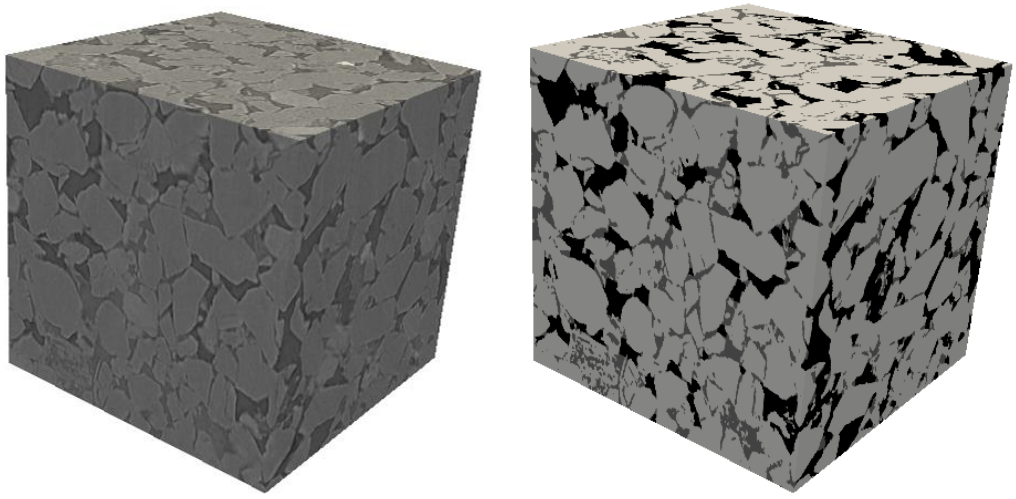

Figure 24. *Experimental CO_2-flooding gray-scale data, on the left-hand side, is compared to MIS-calculations, on the right-hand side. The lightest color corresponds to grains, the darkest color is supercritical carbon dioxide, and the gray color is water. The micro-CT data are courtesy of Jonathan Ajo-Franklin.*

CONCLUSION

The overall conclusions of the LBNL work in ZERT II are that:

(1) Dynamic (time- or history-dependent) processes in geologic carbon sequestration are important as demonstrated by our modeling and simulation studies of CO_2 leakage up a fault, relative permeability hysteresis, reactive geochemical transport, and shallow CO_2 migration. The development of robust simulation capabilities for these processes is essential for defensible design and prediction of storage and migration processes.

(2) Monitoring of CO_2 leakage at the surface is feasible using eddy covariance and accumulation chamber and other methods, subject to limitations in instrument density, temporal aspects of measurements, and proximity of monitoring instruments to the leakage site. In general, our work served to better define the opportunities and limitations of surface monitoring for CO_2 leakage detection.

(3) Pore-scale interfacial forces and processes occurring between fluid phases and rock grains combine to produce predictable flow and trapping effects that can be understood and modeled using computational methods. This work served to motivate continued laboratory studies the results of which need to be upscaled to provide inputs on parameters and models that can be incorporated into numerical simulators for use in large-scale geologic carbon sequestration design and performance assessment.

GRAPHICAL MATERIALS LIST:

REFERENCES

Doughty, C. (2013). Features of relative permeability curves and their use in models of geologic carbon dioxide storage over multiple length scales, Project report, Lawrence Berkeley National Laboratory, 31 pp.

Kneafsey, Timothy J., Dmitriy Silin, and Jonathan B. Ajo-Franklin, (2013). Supercritical CO_2 flow through a layered silica sand/calcite sand system: Experiment and modified maximal inscribed spheres analysis." *International Journal of Greenhouse Gas Control* 14: 141-150.

Lewicki, J.L., G.E. Hilley, L. Dobeck, L. Spangler, (2010). Dynamics of CO_2 fluxes and concentrations during a shallow subsurface CO_2 release, Environmental Earth Sciences, 60, 285-297, doi:, 10.1007/s12665-009-0396-7.

Lewicki, J.L., G.E. Hilley, (2012). Eddy covariance network design for mapping and quantification of surface CO_2 leakage fluxes. International Journal of Greenhouse Gas Control, 7, 137-144, doi:10.1016/j.ijggc.2012.01.010.

Oldenburg, C.M., J.L. Lewicki, L. Dobeck, L. Spangler, (2010). Modeling Gas Transport in the Shallow Subsurface During the ZERT CO_2 Release Test, Transport in Porous Media, 82(1), 77-92, DOI 10.1007/s11242-009-9361-x, LBNL-1529E.

Pruess, K. (2011a). ECO2M: A TOUGH2 Fluid Property Module for Mixtures of Water, NaCl, and CO_2, Including Super- and Sub-Critical Conditions, and Phase Change Between Liquid and Gaseous CO_2, Lawrence Berkeley National Laboratory Report LBNL-4590E, Berkeley, California.

Pruess, Karsten. Integrated modeling of CO_2 storage and leakage scenarios including transitions between super-and subcritical conditions, and phase change between liquid and gaseous CO_2. *Greenhouse Gases: Science and Technology* 1, no. 3 (2011b): 237-247.

Pruess, Karsten, and Jan Nordbotten, (2011). Numerical simulation studies of the long-term evolution of a CO_2 plume in a saline aquifer with a sloping caprock. Transport in porous media 90, no. 1: 135-151.

Silin, Dmitriy, and Tad Patzek, (2006). Pore space morphology analysis using maximal inscribed spheres. Physica A: Statistical Mechanics and its Applications 371.2: 336-360.

Silin, D., L. Tomutsa, S. Benson, T. Patzek, (2010). Microtomography and pore-scale modeling of two-phase fluid distribution, Transport in Porous Media, 1–21, DOI:10.1007/s11242-010-9636-2.

Tokunaga, Tetsu K., Jiamin Wan, Jong-Won Jung, Tae Wook Kim, Yongman Kim, and Wenming Dong, (2013). Capillary pressure and saturation relations for supercritical CO_2 and brine in sand: High-pressure Pc (Sw) controller/meter measurements and capillary scaling predictions. *Water Resources Research* 49, no. 8: 4566-4579.

Tomutsa, Liviu, Dmitriy Borisovich Silin, and Velimir Radmilovic, (2007). Analysis of chalk petrophysical properties by means of submicron-scale pore imaging and modeling. *SPE Reservoir Evaluation & Engineering* 10.03: 285-293.

Xu, T., N. Spycher, E.L. Sonnenthal, G. Zhang, L. Zheng, and K. Pruess, (2011). TOUGHREACT Version 2.0: A Simulator for Subsurface Reactive Transport under Non-isothermal Multiphase Flow Conditions, Computers & Geosciences, 37, 763-774.

LIST OF ACRONYMS AND ABBREVIATIONS

2D	Two Dimensional
3D	Three Dimensional
ALS	Advanced Light Source (at LBNL)
BRGM	Bureau de Recherches Géologiques et Minières
CT	Computer Tomography
ESD	Earth Sciences Division (at LBNL)
LBNL	Lawrence Berkeley National Laboratory
MIS	Maximal Inscribed Spheres
NCG	non-condensible gas
NIST	National Institute of Science and Technology
psi	Pounds per square inch
ZEVCA	Z-factor, enthalpy, viscosity for CO_2 and air

Appendix C

Lawrence Livermore National Laboratory

Analysis of Leakage from a Gas Storage Reservoir

LAWRENCE
LIVERMORE
NATIONAL
LABORATORY

LLNL-JRNL-561016

Analysis of Leakage from a Gas Storage Reservoir: A Case Study at the Leroy Underground Natural Gas Storage Facility

M. Chen, T. A. Buscheck, J. L. Wagoner, Y. Sun, J. A. White, L. Chiaramonte, R. D. Aines

June 14, 2012

International Journal of Greenhouse Gas Control

Disclaimer

Analysis of Leakage from a Gas Storage Reservoir: A Case Study at the Leroy Underground Natural Gas Storage Facility

Mingjie Chen, Thomas A. Buscheck*, Jeffrey L. Wagoner, Yunwei Sun, Joshua A. White, Laura Chiaramonte, and Roger D. Aines

Lawrence Livermore National Laboratory, P.O. Box 808, Livermore, CA 94551, USA

*Corresponding author:

Thomas A. Buscheck
Lawrence Livermore National Laboratory
P.O. Box 808, L-223
Livermore, California 94551
925-423-9390 (office)
925-423-0153 (fax)
buscheck1@llnl.gov

ABSTRACT

Underground natural gas storage reservoirs are useful analogs for identifying and assessing factors that might affect CO_2 leakage during or after deep geological injection in saline formations. We conducted a modeling study of reservoir behavior, examining pressure and gas-inventory histories, as well as gas and brine leakage, and evaluated the sensitivity of that behavior to uncertainty about reservoir properties in an anticlinal, fault-bounded, aquifer-storage system, based on a realistic geological framework model. We chose the Leroy Natural Gas Storage Facility, located in Uinta County in southwest Wyoming, due to its abundant data and observed record of gas seepage (into a creek) and subsequent control by the facility operators. Several hypotheses have been proposed for possible pathways for this leakage, including fault leakage, wellbore leakage, diffuse leakage through an inadequate caprock seal, or some combination of these mechanisms. We focused on the fault leakage hypothesis and investigated the geologic factors affecting such a pathway. Our results are relevant to other natural-gas storage sites, as well as other subsurface storage applications of buoyant fluids, such as CO_2 storage.

For this study we created a three-dimensional model of the geologic structure at the Leroy site, capturing the bounding fault, layered geologic stratigraphy, and surface topography. Using the NUFT code, we developed 2-D and 3-D nonisothermal, two-phase, three-component reservoir models to simulate reservoir pressure and gas-inventory histories, brine and gas leakage from the storage formation, and gas migration to the ground surface. The 3-D reservoir model was validated by virtue of obtaining excellent agreement between the simulated and recorded histories of reservoir pressure and gas inventory, and by predicting gas arrival at the ground surface that was consistent with the timing of observed gas bubbling into a creek. Our analyses also confirmed the facility operators' conclusion that they were able to successfully control the gas leak by reducing reservoir pressures. We then examined the parameters influencing gas leakage up a permeable fault in contact with the gas cap. Given the large uncertainty related to hydrologic properties, such as fault-zone width and permeability, a global sensitivity analysis was performed, ranking the relative importance of various properties in a 15-dimensional parameter space. We also investigated the reservoir-model assumption that the hydrologic properties are static; hence, not dynamically affected by hydro-mechanical coupling. To investigate the likelihood of fault reactivation and whether gas leakage may have occurred up a dynamically created permeable pathway, we used the predicted pressure on the fault plane to drive a geomechanical stability analysis. In general, we show that a discrete leakage pathway, such as through a fault or a leaky wellbore, rather than a diffuse leakage pathway, such as through the caprock, is required to explain the observed gas leakage and its subsequent operational control by reducing reservoir pressures. Specifically, our results indicate that fault leakage is a likely explanation for the observed gas leakage, although the possibility of wellbore leakage has not been ruled out and should still be considered in future work.

Keywords natural gas, underground storage, gas leakage, anticline, fault, brine migration, uncertainty quantification

1. Introduction

Natural gas underground storage plays a vital role in enabling constant, year-round delivery rates (from gas-supply wells), including during the summer (non-heating season), thereby meeting seasonal demands of the consumer and eliminating shortages during the winter (heating season). Over 13% (3.1 trillion cubic feet) of annual natural gas consumption is delivered from over 400 storage reservoirs across the United States (Fig. 1). In the next 20 years, the consumption of natural gas is projected to increase by 1.4% per year (NETL, 2007). Therefore, there will be a need to develop new gas storage reservoirs, as well as safely maintain current ones.

Three main types of underground gas storage are in use today: depleted gas/oil reservoirs, aquifers, and salt caverns (Lord, 2009). Other storage options include abandoned coal mines, lined hard rock caverns and refrigerated mined caverns (PB-KBB, 1998). Several non-traditional types of underground gas storage are also under investigation, such as volcano deposits (Reidel et al., 2003), and caverns with carbonate formations dissolved by hydrochloric acid (Castle et al., 2005). Depleted reservoirs and aquifers have large working gas-storage capacity to meet the base load requirement (long-term demand) and gas is generally cycled only once a year during the winter season. Salt caverns, as well as some small-scale aquifers, are intended to meet peak load requirement (sudden, short-term demand), with

turnover rates as short as a few days or weeks (Beckman et al., 1995). Of the three main types of underground storage, depleted hydrocarbon reservoirs are the cheapest and easiest to develop, operate, and maintain. Their main advantages are (1) infrastructure is already in place, (2) geological characteristics are already reasonably well known, and (3) the need for so-called "cushion-gas", whose sole purpose is to minimize the need for supplemental pressure support for the reservoir, because gas left-in-place can serve towards the cushion requirement. This requirement can be as high as 80% of reservoir capacity. Where major gas-consumption centers are too remote from depleted natural gas or oil fields, natural aquifers are often converted to gas-storage reservoirs, although aquifers lack the advantages of depleted hydrocarbon reservoirs. Moreover, there is also a higher environmental risk for groundwater contamination with gas storage in aquifers.

For any gas storage facility, gas leakage is a concern, both for economic and environmental reasons. Possible leakage pathways include improperly abandoned wells, imperfectly cemented wells, leaking faults, or failed caprock seals (Katz and Tec, 1981). Few leakage pathway analyses have been published for natural gas underground storage. Recently, a number of studies have focused on leakage concerns for geologic CO_2 storage (GCS). Many of these studies utilize idealized conceptual models of generic reservoir systems, with homogeneous permeability within the respective reservoir and seal units. While simplified models can be useful for developing general insight into important processes and parameters, it is recognized that the leakage rate in real geologic settings critically depends on the inherently three-dimensional nature of the reservoir system. To accurately simulate gas leakage for a realistic storage facility, 3-D models capable of simulating the relevant processes must account for site-specific hydrogeological conditions.

In this study, we describe a 3-D reservoir model for gas leakage at the Leroy natural-gas, aquifer-storage facility, which is a unique site because of its history of observed gas leakage at the ground surface, and operational measures taken to minimize that leakage. The objectives of this study are to use the Leroy storage site to (1) investigate the hydrological and geomechanical state of the reservoir during gas injection and extraction, (2) evaluate the sensitivity of the system to various hydrologic and geomechanical parameters, and (3) test the hypothesis that a bounding fault served as a leakage pathway. Insights derived regarding leakage processes at this location, however, are applicable to other underground storage sites as well.

2. Leroy Gas Storage Facility

The Leroy Gas Storage Facility is an aquifer site developed in Uinta County, Wyoming, approximately 100 miles northeast of Salt Lake City (Fig. 1).The reservoir is an anticline bounded on its western side by a fault. Natural gas is injected into and extracted from the T-10 zone, a coarse-grained, porous, high-permeability sandstone aquifer, at a depth of about 900 m, in the lower Thaynes Formation (Fig. 2). The upper and middle Thaynes Formation contains layers of fine-grained sandstone, red shale, siltstone, and dolomite that form a low-permeability caprock for the T-10 aquifer-storage zone. The Ankareh Formation consists of a red bed sequence of shale and siltstone, and also acts as caprock. The Woodside Formation, located beneath the storage aquifer, is a low-permeability sequence of dense, silty shale. The Twin Creek Limestone and Nugget Sandstone Formations contain the low- and high-permeability aquifers lying above the Thaynes Formation caprock. The Knight Formation, comprised of a mixture of sands, silts, and shales, is effectively the overburden that contains the uppermost unconfined aquifer and unsaturated (vadose) zone.

The initial development of the gas-storage reservoir began in 1971. Within the first decade of gas-storage operations several indications of gas leakage were directly or indirectly observed. Of particular interest were observations of gas bubbling in a surface stream in Nov. 1978. Gas-inventory analyses indicated that gas was being lost, and it was believed to be pressure triggered (Araktingi et al., 1984; Sofregaz US, 1998). These observations motivated a number of published papers and in-house studies (Rocky Mountain Petroleum Consultants, 1981; Araktingi et al., 1984, 1987; Sofregaz US, 1998). Since 1981, the facility operators have reduced the maximum reservoir gas pressure enough to successfully control the gas leakage rate.

Several leakage-pathway hypotheses have been proposed to explain the observed gas leakage behavior. The first hypothesis was well leakage, supported by a history of well problems at the Leroy site. In September 1973, gas leakage was observed through a corroded well (Well No. 4), which was subsequently abandoned. This finding motivated a large surface gas detection survey and several tracer tests (Araktingi et al. 1984). During the first round of tracer tests there were indications of a fast-path leakage mechanism in another well (Well 4A), based on observations of tracer migration to the ground surface within only 9 days of tracer release. Two other tracer tests, injected in other locations in the reservoir, resulted in ground-surface detection 32 and 71 days after release. A noise log in Well 4A indicated leakage behind the casing, and during the 1981-1982 season, this well was worked over. Subsequent tracer tests showed much slower migration to the surface, taking 163 days. While these tests indicate that the fast leakage pathway was mitigated, the fact that the tracer still made it to the surface implied that a slower leakage pathway still remained. This pathway could conceivably have been through the well itself, or along some alternative geologic pathway. Unfortunately, it is difficult to directly assess the quality of the well work-over campaign, due to the timing of its completion in 1982. That year, the typical reservoir operating pressure was reduced (Sofregaz US, 1998) and never returned to the high levels of preceding years. Therefore, the possibility that the wells function as pressure-dependent leakage pathways cannot be eliminated based on the available evidence.

A second hypothesis to explain the persistent leakage was that the bounding fault at the site is a vertical permeable pathway. A key piece of evidence supporting this hypothesis is that the observed pattern of surface leakage appeared to align with the surface expression of the main fault (Rocky Mountain Petroleum Consultants, 1981). It should be noted that several wells are also located along the fault trace. Also, if the fault acts as the permeable pathway, other observations would need to be explained. There appears to be some contradiction with a permeable fault passing through the overlying Nugget Formation, which is naturally overpressured (gradient 0.75 psi/ft = 16.96 kPa/m) and contains high-salinity brine, without brine ever being detected in the creek. Of course, the fault may have been naturally sealing, with its permeability becoming dynamically enhanced by reservoir pressurization. Moreover, as the reservoir became overpressured, a gas-only migration pathway could have been established within the fault, with little or no vertical displacement of brine.

A third hypothesis is that a hydrofracture was created at the site due to hydro-mechanical coupling. The Leroy Gas Field was operating at high pressures at the beginning of the project (0.65 psi/m = 14.70 kPa/m) (Sofregaz US, 1998). To properly assess the possibility of either hydrofracturing or fault reactivation requires good estimates of the *in situ* stress in the field. We will discuss this point further in our geomechanical analyses.

A fourth hypothesis is that the permeability of the caprock at the site is not low enough to adequately function as a seal, and that gas may directly flow through it perhaps as diffuse leakage or through an existing fracture network. However, the low permeability and integrity of the caprock seal was confirmed by several pressure interference tests between the caprock and the reservoir, which were conducted during the site's initial development phase. Furthermore, as we will discuss, analyses of pressure observations and of gas-leakage breakthrough times make this particular scenario unlikely.

A fifth hypothesis that has been put forward is that there is a shallow collector zone at the site. That is, gas may migrate to a shallower depth through one or more of the hypothesized leakage pathways, and then accumulate within some trapping structure. This idea was motivated by the observation that some of the surface bubbling appeared to be pressure dependent, while others were not (Araktingi, 1984). However, there was no pressure increase in the observation wells completed in the overlaying Twin Creek, Ankareh, and Nugget Formations that would suggest a collector zone on the same side of the fault. Therefore, it has been postulated that if there is a collector zone, it should be on the other side of the graben, in the Nugget Formation (Sofregaz US, 1998).

Finally, it is conceivable that one or more of the hypothesized leakage mechanisms may have been acting in combination. For example, gas may have leaked through the lower portion of a well to a shallow collector zone, and then migrated to the surface through the fault or some other geologic pathway.

For this study, we focused primarily on the fault-leakage hypothesis and the hydrologic factors affecting such a pathway. Here, we describe those observations that are consistent with a fault-leakage hypothesis, as well as discuss several unexplained observations. Other counter-hypotheses, particular concerning the wellbore-leakage hypothesis, are the subject of future work.

3. Model methodology

The observed gas leakage at the Leroy storage site provides an excellent opportunity to study potential leakage mechanisms that may be applicable to underground gas storage facilities in general. Questar (operator of the Leroy site) provided stratigraphic data, which was used to construct a realistic geologic framework model and numerical mesh. Based on this model, a series of reservoir analyses were performed to investigate the fault leakage hypothesis. The following sections provide relevant details on this methodology, which is summarized in Fig. 3.

3.1. Geological framework model and numerical mesh

EarthVision is a comprehensive family of integrated software used for the analysis, modeling, and visualization of spatial data (Dynamic graphics, Inc., 2008). We used EarthVision to construct a 3-D faulted geological framework model of the Leroy storage reservoir (Fig. 4). The stratigraphic layers were defined by the borehole logs scattered throughout the field. Interpretive structural contour maps of some of the horizons were made available by Questar and these data were used to constrain the geometry of the section. Plan maps of the fault traces were digitized and used for construction of the fault planes. Structural dips of 70 degrees were assigned to the faults. Offset directions of the faults were provided.

With the geometry defined in the geological structural model, the I, J, and K planes were aligned with the geologic features (fault and structure surfaces) within the model. Using EarthVision's cellular meshing module (EVCELL), the treatment of cells along the fault and each stratigraphic layer was defined and the grids calculated. The generated cellular grid consists of irregularly shaped cells, arrayed in I, J, and K dimensions, with the origin in the northwest corner (Fig. 5). The numerical model domain, which was cropped from the initial geological structural model is 3200, 3600, and 2000 m in I, J, and K dimensions respectively, bounded on the west by the fault, on top by the topographic surface, and at the base by bedrock. The cell size in the I dimension increases from west to east, because all of the wells (which provide the majority of the stratigraphic information) are clustered in the western part of the domain, aligned along the major fault. The vertical cell size varies in the respective geological zones: from as small as 8 meters in the T-10 storage-aquifer formation, to as large as over 100 meters at the bedrock surface. The vertical grid resolution for each zone is based on the mean thickness and importance of that zone, as shown in Table 1. The T-10 aquifer is the primary storage formation and has been assigned higher vertical resolution. The 18, 25, and 43 columns and rows in the I, J, and K dimensions result in a total of 19,350 cells. The cells of the first I plane represent the fault zone and the western boundary.

3.2. Reservoir models of gas migration

In this study, the NUFT (Nonisothermal Unsaturated-saturated Flow and Transport) code, developed at Lawrence Livermore National Laboratory, was used as a reservoir simulator (Nitao, 1998; Hao et al., 2011). During the past decade, NUFT has been demonstrated to be robust and accurate in many applications simulating multi-phase multi-component heat and mass transfer and reactive transport (e.g. Buscheck et al., 2003; Johnson et al., 2004, Carroll et al., 2009; Morris et al., 2011; Buscheck et al., 2012). NUFT uses an integral finite difference method for the space discretization, where cell geometry properties, as well as neighboring connectivity, are necessary. An interface code converting the EarthVision generated grids to a NUFT-compatible mesh was developed. Based on the cell geometry information including IJK index, coordinates, and size provided by the grid, neighboring cells were identified and their connectivity (distance, cross area, and connection angle) were calculated by using the interface tool.

3.2.1. 2-D radially-symmetric (RZ) reservoir model

A 2-D radially-symmetric (RZ) numerical mesh was developed to allow more computationally efficient reservoir analyses of the anticlinal aquifer storage reservoir. The apex of anticlinal structure is close to (and slightly east of)

the location of the bounding fault on the west side of the gas cap (Fig. 2). A probability density function of the elevation of the top of the T-10 (aquifer) zone was constructed, which was used to develop the RZ numerical mesh. To capture this shape, the RZ mesh has 103 layers, with 78 layers being 10 m thick and 24 being 40 m thick, and 69 radial (vertical) columns, with an outer radius of 22.88 km, which is a no-flow boundary. Thus, the sloping geometry of the 3-D structure of the anticlinal aquifer was captured in fine detail. The T-10 zone was determined to have an average thickness of 80 m (Table 1), which was honored in the RZ numerical mesh. In the same fashion, the average thickness, along with thickness range of each of the respective stratigraphic formations (Topo, Twin Creek, Nugget, Ankareh, Thaynes, and Woodside) were also honored in the RZ numerical mesh. The injection/withdrawal zone occurs in the inner 26 radial columns, with a total radius of 1.04 km. The fault zone is at the center of the RZ numerical mesh. Different cases were considered with fault-zone radii of 2, 4, 5, 6, 8, 10, 20, and 40 m, respectively.

3.2.2. 3-D reservoir model

The hydrologic parameters for each geological zone were estimated from measurements at the Leroy site or from the radially-symmetric (RZ) model, as listed in Table 2. A schematic representation of a vertical east-west cross section of the Leroy gas storage facility is shown in Fig. 6. Boundary conditions at the land surface (2061 m elevation) are an atmosphere pressure of 7.8×10^4 Pa and a temperature of 8.0^oC. A constant water infiltration flux of 292.8 mm/yr, estimated from the averaged local monthly precipitation, was also assigned to the top boundary. For an unsaturated-saturated flow system as in our study, the pressure on the bottom can usually be estimated from the groundwater level data, which is not available for the Leroy site. However, the initial reservoir pressure (1.03×10^7 Pa) and temperature (27.7^oC) were measured at a depth of 900 m (Araktingi et al., 1984), with which we calibrated the model to determine the pressure and temperature at the bottom boundary to be 1.75×10^7 Pa and 33.0^oC. As shown in Figs. 2 and 6, the western side boundary is the fault zone, where we assumed a no flow (inward or outward) boundary. The cell volumes for the edge cells at the eastern, northern, and southern side boundaries are magnified to minimize pressure changes and thereby eliminate the boundary effect on gas and brine migration. Under these boundary conditions, the model simulates two-phase (gas, liquid), three-component (water, air, methane), thermal flow and transport in an unsaturated-saturated semi-infinite domain. We first ran an initialization simulation for a sufficiently long time period to establish steady-state conditions, from which the spatial distribution of gas pressure, temperature, liquid saturation, and component concentrations were obtained as the initial state of the reservoir before injection/withdrawal operation. Instead of discretely distributing the seasonal sources and sinks along the perforated intervals of each of the 10 injection/withdrawal wells, we combined the sources and sinks, applied to a lumped injection/withdrawal zone containing all the well perforations in the T-10 storage zone (Fig. 7a). In this way, the stability of the numerical simulations is significantly improved with little influence on simulated storage pressure, leakage and inventory history, thanks to the highly permeable storage aquifer (permeability = 1.76×10^{-13} m^2). This simplification is also justified by the results presented in Section 4.

3.2.3. Global sensitivity analyses of reservoir behavior

PSUADE, standing for Problem Solving environment for Uncertainty Analysis and Design Exploration and developed at Lawrence Livermore National Laboratory (Tong, 2009), is a collection of Uncertainty Quantification (UQ) tools, including those for high-dimensional sampling, parameter screening, global sensitivity analysis, response surface analysis, uncertainty assessment, numerical calibration and optimization (Hsieh, 2007; Wemhoff and Hsieh, 2007; Sun et al., 2012). In this study, we used PSUADE to perform a sensitivity analysis, based on a response surface (surrogate model) constructed from a suite of "training" data including input parameter values effectively sampled in hyper-dimensional parameter space and the corresponding NUFT model output (e.g. gas leakage). Following the procedure presented in Fig. 3, fifteen parameters were chosen and sampled 1000 times in a 15-dimensional parameter space using Latin Hypercube sampling method. We consider a two order of magnitude range of permeability of the T-10 storage formation, caprock (Thaynes and Ankareh Formations), and fault zone and of van Genuchten α parameter (for only the T-10 formation and fault zone), following a log-uniform distribution, since these five parameters affect the model dependent variables roughly in a log-scale fashion. The other 10 parameters, including van Genuchten *m* parameter, porosity, residual saturation, compressibility of the T-10 storage

formation, caprock, and fault zone, as well as the fault-zone width, span a one order of magnitude range and were sampled uniformly in the range (Table 3). Based on the training data simulated by NUFT, the response surfaces for outputs (maximum overpressure and gas leakage) were constructed and the importance of 15 parameters were scored and ranked using Multivariate Adaptive Regression Spline (MARS) method. Note that overpressure is defined to be the pressure in excess of initial pressure prior to gas-storage operations. The constructed response surface models were used to evaluate the factors influencing the reservoir overpressure and gas leakage.

3.3. Geomechanical stability analyses

Using the simulated pressure history and geometry of the major bounding fault, we performed a preliminary fault stability analysis in order to assess the possibility of hydro-mechanical coupling. Estimates of the effective normal and tangential tractions acting at each point on the fault were computed, and the potential for slip was estimated using a standard Coulomb slip criterion. A representative coefficient of friction, m = 0.6 and no cohesion was adopted in the absence of further information.

Besides the pressure distribution acting on the fault, a key parameter for the analysis (and a key uncertainty) is the state of stress at depth. Little information regarding the present day stress state was available to us at the time of this study. Maximum horizontal stress orientations (S_{Hmax}) and stress state were available from the World Stress Map (Heidbach et al., 2008), indicating that our area of study is in between two regions with different stress regimes. Approximately 100 km to the southwest, all the measurements indicate a normal faulting (NF) environment, with S_{Hmax} ranging from ~ 150° to 173°Az. These measurements are from geologic fault data, wellbore breakouts, focal mechanisms and hydraulic fracture indicators. Approximately 200 km southeast, most of the measurements indicate a strike slip (SS) environment and a more consistent S_{Hmax} orientation ~110° Az ±5°. These data were mostly derived from borehole breakout analysis and hydraulic fracturing measurements. Given their uncertain nature, these parameter estimates have been used as baseline values within a preliminary uncertainty quantification analysis.

Note that for this analysis, we have used a local approximation, in which slip potential is evaluated point-wise on the fault. It is local in the sense that the analysis does not consider slip interactions and stress re-distribution that would naturally take place as the fault responds. Such a non-local analysis has been deferred until later studies, as the additional detail may not be justified given the very large uncertainties in stress magnitude and orientation at depth, and fault geomechanical properties.

4. Results

4.1. Reservoir Analyses

The simulation of gas leakage from an aquifer-storage site critically depends on the inherently three-dimensional nature of the reservoir system. Nonetheless, it is still possible to assess the sensitivity of reservoir gas-pressure and gas-leakage history to many of the hydrologic parameters using a radially-symmetric RZ model that does not explicitly represent the three-dimensional structure of geologic framework model. Hence, the initial assessment of hydrologic parameters was assisted with the use of the RZ.

Based on the initial flow tests conducted at the Leroy site, the transmissibility of the T-10 storage-aquifer formation was determined to be equal to 53,045 millidarcy-ft/cP (Sofregaz US, 1998). For an assumed pay thickness of 20 ft and water viscosity of 0.87 cP, they determined a permeability of 2310 millidarcy for the T-10 storage formation. Because our 3-D and RZ reservoir models both have an average pay thickness of 80 m for the T-10 formation, this translates to a permeability of 176 millidarcy (1.76×10^{-13} m^2), which we applied to both models.

4.1.1. 2-D radially-symmetric (RZ) reservoir model

The 2-D radially-symmetric (RZ) reservoir model was used to investigate the sensitivity of reservoir overpressure and gas migration to hydrological parameters. The geological formations (Table 1) were treated as two types of hydrogeologic units with respect to hydrological parameters (Table 2), including: (1) aquifer units (Knight, Twin Creek, Nugget and T-10 Formations) and (2) seal (caprock and bedrock) units (Ankareh, Thaynes, and Woodside

Formations). The hydrological parameters of the T-10 storage aquifer were based on the initial aquifer flow tests (Sofregaz US, 1998). Because the Nugget Formation is thicker than the T-10 Formation (225 versus 80 m), it was assumed to be more heterogeneous than the T-10, including less permeable layers, and therefore has lower permeability (1.0×10^{-14} m^2 versus 1.76×10^{-13} m^2). Because the Twin Creek Formation is a limestone aquifer, we assumed it has a lower permeability (1.0×10^{-16} m^2) than the sandstone aquifers (Nugget and T-10 Formations). Because the Knight Formation is the overburden, including both unconsolidated and consolidated rocks, we assumed it has a higher permeability than the Nugget Formation (2.5×10^{-14} m^2 versus 1.0×10^{-14} m^2). The seal units (Ankareh, Thaynes, and Woodside Formations) share the same hydrological parameters (Table 2).

The hydrological parameters listed in Table 2 were used as a starting point to investigate the sensitivity of reservoir overpressure and gas leakage to hydrological parameters, including fault zone permeability and thickness. Note that the fault zone thickness was investigated by varying the radius of the fault zone, located at the center of the RZ model, from 2 to 40 m. We found that the hydrological parameters of the geological formations not in immediate contact with the gas cap in the T-10 storage formation (i.e., all those except the Thaynes and Ankareh Formations and fault zone), have a negligible influence. The permeability of the caprock (Thaynes and Ankareh Formations) influence reservoir overpressure, but do not influence gas leakage (which is further illustrated by the 3-D reservoir analyses). The most influential hydrological parameters affecting overpressure and gas leakage are the permeability and "radius" of the fault zone, together with the permeability of the T-10 storage zone. Details of the parameter sensitivity of the fault zone are best investigated using the 3-D reservoir model (Section 4.1.2.4); consequently, we do not report the sensitivity analysis results obtained with the use of the RZ model.

The lack of parameter sensitivity for the hydrologic parameters in the formations not in direct contact with the gas cap in the T-10 storage zone enabled us to focus on the hydrologic-parameter sensitivity analysis (Section 4.1.2.4) on the formations in direct contact with the gas cap, including the T-10 storage zone, caprock (Thaynes and Ankareh Formations), and fault zone. The bedrock (Woodside Formation) is not in direct contact with the gas cap and its hydrologic properties were not found to sensitively influence reservoir overpressure or gas migration.

4.1.2. 3-D reservoir model

Table 2 lists the hydrological parameters of the base-case 3-D reservoir model. Section 4.1.2.1 describes the validation of the base-case 3-D reservoir model against field measurements of bottom-hole pressure and gas inventory. Sections 4.1.2.2 and 4.1.2.3 describe the reservoir-pressure and gas-inventory histories and gas-leakage-pathway analysis for the base case. Section 4.1.2.4 describes the global hydrologic-parameter sensitivity analysis.

4.1.2.1. Model validation

With the 27 years of injection/withdrawal data, the reservoir pressure and gas leakage to the ground surface were simulated, using the developed 3-D reservoir model, and the gas inventory was calculated by subtracting leakage from the net injection (Fig. 7). The simulated pressure history captures the measured trend quite reasonably (Fig. 8) and the simulated gas-inventory history (influenced by gas leakage out of the T-10 storage zone) match the field data perfectly, particularly after May, 1975, when the reservoir was fully developed and started to be operated in a seasonally cyclical manner (Fig. 9). The small discrepancy between simulated and measured pressures (Fig. 8) is most likely due to the fact that the measured data were obtained in well 3, while the simulated pressure pertains to the center of a lumped injection/withdrawal zone. A lumped zone, containing all the wells, was used instead of discretely representing the 10 individual wells as distinct sources and sinks. Hence, it is reasonable that the simulated pressure differ a bit from the local pressure at wellbore. However, the close match of gas-inventory history indicates that this simplification does not impair the ability to accurately simulate gas leakage out of the T-10 storage aquifer, which is the primary focus of our study.

4.1.2.2. Reservoir history analysis

During the initial phase of gas-storage operations (5/1/1971 through 5/1/1974), reservoir pressure was continuously increasing with the injection of the natural gas (Fig. 7). The gas-storage inventory was increased to 4 BSCF to meet

the requirement for cushion gas. The site operators spent the following year (5/1/1974 through 5/1/1975) evaluating reservoir performance and installing additional facilities, with no injection/withdrawal. However, gas leakage began during this time period, relieving the reservoir overpressure. Because the leakage rate was so small compared to the stored cushion gas inventory, the gas inventory was virtually unaffected (Fig. 7d). The intensive (high amplitude) injection/withdrawal operations, starting 5/1/1975, caused the gas leakage rate to strongly increase, peaking at a rate of 7.0 MMSCF/month at 5/1/1977. From 5/1/1977 to 5/1/1982, the reservoir pressure and gas-inventory histories responded in a cyclical fashion to the injection/withdrawal and gas leakage histories (Fig. 7). After 5/1/1982, the injection/withdrawal rates were substantially reduced, resulting in the reservoir pressure being limited to less than 1600 psi (Fig. 7b) and gas leakage being limited to less than 2 MMSCF/month (Fig. 7c), or ~20 MMSCF/year (Questar's in-house estimation is 20-25 MMSCF/year). The cushion gas increased from 4 to 6 BSCF, and the working gas decreased from 2.2 to ~0.8 BSCF.

Simulated histories indicate that pressure responds immediately to injection/withdrawal rates, while leakage is related to pressure via a two-way feedback mechanism. Leakage increases with pressure, while increased leakage relieves overpressure. This explains why the peak pressure of each successive cycle decreased from the maximum (1975-1976), although the injection rate was not decreased until 1982. After gas leakage rate reached its peak value on 5/1/1977, it relieved the overpressure. When leakage decreased to ~2 MMSCF/month in 1979-1980, the peak pressure of each cycle became nearly constant, corresponding to the constant injection rate. This two-way buffering mechanism leads to a much wider cycling span of gas-leakage history than that of the gas injection/withdrawal and pressure history (Fig. 7). To better illustrate the correlation of leak rate with the pressure, the hysteresis curves of the reservoir pressure versus inventory data during the 1977-1981 time span are plotted (Fig. 10). The slopes of the withdrawal curve (upper curve of the hysteretic cycle) flatten whenever pressure exceeded 1700 psi, suggesting the leakage is triggered when this pressure is exceeded. The slopes of the injection curve (lower curve of the hysteretic cycle) are also very flat whenever the pressure is less than 1400 psi or the inventory is less than 5.5 BSCF, indicating sufficient cushion gas is required to support necessary operating pressure.

4.1.2.3. Leakage pathway analysis

While the focus of our study is on gas leakage, we also analyze brine leakage because of the role it can play in relieving reservoir overpressure. Fig. 11a shows that brine leakage from the T-10 storage aquifer into the fault zone is initially ~37 times greater than that into the caprock and that at later times the ratio declines to ~6. Moreover, the brine flux through the caprock is distributed diffusely over a much wider area than is applicable to the fault zone; consequently, the caprock is not a potential conduit for possible brine migration to shallower groundwater aquifers. Therefore, for the Leroy storage facility, the fault is one of two potential pathways (the other being leaky wellbores) for migrating brine to possibly reach the shallower aquifers in communication with the fault. However, there was no evidence of brine migration affecting the salinity of shallower aquifers at the Leroy site.

Fig. 11b shows that gas leakage into the fault is more than 4 to 5 orders of magnitude greater than into the caprock, and for much of the gas-storage operations, gas leakage into the caprock is zero. Therefore, the caprock is not a significant pathway for gas leakage. Fig. 11 also shows that the cumulative volumes of brine and gas leakage are similar in magnitude, indicating that brine and gas leakage make similar contributions to pressure relief. As discussed in Section 4.1.2.4, these pressure-relief mechanisms are much more significant than that of rock compressibility.

In the T-10 storage aquifer (Fig. 12), the local maximum pressure occurs east of the apex of the anticline because the pressure in the western portion is relieved by gas leakage through the bounding fault zone. Horizontal pressure gradients form in the underlying over-pressured zone near the western fault, through which the gas in the storage zone leaks upward, which reduces the overpressure.

The 3-D spatial distribution of the mole fraction of methane in the gas phase is a good indicator of how natural gas migrates in the system (Fig. 13). According to the simulated gas-leakage history, April 1, 1975 is the time of gas breakthrough at the ground surface, as the leading edge of the gas plume reaches the ground surface (Fig. 13a). On

10/1/1975, when the reservoir pressure reached the peak during injection season, the plume extended horizontally at the ground surface (Fig. 13b). It was also noted that gas started to migrate from the fault zone to the permeable Nugget Formation overlying the caprock (Fig. 13b). After three years of gas leakage (Fig. 13c), most of the fault zone has become the pathway of upward gas migration, and the horizontal distribution of the plume at the ground surface roughly corresponds to the detected gas footprint on November 1978 (Rocky Mountain Petroleum Consultants, Inc., 1981). A significant amount of methane has migrated horizontally along the Nugget Formation from the fault zone by 4/01/1982 (Fig. 13d), the time when gas leakage was controlled by the site operators by limiting the maximum reservoir pressure. The methane contained in the Nugget Formation, in turn, can migrate to the fault and then to the ground surface under some conditions, or through fractures across the overlying low-permeability Twin Creek Formation (permeability = 10^{-16} m^2).

In addition to the fault zone, fractures possibly developing in the caprock during injection could provide another leakage pathway. According to the field monitoring of surface bubbling, some bubbling corresponds to the timing of injection operations, while some do not, indicating the leakage originates not only directly from the aquifer-storage zone, but also from intermediate collector zones. The possibility of gas collector zones in the Nugget Formation was ruled out in previous studies (Araktingi et al., 1984; Sofregaz US, 1998) who noted that gas bubbling appeared to be pressure dependent, which should not be the case if the gas was seeping from a collector zone. They also argued that no collector zones could exist above the caprock, since pressure did not increase in the observation well completed in the overlying formations. This argument would not necessary apply if the well were perforated within lower-permeability layers of a heterogeneous geological formation. Furthermore, it may not be reasonable to rule out the existence of permeable collector zones solely on the basis of observations from a single well. Also, under hydrostatic pressure conditions above the caprock, buoyancy can play an important role for upward gas migration. Finally, barometric pumping may be strong enough to induce some vertical gas migration from shallow collector zones to the ground surface, especially when faults or fractures provide potential pathways (Nilson et al., 1991; Carrigan et al., 1996).

Similarly, brine from the T-10 storage aquifer could be displaced to the Nugget Formation via the fault zone, but not likely to the overburden due to insufficient vertical pressure gradients (Fig. 12). The spatial distributions of the methane fraction in the liquid phase, which can be regarded as a kind of tracer transport in aqueous phase, indicate the possibility of this conclusion (data not shown).

The spatial distribution of mass fraction of methane over the total mass of rock demonstrates our aforementioned conclusion that the fault serves as the primary leakage pathway to the Nugget Formation and the ground (Fig. 14). Unlike the mole fraction in the gas phase (Fig. 13), the total mass fraction in the rock shows a dual-zone methane distribution within the fault zone, separated by the caprock horizon, strongly suggesting gas phase migration encounters bottlenecks in the fault zone adjacent to the caprock formation. The fault-zone permeability in the caprock interval (Thaynes and Ankareh Formations) of the fault is 10^{-14} m^2, one order of magnitude lower than within the T-10, Nugget, Twin Creek, and Knight Formations (the aquifer horizons). During the injection season, the gas phase was driven upward (by overpressure) enough to penetrate the low-permeability portion of the fault zone, but could not be pulled back (by underpressure) during withdrawal season. In this way, the low-permeability portion of the fault zone operates as a one-way “check valve”, which causes methane to be accumulated above the caprock horizon, as manifested by the upper region of methane accumulation (Fig 14).

Gas seepage at the ground surface can be better illustrated by the areal distribution of specific methane flux to the atmosphere (Fig. 15). Although we cannot validate the gas seepage amount due to the lack of quantitative data, the footprint of the dual-zone methane distribution roughly corresponds to the detected gas footprint in November 1978 and November 1979, demonstrating the fault zone as the primary leakage pathway. However, these results cannot rule out the possibility of leakage through other preferential pathways (e.g. leaky wellbores). In fact, the match could be somewhat better if additional gas migration in the center of the leakage footprint were added besides that migrating up the fault zone.

4.1.2.4. Global hydrologic-parameter sensitivity analysis of reservoir behavior

The relative importance of 15 hydrologic input parameters were scored (normalized on 100) and ranked using response surfaces constructed by MARS between the 15-dimensional hydrologic parameters and two reservoir-behavior outputs: (1) accumulated methane leakage to the atmosphere by May 1982 and (2) maximum (seasonal peak) overpressure in the storage aquifer (Table 3). Of the 15 parameters, the bottom 7 ranked parameters had a score of 0.0, indicating no sensitivity. Among the top 6 ranked parameters (whose scores are all larger than 20.0), four of them are related to gas permeability and storage capacity of the storage aquifer, i.e. intrinsic permeability (rank No.1), van Genuchten parameter *m* (No.2), gas residual saturation (No.3), and porosity (No.6). It is expected that permeability (No.4) and width (No.5) of the fault zone, which provides the gas leakage pathway to the ground surface, should significantly influence both accumulated methane leakage and maximum overpressure in the storage reservoir. As shown in Fig. 16, maximum reservoir overpressure increases roughly linearly with decreasing fault-zone permeability and width. Gas leakage increases strongly with increasing fault-zone permeability for low permeability, with the dependence becoming weaker with higher permeability ($> 10^{-13}$ m^2). Accumulated gas leakage exceeds 60 million m^3 for 10^{-12} m^2. The decreasing sensitivity of gas leakage to increasing fault-zone permeability for high permeability is due to the aforementioned two-way feedback that gas leakage has on relieving reservoir overpressure. Gas leakage increases roughly linearly with fault-zone width for width factor greater than 0.4. Gas leakage becomes negligible if fault-zone permeability is below 2×10^{-14} m^2, and width factor is less than 0.4.

For the investigated parameter ranges, storage-aquifer and caprock compressibility are not sensitive parameters for gas leakage and maximum reservoir overpressure, indicating the resulting volume change from pressurization is negligible, compared to the storage volume within the aquifer porosity (No.6). Compared to fault-zone permeability and width, other fault parameters, including van Genuchten *m*, porosity, and residual liquid saturation, are not significant. Neither van Genuchten α nor residual liquid saturation of the storage aquifer is a sensitive parameter, which suggests that storage-aquifer capillary pressure has little influence on gas migration and pressure. In contrast, van Genuchten *m*, and gas residual saturation of the storage aquifer are top-ranked parameters for maximum overpressure and gas leakage, because both properties affect the gas relative permeability, which, together with aquifer intrinsic permeability, play a critical role in gas migration.

Although caprock permeability could be thought to strongly influence gas leakage, it is ranked No. 7 and 8 for gas leakage and overpressure, respectively. To evaluate the relative sensitivity to caprock permeability with greater refinement, reduced-order response surfaces were constructed by sampling in the 2-dimensional parameter space 200 times, spanning the range 10^{-18} to 10^{-16} m^2 for caprock permeability and 10^{-16} to 10^{-14} m^2 for fault-zone permeability (Fig. 17). Note that this is a lower range of fault-zone permeability than considered in the 15-parameter ranking analysis (Table 3). Compared to fault-zone permeability, gas leakage is insensitive to caprock permeability for the range of 10^{-18} to 10^{-16} m^2, indicating that diffusive leakage is negligible, even if the caprock is moderately leaky for brine leakage. This result also indicates that a discrete pathway, such as the fault zone, is required for gas leakage from the Leroy gas storage aquifer. When fault-zone permeability is below 10^{-15} m^2, which means the fault no longer functions as a permeable fault, gas leakage from the T-10 storage zone is close to zero, suggesting that no gas leakage would occur at the Leroy site without the existence of another discrete gas-leakage pathway, such as leaking wellbores.

Fig. 18 is a scatter plot generated for the 200 samples used to develop Fig. 17, with the y axis being the accumulated methane leakage up to April 1, 1982 and the x axis being the maximum overpressure during the first 11 years of storage operation. For maximum overpressure less than 1 MPa, accumulated methane leakage decreases linearly with increasing maximum overpressure (Fig. 18). For maximum overpressure greater than 2 MPa, the gas leakage rate is zero, which shows that such a high pressure can only be maintained in the absence of gas leakage.

4.2. Geomechanical stability analysis

An important question to answer when considering the possibility of fault leakage is the stability of the fault in the in-situ stress regime. An increase in reservoir pressure due to injection could potentially reduce the effective normal

stress acting on the fault, and lead to rupture. This in turn could lead to an increase in permeability as a result of hydro-mechanical coupling.

Unfortunately, the key parameters governing this process are highly uncertain for the Leroy site. In particular, we are unaware of any local estimates of the *in situ* stress magnitude and orientation. As described in Section 3, there are regional estimates that suggest that the Leroy site may lie somewhere between a normal faulting and strike slip regime. Therefore, rather than performing the stability analysis for a specific stress state, we have instead chosen to perform the analysis across a range of stress states that may reasonably be encountered at the site.

Fig. 19 summarizes the results of this study, using two assumptions about the principle stress orientation, one at 150 deg. Az. and another at 170 deg. Az. These two values capture the range of orientations observed from well data approximately 100 km to the southwest of the Leroy site. An additional analysis was also performed at 110 deg. Az to capture the typical stress orientations observed 200 km to the southeast. In this orientation, the maximum horizontal stress is nearly perpendicular to the fault plane, and therefore the fault is found to be stable for almost any reasonable assumption about stress magnitudes. A figure for the 110 deg. Az. case has therefore been omitted.

The vertical stress magnitude was computed by assuming a stress gradient of 23 MPa/km, an approximate value that is reasonable for a sedimentary basin. By assuming particular values of the maximum and minimum horizontal stress at the site, we may compute whether the fault is stable in that particular stress regime. A coefficient of friction m=0.6 was assumed for the fault response, with no cohesion. In the figure, the dark gray regions denote stress states for which the fault would be unstable in the in-situ stress regime. The light gray region shows the expansion of the unstable region due to reservoir pressurization–that is, stress states that are stable under in-situ conditions but unstable when the reservoir is pressurized. From the gas injection simulations, the maximum pressure perturbation at the fault surface was estimated to be approximately 2 MPa.

Depending on the ordering of the principle stress components, we may identify normal faulting, strike-slip, and reverse faulting stress regimes. The triangular shape of figure derives from the assumption that the maximum horizontal stress is greater than the minimum horizontal stress. At this time, our best estimate for the actual stress state at the Leroy site lies somewhere between a strike-slip and normal faulting regime. From the figures, it is clear that the fault is potentially well oriented for slip at realistic stress magnitudes. There is therefore a reasonable likelihood the fault is critically stressed and may represent a permeable pathway. As many of the wellbores at the site pass through this fault plane, there is also some potential for wellbore stability issues.

Clearly, however, nothing definitive can be said without a better estimate of the stress orientations and magnitude for the Leroy site. If the stress is actually rotated closer to the 110 deg. Az. estimate, the fault may in fact be quite stable. It should also be recalled that the fault could be intrinsically permeable even without slip, or relatively impermeable despite being reactivated. Therefore, some care should be taken in interpreting these analyses.

5. Summary and Conclusion

Because of high pressures often associated with natural-gas storage operations in aquifers, gas loss is a possibility via several potential pathways: faults, inadequate caprock seal, or improperly completed wells. Quantitative characterization of the temporal and spatial distribution of potential gas leakage, together with the related uncertainty of reservoir parameters, can provide useful insight and quantitative tools to gas-storage operators to better enable prevention and mitigation of gas leakage. These insights and tools are also useful for analyzing the potential for CO_2 and brine leakage from a geologic CO_2 storage (GCS) site. For this purpose, we developed a comprehensive model framework to investigate the leakage mechanisms and to evaluate the uncertainty due to the lack of knowledge of the reservoir system. The Leroy natural gas storage facility in southwestern Wyoming was chosen to demonstrate the usefulness of our framework and modeling approach, due to its available operating data and information about gas leakage and its subsequent control by the facility operators. A realistic irregular mesh, honoring the faults, layered geological stratigraphy, and surface topography, was built using EVCELL model, upon which a 3-D nonisothermal, multiphase multi-component reservoir model was constructed using the NUFT code to

simulate reservoir pressure and inventory history and natural gas (methane) migration. The reservoir model was validated by virtue of the excellent agreement we obtained between the simulated and recorded histories of reservoir pressure and gas inventory, and by virtue of predicting a gas-arrival time at the ground surface that was consistent with the timing of observed gas bubbling into a creek. The simulated history, as well as the spatial distribution of gas (methane) migration, was analyzed. The possibility of reactivation of the fault by overpressure during the storage operation was also evaluated using the simulated pressure history. Using the PSUADE emulation code, the uncertainty of gas leakage propagated from uncertain hydrogeological input parameters was evaluated based on the "training" data generated by hundreds of reservoir simulations.

Our 3-D reservoir analyses demonstrated the direct dependence of gas leakage on reservoir pressure and confirmed that leakage can be controlled by limiting the operating pressure. Starting in 1981, facility operators took measures to reduce reservoir pressures, resulting in a significant reduction in detected gas leakage. Our simulated results were consistent with those findings, indicating a sharp reduction in leakage rates–to less than 20 MMSCF/year after 1982. Our simulations also showed methane breakthrough at the ground surface occurred around April 1, 1975, which is consistent with the breakthrough-time estimates by the facility operator. The hysteresis curves between bottom-hole pressure and gas inventory indicate leakage was triggered by pressure whenever it exceeds 1700 psi, and that 5.5 BSCF of cushion gas is necessary to support the minimum reservoir pressure of 1400 psi for appropriate gas withdrawal.

Our simulated spatial distributions of methane showed gas leakage occurred via the fault, from the T-10 storage aquifer to the ground surface, as well as through the permeable Nugget Formation overlying the caprock, demonstrating the possibility of both direct reservoir-to-surface leakage and indirect leakage from shallower collector zones in the Nugget Formation. While we focused on evaluating gas leakage through the fault in this study, leaky wellbores could have also contributed to gas migration from the T-10 storage aquifer to the ground surface.

We also analyzed brine leakage from the T-10 storage aquifer, because of its influence on reservoir pressure and its potential influence on the salinity of shallow aquifers. Because brine leakage into the caprock was found to be about an order of magnitude less than into the fault, and because leakage into the caprock occurs diffusely over a very wide area, the caprock is not a likely conduit for brine migrating to shallow aquifers. Hence, the fault is one of two potential pathways for brine leakage from the T-10 storage zone to possibly reach shallow drinking water aquifers (the other being leaky wellbores). However, there was no evidence of brine migration affecting the salinity of shallower aquifers at the Leroy site. Our simulations also showed that the cumulative volumes of brine and gas leakage from the storage aquifer are of similar magnitude, suggesting that brine and gas leakage make similar contributions to pressure relief; moreover, these pressure-relief mechanisms were found to be more significant than that of rock compressibility.

The ranking of the response of accumulated gas leakage and maximum reservoir overpressure to 15 uncertain hydrologic parameters resulted in 7 parameters with a score of zero (no sensitivity) and 8 parameters with finite sensitivity. Of the top 6 ranked parameters, two of them are fault permeability and width, which was expected, and four are related to gas permeability in storage aquifer, which was also expected. The relative sensitivity of fault and caprock permeability indicates that diffusive gas leakage through the caprock is negligible, even when caprock permeability is high enough to be leaky to brine. In general, our results rule out the possibility of a diffuse leakage pathway, such as through the caprock, explaining the observed gas leakage; thus, a discrete pathway, such as through a fault or leaky wellbore, is required. Moreover, if the permeability of the fault zone were low enough (permeability < 10^{-15} m^2) gas leakage would be close to zero without the existence of another discrete gas-leakage pathway, such as leaking wellbores, which will be the focus of future research.

Acknowledgements

This work was sponsored by USDOE Fossil Energy, National Energy Technology Laboratory. The authors want to acknowledge and thank Questar Pipeline for furnishing technical information on the Leroy natural gas-storage

facility. This work was performed under the auspices of the U.S. Department of Energy by Lawrence Livermore National Laboratory under contract DE-AC52-07NA27344.

References

Araktingi, R.E., Benefield, M.E., Bessenyei, Z., Coats, K.H., and Tek, M.R., 1984. Leroy Storage Facility, Uinta County, Wyoming: A case history of attempted gas migration control, Journal of Petroleum Technology, 41(1), 132-140.

Beckman, K.L., Determeyer, P.L., and Mowrey, E.H., 1995. Natural Gas Storage: Historical Development and Expected Evolution: December 1994-February 1995. GRI-95/0214. Gas Research Institute, Houston, TX, June, 1995.

Buscheck, T.A., Glascoe, L.G., Lee, K.H., Gansemer, J., Sun, Y., and Mansoor, K., 2003. Validation of multiscale thermohydrologic model used for analysis of a proposed repository at Yucca Mountain, Journal of Contaminant Hydrology, 62(3), 421-440.

Buscheck, T.A., Sun, Y., Chen M., Hao, Y., Wolery, T.J., Bourcier, W.L., Court, B., Celia, M.A., Friedmann, J.S., and Aines, R.D., 2012. Active CO_2 reservoir management for carbon storage: Analysis of operational strategies to relieve pressure buildup and improve injectivity. International Journal of Greenhouse Gas Control 6, 230-245.

Carrigan, C.R., Heinle, R.A., Hudson, G.B., Nitao, J.J., and Zucca, J.J., 1996. Trace gas emissions on geological faults as indicators of underground nuclear testing, Nature 382(6591), 528-531.

Carroll, S.A., Hao, Y., and Aines, R.D., 2009. Geochemical detection of carbon dioxide in dilute aquifers. Geochemical Transactions 10, 4.

Castle, J.W., Falta, R.W., Bruce, D., Murdoch, l., Foley, J., Brame, S.E., and Brooks, D., 2005. Fracture Dissolution of Carbonate Rock: An Innovative Process for Gas Storage, Topical Report DE-FC26-02NT41299. Clemson University, Clemson, SC.

Dynamic graphics, Inc., 2008. EarthVision 8.0 user manual, Alameda, California.

Hao, Y., Sun, Y., and Nitao, J.J., 2011. Overview of NUFT: a versatile numerical model for simulating flow and reactive transport in porous media, Lawrence Livermore National Laboratory, Groundwater Reactive Transport Models, 213-240.

Heidbach, O., Tingay, M., Barth, A., Reinecker, J., Kurfeß, D. and Müller, B., The World Stress Map database release 2008 doi:10.1594/GFZ.WSM.Rel2008, 2008

Hsieh, H., 2007. Application of the PSUADE tool for sensitivity analysis of an engineering simulation, Lawrence Livermore National Laboratory, UCRL-TR-237205.

Johnson, J.W., Nitao, J.J., and Knauss, K.G., 2004. Reactive transport modeling of CO_2 storage in saline aquifers to elucidate fundamental processes, trapping mechanisms and sequestration partitioning. In: Baines, S.J., Worden, R.H. (Eds.), Geological Storage of Carbon Dioxide, Special Publications, vol. 223. Geological Society, London, 107-128.

Katz, D.L. and Tec, M.R., 1981. Overview on underground storage of natural gas, Journal of Petroleum Technology 33, 9430951.

Lord A.S., 2009. Overview of geologic storage of natural gas with an emphasis on assessing the feasibility of storing hydrogen, Sandia National Laboratory, SAND2009-5878.

Morris J.P., Detwiler, R.L., Friedmann, S.J., Vorobiev, O.Y., and Hao, Y., 2011. The large-scale geomechanical and hydrological effect of multiple CO_2 injection sites on formation stability, International Journal of Greenhouse Gas Control 5, 69-74.

National Energy Technology Laboratory (NETL), 2007.Transmission, distribution, and refining, natural gas storage, http://www.netl.doe.gov/technologies/oil-gas/TDR/Storage/Storage.html, June 27.

Nilson, R.H., Peterson, E.W., Lie. K.H., 1991. Atmospheric pumping: a mechanism causing vertical transport of contaminated gases through fractured permeable media, Journal of Geophysical Research 96(B13), 21933-21948.

Nitao, J.J., 1998. User's manual for the USNT module of the NUFT code, version 2 (NP-phase, NC-component, thermal), Lawrence Livermore National Laboratory, UCRL-MA-130653.

PB-KBB Inc., 1998. Advanced Underground Gas Storage Concepts Refrigerated-Mined Cavern Storage: Final Report. PB-KBB Inc., Houston, TX.

Reidel, S.P., Johnson, V.G., and Spane, F.A., 2003. Natural Gas Storage in Basalt Aquifers of the Columbia Basin: A Guide to Site Characterization, in Gas TIPS, 25-29.

Rocky Mountain Petroleum Consultants, Inc., 1981. Performance study of Leroy gas storage project for Mountain Fuel Supply Company, Unita County, Wyoming.

Sofregaz US, 1998. Leroy natural gas storage history matching, Prepared for Questar Pipeline.

Sun, Y., Tong, C., Duan, Q., Buscheck, T. A., and Blink, J.A., 2012. Combining simulation and emulation for calibrating sequentially reactive transport systems, Transport in Porous Media, DOI 10.1007/s11242-011-99170-4.

Teatini, P., Castelletto, N., Ferronato, M., Gambolati, G., Janna, C., Cairo, E., Marzorati, D., Colombo, D., Ferretti, A., Bagliani, A., and Bottazzi, F., 2011. Geomechanical response to seasonal gas storage in depleted reservoirs: A case study in the Po River basin, Italy, Journal of Geophysical Research-Earth Surface 116.

Tong, C., 2009. PSUADE User's Manual (Version 1.2.0), Lawrence Livermore National Laboratory, LLNL-SM-407882.

Wemhoff, A.P. and Hsieh, H., 2007. TNT Prout-Tompkins kinetics calibration with PSUADE, Lawrence Livermore National Laboratory, UCRL-TR-230194.

Table 1. Thickness and vertical grid resolution of geological formations for the 3-D reservoir model.

Formations[a]	Formation property	Mean thickness (m)[a]	Cell numbers	Cell vertical size (m)
Knight	Overburden	240	6	40
Twin Creek	Limestone aquifer	150	4	38
Nugget	Sandstone aquifer	225	5	45
Ankareh	Seal (caprock)	230	5	46
Thaynes	Seal (caprock)	130	6	22
T-10	Storage aquifer	80	10	8
Woodside	Seal (bedrock)	500	7	70

[a]Note that the mean thicknesses are honored in the 2-D radially-symmetric RZ model.

Table 2. Hydrological parameters of each geological zone are listed for the base case.

Geological Formations	Permeability (m^2)	Porosity	Residual saturation	Van Genuchten *m*	Van Genuchten α (1/Pa)	Solid density (kg/m^3)	Rock compressibility (1/Pa)
Knight	2.5×10^{-14}	0.2	0.3	0.46	5.1×10^{-5}	2000	4.5×10^{-10}
Twin Creek	1.0×10^{-16}	0.1	0.3	0.46	5.1×10^{-5}	2300	4.5×10^{-10}
Nugget	1.0×10^{-14}	0.2	0.3	0.46	5.1×10^{-5}	2500	4.5×10^{-10}
Ankareh	1.0×10^{-17}	0.1	0.3	0.46	5.1×10^{-5}	2300	4.5×10^{-10}
Thaynes	1.0×10^{-17}	0.1	0.3	0.46	5.1×10^{-5}	2500	4.5×10^{-10}
T-10[a]	1.76×10^{-13}	0.138	0.2	0.225	5.1×10^{-5}	2500	4.35×10^{-10}
Woodside	1.0×10^{-17}	0.1	0.3	0.46	5.1×10^{-5}	2200	4.5×10^{-10}
Fault zone[b]	1.0×10^{-13}	0.3	0.01	0.633	1.0×10^{-3}	2300	4.5×10^{-10}

[a]T-10 aquifer parameters are adapted from Sofregas US (1998); The parameters for the other geological formations were evaluated and determined to be reasonable in the RZ model parameter sensitivity study (Section 4.1.1).
[b]Permeability of fault zone within the caprock (Thaynes and Ankareh Formations) is 10^{-14} m^2.

Table 3. Hydrological parameter range, distribution and ranking are listed for the global sensitivity parameter-ranking analyses of reservoir behavior.

Parameter	Range		Distribution	Accumulated gas leakage		Maximum ΔP	
	Low	High		Score	Rank	Score	Rank
1. Fault zone permeability (m^2)[a]	1.0×10^{-14}	1.0×10^{-12}	log-uniform	57.7	4	71.5	3
2. Storage formation permeability (m^2)	1.0×10^{-14}	1.0×10^{-12}	log-uniform	100.0	1	100.0	1
3. Caprock permeability (m^2)	1.0×10^{-18}	1.0×10^{-16}	log-uniform	9.4	7	3.0	8
4. Fault zone van Genuchten α (1/Pa)	1.0×10^{-4}	1.0×10^{-2}	log-uniform	0.0	12	0.0	9
5. Storage formation van Genuchten α (1/Pa)	1.0×10^{-6}	1.0×10^{-4}	log-uniform	0.0	14	0.0	12
6. Fault zone van Genuchten *m*	0.1	0.9	uniform	9.1	8	0.0	14
7. Storage formation van Genuchten *m*	0.1	0.9	uniform	76.3	2	93.8	2
8. Fault zone porosity	0.05	0.5	uniform	0.0	15	0.0	15
9. Storage formation porosity	0.05	0.5	uniform	24.9	6	38.7	5
10. Fault zone residual liquid saturation	0.01	0.1	uniform	0.0	13	0.0	10
11. Storage formation residual liquid saturation	0.05	0.5	uniform	0.0	11	16.2	7
12. Storage formation residual gas saturation	0.02	0.2	uniform	58.8	3	46.2	4
13. Storage formation compressibility (1/Pa)	1.0×10^{-10}	1.0×10^{-9}	uniform	0.0	9	0.0	11
14. Caprock compressibility (1/Pa)	1.0×10^{-10}	1.0×10^{-9}	uniform	0.0	10	0.0	13
15. Fault zone width factor[b]	0.1	1.0	uniform	26.4	5	37.8	6

[a]A wider range of fault-zone permeability (1.0×10^{-16} to 1.0×10^{-12}) was considered in Section 4.1.2.4.
[b]The fault zone widths are multiplied by fault width factor with the original values (average = 60 m).

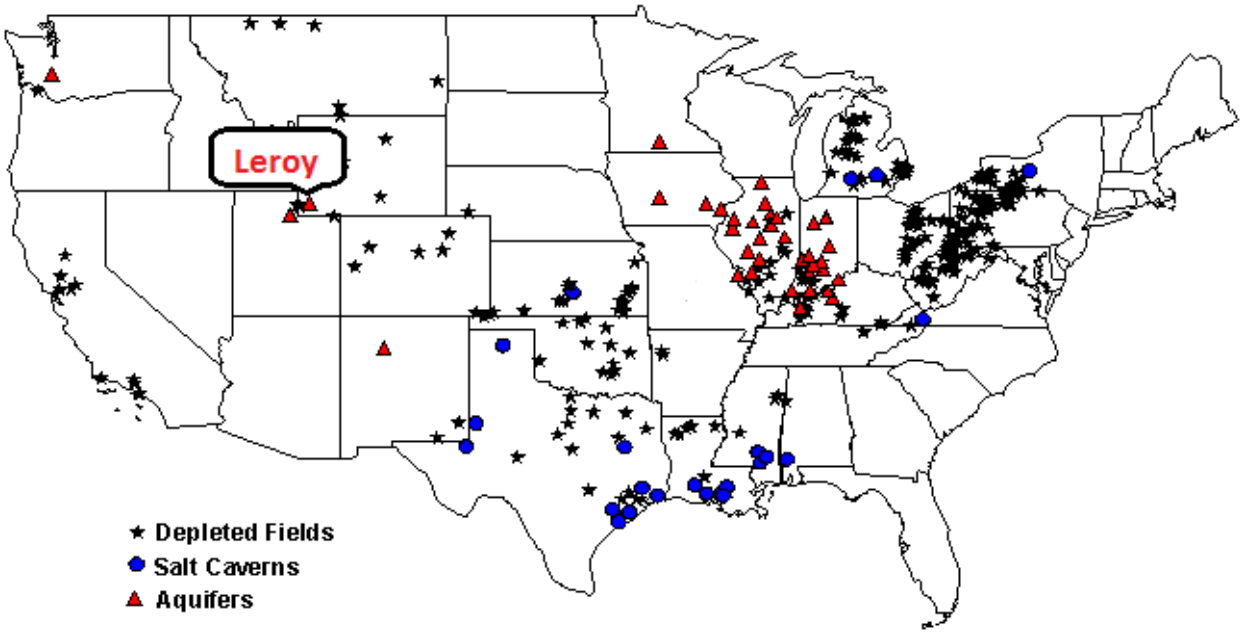

Fig. 1. Underground natural gas storage facilities in the lower 48 states of the United States. This figure is modified from Energy Information Administration (EIA), EIA GasTran geographic information system underground storage database.

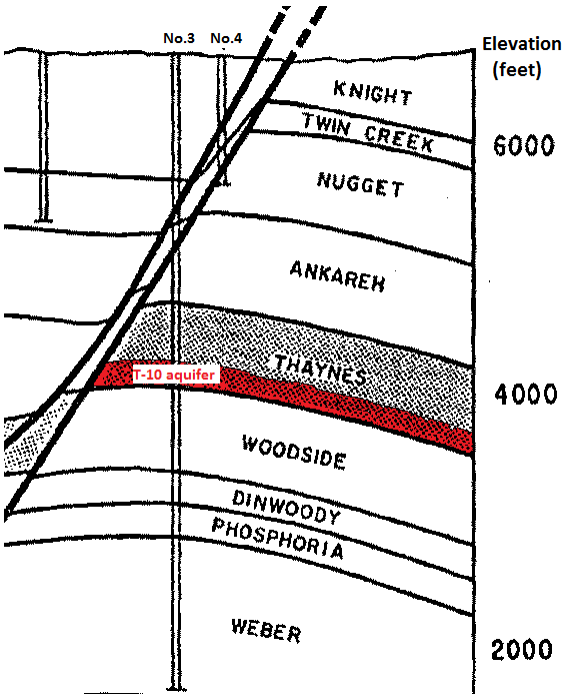

Fig. 2. Lithologic cross section and stratigraphic sequence in Leroy gas storage site. This figure is modified from Rocky Mountain Petroleum Consultants, Inc., 1981.

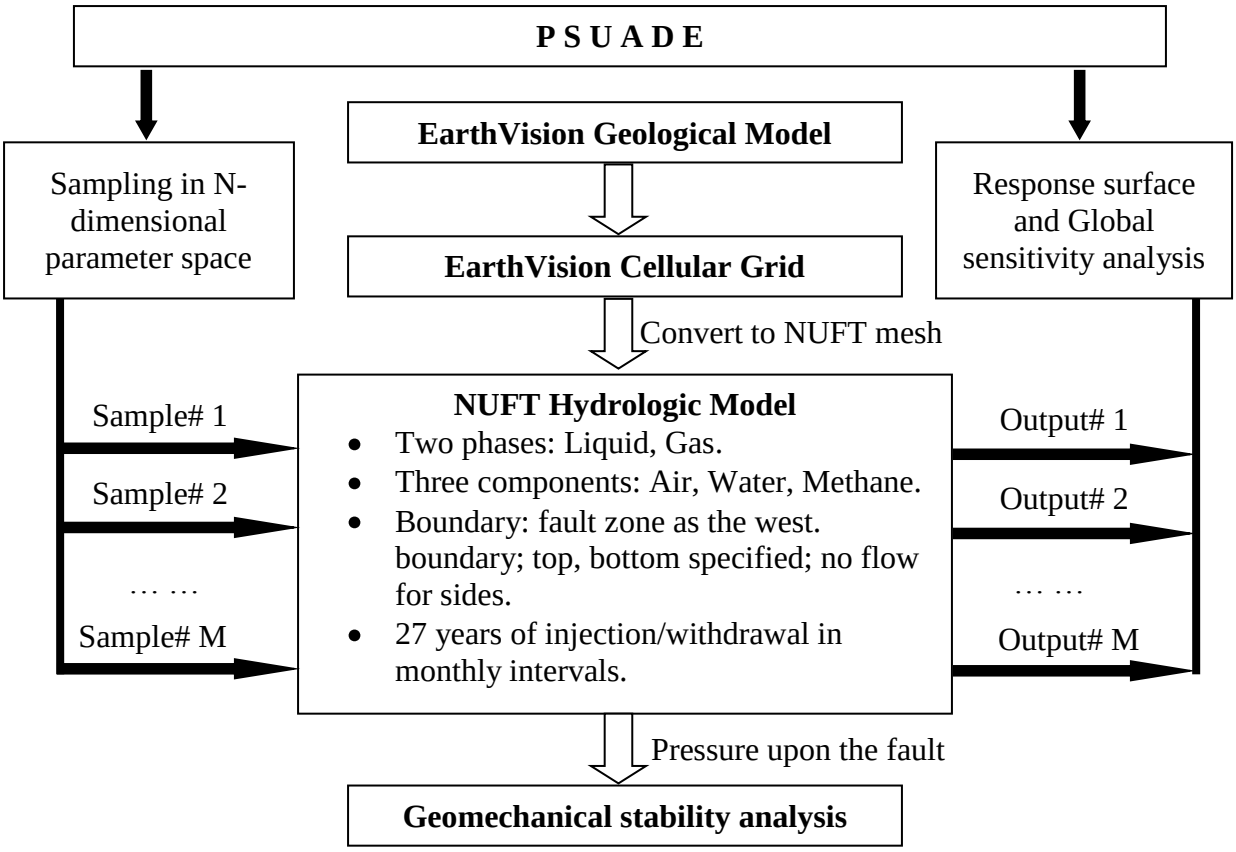

Fig. 3. The model methodology flow chart is shown.

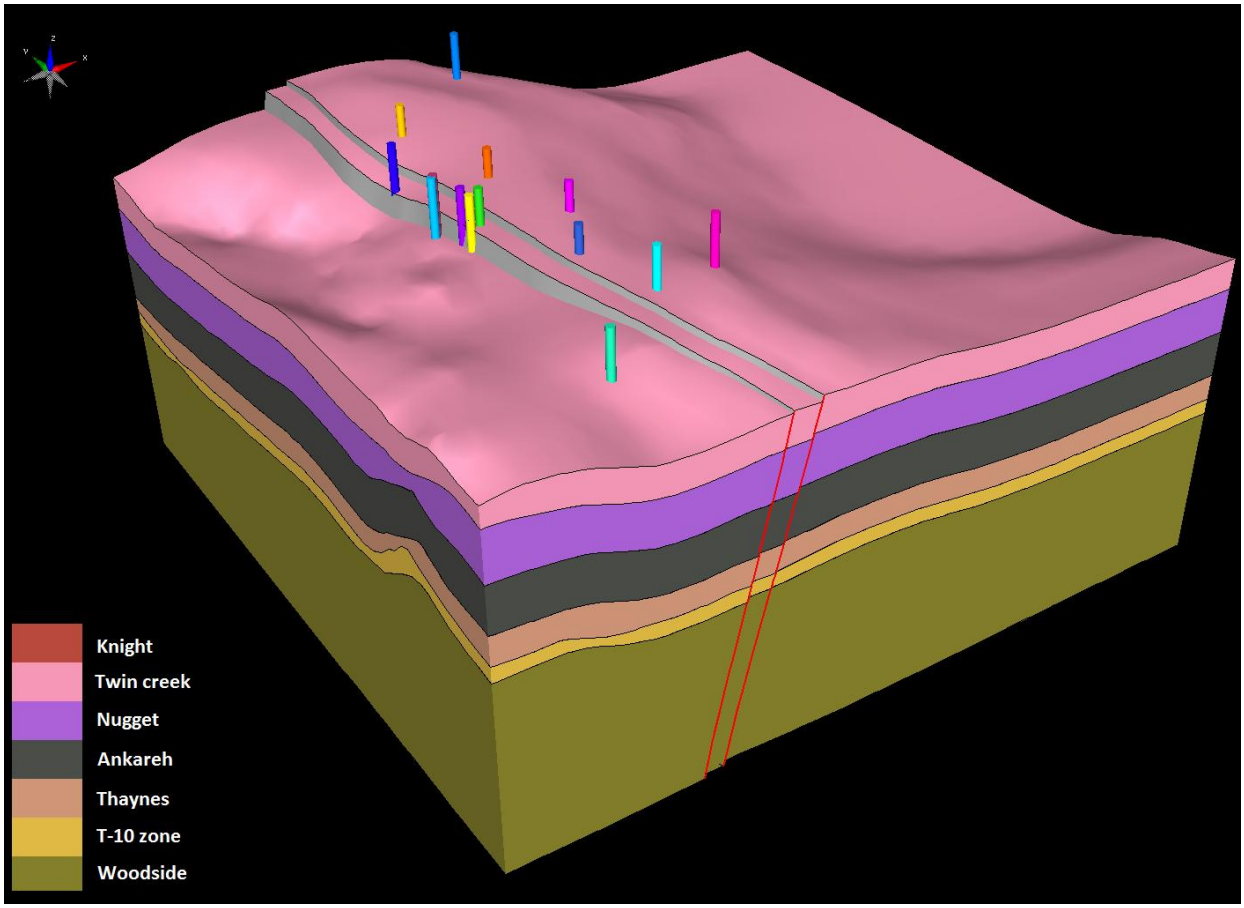

Fig. 4. EarthVision geological framework model is shown for the Leroy gas storage facility. The overburden (Knight Formation) is removed to show the location of injection/production wells and underneath horizons. The storage aquifer (T-10 zone) is formed east of the fault at the depth of 900m. The red lines outline the fault zone.

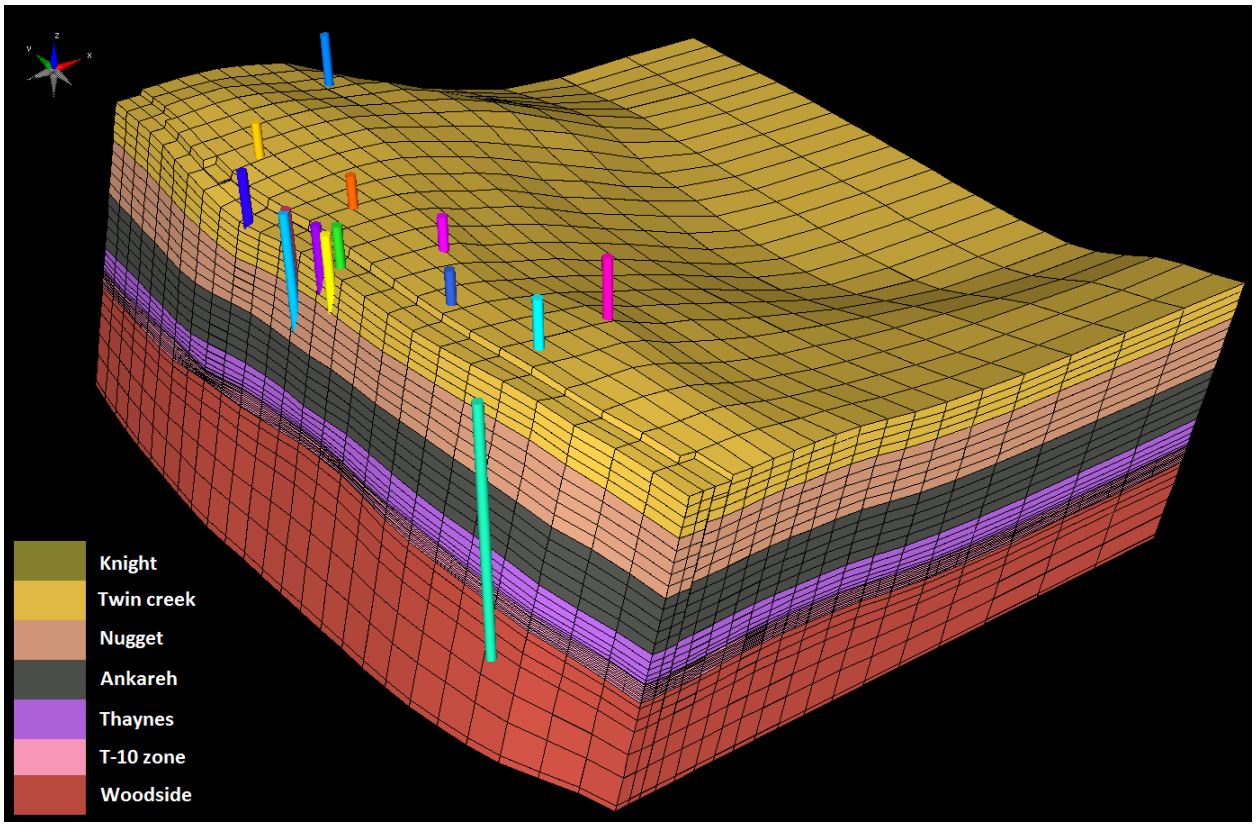

Fig. 5. Cellular grid built on the geological structure is shown. The geology to the west of fault zone is not included in the numerical mesh because the fault is considered to be the western boundary of the model. The overburden (Knight Formation) is removed to show the wells and underneath horizons. The cells are aligned to be conformal to geological layer and fault plane (70^{o} dipped).

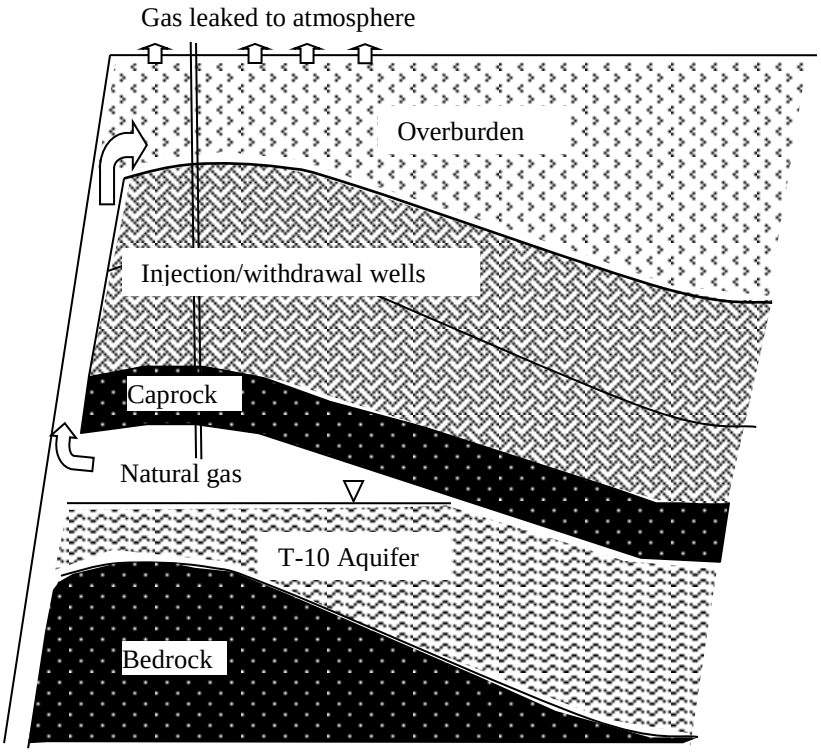

Fig. 6. Cross-sectional view of the Leroy aquifer gas storage is shown, including the direction of gas migration through the fault.

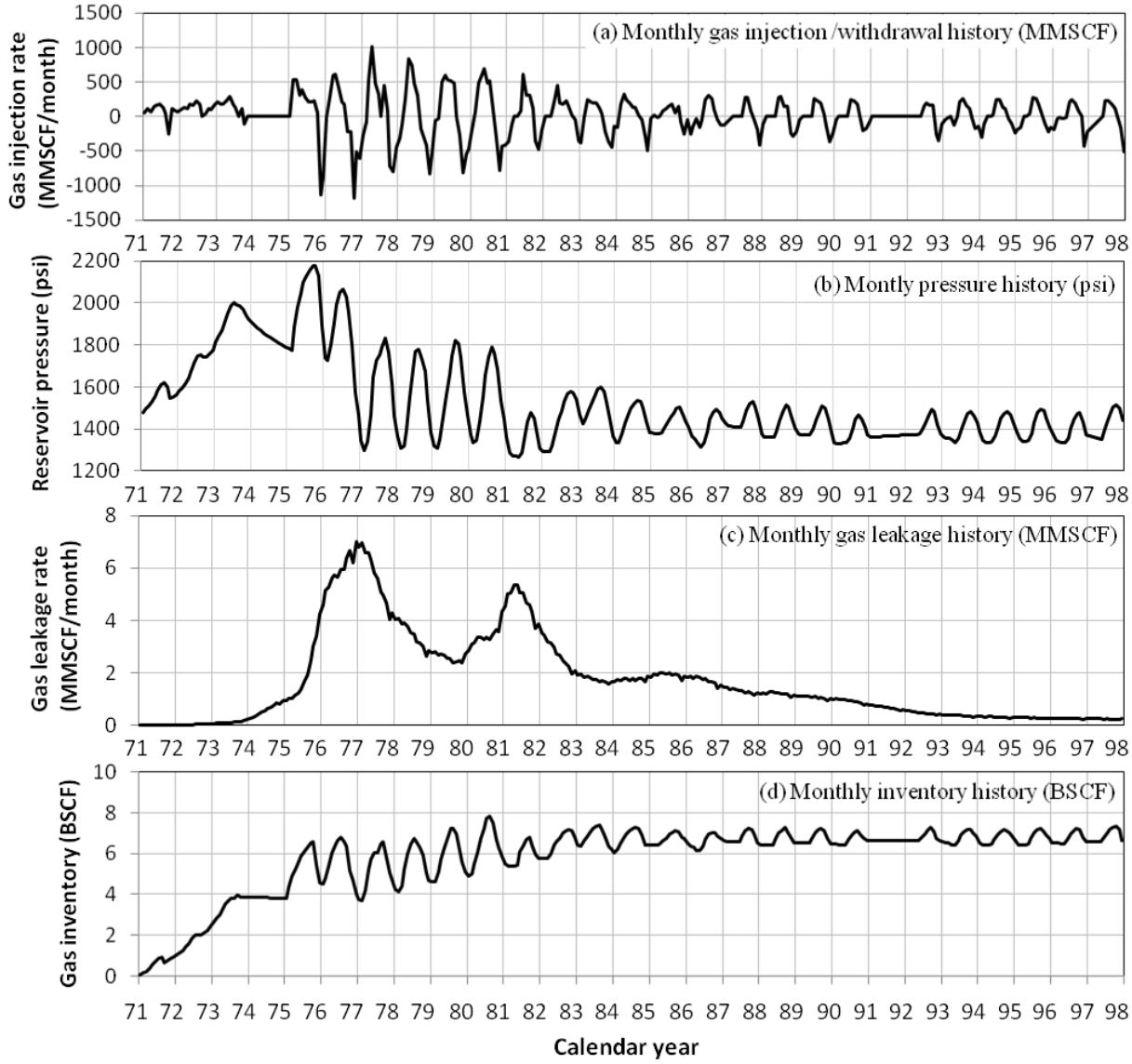

Fig. 7. Time histories are plotted of (a) monthly gas injection/withdrawal summed over 10 wells, (b) simulated reservoir pressure, (c) simulated gas leakage rate at the ground surface, and (d) simulated gas inventory. Positive injection rates correspond to net injection and negative injection rates correspond to net withdrawal. BSCF and MMSCF stand for Billion and Million Standard Cubic Feet, respectively. The calendar-year time axis corresponds to May 1 of that year.

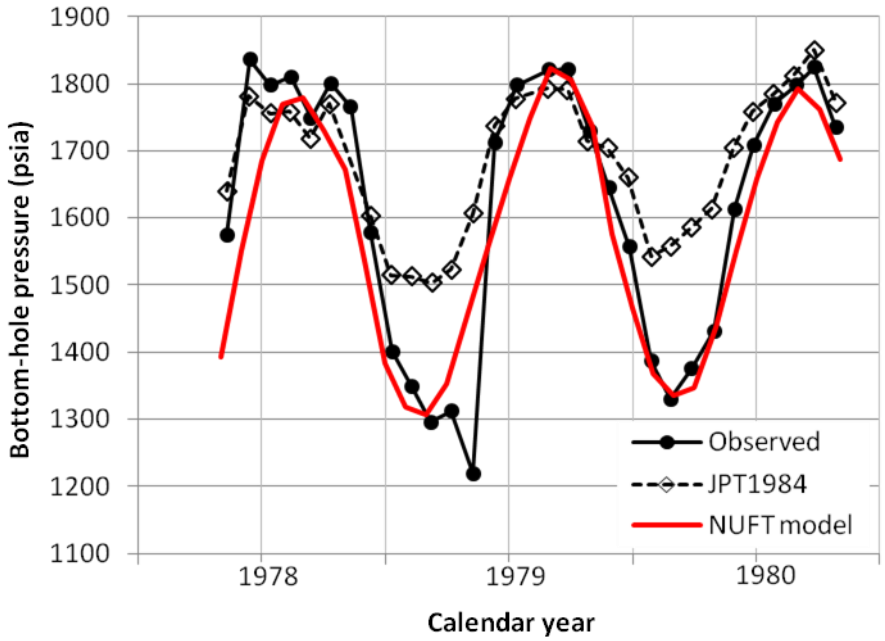

Fig. 8. Simulated bottom-hole pressure (BHP) history in the T-10 aquifer-storage zone is compared with that simulated by Araktingi et al. (1984) and field data. The calendar-year time axis corresponds to April 1 of that year.

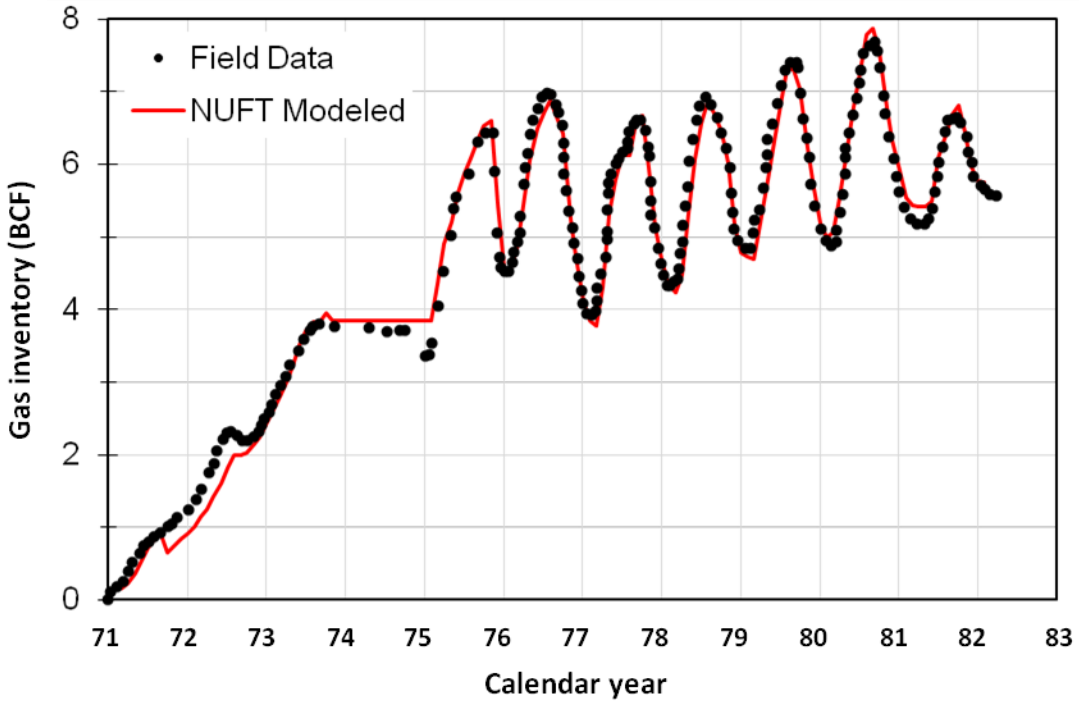

Fig. 9. Simulated gas-inventory history is compared with analyzed field data. BCF stands for Billion Cubic feet.

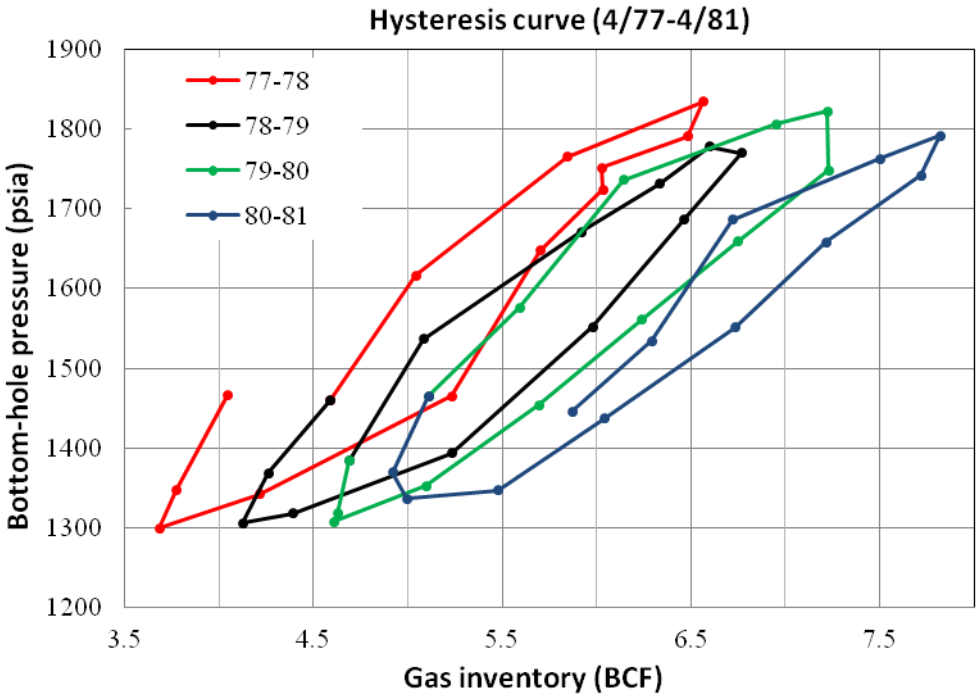

Fig. 10. Simulated cycle of reservoir bottom-hole pressure (BHP) versus gas inventory is plotted for the 1977-1981 season.

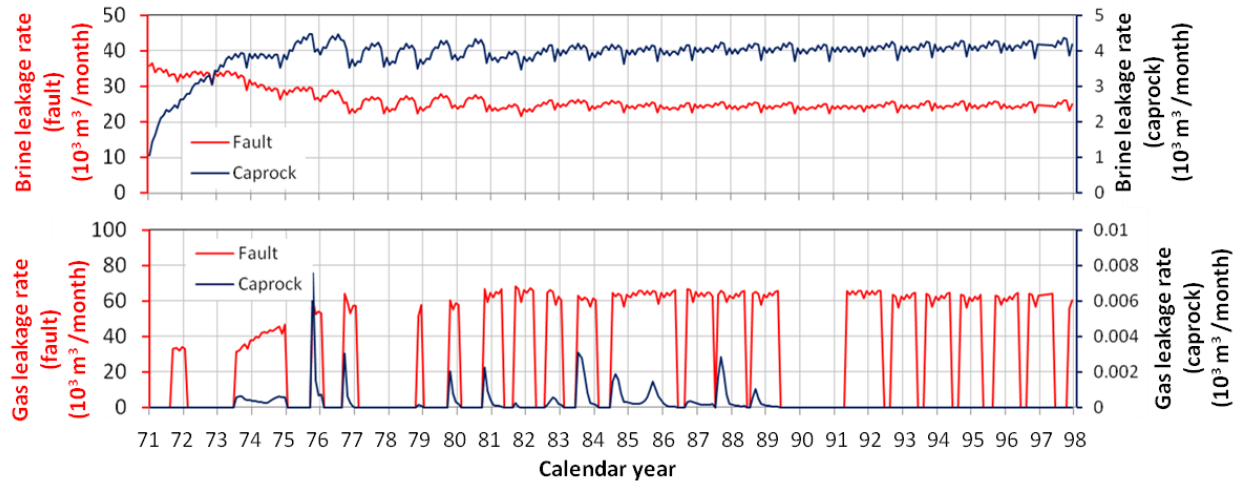

Fig. 11. Time histories are plotted for the monthly rates of (a) brine leakage and (b) gas leakage. The leakage rates are broken down into the leakage into the fault zone and into the caprock, where the leakage rates are determined at the horizon at the top of the T-10 storage reservoir (base of the caprock). The time axis corresponds to calendar year, on May 1 of that year.

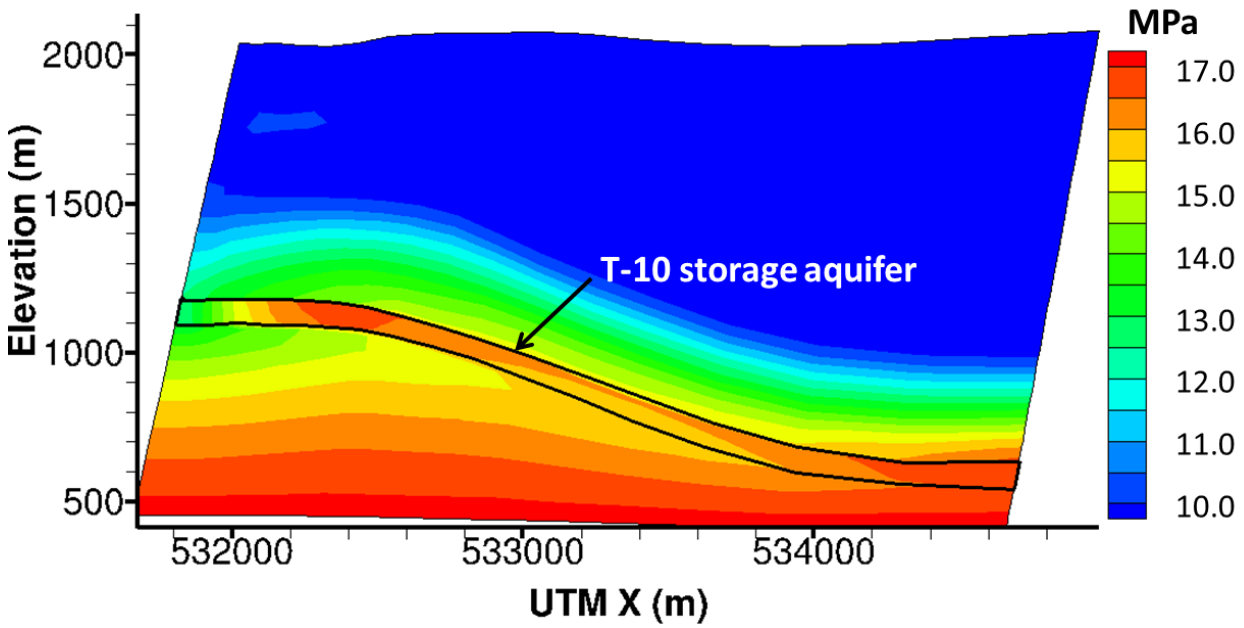

Fig. 12. Vertical east-west cross-section of simulated gas pressure (MPa) is plotted for 10/01/1975, which is when reservoir pressures reached the all-time peak. The T-10 aquifer-storage zone is outlined in black.

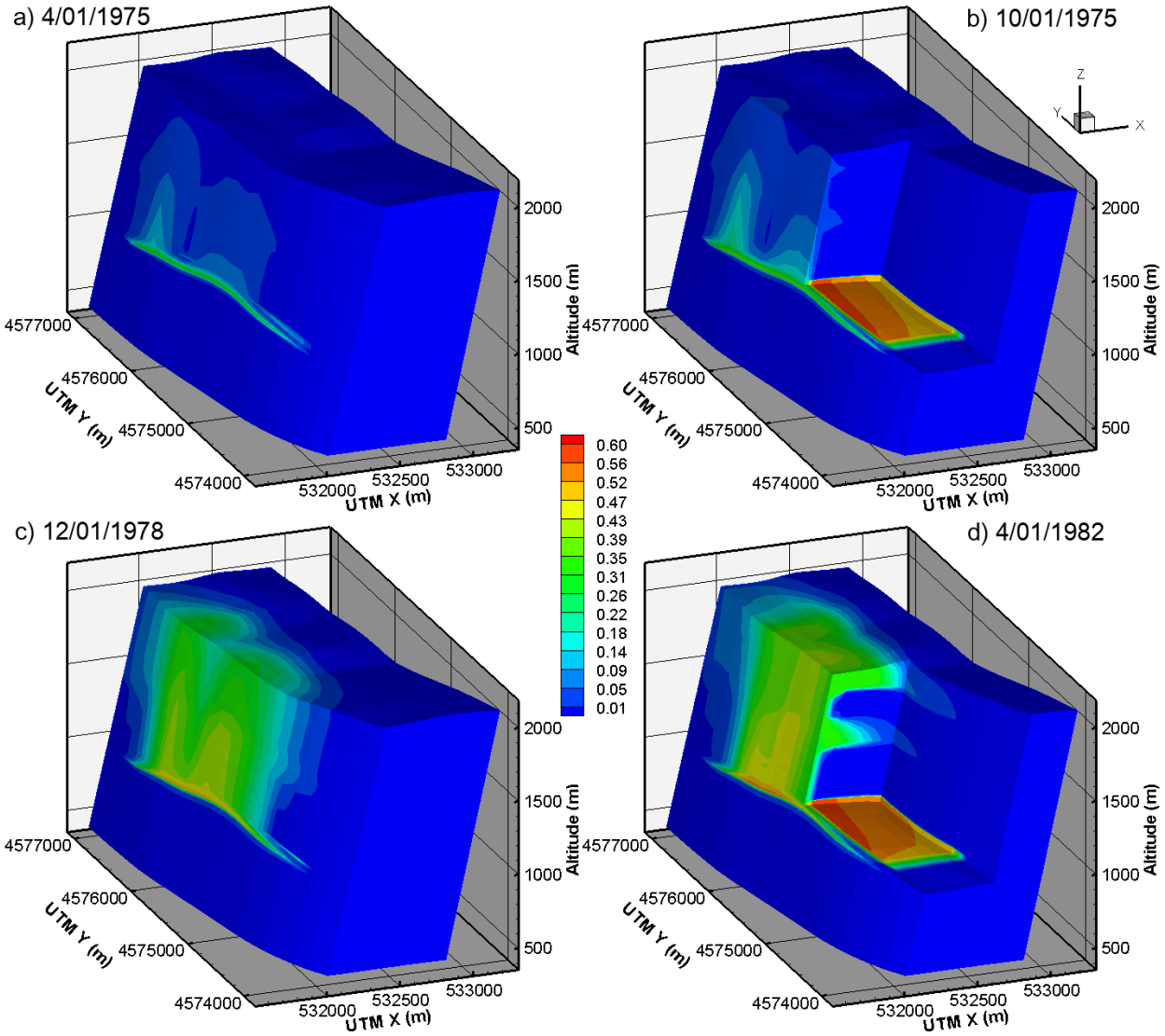

Fig. 13. Three-dimensional contour of simulated mole fraction of methane in gas phase is plotted for (a) 4/1/1975, (b) 10/1/1975, (c) 12/1/1978, and (d) 4/1/1982.

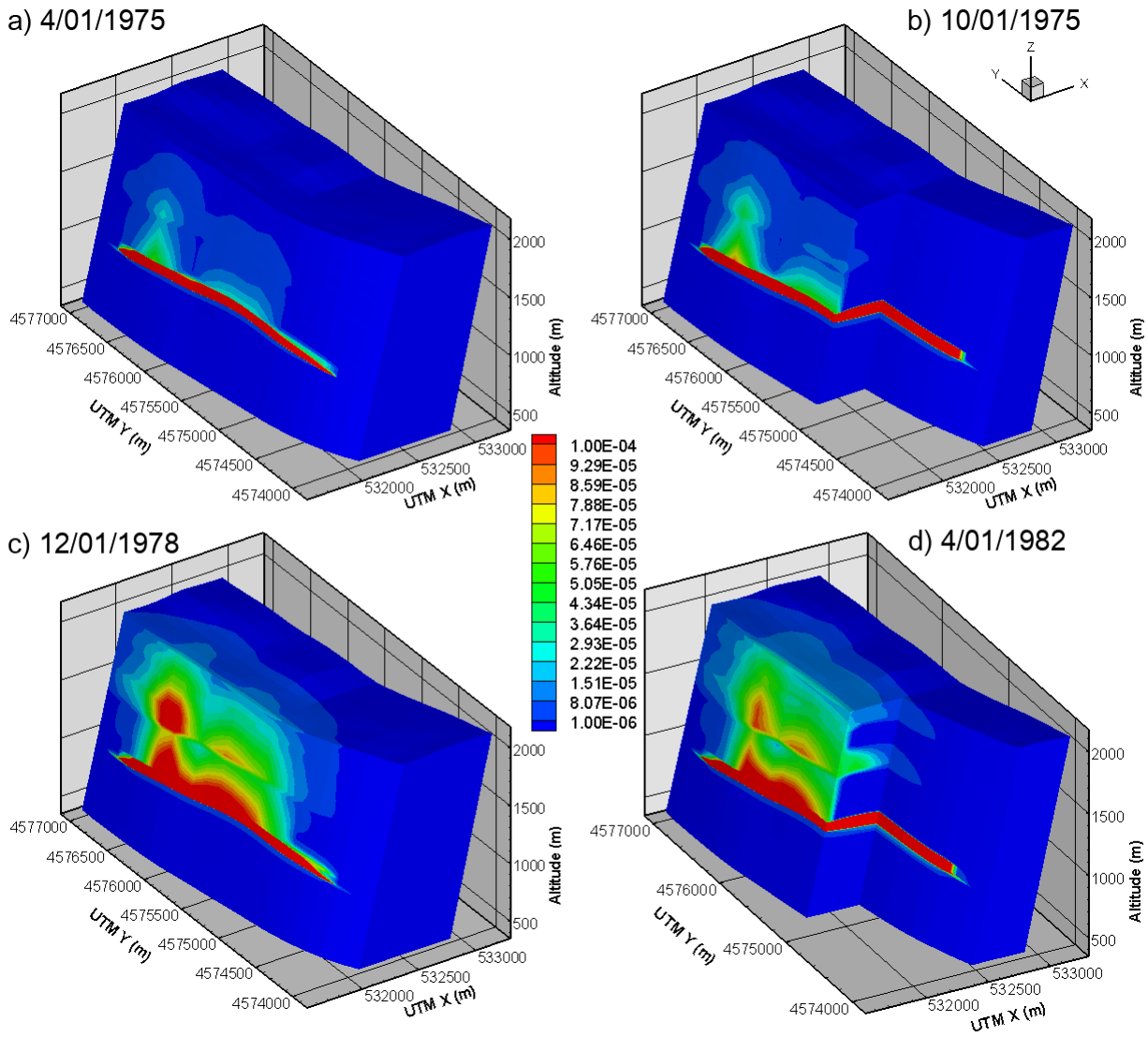

Fig. 14. Three-dimensional contour of simulated mass fraction of methane over the total rock mass is plotted for (a) 4/1/1975, (b) 10/1/1975, (c) 12/1/1978, and (d) 4/1/1982.

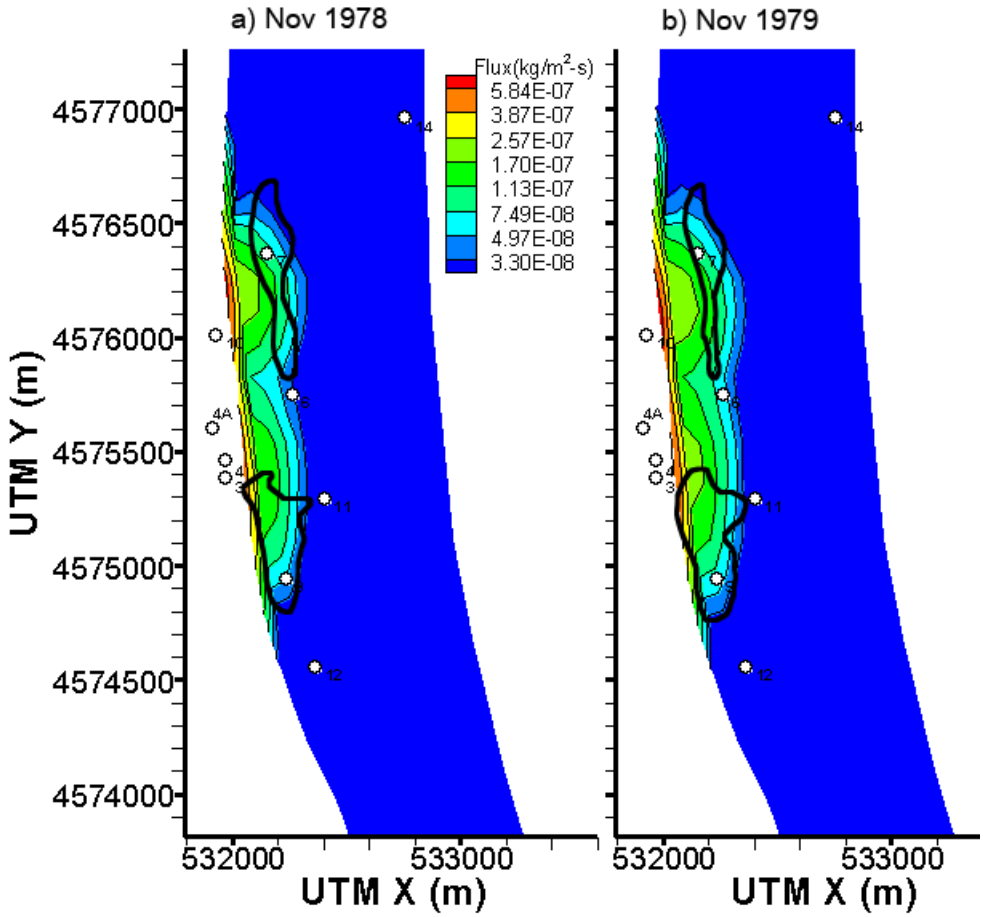

Fig. 15. Contour maps of simulated natural gas leakage to the ground surface are plotted for (a) November 1978, and (b) November 1979. The leakage rate is area-averaged. The locations of injection/withdrawal wells are shown as white circles. The areas encircled by bold solid black lines correspond to the footprint of gas leakage at the ground surface detected by the site operator: Mountain Fuel Supply Company (now Questar), at the indicated times (Rocky Mountain Petroleum Consultants, Inc., 1981).

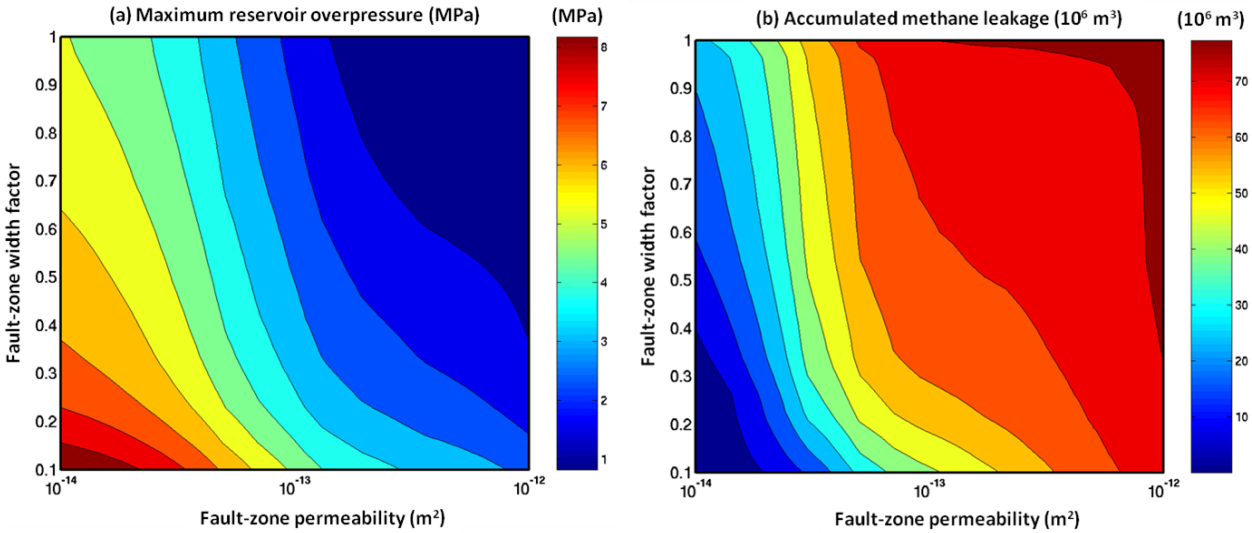

Fig. 16. Response surfaces of sensitivity to fault-zone permeability and width factor are plotted for (a) maximum overpressure, and (b) accumulated methane leakage. The average fault-zone width is equal to 60 m, multiplied by the fault width factor.

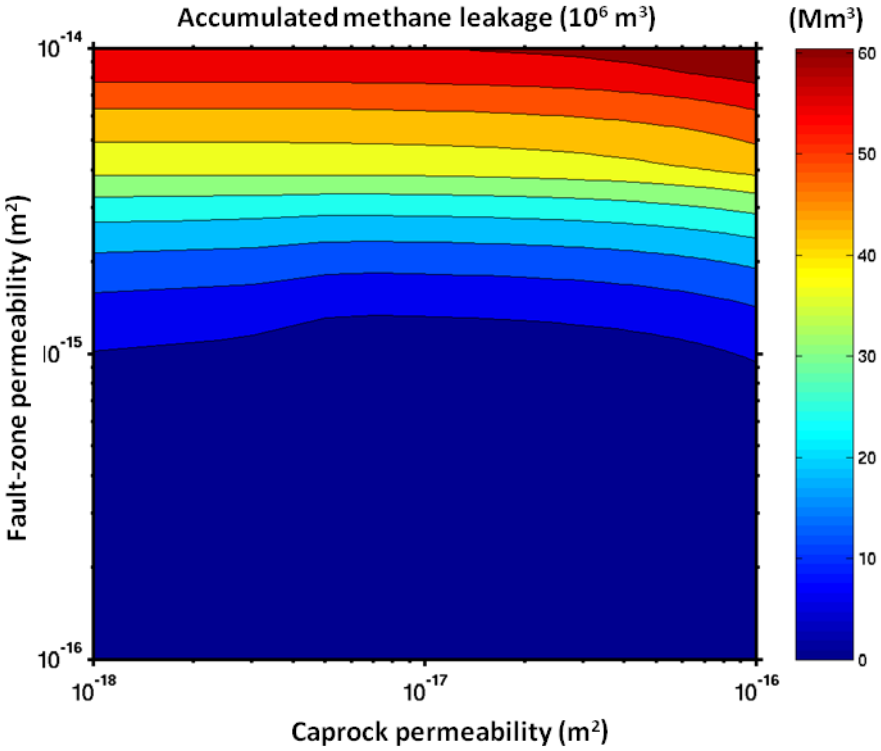

Fig. 17. Response surface of accumulated methane leakage is plotted as a function of caprock and fault permeability.

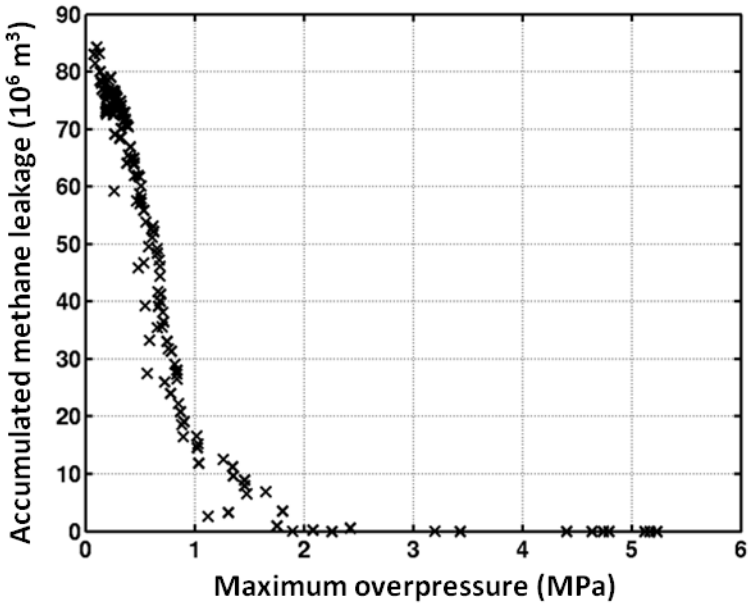

Fig. 18. Scatter plot of accumulated methane leakage versus maximum overpressure is shown. This scatter plot is for the 200 samples used to generate Fig. 17.

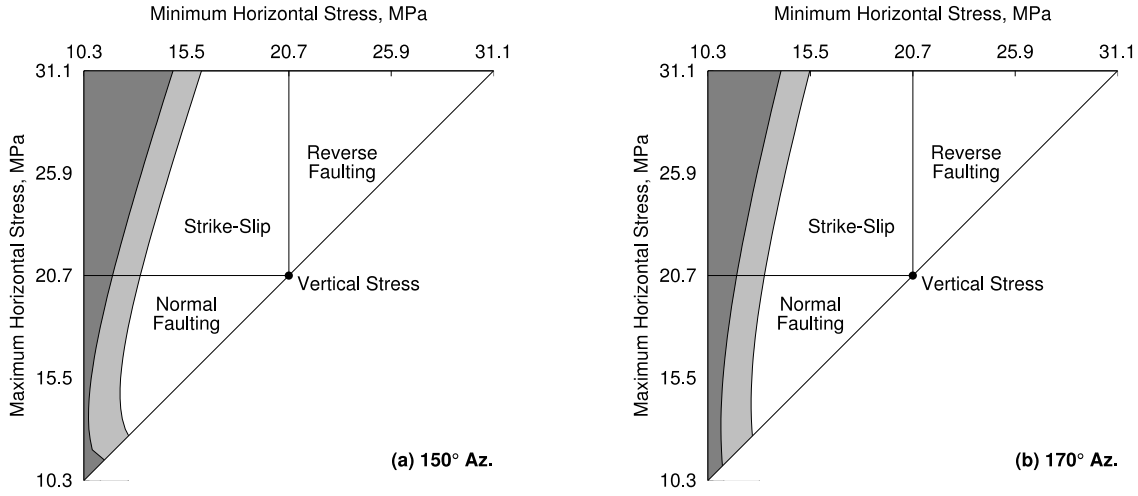

Fig. 19. Assessment of the potential for fault reactivation is shown for given in-situ stress assumptions, including maximum horizontal stress oriented at (a) 150 deg. Az and (b) 170 deg. Az. The dark grey region indicates stress states that would lead to an unstable fault in the in-situ stress regime, while the light gray region shows the expansion of this unstable region due to reservoir pressurization. The white areas in the figures are stable stress regimes. Depending on the ordering of the principle stress components, we may identify normal faulting, strike-slip, and reverse faulting stress regimes. The triangular shape of figure derives from the assumption that the maximum horizontal stress is greater than the minimum horizontal stress.

Appendix D

Los Alamos National Laboratory Final Report

LA-UR Draft

ZERT II Final Scientific Report

DE-FE0000397

Los Alamos National Laboratory

AUTHORS: Rajesh Pawar, Elizabeth Keating, Sharad Kelkar, Hari Viswanathan, Zhenxue Dai

ABSTRACT: This report summarizes results of the work performed at Los Alamos National Laboratory (LANL) for the the Center for Zero Emission Research and Technology–II (ZERT-II). LANL's activities were focused on two topics:

- Characterization of impact of leakage of CO_2 and deeper brines on groundwater quality through natural analogs.
- Coupled fluid-flow and stress simulations to characterize geo-mechanical response of CO_2 injection.

We have used an integrated approach combining field observations at a natural analog site in Chimayo (NM), laboratory experiments and numerical simulations to characterize impacts of CO_2 and brine migration on shallow groundwater quality. We focused on two trace metals, Uranium and Arsenic. Results of our work show that in certain geochemical environment the reactivity of pure CO_2 will not be sufficient to mobilize trace metals such as Uranium and Arsenic beyond background levels. Results of this work were published in two manuscripts, Viswana et al. (2012) and Keating et al. (2013). We have developed capabilities in LANL's FEHM reservoir simulator that are necessary to understand and characterize potential of shear failure and resulting changes in permeability in faults at a CO_2 sequestration site. The capabilities have been validated against field data. These capabilities have been subsequently applied to a number of problems which are part of other CO_2 sequestration projects at LANL and have led to multiple publications on related topics. We have presented results of our work at major conferences including the AGU Fall Meeting, ARMA, GSA meeting and IEAGHG network meetings.

EXECUTIVE SUMMARY: Los Alamos National Laboratory's (LANL) activities for the Center for Zero Emission Research and Technology–II (ZERT-II) were focused on the scientific basis for predicting the performance of engineered geologic CO_2 storage sites. LANL's approach involved using theory, observation, experiment and simulation to characterize the fundamental processes that control large-scale injection and the long-term fate of CO_2 in the subsurface. Specifically, LANL's activities were focused on two topics:

- Characterization of impact of leakage of CO_2 and deeper brines on groundwater quality through natural analogs.
- Coupled fluid-flow and stress simulations to characterize geo-mechanical response of CO_2 injection.

While there have been a number of major milestones achieved as described in the quarterly reports, two of the major accomplishments resulting from LANL's efforts include:

- One of the few field studies to-date focused on understanding impact of CO_2 leakage on shallow groundwater chemistry. Two major conclusions of the study are as follows: the impact of co-contaminants transported with deeper brine on shallow groundwater quality is likely to be much larger than that of the CO_2 and CO_2-induced geochemical reactions and in certain geochemical environment the reactivity of pure CO_2 will not be sufficient to mobilize trace metals such as Uranium and Arsenic beyond background levels.
- Development of the capabilities to simulate the shear failure and associated change in permeability resulting from the geomechanical impacts of large-scale injection of CO_2. These capabilities have been validated against field data.

Approach:

Task 1. Characterization of impact of CO_2 and deeper brine on groundwater quality: We have used a natural analog site in Chimayo, NM to characterize the impact of CO_2 and deeper brine on shallow groundwater quality. Our work was focused on understanding and characterizing behavior of two trace metals, Uranium and Arsenic, due to leakage of CO_2 and deeper brine. Previous quarterly reports have described results to-date related to this effort. We used an integrated approach combining field observations of trace metal concentrations at Chimayo site, laboratory experiments and reactive transport simulations. The uranium focused work was extension of work initiated during ZERT-I and was primarily focused on numerical simulations. The Arsenic study was focused to determine if a set of chemical processes similar to Uranium can be used to model another important trace metal or if a new set of reactive transport processes is required. As with Uranium, Arsenic data exists in the form of laboratory experiments performed at LANL and at NETL. Field observations of arsenic concentration also exist at the Chimayo site. As with Uranium, we developed site-specific batch, 1-D and 3-D reactive transport models to describe the fate of Arsenic at Chimayo. We used inverse geochemical modeling to interpret batch experiment results and field observations on arsenic sorption reactions. The modeling was performed using Phreeqc. We identified the general geochemical reactions for arsenic sorption. The modeling was then used to identify the sorption and cation exchange parameters from batch experiments. Then the field chemical observation data from Chimayo were interpreted to identify the sources of arsenic in field. With the geochemical reaction parameters estimated from the inversion of the batch experiment, we re-do the inversion

of the arsenic reactive transport at the Chimayo site for estimating the recharge concentrations of the major chemical components from the deep aquifer. Results of the inverse modeling were subsequently used to develop a field scale reactive transport model for Chimayo site.

Task 2. Coupled flow and stress simulation capability development: The goal of this task was to extend the coupled flow and stress simulation capabilities in LANL's FEHM simulator specifically for applications related to geomechanical impacts resulting due to large-scale injection at a CO_2 sequestration site. Our focus was to develop a model to simulate permeability changes due to shear failure using Mohr-Coulomb failure criteria and demonstrate how this capability can be potentially used to simulate flow-induced micro-seismicity. We also developed capability to implicitly solve the fluid flow and stress equations, which does not exist in most of the current reservoir simulators.

Shear failure simulation capability development. The intent is to model permeability changes resulting from shear failure along either pre-existing fault planes specified by the user or the plane that maximizes the value of the excess shear stress (τ_{excess})given by

$$\tau_{excess} = |\tau| - S_o + \mu * \sigma$$

where $|\tau|$ is the absolute value of the shear stress on a plane, σ is the effective stress normal to that plane, S_o is shear strength, and μ is the coefficient of friction on the plane. The maximum value of the excess shear stress τ_{excess} is given by (Jaeger and Cook, 1979)

$$\tau_{excess}(\max) = \frac{1}{2}(\sigma_1 - \sigma_3)(\mu^2 + 1)^{1/2} - \frac{1}{2}\mu(\sigma_1 + \sigma_3)$$

and occurs at an orientation β with respect to the maximum principal stress (σ_1) given by

$$\tan(2\beta) = -\frac{1}{\mu}$$

Here σ_3 is the minimum principal stress at the point. For the sake of simplicity, it is assumed that the principal axis of the permeability tensor coincide with those of the stress tensor. When the failure criteria is satisfied, the principal permeabilities are multiplied by a user specified factor as a function of the excess shear stress and then the permeability components along the grid axis are calculated. The failure model was coupled with a permeability-Young's modulus model allowing for material softening and permeability enhancement upon failure. The multiplication factor is ramped over a user specified range of the excess shear stress to avoid step changes. The Young's modulus is decreased by a user specified factor in an analogous manner. We exercised the flow-heat transfer-deformation coupling modules using a permeability-stress model with shear failure using Mohr-Coulomb criteria. This testing was done in an explicitly coupled mode, where the stresses calculated from the previous time step were used for evaluating the permeabilities at the current time step. The approach and model was validated against field data. Given that there is currently no field data available for testing models for coupled fluid flow and deformation coupling, we tested the model with data available for an enhanced geothermal system field test. Although not a CO_2 sequestration study, the site was chosen as an analogue because the site has been well characterized and field data were available

from a hydro-stimulation treatment that involved shear-induced permeability enhancement. The data allowed excellent opportunity to test the newly developed model.

Next, we demonstrate a methodology that employs the stress and damage mechanics modeling capability in FEHM, and integrates these with an ensemble of seismic source terms generating synthetic data. The aim is to model the statistical behavior of induced seismicity, e.g., time-decay, maximum magnitude, and to make predictive statements for proposed operations. Specifically, we wish to model three features of (injection) induced seismicity: (i) a building rate of seismicity as injection operations begin and accelerate; (ii) the limiting, or maximum rate associated with a given injection pressure/flow rate; and (iii) the time decay once injection operations cease (Figure 1).

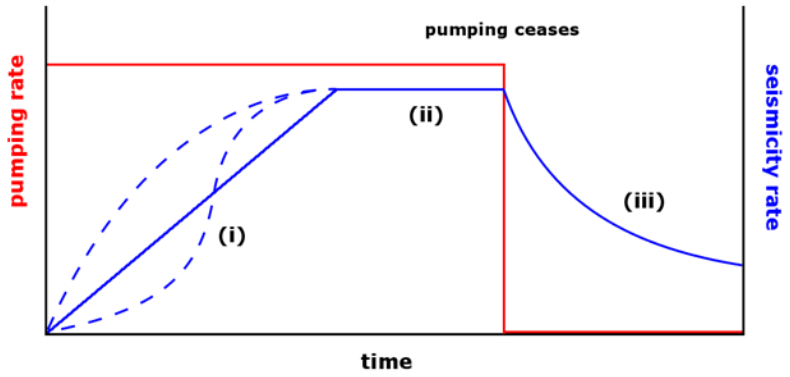

Figure 1. Conceptual relationship between injection (pumping) rate (red line) and induced seismicity (blue line). (i) Seismicity build as injection gets underway (dashed curves are alternative increases), (ii) stabilizes at some rate, and (iii) dies off when pumping ceases.

It has been recognized that seismic activity is typically linked with frictional failure upon fault or fracture surfaces (NRC, 2012). Our conceptual model is that energy released in the form of induced seismicity represents 'in-place' energy that pre-dates injection operations. In other words, the injected fluid acts as a trigger that releases the mechanical energy already in place. The in-place energy is derived from tectonic loading of the crust. This loading occurs over long time-scales; for much shorter operational time-scales, the initial in-place energy will be considered constant. As a consequence, a given volume of rock can only contribute a *limited* amount of seismic energy (and thus induced seismicity). Failure is accompanied by displacement on the failure surfaces, as well as a reduction in the level of stress, called stress drop. A small fraction of the available mechanical energy is radiated as seismic energy and the rest is dissipated in the earth's crust (Dempsey et al., 2012). The fraction of the available mechanical energy that is converted to seismic energy, called 'seismic efficiency' is believed to be in the range of 0.01 to 0.05 (McGarr, 1994). While the triggering mechanism itself depends on the engineering activities; the stress drop, shear slip and the seismic efficiency depend upon the site specific state of earth stress, rock properties and fault properties. The change in the mechanical energy (ΔE) in a volume can be written as

$$\Delta \mathrm{E} = \Delta \int \sigma . \varepsilon \, \mathrm{dV} = \Delta \int \mathrm{D} \cdot \epsilon \cdot \epsilon \, \mathrm{dV}$$

where, Δ denotes a change in the quantity, and ϵ, σ, D are the strain, stress, elasto-plastic coefficient tensors respectively. Thus changes in the mechanical energy can result from changes

in the displacement field in the formation, changes in the state of stress, or changes in the material properties of the formation.

Furthermore, upon satisfaction of a suitable failure criterion, this energy is not released 'all-at-once', but rather as the main shock of some magnitude M followed by a series of aftershocks with diminishing magnitudes. The greatest rate of seismic energy radiation occurs immediately following failure, and decreases with time. A probabilistic law, the so-called Gutenberg-Richter distribution (Gutenberg and Richter, 1944), is used to constrain the distribution of earthquake magnitudes

$$\lambda(M) \propto 10^{-bM}$$

where, λ is the probability of getting an earthquake of magnitude M and b is a site specific phenomenological coefficient with a value often in the neighborhood of 1. For tectonically induced earthquakes, the combined Omori- Gutenberg-Richter law is typically modified by a productivity factor, $A = 10^{\alpha M_{main}}$, that expresses increased aftershock rates associated with larger main shocks, (Helmstetter et al., 2005)

$$\lambda(t, M, A) = A.10^{-\beta M}.(t + c)^{-p}$$

For the case of induced seismicity, the mechanism for raised seismic activity is an ongoing engineering activity, as opposed to a single tectonic event. The productivity factor, A, can't be calculated from an observed main shock magnitude, and will likely need to be calibrated to generate synthetic earthquake catalogues consistent with field data. Furthermore, if this factor is sensitive to rock material properties (e.g., stiffness), in-situ stress state, or size and orientation of failure planes, then the calibration process will be site-specific.

Hanks and Kanamori (1979) proposed that earthquake magnitude be related to radiated seismic energy, E_a, via

$$M = \frac{2}{3}\log\left(\frac{2GE_a}{\Delta\tau}\right) - 10.7$$

where, G is the shear modulus and $\Delta\tau$ the shear stress drop on the plane, which is typically between 0.1 and 10 MPa (*McGarr*, 1994). The probability of aftershocks is governed by an Omori decay law

$$\lambda(t) \propto \frac{1}{(t + c)^p}$$

where, λ a measure of seismicity rate (or probability of getting an earthquake after time t), c is typically less than one day, and p is between 0.8 and 1.2 (Utsu et al., 1995).

In terms of energy balance within the model, we can link the rate at which induced seismic energy is radiated from a given volume to continuum stress changes, $\Delta\boldsymbol{\epsilon}$, within the volume

$$\eta \cdot \Delta E = \eta \cdot \Delta \int_V \mathrm{D} \cdot \Delta\boldsymbol{\epsilon} \cdot \Delta\boldsymbol{\epsilon}\, dV = \int_{M_{min}}^{M_{max}} \int_{t=0}^{\infty} \lambda(t, M) E_a(M) dt dM$$

where, η is seismic efficiency. The approach would be to estimate the various model parameters such as $A, \Delta E, \eta, c, t, and\ \beta$ from historic data for the site and /or analogue sites.

FEHM has the ability to model the coupled set of multi-phase porous flow, heat transfer and static stress balance equations. We have developed in FEHM elastic as well as limited plastic models for this purpose. Of particular relevance for the current discussion is the ability to compute regions of the model where the formation has experienced shear failure and the ability to model permeability enhancement upon failure. FEHM can also model post-failure of the material by changing the Young's modulus. Several models exist (Kelkar et al., 2012) to modify permeability as a function of some evaluated failure criterion, typically Mohr-Coulomb,

$$|\tau| > \mu(\sigma_n - p_f) + S_0$$

where, $|\tau|$ is the absolute value of the shear stress, μ a coefficient of friction, S_0 is the cohesion, σ_n the normal stress taken to be positive in compression, and p_f the pore fluid pressure.

Pumping fluid underground raises pore pressures (and can decrease temperatures) resulting in shear failure of the rock (or at very high pressure, tensile failure, i.e., hydro-fracturing). Associated with this shear failure is measured seismicity. Typically, failure first occurs near the well-bore, where the effects of cooling and high-pressure are immediate. However, in time, the injected fluid is carried further from the well-bore, causing an expanding volume of rock to be affected by failure.

Numerical simulation will require discretization of the integral on the right hand side of the equation above, and application of a stochastic random variable in place of the stress drop $\Delta\tau$. Furthermore, the probability function, λ, instead of being smoothly varying, will be modified by an synthetic noise term, consistent with the irregular and episodic nature of seismicity. By itself, a single failed node would be expected to generate the classic Omori decay curve, with little resemblance to the conceptual seismicity rates shown in Figure 1. However, at early times, as the damaged rock volume expands outward, an increasing number of failed nodes – and thus individual earthquake sources – will outstrip the rate at which the seismicity of any given node is decreasing: total seismicity increases. In time, the expansion of the damage front will slow and may stop (the influence of the injected fluid is finite); stabilization of the total seismicity should be expected where the two opposing processes (addition of new earthquake sources, decay of existing ones) balance. Finally, with the cessation of pumping, observation of time decay may be useful in constraining the persistence of induced seismicity post-operation. As a further caveat, we note that injection need not continue to a point of a stable rate of seismicity. For Enhanced Geothermal Systems, a traffic light risk management system is often observed, where injection operations cease when the rate of seismicity exceeds some tolerable threshold. A similar system has been proposed for CO_2 sequestration and wastewater disposal operations that also carry risks of induced seismicity (NRC, 2012). In these circumstances, the damage front may continue propagating without injection, and a decrease in seismicity may not be immediate. Application of this approach is demonstrated in the Results section.

Implicit coupling of fluid flow and geomechanical deformation: As mentioned earlier, the capability to simulate coupled fluid flow and stress equations exsited in FEHM. These equations

were simulated using an explicit coupling approach. While the explicit coupling approach has been fairly common due to its simplictly, its limitations are known. The approach has time-step size limitations leading to longer simulation times and in certain types of problems the numerical solutions can be in-accurate. In order to overcome these limitations, we initiated developments on implicit solution of flow and stress equations. The numerical algorithm in FEHM uses a control-volume approach for solving the mass and heat transfer equations, where the unknowns are defined at the nodes of the mesh and the mass and energy fluxes are evaluated at the midpoints of the edges connecting neighboring nodes. The control-volume approach makes it easy to use upwinding for advection-dominated flows. The equations of geomechanics on the other hand are solved using a finite-element framework where the stresses are defined at the interior of elements. Given below is the formulation for the mass balance equation for a single component liquid phase, energy balance and multiple phase equations have simillar forms. The derivative of the mass flux q_{ij} between two connected nodes I and J with respect to the displacement vector $\bar{u}_k$ at a node k connected to the node pair is written as,

$$\frac{\partial q^{ij}}{\partial \bar{u}_k} = K^{ij} \cdot \frac{\rho}{\mu} \cdot (A_{ij} / l_{ij}) \cdot (P_j - P_i) * \frac{\partial pF^{ij-e}}{\partial \bar{u}_k}$$

where $\frac{\rho}{\mu}$ is the ratio of fluid density and viscosity, (A_{ij} / l_{ij}) is the ratio of the area and the length associated with the node pair and Pi and Pj are the pressures at the nodes. K^{ij} is the 'effective' permeability between the nodes including multi-phase effects, pF_{ij} is an effective permeability factor representing stress/deformation effects, given by a sum over the elements connected to the edge I-J. Derivatives of this term are related to the nodal displacements within each connected element as:

$$pF_{ij} = \frac{1}{N_{ij-e}} \sum_{elements-ij} pF_{ij}^{e}$$

$$\frac{\partial pF^{ij}}{\partial \bar{u}_k} = \frac{1}{N_{ij-e}} \sum_{elements-ij} \frac{\partial pF^{ij-e}}{\partial \bar{u}_k}$$

$$\frac{\partial pF^{ij-e}}{\partial \bar{u}_k} = \frac{\partial pF^{ij-e}}{\partial \bar{\sigma}_e} \cdot \frac{\partial \bar{\sigma}_e}{\partial \bar{u}_k}$$

$$\frac{\partial \bar{\sigma}_e}{\partial \bar{u}_k} = \frac{1}{Ve} \sum_{gp} |J| \, \bar{\bar{D}} \cdot \bar{\bar{B}} \cdot \bar{\bar{I}}$$

where the sum in the last equation is over the Gauss points of the element e, $\bar{\sigma}_e$ is the element average stress tensor for the element, |J| is the Jacobian for the element, Ve is the volume of the element, and $\bar{\bar{D}}, \bar{\bar{B}}, \bar{\bar{I}}$ are the element elasto-plastic stress-strain matrix, element strain-displacement matrix and the identity matrix respectively. The derivative of the effective

permeability factor with respect to the element stress tensor $\bar{\sigma}_e$, $\frac{\partial pF^{ij-e}}{\partial \bar{\sigma}_e}$, is use specified as a functional dependence of the permeability upon the effective stress.

The equations given above are being incorporated in a fully coupled version of the code FEHM. The definition of stresses and permeabilities at different geometric locations on the grid necessitates the development of suitable averaging schemes to model the changes in permeability due to changes in the stress environment. In particular, we need to represent the element and edge connectivity information so that for any edge, we are able to average the stresses on the set of elements that share that edge. During this quarter we developed the data structures needed for representing these relationships as a set of pointers into the global connectivity matrix. As an example, any hexahedral element in three-dimensions has 12 distinct edges. A set of pointers are created to redirect each of these edges into the matrix that represents global connectivity information. This way, a single loop over the set of the elements can be used efficiently to update the permeabilities over the entire set of edges. This data-structure has been used to implement a simple model of permeability evolution due to tensile effective-stresses.

In the present version of this formulation, five balance equations comprising of one mass balance, one energy balance, and three force balances are considered at each node. The five state variables are pore pressure (P), temperature (T) and three displacements (u,v,w) at each node. In the fully coupled, implicit formulation, the full Jacobian matrix including the derivatives of each term in each of the five equations with respect to each of the five state variables is formed and the Newton-Raphson (NR) scheme is used to iteratively solve for corrections to the values of the variables until convergence is obtained at each time step. This formulation, while more complex to implement, is suitable for handling strongly nonlinear material properties with large gradients. The mass and energy balance equations are based on the Control Volume (CV) approach, while the force balance equations are based on a Finite Element (FE) approach. The mass balance equation contains accumulation and flux term terms. The accumulation term depends on the formation porosity (ϕ). Modules were developed in FEHM to incorporate this term in the fully implicit formulation. The flux terms in the mass balance equation depend additionally on the formation permeability (K). Both ϕ and K can vary with the P, T, stresses (σ), and u,v,w. Several relationships between K and σ/ displacements have been incorporated in FEHM. The force balance equations include the stress-strain relationships for the formation. We are using the linear elastic/plastic models of material deformation. Von Mises plasticity has been included in the fully implicit formulation, handled using an incomplete NR scheme as is commonly done. Also, the Young's modulus (E) in linear elastic model is allowed to vary with temperature and pressure.

Results & Discussions

Task1. Characterization of impact of CO_2 and deeper brine on groundwater quality: Here we will present some of the important findings that were used to determine what reactions control Arsenic release and mobility. Samples of lithesome outcrops from Chimayo were put through the sequential extraction process by Jaqueline Hakala of NETL. The extractions attempt to determine what processes release a trace metal from the rock. These experiments concluded that As can be released due to carbonate or exchange reactions and to a lesser degree redox reactions.

At LANL experiments by Carey et al. (2009) exposed saturated sediments collected in Chimayo to CO_2 and measured the changes in the aqueous geochemistry. For Uranium it was observed that the clay-rich sediments release Uranium once CO_2 was introduced in the system whereas the quartz-rich sediments did not release Uranium. Neither the clay-rich or quartz-rich sediments released Arsenic which is an interesting difference between these trace metals. The literature indicates the Arsenic is mainly an issue under reducing conditions (e.g. Kim et al., 2002). Dissolved oxygen measurements and the pe values shown in Table 1 indicate that the Chimayo aquifer is mostly oxidizing. Figure 1 compares As concentrations to the pe.

Table 1. Observed Arsenic concentrations and pe from groundwater samples collected at Chimayo.

Site	Name	pCo2 / atm (Co2 meter)	low-end pe	As (ug/L)
2	Robert's Well	-0.786284632	12	0.311
3	Robert's Geyser	-0.144568957	7.14	0.743
1	Bradley	-1.278668043	4.29	0.971
6	Mr. Trujillo	-0.97739688	5.5	1.55
7	Carol and Willie Vigil	-1.769094916	12	6.80
5	Old Community Well	-0.004054697	7.02	14.5
8	Rose Vigil	-1.243112304	5.52	32.5

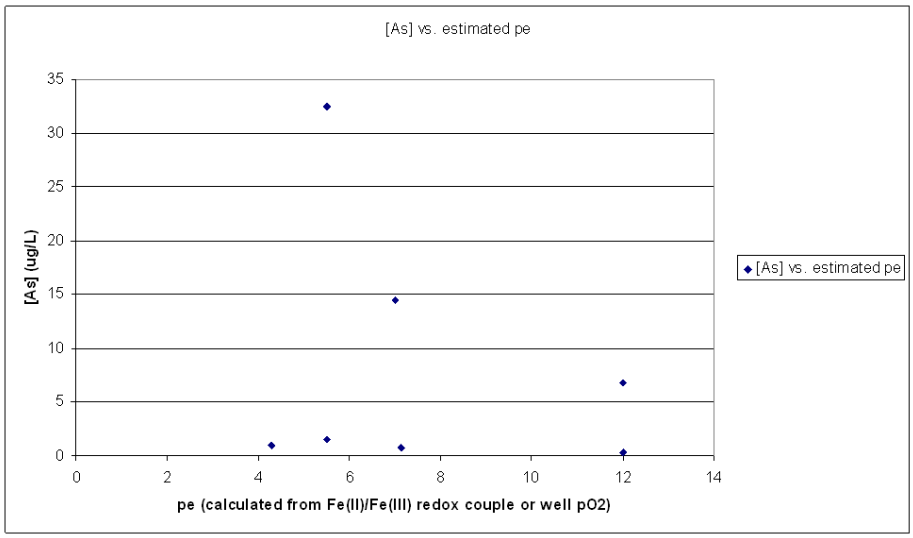

Figure 2. Measured Arsenic concentrations as a function of pe based on groundwater samples collected at Chimayo.

While there is no obvious trend observed in Figure 2, we needed to determine how high arsenic concentrations are possible at Chimayo. Some possibilities include pockets of reducing conditions or redox disequilibrium. For the Uranium work we were able to show that Uranium was co-transported with brine. One piece of evidence that led to this conclusion was that Uranium was linearly varying with chloride concentration (Figure 3). Arsenic also linearly varies with chloride concentration indicating that co-transportation is a possibility in this case as well.

At the Chimayo site, arsenic is mosly in the oxidized form of As(5), which is dominated by aqueous species $H_2AsO_4^-$ and $HAsO_4^{-2}$. According to the study conducted by Manning and Goldberg (1997) and Zheng et al. (2009), $H_2AsO_4^-$ and $HAsO_4^{-2}$ sorb to the iron oxyhydroxides

and clay minerals, when the mineral surfaces are positively charged. These minerals may include goethite, (as well as lepidocrocite and hematite), kaolinite, illite, and semectite.

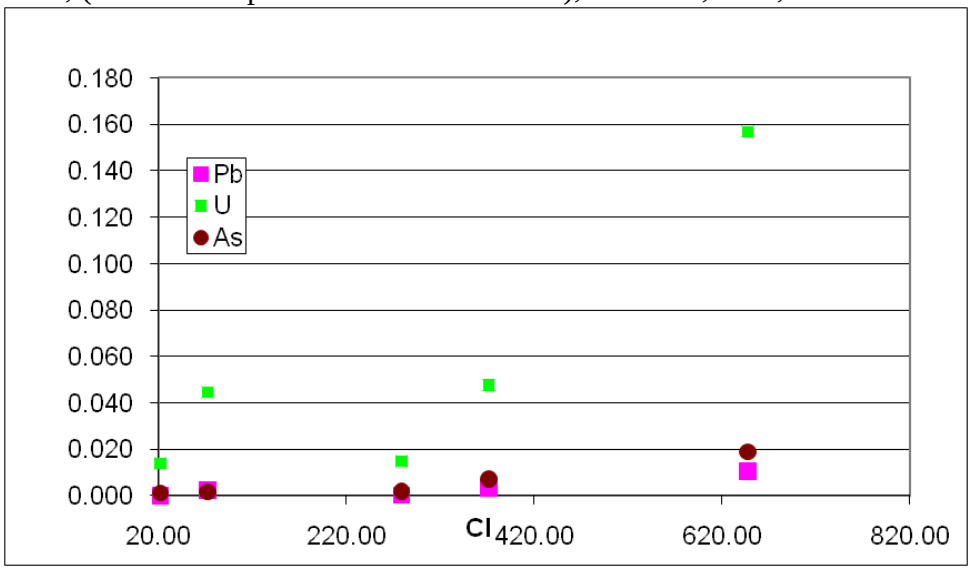

Figure 3. Trace metal trends with Chloride concentration.

Zheng et al. (2009) and Manning and Goldberg (1997) used surface complexation to express those adsorption reactions, such as:

Goethite: Goe_ $H_2AsO_4^-$ + H_2O ↔ Goe_OH + H_3AsO_4 Log(K_{int}) = 7.93 (Dixit and Hering, 2003)
Goethite: Goe_ $HAsO_4^{-2}$ + H_2O + H^+ ↔ Goe_OH + H_3AsO_4 Log(K_{int}) = 14.52 (Dixit and Hering, 2003)
Kaolinite: Kao_ $HAsO_4^{-2}$ + H_2O + H^+↔ Kao_OH + H_3AsO_4 Log(K_{int}) = 4.69 (Goldberg, 2002)
Illite: Ill_ $HAsO_4^{-2}$ + H_2O + H^+↔ Ill_OH + H_3AsO_4 Log(K_{int}) = 5.21 (Goldberg, 2002)
Semectite: Sem_ $H_2AsO_4^-$ + H_2O ↔ Sem_OH + H_3AsO_4 Log(K_{int}) = 4.52 (Goldberg, 2002)

Three more reaction will be included in the data base when we have the equilibrium constants:

Kaolinite: Kao_ $H_2AsO_4^-$ + H_2O ↔ Kao_OH + H_3AsO_4 Log(K_{int}) = ??
Illite: Ill_ $H_2AsO_4^-$ + H_2O ↔ Ill_OH + H_3AsO_4 Log(K_{int}) = ??
Semectite: Sem_ $HAsO_4^{-2}$ + H_2O + H^+↔ Sem_OH + H_3AsO_4 Log(K_{int}) = ??

From the analysis of a few samples collected from the Chimayo site, we know the major minerals that exist at the site include Quartz, K-Feldspar, Plagioclase, Calcite, Hematite, Illite/Mica, Kaolinite and Smectite (Table 2). By ignoring the relatively slow reacting minerals Quartz, K-Feldspar, Plagioclase and the mineral Hematite which has a low volume fraction (<0.2%), we focus on the reactions of calcite and other clay minerals.

The kinetically-controlled mineral dissolution/precipitation are described by:

$Illite = 1.2H^+ + 0.25Mg^{2+} + 0.6K^+ + 3.5SiO_2\ (aq) + 0.4H_2O + 2.3AlO_2^-$
$Kaolinite = 2H^+ + 2SiO_2\ (aq) + H_2O + 2AlO_2^-$
$Smectite\text{-}Ca = 0.96H^+ + 0.26Mg^{2+} + 0.145Ca^{2+} + 3.97SiO_2\ (aq) + 0.52H_2O + 1.77AlO_2^-$
$Smectite\text{-}Na = 0.96H^+ + 0.26Mg^{2+} + 0.29Na^+ + 3.97SiO_2\ (aq) + 0.52H_2O + 1.77AlO_2^-$
$Calcite + H^+ = Ca^{2+} + HCO_3^-$
$Goethite + 3H^+ = 2H_2O + Fe^{3+}$

Table 2. The sample analysis results of mineral components at Chimayo site.

Mineral	R-cut1	R-cut2A	R-cut2B	S2-sand	S2-clay	Average(wt)	Vol Fraction
Quartz	26	48.1	42.3	54	38.8	0.4184	0.4370
K-Feldspar	3.6	6.7	5.6	5.5	4.6	0.052	0.0554
Plagioclase	4.8	10.8	8.9	15.6	5.7	0.0916	0.0470
Calcite	0.4	4.7	1.8	0.6	1.6	0.0182	0.0186
Hematite	0.4	---	0.1	0.5	0.3	0.00325	0.0017
Illite/Mica	43.4	20.3	29.5	11	29.4	0.2672	0.2845
Kaolinite	1.5	---	0.1	0.3	0.9	0.007	0.0075
Smectite	20.2	9.3	11.6	12.5	18.8	0.1448	0.1484

Preliminary chemical speciation calculations were performed with Phreqc (Parkhurst and Appelo, 1999) to identify the most important aqueous complexation reactions. Total 49 aqueous complexes are selected based on the concentration order. Table 3 lists some examples of aqueous complexation reactions.

Table 3. List of geochemical reactions considered for the Chimayo site.

Aqueous complexation reactions	$Log_{10}(K)$ at 25 °C
$OH^- = H_2O - H^+$	13.995
$CO_3^{2-} = HCO_3^- - H^+$	10.329
$CO_2(aq) = HCO_3^- + H^+ - H_2O$	-6.3447
$CaHCO_3^+ = Ca^{2+} + HCO_3^-$	-1.0467
$MgHCO_3^+ = Mg^{2+} + HCO_3^-$	-1.0357
$CaCO_3(aq) = Ca^{2+} + HCO_3^- - H^+$	7.0017
$MgCO_3(aq) = Mg^{2+} + HCO_3^- - H^+$	7.3499
$NaHCO_3(aq) = Na^+ + HCO_3^-$	-0.1541
……	……
Cation exchange:	
$Na^+ + 0.5Ca\text{-}X_2 = 0.5Ca^{2+} + Na\text{-}X$	
$Na^+ + 0.5Mg\text{-}X_2 = 0.5Mg^{2+} + Na\text{-}X$	
$Na^+ + K\text{-}X = K^+ + Na\text{-}X$	
$Na^+ + H\text{-}X = H^+ + Na\text{-}X$	
$Na^+ + 0.5Pb\text{-}X_2 = 0.5Pb^{2+} + Na\text{-}X$	
$Na^+ + 0.5UO\text{-}X_2 = 0.5UO^{2+} + Na\text{-}X$	

The Gaines-Thomas convention was adopted for cation exchange (Appelo and Postma, 1993). It should be pointed out that cation selectivity is defined with respect to a reference species. By adopting Na^+ as the reference cation, cation exchange reactions are listed in Table 3. The symbol ( )-X denotes the cation exchanger or an exchange position. Selectivity coefficients of these reactions, $K_{Na/K}$, $K_{Na/Ca}$, $K_{Na/Mg}$, $K_{Na/H}$, $K_{Na/Pb}$, and $K_{Na/UO2}$, are defined with respect to sodium. The lower the selectivity, the higher the cation is selected compared to sodium. The cation exchange capacity is defined as CEC (meq/100 g of solid).

In order to understand the interactions of CO_2, water and rock, a batch experiment was conducted at LANL. The rock samples collected from Chimayo were stirred with a stir bar in the reaction vessels during the experiment when not being actively sampled. The hydrated CO_2 then was piped to the "w/CO_2" reaction vessels. The samples were allowed to settle before any fluid sampling. The observed concentrations are listed in Table 4.

Table 4. The observation data and the weightings of chemical components from batch experiment.

Time	Hours	0	1	24	240	480	660	840	Weighting
Ca	mg/L	257	277.4	294.5	245.5	234.3	272.9	228.4	0.0413
Fe	ug/L	7.509	8.485	7.61	8.762	100.8	2216	0	0.0012
K	mg/L	8.684	8.967	9.212	4.391	4.406	8.28	7.403	0.4790
Mg	mg/L	14.16	14.79	15.42	8.911	8.496	14.57	12.06	0.3471
Na	mg/L	111.9	110.4	106.6	78.52	77.78	91.41	72.84	0.0595
Cl	mg/l	48	45	43	41	40	38	29	0.1644
SO4	mg/l	91.53	97	91	81	86	81	63	0.0914
U	ug/L	2.57	3.40	3.78	3.97	3.76	3.36	2.99	2.0260
As	ug/L	20.1	18.7	16.9	8.25	5.49	4.09	1.87	0.1318
pH		8.55	5.99	6.06	6.04	5.97	5.90	5.88	1.0244

By using TOUGH-REACT (Xu et el., 2009) as the forward modeling simulator and PEST (Doherty, 2009) as the inverse simulator, we simulate the geochemical reactions and fit the observation data listed in Table 4. The initially estimated geochemical reaction parameters are listed in Table 5, which include the selectivity coefficients, cation exchange capacity, rate constants of mineral dissolution or precipitation and adsorption surface areas of the minerals.

Table 5. The estimated geochemical reaction parameters from the batch experiment.

Parameter	Symbol	Estimated value
Selectivity Coefficient	$K_{Na/H}$	0.1
	$K_{Na/Ca}$	0.26
	$K_{Na/Mg}$	0.38
	$K_{Na/K}$	0.98
	$K_{Na/Pb}$	0.001
	$K_{Na/UO2}$	0.98

Cation exchange capacity (meq/100g s)	CEC	12
Rate constant ($mol/m^2/sec$)	Rfk_goe	4.52E-12
	Rfk_ill	3.71E-13
	Rfk_kao	6.92E-15
Adsorption Surface area (cm^2/g)	Surf_goe	17.1038
	Surf_kao	553.355
	Surf_ill	13920.2
	Surf_sme	737.442

The corresponding fitting results of the nine chemical components are plotted in Figure 4. Due to the complexity of the geochemical reaction patterns, a few of the components are not fit well. This is an ongoing task and we will keep exploring the geochemical reaction patterns and trying to improve the inverse modeling results.

To explore the sources of high arsenic concentrations at the Chimayo site, we established a simplified field-scale reactive transport model as shown in Figure 5. The one-dimensional reactive transport model has a height of 120 m. The CO_2 leaks from the deep aquifer where the groundwater is brine and the exact concentrations of chemical components are unknown. By using some geochemical parameters we initially obtained, we estimate the recharge concentrations of the major chemical components such as Pb, U and As to identify the sources of arsenic. Figures 6 and 7 show the fitting results of the chemical data observed from Robert Geyser. The estimated results are listed in Table 6, which include the estimated recharge concentrations (mol/L), selectivity coefficients (dimensionless) and inflow rate from the deep aquifer and the outflow rate (kg/s). Based on the initial inverse modeling results we simulated the concentration breakthrough curves of the chemical components in the shallow aquifer (in Figure 8). Figure 8A shows at as the CO_2 fraction (from the deep aquifer) increases with time, the pH values in the shallow aquifer decreases. Figure 8B shows the aqueous arsenic concentration increases with time due to the co-transport of arsenic from the deep aquifer. Figure 8C shows that the adsorbed arsenic onto the clay minerals increases when the pH values decreases. Although arsenic adsorption onto clay minerals increase when the pH values decrease, the aqueous arsenic concentrations increase due to the much stronger co-transport of arsenic from the deep aquifer. The estimated high arsenic recharge concentration ($2.54E^{-7}$ mol/L) at the deep aquifer initially indicates that the high arsenic concentrations are co-transported from the deep aquifer.

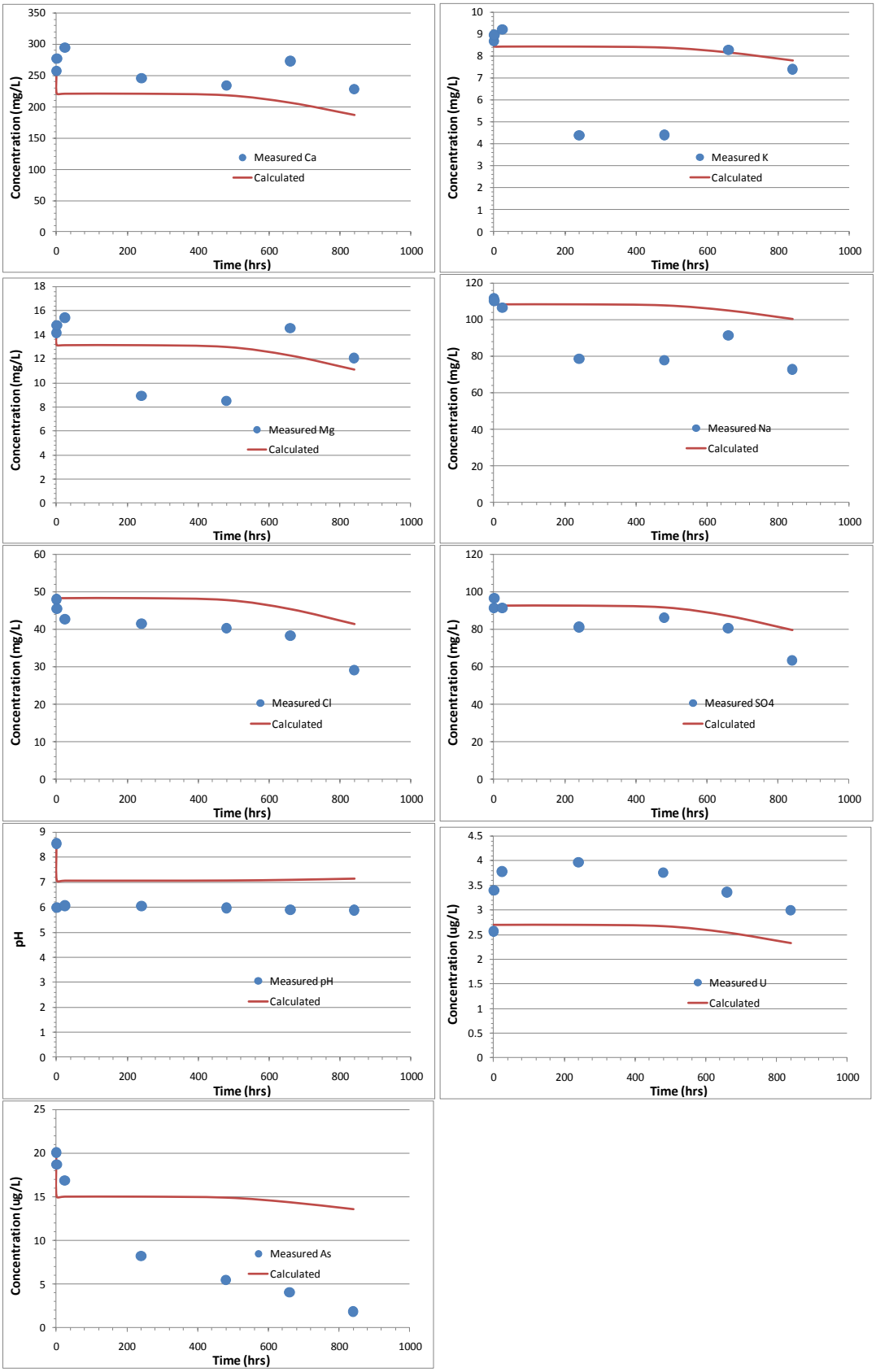

Figure 4. Inverse modeling results of the batch experiment.

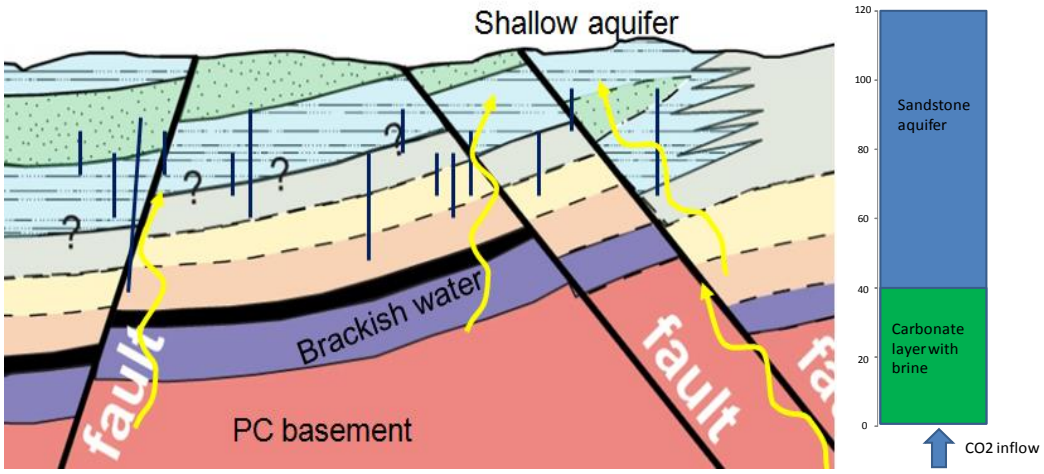

Figure 5. The conceptual model of CO_2 rises from deep aquifer along faults in the Chimayo site (A) and the simplified 1-D reactive transport model (B).

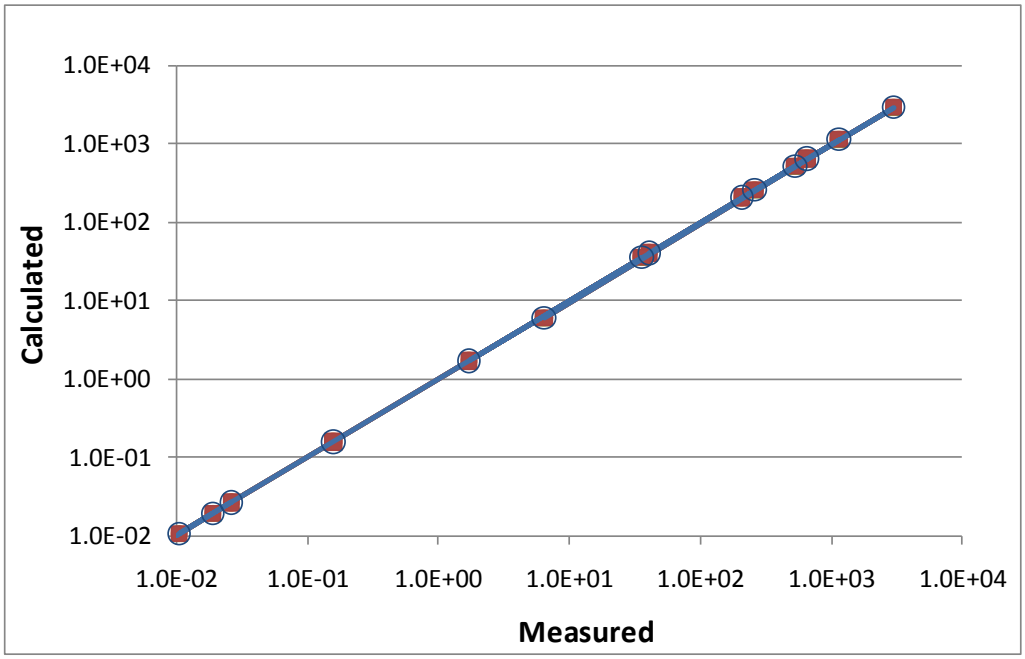

Figure 6. The fitting results of the chemical data observed from Robert Geyser.

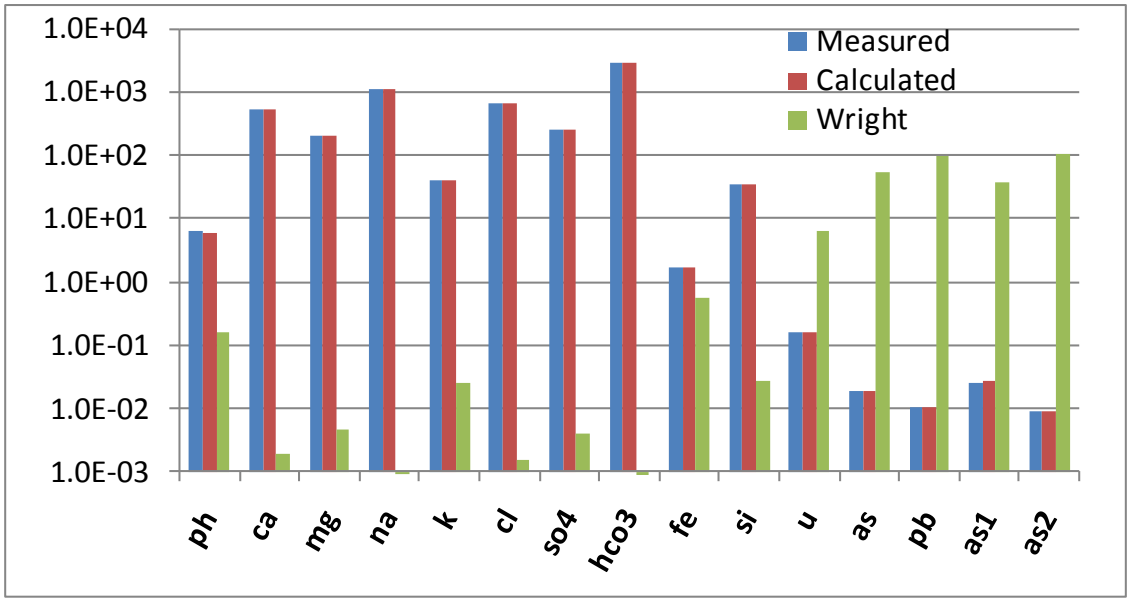

Figure 7. The comparison of measured concentrations and the computed values, as well as their weighting coefficients in the inverse model.

Table 6. Estimated recharge concentrations (mol/L), selectivity coefficients (dimensionless) and inflow rate from the deep aquifer and the outflow rate (kg/s).

h+	alo2-	ca++	cl-	fe+2	hco3-	k+	mg++	na+	sio2(aq)	so4--
1.86E-05	3.48E-07	4.11E-02	1.83E-02	3.06E-05	7.70E-02	1.05E-03	9.17E-03	4.98E-02	5.34E-04	2.69E-03
pb+2	**h3aso4**	**uo2+2**	**goe_soh**	**kao_soh**	**ill_soh**	**sme_soh**	**kpb**	**ku**	**infil1**	**infil2**
1.16E-08	2.54E-07	5.81E-07	2.18E-04	2.18E-04	2.18E-10	2.18E-10	3.48E-03	3.82E-02	4.21E-03	-4.21E-03

By using both TOUGHREACT and PEST, we used the geochemical model to simulate the laboratory batch experiment with background groundwater exposed to CO_2. Specifically, we include equilibrium complexation reactions, kinetic mineral reactions, and surface/cation exchange sorption reactions.

The estimated geochemical reaction parameters are listed in Table 7, which include six selectivity coefficients of cation exchange, cation exchange capacity, six rate constants for the mineral reactions, and four adsorption surface areas of the clay minerals. These were the parameters we felt were most uncertain and would be the key in accurately simulating arsenic concentration in this and other similar systems. The corresponding fitting results of the six key chemical components are plotted in Figure 9. The model fits the change in pH and arsenic concentration as function of time with some discrepancies. As CO_2 is introduced into the system, the pH drops quickly with time but levels out around 6 due to buffering by calcite. This behavior is captured by the model.

The aqueous arsenic concentration drops with pH due to the surface exchange reactions with clays. As the pH decreases and H^+ concentration increases, precipitation of the clay minerals is favored providing more sorption sites (see Figure 10), which enhances the aqueous arsenic sorption onto the clay minerals thereby reducing aqueous arsenic concentrations.

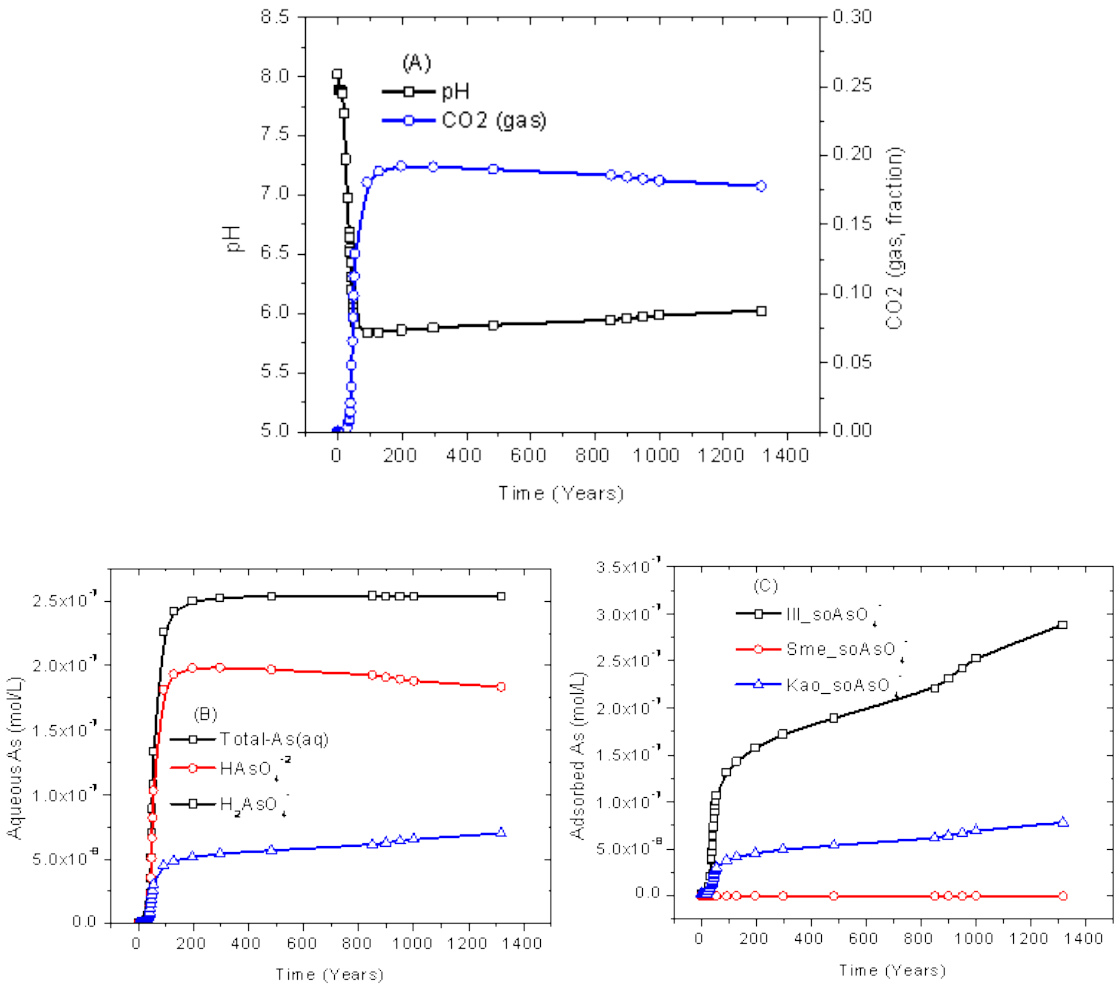

Figure 8. Simulated concentration breakthrough curves of the chemical components in the shallow aquifer: (A) pH and CO_2 fraction; (B) Aqueous arsenic concentrations; and (C) Adsorbed arsenic onto the clay minerals.

The key parameter controlling the rate of arsenic sorption is the illite/$H_2AsO_4^-$ equilibrium constant. This is due to the relatively large volume fraction of illite (43.4%), arsenic (e.g. $H_2AsO_4^-$ and $HAsO_4^{-2}$) sorption onto illite by surface complexation dominates the sorption reactions. We have included two sets of model fits in the pH and arsenic plots in Figure 9. For the solid line, we assume the illite/$H_2AsO_4^-$ surface exchange reaction equilibrium constant is known and this is the case used for the transport calculations in the next section. In this case, the pH is fit accurately but the arsenic concentration drops more quickly in the model than in the experiment. Goldberg (2011) indicates that there is a large amount of uncertainty in this particular equilibrium constant and the fitting correlation coefficient used to determine this parameter was about 0.6. If we allow this parameter to vary, the experimental and modeled arsenic concentrations fit much better with a fit equilibrium constant of 12.48. However, the pH actually does not match as well for this case. The two cases presented illustrate that very few parameter combinations actually fit the experimental data accurately and the presented fits are fairly unique. Because the batch experiment was conducted only for about 14 days, the relatively slow reactions of cation exchanges have only limited impact to the cation concentrations. Although the cations Ca, Na, Mg, Pb and K do not change significantly as CO_2 is introduced into

the system and the model also does not show much change for these species, the cation exchange reactions in the model reasonably predict the magnitude of these species.

Table 7. The estimated geochemical reaction parameters from the batch experiment.

Parameter	Symbol	Estimated value
Cation exchange selectivity coefficient	KNa/H	0.98
	KNa/Ca	0.03
	KNa/Mg	0.99
	KNa/K	0.59
	KNa/Pb	0.1
Cation exchange capacity (meq/100g s)	CEC	86
Mineral dissolution/ precipitation rate constant (mol/m2/sec)	Rfk_goe	1.09E-07
	Rfk_ill	5.07E-09
	Rfk_kao	1.00E-07
	Rfk_sme	1.79E-12
	Rfk_cal	2.11E-06
Adsorption surface (cm2/g)	Surf_hem	1014.41
	Surf_kao	208.50
	Surf_ill	1776
	Surf_sme	59.86

The anions Cl and SO_4 are mainly affected by aqueous complexation and do not show much change during the batch experiment.

To explore the sources of high arsenic concentrations at the Chimayo site, we established a simplified field-scale reactive transport model using the reactions developed from batch experiment. Figure 11 shows the conceptual model where CO_2 leaks from the subsurface through a deep carbonate aquifer into the shallow sandstone aquifer. The one-dimensional reactive transport model has a height of 120 m. CO_2 leaks from the deep aquifer where the groundwater is brine and the exact concentrations of chemical components are unknown. By using geochemical processes and parameters we initially obtained from the batch experiments, we estimate the recharge concentrations of the major chemical components such as Pb, U, As, Ca, Mg, Na, K and Cl to identify the sources of arsenic.

The geochemical processes simulated in this field-scale reactive transport model are the same as those in the batch experiments. When CO_2 inflows into the model from the deep aquifer, the pH in the shallow aquifer drops quickly with time but levels out around 6 due to buffering by calcite. The aqueous arsenic concentration in the shallow aquifer initially increases due to the co-transport (advection, dispersion and diffusion) of arsenic from the deep aquifer. When arsenic concentration increases, the arsenic adsorption onto clay minerals increases due to the surface complexations with clays and hematite.

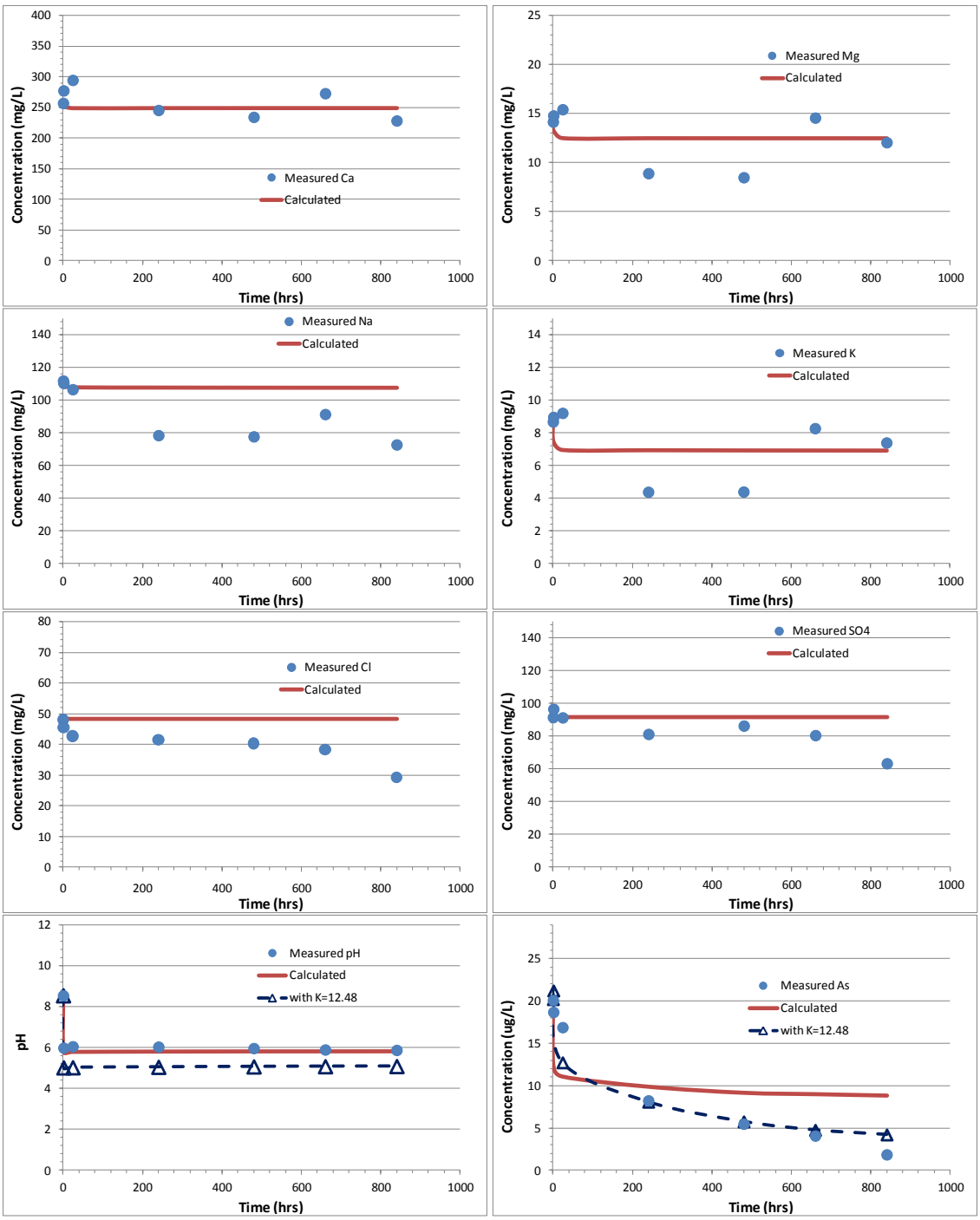

Figure 9. Inverse modeling results of the batch experiment.

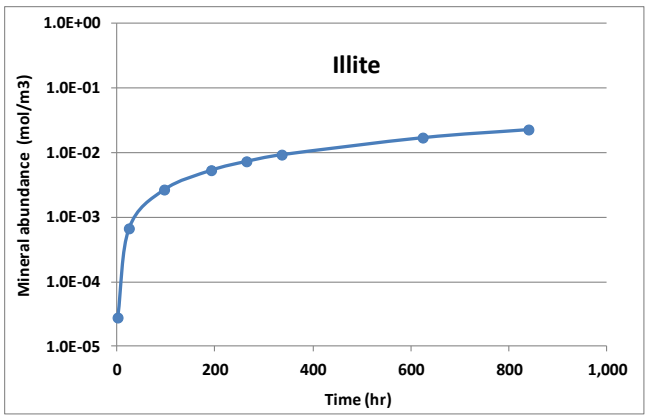

Figure 10. Precipitation of illite during the batch experiment.

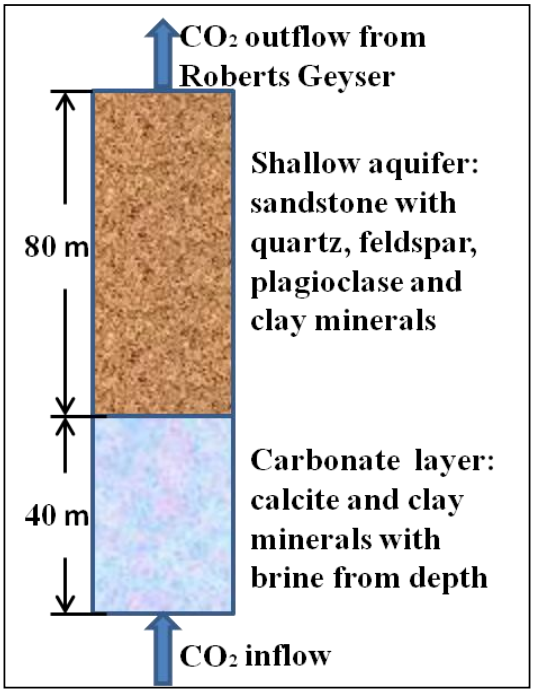

Figure 11. Conceptual model for field-scale reactive transport simulations.

As the pH decreases and H^+ concentration increases, precipitation of the clay minerals is favored providing more sorption sites, which enhances the aqueous arsenic sorption onto the clay minerals. Finally the co-transport of arsenic from deep aquifer reaches equilibrium with the arsenic adsorption onto the clay minerals. The clay mineral illite dominates in the arsenic adsorption process due to the relatively large volume fraction of illite. In the field-scale model an average volume fraction of 28.45% is assigned for illite by considering the heterogeneity of the mineral distributions in the Chimayo site. The other minerals are also assigned their average volume fractions. Figure 12 shows the fitting results of the chemical data observed from Roberts Geyser. The calculated pH and concentrations of other chemical components at the top of the shallow aquifer match the observed data of the Roberts Geyser very well, which demonstrates that the estimated recharge concentrations listed in Table 8 have little uncertainty. The estimated high arsenic recharge concentration (1.58E-6 mol/L) at the deep aquifer indicates that the high

arsenic concentrations in the shallow aquifer are co-transported from the deep aquifer, even though part of co-transported arsenic is adsorbed onto clay minerals. Note that the geochemical parameters estimated from the batch experiments are directly applied for the field-scale reactive transport modeling by ignoring the scaling effects. In fact, most of the reactive transport parameters are scale dependent (Dai et al., 2009).

Table 8. Estimated recharge concentrations (mol/L) from the deep aquifer.

Parameter (mol/L)	Initial value	Lower bound	Upper bound	Estimated value
H+	1.86E-05	1.00E-09	1.00E-03	3.81E-07
AlO2-	3.48E-07	1.00E-11	1.00E-02	7.56E-04
Ca++	4.11E-02	5.86E-06	5.86E-02	1.01E-02
Cl-	1.83E-02	2.82E-05	8.20E-02	1.83E-02
Fe+2	3.06E-05	1.75E-07	1.75E-03	3.06E-05
HCO3-	7.70E-02	5.90E-06	9.90E-02	5.00E-02
K+	1.05E-03	3.09E-06	3.09E-02	1.28E-03
Mg++	9.17E-03	3.82E-06	9.82E-02	7.44E-03
Na+	4.98E-02	2.48E-05	9.90E-02	4.86E-02
SiO2(aq)	5.34E-04	1.14E-06	1.14E-02	9.15E-05
SO4--	2.69E-03	3.84E-05	5.84E-03	2.69E-03
Pb+2	1.16E-08	2.00E-11	2.00E-06	2.31E-09
H3AsO4	2.54E-07	3.82E-09	8.82E-05	1.58E-06
UO2+2	5.81E-07	1.15E-08	1.15E-05	5.81E-07

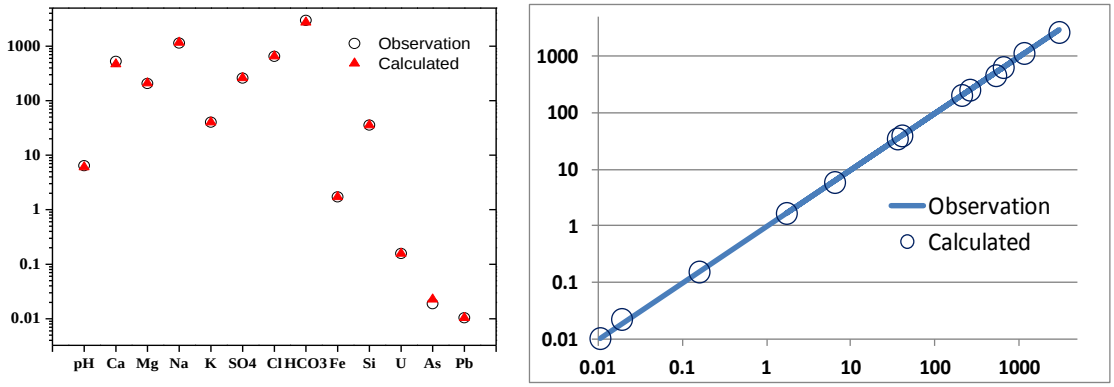

Figure 12. Fitting results of the observed chemical data from Roberts Geyser. The observed and calculated values are in a log scale.

Uranium Reactive Transport Study. The 3-D flow model of the site builds on the conceptual model and hydrologic data presented by Cumming (1997). The extent of the model is indicated in Figure 13, and was chosen so as to include all the wells for which water chemistry data are available, including both CO_2-impacted and background wells.

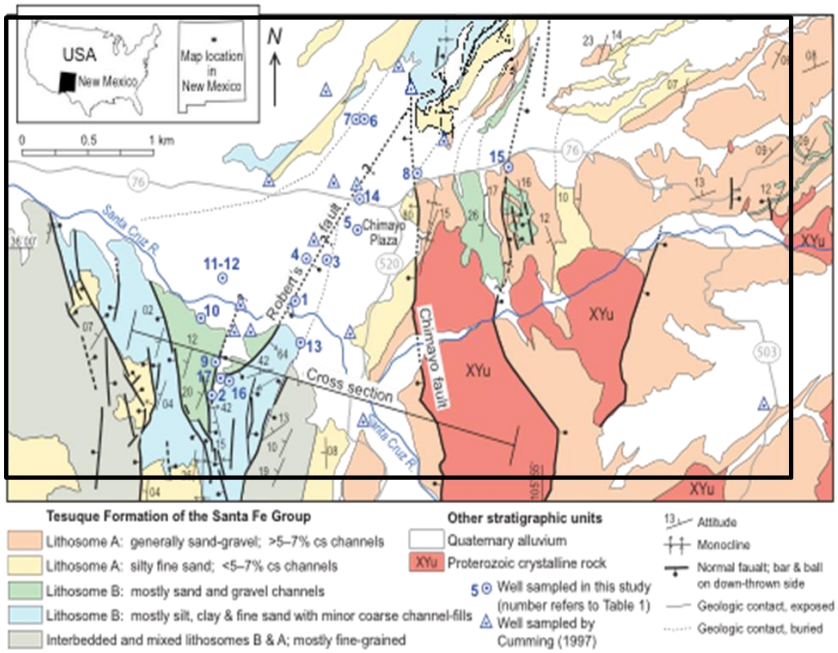

Figure 13. Site map (Koning et al., 2002, Koning 2003). Symbols show location of water samples (Keating 2009 and Cumming 1997). Black rectangle shows model extent.

An orthogonal mesh was generated for the problem, of dimension 5 km X 3.5 km X 0.5 km. East-west resolution varies from 564.8 m at the boundaries to ~70m near the fault. North-south resolution and vertical resolution is uniform (117 m and 30m, respectively). Multi-phase flow and reactive-transport calculations were performed using the simulator FEHM (Finite-Element-Heat-and-Mass-transfer) code (Zyvoloski, 1997). The complex stratigraphy shown in Figure 14 was simplified to a two-layer system: a shallow relatively permeable, sedimentary aquifer underlain by lower permeability carbonate aquifer.

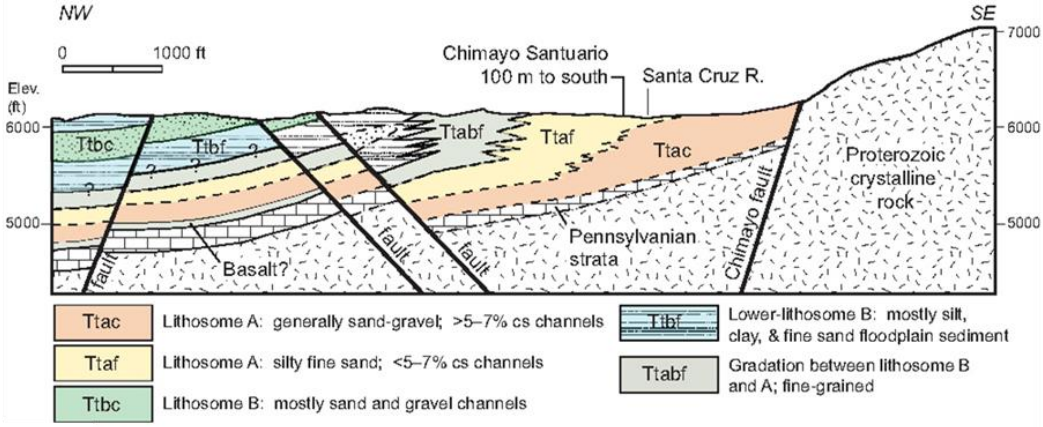

Figure 14. Geologic cross-section (Koning et al. 2002, Koning 2003).

The two units are separated by a thin confining layer, which is broken by a north-south trending, high-permeability conduit representing Roberts Fault (Figure 15).

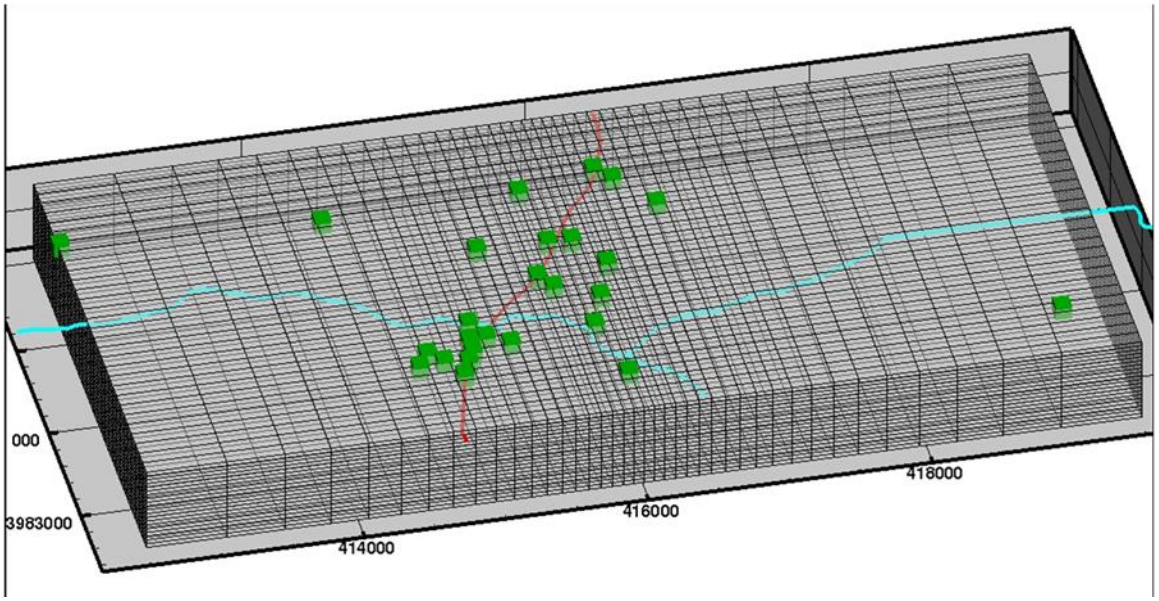

(a)

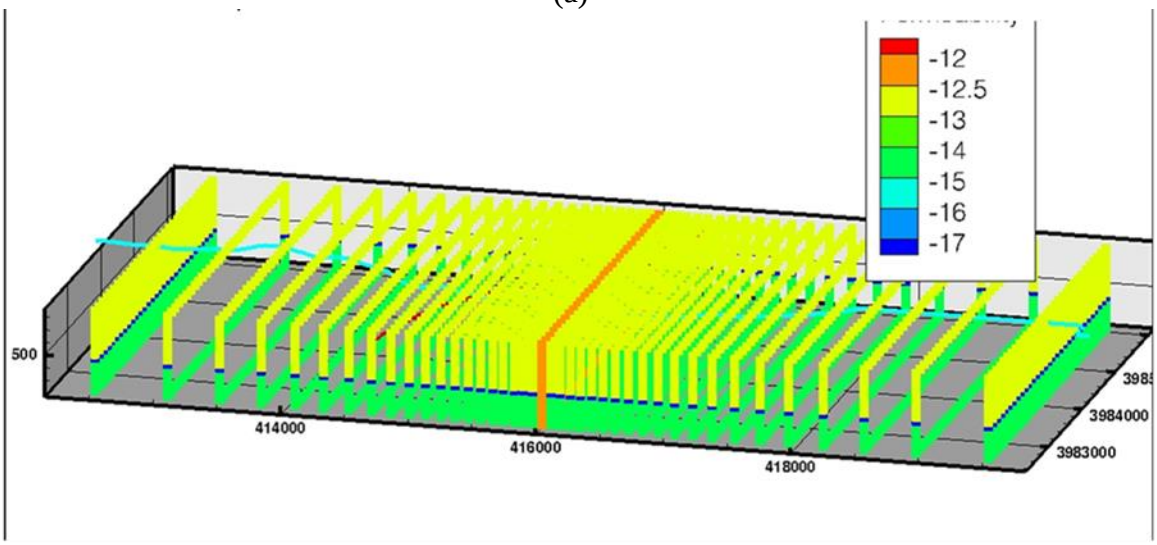

(b)

Figure 15. a) Location of Roberts Fault, Santa Cruz River, and sampled wells in relation to the computational mesh. b). Assumed permeability of model layers.

Inflow to the two horizontal layers is at the eastern edge (roughly corresponding to the contact between the Santa Fe group and the pre-Cambrian); discharge occurs at the western edge. Downward flow occurs along the Santa Cruz River, representing dilute stream recharge. Inflows and permeabilities were specified to achieve approximately the correct gradient in the shallow aquifer is approximately 0.01 m/m, in accordance with estimates provided by Cumming (1997, pg. 19), and to produce slightly higher pressures in the lower units. These parameters are shown in Table 9. Steady-state flow simulations were conducted, followed by transient flow with CO_2 flux applied at the base of the fault.

The specification of reaction networks to include in the simulations was guided by previous batch and 1-D geochemical modeling (Keating et al., 2009) and laboratory experiments (Carey et al., 2009). The aqueous geochemistry of uranium has been the focus of many studies (Langmuir, 1997; Hsi, C-K D. & Langmuir, 1985; Dong et al. 2005; Fox et al. 2006; Rossberg et al., 2009); many of these have focused on sorption reactions. According to Fox et al. (2006), uranium sorbs to mineral surfaces such as ferrihydrite and quartz; however, formation of uranyl-carbonate complexes and U-Ca-CO_3 complexes can inhibit sorption (Dong et al., 2005; Fox et al., 2006). Because of this fact, it is reasonable to expect the introduction of CO_2 could cause uranium desorption and increased concentration of dissolved uranium. Because of potential importance of carbonate chemistry, which is clearly important at Chimayo (Keating et al., 2009) (and will be important in any CO_2-leakage scenario), we include carbonate complexes and U-Ca-CO_3 complexes (Fox et al., 2006) in the reactive-transport model, as listed in Table 10. A common approach to simulating uranium sorption is by surface complexation models (Waite et al, 1994). These models are quite complicated and even when trying to replicate controlled laboratory experiments are not necessarily successful, particularly in the presence of significant uranyl carbonate complexing (Hsi and Langmuir, 1985). The simulator used here (FEHM) does not include a surface complexation module.

Table 9. Hydrologic properties (all boundaries and initial conditions at 15^{o}C).

Hydrologic properties		Permeability (log10 m^2)	
	Shallow aquifer	-12.5	
	Confining unit	-16	
	Carbonate layer	-14.5	
	Fault zone	-12	
Boundary conditions			
Eastern edge	Specified water flux	Shallow aquifer	4 kg/s
		Deep carbonate	0.8 kg/s
Western edge	Specified pressure head	Shallow aquifer	1800 m
		Deep carbonate	1810 m
Santa Cruz River	Specified water flux		1 kg/s
Fault base	Specified CO_2 flux		0.3 kg/s
	Specified water flux		15 kg/s
Relative permeability	Linear: k = KS		

Table 10. Aqueous complexation reactions.

	Log10(Keq)
$HCO_3^- + H^+ \Leftrightarrow H_2CO_3$	-6.3
$CO_3^{2-} + 2H^+ \Leftrightarrow H_2CO_3$	-16.6

$OH^- \Leftrightarrow H^+$	-14.0
$CaUO_2(CO_3)_3^{-2} + 6H^+ <=> 3\ H_2CO_3 + Ca^{2+} + UO_2$	-24.16
$Ca_2UO_2(CO_3)_3 + 6H^+ <=> 3\ H_2CO_3 + 2Ca^{2+} + UO_2$	-20.0
$UO_2(CO3)_2^{-2} + 4H^+ <=> 2H_2CO_3 + UO_2$	-33.68
$UO_2(CO3)_3^{-4} + 6H^+ <=> 3H_2CO_3 + UO_2$	-67.04

As a pragmatic method to approximate pH-dependent sorption/desorption without the computational burden of surface complexation reactions we allowed different aqueous U complexes to sorb at different Kd values. The complex expected to predominate at low pH values, UO_2, was assigned a low sorption value. The complex expected to predominate at neutral and higher pH values was assigned a higher sorption value. This is conceptually consistent with the results of Fox et al. (2006) who found that the presence of $Ca_2UO_2(CO_3)_3$ to reduce sorption onto ferrihydrite and quartz from 83% to 57%. The resulting set of rock/water reactions used is listed in Table 11.

Table 11. Rock/water reactions

$CaCO_3$ (s) + $2H^+ \Leftrightarrow H_2CO_3 + Ca^{2+}$ + **A** UO_2	Log10(Keq)	8.2*
$UO_2 <=> UO_2$ [sorb]	Kd	5.07
$Ca_2UO_2(CO_3)_3 <=> Ca_2UO_2(CO_3)_3$ [sorb]	Kd	0.4

A=2.E-6

* the literature value of 8.2 was increase by 0.71 to reflect the fact that most waters sampled at Chimayo are supersaturated; +0.71 is the calculated SI value at geyser well.

To specify initial geochemical conditions for the shallow aquifer (and lateral recharge to the aquifer from the eastern inflow boundary) we used data collected in 'background' (low pCO_2) wells in Chimayo. Recharge occurring along the Santa Cruz river was also specified using field data. The lower carbonate layer divided into two zones. As described in Keating et al. (2009) one of the striking features of the geochemical trends in the shallow aquifer at Chimayo is that some waters are impacted by CO_2 and others (near the southern end of the fault) are impacted by a mixture of CO_2 and brackish, Na-Cl water. Apparently the upwelling CO_2 entrains Na-Cl water in some locations and not others. To reproduce this feature, we placed Na-Cl-type water in the southern portion of the underlying carbonate. The inflow boundary to the lower carbonate aquifer was set to be equivalent to the initial condition. The lower carbonate aquifer was assumed to be 100% calcite; the upper aquifer was assumed to be 0.4% calcite, in accordance with our XRD results. Table 12 summarizes these initial and boundary conditions.

The simulations were conducted in pairs. The first simulation was used to establish geochemical equilibrium with the reactions listed in Table 11. This produced equilibrium with calcite throughout the model and typically resulted in approximately 50% of uranium sorbed to mineral surfaces. The second simulation perturbed this equilibrium by introducing a flux of CO_2 along the northern portion of the base of Roberts Fault and a flux of CO_2 and brackish water along the southern portion. As CO_2 enters a cell in the model, instantaneous dissolution in water is

assumed to occur. The maximum allowable dissolved concentration is controlled by pressure and temperature of that cell, as defined by tables published by Duan and Sun (2003). If excess CO_2 exists, it flows as a free phase.

Table 12. Initial and boundary conditions (units are mM).

Initial conditions	Ca	C_T	Cl	pH	U
Aquifer	1.52	5.516	0.62	8.5	2.e-4
Deep (northern)	1.52	5.516	0.62	8.5	2.e-4
Deep (southern)	1.52	5.516	20	8.5	7.e-4
Fault base inflow	1.52	100	*	8.5	*
River	1.52	0.1	.62	6.0	2.e-6

* = same as the deep aquifer (north or south)

As a first step we verified that the numerical model is capable of reproducing the general trends observed at Chimayo. Our focus is carbonate and uranium geochemistry and the possible effects of brackish water; therefore we emphasize comparisons with Ca, pH, pCO_2, and Cl.

There are two possible perspectives from which to view the field data. The first is that these data represent a single snapshot in time of an aquifer as a plume of CO_2 (locally, with brackish water) moves through it. In this perspective, the variability in groundwater chemistry is largely due to spatial variability in the characteristics of the CO_2 plume itself, and the spatial relation between the plume and individual wells. Since we do not know how long the CO_2 plume has been in the aquifer, it is difficult to select the appropriate time in the simulation to perform this 'time snapshot' comparison. Another difficulty for this type of comparison is that it requires detailed information about the spatial characteristics of the CO_2 plume, for which we have virtually no information. An alternative perspective is that the data represent waters exposed to the same plume, but for different lengths of time. Using this perspective, we can select points in the model domain corresponding to the sampled wells and compare the time-varying changes in geochemistry to the observed spatial variability in water chemistry at the site.

In Figures 16 and 17 the water chemistry data from the site are compared to time- varying water chemistry in the model domain. The open symbols on these plots are nodes in the model corresponding to the wells (green symbols in Figure 15). The pH/pCO_2 and [C_T]/[Cl] comparisons (Figures 16a & b) show reasonably good agreement. This simply indicates that our conceptual and numerical model is doing a reasonably good job of representing the range of measured pCO_2 and carbonate chemistry. The increasing [Ca] with pCO_2 is due to calcite dissolution. As mentioned above, since calcite precipitation/dissolution is thought to exert a major control on uranium mobility at this site, it is important for the model to capture these trends well. Because of the instantaneous nature of CO_2 dissolution, calcite equilibrium and carbonate complexation, simulated values fall along the measured trends at all times in the simulation.

The comparison with total carbon, uranium, and chloride (Figure 17) is also good, but much more complex because there are significant temporal variations in the simulation results. Generally speaking, total carbon will increase as the CO_2 plume moves through a cell in the model. As discussed above, the measured data fall into two types; one, with a 'pure CO_2' signature, the other impacted by both Na-Cl water and CO_2. The simulated data (Figure 16a) also show both types. A fairly good match to the data occurs between 3 and 5 years after the plume enters the aquifer. At later times, the concentration of C is too high. One possible explanation is that the Chimayo aquifer is not at steady-state with respect to a CO_2 plume, but that total C could continue to rise in the future. Another possible explanation is that there is a C removal process active at the site which is not included in the model.

The simulated trends in uranium and chloride (Figure 17b) also show significant temporal variations. At early times, there is not good agreement with the field data. However, after 80 or 90 years, the simulated trend is very similar to the measured trend. The discrepancy between the timing of a 'good fit' between measured and simulated C_T/Cl and of U/Cl is due to the retarding effect of uranium sorption.

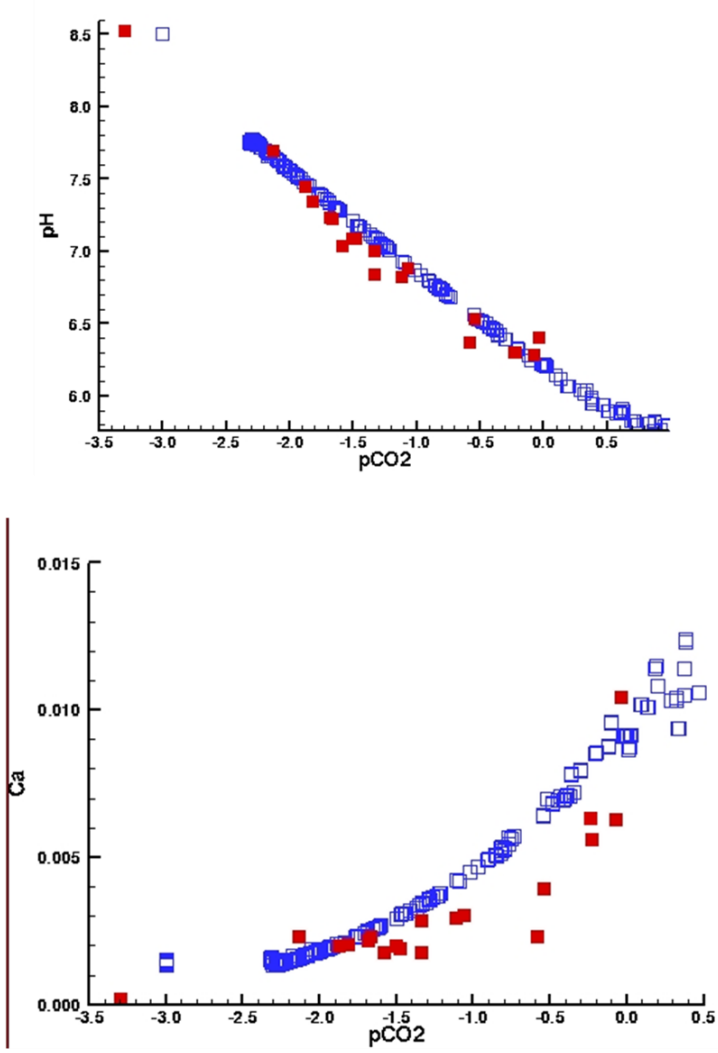

Figure 16. Simulated (blue symbols) and measured (red symbols) pH vs pCO_2 (a) and Ca vs pCO_2 (b). Blue symbols represent all simulation times.

There are a number of possible implications for the Chimayo site, in particular, and for CO_2 leakage scenarios, in general. These will be discussed below. The spatial evolution of the CO_2 plume along a vertical E-W cross-section is shown in Figure 18. At all times, the CO_2 is entirely in the dissolved phase (no free phase). The maximum mass fraction is ~ 4%. By two years, the plume has reached the shallow aquifer and is beginning to spread, mostly in the downstream (western) direction. By one hundred years, there is significant downstream spread. The plume still has not quite reached the top of the aquifer.

The zone where uranium concentrations are changing in response to the plume is smaller, as shown in Figure 18. By inspection of the aqueous complex concentration and sorption results, it is clear that the $Ca_2UO_2(CO_3)_3$ complex dominates everywhere . The fraction of total uranium sorbed does not change significantly in time or space (total variation over all times everywhere in the model: 46.1 % - 47.2 %). This result is consistent with the hypothesis proposed in Keating et al. (2010) that the dominance of the $Ca_2UO_2(CO_3)_3$ complex in this calcium-rich

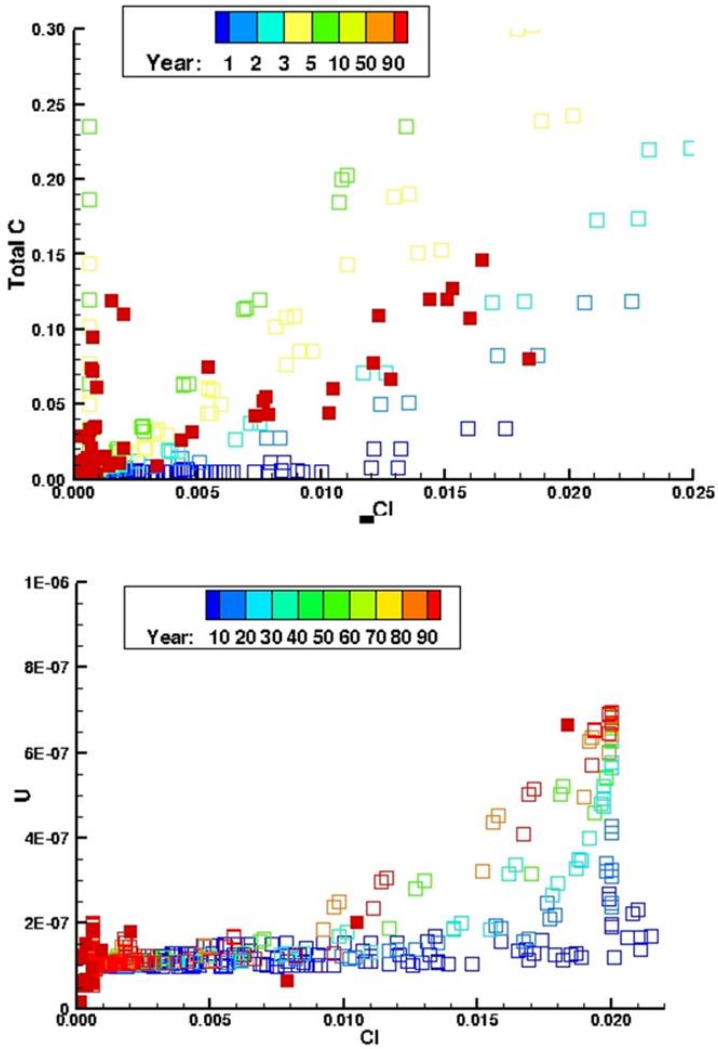

Figure 17. Simulated (open symbols) and measured (closed red symbols) total dissolved carbon vs chloride (a) and uranium vs chloride (b). Simulation results are colored according to the time of model output.

system at all pH values measured at the site will mute the importance of desorption reactions as the aquifer responds to CO_2. In fact, the changes in [U] shown in Figure 19 are entirely due to release of U caused by dissolution of calcite. However, these changes are very small (mostly less than $1.E^{-7}$ M). As shown in Figure 20, the zone of calcite dissolution is much broader than that of increasing uranium. Near the margins of the calcite dissolution 'plume' the increase in [U] (which then partially sorbs to aquifer minerals) is extremely small.

The situation is very different near the southern portion end of the fault (Figure 21). Here changes are about an order of magnitude higher. This is entirely due to the entrainment of brackish water containing elevated [U]. In summary, simulated changes in uranium concentrations in the shallow aquifer are dominated by entrainment of brackish water containing

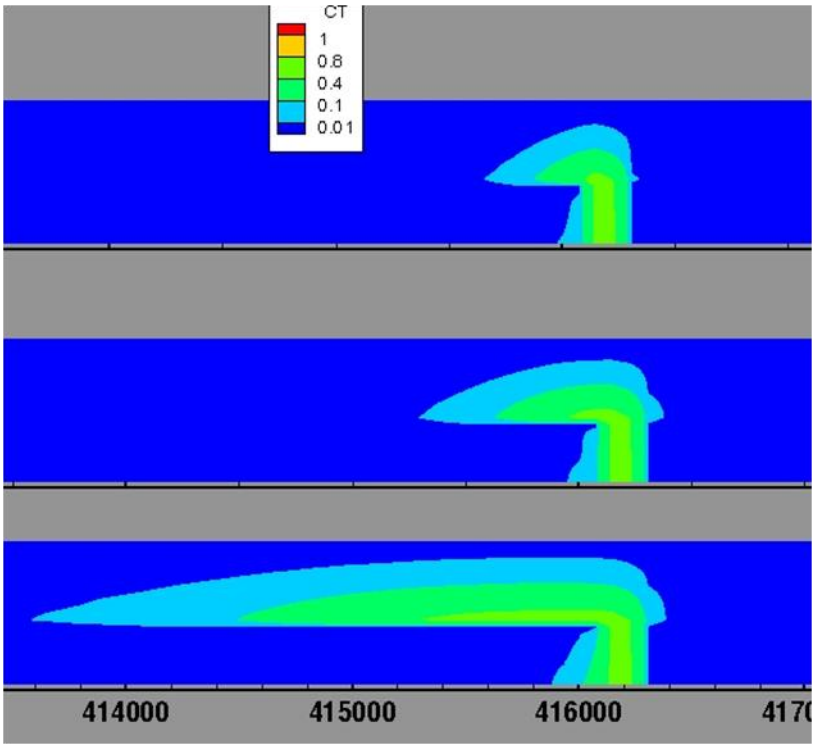

Figure 18. Dissolved mass fraction of CO_2 at 2 years (top figure), 24 years (middle figure) and 100 years (bottom figure). Horizontal line indicates confining beds.

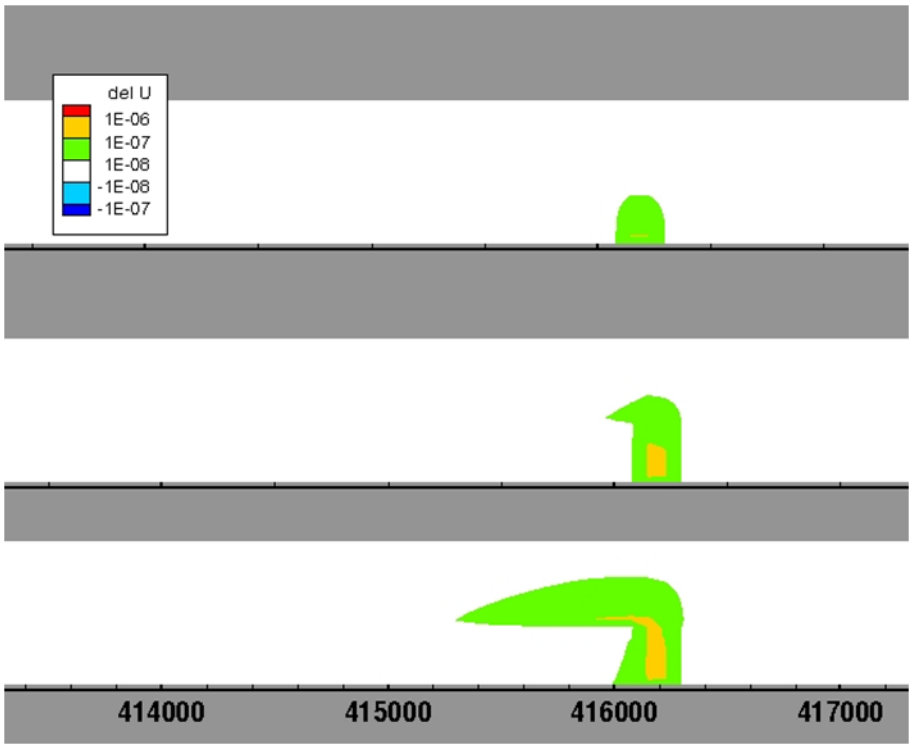

Figure 19. Cumulative changes in U concentrations, along an E-W cross-section in the northern portion of the model.

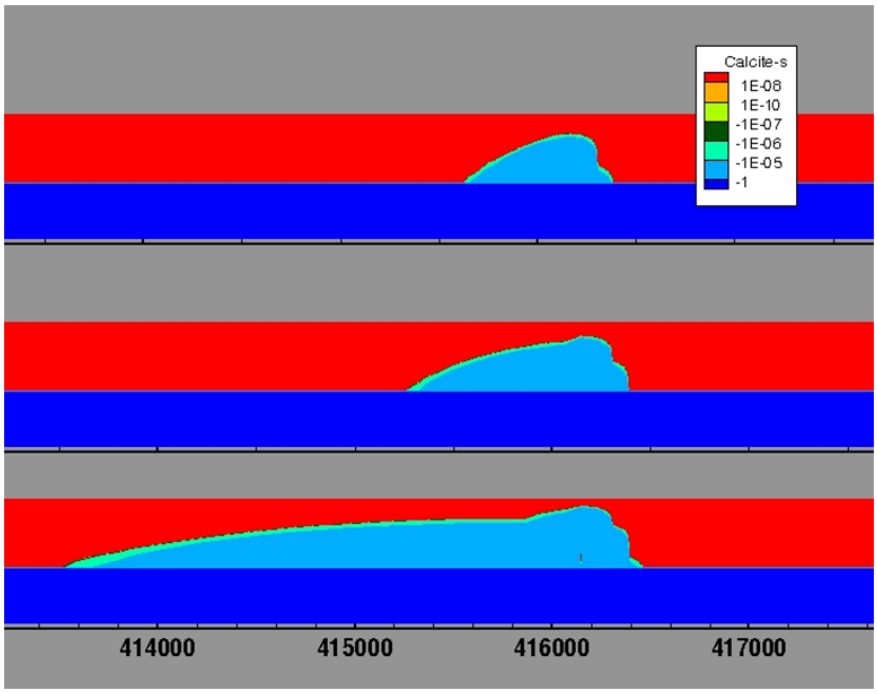

Figure 20. Cumulative amount of calcite dissolved (moles) in the shallow aquifer (note: dark blue area along bottom is below the shallow aquifer – no date here).

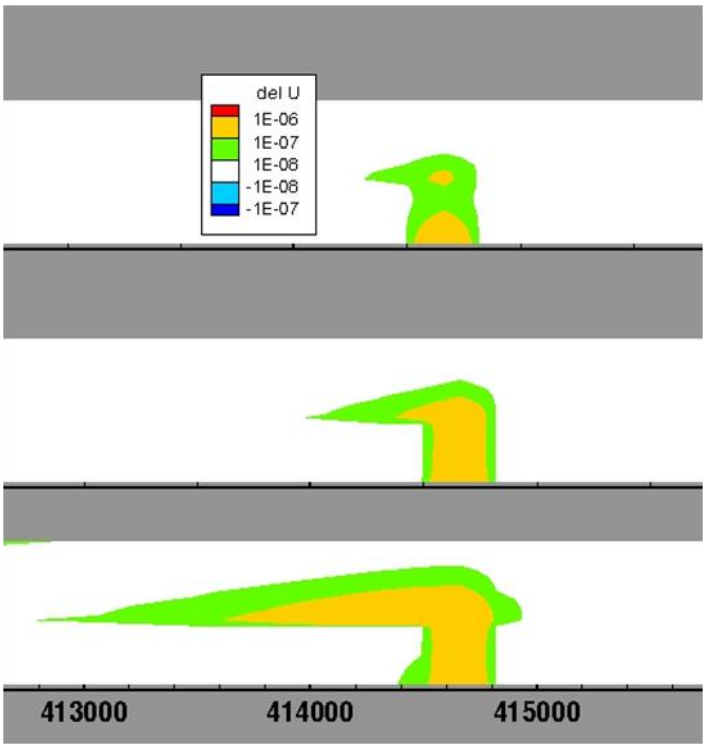

Figure 21. Cumulative changes in U concentrations, along an E-W cross-section in the southern portion of the model.

elevated [U]. Some release of U is caused by dissolution of calcite, but this effect is subtle compared to the entrainment. No significant desorption of [U] occurs, due to the stability of the $Ca_2UO_2(CO_3)_3$ complex at all pH values during the simulation.

Task 2. Coupled flow and stress simulation capability development:

Shear failure simulation capability

First, we used a toy problem to demonstrate the capability to simulate shear failure (Figure 22).

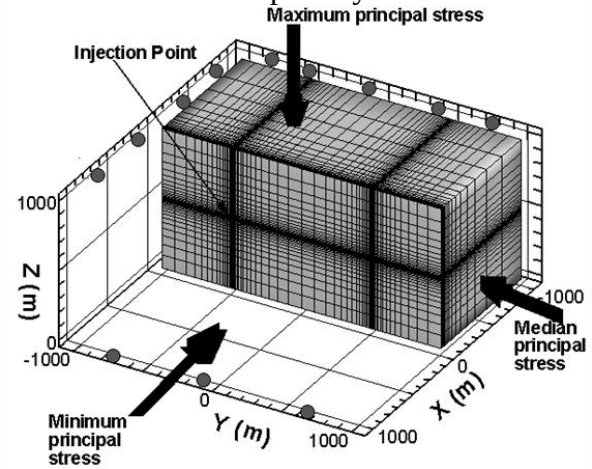

Figure 22. A cut-away view of the computational grid including the stress boundary conditions.

The model domain was 2 km by 2 km in the horizontal directions and 1 km in the vertical direction. The Z axis was aligned with the maximum principal stress, which was taken to be vertical. The X axis was taken to be horizontal and aligned with the least principal stress. There were a total of 79,365 computational nodes. The grid spacing along the X axis was refined near the center. Injection was at a point at the center of the X and Z dimensions, and ¼ of the way from the boundary along the Y axis. The grid spacing along the Y and Z directions was refined near the injection point. Fluid flow boundary conditions were chosen to be such that pressure was held at the constant initial value on the exterior faces of the model volume, and a constant specified pressure was applied at the injection point. The heat flow boundary conditions were taken to be no flow of heat at the external boundaries of the model volume and a constant temperature was specified for the injected flux.

Figure 23 shows the modeled normalized injection rate versus time obtained for the model discussed above. The injection-time history is normalized against convenient values to emphasize different injection rate behaviors (Stages I, II, and III) associated with contributions of distinct processes that operate/dominate at different times in the simulated stimulation. At early times, shown as Stage I in Figure 23, the response is most similar to a system with fixed permeability and fluid properties. Sensitivity analysis reveals that this response is most sensitive to initial permeability and fluid viscosity. In Region II, the injection rate at constant pressure begins to climb in response to the stress-dependence of permeability- derived from simulated Mohr-Coulomb shear failure. This transition results from onset of delivery of cooler fluid to the formation via the injection point, which causes cooling and thermal contraction. The superposition of thermal stresses in the formation promotes shear failure and the associated increase in permeability.

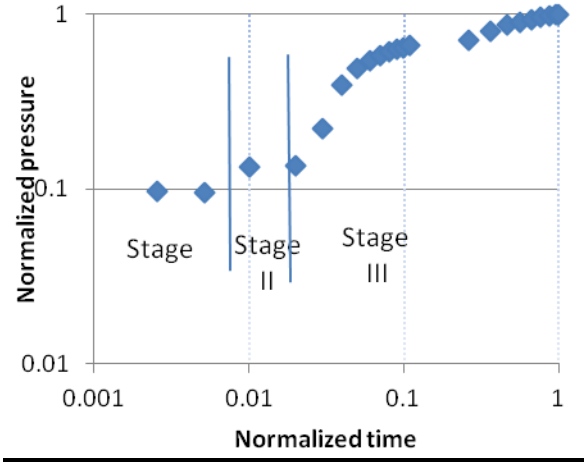

Figure 23. Simulated normalized injection rate versus time.

This produces a positive feedback where higher rates of flow allow for the cooler fluid to reach the formation. In addition to the injection pressure and temperature, the onset of this Stage is most sensitive to the material properties of shear strength, the Young's modulus and the coefficient of thermal expansion. Other properties such conductivity, and heat capacity, have an important, but lesser impact. In Region III, the flow rate continues to increase at a rate lower than that in region II. The rate of increase is lower because the region nearest to the injection point has already gone through permeability enhancement, and the fluid traveling further out gets

warmer and the pressure drops off. The transition from Region II to III is sensitive to the permeability multiplier used in the stress-permeability model.

Next, we used data from the Desert Peak geothermal project for model validation. Although the Desert Peak project is an Enhanced Geothermal System and not a CO_2 sequestration study, we are using it as an analogue for testing the code functionality because the site has been well characterized and field data are available from a hydro-stimulation treatment that involved shear-induced permeability enhancement. Field data included injection rate of water as a function of time.

Figure 24 shows a comparison of the FEHM model predictions against the field data. As can be seen from the figure, we were able to match the field data well using the newly developed shear-induced permeability enhancement capability.

The capability to simulate shear failure was applied to a toy problem to demonstrate how it can be used to study induced micro-seismicity. As mentioned earlier, we use an indirect approach to simulate induced micro-seismicity where the zone of micro-seismicity is correlated to permeability damage zone. The permeability damage zone can be simulated using FEHM by taking into account stress changes resulting from pore-pressure changes as well as thermal effect. In order to demonstrate this approach a three dimensional model domain 50m x 50m x 100m was chosen. CO_2 was injected at a constant mass rate of 3.3 kg/s at the point (0,0, 50m).

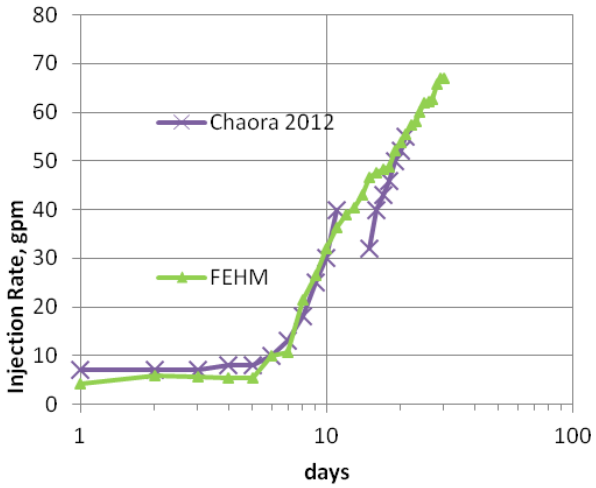

Figure 24. Comparison of FEHM calculations with permeability-shear stress model against field (Chabora et al. 2012) data from the Desert Peak reservoir.

The grid consisted of 2541 nodes, with refinement near the injection interval as shown in Figure 25. The various material properties used in the example are given in Table 13.

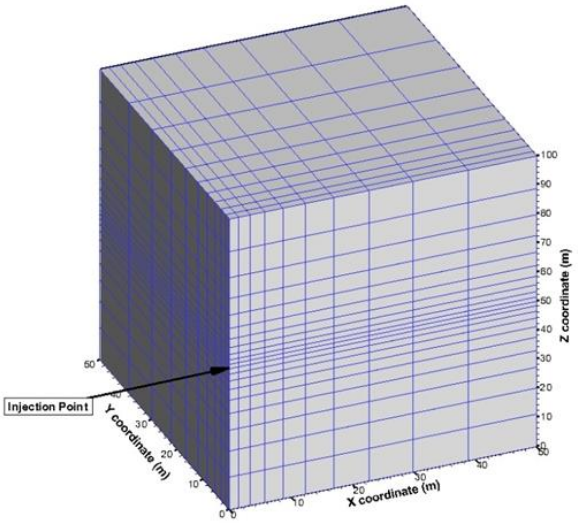

Figure 25. Model domain and the grid used for the CO_2 injection example with shear stress-permeability model.

Table 13. Material properties used for the CO_2 injection example.

PROPERTY	VALUE	PROPERTY	VALUE
Rock Thermal conductivity	3 W/m/^{0}K	Young's modulus	40,000. MPa
Rock density	2480. kg/m^3	Poisson's ratio	0.25
Heat capacity	820. J/kg/^{0}K	Linear Coefficient of thermal expansion	0.633 10^{-5} /^{0}C
Porosity	20%	Biot factor	1
Initial Permeability	10^{-13} m^2	Permeability multiplier	20
Coefficient of friction	0.5	Cohesion	7 MPa

The initial pressure and temperature were 17.5 MPa and 58 °C everywhere in the domain. The domain was initially fully saturated with water. Flow boundary conditions were such that a water pressure of 17.5 MPa and 58 °C were maintained at the X=50m face of the model. All other faces were designated no-flow. CO_2 was injected at the (0, 0, 50m) location at a constant mass rate 3.3 kg/s at a temperature 0f 40 °C. Applied mechanical boundary conditions were such that no X-displacement was allowed at the X=0 m face while it was free to move in the Y and Z directions. Similarly, Y=0 and Z=0 faces were fixed in the Y and Z directions respectively, while being free to mode in the other two directions. A vertical overburden load of 34 MPa was applied to the top of the model at Z=100m. Horizontal compressive stresses of 17.5 MPa were applied on the X=50m and Y=50 faces. As the CO_2 injection continued, a region of cooling and higher pressure developed near the injection point, with accompanying changes in the stress field, and a reduction in the compressive normal stresses. Figure 26 shows the temperature field after 7 days of injection.

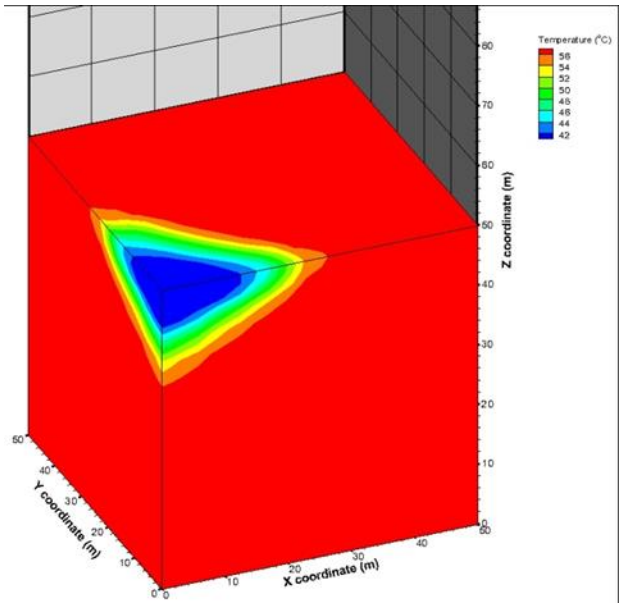

Figure 26. A cut –away through the injection point showing temperature contours after 7 days of CO_2 injection.

When the Mohr-Coulomb criterion was satisfied, this led to the development of a damage zone with enhanced permeability. Figure 27 shows the damage zone developed after 7 days of pumping and Figure 28 shows the zone of enhanced permeability. Figure 29 shows the injection pressure as a function of time – note that as the stimulated zone develops, its permeability increases, thus increasing the overall permeability of the system with time. This is reflected in the reduction of the injection pressure with time. This is in contrast to the behavior expected for a constant permeability system, where the injection pressure is actually expected to rise with time.

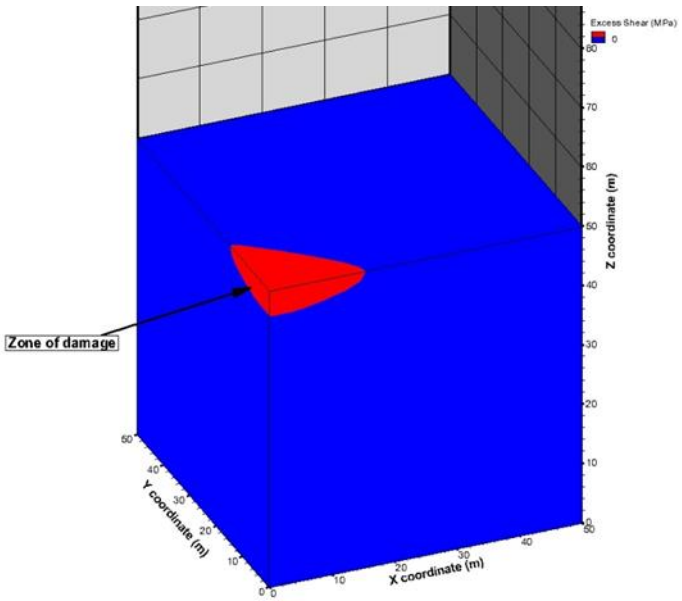

Figure 27. A cut-away through the injection point showing the damage zone.

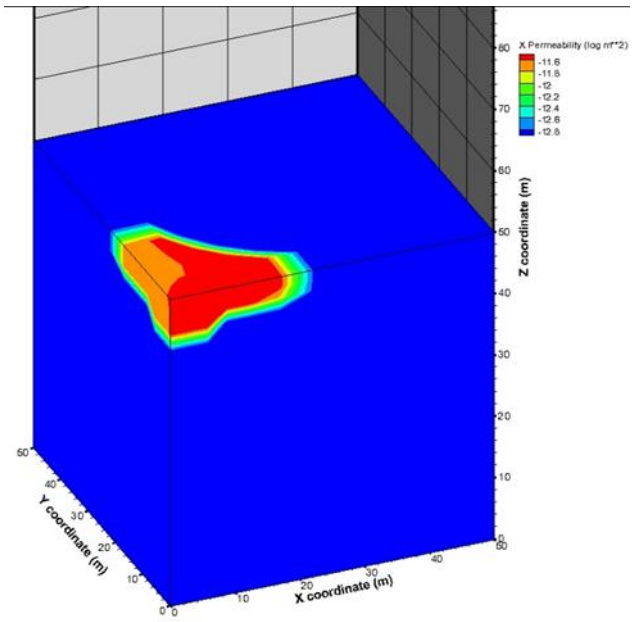

Figure 28. A cut-away through the injection point shown permeability enhancement due to shear stimulation.

Implicit coupling test

We demonstrate the implicit approach of solving the flow and stress equations using a simple model presented in Figure 29. Although the problem being considered is single phase water, a hypothetical permeability-stress model used was used in order to mimic the generation of permeability by fluid pressure build up caused by phase change. The initial permeability was 10^{-14} m^2 everywhere.

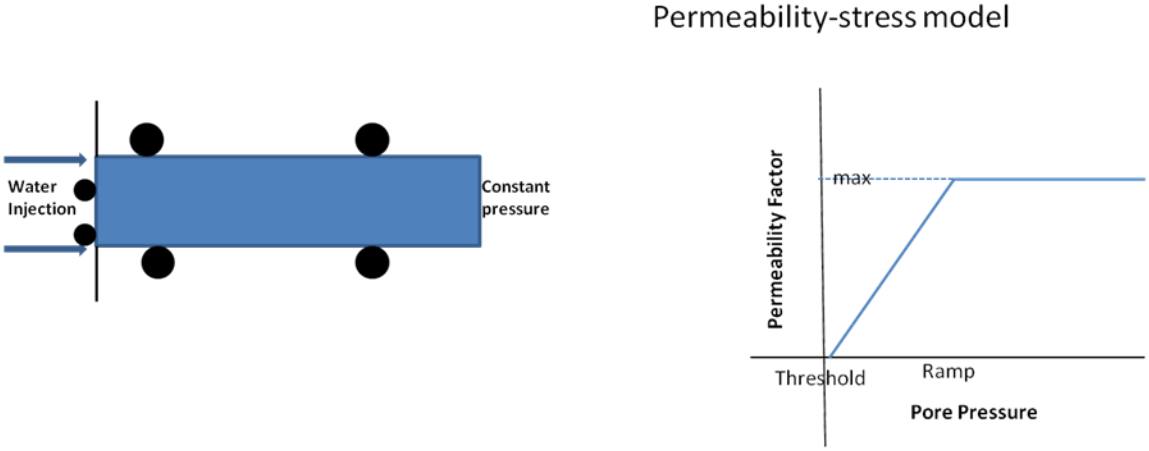

Figure 29. A schematics of the problem used for testing an implicitly coupled 5 DOF formulation in FEHM.

When pore pressure exceeded a prescribed value (in this case 0.01 MPa), the permeability was ramped up over a user specified pressure interval (1 MPa in this case) from the initial value to that multiplied by a user specified factor, which was taken to be 1000 in this case. For this example, porosity was held fixed at 20% throughout the simulation.

The grid had 44 nodes, with dimensions of 10m x 1m x 1m. It was placed on rollers in the y and z directions. In the X direction, the face at X=0 was placed on rollers, and the face at X=10m was free to move. The initial pore pressure everywhere was 10 MPa. Injection was commenced at time=0. The temperature was held constant at 25 °C throughout the simulation.

The resulting pressure at the injection face is shown as a function of time for various values of time step size in Figure 30. The time step was held fixed during each simulation. Results for explicit (solid lines) and fully implicit coupling (symbols) are shown on the same plot. Note that the explicit coupling case does not converge even after 100 Newton-Raphson iterations for time steps larger than about $7x10^{-5}$ days, while the fully implicit coupling stays stable and accurate for time steps at least as large as 1 day.

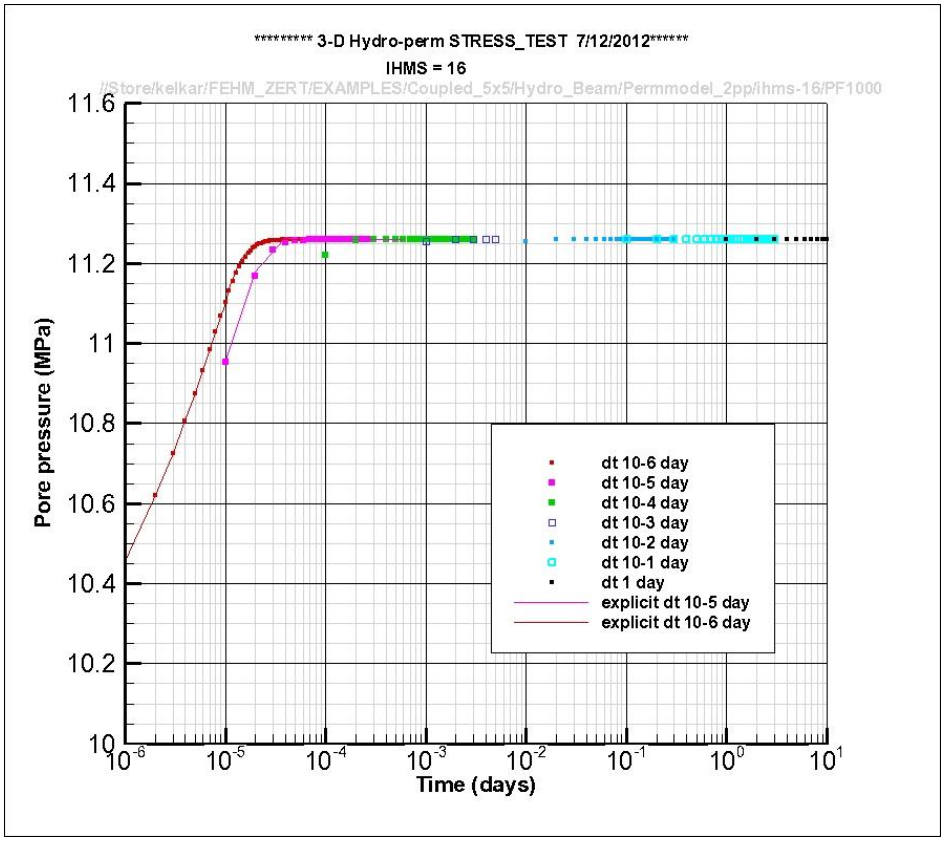

Figure 30. Comparison of the pressure buildup for various time sizes for explicit and implicit coupling for the example from Figure 29.

Conclusions

Task 1 We have made significant advances to address some of the issues related to shallow aquifer impacts due to leakage of CO_2 and deeper brine at a geologic CO_2 sequestration site. We have used an integrated approach combining field observation at a natural analog site with laboratory experiments and numerical simulations. Our research has primarily focused on release of uranium and arsenic. The work related to Uranium builds on earlier work in ZERT-I, while the work related to arsenic is new. We have used inverse modeling to estimate geochemical

reaction parameters for adsorption/desorption behavior of arsenic. Our models for Chimayo field data indicate that the arsenic concentration observed in field samples may be resulting from high arsenic concentration in the deeper brine that is co-transported with CO_2. We have successfully matched the field observed uranium data at Chimayo site with numerical simulations. The results support similar conclusions as arsenic on its transport through deeper brine transport.

Task 2 We have successfully developed for permeability enhancement due to shear failure using Mohr-Coulomb failure criterion and tested it against field data. We have demonstrated how this shear-failure model can be applied to induced micro-seismicity at geologic CO_2 sequestration sites. Additionally, we have also implemented an approach to implicitly solve fluid flow and stress equations. The implicit solution approach overcomes the inherent limitations of time-step size and in-accurate solutions that are present in explicit approach. The problem of inaccuracy can be of importance in cases where there is rupture of fault due to shear failure.

GRAPHICAL MATERIALS LIST(S):

Publications

- Keating, E., Hakala, J., Viswanathan, H., Carey, J., Pawar, R., Guthrie, G., Fessenden-Rahn, J., CO_2 leakage impacts on shallow groundwater: Field-scale reactive transport simulations informed by observations at a natural analog site, Applied Geochemistry, 30, 136-147, 2013.
- Viswanathan, H. S., Dai, Z. X., Lopano, C., Keating, E., Hakala, J. A., Schekel, K. G., Zheng, L., Guthrie, G. D., Pawar, R., Developing a robust geochemical and reactive transport model to evaluate possible sources of arsenic at the CO_2 sequestration analog site in Chimayo, New Mexico, International Journal of Greenhouse Gas Control, 10, 199-214, 2012.
- "Coupled plastic failure and permeability in rocks: a modeling approach", Kelkar et al., Proceedings of 46th US Rock Mechanics/Geomechanics Symposium of the American Rock Mechanics Association, May 24-27, Chicago, IL.

Conference Presentations

- Viswanathan et al., "Mechanisms of arsenic and uranium release at the CO_2 sequestration natural analog site, Chimayo, New Mexico ", Presented at the 10th Annual conference on Carbon Capture & Sequestration, Pittsburgh, PA, May 2-5, 2011.
- Keating et al., "Assessing risk to shallow groundwater from CO_2 leaks: Synthesis of two field studies with contrasting results", Presented at the 10th Annual conference on Carbon Capture & Sequestration, Pittsburgh, PA, May 2-5, 2011.

- Rapaka & Pawar, "Application of Satellite-based Surface Deformation Monitoring for Leakage Detection", Presented at the 10th Annual conference on Carbon Capture & Sequestration, Pittsburgh, PA, May 2-5, 2011.
- Keating et al., "Assessing the impact of CO_2 and brine leakage on shallow groundwater quality: Results from a natural analog study in New Mexico, USA", Invited talk at American Geophysical Union 2011 Fall Meeting, San Francisco.
- Viswanathan et al., "Mechanisms for Arsenic Release at the CO2 Sequestration Natural Analog Site in Chimayo, New Mexico," American Geophysical Union 2011 Fall Meeting, San Francisco.
- Keating et al., "The challenge of predicting groundwater quality impacts in CO_2 leakage scenarios: Results from field, laboratory and modeling studies at a natural analog site in New Mexico, U.S.A.", Invited talk 2010 Geological Society of America Annual Meeting.
- Keating et al., "The challenge of predicting groundwater quality impacts in CO_2 leakage scenarios: Results from field, laboratory and modeling studies at a natural analog site in New Mexico, U.S.A.", Invited talk at Natural release of CO_2: Building knowledge for CO_2 storage environmental impacts assessments – An IEAGHG Workshop, hosted by CO_2GeoNet/BGR 2-4 Nov 2010, Maria Leach, Germany.
- Zyvoloski, et al., "Thermal-Hydrologic-Mechanical behavior of single fracture in EGS reservoirs," Invited talk at the 2010 American Geophysical Union (AGU) Annual Fall Meeting, San Francisco.
- Rapaka et al., "Modeling permeability enhancement due to coupled Thermal-Hydrological-Mechanical processes in geothermal reservoirs, 2010 American Geophysical Union (AGU) Annual Fall Meeting, San Francisco.
- Kelkar et al., "Coupled plastic failure and permeability in rocks: a modeling approach", 46th US Rock Mechanics/Geomechanics Symposium of the American Rock Mechanics Association, May 24-27, Chicago, IL.

References

Appelo, C. A. J., and D. Postma, Geochemistry, Groundwater and pollution, (Ed. Balkema, Rotterdam), 1993.

Carey, J. W., Williams, M. R.; Hakala, A.; Fessenden, J. E.; Keating, E. H., 2009. *Experimental study of sediment-CO_2 reactions with application to changes in groundwater quality due to leakage of sequestered CO_2.* American Geophysical Union, Fall Meeting, abstract #H13A-0913.

Cumming, K.A., 1997. *Hydrogeochemistry of groundwater in Chimayó, New Mexico*, M.S., Northern Arizona University, Flagstaff, AZ.

Dai, Z., A. V. Wolfsberg, Z. Lu and H. Deng, 2009. *Scale dependence of sorption coefficients for radionuclide transport in saturated fractured rock*, Geophys. Res. Lett., 36, L01403, doi:10.1029/2008GL036516.

Dempsey D., Ellis S., Archer R., and Rowland J. (2012), Energetics of normal earthquakes on dip-slip faults, Geology, doi:10.1130/G32643.1

Dixit, S. and J.G. Hering, Comparison of arsenic(V) and arsenic(III) sorption onto iron oxide minerals: implications for arsenic mobility, *Environmental Science & Technology* **37**, pp. 4182–4189, 2003.

Doherty, J., 2010, PEST, *Model-independent parameter estimation*, Watermark Computing, Corinda, Australia, 122p.

Dong, W. et al. , W.P. Ball, C. Liu, Z. Wang, A. Stone, J. Bai, J.M. Zachara, 2005. *Influence of Calcite and Dissolved Calcium on Uranium(VI) Sorption to a Hanford Subsurface Sediment*. Environ. Sci. Technol. 39, 7949-7955.

Duan, Z., Sun, R, 2003. *An improved model calculating CO_2 solubility in pure water and aqueous NaCl solutions from 273 to 533 K and from 0 to 2000 bar*. Chemical Geology 193, pg. 257– 271.

Fox, P.M., Davis, J.A., Zachara, J.M., 2006. *The effect of calcium on aqueous uranium (VI) speciation and adsorption to ferrihydrite and quartz*. Geochimica et Cosmochimica Acta 70, 1379-1387.

Goldberg, S. Competitive adsorption of arsenate and arsenite on oxides and clay minerals, *Soil Science Society of America Journal* **66**, pp. 413–421, 2002.

Goldberg, S., *The optimizations for the intrinsic equilibrium constants of As(V) illite adsorption*, personal communication, 2011.

Guttenberg, B. and Richter, C. F. (1944), Frequency of earthquakes in California, *Bulletin of the Seismological Society of America*, **34**, 185-188.

Hanks, T. C., and Kanamori, H. (1979), A Moment Magnitude Scale, *Journal of Geophysical Research*, **84**, 2348-2350.

Helmstetter, A., Kagan, Y. Y., and Jackson, D. D. (2005), Importance of small earthquakes for stress transfers and earthquake triggering, *Journal of Geophysical Research*, **110**, 10.1029/2004JB003286.

Hsi, C-K D., L. Langmuir, 1985. *Adsorption of uranyl onto ferric oxyhydroxides: Application of the surface complexation site-binding model*, Geochemica Cosmica Arm. Vol. 49. pp. 193

Keating, E.H., Fessenden, J., Kanjorski, N., Koning, D.J., Pawar, R.J., *The impact of CO_2 on shallow groundwater chemistry: observations at a natural analog site and implications for carbon sequestration*, Envrion Earth Sci, 2009.

Keating, E.H., Hakala, J.A., Viswanathan, H., Capo, R., Steward, B., Gerdiner, J., Guthrie, G., Carey, J.W., Fessenden, J., 2010. *The challenge of predicting groundwater quality impacts in a CO2 leakage scenario: Results from field, laboratory, and modeling studies at a natural analog site in New Mexico, U.S.A.* Energy Procedia, Vol.4, p.3239-3245

Koning DJ, Skotnicki S, Nyman M, Horning R, Eppes M, Rogers S, 2002. *Geology of the Cundiyo 7.5-minute quadrangle, Santa Fe County,NewMexico:NewMexico Bureau ofGeology and Mineral Resources*, Open-file Geologic Map OF-GM-56, scale 1:24,000

Kelkar, S., Lewis, K., Hickman, S., Davatzes, N. C., Moos, D., and Zyvoloski, G. (2012), Modeling coupled thermal-hydrological-mechanical processes during shear stimulation of an EGS well, *37th Stanford Geothermal Workshop*, Stanford, Ca.

Koning DJ , 2003. revised Dec-2005, *Geologic map of the Chimayo 7.5-minute quadrangle, Rio Arriba and Santa Fe Counties, New Mexico*: New Mexico Bureau of Geology and Mineral Resources, Open-file Geologic Map OF-GM-71, scale 1:24,000

Langmuir D, 1997. *Aqueous Environmental Chemistry: Upper Addle River, New Jersey*. Prentice-Hall, Englewood Cliffs, 600 pp

Manning, B.A. and S. Goldberg, Adsorption and stability of arsenic(III) at the clay mineral–water interface, *Environmental Science & Technology* **31**, pp. 2005–2011, 1997.

McGarr, A. (1994), Some Comparisons between Mining-induced and Laboratory Earthquakes, *Pure and Applied Geophysics*, **142**, 217-254.

National Research Council (2012), Induced Seismicity Potential in Energy Technologies, *Report of the National Research Council*, The National Academies Press, Washington, D. C.

Parkhurst, D.L., and C.A.J. Appelo, User's guide to PHREEQC (version 2)--A computer program for speciation, batch-reaction, one-dimensional transport, and inverse geochemical calculations: *U.S. Geological Survey Water-Resources Investigations Report* 99-4259, 312 pp., 1999.

Rossberg, A., Ulrich K-U, Weiss, S., Tsushima, S. Hiemstra, T. Scheinost, A.C., 2009. *Identification of uranyl surface complexes on ferrihydrite: advanced EXAFS Data Analysis and CD-MUSIC modeling*. Environ. Sci. Technol. 43,1400-1406.

Tong, C., PSUADE User's Manual (Version 1.2.0), LLNL-SM-407882, Lawrence Livermore National Laboratory, Livermore, CA 94551-0808, May, 2009.

Utsu, T., Ogata, Y. and Matsu'ura, R. S. (1995), The Centenary of the Omori Formula for a Decay Law of Aftershock Activity, *Journal of the Physics of the Earth*, **43**, 1-33.

Viswanathan, H., Z. Dai, C. Lopano, E. Keating, J. A. Hakala, K. Scheckel, L. Zheng and R. Pawar, *Developing a Robust Geochemical and Reactive Transport Model to Evaluate Mechanisms for Arsenic Release at the CO_2 Sequestration Natural Analog Site in Chimayo, New Mexico*, to be submitted to *International Journal of Greenhouse Gas Control*, in internal review, 2011.

Waite, T.D., Davis, J.A., Payne, T.E., Waychunas, G.A., Xu,N., 1994. *Uranium (VI) adsorption to ferrihydrite: Application of a surface complexation model*. Geochimica et Cosmochimica Act, 58(24), 5465-5478.

Xu, T., E.L. Sonnenthal, N. Spycher, and K. Pruess, TOUGHREACT - *A simulation program for non-isothermal multiphase reactive geochemical transport in variably saturated geologic media: Applications to geothermal injectivity and CO_2 geological sequestration*, Computer & Geoscience, v. 32/2 p. 145-165, 2006.

Zheng, L.; Apps, J.A.; Zhang, Y.; Xu, T.; Birkholzer, J.T. On mobilization of lead and arsenic in groundwater in response to CO2 leakage from deep geological storage, Chemical Geology, Volume 268, Issue 3-4, Pages 281-297, November 2009.

Zyvoloski, G. A., et al. , 1997. *Summary of the Models and Methods for the {FEHM} Application --- A Finite-Element Heat- and Mass-Transfer Code*, 72 pp, Los Alamos National Laboratory.

Appendix E

Pacific Northwest National Laboratory

Multi-Channel Auto-Dilution System for Remote Continuous Monitoring of High Soil–CO_2 Fluxes

U.S. DEPARTMENT OF ENERGY

PNNL-18229

Prepared for the U.S. Department of Energy
under Contract DE-AC05-76RL01830

Multi-Channel Auto-Dilution System for Remote Continuous Monitoring of High Soil–CO_2 Fluxes

JE Amonette
JL Barr

April 2009

Pacific Northwest
NATIONAL LABORATORY

DISCLAIMER

PACIFIC NORTHWEST NATIONAL LABORATORY
operated by
BATTELLE
for the
UNITED STATES DEPARTMENT OF ENERGY
under Contract DE-AC05-76RL01830

Printed in the United States of America

Available to DOE and DOE contractors from the
Office of Scientific and Technical Information,
P.O. Box 62, Oak Ridge, TN 37831-0062;
ph: (865) 576-8401
fax: (865) 576-5728
email: reports@adonis.osti.gov

Available to the public from the National Technical Information Service,
U.S. Department of Commerce, 5285 Port Royal Rd., Springfield, VA 22161
ph: (800) 553-6847
fax: (703) 605-6900
email: orders@ntis.fedworld.gov
online ordering: http://www.ntis.gov/ordering.htm

This document was printed on recycled paper.
(9/2003)

PNNL-18229

Multi-Channel Auto-Dilution System for Remote Continuous Monitoring of High Soil–CO_2 Fluxes

JE Amonette
JL Barr

April 2009

Prepared for
the U.S. Department of Energy
under Contract DE-AC05-76RL01830

Pacific Northwest National Laboratory
Richland, Washington 99352

Summary

Geological sequestration has the potential capacity and longevity to significantly decrease the amount of anthropogenic CO_2 introduced into the atmosphere by combustion of fossil fuels such as coal. Effective sequestration, however, requires the ability to verify the integrity of the reservoir and ensure that potential leakage rates are kept to a minimum. Moreover, understanding the pathways by which CO_2 migrates to the surface is critical to assessing the risks and developing remediation approaches. Field experiments, such as those conducted at the Zero Emissions Research and Technology (ZERT) project test site in Bozeman, Montana, require a flexible CO_2 monitoring system that can accurately and continuously measure soil-surface CO_2 fluxes for multiple sampling points at concentrations ranging from background levels to several tens of percent. To meet this need, researchers at Pacific Northwest National Laboratory (PNNL) are developing a multi-port battery-operated system capable of both spatial and temporal monitoring of CO_2 at concentrations from ambient to at least 150,000 ppmv.

The system consists of soil-gas sampling chambers and a sensing unit based on an infrared gas analyzer (IRGA). Headspace gas from the chambers is continuously pumped through a relay-driven manifold that directs gas from individual chambers into the IRGA. A unique feature of the system is its ability, based on feedback from the IRGA, to automatically dilute the sample gas stream with N_2 using a network of gas-flow controllers, thus allowing measurement of CO_2 levels beyond the normal IRGA limit of 3000 ppmv. The entire system is controlled by a programmable datalogger that also stores the output from the IRGA and gas-flow controllers. The system consists of 27 sampling chambers, thus allowing detailed spatial monitoring of a moderately sized test area (~100 m^2). Power can be provided either by an AC source or by an off-grid power-generation system consisting of six deep-cycle batteries charged by both wind and photovoltaic power sources. Dilution gas is provided by a liquid N_2 dewar containing the equivalent of 135,000 L of N_2(g), enough for 4 weeks of continuous operation. The system is remotely controlled and monitored by connecting the datalogger communication port to a cellular-based modem and antenna.

On 27 August 2008, a shallow test injection of CO_2 was started at the ZERT site using a horizontal well located about 2 m below the surface and 1 m below the water table. The PNNL team set up a 27-chamber sampling grid directly above and extending northwest of the injection well. Concentrations were monitored continuously in twenty of these steady-state flux chambers during 13 days of injection (308 h) and for 33 days post injection. These concentration data can be converted directly to flux data using a flow-rate specific constant.

With the 20-chamber setup, data were collected on a 2.7-h cycle continuously for nearly 7 weeks. We centered the southeastern side of the sampling grid on a known leakage spot, and this was clearly borne out by the spatially resolved data. Unfortunately, some of the fluxes were still high enough (> 470 μmol m^{-2} s^{-1}) to saturate the analyzer. In general, the release showed near-immediate breakthrough at the hot spot, and a steady state was obtained after about 1 week of injection. The spatial extent of the emissions was generally less than 5 m laterally from the injection well. After injection ceased, fluxes at the hot spots dropped rapidly. However, at least 2 weeks were needed for the soil system to return to its initial state.

During the injection, we observed several major negative excursions in CO_2 flux data from those expected, based on trends in the data. These excursions were correlated with periods of high wind power

density (proportional to the cube of the wind velocity) and, to a lesser extent, wind direction. Data from our system was compared to that from a LI-8100 non–steady-state flux chamber system (LI-COR Biosciences, Lincoln, NE) located immediately adjacent to five of our chambers and equipped with a special air vent. In some instances, the excursions seem to be artifacts of our chamber design, whereas in others, the excursions seem to represent a real effect of sustained wind power on the CO_2 fluxes emanating from the soil. This comparison also showed that our chambers yielded flux values that were about five times greater than those obtained by the LI-8000 system. Further investigation showed the resistance to air flow inside the narrow vent tubes used to vent ambient air into our chambers, combined with the outflow rates we used, induced a vacuum inside the chambers large enough to cause a significant convective flux of CO_2 from the soil into our chambers, thus explaining the higher flux data we obtained.

Based on these results, we established several priorities for the coming fiscal year. Our primary task will be to modify to our chamber venting system to yield pressure drops of about 0.5 Pa and avoid wind-induced perturbations. Other priorities include developing 1) a two-stage dilution system to expand our range to cover the full range of possible CO_2 concentrations, and 2) an improved data reduction and visualization approach with Internet-based accessibility. During the 2009 field season, we also plan on exploring the impact of moisture content on CO_2 flux patterns.

Acknowledgments

Work was funded by the U.S. Department of Energy (DOE) Office of Fossil Energy as part of the Zero Emissions Research and Technology (ZERT) program, and by the DOE Office of Biological and Environmental Science within the Office of Science as part of the Carbon Sequestration in Terrestrial Ecosystems (CSiTE) program. We thank Dr. Jennifer L. Lewicki (Lawrence Berkeley National Laboratory) for sharing her ZERT-site precipitation data and Dr. Joseph A. Shaw (Montana State University) for all other ZERT-site weather data. Ms. Kadie Gullickson (Montana State University) collected the soil moisture data. Dr. Laura Dobeck (Montana State University) conducted the injection and provided overall site monitoring and expertise. Mr. Steven J. Walsh (Pacific Northwest National Laboratory) generated the two-dimensional plots of the discrete chamber data.

Acronyms and Abbreviations

A-h	ampere-hour(s)
CSiTE	Carbon Sequestration in Terrestrial Ecosystems (program)
DOE	U.S. Department of Energy
IRGA	infrared gas analyzer
MFC	mass flow controller
PNNL	Pacific Northwest National Laboratory
ppmv	parts per million – volumetric
µmol	micromol
WPD	wind power density
ZERT	Zero Emissions Research and Technology

Contents

Figures

Tables

1.0 Introduction

Geological sequestration has the potential capacity and longevity to significantly decrease the amount of anthropogenic CO_2 introduced into the atmosphere by combustion of fossil fuels such as coal (White et al. 2003, 2005; McGrail et al. 2006). Effective sequestration, however, requires the ability to verify the integrity of the reservoir and ensure that potential leakage rates are kept to a minimum. Moreover, understanding the pathways by which CO_2 migrates to the surface is critical to assessing the risks and developing remediation approaches. Field experiments, such as those conducted at the Zero Emissions Research and Technology (ZERT) project test site in Bozeman, Montana, require a flexible CO_2 monitoring system that can accurately and continuously measure soil–surface CO_2 fluxes for multiple sampling points at concentrations ranging from background levels to several tens of percent. To meet this need, we are developing a multi-port battery-operated system capable of both spatial and temporal monitoring of CO_2 at concentrations from ambient to at least 150,000 ppmv.

The system consists of soil surface-flux chambers, a central measurement and control system, and an off-grid power supply system. The flux chambers are connected to the central system by 30-ft lengths of 0.25-in.-OD tubing to transfer gas samples from the chamber interior to the analyzer. The measurement and control system consists of a CO_2/H_2O gas analyzer; a datalogger for measurement recording and system control; a chamber selection and control system composed of latching microvalves, manifold, and AC/DC relays; and a sample dilution system consisting of two flow meters and one flow controller that precisely adjust and measure the incoming sample concentration by dilution with inert gas flow. The off-grid power system is energized by a three-panel photovoltaic array and two wind turbines. This energy is stored in six 12-V deep-cycle batteries and utilized by the system through an AC inverter.

This report summarizes the design of the various components of the system, including the sampling chambers, the measurement and control system, and the off-grid power supply, and then presents the results of a 7-week field test of the integrated system at the ZERT project test site.

2.0 Chamber Design

2.1 Design Considerations

Accurate real-time monitoring of subsurface CO_2 flux and concentration changes associated with CO_2 outflow from a subsurface point or line source requires an appropriately designed sampling chamber. The key considerations for the ZERT field work included

- multi-component chamber construction
- small footprint to improve spatial resolution of measurements and to minimize disturbance to subsurface conditions while sampling
- chamber headspace sized for fast response time necessary for monitoring rapidly changing fluxes and concentrations and compatible with small-sample flow rates necessary for the project
- appropriate headspace mixing for non–steady-state conditions
- low-cost construction utilizing easily obtainable materials to allow placement of multiple chambers throughout the horizontal well injection site.

A multi-component design with a fixed cylindrical base and removable end cap has several advantages. It 1) minimizes long-term disturbance of the subsurface conditions by allowing the enclosure to be open to the atmosphere between sampling campaigns, 2) improves the seal between the chamber base and soil surface, and 3) eliminates uncertainty due to placement of the chamber for successive measurements at a single site. Thus, the same end cap or top can be used sequentially on several fixed base portions inserted and left in the soil at different locations.

The ideal sampling system minimizes disruption of subsurface gas distribution. Disruption can occur by 1) pulling from the sample chamber at a high flow rate, thereby altering flow paths and acting as a sink; 2) subtending a large basal area, which allows pressure differentials to change concentration gradients within a significant volume of the subsurface; and 3) sampling for long periods, which magnifies the previous two disturbances. Reducing the basal area occupied by the sampler minimizes these issues and improves the spatial resolution of the field measurements

The impact of chamber geometric factors varies with the type of flux measurement. For steady-state flux measurements, the basal area of soil surface sampled is used in flux calculations and the chamber volume (in combination with the ambient air influx rate) determines the response rate (i.e., how quickly steady state is attained). For non–steady-state flux measurements, the headspace volume-to-basal-surface-area ratio is part of the flux calculation. In our system, for which both types of flux measurements are desired, all three factors (volume, basal area, and ambient air influx rate) need to be considered. The ratio of the chamber headspace volume to the basal area through which soil gas flux is sampled was sized to provide the fast response time necessary for rapidly changing fluxes/concentrations and small-sample flow rates. A ratio of 0.17 m for chamber headspace volume to basal area was employed and can easily be modified in the field by changing the length of the headspace cylinder if experimental conditions so dictate.

The sample chamber base has inlet and exit ports located above the soil surface that allow for mixing of the headspace gases when used in conjunction with an external diaphragm pump. Mixing homogenizes

gas concentrations in the headspace, provides faster response to changes in gas fluxes and concentrations, and permits sampling of smaller volumes while retaining high accuracy and precision.

2.2 Final Design and Construction

The flux chambers consist of a base and an upper headspace-sampling component (Figure 2.1). The base is constructed of a 4-in.-diameter PVC tube (with a highly beveled end for soil insertion) attached to the male portion of a Spears Union (497-040). The upper component consists of the threaded female portion of the Spears Union, 4-in. PVC pipe, and a PVC cap with machined surfaces to accommodate pass-throughs for a 1/8-in.-OD vent tube and stainless-steel circular perforated sampling tube. Once the base is inserted into the soil, the upper component creates an airtight seal by threading onto the base and compressing the integrated O-ring onto the base sealing surface. Basal area subtended by the chamber is 8.11e-3 m^2, and headspace volume is 1.38e-3 m^3.

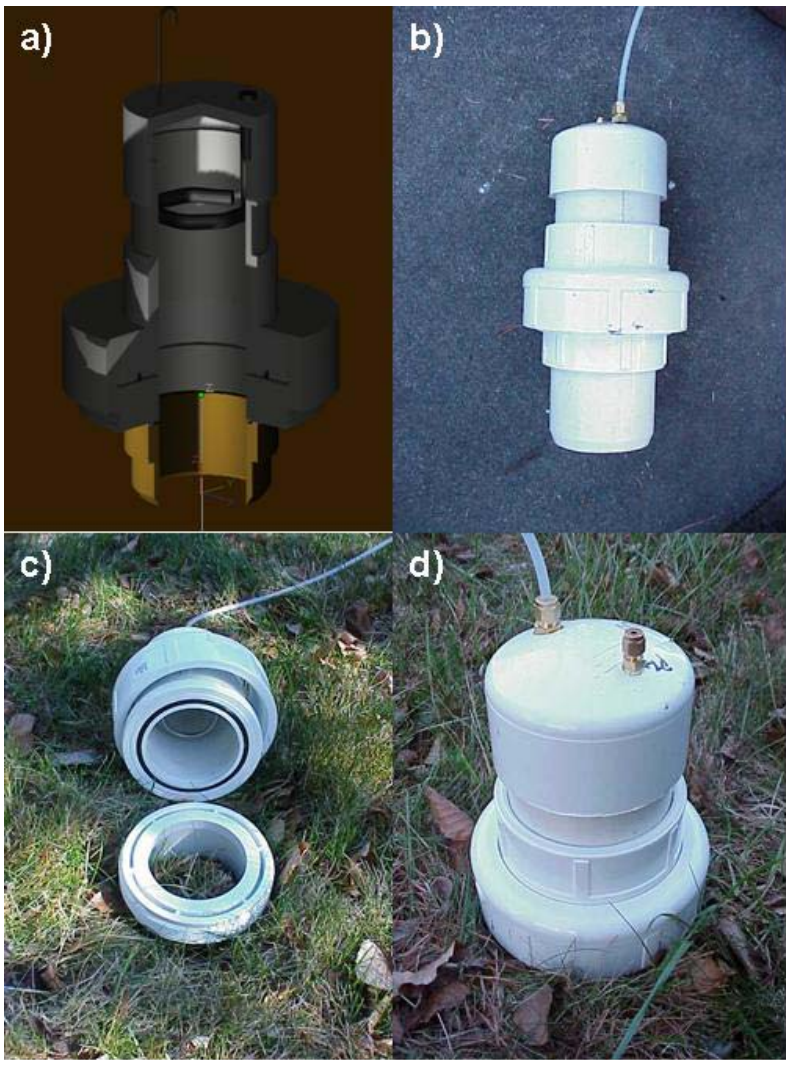

Figure 2.1. Soil Surface-Flux Sampling Chamber: a) cutaway view showing circular perforated sampling tube for headspace mixing, b) pre-installation – assembled, c) installed – top unattached, d) installed – top attached without 4-in.-long, 1/8-in.-OD vent tube

3.0 Measurement and Control System

3.1 Design Considerations

The infrared gas analyzer (IRGA) used to detect CO_2 and H_2O (LI-7000, LI-COR Biosciences, Lincoln, NE) has a maximum detection level of 3000 ppmv (0.3%) for CO_2 in the linear response range. Data collected in the 2006 and 2007 ZERT injection tests demonstrated the need to be able to detect significantly higher concentrations (up to 10–20%) with a steady-state flux-measurement approach. To accommodate this measurement range using the IRGA, we decided to develop an automatic dilution system using N_2 as the diluent. The dilution factor would need to be known precisely to allow accurate calculation of the actual CO_2 concentration and the flux associated with the soil chamber. Moreover, the dilution would need to be automated to allow routine unattended analysis under field conditions.

In our design, the N_2 dilution gas enters the system after the sample gas has been pushed from a sample pump (Aqua Lifter AW-20, Tom Aquarium Products, Gardena, CA) and before sample gas entry into the IRGA optical cell (Figure 3.1). The effect of the dilution on the IRGA response is rapid due to the proximity of the dilution inlet to the optical cell. A datalogger/control system (CR23X, Campbell Scientific, Logan, UT) sets the dilution-gas flow rate through a mass flow controller (MFC) using feedback from the current CO_2 concentration read at the analyzer (Figure 3.2). When the analyzer approaches saturation, the CR23X signals the MFC to start the dilution gas in a staged fashion. The dilution flow increases through several stages in a time-delayed series until the IRGA response is back within the linear operating range (i.e., < 3000 ppmv). From measured flow rates of the incoming sample, dilution gas, and optical cell outflow, the dilution factor is determined and stored, together with the corresponding IRGA response, by the CR23X. Analysis of each chamber is performed during a 6-min cycle time. Successive chambers are selected for analysis by the CR23X, which controls a valve manifold that directs flow to either the IRGA system (from the actively analyzed chamber only) or exhaust (from all other chambers) (Figure 3.1).

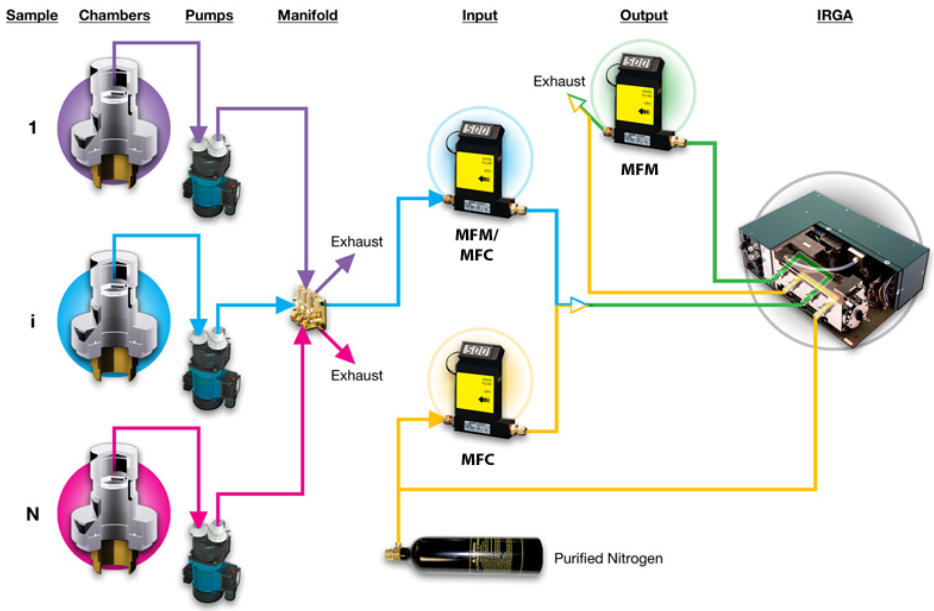

Figure 3.1. Plumbing Schematic for CO_2 Analysis by Automated Sampling and Dilution System

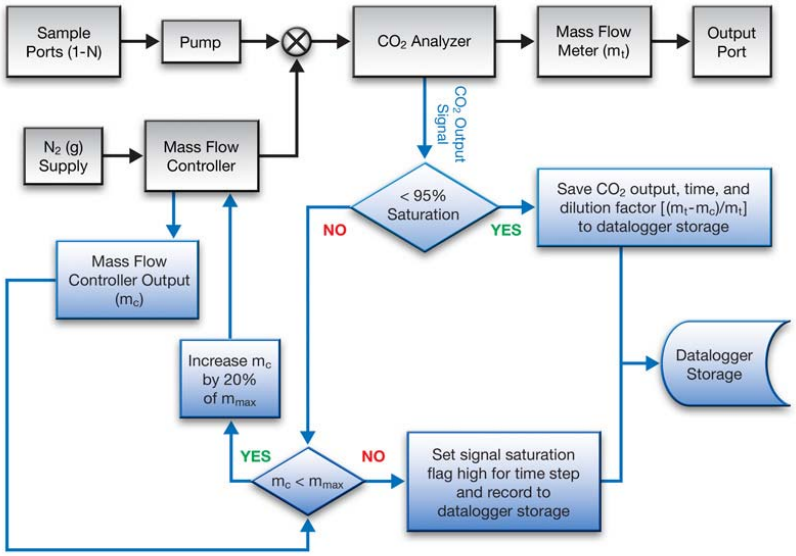

Figure 3.2. Logic and Sample Flow Paths for CO_2 Analysis by Automated Sampling and Dilution System

3.2 Testing and Verification of the System

For the system to work appropriately in the field, several criteria must be met: 1) instrument response should be stable at elevated concentrations, 2) cross-contamination from successive chamber measurements should be negligible, 3) all of the chambers should respond to the same input conditions in the same fashion, and 4) the system should be capable of being calibrated against a known standard.

The capability of the system to accurately dilute samples in real time is demonstrated in Figure 3.3. These data, collected during the 2008 field test at the ZERT site, show the staged activation of the dilution system when the IRGA detector is saturated. In this instance, two of a total of five possible dilution stages were activated. The dilution factors for these two stages were about 20x and 30x. With the higher dilution factor, the sample is diluted below the IRGA saturation limit of 3000 ppmv, and a stable dilution-corrected concentration value of 81,000 ppmv is attained. A slow decay in the dilution factor is balanced by a corresponding increase in the IRGA reading to yield a constant sample concentration as expected. Small oscillations in the sample pump rate impact the dilution factor and sample concentration but do not significantly affect the time-averaged result, which is taken during the last 2 min of the 6-min measurement cycle.

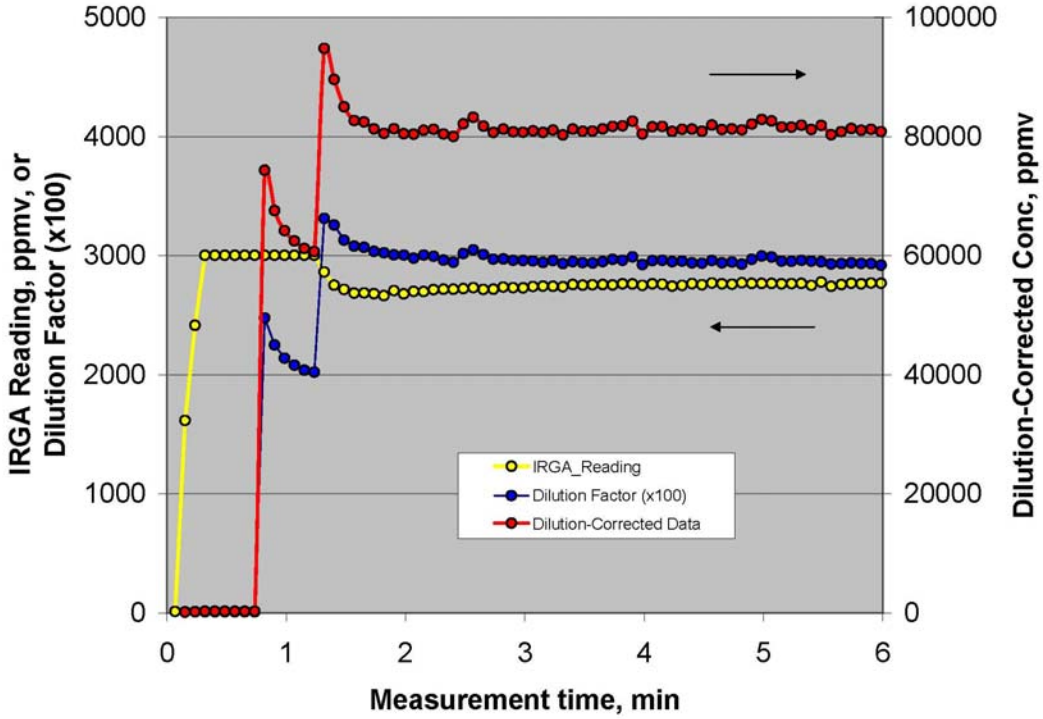

Figure 3.3. Typical Data for Dilution Process Showing Staged Dilution Based on Feedback from IRGA Reading (yellow, left axis). Upon saturation, two dilution stages (five stages are possible) are implemented until IRGA reading drops below saturation level. Dilution factors (about 20x and 30x) are shown (blue, left axis) together with dilution-corrected data (red, right axis).

To conceptually demonstrate the ability of the system to meet the remaining criteria, we conducted a series of laboratory tests on an earlier smaller-scale version of the full field system. The laboratory system differed from the system used in the 2008 ZERT test injections by having only seven channels, each of which was pumped by a separate Aqua-Lifter AW-20 pump located upstream of an eight-channel brass valve manifold.

For the multi-port and real-time dilution capability, we prepared two identical sample chambers filled to the normal depth with quartz sand and connected them to a sample gas inflow. Flow into one of the chambers was controlled by a valve that was closed at the start of the experiment and then opened about 2 h into the experiment. A N_2/CO_2 gas mixture containing about 1.5% CO_2 was used at a nominal flow rate of 41 mL/min. Our control software was programmed to alternate sampling between each sample chamber on a 6-min cycle. At the initialization segment of each sample cycle, the analysis cell in the IRGA was flushed with N_2 for 15 s, and then normal sample flow resumed with staged dilution of the CO_2 by N_2 as needed. The results of the experiment (Figure 3.4, blue and red symbols) show the evolution of the CO_2 concentrations in the headspace of the sample chambers over the course of several hours and demonstrate the breakthrough of the CO_2 plume into the sample chamber headspace. A third dataset in yellow (collected in a separate run) demonstrates the response to both low- and high-flux conditions in the same chamber. For this test the transition to the high-flux condition occurred 93 min after the start of the low-flux condition (Figure 3.4).

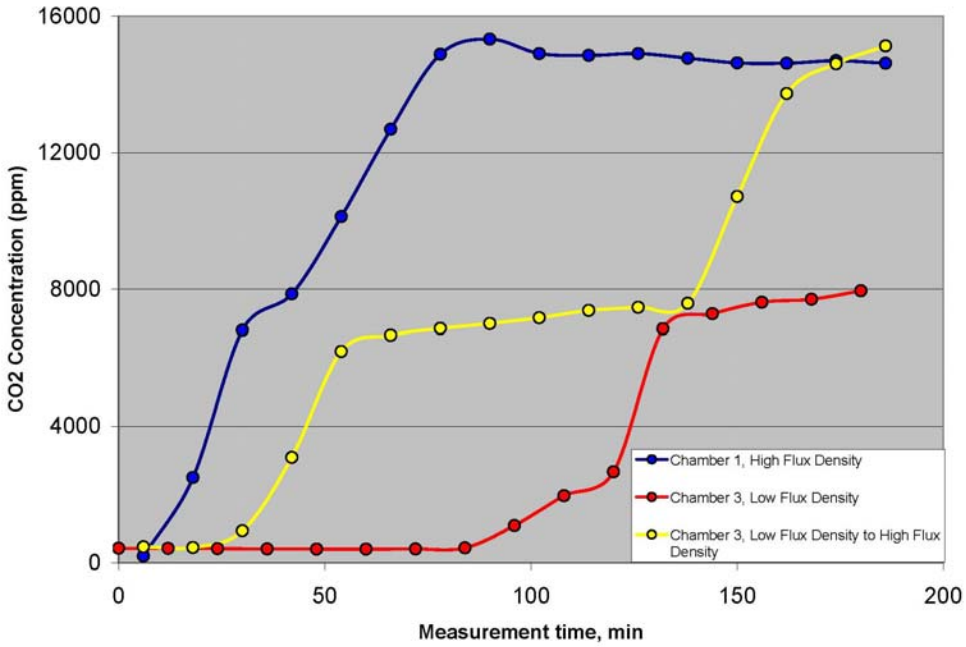

Figure 3.4. Demonstration of Multi-Port Capability and Lack of Cross-Contamination for Two Surface-Flux Chambers Operating at Different Flux Densities

It is important that the system response remain unchanged, regardless of which head unit–base combination is used. Figure 3.5 shows the response of six tests in which various lid and base combinations were examined with identical chamber inlet conditions, two of which were repeated with an active fan circulation, all yielding nearly identical results.

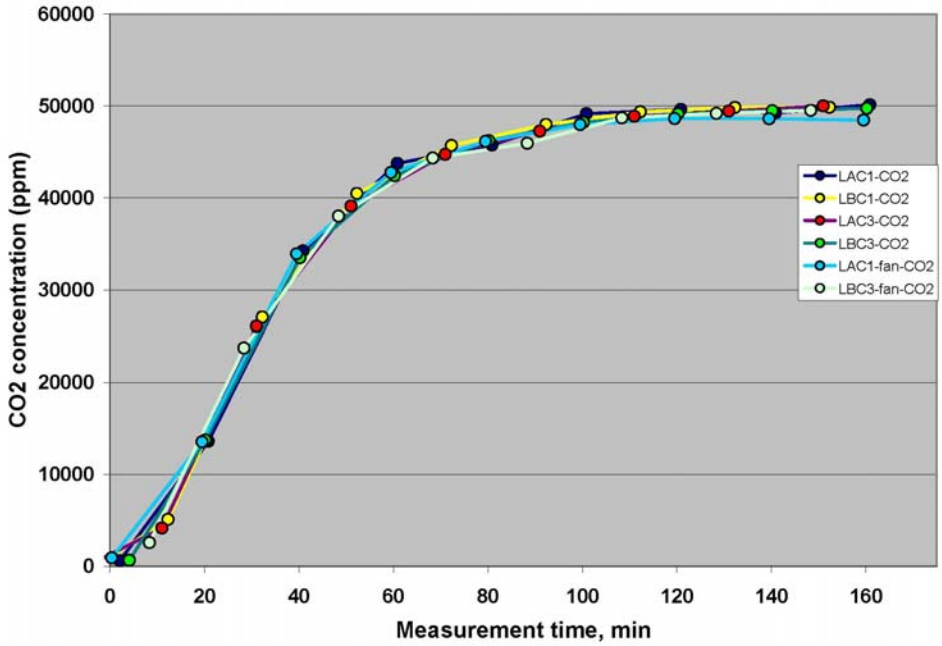

Figure 3.5. System Response to Same Flux-Density Scenario Using Interchangeable Chamber Tops/Bases

To test the accuracy of the staged CO_2-dilution process, we prepared a series of CO_2 standards (1100-86,000 ppm in N_2) and analyzed them using the 6-min procedure. The standards, which had been prepared in 6-L "Summa" canisters, were introduced to the analyzer at constant pressure (10 psi controlled by a regulator) by connection to a sampling port and pump. The results (Figure 3.6) showed that by using the MFC manufacturer's conversion from reading output (V) to flow (mL min^{-1}), there was a deviation in slope for the samples requiring dilution. Using the Solver function in Microsoft Excel, we calculated the correct flow and offset of the flow controllers and meters using the calibrated standards (yellow symbols). This calibration process is readily implemented in the field, and the new slopes and offsets can be substituted easily into the measurement and control code.

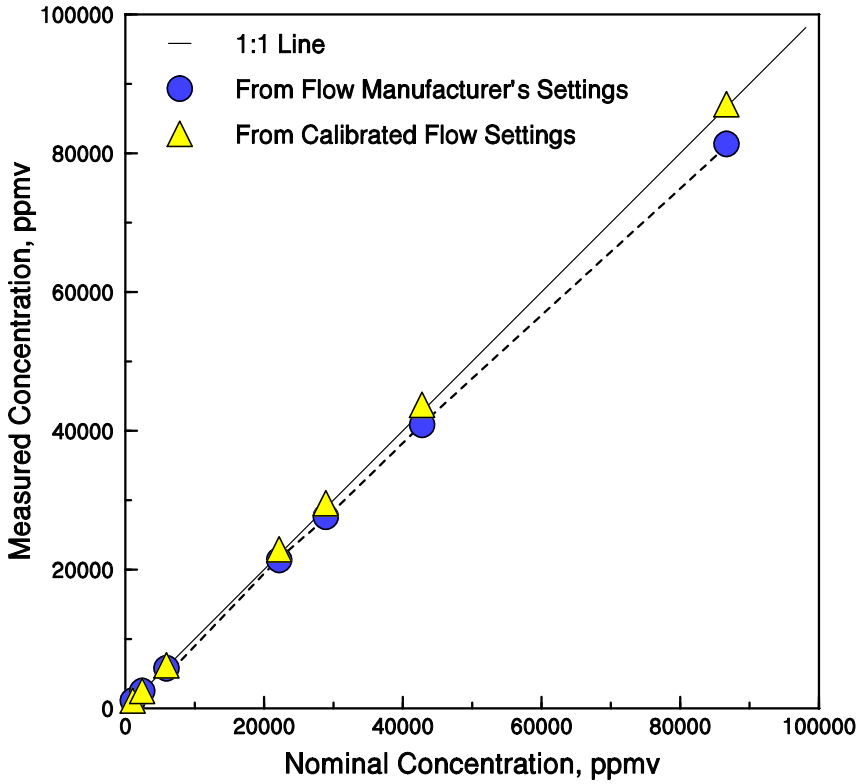

Figure 3.6. Test of Staged-Dilution Accuracy Using CO_2 Standards Prepared in N_2 and Introduced at 10 psi. The blue symbols are the raw readings, and the yellow symbols are the corrected readings.

3.3 Full-Scale Field-Monitoring Version of Measurement and Control System

During the development and testing of the of the portable multi-port real-time CO_2-detection system, we found the system to be a robust, accurate, and useful tool in understanding the dynamics of well injections at the ZERT site in Bozeman, Montana. However, the system was limited by having only seven sampling chambers, requiring a considerable amount of operator interaction to record data, recharge and replace the deep-cycle battery power source, and replace the N_2 gas cylinders that provide both reference and dilution capabilities to the system. The aim of the full-scale field-monitoring version was to create a system that would be capable of continuous unattended subsurface monitoring at remote

sites. Our specific goals were to produce a monitoring system that could be installed easily at remote sites, sample from an ordered dense grid covering a moderate area, operate at sites without available power, be monitored and controlled from offsite continuously in real time, and operate for extended periods between N_2 refills.

The most important changes involved increasing the number of chambers and decreasing the need for frequent operator interactions with the system. Increasing the number of chambers to monitor a moderately sized area in a grid-wise manner, essentially moving from a one-dimensional monitor to a two-dimensional one, was determined to be highly beneficial to understanding subsurface characteristics for transport and to assist in locating small areas of high flux. A modular solution was taken to address the need to increase the sampling chambers from seven to twenty-seven, allowing for the creation of a 5×5 grid with additional soil and ambient-air reference channels. This was accomplished using valved direct-current (DC) relays that were addressable and capable of being daisy-chained, together with valve manifolds that were compact and had exhausts that could easily be tied together. Using addressable and chainable relays allows for future expandability with minimum of changes to system configuration or control software. The relay drivers chosen for this application were Campbell Scientific SDM–CD16AC. These relays have 16 relay ports for device control and can be chained 15 deep for a total of 240 ports or sampling chambers. In the current configuration, two SDM-CD16AC relays are employed, utilizing 27 of the 32 ports for sample valve control. The new manifolds to house the valves are LFMX0510533B and LFMX0510538B manifolds (3- and 8-port manifolds, respectively; Lee Co., Westbrook, CT). These manifolds accept the same microvalves as the custom Campbell Scientific brass manifold at a fraction of the cost and consume very little space in the control and measurement system housing, leaving room for future expansion.

The operator interaction with the previous system involved three activities: 1) charging and rotating deep-cycle batteries every 12 h, 2) transferring data to external storage before the datalogger would overwrite the onboard storage, and 3) replacing cylinders of N_2 every several days (dependent on subsurface concentrations and amount of dilution gas required). Because this level of operator interaction was significant, it would not be feasible for long-term studies. We addressed the first operator-interaction activity by assembling a renewable power system with a large electrical storage capacity, the details of which are described in Section 4.

With respect to the second operator-interaction activity, we developed a two-part solution involving both hardware and software. The Campbell Scientific CR23X datalogger (Campbell Scientific, Logan, UT) stores 5e5 values in 1 MB of flash memory. With the previous system, this translated into 6.5 h of data before an operator would have to perform a memory dump to external memory to prevent overwriting of the data by the datalogger. We connected an Airlink Raven 110 cellular data modem (Sierra Wireless, Richmond, BC, Canada) and a Campbell Scientific 18285 1-dBd Omnidirectional Antenna (Campbell Scientific, Logan, UT) to the datalogger RS232 port, thus allowing data to be pushed or pulled to an Internet Protocol address at 384 kbps. To take advantage of all of the capabilities provided by the cellular data modem, we installed Loggernet 3.1 software (Campbell Scientific, Logan, UT) on the computers used to communicate with the datalogger. With this software, all control programming, communications, and data retrieval can be done remotely, thereby eliminating the need for an on-site presence. However, this approach requires cellular service in the area, the signal of which can be drastically improved if necessary by the use of a Campbell Scientific 14454 9 dBd YAGI unidirectional antenna also available for use with the system.

For the 2008 ZERT injection, we pulled data from the system every 10 min and appended it to a file on the operator's computer. The data file on the computer can contain an unlimited amount of data. However, if viewing data in a spreadsheet, files of less than 18 h of data are most practical to view, due to the limited number of rows available in a spreadsheet.

The third operator-interaction activity involved frequent changing of gas cylinders that supplied the N_2 used in the dilution stage and as a reference gas. Initially we used a type K pressurized cylinder containing approximately 6500 L of N_2. For a typical injection experiment at the ZERT site, this size N_2 cylinder would need to be replaced every 2 to 3 days. To address the need for a larger volume of N_2 than provided by the K-type tank, a Dura-Cyl medium-pressure liquid N_2 cylinder (Chart Industries, Inc., Garfield Heights, OH) containing 209 L of liquid N_2 (yielding approximately 135,000 L of N_2 gas at ambient pressure) was employed. The use of a liquid N_2 cylinder extended the gas maintenance interval by twenty-fold from 2–3 days to more than a month.

4.0 Power System

The power system was designed to provide off-grid power to the measurement and control system throughout the year at the ZERT site. Energy consumption for the complete measurement and control system and subcomponents of that system is detailed in Table 4.1. Total measurement and control system power consumption was determined to be 73.64 A-h. Assuming 80% efficiency, a power supply system would need to provide a minimum of 88.4 ampere-hours (A-h) of power at 12 V. We designed a power supply system that included three 125-W Mitsubishi PV-TE125MF5N solar panels (Mitsubishi Electric and Electronics USA, Cypress, CA), two 400-W Air Industrial wind turbines (Southwest Wind Power, Flagstaff, AZ), and a bank of six Lifeline GPL-4DA 210-A-h deep-cycle 12-V batteries (Lifeline Battery, Azusa, CA).

Table 4.1. Power Consumption of System in Ampere-Hours

Device	Device Current (A-h)
Licor LI-7000 CO_2 gas analyzer	36
SKC pump	9
Omega mass flow controller	6.4
Tom's Aqua Lifter 20 pump	6
Campbell Scientific SDM16AC relay x 2	4.8
Aalborg mass flow meter	4.8
Omega mass flow meter	4.8
Campbell Scientific CR23X datalogger	1.2
Sierra Wireless Airlink Raven	0.64
Total Device Current (A-h)	**73.64**

The system was sized to work solely on solar power throughout the year at the ZERT site in Bozeman, Montana. Using the worst-case equivalent sun hours (i.e., the minimum sun hours for the worst month of the year) for Bozeman (3 h), it was determined that three 125-W 12-V solar panels would be able to deliver an adequate amount of power to the measurement and control system, taking into account 20% system loss (125 W/12 V × 3 h = 93.75 A-h = minimum solar output > 88.4 A-h = adjusted system power need). To supply consistent power (e.g., at night, in winter) to the measurement system, a reserve power battery bank was determined a necessary component of the power system. Given the latitude of the ZERT site (45.68 degrees N), it was determined that a 14-day reserve would be adequate for the system.[1] A battery bank of six 210-A-h deep-cycle batteries (1260 A-h total, 14-day reserve) was attached to the solar array through a Morningstar Tristar solar controller (Morningstar Corp., Washington Crossing, PA). This battery bank feeds 12 V DC into a Xantrex ProWatt 1750 Inverter that converts 12 V DC into the 120-V AC power (at 80% efficiency) that powers the measurement and control system (Xantrex Co, Burnaby, BC, Canada).

[1] http://www.southwestpv.com/Catalog/Home%20Power/SYS_DESIGN.HTM.

To allow for future needs of the measurement and control system, occasional use of power for non-system activities (e.g., power tools, lights), or deployment to a site incapable of providing enough power from the current solar array, two 400-W Air Industrial Wind Turbines mounted on 25-ft towers (RV Mounting Tower, Earthtech Products, Merrick, NY) were tied into the system with individual Tristar Controllers and an external heat load for over-power conditions. The specialized towers make it possible for one person to set up the wind turbines by securing the base under the trailer wheel and rotating the tower into the locked position (Figure 4.1). All of the controls, breakers, battery cases, batteries, heat loads, and power measurement instruments were located in a 6-ft ×-10 ft single-axle trailer (CargoMate, Independence, OR) (Figure 4.1 and Figure 4.2). The trailer can transport all of the hard-mounted electronics, the remainder of the power system (turbines, turbine towers, solar array), the measurement and control system, chambers, chamber tubing, and associated tools with room to store a N_2 dewar if appropriate safety controls are taken.

Figure 4.1. Power Supply System: Wind Turbines, Turbine Towers, Solar Array, and Trailer as Deployed at ZERT Site in 2008

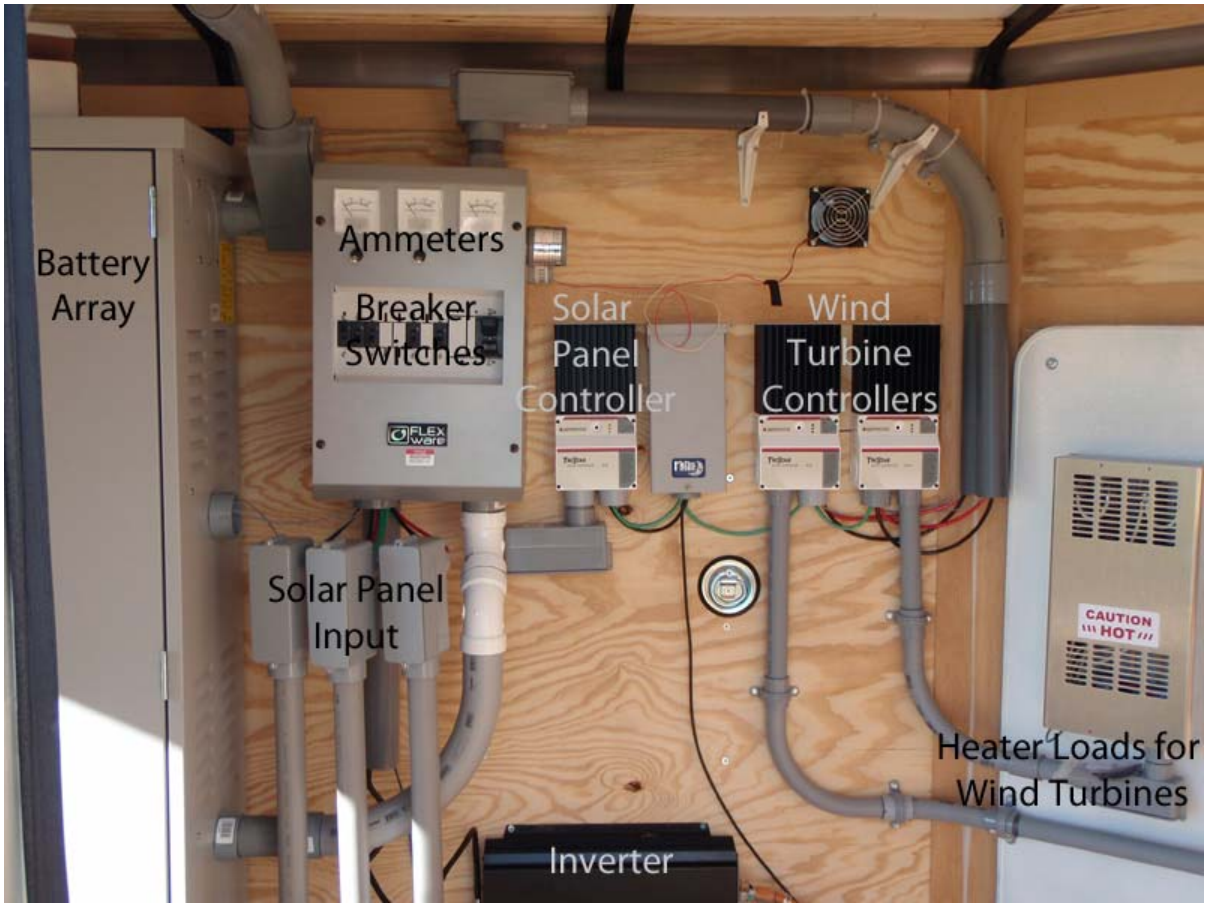

Figure 4.2. Interior View, Power Supply Trailer, Detailing Orientation of Power Supply Components Housed Inside Trailer

5.0 Field Test at ZERT Site, FY 2008

5.1 Experimental Layout

The measurement and control system and components for the off-grid power supply were delivered to the ZERT field test site near Bozeman, Montana, during the third week of June 2008. Limited power availability on the site required that we supply our own power in order to participate in the first test injection scheduled for the second week of July. However, significant delays (10 weeks) in shipping of the power system components prevented assembly and testing beforehand, and the next several weeks were spent assembling the power system onsite. We did not complete assembly in time to participate in the first injection and were fortunate that a sufficient supply of bulk CO_2 remained afterward to allow the ZERT project to schedule a second injection specifically for testing our system.

The 100-m-long horizontal well at the ZERT site used for this experiment is buried approximately 2 m below the surface and divided into six zones by packers that allow independent control of flow rates and gas mixtures in each zone (Figure 5.1). The well is oriented along a northeast–southwest axis, and CO_2 is injected at the northeast end. The water table varies during the year but typically is on the order of 1 m below the surface during mid-summer. As a consequence, CO_2 is injected below the water table, and the pressure differences resulting from small changes in pipe elevation lead to localized emissions or "hot" spots at the higher end of each zone near the packer. In this test, CO_2 was injected only into Zone 3.

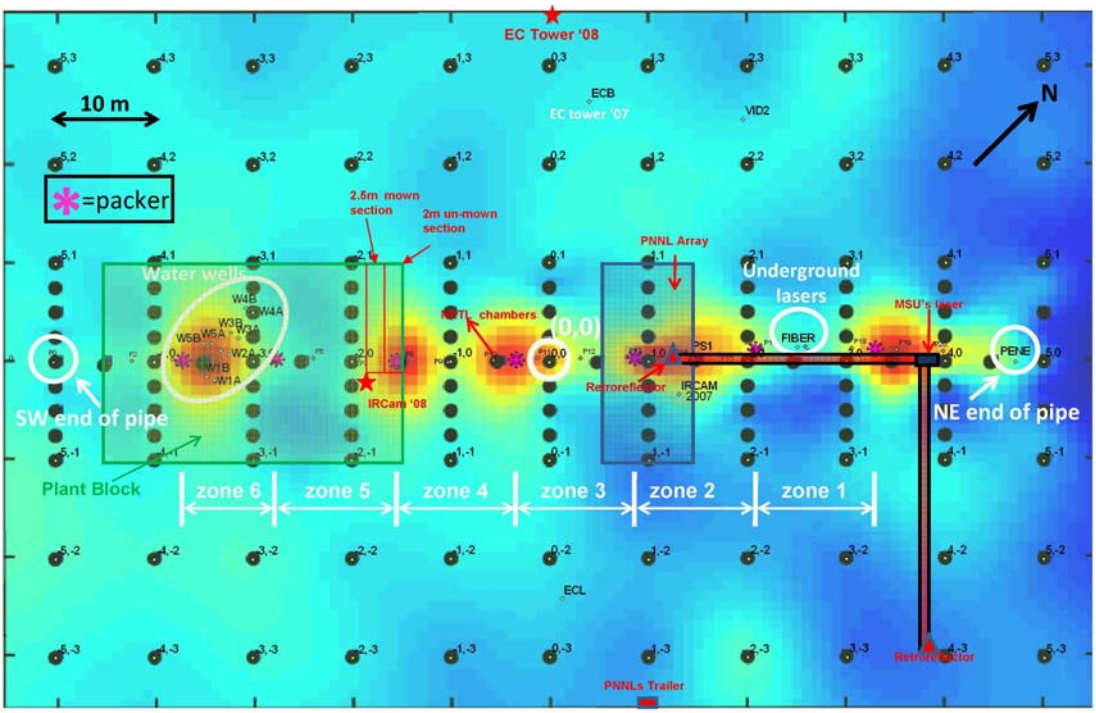

Figure 5.1. ZERT Site Plan View Showing Position of PNNL Experiment (Conducted During Second Injection) Relative to Other Experiments Conducted During First Injection. Also shown in red and orange are the areas in which high CO_2 fluxes were observed during the previous year's injection (data of J. L. Lewicki; map drawn by L. Dobeck).

Based on the results from the previous year's tests, we centered our sampling array directly over a hot spot located near the boundary between zones 2 and 3. Twenty-seven surface-flux chambers were installed to yield a 5×5 sampling array with two reference chambers. A leaking gas valve manifold in the measurement system, however, limited us to twenty chambers for this experiment; their locations are shown in Figure 5.2 and Figure 5.3.

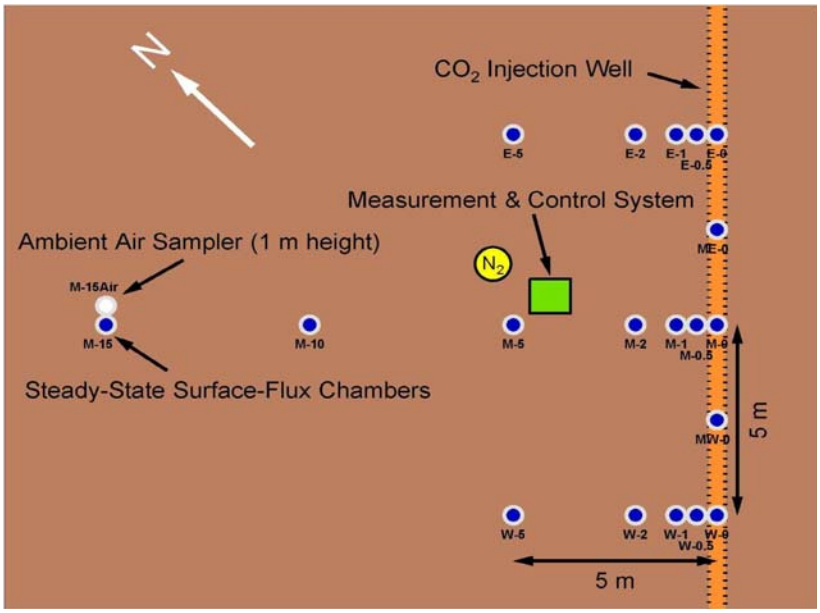

Figure 5.2. Plan View, Surface-Flux Chamber Array and Location of Measurement and Control System with Liquid N_2 Supply

Figure 5.3. Experimental Layout Looking Northeast. Horizontal well is directly beneath rightmost row of flux chambers.

5.2 Injection and Concentration Data

The second injection was started at 12:55 PM on 27 August 2008 (ordinal day 240.54), and continued for nearly 13 days (308.2 h), ending at 9:00 AM on 9 September 2008 (ordinal day 253.38). An injection rate of 52.1 (±0.4) kg CO_2 d^{-1} was maintained for the first 280.8 h, after which the flow monitor failed. A second monitor that measured pressure (rather than flow) showed that the same conditions were maintained except for a 12-h period between 289.4 and 301.4 h, during which pressure increased by 25% over the value maintained for the rest of the injection. Although a 5% increase in measured flux was observed in one of the chambers during this 12-h period, such a change was within the normal noise limits observed, so it is unlikely that the 12-h deviation had a significant impact on the results. The injection was halted about 7 h after the end of the pressure deviation.

We continuously (at 2.7-h intervals) monitored CO_2 concentrations in the twenty chambers starting about 4 h before the injection and for 33 d post-injection. Because these chambers were operating in steady-state flux mode, these concentration data can be converted directly to flux data using a flow-rate specific constant (ca. 0.0031 μmol m^{-2} s^{-1} $ppmv^{-1}$). A plot of data out to 1000 h for all twenty chambers is shown in Figure 5.4. Successive plots (Figure 5.5 through Figure 5.8) focus on subsets of these data.

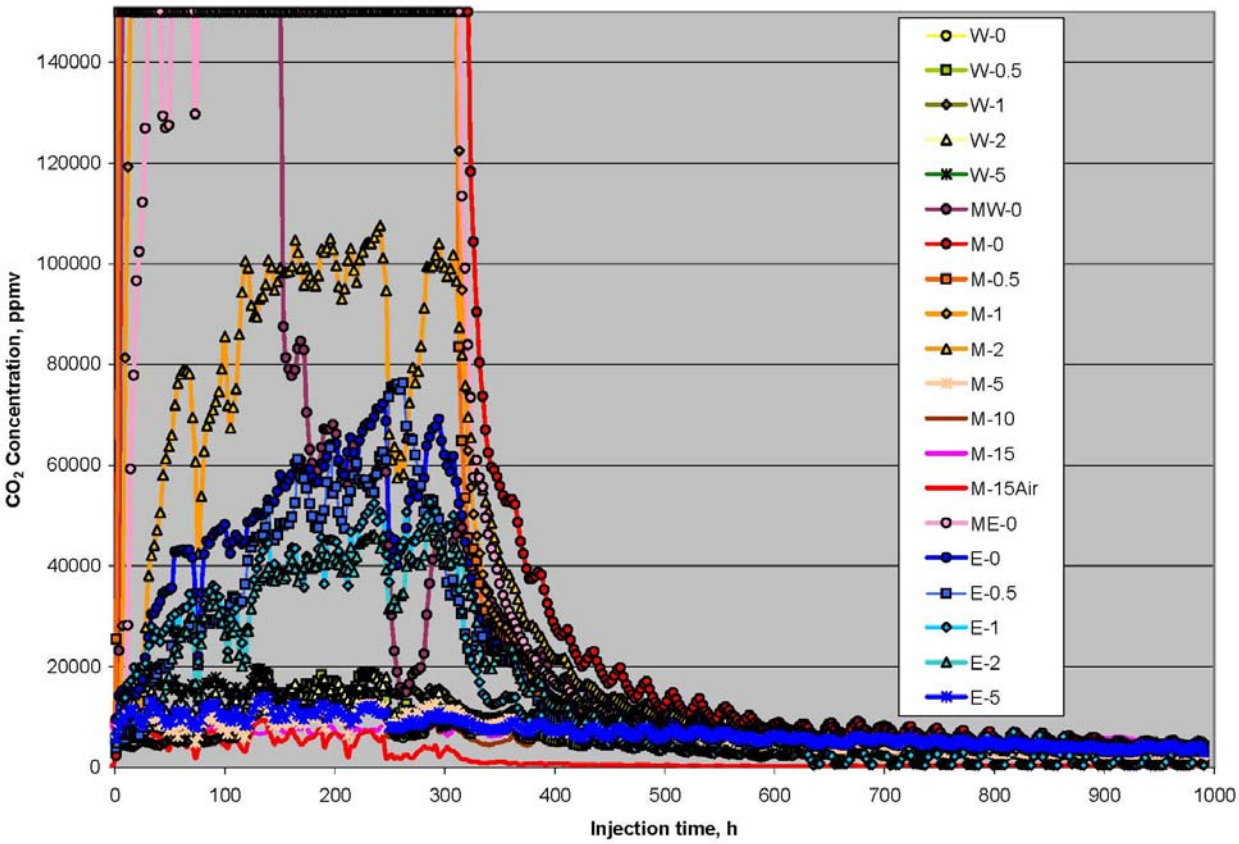

Figure 5.4. CO_2 Concentration Data Collected from Twenty Surface-Flux Chambers During and After Second Injection at ZERT Site. Data collection started on 27 August 2008. Chambers are identified by row (letter) and lateral distance in meters from the horizontal well (number).

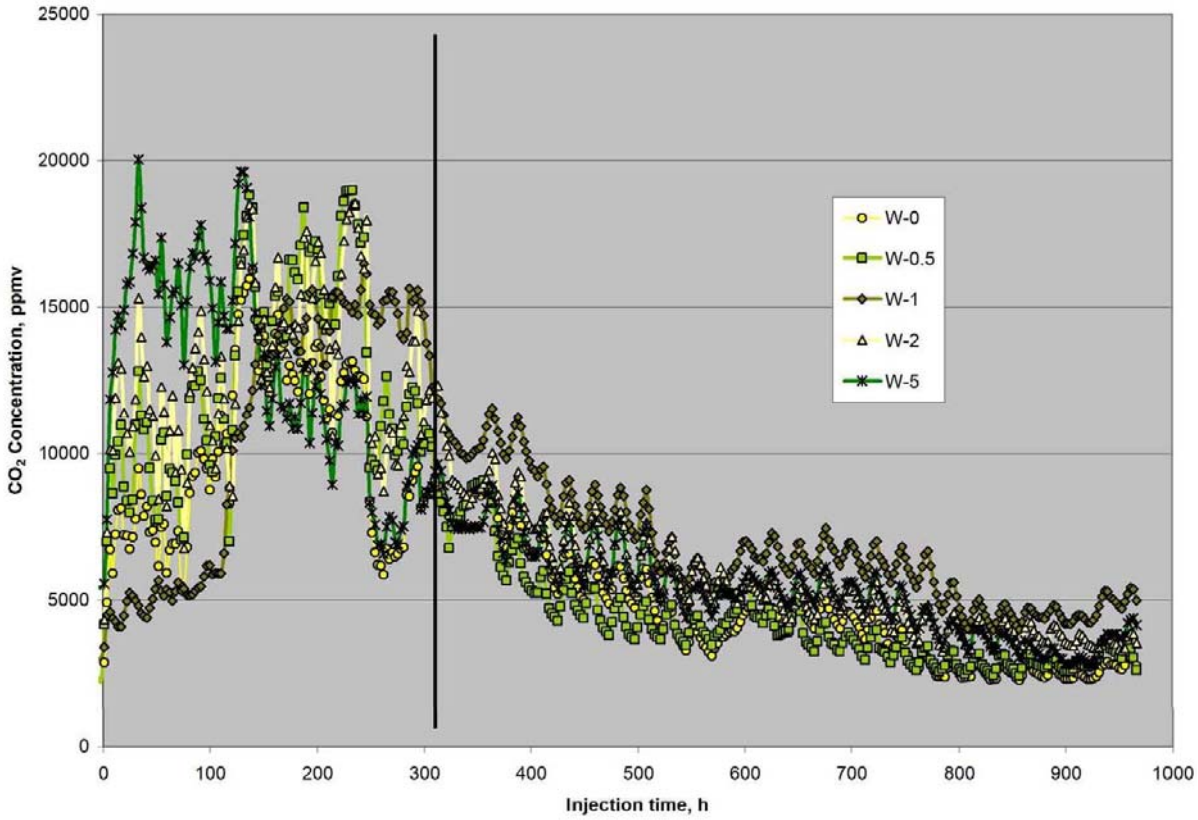

Figure 5.5. CO_2 Concentration Data Collected for West Row (W) of Surface-Flux Chambers. Vertical line indicates end of CO_2 injection. Chambers are identified by row (letter) and lateral distance in meters from the horizontal well (number).

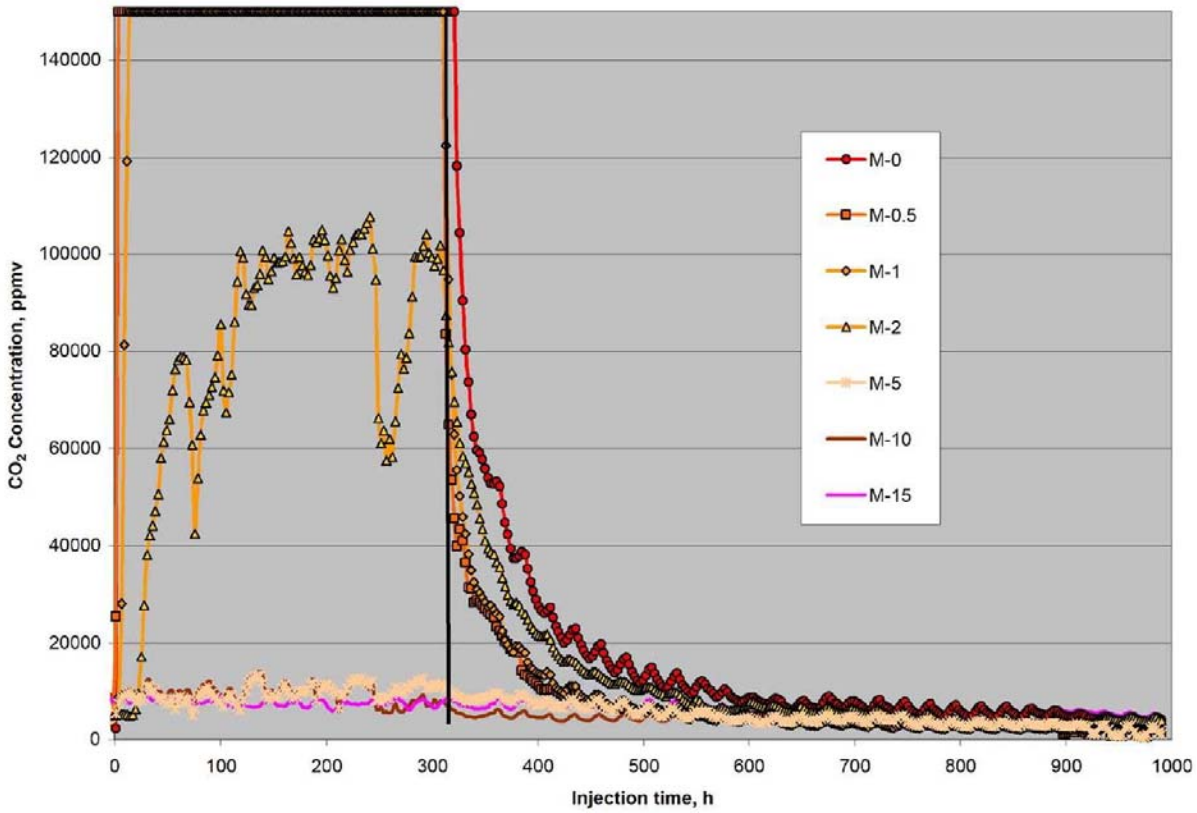

Figure 5.6. CO_2 Concentration Data Collected for Middle Row (M) of Surface-Flux Chambers. Vertical line indicates end of CO_2 injection. Chambers are identified by row (letter) and lateral distance in meters from the horizontal well (number).

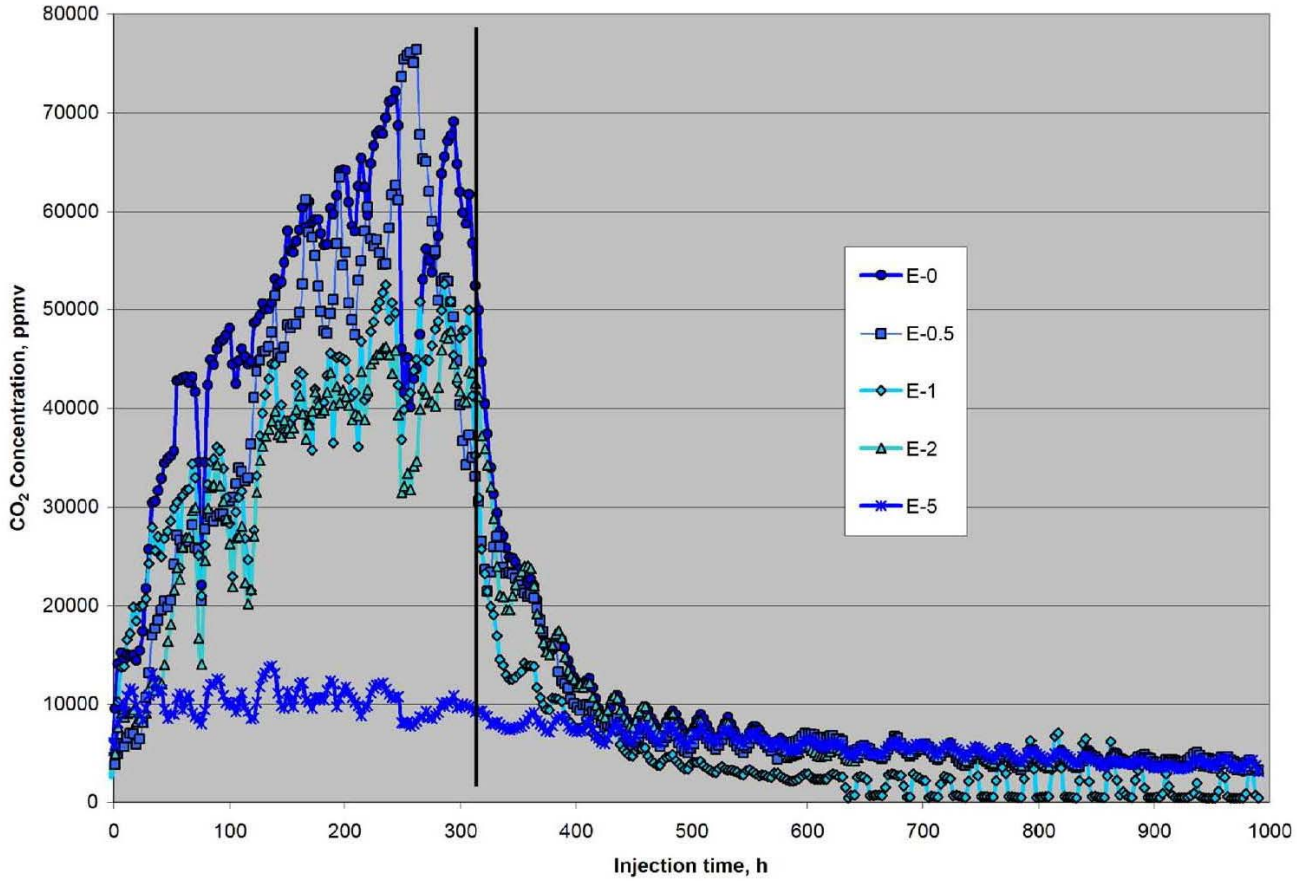

Figure 5.7. CO_2 Concentration Data Collected for East Row (E) of Surface-Flux Chambers. Vertical line indicates end of CO_2 injection. Chambers are identified by row (letter) and lateral distance in meters from the horizontal well (number).

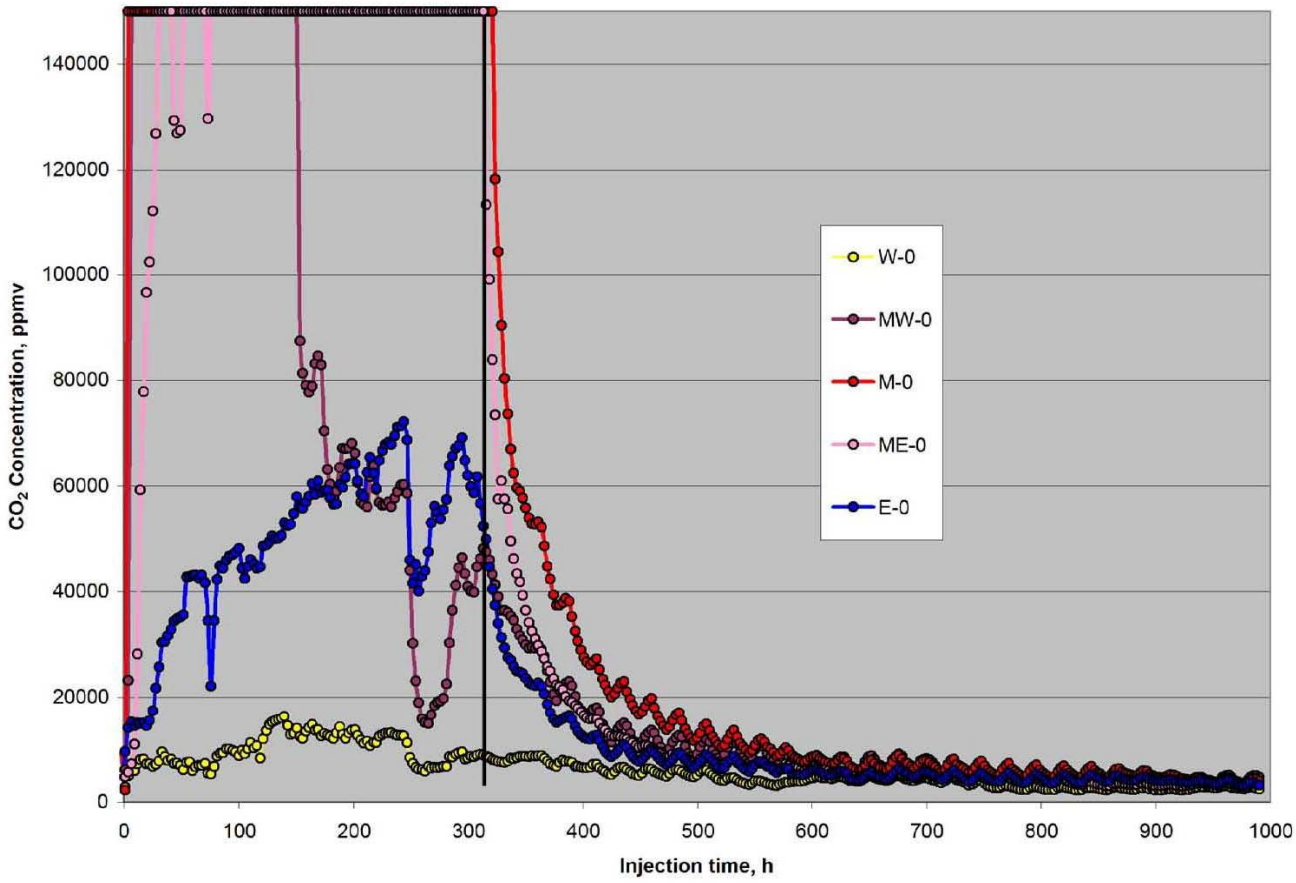

Figure 5.8. CO_2 Concentration Data Collected Surface-Flux Chambers Located Directly Above Horizontal Well. Vertical line indicates end of CO_2 injection. Chambers are identified by row (letter) and lateral distance in meters from the horizontal well (number).

The concentration data in Figure 5.4 to Figure 5.8 show that several chambers reached instrument saturation levels of CO_2 (150,000 ppmv) during the injection period. These chambers were located primarily along the middle row of chambers within 2 m of the horizontal well. The MW-0 and ME-0 chambers also saturated. As would be expected from locating the sampling array over a hot spot, the chambers positioned more than 3 m from this spot (centered at chamber M-0) did not saturate. Although a steady state seemed to be reached for M-2 and some of the W chambers, the CO_2 concentration in the E row continued to increase during the injection, suggesting continued expansion of the plume toward the northeastern end of the sampling array. This result is interesting because the injection occurred only in the southwestern half of the array (i.e., that portion of the horizontal well located in Zone 3). This drift is seen also in the MW-0 data during the injection. Initially (within 7 h), the MW-0 chamber reached saturation, but after 153 h it decreased to about 90,000 ppmv and continued to decline for the remainder of the experiment (Figure 5.8). The northeasterly drift in concentration is consistent with the generally northerly direction of groundwater flow at the ZERT site, which may be a contributing factor.

The concentration data also show significant drops in nearly all the chambers at about 75, 105, and 257 h after injection. As will be discussed in Section 5.3, these drops are likely the result of barometric effects associated with local weather changes.

We took two approaches to help visualize the changes in spatial extent of the plume. In the first, we show the discrete concentration values for each chamber for a particular time arranged in an array that simulates that in the field (Figure 5.9). In the second, we created filled-contour plots for the same time periods using R, a statistical programming language (http://www.r-project.org/) but restricted the spatial range to 0–5 m from the horizontal well (Figure 5.10). Because the contour plots required a full 21×11 data matrix (231 pixels) on a 0.5-m grid spacing and data for only seventeen of these pixels were collected (M-10, M-15, and M-15AIR were excluded), a large number of points needed to be estimated. A two-dimensional Gaussian kernel was used as the smoothing function (essentially a spatial-weighted moving average), and missing values were handled with the Nadaraya/Watson normalization of the kernel (a normalization that diminishes the effects of missing observations). The function was initialized with a 0.5-m spacing of the pixels in the width and height directions and a bandwidth parameter of 1.5 m.

The spatial representations we obtained (Figure 5.9 and Figure 5.10) clearly show a rapid increase to saturation levels within the first 72–168 h of injection for chambers located less than 3 m from the center of the hot spot, as well as the general drift of the plume toward the northeast end of the array (top of plots) with time. Possible evidence for the plume reaching 5 m from the injection well can be seen in the discrete data for the west and east rows in which data rise slightly above background levels.

A rapid system response was observed in the early stages of the injection (Figure 5.11). Within 4 h of the start of injection, the M-0 and M-0.5 chambers had reached instrument saturation levels; the MW-0 and M-1 chambers followed suit at about 7 h and 14 h, respectively. The concentration in the ME-0 chamber rose more slowly and oscillated near saturation from 30 h to 75 h before exceeding 150,000 ppmv for the remainder of the injection.

The rapid response was seen also once the injection ceased. Within 16 h of the injection end, all chamber concentrations were below saturation, and within 133 h, all were below 20,000 ppmv (Figure 5.4 to Figure 5.8). Also, a noticeable diurnal pattern returned to the concentration data once the advective forcing provided by the injection ceased. This pattern presumably reflects the contributions of soil and plant respiration to the surface fluxes measured. Clearly, even in locations where the highest concentrations of CO_2 were observed (e.g., chamber M-0), some living organisms survived. The steady decay of the CO_2 concentrations beneath the diurnal signal continued until background levels were reached 400-600 h after injection ceased.

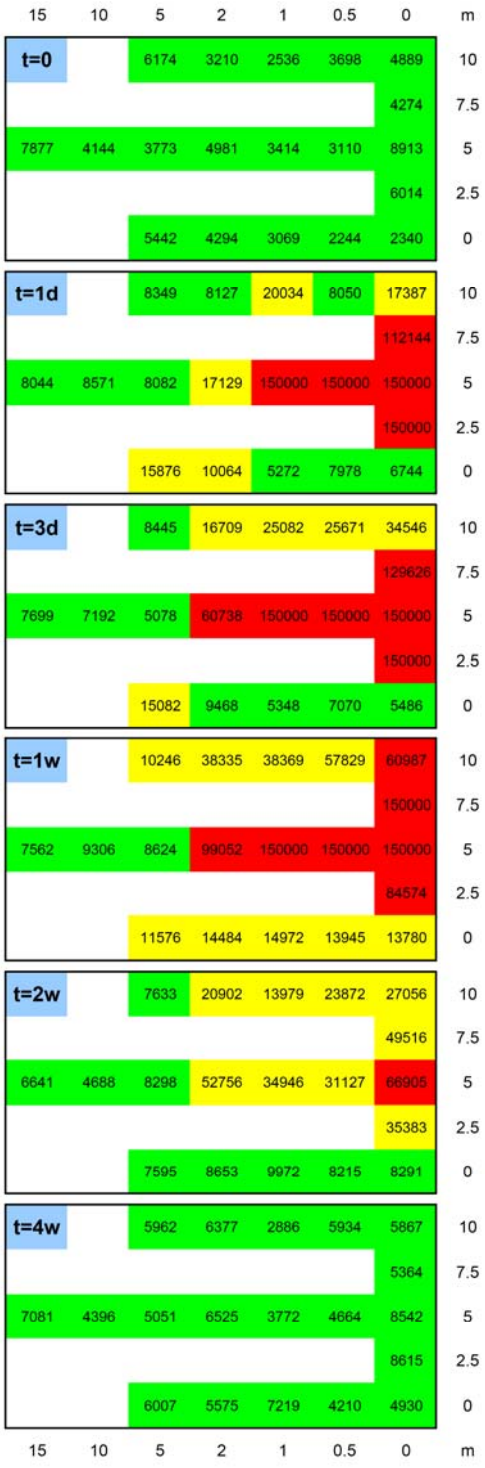

Figure 5.9. Quasi-Spatial Representation of Discrete Chamber Concentration Data at Six Selected Times During the Second Injection Experiment. Values in each rectangle are in parts per million-volumetric of CO_2.

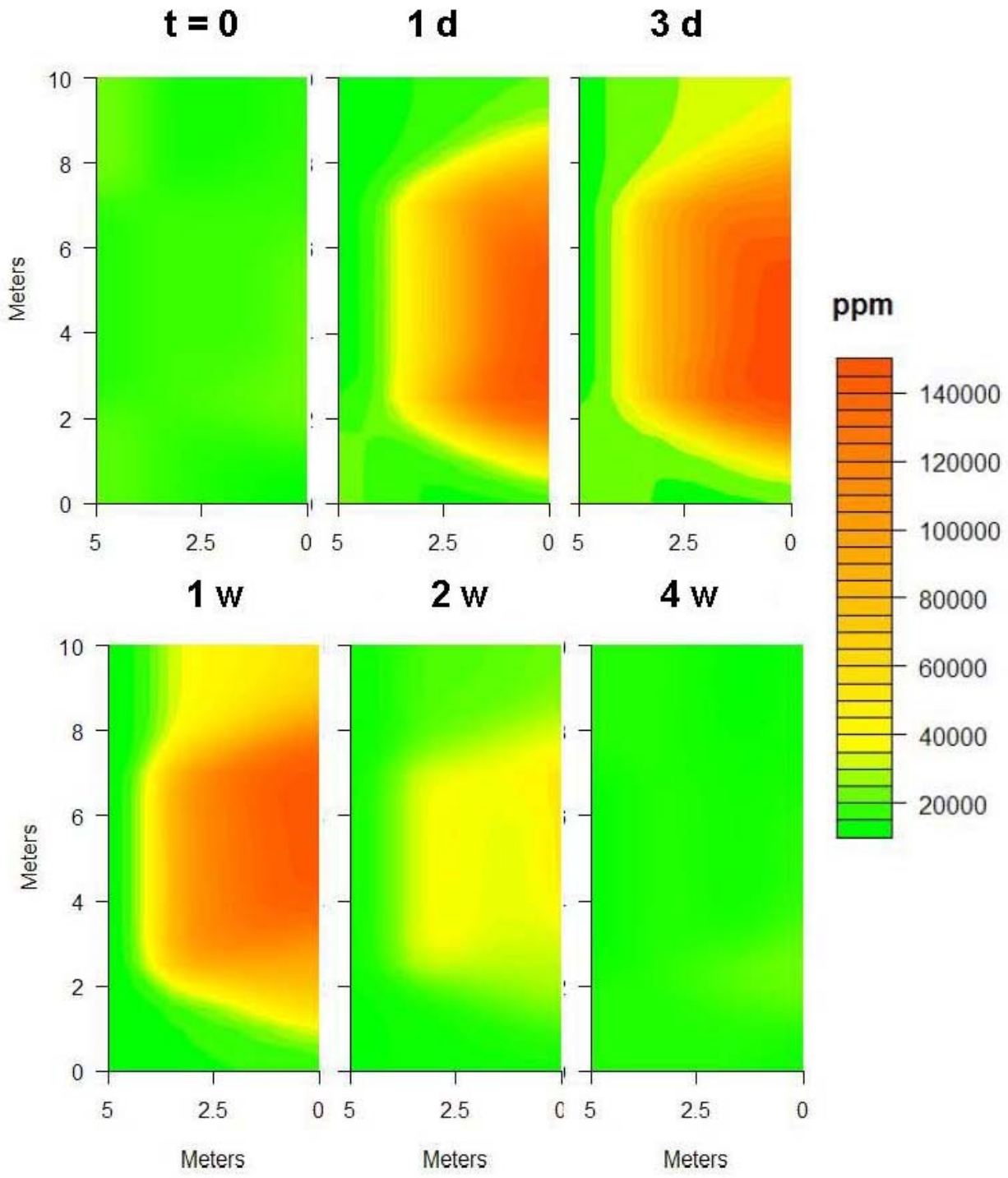

Figure 5.10. Spatially Accurate Two-Dimensional Representation of CO_2 Concentrations Measured Within 5 m of the Horizontal Well During the Second Injection. Data are interpolated from discrete chamber measurements using R statistical software.

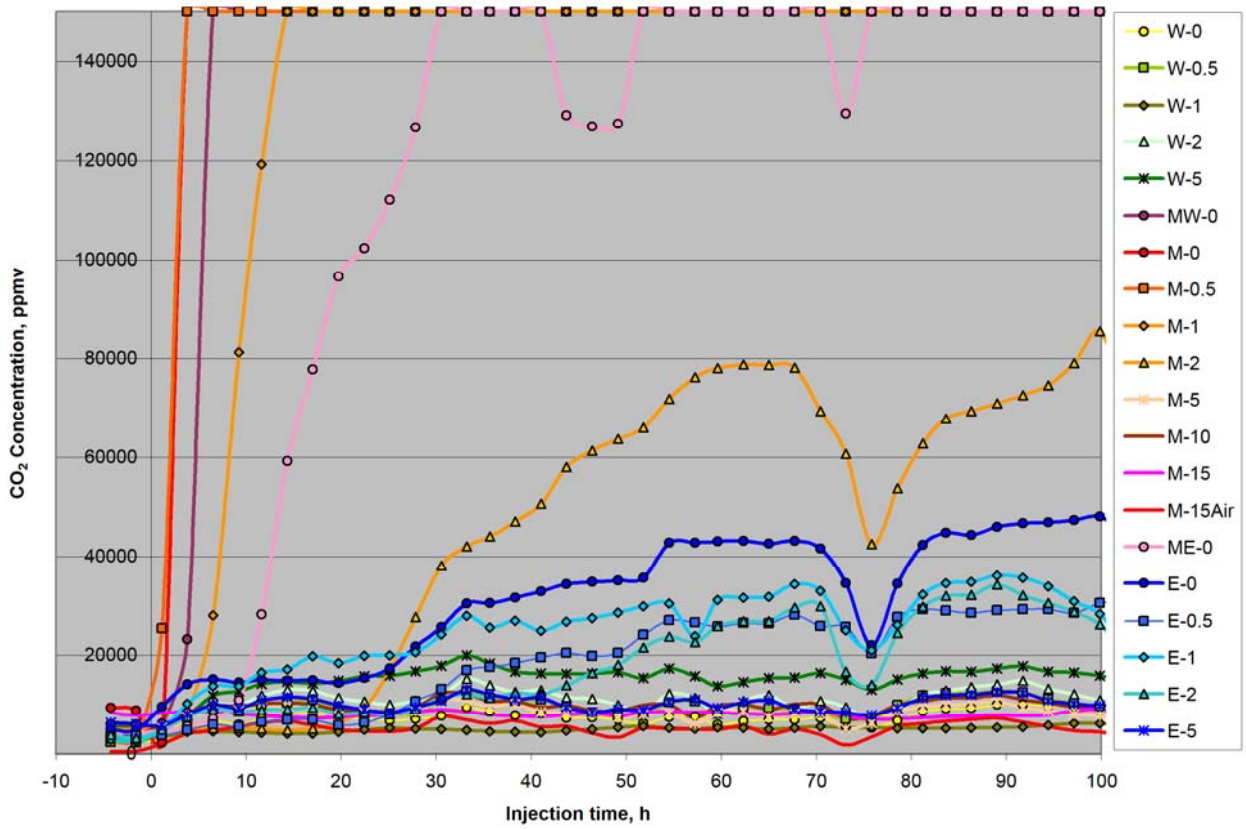

Figure 5.11. CO_2 Concentration Data Collected from twenty Surface-Flux Chambers Immediately Before and During the First 100 h of the Second CO_2 Injection at the ZERT Site. Chambers are identified by row (letter) and lateral distance in meters from the horizontal well (number).

The concentration data for chambers M-10 and M-15 remained at background levels throughout the experiment and retained the diurnal pattern typical of biologically derived CO_2 emissions. The background level for chamber M-15 dropped by about a third as the experiment progressed, in keeping with the overall decline in biological activity with dropping ambient temperature during the fall season (Figure 5.12).

The atmospheric background sample collected at the same location as chamber M-15 but from a chamber suspended 1 m above the ground surface (i.e., chamber M-15Air) should have yielded a similar diurnal pattern (albeit at much lower concentrations) with no impact from the injection. However, the results (Figure 5.12) show much higher concentrations during the injection, falling to normal ambient levels once the injection ceased. The levels observed for chamber M-15Air during the injection are in the range of those expected for normal steady-state soil flux measurements (around 5,000–10,000 ppmv) and clearly do not represent atmospheric conditions. Further evidence for this is the open-path atmospheric concentration data collected directly over the horizontal well in zone 2 (approximately 15-cm height) by Humphries and Repasky during the first injection, which showed typical concentrations near 1000 ppmv and maximum concentrations on the order of 1500 ppmv (K. S. Repasky, Montana State University, personal communication).

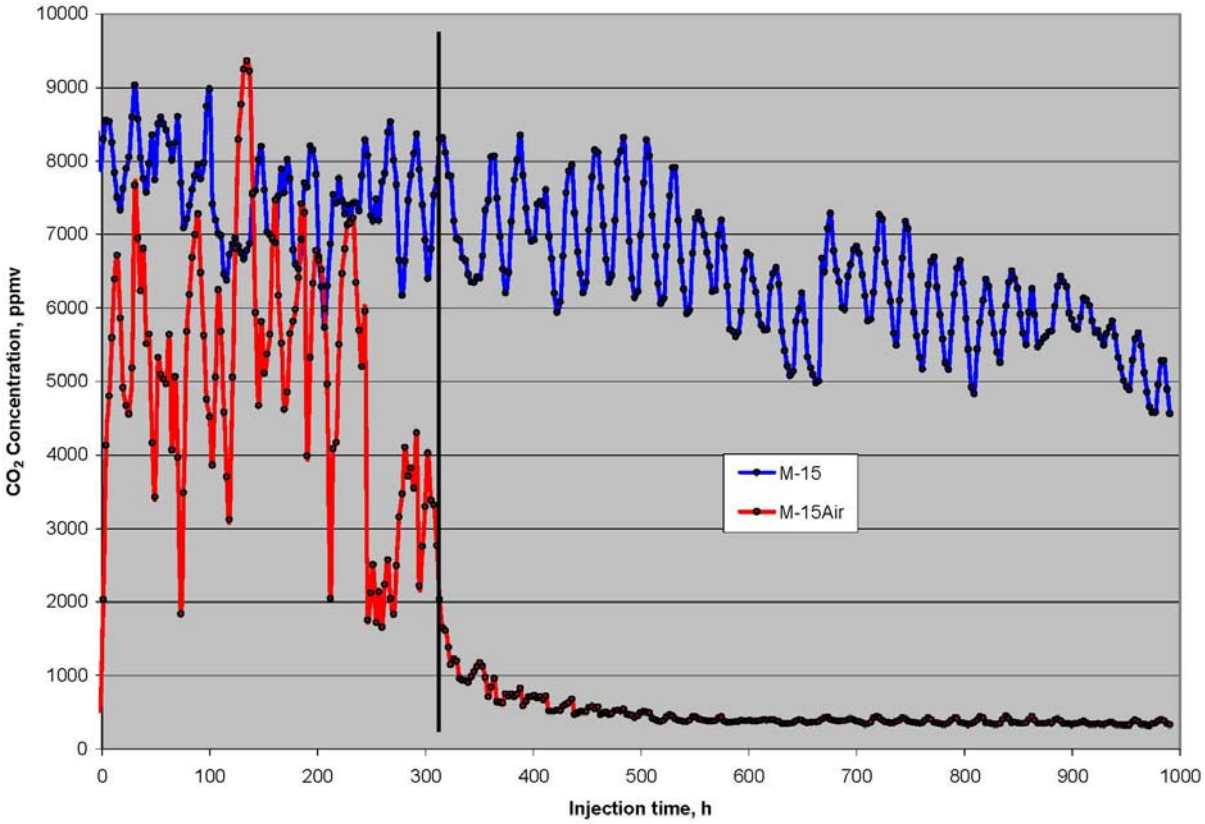

Figure 5.12. CO_2 Concentration Data Collected for Reference Surface-Flux Chamber and Ambient Air 15 m from Horizontal Well. Vertical line indicates end of CO_2 injection.

To explain the chamber M-15Air data, we reexamined other possible sources of CO_2 that could interfere in the analysis. We had eliminated "cross-talk" in earlier versions of the measurement system by having individual pumps for each channel and by flushing the system with 100% N_2 between samples. With our change to a pair of pumps for the entire system (one for exhaust of the chambers not being analyzed, and one for the sample dilution feed) to lower the power consumption of the measurement system, this feature was eliminated. We think there are two possible causes of the high readings. One is sample carryover from the use of a common sample dilution-feed pump. However, we would expect this to be even more of a problem for the chamber M-15 sample because it is analyzed before the M-15A and, thus, closer, in time to the higher-concentration samples. We see no impact of the injection on data for M-15, however, suggesting that carryover is not the likely cause of higher observed concentrations with M-15A. Nevertheless, as a precaution, we have identified a way to automatically flush the sample-handling and dilution system between each sample while retaining the current two-pump configuration and will test it in the next round of instrument enhancements in FY09.

The second possibility is a leak in the valve manifold or tubing. We already know that seven of the channels could not be used due to external air leaks into the sample train. An undetected leak could have been associated with the valve manifold or tubing for the M-15A sample that would allow the take-up of exhaust gas released inside the measurement system box from other samples prior to M-15A analysis, resulting in a contaminated sample. We will be hardening the valve and tubing connections for all channels in the coming year's work, which should eliminate this problem.

5.3 External Factors Affecting CO_2 Concentration Data

As described in Section 5.2, several negative excursions from the expected concentration data were observed simultaneously in essentially all the chambers during the injection. The largest excursions occurred at about 75, 105 and 250–260 h after injection was started and tended to last for tens of hours before the data returned to steady state or otherwise expected patterns. Similar, but positive, excursions were noted by us and the Repasky team during the first injection in summer 2007, and these were hypothesized to be related to changes in soil moisture content stemming from rainfall or dew deposition. With this hypothesis, it was thought that absorption of moisture by the soil particles would decrease the air-filled porosity, thereby increasing the resistance to gas flow in the low-flow regions of a field and promoting higher flow rates in the high-flow regions where moisture absorption would be less likely to occur due to the already high flow rate.

To test the soil-moisture hypothesis in the 2008 field trial, we installed eighteen gypsum-block soil moisture sensors (5201F1 Soilmoisture Gblocks, Soil Moisture Equipment Corporation, Santa Barbara, CA) at a 6-in. depth adjacent to our soil gas-flux chambers in early July 2008. The soil moisture readings from these sensors were obtained manually every 4–7 days using a hand-held meter that registered readings from 0 (dry) to 100 (wet). According to the manufacturer (Soil Moisture Equipment Corporation, 2000), these readings can be converted to soil matric suction (bars). A reading of 70 corresponds to a matric suction of 0.1 bar, that of 19 to 1 bar, that of 4 to 3 bars, and a reading of 1 corresponds to a matric suction of 10 bars (near the permanent wilting point for plants).

Soil moisture measurements were collected over a period of 1800 h (starting at ordinal day 206.65 and ending at ordinal day 282.38) roughly centered on the initiation of the second injection. The results (Figure 5.13) showed a fairly moist soil 800 h before the injection. The soil dried out rapidly, however, and by the time the second injection started, the soil was extremely dry. It remained in that state for the duration of our experiment, thus negating one part of our attempt to address the soil moisture hypothesis. No positive excursions were observed during the second injection of 2008, so the hypothesis remains untested. The sensors remain in place and will be used in the coming field season experiments.

For possible explanations of the negative excursions observed in 2008, we obtained meteorological data from two weather stations located at the ZERT field site (courtesy of J. A. Shaw and J. L. Lewicki). To visually assess relationships between the weather variables and the soil CO_2 excursions, we first isolated the excursions from the "expected" data by fitting a 6th-order polynomial function to the expected data and subtracting the observed from the expected data predicted by the function (Figure 5.14). We then plotted the excursion data on the same time graph as the meteorological variable we were testing and looked for obvious correlations. For this exercise, we selected the data for chamber M-2 as representative for the entire array because the concentrations did not saturate the measurement system and yet were high enough to minimize the contributions of diurnal fluctuations and sampling noise to the overall signal.

The weather variables we tested included relative humidity, temperature, precipitation, wind speed, wind direction, and absolute barometric pressure. Most of these variables had little or no relation to the negative excursion data (Figure 5.15). A clear relationship was seen, however, between wind speed (and, to a lesser extent, change in wind direction) and the observed negative excursions. We believe that the operative variable with respect to wind speed is actually the wind power density (WPD), which has units

of watts per square meter, as this more closely measures the ability of the wind to perform work on the soil gas system. The WPD is calculated as

$$WPD = 0.5 \times \rho_{air} \times \upsilon^3 \quad (5.1)$$

where ρ_{air} is the mass density of air in kg m^{-3}, and υ is the wind velocity in m s^{-1}. A doubling of wind velocity thus produces an eight-fold increase in WPD.

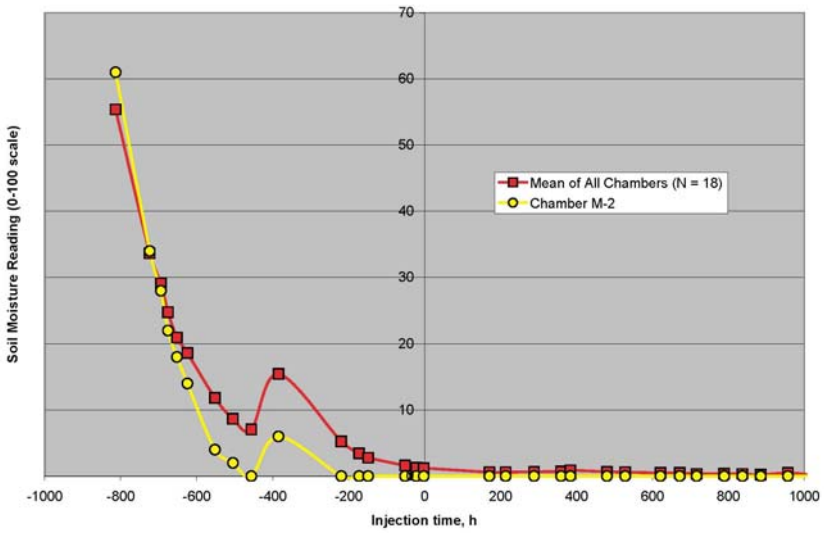

Figure 5.13. Relative Changes in Soil Moisture Content at a 6-in. Depth Before, During, and After Second Injection

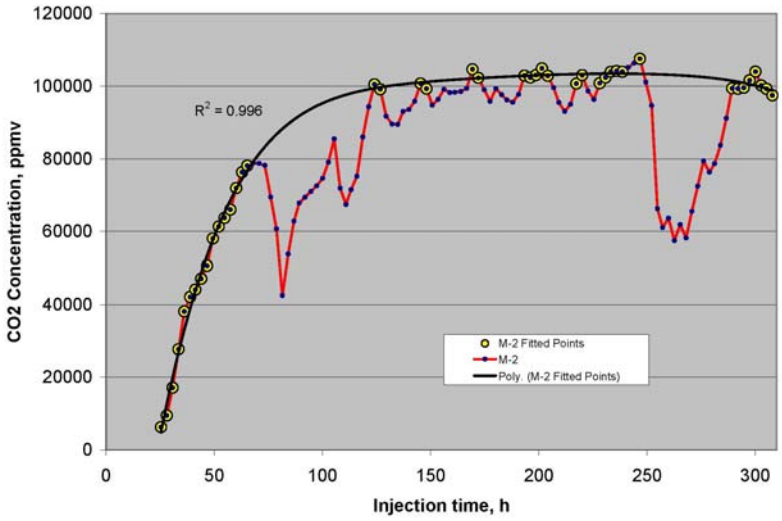

Figure 5.14. Concentration Data for Chamber M-2 Fitted To Obtain a Function Describing the "Expected" Data and Showing the Major Negative Excursions from the Expected Data at 75, 105, and 250–280 h After Injection

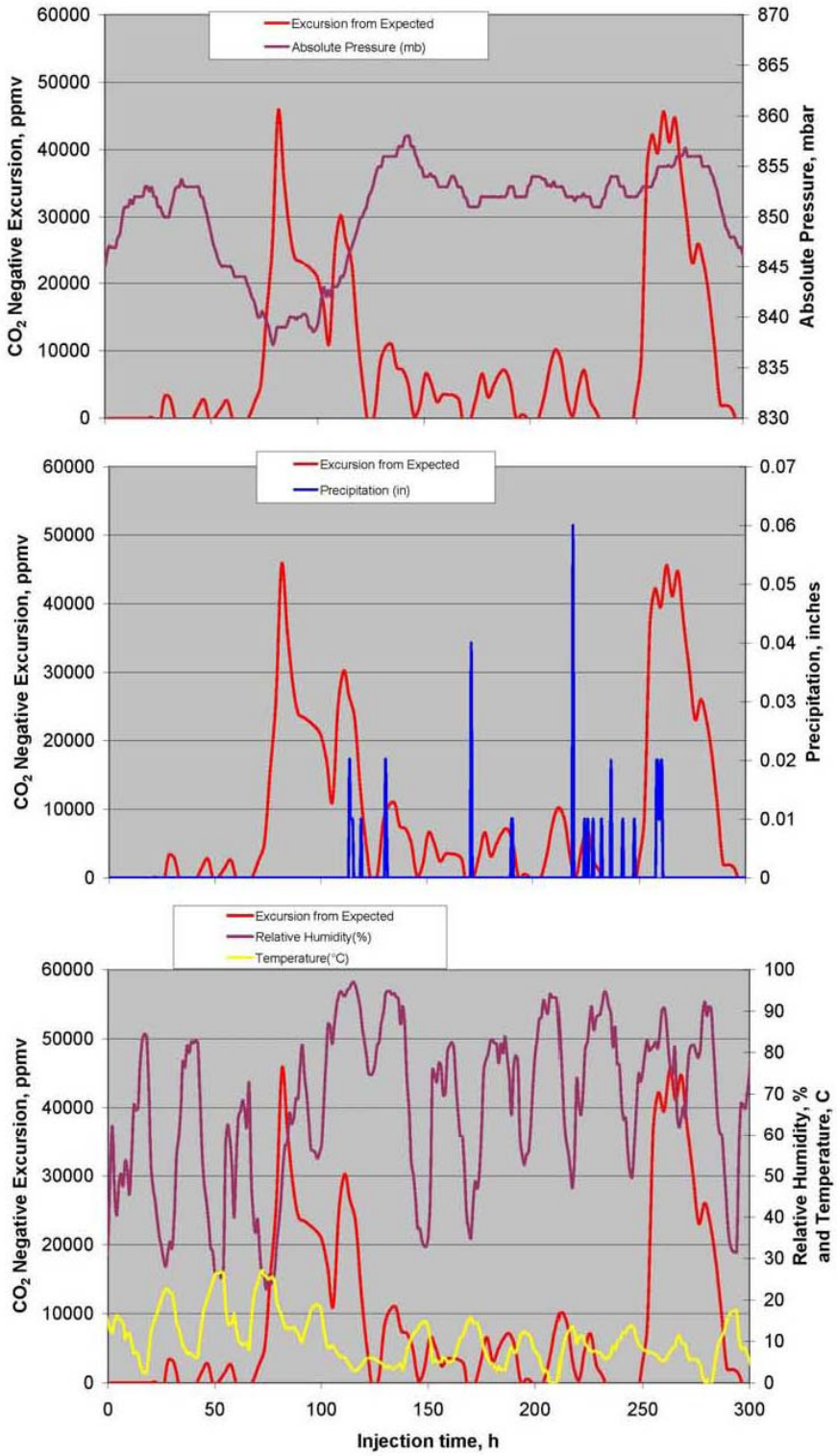

Figure 5.15. Comparison Plots Showing Timing of the Negative Excursions in the CO_2 Concentration Data for Chamber M-2 Relative to the Values for Barometric Pressure (top), Precipitation Amount (middle), and Relative Humidity and Air Temperature (bottom) Collected at the ZERT Site

For wind direction, we calculated the change in wind direction in degrees for a specific time point as the difference between the average of the wind direction 5 h forward from a specific point in time and the average 5 h back. The use of the 5-h differential moving average approach smoothed out variability in the data and helped focus on larger systematic changes. We hypothesized that changes in the wind direction would tend to cause changes in the barometric pumping activity of the wind on the soil, due to the different slope aspect of the soil surface relative to the wind. Wind direction could also affect the venting of the chamber because the 4-in.-long, 1/8-in.-OD vent tubing extended into the air at an angle from the vertical (Figure 5.3).

The results of the comparisons of negative excursion events with wind variables were quite striking. All three major excursions were preceded by or contemporaneous with major bursts of wind power density (Figure 5.16 top). The total energy of the wind (calculated by integrating the area under the power density curve) also seemed to relate well to the size of the excursion event.

The relatively minor excursions did not show much of a correlation with WPD, but the noise in these measurements (2σ) is about 4600 ppmv, so it is unclear whether the minor negative excursions were significantly different from the expected values. Interestingly, however, the frequency of the negative excursions matched nicely with that of the changes in wind direction (Figure 5.16 bottom), suggesting that simply changing the direction of the mass air flow could impact the CO_2 concentrations measured using steady-state methods. We recognize, however, that this periodicity was on the order of 24 h, and some diurnal fluctuations in soil respiration, for example, could have contributed to the minor excursions.

We are uncertain whether the negative excursions that we observed are an artifact of the steady-state flux measurement method or truly represent a process that is occurring in the soil whenever the WPD is high. The evidence supports both possibilities. Data collected using an automated non–steady-state flux chamber (LI-8100, LI-COR Biosciences, Lincoln, NE) located adjacent to our M-2 chamber show a large negative excursion for the 245- to 285-h period comparable to that seen with our chambers (Dr. Laura Dobeck, Montana State University, personal communication). These results suggest that the near-surface portion of the soil reservoir had become depleted due to the high sustained winds and thereby temporarily decreased the measured efflux rates. The LI-8100 chamber was equipped with a novel vent tube (Xu et al. 2006) that minimizes wind effects (transient pressure differentials between chamber interior and ambient air that influence soil gas fluxes) at wind speeds below 7 m s^{-1}. However, the LI-8100 unit did not show negative excursions for the earlier major excursions observed with our chamber that occurred between 73 and 124 h. Moreover, a comparison of flux values obtained by the two chamber types showed the steady-state chamber to have fluxes that were generally five-fold higher than those obtained with the LI-8100.

The combination of wind direction effects, anomalous excursions (i.e., during the 73- to 124-h period), and five-fold higher flux values suggest that our chamber venting system might require modification. For steady-state flow-through flux chambers, pressure differentials of less than a few tenths of a pascal are recommended to avoid artificially enhanced flux results (Kanemasu et al. 1974; Gao and Yates 1998; Rochette and Hutchinson 2005). Reichman and Rolston (2002) obtained accurate data with their chamber at pressure differentials of 0.5–0.8 Pa while noting that soil texture played a significant role in the absolute pressure differential that could be tolerated. The calculated pressure drop (http://www.pressure-drop.com/Online-Calculator/index.html) across the vent tube at the flow rate we used (40 mL min^{-1}) is 8 Pa, which suggests that a relatively substantial vacuum was induced in the chamber under our operating conditions. This vacuum could have caused higher advection from the soil and a correspondingly higher flux rate.

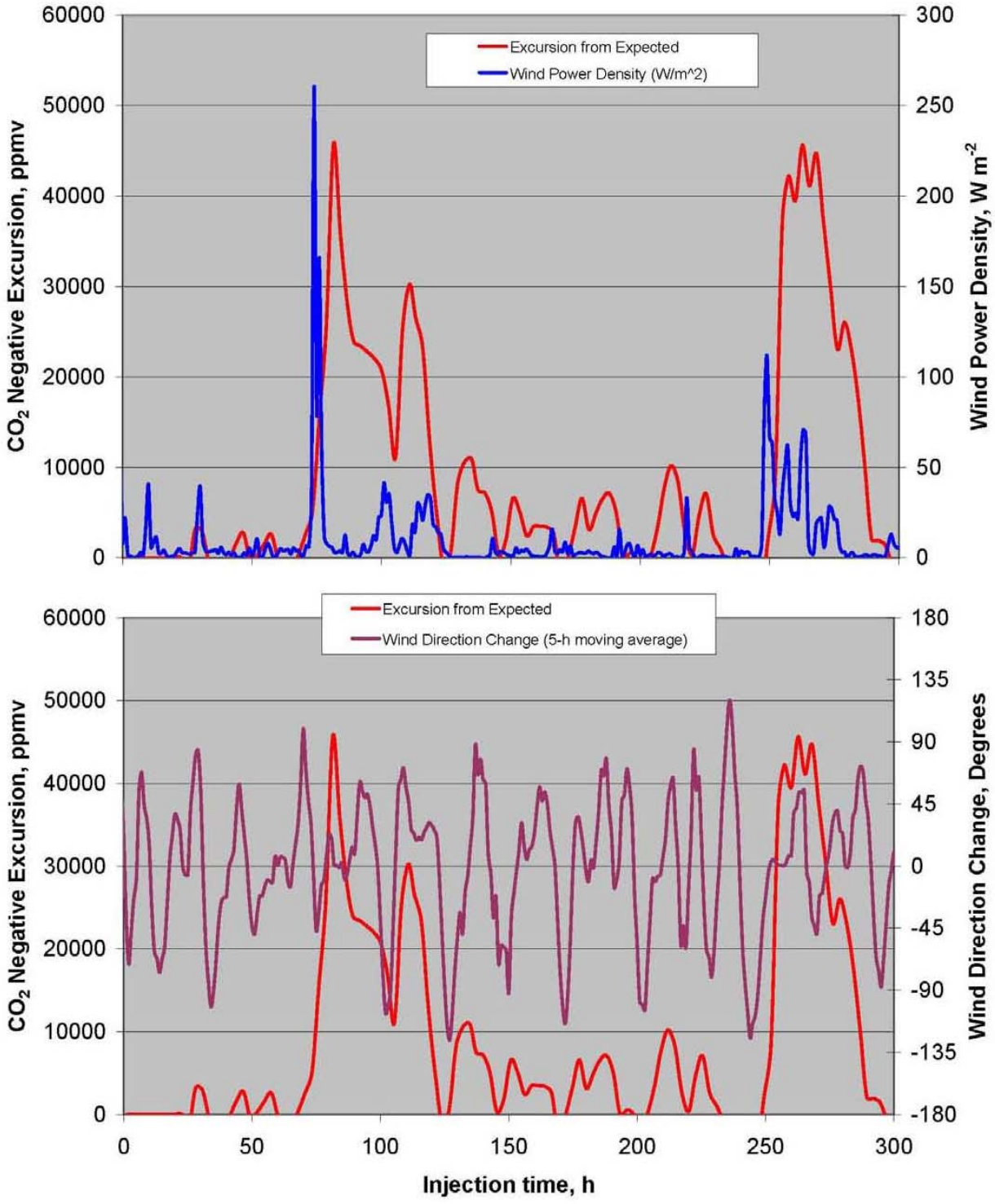

Figure 5.16. Comparison Plots Showing Timing of the Negative Excursions in the CO_2 Concentration Data for Chamber M-2 Relative to the Values for Wind Power Density (top) and Wind Direction Change (bottom) Collected at the ZERT Site

To relieve this pressure drop while also maintaining the ability to buffer transient wind-induced pressure changes, a larger diameter tube is required. For wind speeds of 4 m s^{-1}, Hutchinson and Mosier (1981) calculated that a tube diameter of 3.6 mm and length of 5.8 cm would be needed for a 1.4-L volume chamber. The calculated pressure drop with this sized tube for our flow rate is well below 1 Pa. With the use of vent tubing, however, also comes the risk of pressure changes induced by the Venturi effect at certain wind directions. Xu et al. (2006) eliminated this problem at wind speeds of less than 7 m s^{-1} by a unique split "flying-saucer" vent design oriented normal to the ground and open on all sides, and this design was used to vent the LI-8100 unit. We will explore similar options in modifications to our chamber vent design in the coming year.

6.0 Future Directions

Our interpretation of the results obtained during the second CO_2 test injection in 2008 leads to the following work priorities in FY2009 contingent on funding availability:

- *Chamber Modifications* – The negative pressure inside the chambers resulting from the constricted ambient-air intake tube will need to be reduced to about 0.5 Pa while retaining the ability to minimize Venturi effects from winds. We will explore the use of the vents that behave similarly to those described by Xu et al. (2006) on our chambers, as well as larger-diameter, longer vent tubes based on the calculations in Hutchinson and Mosier (1981). We will use a "flux bucket" fabricated in 2008, based on one described by Evans et al. (2001) to calibrate our flux measurements with those of other flux-monitoring instruments and to explore the impacts of wind and collar depth on our data.
- *Dilution Range* – Assuming that our 2008 flux data are about five times higher than actual (due to the negative pressure inside our chambers), and that the data collected by the LI-8100 system are accurate, we still would need to substantially increase our dilution range to measure fluxes directly over the injection pipe. For example, a maximum flux of about 2500 μmol m^{-2} s^{-1} was measured by the LI-8100 system, which would correspond to a steady-state concentration of more than 800,000 ppmv using our chambers and flow parameters. To expand the current dilution range accurately would require a two-stage dilution system, with each stage capable of one-, five-, and twenty-fold dilution, to yield a maximum dilution of 400-fold and allow us to measure the entire CO_2 concentration range (0–100%). We will add valving and mass-flow controllers to our system so that the full range becomes accessible to our measurements.
- *Data Reduction and Visualization* – The massive amounts of data generated require development of software to process and visualize the data in a more efficient, timely, and spatially organized manner. Further, it will be highly useful to be able to access these data in real time and multiple locations using an Internet-based interface. We will develop the software and interface for use with our system in this summer's experiments.
- *Soil Moisture Experiments* – Due to the very dry soil conditions that occurred during the second test injection, we were not able to test the soil moisture–relative humidity hypothesis in 2008. We anticipate having a fully functional system in time for an injection scheduled during the wetter portion of the summer. In addition, if the weather does not cooperate, we will design an experiment using some form of irrigation to simulate changes in air-filled porosity.
- *Independent and Buried-Chamber Systems* – Although these have lower priority than the previous items, we think it will be important to develop some measurement capabilities that do not require tethering to a central dilution/processing analyzer. Small diffusion-based probes capable of measuring to 200,000 ppmv CO_2 above ground or in the subsurface (noncondensing) are commercially available (e.g., Tang et al. 2003), and we think these could be adapted to transmit output data by radio to a central datalogging system, and from there to the Internet site by cellular modem. Some depth-dependent information would be helpful in delineating the path followed by the CO_2 plume.

7.0 References

Evans WC, ML Sorey, BM Kennedy, DA Stonestrom, JD Rogie, and DL Shuster. 2001. "High CO_2 Emissions through Porous Media: Transport Mechanisms and Implications for Flux Measurement and Fractionation." *Chemical Geology* 177:15–29.

Gao F and SR Yates. 1998. "Laboratory Study of Closed and Dynamic Flux Chambers: Experimental Results and Implications for Field Applications." *Journal of Geophysical Research* 103:26115–26125.

Hutchinson GL and AR Mosier. 1981. "Improved Soil Cover Method for Field Measurement of Nitrous Oxide Fluxes." *Soil Science Society of America Journal* 45:311–316.

Kanemasu ET, WL Powers, and JW Sij. 1974. "Field Chamber Measurements of CO_2 Flux from Soil Surface." *Soil Science* 118:233–237.

McGrail BP, HT Schaef, AM Ho, Y-J Chien, JJ Dooley, and CL Davidson. 2006. "Potential for Carbon Dioxide Sequestration in Flood Basalts." *Journal of Geophysical Research* 111:B12201.

Reichman R and DE Rolston. 2002. "Design and Performance of a Dynamic Gas Flux Chamber." *Journal of Environmental Quality* 31:1774–1781.

Rochette P and GL Hutchinson. 2005. "Measurement of Soil Respiration in Situ: Chamber Techniques." In *Micrometeorology in Agricultural Systems*, JL Hatfield and JM Baker (eds), Agronomy Monograph No. 47, pp. 247–286. American Society of Agronomy, , Madison,Wisconsin.

Soil Moisture Equipment Corporation. 2000. Operating Instructions. 5201F1 Soilmoisture G-blocks. Soil Moisture Equipment Corporation, Santa Barbara,California. Available at http://www.soilmoisture.com/PDF%20Files/85201F1.pdf (April 2009).

Tang J, DD Baldocchi, Y Qi, and L Xu. 2003. "Assessing Soil CO_2 Efflux Using Continuous Measurements of CO_2 Profiles in Soils with Small Solid-State Sensors." *Agricultural Forest Meteorology* 118:207–222.

White CM, BR Strazisar, EJ Granite, JS Hoffman, and HW Pennline. 2003. "Separation and Capture of CO_2 from Large Stationary Sources and Sequestration in Geological Formations – Coalbeds and Deep Saline Aquifers." *Journal of the Air & Waste Management Association* 53:645–715.

White CM, DH Smith, KL Jones, AL Goodman, SA Jikich, RG LaCount, SB DuBose, E Ozdemir, BI Morsi, and KT Schroeder. 2005. "Sequestration of Carbon Dioxide in Coal with Enhanced Coalbed Methane Recovery – a Review." *Energy Fuels* 19:659–724.

Xu L, MD Furtaw, RA Madsen, RL Garcia, DJ Anderson, and DK McDermitt. 2006. "On Maintaining Pressure Equilibrium between a Soil CO_2 Flux Chamber and the Ambient Air." *Journal of Geophysical Research* 111:D08S10, doi: 10.1029/2005JD006435.

Appendix A

System Control Code

```
;{CR23X}
*Table 1 Program
  01: .25       Execution Interval
(seconds)


;Set up time system and cycle times

1:  Time (P18)
 1: 1        Minutes into current
day (maximum 1440)
 2: 1440     Mod/By
 3: 1        Loc [ time_min  ]

2:  Z=X MOD F (P46)
 1: 1        X Loc [ time_min  ]
 2: 162      F
 3: 2        Z Loc [ time_cycl ]

3:  Time (P18)
 1: 0        Seconds into current
minute (maximum 60)
 2: 60       Mod/By
 3: 1        Loc [ time_min  ]

4:  Z=X*F (P37)
 1: 1        X Loc [ time_min  ]
 2: 0.01667  F
 3: 4        Z Loc [ time_add  ]

5:  Z=X+Y (P33)
 1: 2        X Loc [ time_cycl ]
 2: 4        Y Loc [ time_add  ]
 3: 2        Z Loc [ time_cycl ]
;end time set up


;take readings


6:  Volt (Diff) (P2)
 1: 4        Reps
 2: 15       5000 mV, Fast Range
 3: 8        DIFF Channel
 4: 5        Loc [ co2_in    ]
 5: 1        Mult
 6: 0        Offset

;transfer the licor voltage
function output to another variable

7:  Z=X (P31)
 1: 5        X Loc [ co2_in    ]
 2: 47       Z Loc [ CVtest    ]


8:  Volt (Diff) (P2)
 1: 1        Reps
 2: 15       5000 mV, Fast Range
 3: 12       DIFF Channel
 4: 48       Loc [ FlowDil   ]
 5: 0.3994   Mult
 6: -0.0069  Offset

9:  Volt (Diff) (P2)
 1: 1        Reps
 2: 15       5000 mV, Fast Range
 3: 7        DIFF Channel
 4: 49       Loc [ FlowOut   ]
 5: 0.4004   Mult
 6: 0.0121   Offset
;End Read in

10:  Volt (Diff) (P2)
 1: 1        Reps
 2: 15       5000 mV, Fast Range
 3: 1        DIFF Channel
 4: 50       Loc [ flowsamp  ]
 5: -.01     Mult
 6: 0.0      Offset



;Set up Chamber values
11:  If (X<=>F) (P89)
 1: 2        X Loc [ time_cycl ]
 2: 3        >=
 3: 0        F
 4: 30       Then Do

12:  If (X<=>F) (P89)
 1: 2        X Loc [ time_cycl ]
 2: 4        <
 3: 6        F
 4: 30       Then Do
```

```
     13:  Z=F (P30)
      1: 1        F
      2: 00       Exponent of 10
      3: 59       Z Loc [ Chamber
]



14:  End (P95)

15:  End (P95)

16:  If (X<=>F) (P89)
 1: 2        X Loc [ time_cycl ]
 2: 3        >=
 3: 6        F
 4: 30       Then Do

17:  If (X<=>F) (P89)
 1: 2        X Loc [ time_cycl ]
 2: 4        <
 3: 12       F
 4: 30       Then Do



     18:  Z=F (P30)
      1: 2        F
      2: 00       Exponent of 10
      3: 59       Z Loc [ Chamber
]



19:  End (P95)

20:  End (P95)

21:  If (X<=>F) (P89)
 1: 2        X Loc [ time_cycl ]
 2: 3        >=
 3: 12       F
 4: 30       Then Do

22:  If (X<=>F) (P89)
 1: 2        X Loc [ time_cycl ]
 2: 4        <
 3: 18       F
 4: 30       Then Do



     23:  Z=F (P30)
      1: 3        F
      2: 00       Exponent of 10
      3: 59       Z Loc [ Chamber
]



24:  End (P95)

25:  End (P95)

26:  If (X<=>F) (P89)
 1: 2        X Loc [ time_cycl ]
 2: 3        >=
 3: 18       F
 4: 30       Then Do

27:  If (X<=>F) (P89)
 1: 2        X Loc [ time_cycl ]
 2: 4        <
 3: 24       F
 4: 30       Then Do



     28:  Z=F (P30)
      1: 4        F
      2: 00       Exponent of 10
      3: 59       Z Loc [ Chamber
]



29:  End (P95)

30:  End (P95)

31:  If (X<=>F) (P89)
 1: 2        X Loc [ time_cycl ]
 2: 3        >=
 3: 24       F
 4: 30       Then Do

32:  If (X<=>F) (P89)
 1: 2        X Loc [ time_cycl ]
 2: 4        <
 3: 30       F
 4: 30       Then Do



     33:  Z=F (P30)
      1: 5        F
      2: 00       Exponent of 10
      3: 59       Z Loc [ Chamber
]
```

```
34:  End (P95)

35:  End (P95)

36:  If (X<=>F) (P89)
 1: 2        X Loc [ time_cycl ]
 2: 3        >=
 3: 30       F
 4: 30       Then Do

37:  If (X<=>F) (P89)
 1: 2        X Loc [ time_cycl ]
 2: 4        <
 3: 36       F
 4: 30       Then Do

     38:  Z=F (P30)
      1: 6        F
      2: 00       Exponent of 10
      3: 59       Z Loc [ Chamber
]

39:  End (P95)

40:  End (P95)

41:  If (X<=>F) (P89)
 1: 2        X Loc [ time_cycl ]
 2: 3        >=
 3: 36       F
 4: 30       Then Do

42:  If (X<=>F) (P89)
 1: 2        X Loc [ time_cycl ]
 2: 4        <
 3: 42       F
 4: 30       Then Do

     43:  Z=F (P30)
      1: 7        F
      2: 00       Exponent of 10
      3: 59       Z Loc [ Chamber
]

44:  End (P95)

45:  End (P95)

46:  If (X<=>F) (P89)
 1: 2        X Loc [ time_cycl ]
 2: 3        >=
 3: 42       F
 4: 30       Then Do

47:  If (X<=>F) (P89)
 1: 2        X Loc [ time_cycl ]
 2: 4        <
 3: 48       F
 4: 30       Then Do

     48:  Z=F (P30)
      1: 8        F
      2: 00       Exponent of 10
      3: 59       Z Loc [ Chamber
]

49:  End (P95)

50:  End (P95)

51:  If (X<=>F) (P89)
 1: 2        X Loc [ time_cycl ]
 2: 3        >=
 3: 48       F
 4: 30       Then Do

52:  If (X<=>F) (P89)
 1: 2        X Loc [ time_cycl ]
 2: 4        <
 3: 54       F
 4: 30       Then Do

     53:  Z=F (P30)
      1: 9        F
      2: 00       Exponent of 10
      3: 59       Z Loc [ Chamber
]

54:  End (P95)

55:  End (P95)

56:  If (X<=>F) (P89)
 1: 2        X Loc [ time_cycl ]
 2: 3        >=
 3: 54       F
```

```
 4: 30       Then Do

57:  If (X<=>F) (P89)
 1: 2        X Loc [ time_cycl ]
 2: 4        <
 3: 60       F
 4: 30       Then Do


     58:  Z=F (P30)
      1: 10       F
      2: 00       Exponent of 10
      3: 59       Z Loc [ Chamber
]



59:  End (P95)

60:  End (P95)

61:  If (X<=>F) (P89)
 1: 2        X Loc [ time_cycl ]
 2: 3        >=
 3: 60       F
 4: 30       Then Do

62:  If (X<=>F) (P89)
 1: 2        X Loc [ time_cycl ]
 2: 4        <
 3: 66       F
 4: 30       Then Do


     63:  Z=F (P30)
      1: 11       F
      2: 00       Exponent of 10
      3: 59       Z Loc [ Chamber
]



64:  End (P95)

65:  End (P95)

66:  If (X<=>F) (P89)
 1: 2        X Loc [ time_cycl ]
 2: 3        >=
 3: 66       F
 4: 30       Then Do

67:  If (X<=>F) (P89)
 1: 2        X Loc [ time_cycl ]
 2: 4        <
 3: 72       F
 4: 30       Then Do


     68:  Z=F (P30)
      1: 12       F
      2: 00       Exponent of 10
      3: 59       Z Loc [ Chamber
]



69:  End (P95)

70:  End (P95)

71:  If (X<=>F) (P89)
 1: 2        X Loc [ time_cycl ]
 2: 3        >=
 3: 72       F
 4: 30       Then Do

72:  If (X<=>F) (P89)
 1: 2        X Loc [ time_cycl ]
 2: 4        <
 3: 78       F
 4: 30       Then Do


     73:  Z=F (P30)
      1: 13       F
      2: 00       Exponent of 10
      3: 59       Z Loc [ Chamber
]



74:  End (P95)

75:  End (P95)


76:  If (X<=>F) (P89)
 1: 2        X Loc [ time_cycl ]
 2: 3        >=
 3: 78       F
 4: 30       Then Do

77:  If (X<=>F) (P89)
 1: 2        X Loc [ time_cycl ]
 2: 4        <
 3: 84       F
 4: 30       Then Do
```

```
     78:  Z=F (P30)
      1: 14       F
      2: 00       Exponent of 10
      3: 59       Z Loc [ Chamber
]



79:  End (P95)

80:  End (P95)


81:  If (X<=>F) (P89)
 1: 2        X Loc [ time_cycl ]
 2: 3        >=
 3: 84       F
 4: 30       Then Do

82:  If (X<=>F) (P89)
 1: 2        X Loc [ time_cycl ]
 2: 4        <
 3: 90       F
 4: 30       Then Do



     83:  Z=F (P30)
      1: 15       F
      2: 00       Exponent of 10
      3: 59       Z Loc [ Chamber
]



84:  End (P95)

85:  End (P95)


86:  If (X<=>F) (P89)
 1: 2        X Loc [ time_cycl ]
 2: 3        >=
 3: 90       F
 4: 30       Then Do

87:  If (X<=>F) (P89)
 1: 2        X Loc [ time_cycl ]
 2: 4        <
 3: 96       F
 4: 30       Then Do



     88:  Z=F (P30)
      1: 16       F
      2: 00       Exponent of 10
      3: 59       Z Loc [ Chamber
]



89:  End (P95)

90:  End (P95)

91:  If (X<=>F) (P89)
 1: 2        X Loc [ time_cycl ]
 2: 3        >=
 3: 96       F
 4: 30       Then Do

92:  If (X<=>F) (P89)
 1: 2        X Loc [ time_cycl ]
 2: 4        <
 3: 102      F
 4: 30       Then Do



     93:  Z=F (P30)
      1: 17       F
      2: 00       Exponent of 10
      3: 59       Z Loc [ Chamber
]



94:  End (P95)

95:  End (P95)

96:  If (X<=>F) (P89)
 1: 2        X Loc [ time_cycl ]
 2: 3        >=
 3: 102      F
 4: 30       Then Do

97:  If (X<=>F) (P89)
 1: 2        X Loc [ time_cycl ]
 2: 4        <
 3: 108      F
 4: 30       Then Do



     98:  Z=F (P30)
      1: 18       F
      2: 00       Exponent of 10
      3: 59       Z Loc [ Chamber
]
```

```
99:  End (P95)

100:  End (P95)

101:  If (X<=>F) (P89)
 1: 2        X Loc [ time_cycl ]
 2: 3        >=
 3: 108      F
 4: 30       Then Do

102:  If (X<=>F) (P89)
 1: 2        X Loc [ time_cycl ]
 2: 4        <
 3: 114      F
 4: 30       Then Do

    103:  Z=F (P30)
     1: 19       F
     2: 00       Exponent of 10
     3: 59       Z Loc [ Chamber
]

104:  End (P95)

105:  End (P95)

106:  If (X<=>F) (P89)
 1: 2        X Loc [ time_cycl ]
 2: 3        >=
 3: 114      F
 4: 30       Then Do

107:  If (X<=>F) (P89)
 1: 2        X Loc [ time_cycl ]
 2: 4        <
 3: 120      F
 4: 30       Then Do

    108:  Z=F (P30)
     1: 20       F
     2: 00       Exponent of 10
     3: 59       Z Loc [ Chamber
]

109:  End (P95)

110:  End (P95)

111:  If (X<=>F) (P89)
 1: 2        X Loc [ time_cycl ]
 2: 3        >=
 3: 120      F
 4: 30       Then Do

112:  If (X<=>F) (P89)
 1: 2        X Loc [ time_cycl ]
 2: 4        <
 3: 126      F
 4: 30       Then Do

    113:  Z=F (P30)
     1: 21       F
     2: 00       Exponent of 10
     3: 59       Z Loc [ Chamber
]

114:  End (P95)

115:  End (P95)

116:  If (X<=>F) (P89)
 1: 2        X Loc [ time_cycl ]
 2: 3        >=
 3: 126      F
 4: 30       Then Do

117:  If (X<=>F) (P89)
 1: 2        X Loc [ time_cycl ]
 2: 4        <
 3: 132      F
 4: 30       Then Do

    118:  Z=F (P30)
     1: 22       F
     2: 00       Exponent of 10
     3: 59       Z Loc [ Chamber
]

119:  End (P95)

120:  End (P95)

121:  If (X<=>F) (P89)
 1: 2        X Loc [ time_cycl ]
 2: 3        >=
```

```
 3: 132      F
 4: 30       Then Do

122:  If (X<=>F) (P89)
 1: 2        X Loc [ time_cycl ]
 2: 4        <
 3: 138      F
 4: 30       Then Do


     123:  Z=F (P30)
      1: 23       F
      2: 00       Exponent of 10
      3: 59       Z Loc [ Chamber
]



124:  End (P95)

125:  End (P95)

126:  If (X<=>F) (P89)
 1: 2        X Loc [ time_cycl ]
 2: 3        >=
 3: 138      F
 4: 30       Then Do

127:  If (X<=>F) (P89)
 1: 2        X Loc [ time_cycl ]
 2: 4        <
 3: 144      F
 4: 30       Then Do


     128:  Z=F (P30)
      1: 24       F
      2: 00       Exponent of 10
      3: 59       Z Loc [ Chamber
]



129:  End (P95)

130:  End (P95)

131:  If (X<=>F) (P89)
 1: 2        X Loc [ time_cycl ]
 2: 3        >=
 3: 144      F
 4: 30       Then Do

132:  If (X<=>F) (P89)
 1: 2        X Loc [ time_cycl ]
 2: 4        <
 3: 150      F
 4: 30       Then Do


     133:  Z=F (P30)
      1: 25       F
      2: 00       Exponent of 10
      3: 59       Z Loc [ Chamber
]



134:  End (P95)

135:  End (P95)

136:  If (X<=>F) (P89)
 1: 2        X Loc [ time_cycl ]
 2: 3        >=
 3: 150      F
 4: 30       Then Do

137:  If (X<=>F) (P89)
 1: 2        X Loc [ time_cycl ]
 2: 4        <
 3: 156      F
 4: 30       Then Do


     138:  Z=F (P30)
      1: 26       F
      2: 00       Exponent of 10
      3: 59       Z Loc [ Chamber
]



139:  End (P95)

140:  End (P95)

141:  If (X<=>F) (P89)
 1: 2        X Loc [ time_cycl ]
 2: 3        >=
 3: 156      F
 4: 30       Then Do

142:  If (X<=>F) (P89)
 1: 2        X Loc [ time_cycl ]
 2: 4        <
 3: 162      F
 4: 30       Then Do
```

```
     143:  Z=F (P30)
      1: 27       F
      2: 00       Exponent of 10
      3: 59       Z Loc [ Chamber
]


144:  End (P95)

145:  End (P95)




;Open valve 1 operation
146:  If (X<=>F) (P89)
 1: 2        X Loc [ time_cycl ]
 2: 3        >=
 3: .05      F
 4: 30       Then Do

147:  If (X<=>F) (P89)
 1: 2        X Loc [ time_cycl ]
 2: 4        <
 3: .1       F
 4: 30       Then Do

     148:  Do (P86)
      1: 002      Call Subroutine 2


149:  Z=F x 10^n (P30)
 1: 1        F
 2: 0        n, Exponent of 10
 3: 10       Z Loc [ SDM1P_1   ]



150:  End (P95)
151:  End (P95)

152:  If (X<=>F) (P89)
 1: 2        X Loc [ time_cycl ]
 2: 4        <
 3: .2       F
 4: 30       Then Do

153:  If (X<=>F) (P89)
 1: 2        X Loc [ time_cycl ]
 2: 3        >=
 3: .1       F
 4: 30       Then Do

; de-energize valve1
     154:  Do (P86)
      1: 004      Call Subroutine 4


155:  Z=F x 10^n (P30)
 1: 0        F
 2: 0        n, Exponent of 10
 3: 10       Z Loc [ SDM1P_1   ]



156:  End (P95)
157:  End (P95)

158:  If (X<=>F) (P89)
 1: 2        X Loc [ time_cycl ]
 2: 4        <
 3: 5.9      F
 4: 30       Then Do

159:  If (X<=>F) (P89)
 1: 2        X Loc [ time_cycl ]
 2: 3        >=
 3: 5.95     F
 4: 30       Then Do

;close valve1

     160:  Do (P86)
      1: 003      Call Subroutine 3


161:  Z=F x 10^n (P30)
 1: 1        F
 2: 0        n, Exponent of 10
 3: 10       Z Loc [ SDM1P_1   ]



162:  End (P95)
163:  End (P95)


164:  If (X<=>F) (P89)
 1: 2        X Loc [ time_cycl ]
 2: 4        <
 3: 6        F
 4: 30       Then Do

165:  If (X<=>F) (P89)
 1: 2        X Loc [ time_cycl ]
 2: 3        >=
```

```
 3: 5.95     F
 4: 30       Then Do

;de-energize valve1

     166:  Do (P86)
      1: 004      Call Subroutine 4


167:  Z=F x 10^n (P30)
 1: 0        F
 2: 0        n, Exponent of 10
 3: 10       Z Loc [ SDM1P_1   ]



168:  End (P95)
169:  End (P95)

;Open valve 1 operation
170:  If (X<=>F) (P89)
 1: 2        X Loc [ time_cycl ]
 2: 3        >=
 3: .07      F
 4: 30       Then Do

171:  If (X<=>F) (P89)
 1: 2        X Loc [ time_cycl ]
 2: 4        <
 3: .1       F
 4: 30       Then Do

     172:  Do (P86)
      1: 002      Call Subroutine 2


173:  Z=F x 10^n (P30)
 1: 1        F
 2: 0        n, Exponent of 10
 3: 10       Z Loc [ SDM1P_1   ]



174:  End (P95)
175:  End (P95)

176:  If (X<=>F) (P89)
 1: 2        X Loc [ time_cycl ]
 2: 4        <
 3: .2       F
 4: 30       Then Do

177:  If (X<=>F) (P89)
 1: 2        X Loc [ time_cycl ]
 2: 3        >=
 3: .1       F
 4: 30       Then Do

; de-energize valve1
     178:  Do (P86)
      1: 004      Call Subroutine 4


179:  Z=F x 10^n (P30)
 1: 0        F
 2: 0        n, Exponent of 10
 3: 10       Z Loc [ SDM1P_1   ]



180:  End (P95)
181:  End (P95)

182:  If (X<=>F) (P89)
 1: 2        X Loc [ time_cycl ]
 2: 4        <
 3: 5.9      F
 4: 30       Then Do

183:  If (X<=>F) (P89)
 1: 2        X Loc [ time_cycl ]
 2: 3        >=
 3: 5.95     F
 4: 30       Then Do

;close valve1

     184:  Do (P86)
      1: 003      Call Subroutine 3


185:  Z=F x 10^n (P30)
 1: 1        F
 2: 0        n, Exponent of 10
 3: 10       Z Loc [ SDM1P_1   ]



186:  End (P95)
187:  End (P95)

188:  If (X<=>F) (P89)
 1: 2        X Loc [ time_cycl ]
 2: 4        <
 3: 6        F
 4: 30       Then Do

189:  If (X<=>F) (P89)
 1: 2        X Loc [ time_cycl ]
 2: 3        >=
 3: 5.95     F
 4: 30       Then Do
```

```
;de-energize valve1

     190:  Do (P86)
      1: 004      Call Subroutine 4


191:  Z=F x 10^n (P30)
 1: 0        F
 2: 0        n, Exponent of 10
 3: 10       Z Loc [ SDM1P_1   ]



192:  End (P95)
193:  End (P95)


;Open valve 2 operation
194:  If (X<=>F) (P89)
 1: 2        X Loc [ time_cycl ]
 2: 3        >=
 3: 6.07     F
 4: 30       Then Do

195:  If (X<=>F) (P89)
 1: 2        X Loc [ time_cycl ]
 2: 4        <
 3: 6.1      F
 4: 30       Then Do

     196:  Do (P86)
      1: 002      Call Subroutine 2


197:  Z=F x 10^n (P30)
 1: 1        F
 2: 0        n, Exponent of 10
 3: 11       Z Loc [ SDM1P_2   ]



198:  End (P95)
199:  End (P95)

200:  If (X<=>F) (P89)
 1: 2        X Loc [ time_cycl ]
 2: 4        <
 3: 6.2      F
 4: 30       Then Do

201:  If (X<=>F) (P89)
 1: 2        X Loc [ time_cycl ]
 2: 3        >=
 3: 6.1      F
 4: 30       Then Do

; de-energize valve2

     202:  Do (P86)
      1: 004      Call Subroutine 4


203:  Z=F x 10^n (P30)
 1: 0        F
 2: 0        n, Exponent of 10
 3: 11       Z Loc [ SDM1P_2   ]



204:  End (P95)
205:  End (P95)

206:  If (X<=>F) (P89)
 1: 2        X Loc [ time_cycl ]
 2: 4        <
 3: 11.9     F
 4: 30       Then Do

207:  If (X<=>F) (P89)
 1: 2        X Loc [ time_cycl ]
 2: 3        >=
 3: 11.95    F
 4: 30       Then Do

;close valve2

     208:  Do (P86)
      1: 003      Call Subroutine 3


209:  Z=F x 10^n (P30)
 1: 1        F
 2: 0        n, Exponent of 10
 3: 11       Z Loc [ SDM1P_2   ]



210:  End (P95)
211:  End (P95)


212:  If (X<=>F) (P89)
 1: 2        X Loc [ time_cycl ]
 2: 4        <
 3: 12       F
 4: 30       Then Do

213:  If (X<=>F) (P89)
 1: 2        X Loc [ time_cycl ]
 2: 3        >=
 3: 11.95    F
 4: 30       Then Do

;de-energize valve2
```

```
     214:  Do (P86)
      1: 004      Call Subroutine 4


215:  Z=F x 10^n (P30)
 1: 0        F
 2: 0        n, Exponent of 10
 3: 11       Z Loc [ SDM1P_2   ]



216:  End (P95)
217:  End (P95)

;End Valve 2 operation



;Open valve 3 operation
218:  If (X<=>F) (P89)
 1: 2        X Loc [ time_cycl ]
 2: 3        >=
 3: 12.07    F
 4: 30       Then Do

219:  If (X<=>F) (P89)
 1: 2        X Loc [ time_cycl ]
 2: 4        <
 3: 12.1     F
 4: 30       Then Do

     220:  Do (P86)
      1: 002      Call Subroutine 2


221:  Z=F x 10^n (P30)
 1: 1        F
 2: 0        n, Exponent of 10
 3: 12       Z Loc [ SDM1P_3   ]



222:  End (P95)
223:  End (P95)

224:  If (X<=>F) (P89)
 1: 2        X Loc [ time_cycl ]
 2: 4        <
 3: 12.2     F
 4: 30       Then Do

225:  If (X<=>F) (P89)
 1: 2        X Loc [ time_cycl ]
 2: 3        >=
 3: 12.1     F
 4: 30       Then Do

; de-energize valve3
     226:  Do (P86)
      1: 004      Call Subroutine 4


227:  Z=F x 10^n (P30)
 1: 0        F
 2: 0        n, Exponent of 10
 3: 12       Z Loc [ SDM1P_3   ]



228:  End (P95)
229:  End (P95)

230:  If (X<=>F) (P89)
 1: 2        X Loc [ time_cycl ]
 2: 4        <
 3: 17.9     F
 4: 30       Then Do

231:  If (X<=>F) (P89)
 1: 2        X Loc [ time_cycl ]
 2: 3        >=
 3: 17.95    F
 4: 30       Then Do

;close valve3

     232:  Do (P86)
      1: 003      Call Subroutine 3


233:  Z=F x 10^n (P30)
 1: 1        F
 2: 0        n, Exponent of 10
 3: 12       Z Loc [ SDM1P_3   ]



234:  End (P95)
235:  End (P95)


236:  If (X<=>F) (P89)
 1: 2        X Loc [ time_cycl ]
 2: 4        <
 3: 18       F
 4: 30       Then Do

237:  If (X<=>F) (P89)
 1: 2        X Loc [ time_cycl ]
 2: 3        >=
 3: 17.95    F
 4: 30       Then Do

;de-energize valve3
```

```
    238:  Do (P86)
     1: 004      Call Subroutine 4


239:  Z=F x 10^n (P30)
 1: 0        F
 2: 0        n, Exponent of 10
 3: 12       Z Loc [ SDM1P_3   ]



240:  End (P95)
241:  End (P95)

;End Valve 3 operation




;Open valve 4 operation
242:  If (X<=>F) (P89)
 1: 2        X Loc [ time_cycl ]
 2: 3        >=
 3: 18.07    F
 4: 30       Then Do

243:  If (X<=>F) (P89)
 1: 2        X Loc [ time_cycl ]
 2: 4        <
 3: 18.1     F
 4: 30       Then Do

    244:  Do (P86)
     1: 002      Call Subroutine 2


245:  Z=F x 10^n (P30)
 1: 1        F
 2: 0        n, Exponent of 10
 3: 13       Z Loc [ SDM1P_4   ]



246:  End (P95)
247:  End (P95)

248:  If (X<=>F) (P89)
 1: 2        X Loc [ time_cycl ]
 2: 4        <
 3: 18.2     F
 4: 30       Then Do

249:  If (X<=>F) (P89)
 1: 2        X Loc [ time_cycl ]
 2: 3        >=
 3: 18.1     F
 4: 30       Then Do

; de-energize valve4
    250:  Do (P86)
     1: 004      Call Subroutine 4


251:  Z=F x 10^n (P30)
 1: 0        F
 2: 0        n, Exponent of 10
 3: 13       Z Loc [ SDM1P_4   ]



252:  End (P95)
253:  End (P95)

254:  If (X<=>F) (P89)
 1: 2        X Loc [ time_cycl ]
 2: 4        <
 3: 23.9     F
 4: 30       Then Do

255:  If (X<=>F) (P89)
 1: 2        X Loc [ time_cycl ]
 2: 3        >=
 3: 23.95    F
 4: 30       Then Do

;close valve4

    256:  Do (P86)
     1: 003      Call Subroutine 3


257:  Z=F x 10^n (P30)
 1: 1        F
 2: 0        n, Exponent of 10
 3: 13       Z Loc [ SDM1P_4   ]



258:  End (P95)
259:  End (P95)


260:  If (X<=>F) (P89)
 1: 2        X Loc [ time_cycl ]
 2: 4        <
 3: 24       F
 4: 30       Then Do

261:  If (X<=>F) (P89)
 1: 2        X Loc [ time_cycl ]
 2: 3        >=
 3: 23.95    F
```

```
 4: 30       Then Do

;de-energize valve4

     262:  Do (P86)
      1: 004      Call Subroutine 4


263:  Z=F x 10^n (P30)
 1: 0        F
 2: 0        n, Exponent of 10
 3: 13       Z Loc [ SDM1P_4   ]



264:  End (P95)
265:  End (P95)

;End Valve 4 operation




;Open valve 5 operation
266:  If (X<=>F) (P89)
 1: 2        X Loc [ time_cycl ]
 2: 3        >=
 3: 24.07    F
 4: 30       Then Do

267:  If (X<=>F) (P89)
 1: 2        X Loc [ time_cycl ]
 2: 4        <
 3: 24.1     F
 4: 30       Then Do

     268:  Do (P86)
      1: 002      Call Subroutine 2


269:  Z=F x 10^n (P30)
 1: 1        F
 2: 0        n, Exponent of 10
 3: 14       Z Loc [ SDM1P_5   ]



270:  End (P95)
271:  End (P95)

272:  If (X<=>F) (P89)
 1: 2        X Loc [ time_cycl ]
 2: 4        <
 3: 24.2     F
 4: 30       Then Do

273:  If (X<=>F) (P89)
 1: 2        X Loc [ time_cycl ]
 2: 3        >=
 3: 24.1     F
 4: 30       Then Do

; de-energize valve5
     274:  Do (P86)
      1: 004      Call Subroutine 4


275:  Z=F x 10^n (P30)
 1: 0        F
 2: 0        n, Exponent of 10
 3: 14       Z Loc [ SDM1P_5   ]



276:  End (P95)
277:  End (P95)

278:  If (X<=>F) (P89)
 1: 2        X Loc [ time_cycl ]
 2: 4        <
 3: 29.9     F
 4: 30       Then Do

279:  If (X<=>F) (P89)
 1: 2        X Loc [ time_cycl ]
 2: 3        >=
 3: 29.95    F
 4: 30       Then Do

;close valve5

     280:  Do (P86)
      1: 003      Call Subroutine 3


281:  Z=F x 10^n (P30)
 1: 1        F
 2: 0        n, Exponent of 10
 3: 14       Z Loc [ SDM1P_5   ]



282:  End (P95)
283:  End (P95)


284:  If (X<=>F) (P89)
 1: 2        X Loc [ time_cycl ]
 2: 4        <
 3: 30       F
 4: 30       Then Do
```

```
285:  If (X<=>F) (P89)
 1: 2        X Loc [ time_cycl ]
 2: 3        >=
 3: 29.95    F
 4: 30       Then Do

;de-energize valve5

     286:  Do (P86)
      1: 004      Call Subroutine 4


287:  Z=F x 10^n (P30)
 1: 0        F
 2: 0        n, Exponent of 10
 3: 14       Z Loc [ SDM1P_5   ]



288:  End (P95)
289:  End (P95)

;End Valve 5 operation




;Open valve 6 operation
290:  If (X<=>F) (P89)
 1: 2        X Loc [ time_cycl ]
 2: 3        >=
 3: 30.07    F
 4: 30       Then Do

291:  If (X<=>F) (P89)
 1: 2        X Loc [ time_cycl ]
 2: 4        <
 3: 30.1     F
 4: 30       Then Do

     292:  Do (P86)
      1: 002      Call Subroutine 2


293:  Z=F x 10^n (P30)
 1: 1        F
 2: 0        n, Exponent of 10
 3: 15       Z Loc [ SDM1P_6   ]



294:  End (P95)
```

```
295:  End (P95)

296:  If (X<=>F) (P89)
 1: 2        X Loc [ time_cycl ]
 2: 4        <
 3: 30.2     F
 4: 30       Then Do

297:  If (X<=>F) (P89)
 1: 2        X Loc [ time_cycl ]
 2: 3        >=
 3: 30.1     F
 4: 30       Then Do

; de-energize valve6
     298:  Do (P86)
      1: 004      Call Subroutine 4


299:  Z=F x 10^n (P30)
 1: 0        F
 2: 0        n, Exponent of 10
 3: 15       Z Loc [ SDM1P_6   ]



300:  End (P95)
301:  End (P95)

302:  If (X<=>F) (P89)
 1: 2        X Loc [ time_cycl ]
 2: 4        <
 3: 35.9     F
 4: 30       Then Do

303:  If (X<=>F) (P89)
 1: 2        X Loc [ time_cycl ]
 2: 3        >=
 3: 35.95    F
 4: 30       Then Do

;close valve6

     304:  Do (P86)
      1: 003      Call Subroutine 3


305:  Z=F x 10^n (P30)
 1: 1        F
 2: 0        n, Exponent of 10
 3: 15       Z Loc [ SDM1P_6   ]



306:  End (P95)
307:  End (P95)
```

```
308:  If (X<=>F) (P89)
 1: 2        X Loc [ time_cycl ]
 2: 4        <
 3: 36       F
 4: 30       Then Do

309:  If (X<=>F) (P89)
 1: 2        X Loc [ time_cycl ]
 2: 3        >=
 3: 35.95    F
 4: 30       Then Do

;de-energize valve6

     310:  Do (P86)
      1: 004      Call Subroutine 4


311:  Z=F x 10^n (P30)
 1: 0        F
 2: 0        n, Exponent of 10
 3: 15       Z Loc [ SDM1P_6   ]



312:  End (P95)
313:  End (P95)

;End Valve 6 operation




;Open valve 7 operation
314:  If (X<=>F) (P89)
 1: 2        X Loc [ time_cycl ]
 2: 3        >=
 3: 36.07    F
 4: 30       Then Do

315:  If (X<=>F) (P89)
 1: 2        X Loc [ time_cycl ]
 2: 4        <
 3: 36.1     F
 4: 30       Then Do

     316:  Do (P86)
      1: 002      Call Subroutine 2


317:  Z=F x 10^n (P30)
 1: 1        F
 2: 0        n, Exponent of 10
 3: 16       Z Loc [ SDM1P_7   ]



318:  End (P95)
319:  End (P95)

320:  If (X<=>F) (P89)
 1: 2        X Loc [ time_cycl ]
 2: 4        <
 3: 36.2     F
 4: 30       Then Do

321:  If (X<=>F) (P89)
 1: 2        X Loc [ time_cycl ]
 2: 3        >=
 3: 36.1     F
 4: 30       Then Do

; de-energize valve7
     322:  Do (P86)
      1: 004      Call Subroutine 4


323:  Z=F x 10^n (P30)
 1: 0        F
 2: 0        n, Exponent of 10
 3: 16       Z Loc [ SDM1P_7   ]



324:  End (P95)
325:  End (P95)

326:  If (X<=>F) (P89)
 1: 2        X Loc [ time_cycl ]
 2: 4        <
 3: 41.9     F
 4: 30       Then Do

327:  If (X<=>F) (P89)
 1: 2        X Loc [ time_cycl ]
 2: 3        >=
 3: 41.95    F
 4: 30       Then Do

;close valve7

     328:  Do (P86)
      1: 003      Call Subroutine 3


329:  Z=F x 10^n (P30)
 1: 1        F
 2: 0        n, Exponent of 10
 3: 16       Z Loc [ SDM1P_7   ]
```

```
330:  End (P95)
331:  End (P95)


332:  If (X<=>F) (P89)
 1: 2        X Loc [ time_cycl ]
 2: 4        <
 3: 42       F
 4: 30       Then Do

333:  If (X<=>F) (P89)
 1: 2        X Loc [ time_cycl ]
 2: 3        >=
 3: 41.95    F
 4: 30       Then Do

;de-energize valve7

     334:  Do (P86)
      1: 004      Call Subroutine 4


335:  Z=F x 10^n (P30)
 1: 0        F
 2: 0        n, Exponent of 10
 3: 16       Z Loc [ SDM1P_7   ]


336:  End (P95)
337:  End (P95)

;End Valve 7 operation




;Open valve 8 operation
338:  If (X<=>F) (P89)
 1: 2        X Loc [ time_cycl ]
 2: 3        >=
 3: 42.07    F
 4: 30       Then Do

339:  If (X<=>F) (P89)
 1: 2        X Loc [ time_cycl ]
 2: 4        <
 3: 42.1     F
 4: 30       Then Do

     340:  Do (P86)
      1: 002      Call Subroutine 2


341:  Z=F x 10^n (P30)
 1: 1        F
 2: 0        n, Exponent of 10
 3: 17       Z Loc [ SDM1P_8   ]


342:  End (P95)
343:  End (P95)

344:  If (X<=>F) (P89)
 1: 2        X Loc [ time_cycl ]
 2: 4        <
 3: 42.2     F
 4: 30       Then Do

345:  If (X<=>F) (P89)
 1: 2        X Loc [ time_cycl ]
 2: 3        >=
 3: 42.1     F
 4: 30       Then Do

; de-energize valve8
     346:  Do (P86)
      1: 004      Call Subroutine 4


347:  Z=F x 10^n (P30)
 1: 0        F
 2: 0        n, Exponent of 10
 3: 17       Z Loc [ SDM1P_8   ]


348:  End (P95)
349:  End (P95)

350:  If (X<=>F) (P89)
 1: 2        X Loc [ time_cycl ]
 2: 4        <
 3: 47.9     F
 4: 30       Then Do

351:  If (X<=>F) (P89)
 1: 2        X Loc [ time_cycl ]
 2: 3        >=
 3: 47.95    F
 4: 30       Then Do

;close valve8

     352:  Do (P86)
```

```
     1: 003      Call Subroutine 3


353:  Z=F x 10^n (P30)
 1: 1        F
 2: 0        n, Exponent of 10
 3: 17       Z Loc [ SDM1P_8   ]



354:  End (P95)
355:  End (P95)


356:  If (X<=>F) (P89)
 1: 2        X Loc [ time_cycl ]
 2: 4        <
 3: 48       F
 4: 30       Then Do

357:  If (X<=>F) (P89)
 1: 2        X Loc [ time_cycl ]
 2: 3        >=
 3: 47.95    F
 4: 30       Then Do

;de-energize valve8

     358:  Do (P86)
      1: 004      Call Subroutine 4


359:  Z=F x 10^n (P30)
 1: 0        F
 2: 0        n, Exponent of 10
 3: 17       Z Loc [ SDM1P_8   ]



360:  End (P95)
361:  End (P95)

;End Valve 8 operation









;Open valve 9 operation
362:  If (X<=>F) (P89)
 1: 2        X Loc [ time_cycl ]
 2: 3        >=
 3: 48.07    F
 4: 30       Then Do
```

```
363:  If (X<=>F) (P89)
 1: 2        X Loc [ time_cycl ]
 2: 4        <
 3: 48.1     F
 4: 30       Then Do

     364:  Do (P86)
      1: 002      Call Subroutine 2


365:  Z=F x 10^n (P30)
 1: 1        F
 2: 0        n, Exponent of 10
 3: 18       Z Loc [ SDM1P_9   ]



366:  End (P95)
367:  End (P95)

368:  If (X<=>F) (P89)
 1: 2        X Loc [ time_cycl ]
 2: 4        <
 3: 48.2     F
 4: 30       Then Do

369:  If (X<=>F) (P89)
 1: 2        X Loc [ time_cycl ]
 2: 3        >=
 3: 48.1     F
 4: 30       Then Do

; de-energize valve9
     370:  Do (P86)
      1: 004      Call Subroutine 4


371:  Z=F x 10^n (P30)
 1: 0        F
 2: 0        n, Exponent of 10
 3: 18       Z Loc [ SDM1P_9   ]



372:  End (P95)
373:  End (P95)

374:  If (X<=>F) (P89)
 1: 2        X Loc [ time_cycl ]
 2: 4        <
 3: 53.9     F
 4: 30       Then Do

375:  If (X<=>F) (P89)
 1: 2        X Loc [ time_cycl ]
 2: 3        >=
 3: 53.95    F
```

```
 4: 30       Then Do

;close valve9

     376:  Do (P86)
      1: 003      Call Subroutine 3


377:  Z=F x 10^n (P30)
 1: 1        F
 2: 0        n, Exponent of 10
 3: 18       Z Loc [ SDM1P_9   ]



378:  End (P95)
379:  End (P95)


380:  If (X<=>F) (P89)
 1: 2        X Loc [ time_cycl ]
 2: 4        <
 3: 54       F
 4: 30       Then Do

381:  If (X<=>F) (P89)
 1: 2        X Loc [ time_cycl ]
 2: 3        >=
 3: 53.95    F
 4: 30       Then Do

;de-energize valve9

     382:  Do (P86)
      1: 004      Call Subroutine 4


383:  Z=F x 10^n (P30)
 1: 0        F
 2: 0        n, Exponent of 10
 3: 18       Z Loc [ SDM1P_9   ]



384:  End (P95)
385:  End (P95)

;End Valve 9 operation




;Open valve 10 operation
386:  If (X<=>F) (P89)
 1: 2        X Loc [ time_cycl ]
 2: 3        >=
 3: 54.07    F
 4: 30       Then Do

387:  If (X<=>F) (P89)
 1: 2        X Loc [ time_cycl ]
 2: 4        <
 3: 54.1     F
 4: 30       Then Do

     388:  Do (P86)
      1: 002      Call Subroutine 2


389:  Z=F x 10^n (P30)
 1: 1        F
 2: 0        n, Exponent of 10
 3: 19       Z Loc [ SDM1P_10  ]



390:  End (P95)
391:  End (P95)

392:  If (X<=>F) (P89)
 1: 2        X Loc [ time_cycl ]
 2: 4        <
 3: 54.2     F
 4: 30       Then Do

393:  If (X<=>F) (P89)
 1: 2        X Loc [ time_cycl ]
 2: 3        >=
 3: 54.1     F
 4: 30       Then Do

; de-energize valve10
     394:  Do (P86)
      1: 004      Call Subroutine 4


395:  Z=F x 10^n (P30)
 1: 0        F
 2: 0        n, Exponent of 10
 3: 19       Z Loc [ SDM1P_10  ]



396:  End (P95)
397:  End (P95)

398:  If (X<=>F) (P89)
 1: 2        X Loc [ time_cycl ]
 2: 4        <
 3: 59.9     F
 4: 30       Then Do
```

```
399:  If (X<=>F) (P89)
 1: 2        X Loc [ time_cycl ]
 2: 3        >=
 3: 59.95    F
 4: 30       Then Do

;close valve10

     400:  Do (P86)
      1: 003      Call Subroutine 3


401:  Z=F x 10^n (P30)
 1: 1        F
 2: 0        n, Exponent of 10
 3: 19       Z Loc [ SDM1P_10  ]



402:  End (P95)
403:  End (P95)


404:  If (X<=>F) (P89)
 1: 2        X Loc [ time_cycl ]
 2: 4        <
 3: 60       F
 4: 30       Then Do

405:  If (X<=>F) (P89)
 1: 2        X Loc [ time_cycl ]
 2: 3        >=
 3: 59.95    F
 4: 30       Then Do

;de-energize valve10

     406:  Do (P86)
      1: 004      Call Subroutine 4


407:  Z=F x 10^n (P30)
 1: 0        F
 2: 0        n, Exponent of 10
 3: 19       Z Loc [ SDM1P_10  ]



408:  End (P95)
409:  End (P95)

;End Valve 10 operation
```

```
;Open valve 11 operation
410:  If (X<=>F) (P89)
 1: 2        X Loc [ time_cycl ]
 2: 3        >=
 3: 60.07    F
 4: 30       Then Do

411:  If (X<=>F) (P89)
 1: 2        X Loc [ time_cycl ]
 2: 4        <
 3: 60.1     F
 4: 30       Then Do

     412:  Do (P86)
      1: 002      Call Subroutine 2


413:  Z=F x 10^n (P30)
 1: 1        F
 2: 0        n, Exponent of 10
 3: 20       Z Loc [ SDM1P_11  ]



414:  End (P95)
415:  End (P95)

416:  If (X<=>F) (P89)
 1: 2        X Loc [ time_cycl ]
 2: 4        <
 3: 60.2     F
 4: 30       Then Do

417:  If (X<=>F) (P89)
 1: 2        X Loc [ time_cycl ]
 2: 3        >=
 3: 60.1     F
 4: 30       Then Do

; de-energize valve11
     418:  Do (P86)
      1: 004      Call Subroutine 4


419:  Z=F x 10^n (P30)
 1: 0        F
 2: 0        n, Exponent of 10
 3: 20       Z Loc [ SDM1P_11  ]



420:  End (P95)
421:  End (P95)

422:  If (X<=>F) (P89)
```

```
 1: 2        X Loc [ time_cycl ]
 2: 4        <
 3: 65.9     F
 4: 30       Then Do

423:  If (X<=>F) (P89)
 1: 2        X Loc [ time_cycl ]
 2: 3        >=
 3: 65.95    F
 4: 30       Then Do

;close valve11

     424:  Do (P86)
      1: 003      Call Subroutine 3


425:  Z=F x 10^n (P30)
 1: 1        F
 2: 0        n, Exponent of 10
 3: 20       Z Loc [ SDM1P_11  ]



426:  End (P95)
427:  End (P95)


428:  If (X<=>F) (P89)
 1: 2        X Loc [ time_cycl ]
 2: 4        <
 3: 66       F
 4: 30       Then Do

429:  If (X<=>F) (P89)
 1: 2        X Loc [ time_cycl ]
 2: 3        >=
 3: 65.95    F
 4: 30       Then Do

;de-energize valve11

     430:  Do (P86)
      1: 004      Call Subroutine 4


431:  Z=F x 10^n (P30)
 1: 0        F
 2: 0        n, Exponent of 10
 3: 20       Z Loc [ SDM1P_11  ]



432:  End (P95)
433:  End (P95)

;End Valve 11 operation
```

```
;Open valve 12 operation
434:  If (X<=>F) (P89)
 1: 2        X Loc [ time_cycl ]
 2: 3        >=
 3: 66.07    F
 4: 30       Then Do

435:  If (X<=>F) (P89)
 1: 2        X Loc [ time_cycl ]
 2: 4        <
 3: 66.1     F
 4: 30       Then Do

     436:  Do (P86)
      1: 002      Call Subroutine 2


437:  Z=F x 10^n (P30)
 1: 1        F
 2: 0        n, Exponent of 10
 3: 21       Z Loc [ SDM1P_12  ]



438:  End (P95)
439:  End (P95)

440:  If (X<=>F) (P89)
 1: 2        X Loc [ time_cycl ]
 2: 4        <
 3: 66.2     F
 4: 30       Then Do

441:  If (X<=>F) (P89)
 1: 2        X Loc [ time_cycl ]
 2: 3        >=
 3: 66.1     F
 4: 30       Then Do

; de-energize valve12
     442:  Do (P86)
      1: 004      Call Subroutine 4


443:  Z=F x 10^n (P30)
 1: 0        F
 2: 0        n, Exponent of 10
 3: 21       Z Loc [ SDM1P_12  ]
```

```
444:  End (P95)
445:  End (P95)

446:  If (X<=>F) (P89)
 1: 2        X Loc [ time_cycl ]
 2: 4        <
 3: 71.9     F
 4: 30       Then Do

447:  If (X<=>F) (P89)
 1: 2        X Loc [ time_cycl ]
 2: 3        >=
 3: 71.95    F
 4: 30       Then Do

;close valve12

     448:  Do (P86)
      1: 003      Call Subroutine 3


449:  Z=F x 10^n (P30)
 1: 1        F
 2: 0        n, Exponent of 10
 3: 21       Z Loc [ SDM1P_12  ]



450:  End (P95)
451:  End (P95)


452:  If (X<=>F) (P89)
 1: 2        X Loc [ time_cycl ]
 2: 4        <
 3: 72       F
 4: 30       Then Do

453:  If (X<=>F) (P89)
 1: 2        X Loc [ time_cycl ]
 2: 3        >=
 3: 71.95    F
 4: 30       Then Do

;de-energize valve12

     454:  Do (P86)
      1: 004      Call Subroutine 4


455:  Z=F x 10^n (P30)
 1: 0        F
 2: 0        n, Exponent of 10
 3: 21       Z Loc [ SDM1P_12  ]
```

```
456:  End (P95)
457:  End (P95)

;End Valve 12 operation




;Open valve 13 operation
458:  If (X<=>F) (P89)
 1: 2        X Loc [ time_cycl ]
 2: 3        >=
 3: 72.07    F
 4: 30       Then Do

459:  If (X<=>F) (P89)
 1: 2        X Loc [ time_cycl ]
 2: 4        <
 3: 72.1     F
 4: 30       Then Do

    460:  Do (P86)
     1: 002      Call Subroutine 2


461:  Z=F x 10^n (P30)
 1: 1        F
 2: 0        n, Exponent of 10
 3: 22       Z Loc [ SDM1P_13  ]



462:  End (P95)
463:  End (P95)

464:  If (X<=>F) (P89)
 1: 2        X Loc [ time_cycl ]
 2: 4        <
 3: 72.2     F
 4: 30       Then Do

465:  If (X<=>F) (P89)
 1: 2        X Loc [ time_cycl ]
 2: 3        >=
 3: 72.1     F
 4: 30       Then Do

; de-energize valve13
     466:  Do (P86)
      1: 004      Call Subroutine 4


467:  Z=F x 10^n (P30)
```

```
 1: 0        F
 2: 0        n, Exponent of 10
 3: 22       Z Loc [ SDM1P_13  ]
```

```
468:  End (P95)
469:  End (P95)
```

```
470:  If (X<=>F) (P89)
 1: 2        X Loc [ time_cycl ]
 2: 4        <
 3: 77.9     F
 4: 30       Then Do
```

```
471:  If (X<=>F) (P89)
 1: 2        X Loc [ time_cycl ]
 2: 3        >=
 3: 77.95    F
 4: 30       Then Do
```

```
;close valve13
```

```
     472:  Do (P86)
      1: 003      Call Subroutine 3
```

```
473:  Z=F x 10^n (P30)
 1: 1        F
 2: 0        n, Exponent of 10
 3: 22       Z Loc [ SDM1P_13  ]
```

```
474:  End (P95)
475:  End (P95)
```

```
476:  If (X<=>F) (P89)
 1: 2        X Loc [ time_cycl ]
 2: 4        <
 3: 78       F
 4: 30       Then Do
```

```
477:  If (X<=>F) (P89)
 1: 2        X Loc [ time_cycl ]
 2: 3        >=
 3: 77.95    F
 4: 30       Then Do
```

```
;de-energize valve13
```

```
     478:  Do (P86)
      1: 004      Call Subroutine 4
```

```
479:  Z=F x 10^n (P30)
 1: 0        F
 2: 0        n, Exponent of 10
 3: 22       Z Loc [ SDM1P_13  ]
```

```
480:  End (P95)
481:  End (P95)
```

```
;End Valve 13 operation
```

```
;Open valve 14 operation
482:  If (X<=>F) (P89)
 1: 2        X Loc [ time_cycl ]
 2: 3        >=
 3: 78.07    F
 4: 30       Then Do
```

```
483:  If (X<=>F) (P89)
 1: 2        X Loc [ time_cycl ]
 2: 4        <
 3: 78.1     F
 4: 30       Then Do
```

```
     484:  Do (P86)
      1: 002      Call Subroutine 2
```

```
485:  Z=F x 10^n (P30)
 1: 1        F
 2: 0        n, Exponent of 10
 3: 23       Z Loc [ SDM1P_14  ]
```

```
486:  End (P95)
487:  End (P95)
```

```
488:  If (X<=>F) (P89)
 1: 2        X Loc [ time_cycl ]
 2: 4        <
 3: 78.2     F
 4: 30       Then Do
```

```
489:  If (X<=>F) (P89)
 1: 2        X Loc [ time_cycl ]
 2: 3        >=
 3: 78.1     F
```

```
 4: 30       Then Do

; de-energize valve14
     490:  Do (P86)
      1: 004      Call Subroutine 4


491:  Z=F x 10^n (P30)
 1: 0        F
 2: 0        n, Exponent of 10
 3: 23       Z Loc [ SDM1P_14  ]



492:  End (P95)
493:  End (P95)

494:  If (X<=>F) (P89)
 1: 2        X Loc [ time_cycl ]
 2: 4        <
 3: 83.9     F
 4: 30       Then Do

495:  If (X<=>F) (P89)
 1: 2        X Loc [ time_cycl ]
 2: 3        >=
 3: 83.95    F
 4: 30       Then Do

;close valve14

     496:  Do (P86)
      1: 003      Call Subroutine 3


497:  Z=F x 10^n (P30)
 1: 1        F
 2: 0        n, Exponent of 10
 3: 23       Z Loc [ SDM1P_14  ]



498:  End (P95)
499:  End (P95)


500:  If (X<=>F) (P89)
 1: 2        X Loc [ time_cycl ]
 2: 4        <
 3: 84       F
 4: 30       Then Do

501:  If (X<=>F) (P89)
 1: 2        X Loc [ time_cycl ]
 2: 3        >=
 3: 83.95    F
 4: 30       Then Do
```

```
;de-energize valve14

     502:  Do (P86)
      1: 004      Call Subroutine 4


503:  Z=F x 10^n (P30)
 1: 0        F
 2: 0        n, Exponent of 10
 3: 23       Z Loc [ SDM1P_14  ]



504:  End (P95)
505:  End (P95)

;End Valve 14 operation



;Open valve 15 operation
506:  If (X<=>F) (P89)
 1: 2        X Loc [ time_cycl ]
 2: 3        >=
 3: 84.07    F
 4: 30       Then Do

507:  If (X<=>F) (P89)
 1: 2        X Loc [ time_cycl ]
 2: 4        <
 3: 84.1     F
 4: 30       Then Do

     508:  Do (P86)
      1: 002      Call Subroutine 2


509:  Z=F x 10^n (P30)
 1: 1        F
 2: 0        n, Exponent of 10
 3: 24       Z Loc [ SDM1P_15  ]



510:  End (P95)
511:  End (P95)

512:  If (X<=>F) (P89)
 1: 2        X Loc [ time_cycl ]
 2: 4        <
 3: 84.2     F
 4: 30       Then Do

513:  If (X<=>F) (P89)
 1: 2        X Loc [ time_cycl ]
 2: 3        >=
```

```
 3: 84.1     F
 4: 30       Then Do

; de-energize valve15
     514:  Do (P86)
      1: 004      Call Subroutine 4


515:  Z=F x 10^n (P30)
 1: 0        F
 2: 0        n, Exponent of 10
 3: 24       Z Loc [ SDM1P_15  ]



516:  End (P95)
517:  End (P95)

518:  If (X<=>F) (P89)
 1: 2        X Loc [ time_cycl ]
 2: 4        <
 3: 89.9     F
 4: 30       Then Do

519:  If (X<=>F) (P89)
 1: 2        X Loc [ time_cycl ]
 2: 3        >=
 3: 89.95    F
 4: 30       Then Do

;close valve15

     520:  Do (P86)
      1: 003      Call Subroutine 3


521:  Z=F x 10^n (P30)
 1: 1        F
 2: 0        n, Exponent of 10
 3: 24       Z Loc [ SDM1P_15  ]



522:  End (P95)
523:  End (P95)


524:  If (X<=>F) (P89)
 1: 2        X Loc [ time_cycl ]
 2: 4        <
 3: 90       F
 4: 30       Then Do

525:  If (X<=>F) (P89)
 1: 2        X Loc [ time_cycl ]
 2: 3        >=
 3: 89.95    F
 4: 30       Then Do

;de-energize valve15

     526:  Do (P86)
      1: 004      Call Subroutine 4


527:  Z=F x 10^n (P30)
 1: 0        F
 2: 0        n, Exponent of 10
 3: 24       Z Loc [ SDM1P_15  ]



528:  End (P95)
529:  End (P95)

;End Valve 15 operation




;Open valve 16 operation
530:  If (X<=>F) (P89)
 1: 2        X Loc [ time_cycl ]
 2: 3        >=
 3: 90.07    F
 4: 30       Then Do

531:  If (X<=>F) (P89)
 1: 2        X Loc [ time_cycl ]
 2: 4        <
 3: 90.1     F
 4: 30       Then Do

     532:  Do (P86)
      1: 002      Call Subroutine 2


533:  Z=F x 10^n (P30)
 1: 1        F
 2: 0        n, Exponent of 10
 3: 25       Z Loc [ SDM1P_16  ]



534:  End (P95)
535:  End (P95)

536:  If (X<=>F) (P89)
 1: 2        X Loc [ time_cycl ]
 2: 4        <
```

```
 3: 90.2     F
 4: 30       Then Do

537:  If (X<=>F) (P89)
 1: 2        X Loc [ time_cycl ]
 2: 3        >=
 3: 90.1     F
 4: 30       Then Do

; de-energize valve16
     538:  Do (P86)
      1: 004      Call Subroutine 4


539:  Z=F x 10^n (P30)
 1: 0        F
 2: 0        n, Exponent of 10
 3: 25       Z Loc [ SDM1P_16  ]



540:  End (P95)
541:  End (P95)

542:  If (X<=>F) (P89)
 1: 2        X Loc [ time_cycl ]
 2: 4        <
 3: 95.9     F
 4: 30       Then Do

543:  If (X<=>F) (P89)
 1: 2        X Loc [ time_cycl ]
 2: 3        >=
 3: 95.95    F
 4: 30       Then Do

;close valve16

     544:  Do (P86)
      1: 003      Call Subroutine 3


545:  Z=F x 10^n (P30)
 1: 1        F
 2: 0        n, Exponent of 10
 3: 25       Z Loc [ SDM1P_16  ]



546:  End (P95)
547:  End (P95)


548:  If (X<=>F) (P89)
 1: 2        X Loc [ time_cycl ]
 2: 4        <
 3: 96       F
 4: 30       Then Do

549:  If (X<=>F) (P89)
 1: 2        X Loc [ time_cycl ]
 2: 3        >=
 3: 95.95    F
 4: 30       Then Do

;de-energize valve16

     550:  Do (P86)
      1: 004      Call Subroutine 4


551:  Z=F x 10^n (P30)
 1: 0        F
 2: 0        n, Exponent of 10
 3: 25       Z Loc [ SDM1P_16  ]



552:  End (P95)
553:  End (P95)

;End Valve 16 operation

;Open valve 17 operation
554:  If (X<=>F) (P89)
 1: 2        X Loc [ time_cycl ]
 2: 3        >=
 3: 96.07    F
 4: 30       Then Do

555:  If (X<=>F) (P89)
 1: 2        X Loc [ time_cycl ]
 2: 4        <
 3: 96.1     F
 4: 30       Then Do

     556:  Do (P86)
      1: 002      Call Subroutine 2


557:  Z=F x 10^n (P30)
 1: 1        F
 2: 0        n, Exponent of 10
 3: 26       Z Loc [ SDM2P_1   ]
```

```
558:  End (P95)
559:  End (P95)

560:  If (X<=>F) (P89)
 1: 2        X Loc [ time_cycl ]
 2: 4        <
 3: 96.2     F
 4: 30       Then Do

561:  If (X<=>F) (P89)
 1: 2        X Loc [ time_cycl ]
 2: 3        >=
 3: 96.1     F
 4: 30       Then Do

; de-energize valve17
     562:  Do (P86)
      1: 004      Call Subroutine 4


563:  Z=F x 10^n (P30)
 1: 0        F
 2: 0        n, Exponent of 10
 3: 26       Z Loc [ SDM2P_1   ]



564:  End (P95)
565:  End (P95)

566:  If (X<=>F) (P89)
 1: 2        X Loc [ time_cycl ]
 2: 4        <
 3: 101.9    F
 4: 30       Then Do

567:  If (X<=>F) (P89)
 1: 2        X Loc [ time_cycl ]
 2: 3        >=
 3: 101.95   F
 4: 30       Then Do

;close valve17

     568:  Do (P86)
      1: 003      Call Subroutine 3


569:  Z=F x 10^n (P30)
 1: 1        F
 2: 0        n, Exponent of 10
 3: 26       Z Loc [ SDM2P_1   ]
```

```
570:  End (P95)
571:  End (P95)


572:  If (X<=>F) (P89)
 1: 2        X Loc [ time_cycl ]
 2: 4        <
 3: 102      F
 4: 30       Then Do

573:  If (X<=>F) (P89)
 1: 2        X Loc [ time_cycl ]
 2: 3        >=
 3: 101.95   F
 4: 30       Then Do

;de-energize valve17

     574:  Do (P86)
      1: 004      Call Subroutine 4


575:  Z=F x 10^n (P30)
 1: 0        F
 2: 0        n, Exponent of 10
 3: 26       Z Loc [ SDM2P_1   ]



576:  End (P95)
577:  End (P95)

;End Valve 17 operation




;Open valve 18 operation
578:  If (X<=>F) (P89)
 1: 2        X Loc [ time_cycl ]
 2: 3        >=
 3: 102.07   F
 4: 30       Then Do

579:  If (X<=>F) (P89)
 1: 2        X Loc [ time_cycl ]
 2: 4        <
 3: 102.1    F
 4: 30       Then Do

     580:  Do (P86)
      1: 002      Call Subroutine 2
```

```
581:  Z=F x 10^n (P30)
 1: 1        F
 2: 0        n, Exponent of 10
 3: 27       Z Loc [ SDM2P_2   ]


582:  End (P95)
583:  End (P95)

584:  If (X<=>F) (P89)
 1: 2        X Loc [ time_cycl ]
 2: 4        <
 3: 102.2    F
 4: 30       Then Do

585:  If (X<=>F) (P89)
 1: 2        X Loc [ time_cycl ]
 2: 3        >=
 3: 102.1    F
 4: 30       Then Do

; de-energize valve18
     586:  Do (P86)
      1: 004      Call Subroutine 4


587:  Z=F x 10^n (P30)
 1: 0        F
 2: 0        n, Exponent of 10
 3: 27       Z Loc [ SDM2P_2   ]


588:  End (P95)
589:  End (P95)

590:  If (X<=>F) (P89)
 1: 2        X Loc [ time_cycl ]
 2: 4        <
 3: 107.9    F
 4: 30       Then Do

591:  If (X<=>F) (P89)
 1: 2        X Loc [ time_cycl ]
 2: 3        >=
 3: 107.95   F
 4: 30       Then Do

;close valve18

     592:  Do (P86)
      1: 003      Call Subroutine 3


593:  Z=F x 10^n (P30)
 1: 1        F
 2: 0        n, Exponent of 10
 3: 27       Z Loc [ SDM2P_2   ]


594:  End (P95)
595:  End (P95)

596:  If (X<=>F) (P89)
 1: 2        X Loc [ time_cycl ]
 2: 4        <
 3: 108      F
 4: 30       Then Do

597:  If (X<=>F) (P89)
 1: 2        X Loc [ time_cycl ]
 2: 3        >=
 3: 107.95   F
 4: 30       Then Do

;de-energize valve18

     598:  Do (P86)
      1: 004      Call Subroutine 4


599:  Z=F x 10^n (P30)
 1: 0        F
 2: 0        n, Exponent of 10
 3: 27       Z Loc [ SDM2P_2   ]


600:  End (P95)
601:  End (P95)

;End Valve 18 operation


;Open valve 19 operation
602:  If (X<=>F) (P89)
 1: 2        X Loc [ time_cycl ]
 2: 3        >=
 3: 108.07   F
 4: 30       Then Do

603:  If (X<=>F) (P89)
 1: 2        X Loc [ time_cycl ]
 2: 4        <
```

```
 3: 108.1    F
 4: 30       Then Do

     604:  Do (P86)
      1: 002      Call Subroutine 2


605:  Z=F x 10^n (P30)
 1: 1        F
 2: 0        n, Exponent of 10
 3: 28       Z Loc [ SDM2P_3   ]



606:  End (P95)
607:  End (P95)

608:  If (X<=>F) (P89)
 1: 2        X Loc [ time_cycl ]
 2: 4        <
 3: 108.2    F
 4: 30       Then Do

609:  If (X<=>F) (P89)
 1: 2        X Loc [ time_cycl ]
 2: 3        >=
 3: 108.1    F
 4: 30       Then Do

; de-energize valve19
     610:  Do (P86)
      1: 004      Call Subroutine 4


611:  Z=F x 10^n (P30)
 1: 0        F
 2: 0        n, Exponent of 10
 3: 28       Z Loc [ SDM2P_3   ]



612:  End (P95)
613:  End (P95)

614:  If (X<=>F) (P89)
 1: 2        X Loc [ time_cycl ]
 2: 4        <
 3: 113.9    F
 4: 30       Then Do

615:  If (X<=>F) (P89)
 1: 2        X Loc [ time_cycl ]
 2: 3        >=
 3: 113.95   F
 4: 30       Then Do

;close valve19
```

```
     616:  Do (P86)
      1: 003      Call Subroutine 3


617:  Z=F x 10^n (P30)
 1: 1        F
 2: 0        n, Exponent of 10
 3: 28       Z Loc [ SDM2P_3   ]



618:  End (P95)
619:  End (P95)


620:  If (X<=>F) (P89)
 1: 2        X Loc [ time_cycl ]
 2: 4        <
 3: 114      F
 4: 30       Then Do

621:  If (X<=>F) (P89)
 1: 2        X Loc [ time_cycl ]
 2: 3        >=
 3: 113.95   F
 4: 30       Then Do

;de-energize valve19

     622:  Do (P86)
      1: 004      Call Subroutine 4


623:  Z=F x 10^n (P30)
 1: 0        F
 2: 0        n, Exponent of 10
 3: 28       Z Loc [ SDM2P_3   ]



624:  End (P95)
625:  End (P95)

;End Valve 19 operation
```

```
;Open valve 20 operation
626:  If (X<=>F) (P89)
 1: 2        X Loc [ time_cycl ]
 2: 3        >=
 3: 114.07   F
 4: 30       Then Do

627:  If (X<=>F) (P89)
 1: 2        X Loc [ time_cycl ]
 2: 4        <
 3: 114.1    F
 4: 30       Then Do

     628:  Do (P86)
      1: 002      Call Subroutine 2


629:  Z=F x 10^n (P30)
 1: 1        F
 2: 0        n, Exponent of 10
 3: 29       Z Loc [ SDM2P_4   ]



630:  End (P95)
631:  End (P95)

632:  If (X<=>F) (P89)
 1: 2        X Loc [ time_cycl ]
 2: 4        <
 3: 114.2    F
 4: 30       Then Do

633:  If (X<=>F) (P89)
 1: 2        X Loc [ time_cycl ]
 2: 3        >=
 3: 114.1    F
 4: 30       Then Do

; de-energize valve20
     634:  Do (P86)
      1: 004      Call Subroutine 4


635:  Z=F x 10^n (P30)
 1: 0        F
 2: 0        n, Exponent of 10
 3: 29       Z Loc [ SDM2P_4   ]



636:  End (P95)
637:  End (P95)

638:  If (X<=>F) (P89)
 1: 2        X Loc [ time_cycl ]
 2: 4        <
 3: 119.9    F
 4: 30       Then Do

639:  If (X<=>F) (P89)
 1: 2        X Loc [ time_cycl ]
 2: 3        >=
 3: 119.95   F
 4: 30       Then Do

;close valve20

     640:  Do (P86)
      1: 003      Call Subroutine 3


641:  Z=F x 10^n (P30)
 1: 1        F
 2: 0        n, Exponent of 10
 3: 29       Z Loc [ SDM2P_4   ]



642:  End (P95)
643:  End (P95)


644:  If (X<=>F) (P89)
 1: 2        X Loc [ time_cycl ]
 2: 4        <
 3: 120      F
 4: 30       Then Do

645:  If (X<=>F) (P89)
 1: 2        X Loc [ time_cycl ]
 2: 3        >=
 3: 119.95   F
 4: 30       Then Do

;de-energize valve20

     646:  Do (P86)
      1: 004      Call Subroutine 4


647:  Z=F x 10^n (P30)
 1: 0        F
 2: 0        n, Exponent of 10
 3: 29       Z Loc [ SDM2P_4   ]



648:  End (P95)
649:  End (P95)

;End Valve 20 operation
```

```
;Open valve 21 operation
650:  If (X<=>F) (P89)
 1: 2        X Loc [ time_cycl ]
 2: 3        >=
 3: 120.07   F
 4: 30       Then Do

651:  If (X<=>F) (P89)
 1: 2        X Loc [ time_cycl ]
 2: 4        <
 3: 120.1    F
 4: 30       Then Do

     652:  Do (P86)
      1: 002      Call Subroutine 2


653:  Z=F x 10^n (P30)
 1: 1        F
 2: 0        n, Exponent of 10
 3: 30       Z Loc [ SDM2P_5   ]



654:  End (P95)
655:  End (P95)

656:  If (X<=>F) (P89)
 1: 2        X Loc [ time_cycl ]
 2: 4        <
 3: 120.2    F
 4: 30       Then Do

657:  If (X<=>F) (P89)
 1: 2        X Loc [ time_cycl ]
 2: 3        >=
 3: 120.1    F
 4: 30       Then Do

; de-energize valve21
     658:  Do (P86)
      1: 004      Call Subroutine 4


659:  Z=F x 10^n (P30)
 1: 0        F
 2: 0        n, Exponent of 10
 3: 30       Z Loc [ SDM2P_5   ]



660:  End (P95)
661:  End (P95)

662:  If (X<=>F) (P89)
 1: 2        X Loc [ time_cycl ]
 2: 4        <
 3: 125.9    F
 4: 30       Then Do

663:  If (X<=>F) (P89)
 1: 2        X Loc [ time_cycl ]
 2: 3        >=
 3: 125.95   F
 4: 30       Then Do

;close valve21

     664:  Do (P86)
      1: 003      Call Subroutine 3


665:  Z=F x 10^n (P30)
 1: 1        F
 2: 0        n, Exponent of 10
 3: 30       Z Loc [ SDM2P_5   ]



666:  End (P95)
667:  End (P95)


668:  If (X<=>F) (P89)
 1: 2        X Loc [ time_cycl ]
 2: 4        <
 3: 126      F
 4: 30       Then Do

669:  If (X<=>F) (P89)
 1: 2        X Loc [ time_cycl ]
 2: 3        >=
 3: 125.95   F
 4: 30       Then Do

;de-energize valve21

     670:  Do (P86)
      1: 004      Call Subroutine 4


671:  Z=F x 10^n (P30)
 1: 0        F
 2: 0        n, Exponent of 10
```

```
 3: 30       Z Loc [ SDM2P_5   ]


672:  End (P95)
673:  End (P95)

;End Valve 21 operation




;Open valve 22 operation
674:  If (X<=>F) (P89)
 1: 2        X Loc [ time_cycl ]
 2: 3        >=
 3: 126.07   F
 4: 30       Then Do

675:  If (X<=>F) (P89)
 1: 2        X Loc [ time_cycl ]
 2: 4        <
 3: 126.1    F
 4: 30       Then Do

     676:  Do (P86)
      1: 002      Call Subroutine 2


677:  Z=F x 10^n (P30)
 1: 1        F
 2: 0        n, Exponent of 10
 3: 31       Z Loc [ SDM2P_6   ]



678:  End (P95)
679:  End (P95)

680:  If (X<=>F) (P89)
 1: 2        X Loc [ time_cycl ]
 2: 4        <
 3: 126.2    F
 4: 30       Then Do

681:  If (X<=>F) (P89)
 1: 2        X Loc [ time_cycl ]
 2: 3        >=
 3: 126.1    F
 4: 30       Then Do

; de-energize valve22
     682:  Do (P86)
      1: 004      Call Subroutine 4


683:  Z=F x 10^n (P30)
 1: 0        F
 2: 0        n, Exponent of 10
 3: 31       Z Loc [ SDM2P_6   ]



684:  End (P95)
685:  End (P95)

686:  If (X<=>F) (P89)
 1: 2        X Loc [ time_cycl ]
 2: 4        <
 3: 131.9    F
 4: 30       Then Do

687:  If (X<=>F) (P89)
 1: 2        X Loc [ time_cycl ]
 2: 3        >=
 3: 131.95   F
 4: 30       Then Do

;close valve22

     688:  Do (P86)
      1: 003      Call Subroutine 3


689:  Z=F x 10^n (P30)
 1: 1        F
 2: 0        n, Exponent of 10
 3: 31       Z Loc [ SDM2P_6   ]



690:  End (P95)
691:  End (P95)

692:  If (X<=>F) (P89)
 1: 2        X Loc [ time_cycl ]
 2: 4        <
 3: 132      F
 4: 30       Then Do

693:  If (X<=>F) (P89)
 1: 2        X Loc [ time_cycl ]
 2: 3        >=
 3: 131.95   F
 4: 30       Then Do

;de-energize valve22

     694:  Do (P86)
```

```
     1: 004      Call Subroutine 4


695:  Z=F x 10^n (P30)
 1: 0        F
 2: 0        n, Exponent of 10
 3: 31       Z Loc [ SDM2P_6   ]



696:  End (P95)
697:  End (P95)

;End Valve 22 operation









;Open valve 23 operation
698:  If (X<=>F) (P89)
 1: 2        X Loc [ time_cycl ]
 2: 3        >=
 3: 132.07   F
 4: 30       Then Do

699:  If (X<=>F) (P89)
 1: 2        X Loc [ time_cycl ]
 2: 4        <
 3: 132.1    F
 4: 30       Then Do

    700:  Do (P86)
     1: 002      Call Subroutine 2


701:  Z=F x 10^n (P30)
 1: 1        F
 2: 0        n, Exponent of 10
 3: 32       Z Loc [ SDM2P_7   ]



702:  End (P95)
703:  End (P95)

704:  If (X<=>F) (P89)
 1: 2        X Loc [ time_cycl ]
 2: 4        <
 3: 132.2    F
 4: 30       Then Do

705:  If (X<=>F) (P89)
 1: 2        X Loc [ time_cycl ]
 2: 3        >=
 3: 132.1    F
 4: 30       Then Do

; de-energize valve23
    706:  Do (P86)
     1: 004      Call Subroutine 4


707:  Z=F x 10^n (P30)
 1: 0        F
 2: 0        n, Exponent of 10
 3: 32       Z Loc [ SDM2P_7   ]



708:  End (P95)
709:  End (P95)

710:  If (X<=>F) (P89)
 1: 2        X Loc [ time_cycl ]
 2: 4        <
 3: 137.9    F
 4: 30       Then Do

711:  If (X<=>F) (P89)
 1: 2        X Loc [ time_cycl ]
 2: 3        >=
 3: 137.95   F
 4: 30       Then Do

;close valve23

    712:  Do (P86)
     1: 003      Call Subroutine 3


713:  Z=F x 10^n (P30)
 1: 1        F
 2: 0        n, Exponent of 10
 3: 32       Z Loc [ SDM2P_7   ]



714:  End (P95)
715:  End (P95)


716:  If (X<=>F) (P89)
 1: 2        X Loc [ time_cycl ]
 2: 4        <
 3: 138      F
 4: 30       Then Do

717:  If (X<=>F) (P89)
 1: 2        X Loc [ time_cycl ]
```

```
 2: 3        >=
 3: 137.95   F
 4: 30       Then Do

;de-energize valve23

     718:  Do (P86)
      1: 004      Call Subroutine 4


719:  Z=F x 10^n (P30)
 1: 0        F
 2: 0        n, Exponent of 10
 3: 32       Z Loc [ SDM2P_7   ]



720:  End (P95)
721:  End (P95)

;End Valve 23 operation




;Open valve 24 operation
722:  If (X<=>F) (P89)
 1: 2        X Loc [ time_cycl ]
 2: 3        >=
 3: 138.07   F
 4: 30       Then Do

723:  If (X<=>F) (P89)
 1: 2        X Loc [ time_cycl ]
 2: 4        <
 3: 138.1    F
 4: 30       Then Do

     724:  Do (P86)
      1: 002      Call Subroutine 2


725:  Z=F x 10^n (P30)
 1: 1        F
 2: 0        n, Exponent of 10
 3: 33       Z Loc [ SDM2P_8   ]



726:  End (P95)
727:  End (P95)

728:  If (X<=>F) (P89)
 1: 2        X Loc [ time_cycl ]
 2: 4        <
 3: 138.2    F
 4: 30       Then Do

729:  If (X<=>F) (P89)
 1: 2        X Loc [ time_cycl ]
 2: 3        >=
 3: 138.1    F
 4: 30       Then Do

; de-energize valve24
     730:  Do (P86)
      1: 004      Call Subroutine 4


731:  Z=F x 10^n (P30)
 1: 0        F
 2: 0        n, Exponent of 10
 3: 33       Z Loc [ SDM2P_8   ]



732:  End (P95)
733:  End (P95)

734:  If (X<=>F) (P89)
 1: 2        X Loc [ time_cycl ]
 2: 4        <
 3: 143.9    F
 4: 30       Then Do

735:  If (X<=>F) (P89)
 1: 2        X Loc [ time_cycl ]
 2: 3        >=
 3: 143.95   F
 4: 30       Then Do

;close valve24

     736:  Do (P86)
      1: 003      Call Subroutine 3


737:  Z=F x 10^n (P30)
 1: 1        F
 2: 0        n, Exponent of 10
 3: 33       Z Loc [ SDM2P_8   ]



738:  End (P95)
739:  End (P95)


740:  If (X<=>F) (P89)
 1: 2        X Loc [ time_cycl ]
 2: 4        <
 3: 144      F
 4: 30       Then Do
```

```
741:  If (X<=>F) (P89)
 1: 2        X Loc [ time_cycl ]
 2: 3        >=
 3: 143.95   F
 4: 30       Then Do

;de-energize valve24

     742:  Do (P86)
      1: 004      Call Subroutine 4


743:  Z=F x 10^n (P30)
 1: 0        F
 2: 0        n, Exponent of 10
 3: 33       Z Loc [ SDM2P_8   ]



744:  End (P95)
745:  End (P95)

;End Valve 24 operation




;Open valve 25 operation
746:  If (X<=>F) (P89)
 1: 2        X Loc [ time_cycl ]
 2: 3        >=
 3: 144.07   F
 4: 30       Then Do

747:  If (X<=>F) (P89)
 1: 2        X Loc [ time_cycl ]
 2: 4        <
 3: 144.1    F
 4: 30       Then Do

     748:  Do (P86)
      1: 002      Call Subroutine 2


749:  Z=F x 10^n (P30)
 1: 1        F
 2: 0        n, Exponent of 10
 3: 34       Z Loc [ SDM2P_9   ]


750:  End (P95)
751:  End (P95)

752:  If (X<=>F) (P89)
 1: 2        X Loc [ time_cycl ]
 2: 4        <
 3: 144.2    F
 4: 30       Then Do

753:  If (X<=>F) (P89)
 1: 2        X Loc [ time_cycl ]
 2: 3        >=
 3: 144.1    F
 4: 30       Then Do

; de-energize valve25
     754:  Do (P86)
      1: 004      Call Subroutine 4


755:  Z=F x 10^n (P30)
 1: 0        F
 2: 0        n, Exponent of 10
 3: 34       Z Loc [ SDM2P_9   ]



756:  End (P95)
757:  End (P95)

758:  If (X<=>F) (P89)
 1: 2        X Loc [ time_cycl ]
 2: 4        <
 3: 149.9    F
 4: 30       Then Do

759:  If (X<=>F) (P89)
 1: 2        X Loc [ time_cycl ]
 2: 3        >=
 3: 149.95   F
 4: 30       Then Do

;close valve25

     760:  Do (P86)
      1: 003      Call Subroutine 3


761:  Z=F x 10^n (P30)
 1: 1        F
 2: 0        n, Exponent of 10
 3: 34       Z Loc [ SDM2P_9   ]



762:  End (P95)
```

```
763:  End (P95)


764:  If (X<=>F) (P89)
 1: 2        X Loc [ time_cycl ]
 2: 4        <
 3: 150      F
 4: 30       Then Do

765:  If (X<=>F) (P89)
 1: 2        X Loc [ time_cycl ]
 2: 3        >=
 3: 149.95   F
 4: 30       Then Do

;de-energize valve25

     766:  Do (P86)
      1: 004      Call Subroutine 4


767:  Z=F x 10^n (P30)
 1: 0        F
 2: 0        n, Exponent of 10
 3: 34       Z Loc [ SDM2P_9   ]


768:  End (P95)
769:  End (P95)

;End Valve 25 operation




;Open valve 26 operation
770:  If (X<=>F) (P89)
 1: 2        X Loc [ time_cycl ]
 2: 3        >=
 3: 150.07   F
 4: 30       Then Do

771:  If (X<=>F) (P89)
 1: 2        X Loc [ time_cycl ]
 2: 4        <
 3: 150.1    F
 4: 30       Then Do

     772:  Do (P86)
      1: 002      Call Subroutine 2


773:  Z=F x 10^n (P30)
 1: 1        F
 2: 0        n, Exponent of 10
 3: 35       Z Loc [ SDM2P_10  ]


774:  End (P95)
775:  End (P95)

776:  If (X<=>F) (P89)
 1: 2        X Loc [ time_cycl ]
 2: 4        <
 3: 150.2    F
 4: 30       Then Do

777:  If (X<=>F) (P89)
 1: 2        X Loc [ time_cycl ]
 2: 3        >=
 3: 150.1    F
 4: 30       Then Do

; de-energize valve26
     778:  Do (P86)
      1: 004      Call Subroutine 4


779:  Z=F x 10^n (P30)
 1: 0        F
 2: 0        n, Exponent of 10
 3: 35       Z Loc [ SDM2P_10  ]


780:  End (P95)
781:  End (P95)

782:  If (X<=>F) (P89)
 1: 2        X Loc [ time_cycl ]
 2: 4        <
 3: 155.9    F
 4: 30       Then Do

783:  If (X<=>F) (P89)
 1: 2        X Loc [ time_cycl ]
 2: 3        >=
 3: 155.95   F
 4: 30       Then Do

;close valve26

     784:  Do (P86)
      1: 003      Call Subroutine 3


785:  Z=F x 10^n (P30)
```

```
 1: 1        F
 2: 0        n, Exponent of 10
 3: 35       Z Loc [ SDM2P_10  ]



786:  End (P95)
787:  End (P95)


788:  If (X<=>F) (P89)
 1: 2        X Loc [ time_cycl ]
 2: 4        <
 3: 156      F
 4: 30       Then Do

789:  If (X<=>F) (P89)
 1: 2        X Loc [ time_cycl ]
 2: 3        >=
 3: 155.95   F
 4: 30       Then Do

;de-energize valve26

     790:  Do (P86)
      1: 004      Call Subroutine 4


791:  Z=F x 10^n (P30)
 1: 0        F
 2: 0        n, Exponent of 10
 3: 35       Z Loc [ SDM2P_10  ]



792:  End (P95)
793:  End (P95)

;End Valve 26 operation



;Open valve 27 operation
794:  If (X<=>F) (P89)
 1: 2        X Loc [ time_cycl ]
 2: 3        >=
 3: 156.07   F
 4: 30       Then Do

795:  If (X<=>F) (P89)
 1: 2        X Loc [ time_cycl ]
 2: 4        <
 3: 156.1    F
 4: 30       Then Do

     796:  Do (P86)
      1: 002      Call Subroutine 2


797:  Z=F x 10^n (P30)
 1: 1        F
 2: 0        n, Exponent of 10
 3: 36       Z Loc [ SDM2P_11  ]



798:  End (P95)
799:  End (P95)

800:  If (X<=>F) (P89)
 1: 2        X Loc [ time_cycl ]
 2: 4        <
 3: 156.2    F
 4: 30       Then Do

801:  If (X<=>F) (P89)
 1: 2        X Loc [ time_cycl ]
 2: 3        >=
 3: 156.1    F
 4: 30       Then Do

; de-energize valve27
     802:  Do (P86)
      1: 004      Call Subroutine 4


803:  Z=F x 10^n (P30)
 1: 0        F
 2: 0        n, Exponent of 10
 3: 36       Z Loc [ SDM2P_11  ]



804:  End (P95)
805:  End (P95)

806:  If (X<=>F) (P89)
 1: 2        X Loc [ time_cycl ]
 2: 4        <
 3: 161.9    F
 4: 30       Then Do

807:  If (X<=>F) (P89)
 1: 2        X Loc [ time_cycl ]
 2: 3        >=
 3: 161.95   F
 4: 30       Then Do

;close valve27

     808:  Do (P86)
      1: 003      Call Subroutine 3
```

```
809:  Z=F x 10^n (P30)
 1: 1        F
 2: 0        n, Exponent of 10
 3: 36       Z Loc [ SDM2P_11  ]

810:  End (P95)
811:  End (P95)

812:  If (X<=>F) (P89)
 1: 2        X Loc [ time_cycl ]
 2: 4        <
 3: 162      F
 4: 30       Then Do

813:  If (X<=>F) (P89)
 1: 2        X Loc [ time_cycl ]
 2: 3        >=
 3: 161.95   F
 4: 30       Then Do

;de-energize valve27

     814:  Do (P86)
      1: 004      Call Subroutine 4

815:  Z=F x 10^n (P30)
 1: 0        F
 2: 0        n, Exponent of 10
 3: 36       Z Loc [ SDM2P_11  ]

816:  End (P95)
817:  End (P95)

;End Valve 27 operation

;purge sample flow controller-
taken out until
;wired into SDM as aopposed to
direct connect to V_hi
;689:  Do (P86)
; 1: 45       Set Port 5 High

;scale variables
818:  Z=X*F (P37)
 1: 6        X Loc [ Tin       ]
 2: .011     F
 3: 6        Z Loc [ Tin       ]

819:  Z=X+F (P34)
 1: 6        X Loc [ Tin       ]
 2: 0        F
 3: 6        Z Loc [ Tin       ]

820:  Z=X*F (P37)
 1: 5        X Loc [ co2_in    ]
 2: .6       F
 3: 5        Z Loc [ co2_in    ]

821:  Z=X+F (P34)
 1: 5        X Loc [ co2_in    ]
 2: 0        F
 3: 5        Z Loc [ co2_in    ]

822:  Z=X*F (P37)
 1: 7        X Loc [ H2Oin     ]
 2: .014     F
```

```
 3: 7        Z Loc [ H2Oin     ]

823:  Z=X+F (P34)
 1: 7        X Loc [ H2Oin     ]
 2: 0        F
 3: 7        Z Loc [ H2Oin     ]

824:  Z=X*F (P37)
 1: 8        X Loc [ Pin       ]
 2: .03058   F
 3: 8        Z Loc [ Pin       ]

825:  Z=X+F (P34)
 1: 8        X Loc [ Pin       ]
 2: 58.564   F
 3: 8        Z Loc [ Pin       ]

826:  If (X<=>F) (P89)
 1: 51       X Loc [ F_Volt    ]
 2: 1        =
 3: 0        F
 4: 30       Then Do

     827:  Z=F (P30)
      1: 0.0      F
      2: 00       Exponent of 10
      3: 48       Z Loc [ FlowDil
]

828:  End (P95)


829:  Z=X/Y (P38)
 1: 49       X Loc [ FlowOut   ]
 2: 50       Y Loc [ flowsamp  ]
 3: 55       Z Loc [ DILconst  ]



830:  Z=X*F (P37)
 1: 55       X Loc [ DILconst  ]
 2: 0.001    F
 3: 56       Z Loc [ DILscalar ]


831:  Z=X*Y (P36)
 1: 5        X Loc [ co2_in    ]
 2: 56       Y Loc [ DILscalar ]
 3: 57       Z Loc [ CO2norm   ]

832:  Z=X*Y (P36)
 1: 5        X Loc [ co2_in    ]
 2: 55       Y Loc [ DILconst  ]
 3: 58       Z Loc [ FlowOut2  ]

; end scale variables

833:  If time is (P92)
 1: 4     -- Minutes (Seconds --)
into a
 2: 5        Interval (same units
as above)
 3: 30       Then Do



834:  Do (P86)
 1: 10       Set Output Flag High
(Flag 0)



835:  Set Active Storage Area
(P80)^7165
 1: 1        Final Storage Area 1
 2: 101      Array ID

836:  Real Time (P77)^25091
 1: 11       Hour/Minute,Seconds
(midnight = 0000)

837:  Resolution (P78)
 1: 1        High Resolution

838:  Sample (P70)^23897
 1: 1        Reps
 2: 1        Loc [ time_min  ]

839:  Sample (P70)^1564
 1: 1        Reps
 2: 65       Loc [ time_cyc2 ]

840:  Sample (P70)^4171
 1: 1        Reps
 2: 59       Loc [ Chamber   ]


841:  Sample (P70)^4459
 1: 1        Reps
 2: 5        Loc [ co2_in    ]


842:  Sample (P70)^11467
 1: 1        Reps
 2: 48       Loc [ FlowDil   ]

843:  Sample (P70)^3149
 1: 1        Reps
 2: 49       Loc [ FlowOut   ]

844:  Sample (P70)^19604
```

```
 1: 1        Reps
 2: 50       Loc [ flowsamp  ]


845:  Sample (P70)^4944
 1: 1        Reps
 2: 56       Loc [ DILscalar ]

846:  Sample (P70)^9719
 1: 1        Reps
 2: 55       Loc [ DILconst  ]

847:  Sample (P70)^1936
 1: 1        Reps
 2: 57       Loc [ CO2norm   ]

848:  Sample (P70)^29257
 1: 1        Reps
 2: 58       Loc [ FlowOut2  ]

849:  Sample (P70)^22202
 1: 1        Reps
 2: 51       Loc [ F_Volt    ]


850:  Sample (P70)^15552
 1: 1        Reps
 2: 6        Loc [ Tin       ]

851:  Sample (P70)^1768
 1: 1        Reps
 2: 7        Loc [ H2Oin     ]

852:  Sample (P70)^9842
 1: 1        Reps
 2: 8        Loc [ Pin       ]



853:  Sample (P70)^13983
 1: 1        Reps
 2: 3        Loc [ CAO2      ]


854:  Do (P86)
 1: 20       Set Output Flag Low
(Flag 0)



855:  End (P95)
```

```
*Table 2 Program
  01: 0.01      Execution Interval
(seconds)

;Set up time system and cycle times

1:  Time (P18)
 1: 1        Minutes into current
day (maximum 1440)
 2: 1440     Mod/By
 3: 1        Loc [ time_min  ]

2:  Z=X MOD F (P46)
 1: 1        X Loc [ time_min  ]
 2: 6        F
 3: 65       Z Loc [ time_cyc2 ]

3:  Time (P18)
 1: 0        Seconds into current
minute (maximum 60)
 2: 60       Mod/By
 3: 1        Loc [ time_min  ]

4:  Z=X*F (P37)
 1: 1        X Loc [ time_min  ]
 2: 0.01667  F
 3: 4        Z Loc [ time_add  ]

5:  Z=X+Y (P33)
 1: 65       X Loc [ time_cyc2 ]
 2: 4        Y Loc [ time_add  ]
 3: 65       Z Loc [ time_cyc2 ]
;end time set up

;set ports for clean out

;Setup SDM 16AC port flags

6:  If (X<=>F) (P89)
 1: 65       X Loc [ time_cyc2 ]
 2: 4        <
 3: 0.02     F
 4: 30       Then Do

7:  If (X<=>F) (P89)
 1: 65       X Loc [ time_cyc2 ]
 2: 3        >=
 3: 0        F
 4: 30       Then Do


;Initialize SDM array


     8:  Do (P86)
```

```
      1: 005      Call Subroutine 5

9:  End (P95)
10:  End (P95)

;Setup SDM 16AC port flags

11:  If (X<=>F) (P89)
 1: 65       X Loc [ time_cyc2 ]
 2: 4        <
 3: 0.04     F
 4: 30       Then Do

12:  If (X<=>F) (P89)
 1: 65       X Loc [ time_cyc2 ]
 2: 3        >=
 3: 0.02     F
 4: 30       Then Do

;Initialize SDM array


     13:  Do (P86)
      1: 001      Call Subroutine 1

14:  End (P95)
15:  End (P95)

;Execute valve operation

16:  SDM-CD16 / SDM-CD16AC (P104)
 1: 2        Reps
 2: 00       SDM Address
 3: 10       Loc [ SDM1P_1   ]

;Start clean out sample 1

17:  If (X<=>F) (P89)
 1: 65       X Loc [ time_cyc2 ]
 2: 4        <
 3: .1       F
 4: 30       Then Do

18:  If (X<=>F) (P89)
 1: 65       X Loc [ time_cyc2 ]
 2: 3        >=
 3: .06      F
 4: 30       Then Do

     19:  Z=F (P30)
      1: 5        F
      2: 03       Exponent of 10
      3: 51       Z Loc [ F_Volt
]

     20:  Analog Out (P133)
      1: 1        CAO1
      2: 51       mV Loc [ F_Volt
]

21:  End (P95)
22:  End (P95)

;end clean out sample 1

;Initial dilution prep between
switching samples (first 2.25 min)


;close down dilution to get
preliminary read on sample conc

23:  If (X<=>F) (P89)
 1: 65       X Loc [ time_cyc2 ]
 2: 3        >=
 3: .1       F
 4: 30       Then Do

24:  If (X<=>F) (P89)
 1: 65       X Loc [ time_cyc2 ]
 2: 4        <
 3: 0.25     F
 4: 30       Then Do

     25:  Z=F (P30)
      1: 0.0      F
      2: 00       Exponent of 10
      3: 51       Z Loc [ F_Volt
]

     26:  Analog Out (P133)
      1: 1        CAO1
      2: 51       mV Loc [ F_Volt
]

27:  End (P95)

28:  End (P95)
;end priliminary read sample


;Dilution stage 1 for sample 1

29:  If (X<=>F) (P89)
 1: 65       X Loc [ time_cyc2 ]
 2: 3        >=
 3: .25      F
 4: 30       Then Do

30:  If (X<=>F) (P89)
```

```
 1: 65       X Loc [ time_cyc2 ]
 2: 4        <
 3: 0.75     F
 4: 30       Then Do

31:  If (X<=>F) (P89)
 1: 5        X Loc [ co2_in    ]
 2: 3        >=
 3: 4800     F
 4: 30       Then Do


     32:  Z=F (P30)
      1: 1.2      F
      2: 3        Exponent of 10
      3: 51       Z Loc [ F_Volt
]

     33:  Analog Out (P133)
      1: 1        CAO1
      2: 51       mV Loc [ F_Volt
]

34:  End (P95)

35:  End (P95)

36:  End (P95)
;Dilution stage 1 for sample 1




;Dilution stage 2 for sample 1

37:  If (X<=>F) (P89)
 1: 65       X Loc [ time_cyc2 ]
 2: 3        >=
 3: .75      F
 4: 30       Then Do

38:  If (X<=>F) (P89)
 1: 65       X Loc [ time_cyc2 ]
 2: 4        <
 3: 1.25     F
 4: 30       Then Do

39:  If (X<=>F) (P89)
 1: 47       X Loc [ CVtest    ]
 2: 3        >=
 3: 4800     F
 4: 30       Then Do


     40:  Z=F (P30)
      1: 2.4      F
      2: 3        Exponent of 10
      3: 51       Z Loc [ F_Volt
]

     41:  Analog Out (P133)
      1: 1        CAO1
      2: 51       mV Loc [ F_Volt
]

42:  End (P95)

43:  End (P95)

44:  End (P95)
;Dilution stage 2 for sample 1


;Dilution stage 3 for sample 1

45:  If (X<=>F) (P89)
 1: 65       X Loc [ time_cyc2 ]
 2: 3        >=
 3: 1.25     F
 4: 30       Then Do

46:  If (X<=>F) (P89)
 1: 65       X Loc [ time_cyc2 ]
 2: 4        <
 3: 1.75     F
 4: 30       Then Do

47:  If (X<=>F) (P89)
 1: 47       X Loc [ CVtest    ]
 2: 3        >=
 3: 4800     F
 4: 30       Then Do


     48:  Z=F (P30)
      1: 3.6      F
      2: 3        Exponent of 10
      3: 51       Z Loc [ F_Volt
]

     49:  Analog Out (P133)
      1: 1        CAO1
      2: 51       mV Loc [ F_Volt
]

50:  End (P95)

51:  End (P95)

52:  End (P95)
;Dilution stage 3 for sample 1
```

```
;Dilution stage 4 for sample 1

53:  If (X<=>F) (P89)
 1: 65       X Loc [ time_cyc2 ]
 2: 3        >=
 3: 1.75     F
 4: 30       Then Do

54:  If (X<=>F) (P89)
 1: 65       X Loc [ time_cyc2 ]
 2: 4        <
 3: 2.25     F
 4: 30       Then Do

55:  If (X<=>F) (P89)
 1: 47       X Loc [ CVtest    ]
 2: 3        >=
 3: 4800     F
 4: 30       Then Do


     56:  Z=F (P30)
      1: 4.8      F
      2: 3        Exponent of 10
      3: 51       Z Loc [ F_Volt
]

     57:  Analog Out (P133)
      1: 1        CAO1
      2: 51       mV Loc [ F_Volt
]

58:  End (P95)

59:  End (P95)

60:  End (P95)
;end Dilution stage 4 for sample 1
```

```
;Dilute if CO2 is saturated for
sample 1
61:  If (X<=>F) (P89)
 1: 65       X Loc [ time_cyc2 ]
 2: 3        >=
 3: 2.25     F
 4: 30       Then Do

62:  If (X<=>F) (P89)
 1: 65       X Loc [ time_cyc2 ]
 2: 4        <
 3: 6        F
 4: 30       Then Do

63:  If (X<=>F) (P89)
 1: 47       X Loc [ CVtest    ]
 2: 3        >=
 3: 4800     F
 4: 30       Then Do

64:  If (X<=>F) (P89)
 1: 51       X Loc [ F_Volt    ]
 2: 4        <
 3: 4800     F
 4: 30       Then Do


          65:  Z=X+F (P34)
           1: 51       X Loc [
F_Volt    ]
           2: 1200     F
           3: 51       Z Loc [
F_Volt    ]

     66:  Analog Out (P133)
      1: 1        CAO1
      2: 51       mV Loc [ F_Volt
]

     67:  End (P95)
;end if 1
     68:  End (P95)
;end if 2
69:  End (P95)
;end if 3
70:  End (P95)
;end if 4

;This should increase the dilution
and wait to see if the
;action is effective



;Reduce dilution if CO2 is over
diluted for sample 1
```

```
71:  If (X<=>F) (P89)
 1: 65       X Loc [ time_cyc2 ]
 2: 3        >=
 3: 2.25     F
 4: 30       Then Do

72:  If (X<=>F) (P89)
 1: 65       X Loc [ time_cyc2 ]
 2: 4        <
 3: 6        F
 4: 30       Then Do

73:  If (X<=>F) (P89)
 1: 47       X Loc [ CVtest    ]
 2: 4        <
 3: 500      F
 4: 30       Then Do

74:  If (X<=>F) (P89)
 1: 51       X Loc [ F_Volt    ]
 2: 3        >=
 3: 1200     F
 4: 30       Then Do

          75:  Z=X+F (P34)
           1: 51       X Loc [
F_Volt    ]
           2: -1200    F
           3: 51       Z Loc [
F_Volt    ]

     76:  Analog Out (P133)
      1: 1        CAO1
      2: 51       mV Loc [ F_Volt
]

     77:  End (P95)
;end if 1
     78:  End (P95)
;end if 2
79:  End (P95)
;end if 3
80:  End (P95)
;end if 4

;This should decrease the dilution
and wait to see if the
;action is effective



81:  Do (P86)
 1: 10       Set Output Flag High
(Flag 0)
```

```
;End Table 2



*Table 3 Subroutines

1:  Beginning of Subroutine (P85)
 1: 01       Subroutine 1
;Initialize SDM arrays to zero
2:  Z=F x 10^n (P30)
 1: 0.0      F
 2: 00       n, Exponent of 10
 3: 10       Z Loc [ SDM1P_1   ]

3:  Z=F x 10^n (P30)
 1: 0.0      F
 2: 00       n, Exponent of 10
 3: 11       Z Loc [ SDM1P_2   ]

4:  Z=F x 10^n (P30)
 1: 0.0      F
 2: 00       n, Exponent of 10
 3: 12       Z Loc [ SDM1P_3   ]

5:  Z=F x 10^n (P30)
 1: 0.0      F
 2: 00       n, Exponent of 10
 3: 13       Z Loc [ SDM1P_4   ]

6:  Z=F x 10^n (P30)
 1: 0.0      F
 2: 00       n, Exponent of 10
 3: 14       Z Loc [ SDM1P_5   ]

7:  Z=F x 10^n (P30)
 1: 0.0      F
 2: 00       n, Exponent of 10
 3: 15       Z Loc [ SDM1P_6   ]

8:  Z=F x 10^n (P30)
 1: 0.0      F
 2: 00       n, Exponent of 10
 3: 16       Z Loc [ SDM1P_7   ]

9:  Z=F x 10^n (P30)
 1: 0.0      F
 2: 00       n, Exponent of 10
 3: 17       Z Loc [ SDM1P_8   ]

10:  Z=F x 10^n (P30)
 1: 0.0      F
 2: 00       n, Exponent of 10
 3: 18       Z Loc [ SDM1P_9   ]
```

```
11:  Z=F x 10^n (P30)
 1: 0.0      F
 2: 00       n, Exponent of 10
 3: 19       Z Loc [ SDM1P_10  ]

12:  Z=F x 10^n (P30)
 1: 0.0      F
 2: 00       n, Exponent of 10
 3: 20       Z Loc [ SDM1P_11  ]

13:  Z=F x 10^n (P30)
 1: 0.0      F
 2: 00       n, Exponent of 10
 3: 21       Z Loc [ SDM1P_12  ]

14:  Z=F x 10^n (P30)
 1: 0.0      F
 2: 00       n, Exponent of 10
 3: 22       Z Loc [ SDM1P_13  ]

15:  Z=F x 10^n (P30)
 1: 0.0      F
 2: 00       n, Exponent of 10
 3: 23       Z Loc [ SDM1P_14  ]

16:  Z=F x 10^n (P30)
 1: 0.0      F
 2: 00       n, Exponent of 10
 3: 24       Z Loc [ SDM1P_15  ]

17:  Z=F x 10^n (P30)
 1: 0.0      F
 2: 00       n, Exponent of 10
 3: 25       Z Loc [ SDM1P_16  ]

18:  Z=F x 10^n (P30)
 1: 0.0      F
 2: 00       n, Exponent of 10
 3: 26       Z Loc [ SDM2P_1   ]

19:  Z=F x 10^n (P30)
 1: 0.0      F
 2: 00       n, Exponent of 10
 3: 27       Z Loc [ SDM2P_2   ]

20:  Z=F x 10^n (P30)
 1: 0.0      F
 2: 00       n, Exponent of 10
 3: 28       Z Loc [ SDM2P_3   ]

21:  Z=F x 10^n (P30)
 1: 0.0      F
 2: 00       n, Exponent of 10
 3: 29       Z Loc [ SDM2P_4   ]

22:  Z=F x 10^n (P30)
 1: 0.0      F
 2: 00       n, Exponent of 10
 3: 30       Z Loc [ SDM2P_5   ]

23:  Z=F x 10^n (P30)
 1: 0.0      F
 2: 00       n, Exponent of 10
 3: 31       Z Loc [ SDM2P_6   ]

24:  Z=F x 10^n (P30)
 1: 0.0      F
 2: 00       n, Exponent of 10
 3: 32       Z Loc [ SDM2P_7   ]

25:  Z=F x 10^n (P30)
 1: 0.0      F
 2: 00       n, Exponent of 10
 3: 33       Z Loc [ SDM2P_8   ]

26:  Z=F x 10^n (P30)
 1: 0.0      F
 2: 00       n, Exponent of 10
 3: 34       Z Loc [ SDM2P_9   ]

27:  Z=F x 10^n (P30)
 1: 0.0      F
 2: 00       n, Exponent of 10
 3: 35       Z Loc [ SDM2P_10  ]

28:  Z=F x 10^n (P30)
 1: 0.0      F
 2: 00       n, Exponent of 10
 3: 36       Z Loc [ SDM2P_11  ]

29:  Z=F x 10^n (P30)
 1: 0.0      F
 2: 00       n, Exponent of 10
 3: 37       Z Loc [ SDM2P_12  ]

30:  Z=F x 10^n (P30)
 1: 0.0      F
 2: 00       n, Exponent of 10
 3: 38       Z Loc [ SDM2P_13  ]

31:  Z=F x 10^n (P30)
 1: 0.0      F
 2: 00       n, Exponent of 10
 3: 39       Z Loc [ SDM2P_14  ]

32:  Z=F x 10^n (P30)
 1: 0        F
 2: 00       n, Exponent of 10
 3: 40       Z Loc [ SDM2P_15  ]

33:  Z=F x 10^n (P30)
 1: 0.0      F
 2: 00       n, Exponent of 10
 3: 41       Z Loc [ SDM2P_16  ]
```

```
34:  End (P95)

35:  Beginning of Subroutine (P85)
 1: 02       Subroutine 2

;Power latch open

36:  Z=F x 10^n (P30)
 1: 0.0      F
 2: 00       n, Exponent of 10
 3: 40       Z Loc [ SDM2P_15  ]

37:  Z=F x 10^n (P30)
 1: 1        F
 2: 00       n, Exponent of 10
 3: 41       Z Loc [ SDM2P_16  ]


38:  End (P95)

39:  Beginning of Subroutine (P85)
 1: 03       Subroutine 3

;Power latch close

40:  Z=F x 10^n (P30)
 1: 1        F
 2: 00       n, Exponent of 10
 3: 40       Z Loc [ SDM2P_15  ]

41:  Z=F x 10^n (P30)
 1: 0        F
 2: 00       n, Exponent of 10
 3: 41       Z Loc [ SDM2P_16  ]



42:  End (P95)

43:  Beginning of Subroutine (P85)
 1: 04       Subroutine 4

;Valve SS (non-powered)

44:  Z=F x 10^n (P30)
 1: 0        F
 2: 00       n, Exponent of 10
 3: 40       Z Loc [ SDM2P_15  ]

45:  Z=F x 10^n (P30)
 1: 0        F
 2: 00       n, Exponent of 10
 3: 41       Z Loc [ SDM2P_16  ]

46:  End (P95)

47:  Beginning of Subroutine (P85)
 1: 05       Subroutine 5
;Initialize SDM arrays to exhaust

48:  Z=F x 10^n (P30)
 1: 1        F
 2: 00       n, Exponent of 10
 3: 40       Z Loc [ SDM2P_15  ]

49:  Z=F x 10^n (P30)
 1: 1        F
 2: 00       n, Exponent of 10
 3: 10       Z Loc [ SDM1P_1   ]

50:  Z=F x 10^n (P30)
 1: 1        F
 2: 00       n, Exponent of 10
 3: 11       Z Loc [ SDM1P_2   ]

51:  Z=F x 10^n (P30)
 1: 1        F
 2: 00       n, Exponent of 10
 3: 12       Z Loc [ SDM1P_3   ]

52:  Z=F x 10^n (P30)
 1: 1        F
 2: 00       n, Exponent of 10
 3: 13       Z Loc [ SDM1P_4   ]

53:  Z=F x 10^n (P30)
 1: 1        F
 2: 00       n, Exponent of 10
 3: 14       Z Loc [ SDM1P_5   ]

54:  Z=F x 10^n (P30)
 1: 1        F
 2: 00       n, Exponent of 10
 3: 15       Z Loc [ SDM1P_6   ]

55:  Z=F x 10^n (P30)
 1: 1        F
 2: 00       n, Exponent of 10
 3: 16       Z Loc [ SDM1P_7   ]

56:  Z=F x 10^n (P30)
 1: 1        F
 2: 00       n, Exponent of 10
 3: 17       Z Loc [ SDM1P_8   ]

57:  Z=F x 10^n (P30)
 1: 1        F
 2: 00       n, Exponent of 10
 3: 18       Z Loc [ SDM1P_9   ]
```

```
58:  Z=F x 10^n (P30)
 1: 1        F
 2: 00       n, Exponent of 10
 3: 19       Z Loc [ SDM1P_10  ]

59:  Z=F x 10^n (P30)
 1: 1        F
 2: 00       n, Exponent of 10
 3: 20       Z Loc [ SDM1P_11  ]

60:  Z=F x 10^n (P30)
 1: 1        F
 2: 00       n, Exponent of 10
 3: 21       Z Loc [ SDM1P_12  ]

61:  Z=F x 10^n (P30)
 1: 1        F
 2: 00       n, Exponent of 10
 3: 22       Z Loc [ SDM1P_13  ]

62:  Z=F x 10^n (P30)
 1: 1        F
 2: 00       n, Exponent of 10
 3: 23       Z Loc [ SDM1P_14  ]

63:  Z=F x 10^n (P30)
 1: 1        F
 2: 00       n, Exponent of 10
 3: 24       Z Loc [ SDM1P_15  ]

64:  Z=F x 10^n (P30)
 1: 1        F
 2: 00       n, Exponent of 10
 3: 25       Z Loc [ SDM1P_16  ]

65:  Z=F x 10^n (P30)
 1: 1        F
 2: 00       n, Exponent of 10
 3: 26       Z Loc [ SDM2P_1   ]

66:  Z=F x 10^n (P30)
 1: 1        F
 2: 00       n, Exponent of 10
 3: 27       Z Loc [ SDM2P_2   ]

67:  Z=F x 10^n (P30)
 1: 1        F
 2: 00       n, Exponent of 10
 3: 28       Z Loc [ SDM2P_3   ]

68:  Z=F x 10^n (P30)
 1: 1        F
 2: 00       n, Exponent of 10
 3: 29       Z Loc [ SDM2P_4   ]

69:  Z=F x 10^n (P30)
 1: 1        F
 2: 00       n, Exponent of 10
 3: 30       Z Loc [ SDM2P_5   ]

70:  Z=F x 10^n (P30)
 1: 1        F
 2: 00       n, Exponent of 10
 3: 31       Z Loc [ SDM2P_6   ]

71:  Z=F x 10^n (P30)
 1: 1        F
 2: 00       n, Exponent of 10
 3: 32       Z Loc [ SDM2P_7   ]

72:  Z=F x 10^n (P30)
 1: 1        F
 2: 00       n, Exponent of 10
 3: 33       Z Loc [ SDM2P_8   ]

73:  Z=F x 10^n (P30)
 1: 1        F
 2: 00       n, Exponent of 10
 3: 34       Z Loc [ SDM2P_9   ]

74:  Z=F x 10^n (P30)
 1: 1        F
 2: 00       n, Exponent of 10
 3: 35       Z Loc [ SDM2P_10  ]

75:  Z=F x 10^n (P30)
 1: 1        F
 2: 00       n, Exponent of 10
 3: 36       Z Loc [ SDM2P_11  ]

76:  End (P95)

End Program

-Input Locations-
1 time_min  1 5 2
2 time_cycl 1 135 2
3 CAO2      1 0 0
4 time_add  1 2 2
5 co2_in    5 7 3
6 Tin       9 3 3
7 H2Oin     9 3 3
8 Pin       17 3 3
9 _________ 0 0 0
10 SDM1P_1   3 1 9
11 SDM1P_2   3 1 6
```

```
12 SDM1P_3   3 1 6
13 SDM1P_4   3 1 6
14 SDM1P_5   3 1 6
15 SDM1P_6   3 1 6
16 SDM1P_7   3 1 6
17 SDM1P_8   3 1 6
18 SDM1P_9   3 1 6
19 SDM1P_10  3 1 6
20 SDM1P_11  3 1 6
21 SDM1P_12  3 1 6
22 SDM1P_13  3 1 6
23 SDM1P_14  3 1 6
24 SDM1P_15  3 1 6
25 SDM1P_16  3 1 6
26 SDM2P_1   3 2 6
27 SDM2P_2   3 2 6
28 SDM2P_3   3 2 6
29 SDM2P_4   3 2 6
30 SDM2P_5   3 2 6
31 SDM2P_6   3 2 6
32 SDM2P_7   3 2 6
33 SDM2P_8   3 2 6
34 SDM2P_9   3 2 6
35 SDM2P_10  3 2 6
36 SDM2P_11  3 2 6
37 SDM2P_12  3 2 1
38 SDM2P_13  3 2 1
39 SDM2P_14  3 2 1
40 SDM2P_15  11 2 5
41 SDM2P_16  19 2 4
42 c2o2_1    1 0 0
43 co2_2     1 0 0
44 co2_3     1 0 0
45 co2_4     1 0 0
46 c2o2_in   1 0 0
47 CVtest    1 5 1
48 FlowDil   1 1 2
49 FlowOut   1 2 1
50 flowsamp  1 2 1
51 F_Volt    1 14 8
52 T2in      1 1 0
53 H22Oin    1 0 0
54 P2in      1 0 0
55 DILconst  1 3 1
56 DILscalar 1 2 1
57 CO2norm   1 1 1
58 FlowOut2  1 1 1
59 Chamber   1 1 28
60 CO2normhi 1 0 0
61 co2_1     1 0 0
62 co2_2     1 0 0
63 co2_3     1 0 0
64 co2_4     1 0 0
65 time_cyc2 1 76 2
-Program Security-
0
0
0
-Mode 4-
-Final Storage Area 2-
0
-CR10X ID-
0
-CR10X Power Up-
0
-CR10X Compile Setting-
13
-CR10X RS-232 Setting-
-1
-DLD File Labels-
0
-Final Storage Labels-
0,101,7165
1,Hour_Minute_RTM,25091
1,Seconds_RTM
2,time_min~1,23897
3,time_cyc2~65,1564
4,Chamber~59,4171
5,co2_in~5,4459
6,FlowDil~48,11467
7,FlowOut~49,3149
8,flowsamp~50,19604
9,DILscalar~56,4944
10,DILconst~55,9719
11,CO2norm~57,1936
12,FlowOut2~58,29257
13,F_Volt~51,22202
14,Tin~6,15552
15,H2Oin~7,1768
16,Pin~8,9842
17,CAO2~3,13983
```

Distribution

No. of Copies

1 National Energy Technology Laboratory
Morgantown, WV
D Deel (PDF)

2 National Energy Technology Laboratory
Pittsburg, PA
BL Strazisar (PDF)
AW Wells (PDF)

5 Montana State University
Bozeman, MT 59717
LH Spangler (PDF)
LM Dobeck (PDF)
JA Shaw (PDF)
KS Repasky (PDF)
AB Cunningham (PDF)

2 Lawrence Berkeley National Laboratory
Berkeley, CA 94720
JL Lewicki (PDF)
CM Oldenburg (PDF)

1 University of California Santa Cruz
Santa Cruz, CA 94019
WL Pickles (PDF)

2 Los Alamos National Laboratory
Los Alamos, NM 87545
SD Humphries (PDF)
JE Fessenden (PDF)

No. of Copies

6 **Local Distribution**
Pacific Northwest National Laboratory
JE Amonette (PDF)
JL Barr (PDF)
RT Dahowski (PDF)
BP McGrail (PDF)
HT Schaef (PDF)
C Sullivan (PDF)
FA Spane (PDF)

Pacific Northwest
NATIONAL LABORATORY

U.S. DEPARTMENT OF
ENERGY

902 Battelle Boulevard
P.O. Box 999
Richland, WA 99352
1-888-375-PNNL (7665)
www.pnl.gov

Appendix F

Pacific Northwest National Laboratory

Soret Effect Study on High-Pressure CO_2-Water Solutions Using UVRaman Spectroscopy and a Concentric-Tube Optical Cell

U.S. DEPARTMENT OF ENERGY

PNNL-21156

Prepared for the U.S. Department of Energy
under Contract DE-AC05-76RL01830

Soret Effect Study on High-Pressure CO_2-Water Solutions Using UV-Raman Spectroscopy and a Concentric-Tube Optical Cell

CF Windisch Jr.
BP McGrail
GD Maupin

January 2012

Pacific Northwest
NATIONAL LABORATORY

Proudly Operated by Battelle *Since 1965*

PACIFIC NORTHWEST NATIONAL LABORATORY
operated by
BATTELLE
for the
UNITED STATES DEPARTMENT OF ENERGY
under Contract DE-AC05-76RL01830

Printed in the United States of America

Available to DOE and DOE contractors from the
Office of Scientific and Technical Information,
P.O. Box 62, Oak Ridge, TN 37831-0062;
ph: (865) 576-8401
fax: (865) 576-5728
email: reports@adonis.osti.gov

Available to the public from the National Technical Information Service
5301 Shawnee Rd., Alexandria, VA 22312
ph: (800) 553-NTIS (6847)
email: orders@ntis.gov <http://www.ntis.gov/about/form.aspx>
Online ordering: http://www.ntis.gov

This document was printed on recycled paper.
(8/2010)

PNNL-21156

Soret Effect Study on High-Pressure CO_2-Water Solutions Using UV-Raman Spectroscopy and a Concentric-Tube Optical Cell

CF Windisch Jr.
BP McGrail
GD Maupin

January 2012

Prepared for
the U.S. Department of Energy
under Contract DE-AC05-76RL01830

Pacific Northwest National Laboratory
Richland, Washington 99352

Abstract

Spatially resolved deep-UV Raman spectroscopy was applied to solutions of CO_2 and H_2O (or D_2O), which were subject to a temperature gradient in a thermally regulated high-pressure concentric-tube Raman cell in an attempt to measure a Soret effect in the vicinity of the critical point of CO_2. Although Raman spectra of solutions of CO_2 dissolved in D_2O at 10 MPa and temperatures near the critical point of CO_2 had adequate signal-to-noise and spatial resolution to observe a Soret effect with a Soret coefficient with magnitude of $|S_T| > 0.03$, no evidence for an effect of this size was obtained for applied temperature gradients up to 19^oC. The presence of 1 M NaCl did not make a difference. In contrast, the concentration of CO_2 dissolved in H_2O was shown to vary significantly across the temperature gradient when excess CO_2 was present, but the results could be explained simply by the variation in CO_2 solubility over the temperature range and not to kinetic factors. For mixtures of D_2O dissolved in scCO_2 at 10 MPa and temperatures close to the critical point of CO_2, the Raman peaks for H_2O were too weak to measure with confidence even at the limit of D_2O solubility.

Acknowledgments

This work was supported by the U.S. Department of Energy (DOE), Office of Fossil Energy. The Pacific Northwest National Laboratory (PNNL) is operated by Battelle for the DOE under Contract DE-AC05-76RL01830.

Acronyms and Abbreviations

BBO	beta barium borate
cm	centimeter
CO_2	carbon dioxide
D_2O	heavy water
H_2O	water
mm	millimeter
MPa	megapascals
NaCl	sodium chloride
$scCO_2$	supercritical carbon dioxide
μm	micron
UV	ultraviolet
ZERT	Zero Emissions Research and Technology

Contents

Figures

1.0 Introduction

1.1 Overall program objective

Considerable work on flow processes in CO_2-water[1] systems has been done in geothermal reservoir engineering. However, significant uncertainties remain with respect to mixing processes that occur in supercritical CO_2-water systems, especially in porous media. For the case where supercritical CO_2 is injected into a deep saline formation, the important processes to be considered include the following: (1) forced convective flow around the injection well, (2) dissolution rate of CO_2 into the brine, and (3) heat of solution as CO_2 dissolves into the formation brine.

As CO_2 dissolves into water, the negative heat of solution consumes approximately 17 kJ/mol at typical reservoir conditions (Bastelli 1997; White 2002). Also, pipeline supply of CO_2 will result in cold CO_2 reaching the wellhead. Reservoir calculations suggest that temperature gradients on the order of 5 to 10°C cm^{-1} can easily be generated as a result. A temperature gradient induces coupled feedback effects on the rate of convective mixing in two ways: (1) through changes in physical properties (density, viscosity, surface tension) and (2) nonlinear thermal diffusion or Soret effects (Kempers 2001; Nejad 2001). The Soret effect is the tendency of a mixture of two or more components to separate under the influence of a temperature gradient. The effect is quantified by the Soret coefficient, S_T, which is derived by considering Fick's law under conditions where the flux results from a combination of thermal and concentration gradients.

Empirical descriptions treat the mass flux associated with a thermal gradient, $\mathbf{j_T}$, as

$$\mathbf{j_T} = -D_T c \nabla T \qquad (1)$$

where D_T is the thermal diffusion coefficient of the diffusing species in the solution, c is the concentration and T is the temperature. It is considered a separate process from the mass flux associated with a concentration gradient, $\mathbf{j_c}$, which is given by

$$\mathbf{j_c} = -D \nabla c \qquad (2)$$

where D is the ordinary (mass) diffusion coefficient. Under steady-state conditions, $\mathbf{j_T} = -\mathbf{j_c}$, yielding (Duhr 2006):

$$\nabla c = -c S_T \nabla T \qquad (3)$$

where $S_T = D_T/D$ and is called the Soret coefficient. In concentrated mixtures, S_T is also a function of the solute concentration and can even change sign (Kolodner et al. 1988; Slavtchev et al. 1999).

[1] CO_2-water is the general term for the solutions studied here. Both isotopic forms of water, H_2O and D_2O, were used for reasons discussed in the text. For specific experiments, the form of water is called out in the notation, e.g., CO_2-D_2O.

Because of rapid changes in thermochemical properties near critical points (Zhang 2002) and based on independent measurements of supercritical CO_2 fluids (Swinney 1968), Soret effects have been predicted to be strong in near-critical liquids (Kempers 2001). The primary objective of the Fundamental Studies Task of Zero Emissions Research and Technology (ZERT) was to use laser Raman spectroscopy to study the Soret effect in CO_2-water mixtures across a temperature gradient near the critical point of CO_2. The proposed approach is based on other optical studies of the phenomenon (Xu 2003; Duhr 2006; Ning 2006; Koniger 2010) and the recognition that Raman spectroscopy is very sensitive to both H_2O and CO_2 under both subcritical and supercritical conditions (Cabaco 2007, 2010a, 2010b). Two specific goals of the Task were (1) to determine whether the technique can be used to substantiate thermal diffusion in CO_2-water mixtures and, if so, (2) to quantify the Soret effect as a function of conditions.

1.2 Summary of ZERT I results

In ZERT I, a specially designed high-pressure Raman cell suitable for supercritical studies with an imposed temperature gradient, specifically a 10-20^{o}C temperature gradient across an optical window through which Raman measurements could be acquired as a function of position, was built and applied to CO_2-water mixtures over a range of experimental conditions. Results were inconclusive over the range of conditions studied. In particular, even though variations in composition (CO_2 in H_2O) were measured between the two temperatures across the cell, the magnitude of the variations was very small. Soret coefficients calculated from this data were on the order of 10^{-3}, several orders of magnitude less than expected from published values of the ordinary and thermal diffusion coefficients of the components (Xu 2003; Amirkhanov 1987; Swinney 1968).

The surprisingly small values of S_T were attributed to two experimental difficulties. The first involved the design of the Raman cell, which appeared to offer insufficient thermal management under the imposed temperature gradient. The large size of the cell and its windows were speculated to induce convection currents that interfered with the measurements by evening out the concentrations across the cell. The second problem related to the range of compositions of the mixtures that were “accessible” in the study. The solubility of H_2O in scCO_2 is too low (mole fraction ~ 10^{-3}) to obtain Raman spectra with sufficient S/N for quantitative measurements. On the other hand, CO_2 dissolves in liquid H_2O to a degree that is an order of magnitude higher under similar pressure and temperature conditions. Research under ZERT II addressed these difficulties as follows: (1) a new Raman cell was designed and built with a smaller volume, better spatial resolution, and improved thermal management through the use of temperature-controlled windows, and (2) measurements were largely confined to the system “CO_2 dissolved in water” under conditions where CO_2 is either liquid or a supercritical fluid.

1.3 Justification and description of approach for ZERT II

The Raman cell in ZERT II consisted of a set of three concentric tubes. The CO_2-water mixture was contained in the annulus (white region in Figure 1) between a tube of transparent sapphire on the outside, which also served part of the optical window, and an inner tube of stainless steel on the other. Temperature-controlled water circulated through the outer annulus between the sapphire tube and an outer tube of transparent quartz (blue region in Figure 1) and also through the inner stainless steel tube (red region in Figure 1). With the two water streams held at two different temperatures by external temperature controllers, a temperature gradient was established across the inner annulus containing the

CO_2-water mixture. A simplified schematic of this Raman cell and the scattering configuration is shown in Figure 1.

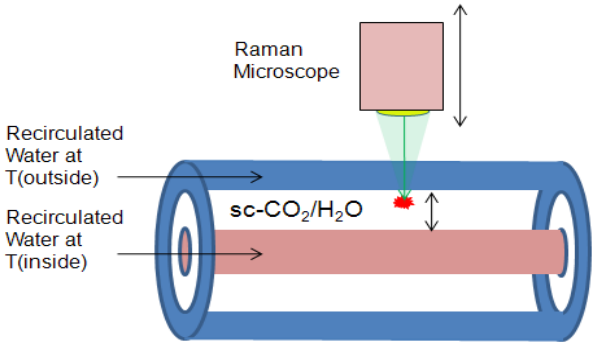

Figure 1. Simplified schematic of concentric-tube Raman cell.

A high-resolution UV-Raman microscope system was used to make the measurements in this study. The beam was focused within the bulk of a static CO_2-water solution contained in the inner annulus of the concentric-tube cell, positioned directly under the Raman microscope. As describe above, the central stainless steel tube and the outer annulus contained water at near-ambient pressure circulated between two thermostatically controlled temperature baths, separated in temperature by the desired gradient for the Soret study. The result was a temperature gradient imposed across the solution in the inner annulus ***without the presence of thermally unregulated windows***. Thermal regulation of the windows is one of the features that distinguished this design from that of the cell employed in ZERT I. The optical window consisted of the outer quartz tube, the circulating water circulating through the outer annulus, and the sapphire tube containing the CO_2-water solution.

Using the microscope, Raman spectra were collected as a function of depth, or distance between the thermally controlled walls of the inner annulus containing the CO_2-water solution. From these measurements, composition profiles (based on spectral features from CO_2 and water) within the solution and across the inner annulus were determined and, from the imposed temperature gradient, the occurrence and magnitude of the Soret effect was determined.

The depth resolution of Raman microscopes have improved significantly over the past few years, particularly with the advent of UV-Raman spectroscopy. PNNL recently acquired a Horiba Jobin Yvon LabRAM HR high-resolution UV-Raman system that was considered suitable for these measurements. This instrument, which has all reflective optics providing excellent quality Raman spectra with minimal signal distortion and resolution of +/- 2 cm^{-1}, also has distinct advantages in depth profiling. Studies on polished Si have demonstrated (Horiba Jobin Yvon Raman Application Note 2011) depth resolution of a fraction of a micrometer is achievable, depending on the excitation wavelength (shorter is better and our system uses deep-UV excitation at 244 nm), the characteristics of the material under study and the configuration of the optics, especially the size of the pinhole used for confocal measurements. In these measurements where a larger pinhole was required to achieve acceptable signal strength, we estimated a sampling volume (taken as spherical) with a diameter of about 500 μm. Although significantly poorer than anticipated, this depth-resolution was more than adequate to obtain several Raman spectra as a function of reasonable distinct distances between the two temperature reservoirs.

2.0 Experimental Procedure

2.1 Concentric-tube Raman cell design

The Raman cell used in these experiments was designed to withstand pressures of 10 MPa at temperatures up to about 45°C. This allowed measurements to be obtained on mixtures of CO_2 and water at 10 MPa (above the critical pressure of CO_2, 7.38 MPa) and temperatures in the regions below and above the critical temperature of CO_2 (31.04°C). The cell consisted of three concentric tubes: an outer tube made of quartz, a middle tube of sapphire and an inner tube of 316 stainless steel. A diagram of the configuration with dimensions of the components is given in Figure 2.

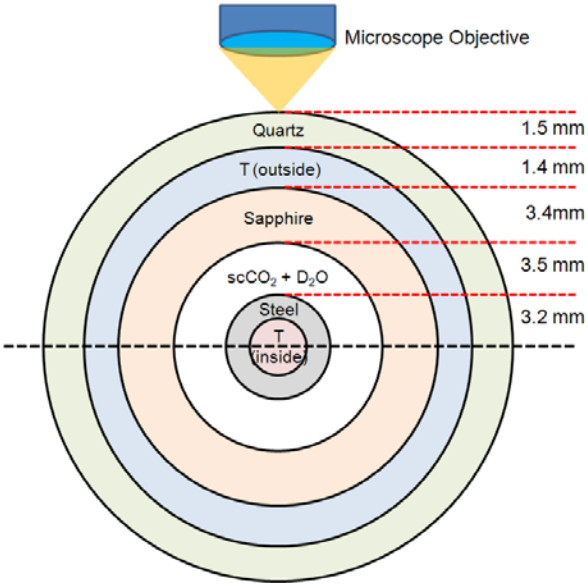

Figure 2. Concentric-tube Raman cell in cross-section showing thicknesses of the tubes and the annuli.

The steel tube in the center (gray in Figure 2) was used to carry constant temperature water (red in Figure 2), at T(inside), controlled by a Julabo (Vista, California) F12ED Refrigerated/Heating Circulator. The outer annulus with an outer wall of quartz (green in Figure 2) and an inner wall of sapphire (tan in Figure 2) contained water (blue in Figure 2) controlled at the second temperature T(outside) set with a separate Julabo circulator. The inner annulus contained the static mixture of CO_2 and water. It had an inner wall of steel (controlled at T(inside)) and an outer wall of sapphire (controlled at T(outside)). The dimensions of the sapphire tube were those required to withstand pressures up to 10 MPa and temperatures to 45°C. Pressure testing of the system was performed with water and nitrogen gas prior to the experiments to establish compatibility of this design with the test conditions.

In each measurement, the laser beam was imaged at different positions within the inner annulus containing the CO_2-water mixture. In this configuration, there were three components of the optical windows: (1) the outer quartz tube, (2) the thermally regulated H_2O circulating in the outer annulus, and (3) the sapphire tube. Since one of these components was H_2O, it was necessary to modify the procedure so that water in the inner annulus could be distinguished spectroscopically from water in the window. Consequently, D_2O was used in place of H_2O in most of the mixtures under study (i.e., in the inner

annulus). Figure 3 shows the spectra of H_2O and D_2O in the spectral region under study. Positions of the principal peaks of CO_2 (the Fermi dyad) are also shown to illustrate that all of the key peaks of these three Raman-active components (CO_2, D_2O, and H_2O) can be distinguished when all are present together. Sapphire also gave rise to distinct Raman bands that, with the one exception discussed below, are also sufficiently spaced from the peaks of the solution components to be unambiguous.

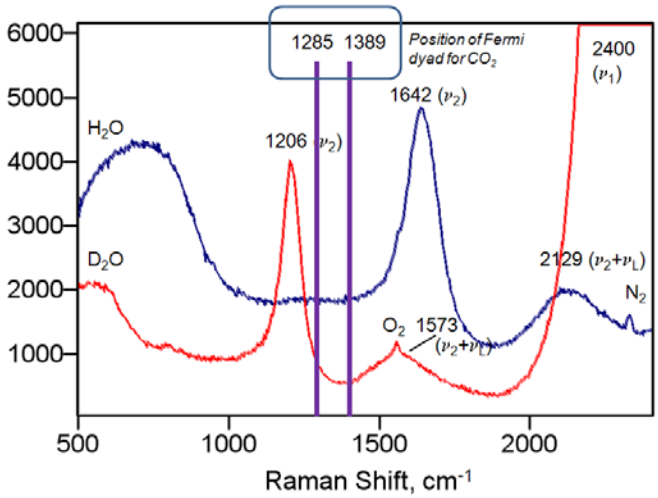

Figure 3. Comparisons of the UV-Raman spectra of H_2O and D_2O, at room temperature and atmospheric pressure, with the principal peaks of CO_2 (Fermi dyad) also shown.

The sapphire tube was purchased from Saint-Gobain (Hiram, Ohio) in a 6-inch length, machined slightly at the ends, and capped with specialized Swagelok (Solon, Ohio) 316 stainless steel fittings at the ends using Viton seals. The specialized fittings allowed a length of ¼ inch outside diameter. stainless steel tubing to be inserted through the center of the sapphire tube (used for carrying one of the circulated water streams) and also accommodated a section of stainless steel tubing at 90° to the sapphire tube (used for filling/emptying the cell with the CO_2-water solution). Approximately 1 inch at each end of the sapphire tube was retained within the fittings, leaving approximately 10 cm exposed for imaging and spectral study. A wider-diameter quartz tube was used as the container for the outer circulated water stream. It was equipped with quartz-tube side ports (for connecting to the circulator) and was sealed to the sapphire tube at the ends with epoxy. Remaining cell parts included 316 stainless steel fittings, valves and tubing purchased from Swagelok Inc. as well as a Cecomp Electronics (Libertyville, Illinois) digital pressure gauge, assembled as shown in Figure 4. An ISCO Inc. (Lincoln, Nebraska) 1000D pump was used to pressurize the cell with the CO_2-water mixtures. The cell assembly was mounted on a floating optical table using position-adjustable Newport Inc. (Irvine, California) stages to provide stability and facilitate alignment of the laser beam on the sample. Lexan blast shields were incorporated for safety. A photograph of the assembled cell (positioned under the UV-Raman microscope) is shown in Figure 5. The volume of the cell and all tubing leading from (but not including) the pump and to a Tescom (Elk River, Minnesota) back pressure regulator, used to control back pressure and empty the cell, was approximately 70 mL. The D_2O used in the study was 99.9% pure and obtained from Sigma-Chemical Company (St. Louis, Missouri), while the CO_2 gas was 99.99% pure and purchased from Polar Cryogenics (Portland, Oregon).

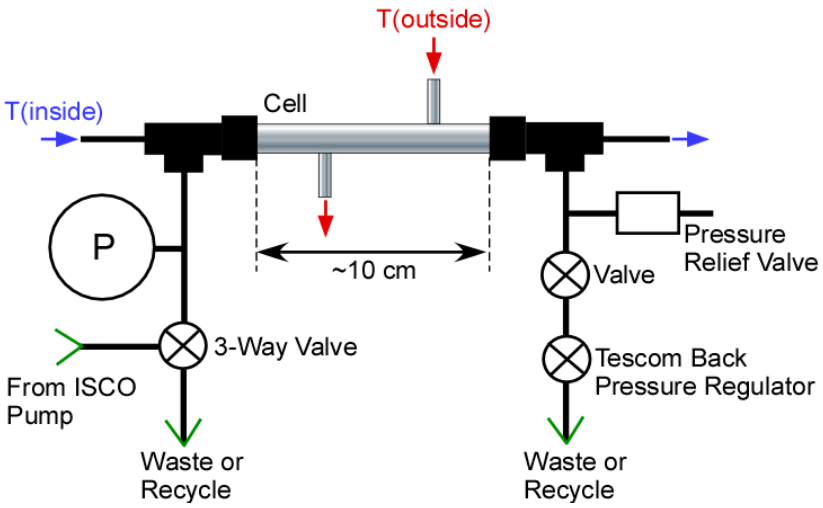

Figure 4. Schematic of the concentric-tube Raman cell within its assembly.

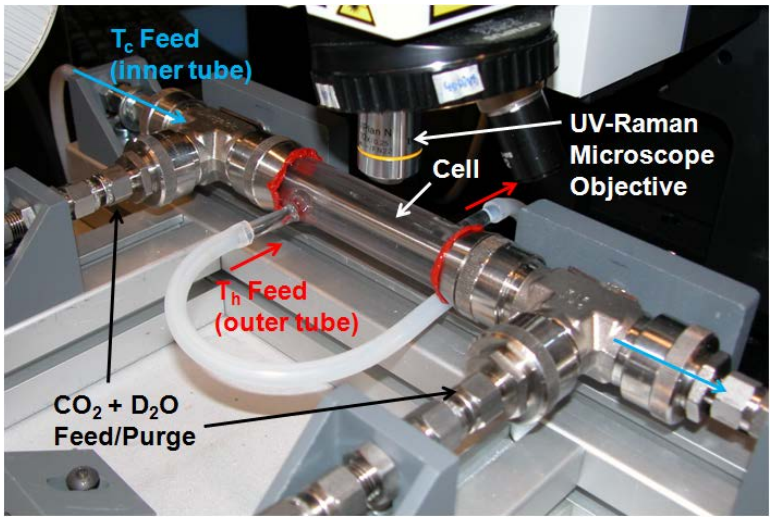

Figure 5. Photograph of the concentric-tube Raman cell assembly positioned under the UV-Raman spectrometer microscope objective.

To minimize specular reflection and elastic scattering from the stainless steel tube (both are potential interferences in Raman spectroscopy), the stainless steel tube was coated with black oxide using a proprietary method similar to "bluing." The resulting coating, consisting of transition metal oxides, was black and gave no significant Raman spectrum in the region of interest. Figure 6 illustrates the degree to which specular reflection was attenuated by the coating.

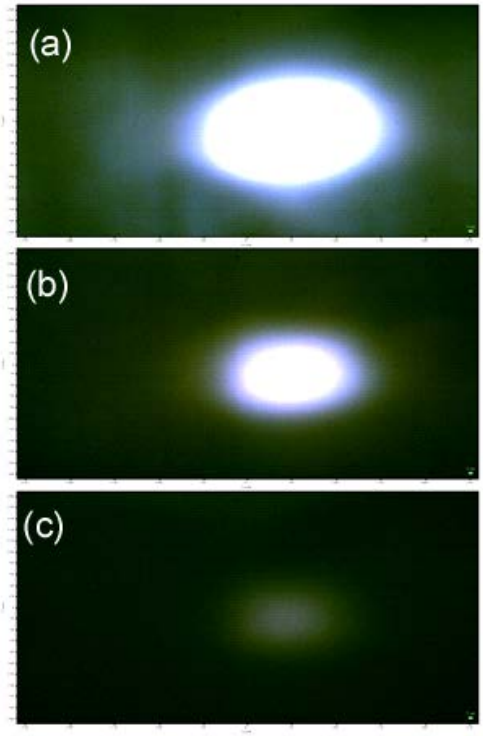

Figure 6. Images of the reflected laser light from the stainless steel tube in the center of the Raman cell, (a) with the incident light focus on the bare steel, (b) with the incident light focused on the steel with a high-temperature air-formed film (held at 600°C overnight), and (c) with the incident light focused on a "blued" steel surface.

2.2 UV-Raman spectrometer

Raman spectra were collected using a Horiba JY (Edison, New Jersey) LabRAM HR (high-resolution) Raman (confocal) microscope system. With a focal length of 0.8 m and dual gratings with groove density of 2400 grooves/mm the instrument can achieve a nominal spectral resolution of 1-2 cm^{-1}. Excitation was provided by the deep-UV 244-nm line of a Lexel (Fremont, California) Model 85-SHG frequency-doubled Ar^{+} ion laser equipped with a non-linear beta barium borate (BBO) crystal. Laser power was 25 mW at the source and approximately 1 mW at the objective. Significant further attenuation of power is expected through the Raman cell. A 10x UV-compatible microscope objective (numerical aperture = 0.25) with a working distance of 15 mm was used. The spectrometer pinhole was kept fairly large, at 400 μm, resulting in less-than-optimal depth and lateral resolution. However, laser throughput was improved with the larger pinhole, giving acceptable band intensities when collected with an exposure time of 500 s. The spectral range was restricted to Raman shift above 450 cm^{-1}. Measurements at lower frequencies were not possible because of the presence of a factory-installed edge filter for eliminating the exciting line. Spectral analysis, including curve fitting, was performed using Thermo Scientific (Waltham, Massachusetts) Grams/32 AI software. Any curve fitting used the Levenburg-Marquardt non-linear peak fitting method (Levenberg 1944) with baseline correction to remove background from Rayleigh scattering or fluorescence. A photograph of the spectrometer with a cell positioned for data collection is given in Figure 7.

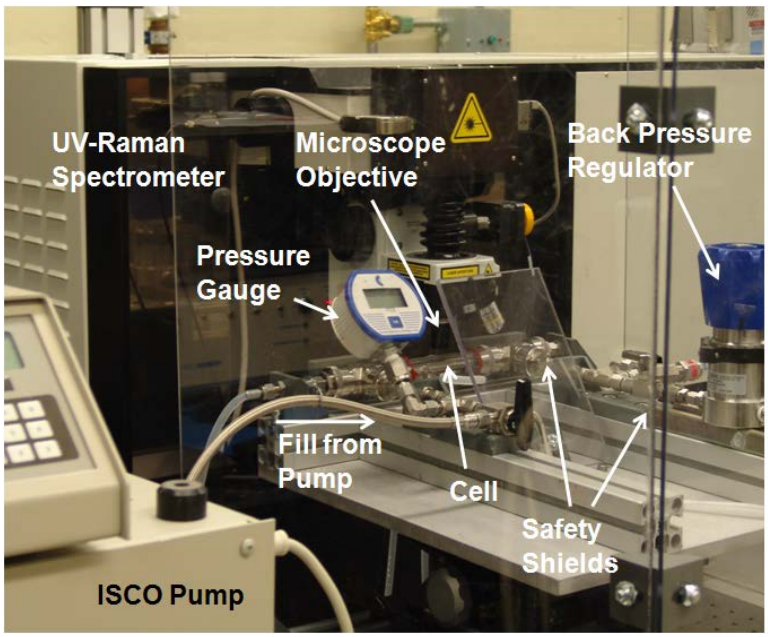

Figure 7. Photograph of the concentric-tube Raman cell assembly, UV-Raman spectrometer, and ancillary equipment.

2.3 Typical experiment and variables

The following procedures were used in the collection of spectra in most of the experiments:

- The pump, then cell, were filled with pure D_2O under ambient conditions and pressurized to the pressure of the experiment, 10 MPa. The cell was then valved off from the ISCO pump.
- The pump pressure was reduced to the pressure of the CO_2 cylinder and the volume of D_2O remaining in the pump was noted. A volume of CO_2 gas at this pressure (approximately 5.8 MPa) was then added to the pump to give the required concentration of CO_2 in the final test mixture. Following this, the pump was sealed off from the CO_2 cylinder and the pump pressure increased to 10 MPa. To help mix the CO_2 and D_2O, the pressure in the pump was dropped back to 5.8 MPa and then returned to 10 MPa, and this procedure was repeated approximately five times.
- The mixture in the pump was allowed to sit overnight so the CO_2 could dissolve in the D_2O at 10 MPa. During this time, the cell itself still contained pure D_2O at 10 MPa.
- On the following day, the valve between the pump and cell was opened, and the mixture in the pump was slowly metered into the cell to replace the pure D_2O in the cell. The metering was done by slowly opening and closing the pressure reducing valve at the exit of the cell. The procedure was performed carefully to minimize any flashing of CO_2 in the cell. Done properly, the solution in the cell remained homogeneous with no gas bubbles or liquid CO_2 separating from solution. (Phase separation was evident by the appearance of a second phase in the sapphire tube.) After flowing about 150 mL through the cell, the cell was considered completely charged with the fluid mixture. The pump remained on and connected to the cell to maintain pressure at 10 MPa throughout the experiment.
- The temperature controllers were turned on and thermostated water was circulated through the two thermal reservoirs at the desired temperatures.

- Raman spectra were collected after waiting at least two hours for thermal equilibration.
- The Raman spectrometer was first calibrated by focusing on the sapphire tube and using the Raman bands of sapphire (e.g., the strong sapphire peak at 746 cm^{-1}).
- The microscope objective was then moved so that the bottom of the sapphire tube was put in visible focus using an objective suited to visible light. This position was defined as z = 0 μm.
- The UV objective was then substituted, with its position configured to retain z = 0 μm, at the focal position without further adjustment of the microscope.
- Raman spectra were acquired as a function of position across the annulus containing the CO_2-D_2O solution. The first measurement was usually obtained at the inside surface of the sapphire tube (z = 0), taken as T = T(outside), or very near to it (z = 200 μm). Subsequent measurements were usually made at increments of 200 μm from this position (here reported as positive values of z) and toward the stainless steel tube (shown to be at z = 2000 μm, as discussed below), where T = T(inside). Because of optical and cell geometry constrains, no independent temperature measurements could be made at the exact positions from where the spectra were acquired. However, calculations predicted that minimal temperature drop occurred across the sapphire and the stainless steel tubes, so the assumption of thermal equilibration between the temperature reservoirs and fluid at z = 0 and z = 2000 μm was considered valid.
- Immediately after collecting Raman spectra in the increasing-z direction, a series of spectra were collected in the decreasing-z direction ending up at the position z = 0, or close to it.

Some experiments employed special procedures as follows:

- To lower the possibility of condensation of water vapor on the outside of the cell, T(outside) was usually kept higher than T(inside). Some experiments used T(inside) greater than T(outside) to make sure that there was no unexpected effect of the direction of the thermal gradient.
- A series of experiments were performed with T(outside) = T(inside) to account for the possibility of any spectral variations across the annulus in the absence of an applied temperature gradient.
- A series of experiments were performed with the outer quartz jacket removed. This permitted the use of CO_2-H_2O instead of CO_2-D_2O mixtures since there was no spectral interference from the H_2O in the outer thermal reservoir. The configuration had the added advantage of much higher signal-to-noise since there was no loss of signal by scattering from the quartz, reservoir water, and the accompanying interfaces. In these experiments, T(outside) was taken at the value measured on the outside of the sapphire tube with a thermocouple.
- A series of experiments (2-position measurements) were performed on a given CO_2-D_2O mixture in which spectra were acquired at two positions (e.g., z = 500 μm and 2000 μm) with varying temperature gradients imposed across the cell. T(inside) was held constant while T(outside) was changed). These experiments provided data on a single mixture over a wider variety of thermal conditions than those in which more extensive data as a function of z were acquired.
- Mixtures of D_2O dissolved in $scCO_2$, instead of CO_2 dissolved in D_2O or H_2O, were also performed. These were considered more challenging for two reasons: (1) the solubility of D_2O in $scCO_2$ was about an order of magnitude less than CO_2 in D_2O (mole fraction 10^{-3} vs. 10^{-2}) under the same conditions of temperature and pressure (i.e., 10 MPa, and 12°C to 45°C), (2) with mostly $scCO_2$, the

amount of stored energy in the cell increased significantly and, with it, the level of safety concerns. Nevertheless, experiments of this sort were still conducted to determine if D_2O could be detected at these concentrations (the stronger C-D stretching bands were used in an attempt to compensate for the lower concentration) and, if so, whether a Soret effect was observed at "the other end" of the phase diagram of the mixture.

- Some experiments used deuterated brine (D_2O + 1 M NaCl) instead of pure D_2O.

The key variables in this study were:

- ***Position*** (z) relative to the top of the sapphire tube. Values of z with increments of 200 μm were usually used.
- ***Direction of scan***, i.e., either increasing z or decreasing z. In most cases, data were collected in both directions during the same experiment.
- ***Values of temperature*** and ***size of temperature gradient***. In most cases, a given experiment spanned a temperature range below the critical point of CO_2 (31.04^{o}C) or above it, to avoid the effects of density fluctuations (on the relative intensities of the Fermi dyad components in CO_2) known to occur at this temperature. A series of two-position experiments were also conducted where the temperature gradient was changed in increasing increments, while making measurements at only two positions in the cell.
- ***Direction of temperature gradient***, i.e., T(outside) > T(inside) or T(inside) > T(outside).
- ***Concentration of CO_2*** in the mixture (i.e., mole fraction CO_2 or X(CO_2)). In most cases the concentration was kept below the solubility of CO_2 in H_2O (approximately 0.028 mole fraction under these conditions). Some experiments were run with H_2O saturated with CO_2. A few experiments were also performed with scCO_2 saturated with D_2O (i.e., X(H_2O) ~ 0.003). A solution of CO_2 dissolved ***in brine***, D_2O + 1 M NaCl, was also tested.
- A few experiments were conducted where ***pressure was varied*** while holding the temperature values constant.

3.0 Results

3.1 Assessment of Raman cell

3.1.1 Position of the microscope objective vs. focal point of the measurement

During preliminary testing, it became clear that increments in the vertical position of the microscope objective (denoted by the z value) did not correspond to increments in the position of the focus spot within the annulus of the cell. This is attributed to refraction of the laser beam through the three components of the window (quartz tube, water layer, and sapphire tube) between the objective and the fluid. It was estimated by Snell's law that the major deviation was caused by refraction through the relatively thick sapphire tube. Calculations indicated that a z value of 3000 μm actually corresponded to a distance of 2000 μm within the fluid, and this was born out by experiment. First, when using white light illumination, visual images of a "surface" were obtained at approximately these two locations (i.e., z = 0 and 2000 μm). Second, as shown in Figure 8 (for an experiment with $X(CO_2)$ = 0.0027, P = 10 MPa, and T(outside) = T(inside) = 40°C), the total integrated intensity of peaks (from both CO_2 and D_2O) at z = 0 μm is roughly half its maximum value and the sapphire peaks show a markedly sudden decrease in intensity. For z > 2000 μm, the total signal drops significantly due to focusing beyond the stainless steel tube, but does not completely disappear because there is still some out-of-focus Raman scattering.

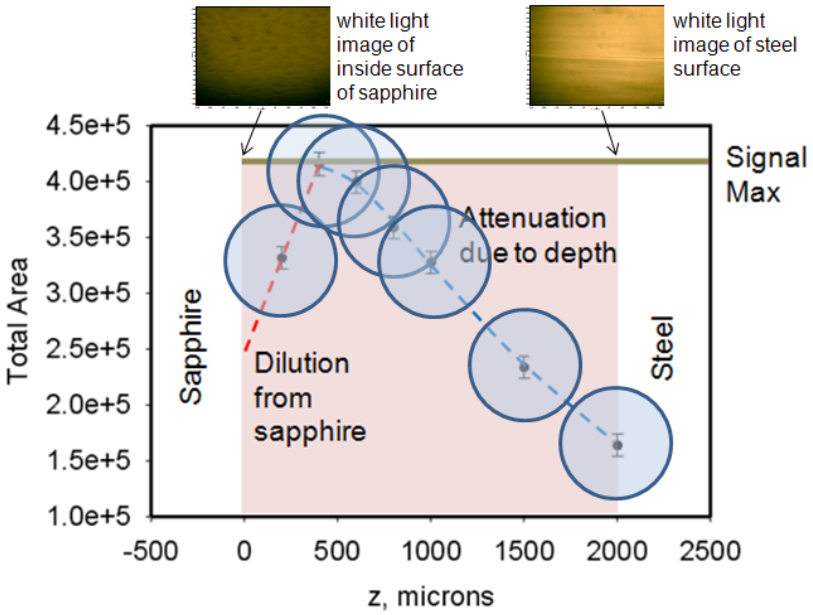

Figure 8. Total Raman scattering signal strength (from both CO_2 and D_2O) as a function of the position of the objective (z value). In relationship to position within the annulus, z = 0 μm corresponds to the inside surface of the sapphire tube, whereas z = 2000 μm is near the outside surface of the stainless steel tube. The photographs are white-light images at these two positions. Circles around each point indicate the approximate sampling volumes.

In each experiment, Raman spectra were acquired between z = 0 and z = 2000 μm (pink region in Figure 8), usually at increments of z = 200 μm. Given that width of the annulus was 3.4 mm, that the

range of z-values relevant to the annulus was 2000 μm, and also that the relationship between the two scales is probably non-linear, it was difficult to correlate exactly the position of the focused beam with the z value. However, the important variable in this study was temperature and not position. For this reason, we took the following approach in our analysis: (1) the spectrum corresponding to T(outside) was taken as the spectrum at z = 0 μm; (2) the spectrum corresponding to T(inside) was taken as the spectrum at z = 2000 μm; and (3) the spectra for positions with z between 0 and 2000 μm (pink region in Figure 8) were deemed to vary continuously between these two limits. To estimate the Soret coefficient, we used the spectra at the end points. If spectra at these positions could not be obtained directly, they were determined by extrapolation from the observed variations in the spectra within the annulus.

3.1.2 Estimate of sampling volume

Figure 8 also illustrates the effects of the two principal causes of signal attenuation in the Raman cell. The first was important for z values between 0 and 500 μm, where the Raman scattered signal was "diluted" by the contribution of the sapphire tube. Peaks from the sapphire (including the very strong one at 746 cm^{-1}) were still strong in this region due to contribution from significant out-of-focus scattering. At positions greater than 500 μm, almost all of the signal came from the fluid. The results not only explain the loss of signal near the sapphire tube, but help establish an approximate volume from which most of the scattering occurred. In the present case, the volume (approximated by a sphere) had a likely diameter of about 500 μm (or about 25% of the annulus distance). This suggests that increments less than z = 500 μm exhibit marked overlap of scattered signals. Since the total thickness of the annulus is 2000 μm, about 4 unique measurements were therefore possible across it, sufficient for a reasonably good estimate of a significant gradient in any of the spectral parameters. To illustrate this, a circle with a diameter of 500 μm is drawn around each data point in Figure 8. Even though the circles overlap, there is "enough z" represented to capture the variation across the annulus. The same could be argued for individual spectra collected at these positions.

For z values greater than about 500 μm but less than 2000 μm, the total signal strength again decreases. This is attributed to additional scattering of the Raman light as it *returns* to the objective from positions deep within the sample. The deeper the focal point, the more significant the losses will be from this phenomenon.

Finally, it is important to note that any changes in the *ratios of individual band intensities* (e.g., CO_2 band relative to D_2O band) arising from variation in composition of the mixture across the annulus should be unaffected by variations in the total Raman scattering signal. Consequently, the only effect that variations in the *total spectral intensity* will have on determining Soret coefficient is with regard to signal-to-noise. A smaller total scattering intensity, in most cases, resulted in a smaller signal-to-noise and a greater uncertainty in measured or calculated spectral parameters.

3.2 Raman spectra

3.2.1 Experiments on D_2O containing CO_2 below saturation

Raman spectra were obtained as a function of distance (related to the z value) across annulus containing the CO_2 + D_2O mixture with concentrations of CO_2 in D_2O below its solubility value. For the

conditions of this study, this value corresponds to $X(CO_2)$, approximately 0.028. The specific compositions studied in this work were $X(CO_2)$ equal to 0.0014, 0.0027, and 0.0054, corresponding to approximately 5%, 11%, and 22% of saturation. Spectra are shown in Figures 9 and 10 as a function of the z value $X(CO_2)$ = 0.0054, and 0.0027, respectively, and with two different temperature gradients. The results for 0.0014 showed similar trends but the CO_2 peaks were extremely weak. Spectra were also collected with different temperatures and temperature gradients applied. Generally, for a given experiment, the temperature gradient was maintained on one or the other side of the critical temperature, 31.1°C. For measurements below the critical point, the reservoir temperatures were 30°C and 12°C (clathrates form below 12°C); for measurements above the critical point, the temperature reservoirs were at 33°C and 45°C (the approximate upper limit for the cell). Spectra shown in Figures 9 and 10 are for one of the temperature gradients for each composition. Results for other temperature gradients showed the same results. Spectra collected upon increasing the z value are shown, although spectra for decreasing z, with all other conditions the same, were essentially identical.

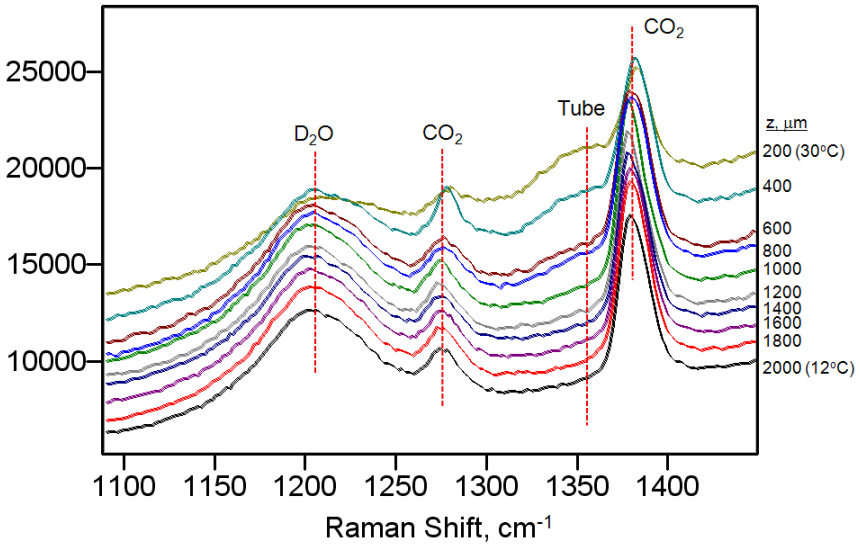

Figure 9. UV-Raman spectra as a function of position within the annulus (in terms of the microscope position, z), with $X(CO_2)$ = 0.0054, T(inside) = 12°C and T(outside) = 30°C. Higher temperature is outside. The spectra were acquired in the direction of increasing z. CO_2 is a liquid under these conditions.

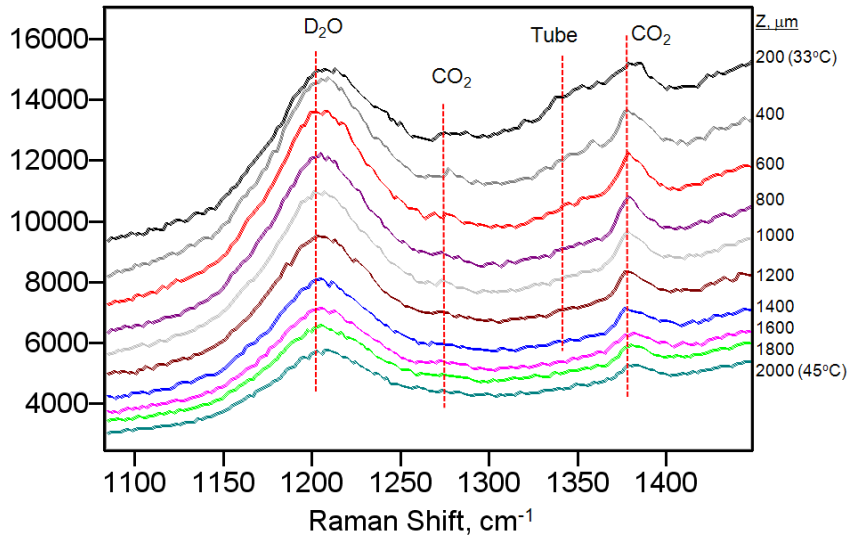

Figure 10. UV-Raman spectra as a function of position within the annulus (in terms of the microscope position, z), with X(CO_2) = 0.0027, T(inside) = 45°C and T(outside) = 33°C. The higher temperature is inside. The spectra were acquired in the direction of increasing z. CO_2 is supercritical under these conditions.

Each spectrum in Figures 9 and 10 contains three bands of interest: the two peaks corresponding to the Fermi dyad of CO_2, positioned at approximately 1273 and 1377 cm^{-1}, respectively, and the band at 1203 cm^{-1} from the bending mode of D_2O. The band positions are a little lower than those indicated in Figure 3 for neat compounds, especially the Fermi dyad of CO_2. The variance, which was reproducible for all mixtures with concentrations of CO_2 below saturation, was surprising and its cause unknown at this time. However, as discussed later in this report, the peak frequencies from mixtures with high scCO_2 concentrations are closer to the values in Figure 3, suggesting the likely explanation involves molecular interactions, arguably different for CO_2 surrounded by other CO_2 molecules (at high CO_2 concentration) and CO_2 surrounded by water molecules (at low CO_2 concentration).

A band at approximately 1350 cm^{-1} also appears in the spectra for measurements taken close to the sapphire tube (small z). The Raman spectrum of sapphire does not normally have a peak at this frequency, however no published spectra of sapphire with UV excitation have been previously reported, to our knowledge. It is possible that the peak is due to sapphire, observed here because of resonant enhancement in the UV. Another possibility is that it arises from a carbon impurity associated with the surface of the sapphire. Amorphous carbon has a strong peak due to sp^3 carbon (C-C stretch) at approximately 1360 cm^{-1}. Regardless of the cause, this peak appears to be associated with the surface of the sapphire and is disregarded in this study. Another observation that may be of fundamental significance, but is not addressed further in this study, is the apparent asymmetry of some of the peaks, particularly the stronger Fermi dyad component at 1377 cm^{-1}, in spectra of mixtures where the CO_2 peaks are weak relative to D_2O (see Figure 10). This characteristic of the Fermi dyad probably relates to molecular interactions and how they change with concentration, particularly when CO_2 concentrations are low. Similar to the effect on peak frequencies, reported above, a definitive explanation of the band shape is not forthcoming from this study, nor is it within its scope.

The primary objective of this study was to determine whether changes in the Raman spectra occur as a function of position across the annulus when a temperature gradient is applied. ***As indicated by Figures 9 and 10, the spectra exhibit no obvious changes as a function of position (other than overall intensity changes and changes related to the contribution from extraneous bands) for a given solution composition. This is the first qualitative evidence that a Soret effect is not inordinately pronounced for solutions studied in this work.***

Several characteristics of the spectra, including relative peak areas, intensities and band shapes, were scrutinized quantitatively and none showed significant change across the annulus. Figure 11, for example, shows the variation of the ratio of the intensity of the strongest peak in the Fermi dyad of CO_2 (1377 cm^{-1}) to the intensity of the peak due to D_2O (1203 cm^{-1}) for solutions with $X(CO_2)$ = 0.0014 and 0.0027. Figure 12 shows the variation in the same ratio for solutions with $X(CO_2)$ = 0.0054. Data for several temperature gradients are shown, as are data from experiments with increasing-z and decreasing-z, and with the gradient imposed in two directions (higher temperature inside and outside). The results all point to the same conclusion: regardless of the way the experiment was performed, there was no significant variation of the intensity ratio across the annulus for a given value of $X(CO_2)$. (Variation of the ratio with the $X(CO_2)$ value of each experiment is discussed later in this report.) Uncertainties were taken as twice the standard deviation of the intensity of peaks calculated from the curve fits. Note that the uncertainties are much greater for small z. This is due to the relative weakness of the bands in spectra acquired at these locations, as well as the need to subtract a correspondingly larger background with stronger extraneous bands (i.e., from the sapphire tube) in determining the CO_2 and D_2O peak intensities.

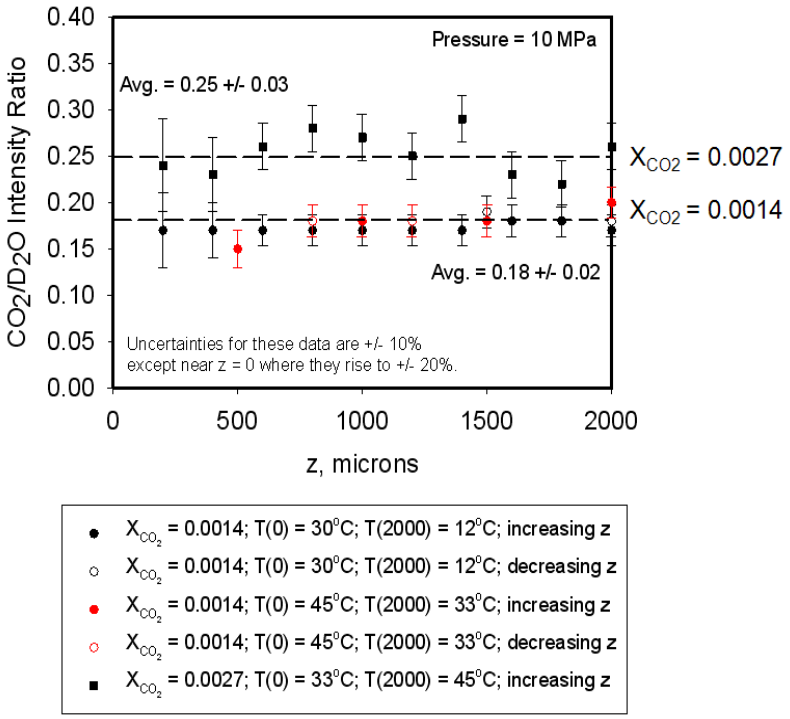

Figure 11. CO_2/D_2O peak intensity ratio calculated from the Raman spectra as a function of position for $X(CO_2)$ = 0.0014 and 0.0027, with different temperature gradients and direction of scan.

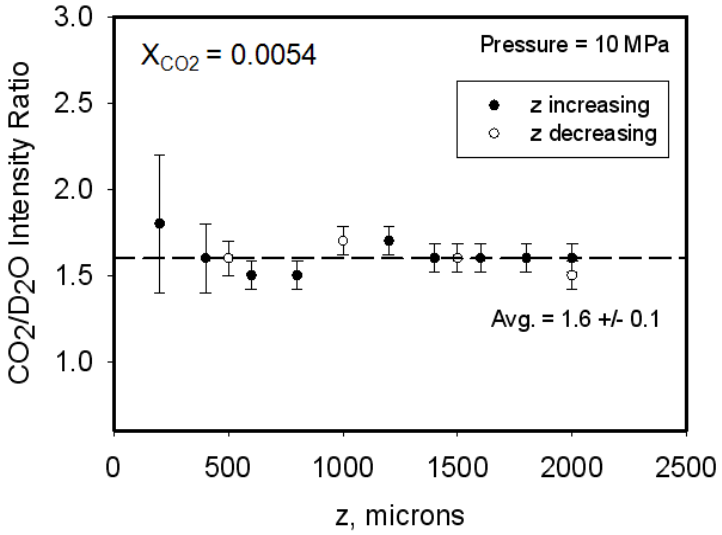

Figure 12. CO_2/D_2O peak intensity ratio calculated from the Raman spectra as a function of position for $X(CO_2)$ = 0.0054, T(outside) = 30°C and T(inside) = 12°C, in both increasing- and decreasing-z directions.

Spectra as a function of z were also acquired in a series of experiments where the same temperature was imposed on both sides of the annulus, i.e., T(outside) = T(inside). Results from two of these studies, at 23°C and 40°C, are shown in Figure 13. The intended purpose of these "isothermal" measurements was to address questions that might arise in the event the relative Raman intensities showed a significant and reproducible trend as a function of position within the annulus. In particular, could this variation be due to something other than the temperature gradient? Given the lack of variation shown in Figures 11 and 12, the results in Figure 13 are expected, and therefore, somewhat academic. They also show no significant difference in the Raman intensity ratio as a function of position across the annulus.

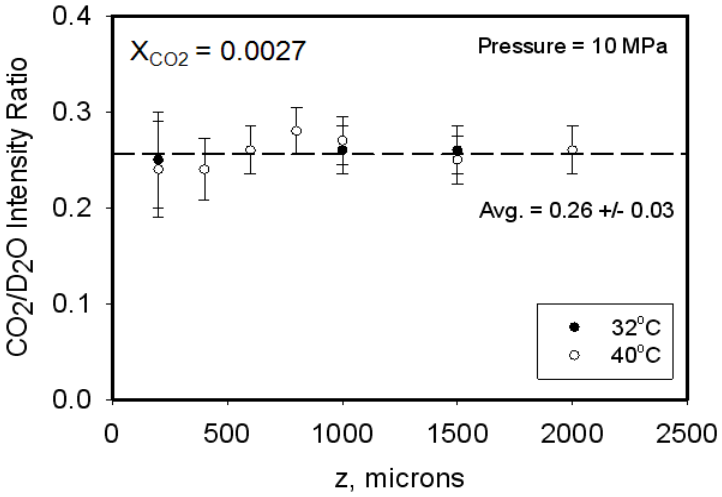

Figure 13. CO_2/D_2O peak intensity ratio calculated from the Raman spectra as a function of position for $X(CO_2)$ = 0.0027 with T(outside) = T(inside) at 32°C and 40°C. Spectra were collected in the direction of increasing z.

As a further confirmation of the lack of significant variation in the relative Raman intensities across the annulus, a series of "2-point temperature ramps" were performed. In this study, Raman spectra of a CO_2-D_2O mixture were obtained at only two positions (z values) within the annulus containing a given solution but using different temperature gradients. For the data in Figure 14, T(outside) was held at 45°C and T(inside) was varied as indicated. A Raman spectrum was acquired at the two positions for each gradient, after allowing sufficient time (about 2 hours) for thermal equilibration. The spectra shown in the figure were background-adjusted and intensity-normalized so the D_2O peak overlapped for measurements at the two positions (different color correspond to the different temperature gradients and positions). Inspection of the CO_2 peaks under these conditions indicates no significant change in the spectra results from changing the temperature gradient over a significant range of values, other than the single case (red spectrum in Figure 14) that appears to have a slightly smaller background toward higher frequencies. The results are consistent with the spectra in Figures 9-13 that showed no significant variation in the relative intensities of the CO_2 and D_2O peaks across the annulus.

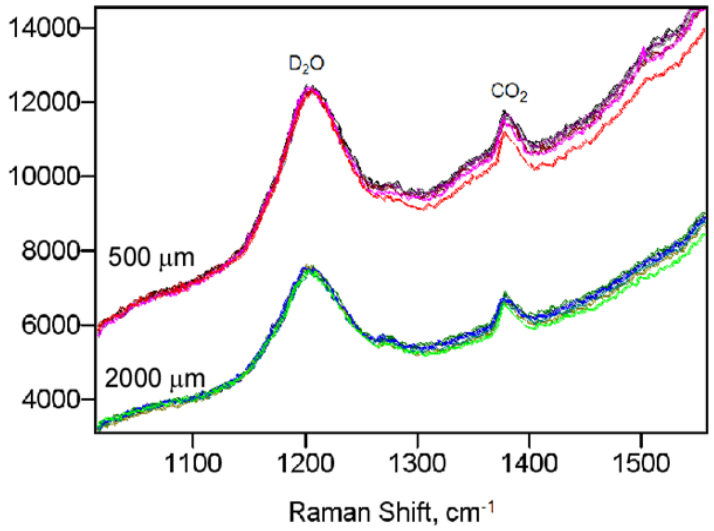

Figure 14. UV-Raman spectra at two positions within the annulus with X(CO_2) = 0.0027 and T(outside) = T(0 μm) = 45°C and with varying T(inside). Spectra are shown for T(inside) = T(2000 μm) = 45°C, 40°C, 35°C, 30°C, 25°C, and 20°C.

3.2.2 Experiments on D_2O + 1 M NaCl containing CO_2 below saturation

Results similar to the aforementioned experiments, but using 1 M NaCl in D_2O instead of pure D_2O, are shown in Figure 15. The presence of the NaCl does not appear to make a difference in the response of the Raman intensity ratios to a temperature gradient imposed across the annulus. Similar to results without the NaCl, there is no significant change in the intensity ratios.

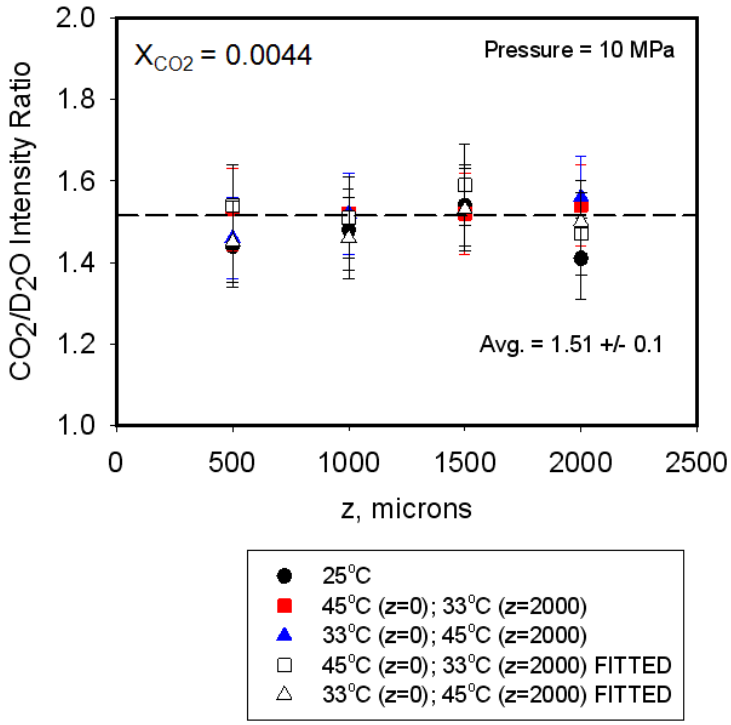

Figure 15. CO_2/D_2O peak intensity ratio, for solutions containing 1 M NaCl, as a function of position with $X(CO_2)$ = 0.0044, and various temperature gradients. Open symbols are ratios for the same experiments as the corresponding closed symbols, but were calculated using integrated intensities from curve fitting results.

3.2.3 Varied pressure study

Raman spectra were also acquired in an experiment with $X(CO_2)$ = 0.0027 and temperature held constant at 40°C (above the critical temperature with no temperature gradient), but where the cell pressure was changed. The purpose of this experiment was to see if pressure had an effect, independent of concentration, on the relative intensities of the CO_2 and D_2O bands. The lowest pressure studied was 1 MPa, where the solubility of CO_2 in water at 40°C is approximately 0.004. Since $X(CO_2)$ = 0.0027, a single phase was maintained throughout this study and this was confirmed by the absence phase separation in the cell at any time. Spectra were measured in the center of the cell (z = 1000 μm) for each pressure. The results, shown in Figure 16, indicate that there was no significant variation in the CO_2/D_2O intensity ratio with cell pressure, for a single-phase solution, over the range of pressures studied in this work.

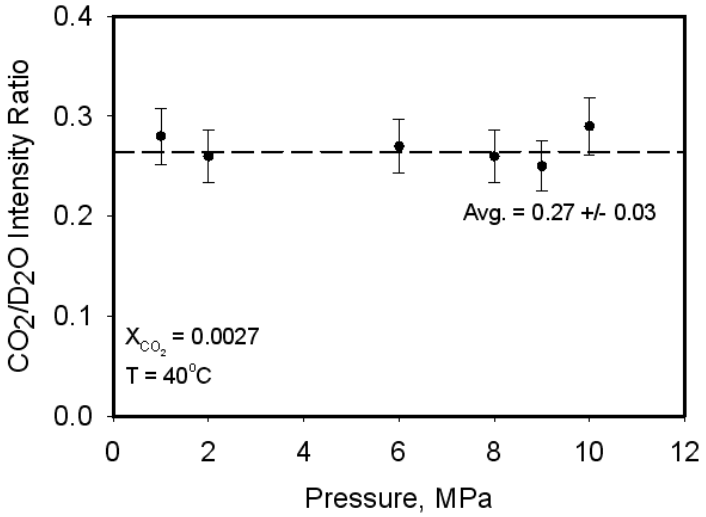

Figure 16. CO_2/D_2O peak intensity ratio, for solution with $X(CO_2) = 0.0027$ and T(inside) = T(outside) = 40°C, as a function of cell pressure.

3.2.4 H_2O containing CO_2 at saturation

Raman spectra as a function of position across the annulus, between T(inside) = 11°C and T(outside) = 15°C, were also obtained for a solution of H_2O saturated with CO_2 at 10 MPa and the two temperatures, roughly corresponding to $X(CO_2) = 0.029$ and 0.028, respectively. The results are shown in Figures 17 and 18.

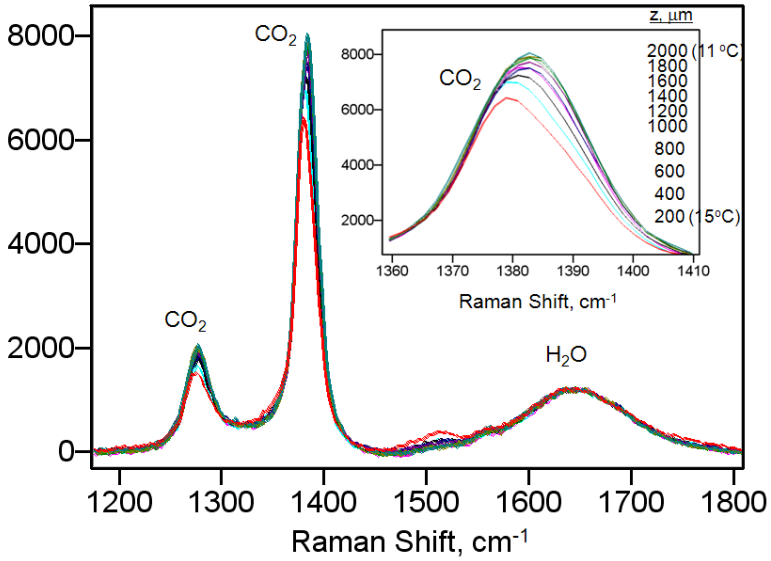

Figure 17. UV-Raman spectra as a function of position within the annulus (in terms of the microscope position, z), for H_2O saturated with CO_2, i.e., $X(CO_2) \sim 0.028$. T(inside) = 11°C and T(outside) = 15°C. Spectra were acquired in the direction of increasing z. Spectral intensities are normalized with respect to the H_2O peak at 1640 cm-1.

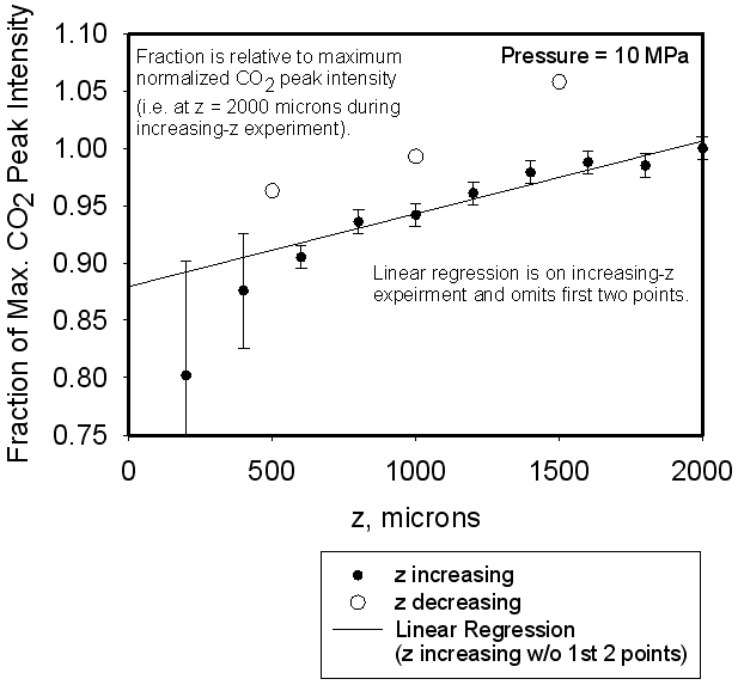

Figure 18. $CO_2/(CO_2 + D_2O)$ peak intensity fraction calculated from the Raman spectra as a function of position, for H_2O saturated with CO_2, i.e., $X(CO_2) \sim 0.028$. Results are shown for measurements made with both increasing and decreasing z. Linear regression in the absence of the two low-z points is shown.

H_2O was used instead of D_2O in these studies because they were performed in the absence of the outer temperature reservoir. T(outside) was controlled by the air temperature and measured with a thermocouple as equal to 15°C. Unlike the experiments on solutions with lower concentrations of CO_2, these results show a clear trend with changing z. The ratio of intensities of the CO_2 to H_2O peaks increases in going from the higher temperature side, T(outside) or z = 0 μm, to the lower temperature side, T(inside) = 11°C or z = 2000 μm. Because the CO_2 peaks are so large in this study, it was more prudent to plot the CO_2 peak intensity (1389 cm^{-1}) in terms of the fraction of total intensity of the H_2O (1640 cm^{-1}) + CO_2 (1389 cm^{-1}) peaks, rather than using the CO_2/H_2O intensity ratio. The results, shown in Figure 18, clearly illustrate the significant and consistent trend in the relative size of the CO_2 peak as function of position, and therefore temperature, within the annulus. Assuming the relative intensity scales with concentration, Figure 18 indicates a preferential segregation of CO_2 to the colder side of the annulus in this experiment.

3.2.5 $scCO_2$ containing D_2O at saturation

Experiments were also performed on the other side of the phase diagram of the CO_2-water solution, i.e., with D_2O dissolved in $scCO_2$. The CO_2 was the majority species in these studies and was in the supercritical state. Since the solubility of D_2O in $scCO_2$ is much lower than CO_2 in D_2O, i.e., $X(D_2O) = 0.003$ compared to $X(CO_2) = 0.028$ to 0.029, under similar conditions, using the C-D stretching mode, instead of the much weaker bending mode, for quantitative analysis seemed prudent. The results of a series of measurement across the annulus of one of these studies, with T(outside) = 40°C and T(inside) = 32°C, are shown in Figure 19.

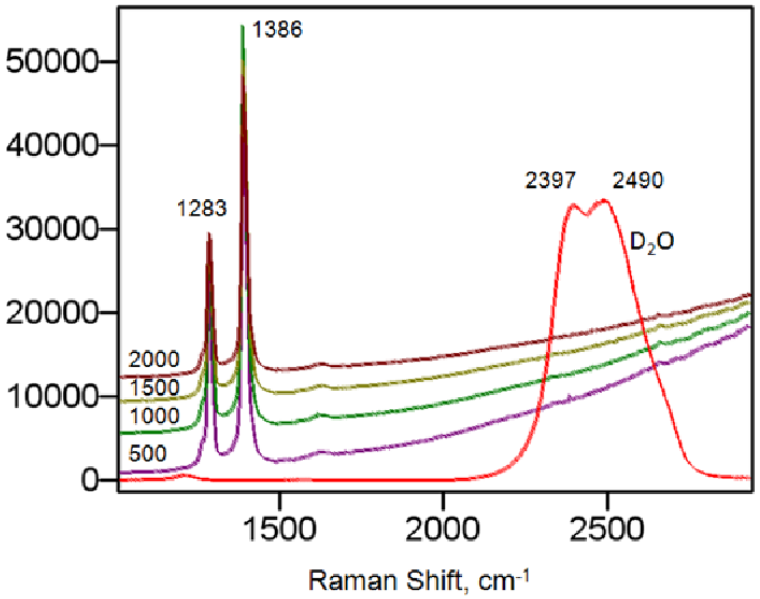

Figure 19. UV-Raman spectra as a function of position within the annulus for solutions of $scCO_2$ containing D_2O at saturation (i.e., $X(D_2O) \sim 0.003$). T(inside) = 32°C and T(outside) = 40°C.

As expected from the concentration, the CO_2 Fermi dyad is very strong in these spectra. Unfortunately, the D_2O peaks are also extremely weak. The expected position of the C-D stretching bands, around 2500 cm^{-1}, is illustrated by the spectrum of neat D_2O that is also plotted in the figure. It is difficult to discern even the slightest contribution from these modes to the spectra obtained from the solution, precluding the determination of the relative intensities of bands from the two components and, consequently, concentration trends across the annulus.

4.0 Discussion

4.1 Solutions of CO_2 in D_2O with CO_2 below saturation

Raman spectra showed no significant variation with respect to the relative intensities and areas of peaks associated with CO_2 and D_2O as a function of position within the cell annulus between the two imposed temperatures, regardless of the concentration of CO_2, as long as it was below saturation. The behavior was obtained independent of the direction of the scan (increasing or decreasing z), the size of the temperature gradient (between 11°C and 45°C), whether the data was collected below or above the critical temperature of CO_2, the direction of the temperature gradient (higher temperature or colder temperature on the outside), pressure (up to 10 MPa), or in the presence of 1 M NaCl. These results argue to the presence of no detectable Soret effect, corresponding to $S_T \sim 0$ within the uncertainty of the measurements.

An estimate of uncertainty in S_T can be obtained by inspection of the uncertainties in the intensity ratio vs. z-position plots. As illustrated in the case of the study with X(CO_2 = 0.0014), T(outside, z = 0 μm) = 30°C and T(inside, z = 2000 μm) = 12°C, shown in Figure 20, straight lines are easily drawn to bracket the error bars in an experiment. We now make use of Equation (3), after rearranging and integrating between the two temperatures T_o = T(outside, z = 0 μm) = 30°C and T = T(inside, z = 2000 μm) = 12°C where concentrations are c_o and c, respectively:

$$\ln\left(\frac{c}{c_o}\right) = -S_T\left(T - T_o\right) \tag{4}$$

or, in terms of the absolute magnitude of S_T:

$$\left|S_T\right| = \left|\left[\frac{1}{\left(T - T_o\right)}\right]\ln\left(\frac{c}{c_o}\right)\right| \tag{5}$$

Applying Equation (5) to the endpoints of the error-bracketing lines in Figure 20 gives an estimate of the maximum slope of the relationship (assuming linearity) as well as an estimate of the ratio of the intensities of the CO_2 and D_2O peaks at T_o = T(outside, z = 0 μm) and T = T(inside, z = 2000 μm). Since the concentration of CO_2 is always small, the intensity ratios approximate the mole fraction of CO_2 in D_2O and can be substituted for the concentrations in Equation (5). Substituting these ratios, 0.124 and 0.210, and the respective temperatures, 30°C and 12°C, gives:

$$\left|S_T\right|_{\max} = \left|\left[\frac{1}{(12 - 30)}\right]\ln\left(\frac{0.210}{0.125}\right)\right| = 0.03 \tag{6}$$

Similar results are obtained from the uncertainty values in the other plots, providing a reasonable estimate of the minimum absolute value for S_T than can be measured in these experiments. In conclusion, the results of this study indicate that

$$-0.03 < S_T < 0.03 \qquad (7)$$

If the absolute magnitude of S_T is smaller than 0.03, it is unlikely that it could be measured using the experimental approach employed here.

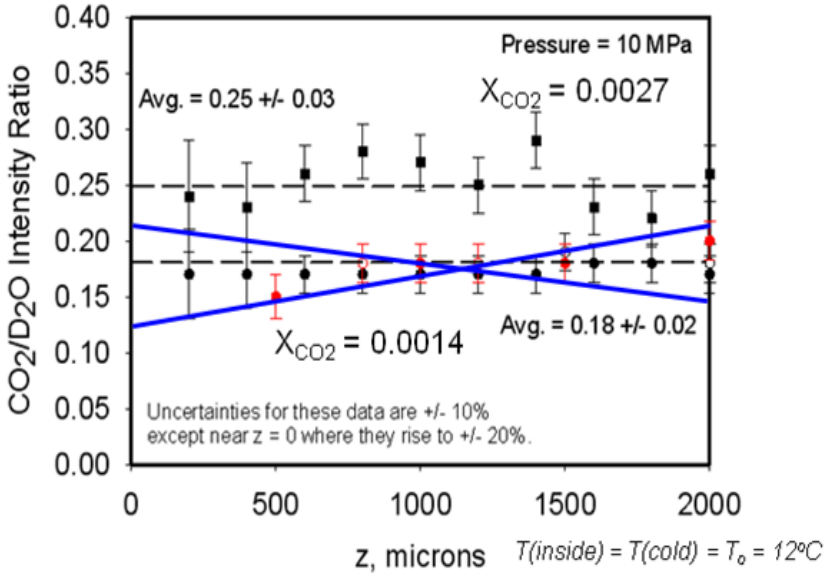

Figure 20. Re-plot of Figure 11 showing straight lines fitted by eye to limits of error bars of the data for $X(CO_2) = 0.0014$.

On the other hand, the results indicate that solutions of CO_2 dissolved in water do not exhibit S_T values as large as those determined for some other mixtures near their critical point of one of the components. Kempers (Kempers 2001) reported values of the thermal diffusion factor, α_T, significantly above 10 for mixtures of methane and propane above the critical point of methane. Given that α_T is related S_T in Equation (3) by $S_T \sim \alpha_T/T$ for dilute solutions, similar values of α_T in our experiments would have led to $|S_T| > 0.03$ (using an average temperature of 35°C). The sensitivity analysis performed above indicates that values of S_T of this magnitude should have been observable with the experimental approach used here. Consequently, it appears that solutions of CO_2 dissolved in water solutions do not exhibit the inordinately large Soret effect of other mixtures under conditions near the critical point of one of the components. This could be partly attributed to the low concentration of the "supercritical" component CO_2 compared to mixtures studied by Kempers where components were present at mole fractions exceeding 0.1.

4.2 Solutions of H_2O saturated with CO_2

Figures 17 and 18 seem to suggest the presence of a Soret effect in solutions of H_2O containing CO_2 above its solubility. The peak intensity parameter related to CO_2 is clearly smaller close to z = 0 μm (where T = 15°C) than it is near z = 2000 μm (where T = 11°C). The slope of the line connecting the two limiting positions is positive. However, it is important to remember that these experiments were conducted with excess CO_2 present. The H_2O phase was saturated with CO_2 at all temperatures and, since all temperatures were below the critical temperature of CO_2, the excess CO_2 was in the form of a

secondary liquid phase. For this reason, it seems more likely that the variation in Figures 16 and 17 is due to the relationship between solubility and temperature (i.e., position), rather than kinetic parameters. To check this possibility, we compared the fractional variation in concentration with temperature observed in this experiment with that expected from the variation in solubility.

Using the endpoints of the data in Figure 18, shown again in Figure 21, and substituting intensities for concentrations as discussed previously,

$$\frac{\Delta c / c_o}{\Delta T} = \frac{1}{T - T_o}\left(\frac{c - c_o}{c_o}\right) \approx \frac{1}{T - T_o}\left(\frac{I - I_o}{I_o}\right) = \frac{1}{11 - 15}\left(\frac{1 - 0.876}{1}\right)$$
$$\frac{\Delta c / c_o}{\Delta T} \approx -0.03 \pm 0.01\,^{o}C^{-1} \qquad (8)$$

Performing the same calculate using solubility data for CO_2 in H_2O at 10 MPa between 12°C and 15°C (Spycher 2002) gives

$$\frac{\Delta c / c_o}{\Delta T} = \frac{1}{T - T_o}\left(\frac{c - c_o}{c_o}\right) \approx \frac{1}{12 - 15}\left(\frac{0.001}{0.028}\right)$$
$$\frac{\Delta c / c_o}{\Delta T} \approx -0.01 \pm 0.01\,^{o}C^{-1} \qquad (9)$$

A good case is made from the above comparative calculations that the trend in CO_2 concentrations within the annulus, in the case of H_2O saturated with CO_2 and excess liquid CO_2 present, is a simple consequence of the variation in solubility of CO_2 as a function of temperature.

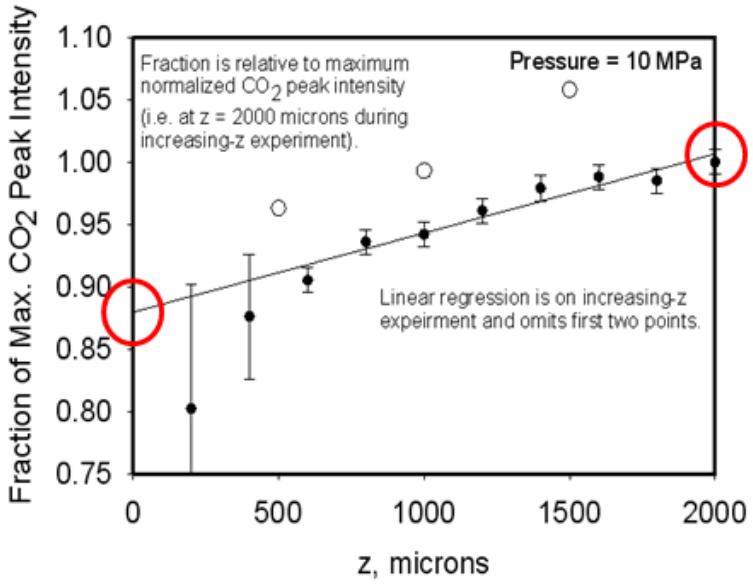

Figure 21. Re-plot of Figure 17 noting intensity values at z = 0 μm and z = 2000 μm that were used to compare the observed variation with temperature to predictions based on solubility.

4.2 Concentration calibration plots

The final calculations performed in this work concern the values of the relative Raman intensities measured over the course of several experiments with different mole fraction CO_2. Values of the intensity ratios (for the strongest peak of CO_2 to the D_2O or H_2O peak) were amassed and plotted versus the mole fraction of CO_2 in each mixture. Since minimal variation in concentration occurred within the annulus for experiments where a temperature gradient was applied, the ratios from both isothermal experiments and experiments with a temperature gradient were all used. The ratios were converted to the fraction of total intensity associated with CO_2 (to be slightly more quantitative relative to concentration) and results are shown in Figure 22.

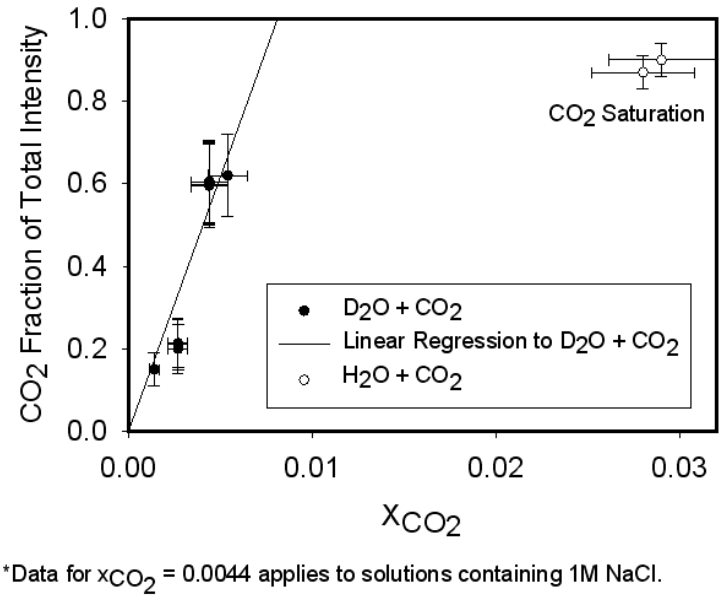

Figure 22. Plot of the fraction of total Raman scattering intensity attributed to CO_2 versus the mole fraction of CO_2 in the mixture as calculated from the quantities used in preparation.

As shown in Figure 22, the CO_2 intensity fraction scales linearly with the mole fraction of CO_2 for concentrations less than about 0.005. When the values for the CO_2-saturated solutions are included (at two temperatures), significant non-linearity is observed. The non-linearity is due to two factors. First, the CO_2-saturated solutions contained H_2O instead of D_2O and, consequently, the H-O-H bending mode instead of the D-O-D bending mode was used. Slight differences between the scattering cross sections for H_2O and D_2O may exist. Second, and most important, the CO_2 Fermi dyad has a significantly greater scattering cross section than the H-O-H bending mode. The impact of this difference is illustrated by calculations for the two extreme of CO_2 concentration as given below:

Low concentration of CO_2: $$\frac{c_{CO_2}}{c_{CO_2}+c_{H_2O}} \approx \frac{c_{CO_2}}{c_{H_2O}(\sim 1)} = \frac{s_{CO_2} I_{CO_2}}{s_{H_2O} I_{H_2O}} = const.\left(\frac{I_{CO_2}}{I_{H_2O}}\right)$$

High concentration of CO_2: $$\frac{s_{CO_2} I_{CO_2}}{s_{CO_2} I_{CO_2} + s_{H_2O} I_{H_2O}} \approx \frac{s_{CO_2} I_{CO_2}}{s_{CO_2} I_{CO_2}} = 1$$

At low CO_2 concentrations, the intensity ratio (or fraction) should scale directly with the concentration. At high CO_2 concentrations, the ratio will approach unity. Given the relative size of the scattering coefficients, $s_{CO2} >> s_{H2O}$, the transition to asymptotic behavior (curve approaching unity) should occur at relatively small CO_2 concentrations. In this case, the CO_2 bands come to dominate the spectra at mole fractions significantly below the saturation concentration.

The alternative calibration plot shown in Figure 23 corroborates the statements made above. In this figure, the measured intensity ratios were converted to ratios of the mole fractions (CO_2/D_2O) using the solubility of CO_2 in H_2O as a single calibration point (i.e., $X(CO_2) = 0.028$). The formula used for the conversion is shown in the figure, were f is the conversion factor determined from the CO_2 solubility. The converted intensities ratios were then plotted against the ratios of concentrations calculated from the amounts of CO_2 and D_2O (or H_2O) mixed during sample preparation. The resulting plot is near-linear as expected, with some small deviations near the origin attributed to difficulties in quantitative transfer of the gas to the pump, assurance of complete dissolution of the CO_2 in the water during mixing, and the presence of a systematic uncertainty in the pump volume.

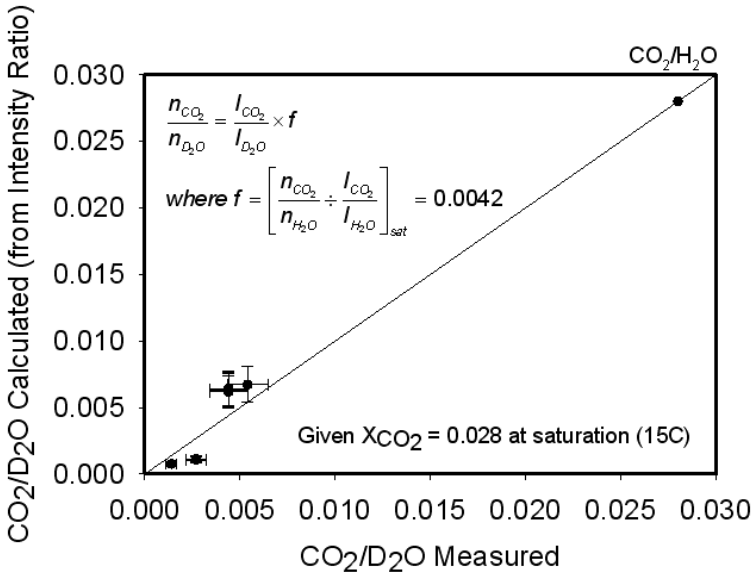

Figure 23. Plot of the fraction of total Raman scattering intensity attributed to CO_2 versus the mole fraction of CO_2 in the mixture as calculated from the quantities used in preparation.

5.0 References

Amirkhanov DG and AG Usmanov. 1987. "Thermal Diffusivity of Hydrocarbon in the Near-Critical Region." *Inzhenerno-Fizicheskii Zhurnal* 52(1):106-107.

Battestelli A, C Calore, and K Pruess. 1997. "The Simulator TOUGH2/EWASG for Modelling Geothermal Reservoirs with Brines and Non-Condensible Gas." *Geothermics* 26(4): 437-464. Available at http://dx.doi.org/10.1016/S0375-6505(97)00007-2.

Cabaco MI, M Besnard, S Longelin, and Y Danten. 2010a. "Evolution with the Density of CO_2 Clustering Studied by Raman Spectroscopy." *Journal of Molecular Liquids* 153(1):15-19. Available at http://dx.doi.org/10.1016/j.molliq.2009.09.007.

Cabaco MI and M Musso. 2010b. "Preface." *Journal of Molecular Liquids* 153(1):1. Available at http://dx.doi.org/10.1016/j.molliq.2010.03.013.

Cabaco MI, S Longelin, Y Danten, and M Besnard. 2007. "Local Density Enhancement in Supercritical Carbon Dioxide Studied by Raman Spectroscopy." *Journal of Physical Chemistry A* 111(50):12966. DOI: 10.1021/jp0756707.

Duhr S and D Braun. 2006. "Why Molecules Move Along a Temperature Gradient." *Proceedings of the National Academy of Sciences* 103(52):19678-19682. DOI: 10.1073/pnas.0603873103.

Horiba Jobin Yvon Raman Application Note. "Strain Measurements of a Si cap Layer Deposited on a SiGe Substrate Determination of Ge Content." *Semiconductor 01*. Available at http://www.horiba.com/fileadmin/uploads/Scientific/Documents/Raman/Semiconductors01.pdf

Kempers LJTM. 2001. "A Comprehensive Thermodynamic Theory of the Soret Effect in a Multicomponent Gas, Liquid, or Solid." *Journal of Chemical Physics* 115(14):6330. DOI: 10.1063/1.1398315.

Kolodner P, H Williams, and C Moe. 1988. "Optical Measurement of the Soret Coefficient of Ethanol/Water Solutions." *Journal of Chemical Physics* 88(10):6512. DOI:10.1063/1.454436.

Slavtchev S, G Simeonov, and S Van Vaerenbergh. 1999. "Technical Note: Marangoni Instability of a Layer of Binary Liquid in the Presence of Nonlinear Soret Effect." *International Journal of Heat and Mass Transfer* 42(15):3007-3011. Available at http://dx.doi.org/10.1016/S0017-9310(98)00353-6.

Koniger A, H Wunderlich, and W Kohler. 2010. "Measurement of Diffusion and Thermal Diffusion in Ternary Fluid Mixtures using a Two-Color Optical Beam Deflection Technique." *Journal of Chemical Physics* 132(17):174506. DOI: 10.1063/1.3421547.

Levenberg. 1944. "A Method for the Solution of Certain Non-Linear Problems in Least Squares." *The Quarterly of Applied Mathematics* 2: 164-168.

Nejad M, MZ Saghir, and MR Islam. 2001. “Role of Thermal Diffusion on Heat and Mass Transfer in Porous Media.” *International Journal of Computational Fluid Dynamics* 15:157. DOI:10.1080/10618560108970025.

Ning H and S Wiegand. 2006. “Experimental Investigation of the Soret Effect in Acetone/Water and Dimethylsulfoxide/Water Mixtures.” *Journal of Chemical Physics* 125(22):221102. DOI:10.1063/1.2402159.

Spycher N, K Pruess, and J Ennis-King. 2002, July. *CO_2-H_2O Mixtures in the Geological Sequestration of CO_2. I. Assessment and Calculation of Mutual Solubilities from 12 to 100°C and up to 600 bar*. LBNL-50991, Lawrence Berkeley National Laboratory, Berkeley, California.

Swinney HL and HZ Cummins. 1968. “Thermal Diffusivity of CO_2 in the Critical Region.” *Physical Review* 171(1):152-160. DOI:10.1103/PhysRev.171.152.

White MD and BP McGrail. 2002. “Numerical Investigations of Multifluid Hydrodynamics During Injection of Supercritical CO_2 into Porous Media.” In *Sixth International Conference on Greenhouse Gas Control Technologies*, pp. 449-455, ed. N Matsumiya, Research Institute of Innovative Technology for the Earth, October 1-4, 2002, Kyoto, Japan. http://dx.doi.org/10.1016/B978-008044276-1/50072-6.

Xu B, K Nagashima, JM DeSimone, and CS Johnson. 2003.“Diffusion of Water in Liquid and Supercritical Carbon Dioxide: An NMR Study.” *Journal of Physical Chemistry A* 107(1):1-3.

Zhang JL, XG Zhang, and BX Han. 2002. “Study on Intermolecular Interactions in Supercritical Fluids by Partial Molar Volume and Isothermal Compressibility.” *Journal of Supercritical Fluids* 22(1):15-19.

Pacific Northwest
NATIONAL LABORATORY

U.S. DEPARTMENT OF
ENERGY

Proudly Operated by Battelle *Since 1965*

902 Battelle Boulevard
P.O. Box 999
Richland, WA 99352
1-888-375-PNNL (7665)
www.pnl.gov